Lecture Notes in Civil Engineering

Ravi Sundaram
Jagdish Telangrao Shahu
Vasant Havanagi *Editors*

Geotechnics for Transportation Infrastructure

Recent Developments, Upcoming Technologies and New Concepts, Volume 1

Springer

Lecture Notes in Civil Engineering

Volume 28

Lecture Notes in Civil Engineering (LNCE) publishes the latest developments in Civil Engineering—quickly, informally and in top quality. Though original research reported in proceedings and post-proceedings represents the core of LNCE, edited volumes of exceptionally high quality and interest may also be considered for publication. Volumes published in LNCE embrace all aspects and subfields of, as well as new challenges in, Civil Engineering. Topics in the series include:

- Construction and Structural Mechanics
- Building Materials
- Concrete, Steel and Timber Structures
- Geotechnical Engineering
- Earthquake Engineering
- Coastal Engineering
- Hydraulics, Hydrology and Water Resources Engineering
- Environmental Engineering and Sustainability
- Structural Health and Monitoring
- Surveying and Geographical Information Systems
- Heating, Ventilation and Air Conditioning (HVAC)
- Transportation and Traffic
- Risk Analysis
- Safety and Security

To submit a proposal or request further information, please contact the appropriate Springer Editor:

– Mr. Pierpaolo Riva at pierpaolo.riva@springer.com (Europe and Americas);
– Ms. Swati Meherishi at swati.meherishi@springer.com (India);
– Ms. Li Shen at li.shen@springer.com (China);
– Dr. Loyola D'Silva at loyola.dsilva@springer.com (Southeast Asia and Australia/NZ).

Indexed by Scopus

More information about this series at http://www.springer.com/series/15087

Ravi Sundaram · Jagdish Telangrao Shahu ·
Vasant Havanagi
Editors

Geotechnics for Transportation Infrastructure

Recent Developments, Upcoming Technologies and New Concepts, Volume 1

Springer

Editors
Ravi Sundaram
Cengrs Geotechnica Pvt. Ltd.
Noida, Uttar Pradesh, India

Vasant Havanagi
Geotechnical Engineering Division
CSIR Central Road Research Institute
New Delhi, Delhi, India

Jagdish Telangrao Shahu
Department of Civil Engineering
Indian Institute of Technology Delhi
New Delhi, Delhi, India

ISSN 2366-2557 ISSN 2366-2565 (electronic)
Lecture Notes in Civil Engineering
ISBN 978-981-13-6700-7 ISBN 978-981-13-6701-4 (eBook)
https://doi.org/10.1007/978-981-13-6701-4

Library of Congress Control Number: 2019931960

This Springer imprint is published by the registered company Springer Nature Singapore Pte Ltd.
The registered company address is: 152 Beach Road, #21-01/04 Gateway East, Singapore 189721, Singapore

Foreword

Transportation Geotechnics has evolved as an important discipline in geotechnical engineering contributing to design and construction of highways, railways, airports and metro-rail facilities. In order to strengthen and promote work in this area, the International Society of Soil Mechanics and Geotechnical Engineering (ISSMGE) has constituted a Technical Committee, designated as TC-202 on Transportation Geotechnics.

As a fast-growing economy, Indian developments in "Transportation Geotechnics" have been substantial. The accelerated pace of infrastructure construction, particularly highways, railways, metro-lines and airport runways has pushed up the need for advanced design and construction methodologies. In the design and construction of transportation infrastructure in urban areas, geotechnical engineers face many difficult problems related to ground conditions, geology, groundwater, the presence of adjacent structures, etc. In mountainous and hilly areas, construction of roads throws challenges of hill-slope stability, landslides and safety issues.

To strengthen and promote work on this subject, Indian Geotechnical Society (IGS) organized the *International Symposium on Geotechnics for Transportation Infrastructure (ISGTI 2018)* in April 2018 under the aegis of TC-202. While commemorating 70 years of Indian Geotechnical Society's accomplishments, ISGTI 2018 served as a significant platform for academic exploration, experience exchange and thought-inspiration amongst practitioners, researchers, academics and students. The goal was to apply broad engineering principles to bridge the gap between pavement and railway engineering and geotechnical engineering.

This publication, in two volumes, compiles the latest research and development on geotechnical aspects of design, construction, maintenance, monitoring and upgrading of roads, railways, metro-lines and other transportation infrastructure.

I congratulate the editors for the compilation of contributions from various authors, and I am sure that it will lead to a better understanding of the subject, making this publication a valuable treatise on Transportation Geotechnics.

Bengaluru, India

G. L. Sivakumar Babu
President, Indian Geotechnical Society

Professor, Indian Institute of Science

Preface

Transportation Geotechnics encompasses various disciplines of civil engineering such as pavement engineering, bridge engineering, hill area development, underground structures and geosynthetics. It is an important aspect in the construction of road and railway pavements and embankments, metro facilities, waterways, airports and pipelines.

To bring together professional experts including academicians, students, consultants and practising engineers on the subject on a common platform, Indian Geotechnical Society organized the International Symposium on Transportation Geotechnics in April 2018 at IIT Delhi.

Papers received from over 100 experts from 20 countries have been compiled in this publication to document the latest developments on the subject of Transportation Geotechnics. It covers nine parts as given below:

Part I: Challenges in Design and Construction of Pavements and Embankments.

Part II: Design and Construction of High-Speed Railway and Metro Track Substructures.

Part III: Advances in Waterways and Pipeline Geotechnics.

Part IV: Slope Stability, Landslides, Debris Flows and Avalanches on Hilly Roads and Remedial Measures.

Part V: Subsurface Sensing, Investigations and Monitoring in Transport Geotechnics.

Part VI: Use of Geosynthetics and Non-Traditional Materials in Transport Geotechnics.

Part VII: Transport Geotechnics in Underground Construction.

Part VIII: Ground Improvement Techniques for Transport Geotechnics.

Part IX: Emerging Trends in Transport Geotechnics—Unsaturated Soil Mechanics, Macro- and Nanotechnology, Climate Change and Sustainability.

This publication is presented in two volumes. Parts I–IV are covered in Volume 1, and Parts V–IX are included in Volume 2.

Volume 1 covering Parts I–IV includes 45 papers and includes the following expert lectures:

- Field Performance Evaluations of Sustainable Aggregate By-product Applications by Erol Tutumluer
- Challenges in Design and Construction of Embankments and Pavements by Sharokh Bagli
- Concepts and Methodologies for Track Improvement and Associated Physical Modelling and Field Monitoring by Buddhima Indraratna
- Damage of Heavy Rain on Local Transportation Line by Ikuo Towhata
- Surfactant Grout and Its Application in CIP for Metro Construction Project by E.C. Shin
- Evaluation of Geosynthetic Reinforced Tracks on Clayey Subgrade by Jagdish Telangrao Shahu
- Applicability Evaluation of Slope Disaster Risk Assessment Method in Snowy Cold Regions by Tatsuya Ishikawa
- Unified Prediction Method for the Rainfall-Induced Landslides and Debris Flows by Sangseom Jeong
- Design Approach to Rockfall-Related Problems by Giorgio Giacchetti

All the articles were subjected to an extensive review. The peer review of the articles really helped to improve the quality of the research papers. We thankfully acknowledge the dedicated work of all the reviewers.

We deeply acknowledge the consistent efforts and the support provided by the publishers for bringing out a quality publication of this volume. We are also thankful to Macaferri Environmental Solutions Pvt. Ltd., Strata Geosystems (India) Pvt. Ltd. and various other sponsors and exhibitors for their support and financial aid.

We hope that this volume, a storehouse of valuable information, will help to fast-track dissemination of knowledge so that students, researchers, practising structural, geotechnical and transportation engineers and other professionals definitely benefit from latest research and developments in this specialized subject. We hope the readers will find the proceedings very useful in their day-to-day research and professional life.

Noida, India — Ravi Sundaram
New Delhi, India — Jagdish Telangrao Shahu
New Delhi, India — Vasant Havanagi

About the International Symposium on Geotechnics for Transportation Infrastructure

This publication forms the proceedings of the first "International Symposium on Geotechnics of Transportation Infrastructure (ISGTI 2018)". The Technical Committee TC-202 of International Society for Soil Mechanics and Geotechnical Engineering (ISSMGE) along with Indian Geotechnical Society (IGS) and Indian Institute of Technology Delhi (IIT Delhi) organized ISGTI 2018 at IIT Delhi, New Delhi, India, on 7–8 April 2018. The symposium was organized in commemoration of 70 years of formation of IGS. The main part of the symposium was Transportation Geotechnics for Infrastructure Development.

Around 230 delegates registered for the symposium, out of which 40 delegates were from abroad representing 28 countries. A total of 185 abstracts were submitted, out of which finally 115 papers were presented by the delegates. Every paper was reviewed by two experts, and the authors incorporated the reviewers' comments and submitted the final paper. The delegates deliberated upon emerging challenges in the field of transportation geotechnical engineering for 2 days of the symposium. Seven awards were given to outstanding papers by young geotechnical engineers sponsored by Centre for Geomechanics and Railway Engineering, University of Wollongong, Australia, and the Symposium Organizing Committee.

The symposium is comprised of 4 plenary sessions consisting of 10 keynote lectures and 2 corporate presentations, 12 parallel sessions consisting of 11 invited lectures and general paper presentations, and the technical exhibition. The exhibition had a total of 21 stalls put up by multinational and Indian organizations for showcasing their products and equipment. Overall, ISGTI was well supported by sponsors and exhibitors who played a crucial role in making the event a success.

The need for building a strong and stable transportation infrastructure has become more critical than ever for sustainable engineering practices. Transportation Geotechnics provide key knowledge to building sustainable pavement and railroad track infrastructure. With recent major investments expected in road construction and high-speed railways in India and many other countries, this was an appropriate juncture for organizing ISGTI in India.

We would like to express our sincere gratitude to TC-202 of ISSMGE for their contribution in overall planning of the symposium. The organization of the

symposium was managed by an Organizing Committee guided by National and International Advisory Committees. We express our deep appreciation to the members of Organizing and Advisory Committees. The paper reviewers went through 185 abstracts and 115 full-length papers. Their untiring efforts are gratefully acknowledged. The contributions made by the keynote and invited speakers and the authors of papers as well as of the session chairmen and coordinators are also gratefully acknowledged. The symposium proceedings have been published by Springer. Their efficient and high-quality work is appreciated.

Ravi Sundaram
Jagdish Telangrao Shahu
Vasant Havanagi

Contents

About the Editors

Mr. Ravi Sundaram did his B.Tech. (1978) and M.Tech. (1980) from IIT Delhi. He started his career with McClelland Suhaimi Ltd. at Saudi Arabia and Qatar. He has 38 years experience as practicing geotechnical engineer and is a founder director of Cengrs Geotechnica Pvt. Ltd. His expertise includes geotechnical investigations, geophysical surveys, ground improvement and bored piles. He has worked on problems of collapsible soils, soft clays, expansive soils, weak rocks, artesian conditions and liquefiable soils. His interests include foundations for bridges, high rise buildings, large-diameter tanks, power plants, etc. He has published over 60 technical papers that reflect his experience in geotechnical engineering practice. He was awarded the IGS Delhi Chapter Lifetime Achievement Award for the year 2014–2015. He delivered the prestigious Sixth Madhav Lecture at Hyderabad in October 2017. He received Indian Geotechnical Society's IGS-Prof. Dinesh Mohan Memorial Award for Excellence in Professional Practice for the years 2016–2017.

Dr. Jagdish Telangrao Shahu graduated in 1986 from Nagpur University, India and obtained his M.Tech. and Ph.D. degrees from IIT Kanpur, India in 1988 and 1994, respectively. He did his post doctoral research at Institute of Lowland Technology, Japan from 1996 to 1999 and again visited Japan in 2006–2007 as Visiting Professor. Dr. Shahu joined IIT Delhi in 2002 as Assistant Professor. Since 2012, he is Professor at IIT Delhi. His main research interests are geotechnology for roads and railway tracks, ground improvement and geosynthetic applications. He has more than 50 papers in journals. He has also co-edited four book volumes. He has guided 50 M.Tech. and 9 Ph.D. theses.

Dr. Vasant Havanagi did his M.Tech. in Highway Engineering in the year 1988, from IIT, Kharagpur and completed his Doctorate in Geotechnical Engineering from IIT, Delhi in the year 2000. Presently he is a Senior Principal Scientist at CSIR-Central Road Research Institute, New Delhi. He has over 27 years of experience in R&D activities related to Geotechnical investigations, Ground improvement, Waste material utilization, Pavement design, Quality supervision,

Audit of highway projects etc. He has published more than 65 Research papers in National and International Journals, Conferences and Seminars etc. Awards for his R&D contribution/achievements included; DAAD (German Academic Exchange), IRC, SKOCH order of merit, CIDC etc. He is also involved activities of Indian Roads Congress (IRC), Bureau of Indian Standards (BIS), and Indian Geotechnical Society, Delhi chapter.

Part I
Challenges in Design and Construction of Pavements and Embankments

Field Performance Evaluations of Sustainable Aggregate By-product Applications

Erol Tutumluer, Issam I. A. Qamhia and Hasan Ozer

Abstract Recent research efforts at the Illinois Center for transportation focused on evaluating new sustainable applications of quarry by-products (QBs) or QB mixed with other marginal, virgin, or recycled aggregate materials in pavements as unbound or chemically stabilized pavement layers. Sixteen full-scale test sections were constructed to evaluate the use of QB in base, subbase, and aggregate subgrade applications. The chemically stabilized test sections utilizing QB were stabilized with 3% cement or 10% Class 'C' fly ash, by dry weight and were constructed over a subgrade having an engineered unsoaked California bearing ratio (CBR) of 6% to study their effectiveness in low to medium volume flexible pavements. The unbound applications of QB investigated the use of QB to fill the voids between large rocks commonly used for rockfill applications on top of very soft subgrade soils, as well as using dense-graded aggregate subgrade layers with higher fines content up to 15% passing No. 200 sieve for soft subgrade remediation. These unbound test sections were constructed over a CBR = 1% subgrade soil to investigate their effectiveness in both construction platforms and low volume road applications. All the field test sections were then evaluated in rutting and fatigue by applying traffic loading using a super-single wheel in accelerated pavement testing. In general, the satisfactory results obtained from the field rutting performance evaluations indicate that the proposed QB applications can be successfully incorporated in standard pavement construction/rehabilitation practices.

Keywords Quarry · By-products · Accelerated pavement testing · Sustainable construction practices · Field performance · Chemical stabilization

E. Tutumluer (✉) · H. Ozer
Department of Civil and Environmental Engineering, University of Illinois at Urbana-Champaign, 205 N. Mathews, Urbana, IL 61801, USA
e-mail: tutumlue@illinois.edu

H. Ozer
e-mail: hozer2@illinois.edu

I. I. A. Qamhia
Department of Civil and Environmental Engineering, University of Illinois at Urbana-Champaign, 1611 Titan Dr., Rantoul, IL 61866, USA
e-mail: qamhia2@illinois.edu

R. Sundaram et al. (eds.), *Geotechnics for Transportation Infrastructure*, Lecture Notes in Civil Engineering 28, https://doi.org/10.1007/978-981-13-6701-4_1

1 Introduction

Quarry by-products, usually less than 6 mm in size, are produced during quarry operations such as blasting, crushing, screening, and washing operations. QB are mostly coarse-, medium-, and fine-grained sand particles, with a small fraction of silts and clays. QB can exist in aggregate production sites in three distinct types: screenings, pond fines, and baghouse fines (Chesner et al. 1998). During the crushing stages, QBs are generally carried out in three stages, i.e., primary, secondary, and tertiary crushing (Petavratzi and Wilson 2007).

The importance of utilizing aggregate quarry by-products in pavement applications stem from the vast quantities that are produced and remain excessive with many quarries each year. QB stockpiling and disposal is a serious issue facing the aggregate industry as they accumulate in stockpiles and interfere with quarry operations (Hudson et al. 1997). A report by the Federal Highway Administration estimated the quantity of quarry by-products generated in the USA each year to exceed 159 million metric tons, little of which is being put into use for pavement applications (Chesner et al. 1998). The same report also estimated that aggregate QB accumulation in the USA alone exceeded 3.6 billion metric tons from the 3000 operating quarries. In the state of Illinois, where this study was conducted, the annual production of crushed stone QB was estimated through a survey conducted among aggregate producers in the state and was found to be as high as 855,000 tonnes (950,000 US short tons) (Tutumluer et al. 2015). Research conducted by Kumar and Hudson (1992) showed that stockpiled fines comprised an average of approximately 12% of the total annual aggregate production. More recently, NCHRP Synthesis 435 (volume 4) reported that, depending on the type of rock quarried, QB could make up to 25% of the total aggregates produced (Stroup-Gardiner and Wattenberg-Komas 2013).

Given these massive quantities, the investigation of successful applications of QB as a sustainable and inexpensive construction alternative for pavements has become imperative. However, only a few numbers of research studies have been conducted to date to evaluate the use of QB as a geotechnical pavement material in subgrade, subbase or base applications, and especially the use of QB as an unbound material, which was found to be scarce in the literature. NCHRP synthesis 435 (volume 4) being a main source of information on the QB use summarizes the different QB applications in pavements by the different states in the USA (Stroup-Gardiner and Wattenberg-Komas 2013). Other noteworthy studies found in the literature are summarized hereafter.

A study in Brazil used quarry waste to construct a 203-mm-thick base layer, topped with 30 mm of surface treatment for a low traffic volume roadway (De Rezende and Carvalho 2003). The QB evaluated in this study had around 45% of material passing the No. 4 sieve (4.75 mm), meaning that it is coarser than what QB normally entails. It also had relatively high percentages of silts and clays (22%). Nonetheless, any structural damage of the constructed low-volume pavement after more than three years of operation was insignificant.

Few field evaluation studies also investigated chemically stabilized layers of QB. Nelson et al. (1994) investigated using emulsion-stabilized limestone screenings as a base material. Different test sections with varying base thicknesses ranging from 100 to 150 mm were constructed. Three binder contents of the stabilized QB bases were considered 2.5, 3.5, and 4.5%. The recommendation of the study was to use a base thickness of 150 mm, having a binder content of 3.5% or higher, topped with 50 mm of hot-mix asphalt (HMA) surface coarse in order to provide a good performing roadway, requiring low maintenance. Another major study that investigated the use of chemically stabilized QB for pavement applications was conducted in Arlington, Texas. The study used limestone QB fines as a base material for sections of State Highway No. 360 (Puppala et al. 2008). A 914-mm-thick quarry fines base layer, stabilized with 2.3% cement was constructed and topped with 100-mm HMA and 200-mm continuously reinforced concrete pavement (CRCP) layers. Field monitoring was conducted using a horizontal inclinometer, and the sections experienced low permanent deformation levels during the servicing of the highway. After 30 months of service, the measured International Roughness Index (IRI) was 0.5–2.5 m/km which indicated a good performance (Puppala et al. 2011).

Several research studies also proposed field applications for QB based on determining mechanical and physical properties and laboratory performance evaluations. Kumar and Hudson (1992) concluded that stabilizing QBs with cement could produce the adequate compressive strength, modulus of elasticity, and tensile strength properties required for subbase materials. They also proposed base course material additive, flowable fill, under slab granular fill, and cement-stabilized subbase/base layers as possible pavement applications of QB (Kumar and Hudson 1992). McClellan et al. (2002) suggested using QB for engineering backfill applications and as a direct additive to concrete mixes as a filler or fine aggregates. Another potential use area for QB includes self-consolidating concrete (Wood 1995; Naik et al. 2005) and the replacement of sand in concrete to enhance pozzolanic reactions and durability (Lohani et al. 2012).

More recently, Qamhia et al. (2017a) evaluated using QB as a stabilized base/subbase material and as a filler for the voids between large aggregate subgrade rocks constructed over weak soils for improving subgrade stability under moving loads (Qamhia et al. 2016, 2017a, b, c). The Illinois Department of Transportation (IDOT) intends to use a certain percentage of QBscreenings as filler materials for the large rocks over soft subgrade. To this point, there are no clear established guidelines to dictate the appropriate percentage of QB for filling up the voids in rockfill applications. Only a few studies dealt with the packing perspective in typical base course or railway ballast granular materials (Boler et al. 2014; Xiao and Tutumluer 2016). However, none of these studies involved utilizing QB as a filler material of large rocks and QBfines.

2 Quarry By-product Applications Studied

In total, sixteen full-scale pavement test sections were built at the Illinois Center for Transportation to study the proposed low to medium volume road and construction platform applications of QB in pavement foundation layers, also including one control section. The sections were divided into three cells: Cell 1 (1N and 1S), Cell 2, and Cell 3, where each cell consisted of four test sections. Each cell also established one parked location of the accelerated pavement testing field equipment which was used to evaluate the performance trends of all four test sections in a cell under moving wheel traffic loading. Cell 1S investigated construction platforms of QB materials used in aggregate subgrade layers, while Cell 1N consisted of the same test sections as Cell 1S, but they were paved on with a 100-mm (4-in.) thick HMA surface course to investigate asphalt pavement applications of the QB materials utilized with large rocks and high fines base courses. All test sections were constructed on top of a CBR = 1% silty subgrade. The subsurface layers investigating QB applications for subgrade remediation were 530 mm (21 in.) thick, and all test sections were topped with a 75-mm (3-in.) thick dolomite capping. The capping layer was a dense-graded aggregate (CA06 Illinois DOT designation) having 10% non-plastic fines (passing No. 200 sieve or finer than 0.075 mm). The 100-mm-thick HMA in Cell 1N was paved on top of the capping layer. Table 1 gives descriptions of the four test sections constructed in Cell 1. Note that the same four sections were constructed for both Cell 1S and Cell 1N. Descriptions of the materials used in the construction and their material properties are provided in the following subsection.

The test sections investigating chemically stabilized applications of QB were constructed in Cells 2 and 3, with each cell having four test sections. Cell 2 investigated the use of QB in chemically treated base materials, stabilized with 3% cement, or 10% Class 'C' fly ash, while Cell 3 studied treated base and subbase applications of QB. All test sections were constructed on top of a CBR = 6% silty soil and were paved on top with a 100-mm-thick HMA constructed in two lifts. The last test section in Cell 3 was a control section, a standard unbound aggregate base layer commonly

Table 1 Descriptions of the unbound aggregate QB applications constructed in Cell 1

Section ID	Description
C1S1	Primary Crusher Run (PCR) rocks with 25% QB1 by weight constructed in two lifts using a vibratory compactor; QB placed into the large voids of the PCR from the top of constructed layer
C1S2	PCR with 16.7% QB1 by weight, constructed in a single lift in a similar manner as C1S1
C1S3	CA06_15PF: Dense-graded CA06 aggregates with 15% plastic fines content (passing No. 200 sieve) with a plasticity index (PI) of 8 constructed in three equal lifts
C1S4	CA06_15NPF: Dense-graded CA06 aggregates with 15% non-plastic fines content (passing No. 200 sieve) constructed in three equal lifts

Table 2 Descriptions of the base and subbase QB applications constructed in Cells 2 and 3

Section ID	Description[a]
C2S1	A blend of 70% QB2 and 30% fractionated reclaimed asphalt pavements (FRAP) by weight, mixed with 3% Type I cement by weight
C2S2	A blend of 70% QB2 and 30% fractionated recycled concrete aggregates (FRCA) by weight, mixed with 3% Type I cement by weight
C2S3	A blend of 70% QB2 and 30% FRAP by weight, mixed with 10% Class 'C' fly ash by weight
C2S4	A blend of QB2 and 3% Type I cement by weight
C3S1	A blend of QB3 and 3% Type I cement by weight
C3S2	Subbase layer: A blend of QB2 and 3% Type I cement by weight Base layer: CA06_R (a dense-graded unbound dolomite aggregate layer conforming to the CA06 aggregate gradation band of the Illinois Department of Transportation)
C3S3	Subbase layer: A blend of QB2 and 10% Class 'C' fly ash by weight Base layer: CA06_R
C3S4	CA06_R

[a]All sections are 300 mm (12 in.) thick. Sections C3S2 and C3S3 have a 150-mm (6-in.) base layer on top of a 150-mm (6-in.) subbase layer aimed to investigate chemically stabilized QB applications

constructed in Illinois. The subsurface layers which targeted QB applications for base and subbase applications were 300 mm (12 in.) thick. Table 2 provides descriptions of the eight test sections constructed in Cells 2 and 3. Descriptions of the materials used in the construction and their material properties are provided in the following subsection.

The typical cross sections of the constructed test sections in each test cell are shown in Fig. 1.

2.1 Criteria for Materials Selection and Laboratory Characterization

In total, nine different aggregate construction materials were used for the construction of the different test sections. The QB materials were selected from three crushed stone quarries in the State of Illinois. The objective has been to study the variations in QB properties and the effect of the type of QB on-field performance, especially for two of the sections (C2S4 and S2S1) where QB is used as a cement-stabilized base material.

Cell 1 studied sustainable applications of QB as an unbound material for subgrade remediation. Two of the sections encompass QB utilization to fill the large in PCR aggregates to increase stability and reduce settlements. For the other two sections in Cell 1, the goal was to evaluate the effect of increasing fines (passing No. 200 or finer than 0.075 mm) from 12 to 15% on pavement performance. If minor influence, this

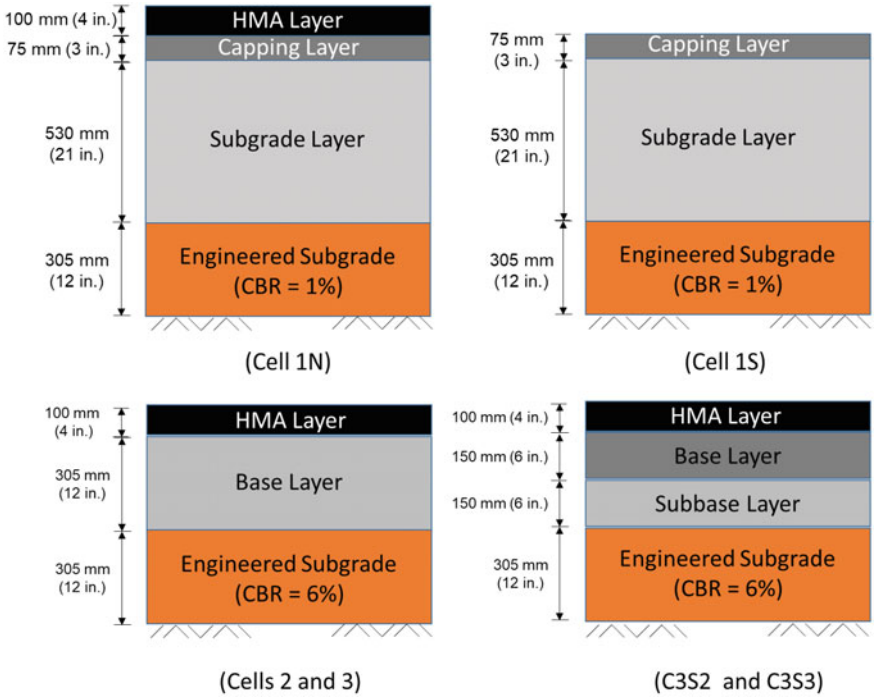

Fig. 1 Typical cross sections for the constructed test sections in each test Cell

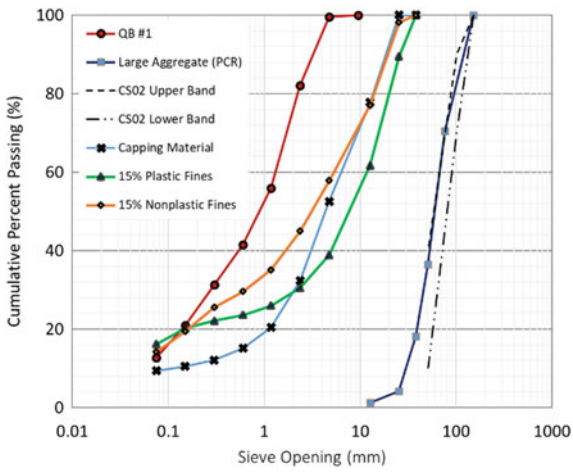

Fig. 2 Particle size distributions of the materials used in the construction of Cell 1 pavement test sections

could ultimately lead to lower excess QB generation and less stockpiling of QB at the quarries. The particle size distributions of all the materials used in the construction of Cell 1 are shown in Fig. 2.

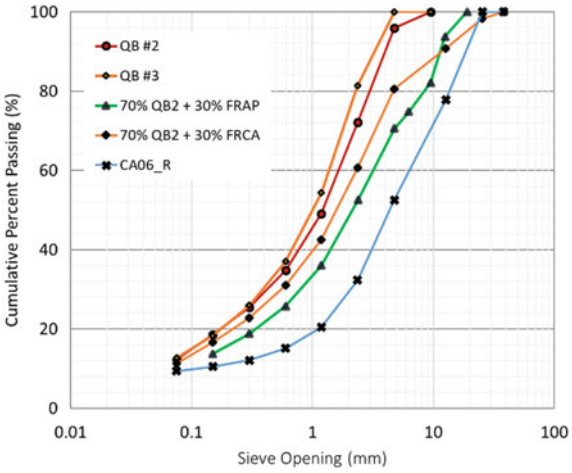

Fig. 3 Particle size distributions of the materials used in the construction of Cells 2 and 3 test sections

Cells 2 and 3 studied the use of QB in treated base materials, stabilized with 3% cement or 10% Class 'C' fly ash. Three of the sections had the QB blended with other recycled materials (FRAP and FRCA). The other sections studied the uses of QB as base or subbase materials (i.e., in inverted pavements). Two of the sections had cement and fly ash-stabilized QB as subbase materials. One test section was a control section with an unbound granular base. The particle size distributions of all the materials used in the construction of Cell 2 and Cell 3 pavement test sections are shown in Fig. 3.

The HMA structural layer had an asphalt binder with a performance grade of PG 64-22 used in two HMA lifts. Both the binder course and the surface course had the same mix, with a 9.5-mm (0.375-in.) nominal aggregate size.

2.1.1 Moisture-Density Relationships

The maximum dry densities (MDD) and corresponding optimum moisture contents (OMC) were obtained for all material combinations used for constructing the full-scale test sections using the standard Proctor compaction test procedure (ASTM D698). The determination of the moisture-density relationships was deemed very critical for the construction phase because the constructed test sections were compacted at the optimum moisture content, and the field densities were checked for the relative compaction, where 95% of the MDD was specified by IDOT for a passing field density. The compaction at the OMC was also deemed critical for the stabilized test sections to ensure that sufficient water was available for the proper hydration of the stabilized test sections.

Table 3 summarizes the compaction characteristics (MDD and OMC) of the different material combinations used in the construction of the full-scale test sections. Out of the three different CA06 materials, CA06_15NPF has the highest MDD and

Table 3 Compaction characteristics (MDD and OMC) for the different material combinations used in the construction of the full-scale test sections

Material combinations	MDD kN/m^3	OMC (%)
CA06_R	20.8	5.4
CA06_15NPF	21.7	6.8
CA06_15PF	21.2	6.5
QB2 + 3% cement	21.7	9.1
QB2 + 10% fly ash	21.6	8.0
QB3 + 3% cement	20.4	8.4
70% QB2 + 30% FRAP + 3% cement	21.2	8.0
70% QB2 + 30% FRCA + 3% cement	20.3	9.8
70% QB2 + 30% FRAP + 10% fly ash	21.4	7.5

OMC of 21.7 kN/m^3 (138.4 pcf) and 6.8%, respectively, which can be related to CA06_15NPF having the finest gradations of the three materials. For cement and fly ash-stabilized QB2 and QB3 combinations, QB2 + 3% cement had the highest MDD value. QB2 samples, blended with FRAP or FRCA in a 70:30 ratio by weight and stabilized with 3% cement or 10% fly ash, showed similar trends to those of stabilized QB2 material, where the fly ash-stabilized QB2/FRAP had a lower OMC compared to the 3% cement-stabilized QB2/FRAP (7.5% vs. 8.0%, respectively). However, the fly ash-stabilized QB2/FRAP showed a higher MDD than the cement-stabilized QB2/FRAP (21.4 kN/m^3 vs. 21.2 kN/m^3). For the 3% cement-stabilized QB2/FRCA material, the OMC of 9.8% is significantly higher than the cement-stabilized QB2/FRAP material, while the MDD of 20.3 kN/m^3 (129 pcf) is significantly lower. One possible explanation is the higher fines content, and the finer grain size distribution of the QB2/FRCA blends. Note that the specific gravity of the used FRAP and FRCA has not been checked.

2.1.2 Packing Study of PCR with QB

A laboratory investigation was conducted to ascertain the optimized blends of the large PCR rocks and QB materials constructed in a single lift and in two lifts. A customized steel box (UIUC Packing Box) was built to investigate the packing efficiency of the PCR and QB blends. The steel box has a 610 mm (24 in.) long square base and is 530 mm (21 in.) in height. One side of the box is made of plexiglass to monitor the quality of the blending of the two materials after compaction. A high-resolution image of the cross section was taken to further study the packing and percolation of QB through the large rocks. The PCR rocks are placed first, followed by spreading the QB on the surface of each lift, and shaking it into the voids using a laboratory-sized vibratory roller compactor. The vibratory action simulated the construction

procedure in the field, where a vibratory roller compactor was used after spreading the QB on the surface of the PCR rocks in single-lift and two-lift applications.

The test matrix involved conducting fourteen distinct tests with the UIUC Packing Box. Four variables were primarily changed to examine the factors that might contribute to the quality of blending of the QB with the large rocks, and the maximum possible quantity of QB that could be practically intermixed with the large PCR aggregates by shaking from the top of the lift. The four variables that were studied in the laboratory are:

(1) The number of constructed lifts, which was varied between a single 530-mm (21-in.) lift and two 265-mm (10.5-in.) lifts.
(2) The quantity of the QB measured and reported as a percentage of the dry weight of the large rocks. This quantity was varied from 20 to 40%.
(3) The moisture content w (%) of the QB, which was varied between 0 and 2.5%, where the latter was the measured moisture content of the QB samples as received from the source quarry.
(4) The support conditions (foundation rigidity) on top of which the experiments were conducted. Both a rigid steel bottom and a very soft (CBR = 1%) subgrade soil were considered to study the effect of stiff and soft bottom.

The conducted experiments did not show a significant difference in densities and percolation between the single-lift and two-lift arrangements when dry QB ($w = 0\%$) was used. However, as the moisture content of the QB was increased to natural $w = 2.5\%$, the presence of moisture reduced the ability of the QB to percolate and fill the voids at higher depths with a single-lift arrangement. For tests with varying QB content, 30% by weight was found to be an optimum quantity of QB to be mixed with the PCR in the case of dry QB. However, this quantity was found to result in relatively large amount of QB left on the surface for wet QB with natural $w = 2.5\%$. Over the CBR = 1% subgrade, the optimum quantity of QB, having a moisture content of $2.5 \pm 0.2\%$, was found to be 25% by the dry weight of the large PCR aggregates for a single-lift construction. Figure 4 shows a cross section of the compacted PCR aggregates without QB, and with 25% of QB by dry weight of the PCR aggregates, having a moisture content of 2.5–2.6%, compacted in a single lift on top of soft compacted subgrade soil. More details of the laboratory matrix and the test results were presented elsewhere (Qamhia et al. 2017a, b).

2.1.3 Unconfined Compressive Strength of the Chemically Stabilized QB Applications

Stabilized samples were tested for the 7-day unconfined compressive strength (UCS) using the procedure outlined in ASTM D1633. Prior to testing, samples were completely soaked in water for 4 h, surface-dried and capped at the ends using a sulfuric compound, then tested for compressive strength on a Forney loading frame at a rate of 18–49 kN/min (4000–11,000 lbs./min). Figure 5 compares the 7-day achieved unconfined compressive strengths of the stabilized samples. Following these tests, it

Fig. 4 Cross section of the compacted PCR rocks without QB (left), and with 25% of wet QB ($w = 2.5\%$) in a single-lift on top of soft compacted subgrade soil (right)

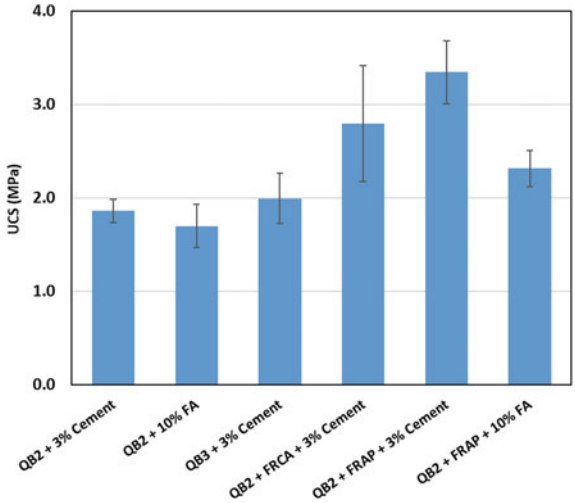

Fig. 5 Seven-day unconfined compressive strength (UCS) values for the material combinations used in constructing the full-scale test sections in Cells 2 and 3

was decided that samples stabilized with 3% cement or 10% class 'C' fly ash could achieve adequate strengths.

For the test sections constructed with QB mixed with recycled materials (FRAP or FRCA), a study was performed to determine a suitable mix ratio of the two materials that maximized the packing density (minimizes voids content) and utilized high quantities of QB in the mix. The tests were performed by dry mixing of QB2 in different percentages by weight with FRAP/FRCA and compacting those mixes using the modified compactive effort in a standard CBR mold in five equal lifts. The quantity of QB was varied from 30 to 100% by weight of the total mix, in increments of 10%, and the results indicated that the density started to stabilize/maximize at

a mix ratio of QB: [FRAP/FRCA] of 70:30. Thus, it was decided to use the 70:30 blend for the field construction.

Excluding the samples for FRCA + QB2 + 3% cement, which had a coefficient of variation of 22.9%, all the other samples had a coefficient of variation lower than 13.5%. Samples for FRAP + QB2 + 3% cement achieved the highest 7-day UCS, and their strength values were statistically different from all other combinations except FRCA + QB2 + 3% cement obtained using a two-sided t-test with a 95% confidence interval. The mean UCS values for[FRAP + QB2 + 10% fly ash] and [FRCA + QB2 + 3% cement] were also statistically different from all stabilized QB2 and QB3 samples, while the strength values of the stabilized QB2 and QB3 samples were not statistically different with a t-test with a 95% confidence interval. Additionally, the UCS of [FRAP + QB2 + 10% fly ash] and [FRCA + QB2 + 3% cement] are not statistically different, partly due to the high variability in the achieved strengths of the [FRCA + QB2 + 3% cement] samples.

3 Construction of the Full-Scale Test Sections

In the field, sixteen test sections, each approximately 6.1 m long (20 ft.), were constructed to study the proposed low to medium volume roads and construction platform applications of QB. Each test section had two locations at which field properties and performance trends were measured. Figure 6 shows a typical plan view for each of the three constructed test cells.

The construction steps of the test sections in the field included the subgrade preparation, construction of the aggregate subgrade layers, and the quality control measures to be discussed in the following subsections.

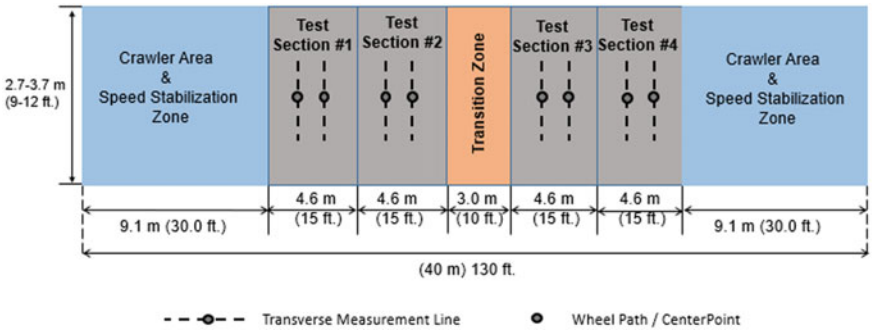

Fig. 6 Typical plan view of a full-scale test Cell

3.1 Subgrade Engineering and Preparation

The subgrade soil on top of which the proposed test sections were constructed was engineered to specified strength levels. Cell 1 subgrade was engineered to a CBR of 1% or less, while Cells 2 and 3 were engineered to a CBR of 6%. The required subgrade CBR was achieved through a moisture adjustment procedure for the in situ soil. The process was iterative and required wetting the existing subgrade soil to specified moisture levels that conformed to the required CBR levels, followed by tilling the top 355 mm (14 in.) of the soil with a tiller to ensure homogeneity, and then compacting the soil with a sheepsfoot roller compactor. Several trials were required, and the strength profile across the top 305 mm (12 in.) along the length of each test cell was checked after each trial using dynamic cone penetrometer (DCP) tests to a depth of 305 mm (12 in.), to assess subgrade strength and uniformity. Penetration rate (PR) of the DCP in mm/blow is related to CBR using the original South African Kleyn equation (Kleyn 1975).

Figure 7 outlines the final achieved CBR profiles along each of the constructed test Cells. The test sections used for studying the different proposed QB applications were constructed on top of the engineered subgrade soil. In order to minimize moisture loss until the other pavement layers were constructed, the surface of the engineered subgrade was covered with an insulating layer of tack coat, sprayed at a rate of 1.95 kg/m^2 (3.6 lbs./yd^2). The sections were also further covered with plastic sheets to minimize any moisture or humidity infiltration.

3.2 Construction of the Subsurface Layers Utilizing QB Applications

First, the two test sections studying the blending of PCR large aggregates with QB were constructed on top of the engineered subgrade in a 530-mm (21-in.) single lift, and in two 265-mm (10.5-in.) lifts. The target dry QB quantity to be added was 25% by the weight of the large rocks, as recommended from the laboratory packing study. Samples of QB were collected and tested for their natural moisture contents, and the average moisture content was 3.2%.

For the construction of the first lift in the two-lift test section (C1S1), the large rocks were placed first and then 25% QB materials by weight were evenly distributed on the surface. A vibratory compactor was supposed to shake the QB into the inherent voids in the PCR skeleton. Instead, the compactive effort resulted in a dense layer of QB forming on the surface and preventing any further percolation of QB into the voids.

To overcome this issue, the QB was intermixed with the large rocks using the teeth of an excavator bucket. For the second lift of the two-lift test section (C1S1), and for the section constructed in one lift (C1S2), the QB was manually spread using shovels on the surface of the large rocks, in smaller increments. The QB was then shaken

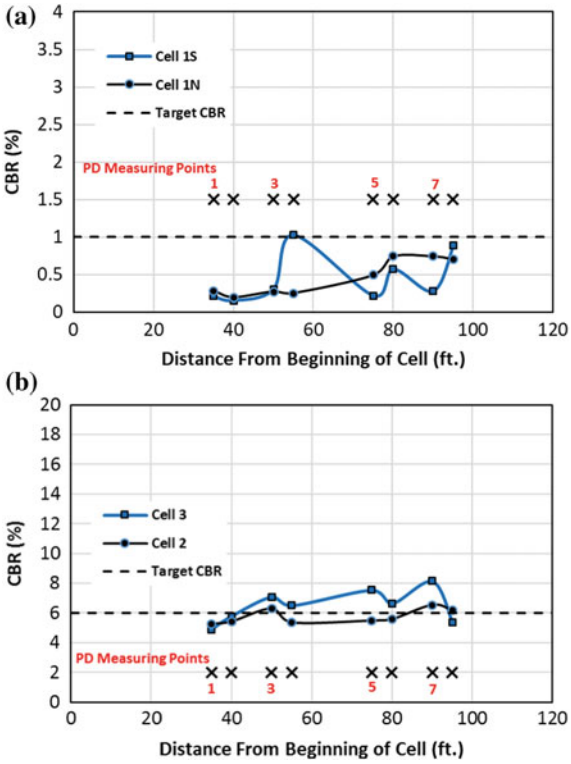

Fig. 7 Average CBR for the Top 30.5-cm (12-in.) subgrade for **a** Cell 1N and Cell 1S, showing the final trial with CBR values <1% at all measuring points and **b** Cells 2 and 3 showing final achieved CBR of ~6%

into the voids of the PCR using a standard size vibratory roller, and the process was repeated several times until the full quantity of QB was added (25% by dry weight of the PCR). However, for the section constructed in a single lift, the maximum amount of QB that could be packed was 16.7%. A possible reason could be the moisture content of the QB used in the field construction, which was higher than that investigated during the laboratory experiments (3.2% vs. 2.5–2.6%). The higher moisture content might have prevented the QB from percolating the full depth. The successful application when the QB was added in smaller increments suggests the need of developing an automated technique to spread the QB uniformly and more slowly on the surface, accompanied with continuous vibration. The construction procedure is outlined in Fig. 8.

For the other two test sections constructed in Cell 1 with dense-graded aggregate materials (C1S3 and C1S4), the layers were compacted in three equal 178-mm (7-in.) lifts. All test sections in Cell 1 were then topped with a 76-mm (3-in.) dense-graded CA06_R aggregate layer, compacted at the optimum moisture content. Further, test sections in Cell 1N, studying the low-volume road applications of QB, were paved with a 102-mm (4-in.) thick HMA layer.

(a) Construction of C1S1 and C1S2 test sections

(b) Construction of cement and fly ash stabilized sections

Fig. 8 Construction of the foundation layers utilizing the various unstabilized and stabilized QB applications

For the admixture stabilized QB test sections constructed in Cells 2 and 3, the process involved dry mixing the construction materials several times with the bucket of a backhoe to ensure uniformity of moisture and particle size distribution. Note that for test sections comprising QB intermixed with other recycled materials (FRAP or FRCA), the 70:30 blending was performed off-site in a local asphalt plant. Moisture samples were taken to assess the in situ moisture contents of the stockpiles. The stabilizing agent (cement or fly ash) was then added in the required quantities by weight, and the stabilizing agents were mixed with the QB blends for uniformity

using a backhoe bucket. Moisture was added to the mixed stockpiles from a water truck to raise the moisture content to the OMC. The blends were further mixed to uniformly distribute the moisture and the stabilizing agents. The uniform mixes were transferred to the construction site, placed, and tilled several times using a soil tiller to ensure uniformity. The test sections were constructed and compacted in two equal lifts. For the control test section, and the base layers of sections CS2 and C3S3 constructed with the dense-graded CA06_R aggregate materials, the layers were compacted in 152-mm (6-in.) lifts. The construction procedure is outlined in Fig. 8.

4 Performance Monitoring and Evaluation

Following the construction of the aggregate layers utilizing QB applications, the composite surface moduli were measured/backcalculated for each test section using a lightweight deflectometer (LWD). Figure 9 shows the average LWD composite moduli of all the test sections. As shown in Fig. 9, the backcalculated surface modulus for sections in Cell 1 ranged between 171 and 260.3 MPa. Section 4 constructed with CA06_15NPF had the highest surface moduli for both C1N and S1S. Sections constructed with stabilized layers utilizing QB applications in Cells 2 and 3 showed significantly higher modulus values. Out of all sections studying base layer applications of QB or QB blended with other recycled materials (C2S1–C3S1), C1S1 constructed with QB blended with FRAP and cement had the highest modulus, and C1S3 constructed with QB blended with FRAP and fly ash showed the lowest modulus. Section C3S3 for the subbase application of QB mixed with fly ash had a relatively similar modulus to C3S4 constructed with dense-graded unbound aggregate CA06_R material. On the other hand, section C3S3 for the subbase application of QB mixed with cement had a significantly higher modulus than C3S4. The backcalculated LWD modulus and the rut development in the different test sections were often closely related. Note that for the admixture stabilized test sections in Cells 2 and 3 (i.e. C2S1–C3S3), the LWD measurements indicated were taken after 11–14 days of the placement and compaction of the test sections.

The constructed test sections were monitored for rutting performance through accelerated pavement testing. Heavy wheel loads were applied using a constant unidirectional wheel load of 44.5 kN (10 kip), a tire pressure of 760 kPa (110 psi), and a constant speed of 8 km/h (5 mph) from the Accelerated Transportation Loading Assembly (ATLAS) at the Illinois Center for Transportation. A super-single tire (455/55R22.5) was used, where the first number (455) refers to the tire width from wall to wall in mm, the second number (55) corresponds to the sidewall height expressed in terms of percentage of tire width, and the third number (22.5) is the rim diameter in inches.

The surface profiles for the construction platforms in Cell 1S were measured using a customized surface rut measurement device, which consisted of a hollow channel perforated at 50.8-mm (2-in.) intervals, and equipped with slide calipers that measured the change in depth with loading. The surface profile was first measured at

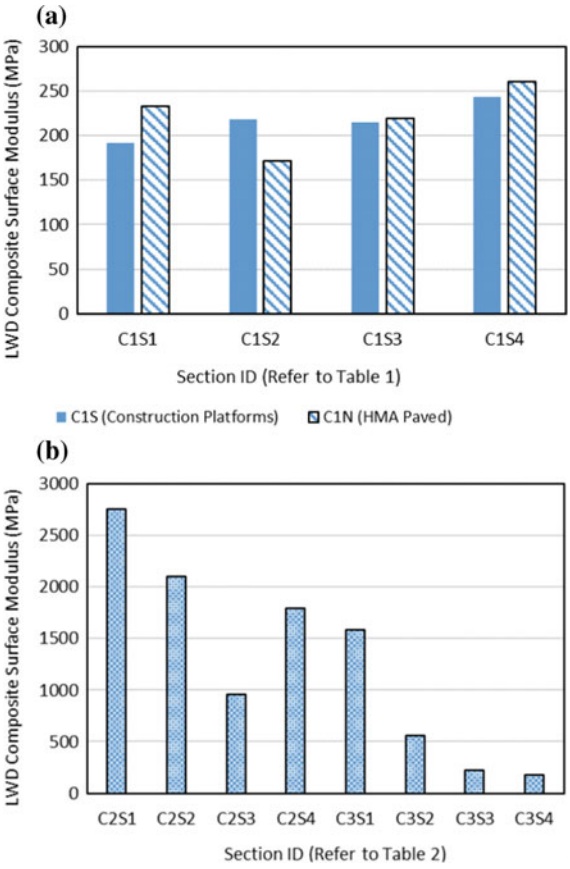

Fig. 9 Average composite surface moduli measured by LWD for all the constructed test sections

zero load applications, and consecutive rut depths at different number of passes were calculated by subtracting the depths measured at the corresponding number of passes from the depths at zero passes. Measurements were taken laterally up to 760 mm (30 in.) on each side of the wheel path to capture any possible heaving on the sides of the wheel path, which was not noticeable at any of the sections for up to 20,000-wheel passes. For the paved test sections (i.e., Cell 1N, Cell 2 and Cell 3), the changes in surface profiles with increased number of passes were measured using an automated laser profiler. Measurements were taken along an 810-mm transverse distance, with 405 mm on each side of the wheel path. A total of six 810-mm lateral scans were performed at 5-mm spacing for each measurement point in each section. Figure 10 shows ATLAS accelerated pavement test equipment, the customized measurement device for rutting measurements of the construction platforms, and the laser profiler for rutting measurements for the HMA-paved test sections. The rut depths in all sections are summarized in Fig. 11 after 10,000-wheel passes. Note that the reported

Fig. 10 ATLAS test equipment setup (right), the customized rutting measurement device for construction platforms (top left), and the laser profiler used for measuring rutting for the HMA-paved test sections (bottom left)

values indicate the average rutting of the centermost 150 mm in the wheel path, averaged for both measurement points in each section.

As shown in Fig. 11a, all HMA-paved test sections in Cell 1N accumulated relatively similar levels of permanent deformation after 10,000-wheel passes. The construction platform sections in Cell 1S, on the other hand, showed significantly higher levels of permanent deformation and more variability in performance between the different sections. C1S3 with plastic fines accumulated the highest rutting, while C1S4 with non-plastic fines accumulated the lowest permanent deformation after 10,000 load applications. The detrimental effect of using plastic fines can be clearly seen from the results.

As seen in Fig. 11b, satisfactory rutting accumulation was achieved for all test sections utilizing QB applications. Except test section C2S3, having the blend of 70% QB2 and 30% FRAP by weight and stabilized with 10% class 'C' fly ash, the other six test sections utilizing admixture stabilized applications of QB accumulated less than 2 mm of rutting after 10,000 load applications, which is considered a low rut accumulation. C2S3 had higher rut depths exceeding 3 mm after 10,000 passes, but showed a significantly slower rate of rutting progression after 1000 passes (which is not shown here). The control section, on the other hand, had the highest rate of rut accumulation (highest slope) and accumulated the maximum rut crater after 10,000 passes, which exceeded 4.5 mm. Note that further investigation is required for the as-constructed thicknesses of the HMA, especially for the control section, which was paved the last and might have a lower achieved thickness, compared with the other full-scale test sections.

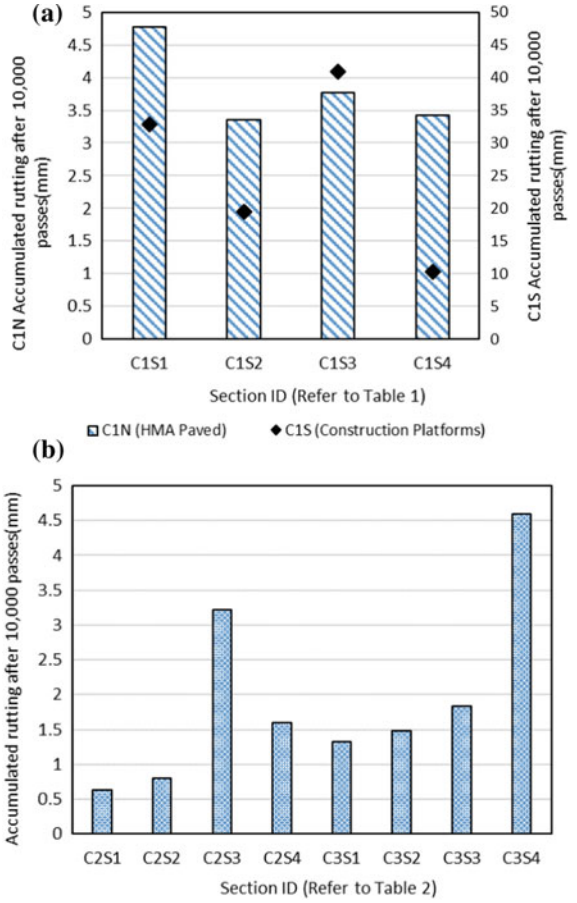

Fig. 11 Average rutting accumulation for all constructed test sections after 10,000-wheel passes

5 Summary and Conclusions

This paper presented results from an ongoing study at the Illinois Center for Transportation focusing on the sustainable use of quarry by-products (QB) in pavement applications. Fifteen different applications were proposed for using QB as an unbound material for subgrade remediation applications and as a chemically stabilized construction material for base and subbase applications. The applications proposed and evaluated for subgrade remediation for low-volume flexible pavement and construction platform applications included: (1) QB used as a filler material in the voids of large, unconventional, uniformly graded 'aggregate subgrade' materials to improve strength and reduce potential settlement, and (2) the construction of commonly used dense-graded aggregate base/subbase materials with higher fines content, i.e., 15% passing the No. 200 sieve on top of a very soft (CBR $\leq$ 1) subgrade. The applications proposed and evaluated for base and subbase materials for

low to medium volume flexible pavement roadways included QB or blends of QB and other recycled materials such as FRAP and FRCA in cement or fly ash-stabilized subsurface pavement layers, constructed on top of a CBR = 6% subgrade soil.

Seven full-scale pavement test sections, utilizing stabilized applications of QB, and an eight control section, were constructed and evaluated for performance under accelerated pavement testing. A laboratory study conducted prior to the field construction concluded that sufficient unconfined compressive strength values could be achieved for the QB applications when chemically stabilized with 3% cement and 10% fly ash, by dry weight. Performance monitoring with accelerated pavement testing showed satisfactory results with low rut accumulations for all the test sections utilizing QB applications, with six of the seven test sections utilizing QB accumulating less than 2 mm of permanent deformation after 10,000-wheel load cycles.

Another set of eight full-scale pavement test sections utilizing unbound applications of QB for subgrade remediation were also constructed to evaluate construction platforms and low volume road pavement applications. The large PCR rocks with QB test sections were built by shaking the QB on top of the large aggregate subgrade rockfill in a single lift and in two equal lifts using a vibratory roller. Approximately, 25% QB with a moisture content of 3.2% were packed in the two-lift test section, while only 16.7% QB by the dry weight of the large rocks could be packed in the single-lift test section. The presence of moisture in the QB probably increased resistance for the QB to percolate through the voids over the full depth of the single-lift test section and caused less QB packing in the inherent voids. The successful packing of the QB with manual spreading, followed by proper shaking with a vibratory roller proves the need for a uniform and slow spreading technique of the QB, followed by continuous vibration, for the optimal packing to apply this construction technique in standard practice. Performance monitoring with accelerated pavement testing for these test sections showed satisfactory results for all construction platforms and flexible pavement sections. All construction platform sections in Cell 1S accumulated less than 50-mm (2-in.) permanent deformation after 10,000-wheel passes, while all paved sections in Cell 1N had less than 5 mm or 0.2 in. of rutting after 10,000 passes.

Acknowledgements The support for this study was provided by the Illinois Department of Transportation (IDOT) as part of the Illinois Center for Transportation (ICT) R27-168 research project. The authors would like to acknowledge the members of IDOT Technical Review Panel (TRP) for their useful advice at the various stages of this research. Special thanks go to Dr. Imad Al-Qadi, Greg Renshaw, Shenghua Wu, James Meister, John Hart, and all the ICT students for their help during construction and testing at the Advanced Transportation Research and Engineering Laboratory (ATREL). The contents of this paper reflect the views of the authors who are responsible for the facts and the accuracy of the data presented. This paper does not constitute a standard, specification, or regulation.

References

Boler H, Qian Y, Tutumluer E (2014) Influence of size and shape properties of railroad ballast on aggregate packing. Transp Res Rec: J Transp Res Board 94–104. https://doi.org/10.3141/2448-12(2448)

Chesner WH, Collins RJ, MacKay MH (1998) User guidelines for waste and by-product materials in pavement construction (No. FHWA-RD-97-148)

De Rezende LR, de Carvalho JC (2003) The use of quarry waste in pavement construction. Resour Conserv Recycl 39(1):91–105

Hudson WR, Little DN, Razmi AM, Anderson V, Weissmann AJ (1997). An investigation of the status of by-product fines in the United States. University of Texas at Austin. International Center for Aggregates Research

Kleyn E (1975) The use of the dynamic cone penetrometer (DCP), s.n, Pretoria, South Africa

Kumar DS, Hudson WR (1992) Use of Quarry fines for engineering and environmental applications: special re-port for the national stone association. Center for Transportation Research, University of Texas at Austin, Austin, TX

Lohani TK (2012) Optimum utilization of Quarry dust as partial replacement of sand in concrete. Int J Appl Sci Eng Res

McClellan GH, Eades JL, Fountain KB, Kirk P, Roth-fuss C (2002) Research and techno-economic evaluation: uses of limestone byproducts (No. WPI 0510798)

Naik TR, Rudolph NK, Chun YM, Fethullah C, Bruce WR (2005) Use of fly ash and limestone quarry byproducts for developing economical self-compacting concrete. In: International congress on fly ash utilization, 4th–7th December

Nelson JD, Tymkowicz S, Callahan M (1994) An investigation of emulsion stabilized limestone screenings. Office of Materials, Highway Division, Iowa Department of Transportation

Petavratzi E, Wilson S (2007) Incinerated sewage sludge ash in facing bricks. In: Characterization of mineral wastes, resources and processing technologies–integrated waste management for the production of construction material. WRT177/WR0115

Puppala AJ, Saride S, Sirigiripet SK, Williammee R, Dronamraju VS (2008) Evaluation of cemented quarry fines as a pavement base material. In: GeoCongress 2008: geotechnics of waste management and remediation, pp 312–319

Puppala AJ, Saride S, Williammee R (2011) Sustainable reuse of limestone quarry fines and RAP in pavement base/subbase layers. J Mater Civ Eng 24(4):418–429

Qamhia I, Cheung J, Hou W, Mwumvaneza V, Ozer H, Tutumluer E (2016) Gradation effects on the strength properties of cement and fly ash stabilized Quarry by-products. In: Geo-Chicago 2016, pp 610–620

Qamhia I, Kazmee H, Tutumluer E, Ozer H (2017a) Sustainable application of Quarry by-products mixed with large size unconventional aggregates for improved performance. In: International congress and exhibition: sustainable civil infrastructures: innovative infrastructure geotechnology, Springer, Cham, pp 262–273

Qamhia I, Tutumluer E, Ozer H, Kazmee H (2017b) Field performance evaluation of pavement Construction platforms utilizing unconventional large size aggregates packed with Quarry byproducts, and higher fines aggregate subgrade layers. In Airfield and highway pavements 2017, pp 334–347

Qamhia I, Tutumluer E, Ozer H, Kazmee H (2017c) Field performance evaluation of pavement construction platforms utilizing unconventional large size aggregates packed with Quarry byproducts, and higher fines aggregate subgrade. In: Airfield and highway pavements, 2017

Tutumluer E, Ozer H, Hou W, Mwumvaneza V (2015) Sustainable aggregates production: green applications for aggregate by-products. Illinois Center for Transportation/Illinois Department of Transportation

Stroup-Gardiner M, Wattenberg-Komas (2013) Recycled materials and byproducts in highway applications. Transportation Research Board, Washington, DC. (vol 4, no 435)

Wood SA, Marek CR (1995) Recovery and utilization of quarry by-products for use in highway construction. In: ICAR 3rd annual symposium, vol 10

Xiao Y, Tutumluer E (2016) Gradation and packing characteristics affecting stability of granular materials: aggregate imaging-based discrete element modeling approach. ASCE Int J Geomech. http://dx.doi.org/10.1061/(ASCE)GM1943-5622.0000735

Challenges in Design and Construction of Embankments and Pavements

Shahrokh P. Bagli

Abstract This Paper discusses various concerns relating to embankments and pavements in the Indian context. With expansion of existing carriageways into multi-lane expressways, new road routes and development of rural roads to carry motorised vehicles instead of traditional animal-drawn carts, the challenge is compounded by difficult ground conditions, scarce road building materials, high costs of diversions and environment considerations. Considering a significant portion of capital costs being fixed costs, time is of the essence and even a week's delay can upset financial computations. There are several examples where delays ultimately affect commercial viability of an infrastructure project, with serious consequences on its very completion. This Paper attempts to highlight possible technical issues on pavement design with geosynthetics and how these can be circumvented. It discusses options that could optimise costs and/or reduce the project completion time. It may be noted that solutions, particularly for embankments would require more than one type of geosynthetics for a complete solution. Likewise, solutions may require a holistic approach rather than a piecemeal solution, which in totality may not gel with the entire system. Considering scarcity of construction materials, the Paper also discusses how traditionally waste and marginal materials can be used.

Keywords Weak soils · Embankment · Pavement · Geogrids · Geocells

1 Introduction

Roads are an essential component of development and are essential for the economic growth of the country. These are essential systems for transfer of goods and passengers across the country and unlike the railway network, various classes of roads from expressways to rural roads assure the last mile connectivity. The growing economy requires expansion of existing carriageways into multi-lane expressways, new road routes and development of rural roads to carry motorised vehicles instead of the

S. P. Bagli (✉)
Strata Geosystems (India) Pvt. Ltd., Mumbai 400093, India
e-mail: shahrokh.bagli@strataindia.com

R. Sundaram et al. (eds.), *Geotechnics for Transportation Infrastructure*, Lecture Notes in Civil Engineering 28, https://doi.org/10.1007/978-981-13-6701-4_2

traditional animal-drawn carts. However, difficult subsoil conditions along with high economic and social costs of diversions, and dearth of good construction material coupled with environmental constraints pose major challenges to development of the road network.

A typical road project has two major components:

(1) The embankment supporting the carriageway;
(2) The pavement which is the structural entity of the carriageway; there are several cases though where the pavement is supported directly on the treated/untreated dressed natural subgrade.

The embankment may be a typical earth structure with a trapezoidal profile, or a reinforced soil structure with slopes steeper than 27° and invariably about 70°. The pavement may be flexible or rigid; this paper discusses the commonly adopted flexible pavement. The embankment and the pavement are structural entities and need to be designed accordingly. As in any other structure, two essential conditions need to be satisfied—strength and serviceability. The two structural entities are discussed separately.

2 Embankment Component of the Road

The embankment makes up for the difference in levels between the bottom of the pavement and natural ground. It also spreads the loads from the pavement such that the stresses at ground level are within the limits of its safe-bearing capacity. The embankment, whether it is a conventional earth structure, or a reinforced soil structure needs to be checked for its structural integrity (stability) as well as deformation (serviceability). These two aspects must be considered in conjunction with the supporting foundation subsoil, untreated or treated. Various methods of subsoil treatment for the embankment are shown in Fig. 1a–g. These procedures may be used appropriately in conjunction with each other. The Paper in particular addresses construction of the structure in stages along with the use of prefabricated drains for subsoil stabilisation and basal reinforcement for countering shear failure of the embankment and subsoil, as well as reinforcing the earth structure against lateral slide.

2.1 Types of Embankment Failure

An embankment on weak-soil foundation is susceptible to the following modes of failure:

(1) Foundation bearing capacity failure;
(2) Lateral sliding of embankment;

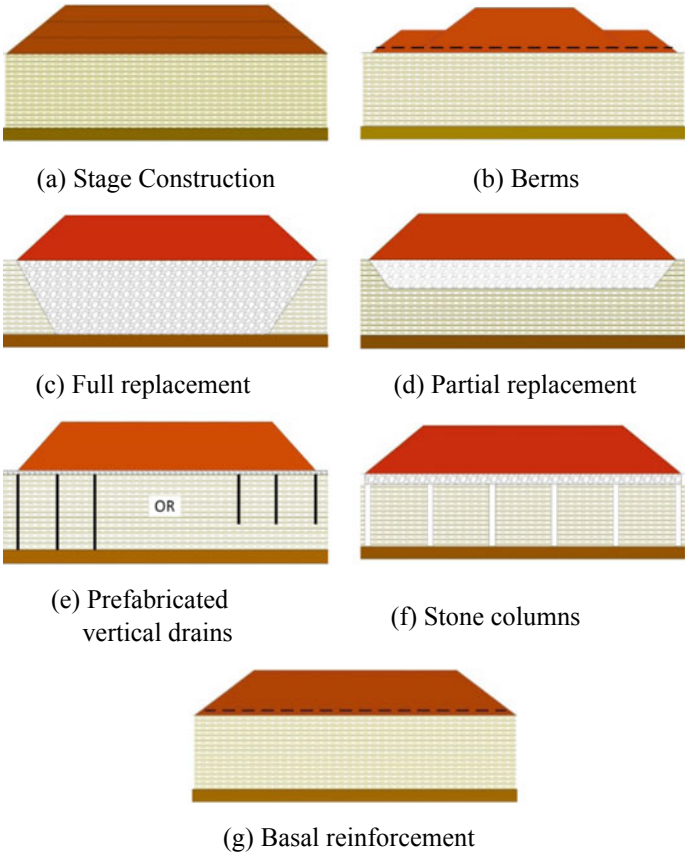

Fig. 1 Methods for constructing embankments over weak soils

(3) Global failure.

A single solution with geosynthetic reinforcement may cater to two or all three potential failure modes.

In addition, settlements during the service life of the embankment structure should be within limits permissible to the application.

2.1.1 Foundation Bearing Capacity Failure

Like in any structure, it is essential to check the bearing capacity of the foundation of the embankment. This will not be confined to shear failures from embankment loads; short-term and long-term settlements need to be reviewed.

There are basically two solutions:

(1) providing basal reinforcement to act as a rigid layer to spread the load from the embankment;
(2) improving the shear strength of the weak soil below by consolidation.

Both solutions may be adapted simultaneously to advantage. An embankment with basal reinforcement may be considered equivalent to a footing with a rough base on weak soil—Almeida et al. (2013). Notwithstanding using reinforcement at the base, it is recommended that the bearing capacity required for the unreinforced embankment be lower than the permissible stress of the underlying strata, so that the factor is safety of the unreinforced embankment is at least equal to one. The basal reinforcement is required only to increase the factor is safety to the required value beyond one, or from marginally below one.

Regarding settlements, the earth embankment, both unreinforced and reinforced are flexible structures and can tolerate differential settlements better than a rigid concrete or masonry structure. Even then, service conditions may require limiting these settlements during operations and major settlements are best catered to during construction of the embankment. This is highlighted in the case study for embankments herein.

2.1.2 Failure Due to Lateral Sliding of Embankment

This is an often neglected check for both unreinforced as well as reinforced embankments/earth structures. Forces that come to play in sliding are illustrated in Fig. 2—Almeida et al. (2013).

With respect to Fig. 2, Eqs. (1) and (2) give the factors of safety against lateral sliding for the two conditions of embankment base unreinforced and reinforced, respectively.

$$F_s = \frac{0.5 * n * \gamma_{emb} * h_{emb} * \tan \varphi_d}{K_{aemb}(0.5 * \gamma_{emb} * h_{emb} + q)} \tag{1}$$

$$F_s = \frac{n * S_{clay} + T}{K_{aemb}(0.5 * \gamma_{emb} * h_{emb} + q)} \tag{2}$$

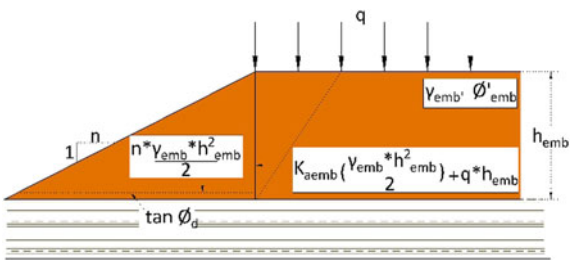

Fig. 2 Sliding in an embankment

where

n	is the horizontal component of the slope ratio 1: n;
K_{aemb}	is the active earth pressure coefficient for the embankment material;
φ_d	is the soil friction angle;
h_{emb} and γ_{emb}	are height and material unit weight, respectively, of the embankment;
q	is the surcharge on top of the embankment;
T	is the long-term design strength of the geosynthetic reinforcement;
S_{clay}	as a term, is explained below.

Equation (1) clearly underscores that the resisting force is by virtue of friction within the embankment material, whereas Eq. (2) highlights the interaction between the clay and the reinforcement, S_{clay}, and the long-term design strength of the reinforcement T.

A word of caution here; as a matter of detailing on the design drawing, the designer is bound to place a nonwoven geotextile at the interface of the embankment and the underlying weak soil. Hence, S_{clay} must be the force mobilised between the underlying weak clay and the geotextile considered as separation, if any.

Where geocells are concerned, total lateral resistance is by virtue of friction between the underlying soil and the infill material (if there is no separation geosynthetic in between), plus the tensile characteristic of the geocell material, symbolically T. If there is a separation layer, the preceding paragraph applies.

For geocells, the philosophy of considering T will be governed by the orientation of the geocells with respect to the embankment cross section:

(1) When the straps of the geocell are oriented along the cross section of the embankment—Fig. 3a, lateral forces from the embankment are transferred to the infill through friction, and the infill transfers these forces to the geocell profile. Hence, the design tensile strength of the straps is to be considered. It is to be noted that the strap is parallel to the lateral force exerted by the embankment block; otherwise, roughly at 45° at the most. Hence, the resistance offered by the straps alone would be an average of 0.85 T.
All cells of the geocells are infilled. The infill, being totally confined, will transfer the forces to the geocell straps. During the transfer of forces, the weld seam also is stressed. Hence, the weld seam strength is also significant.
T needs to be checked not only with respect to the design tensile strength of the perforated strap, but also the weld seam peel strength of the geocell. In this case, weld seam peel strength should be determined by "Method A" as per EN ISO 13426-1 "Geotextiles and geotextiles related products—Strength of internal structural junctions—Part 1: Geocells"—Fig. 3b.

(2) When the straps of the geocell are oriented along the embankment longitudinal axis—Fig. 3c, as in the previous case, lateral forces from the embankment are transferred to the infill through friction, and the infill transfers these forces to the geocell profile. However, in this case, tensile resistance from the straps will not be significant, and the lateral forces other than the component resisted by friction will be resisted essentially by the geocell weld seams. In this case,

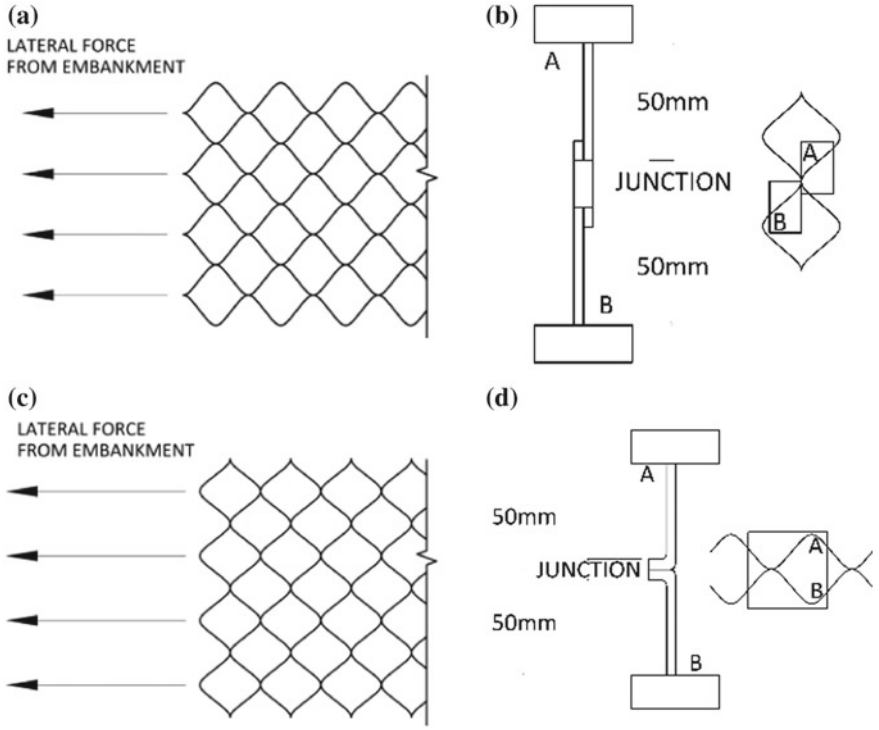

Fig. 3 **a** Geocell straps along lateral direction, **b** weld seam peel strength—Method A, **c** geocell straps along longitudinal direction, **d** weld seam peel strength—Method B

weld seam peel strength should be determined by "Method B" as per EN ISO 13426-1—Fig. 3d.

It may be noted that stresses on the welded seams will be reduced owing to the confined infilling in all the cells. The reduction can be significant but difficult to determine at this juncture. Not much work has been done regarding geocells stressed along the plane in either direction and research is still in progress.

2.1.3 Global Failure

Several computer programs are available for global stability, also incorporating geosynthetic reinforcement within the embankment and along the base. In the case of embankments, Bishop's method, considering circular slips would suffice.

Geogrids are essentially two-dimensional geogrids with their major strength in either one direction (uniaxial geogrids) or two orthogonal directions (biaxial geogrids). When geogrids are used, the long-term design tensile strength T is considered as an additional factor as resisting force along the shear surface.

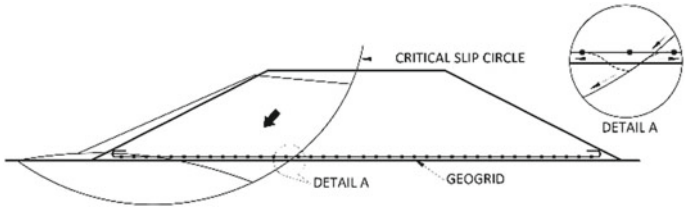

Fig. 4 Geogrid as basal reinforcement and critical slip circle

It must be noted that the total tension to be taken by the geogrid must be a sum of the tension induced in the geogrid due to its providing lateral resistance plus the tension induced in the geogrid induced by the incipient shear failure surface determined by global failure analysis. Hence,

$$T_{\text{gr design}} \geq T_{\text{gr lateral}} + T_{\text{gr critical global}} \tag{3}$$

where

$T_{\text{gr design}}$ is the long-term design tensile strength of the geogrid;
$T_{\text{gr lateral}}$ is the tension developed in the geogrid due to resisting incipient lateral slide of the embankment for the required safety factor;
$T_{\text{gr critical global}}$ is the tension developed in the geogrid due to resisting incipient global shear failure of the embankment for the minimum safety factor as analysed (Fig. 4).

Geocells are three-dimensional geosynthetics providing cellular confinement to infilled soil. The cells are curvilinear rhomboids in shape. There is a distinct depth to a geocell h_g, and the confinement within the curvilinear rhomboid has an average diagonal distance d. Hence, the geocell cannot be considered as a two-dimensional system in any mathematical modelling. When considered in cross section of an embankment, the geocell is depicted as a distinct stratum with a thickness equal to h_g, or in case a number of layers of geocells have to be considered, then $\sum h_g$. It has been determined by Bathurst and Rajagopal (1993) and confirmed by laboratory tests that a geocell layer infilled with non-plastic soil can be considered as a stratum with an equivalent cohesion term c_τ, which is initiated by virtue of enhanced strength of the soil infill confined by the geocell walls. The geocell-infill system is best explained by the normal stress versus shear stress diagram in Fig. 5. Figure 5 illustrates the effect of lateral confining stress within the cell, $\Delta\sigma_3$ on reinforced soil to generate a larger circle, whose parallel tangent intercept is at c_τ on the shear stress axis; c_τ is also called "apparent cohesion".

It can be derived from Fig. 5 that

$$c_\tau = \frac{\Delta\sigma_3{}^*}{2} \tan\left(45^\circ + \frac{\varphi}{2}\right) \tag{4}$$

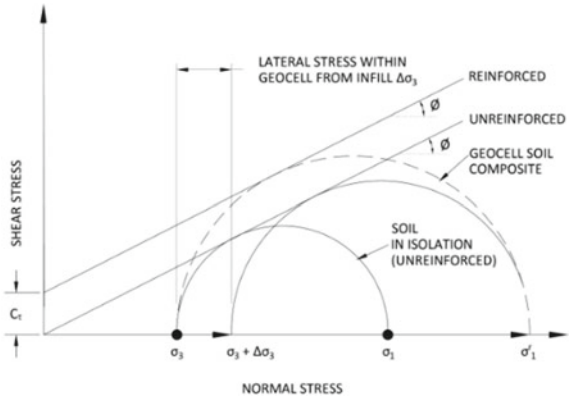

Fig. 5 Effect of cell confinement on non-plastic soil—"apparent cohesion"

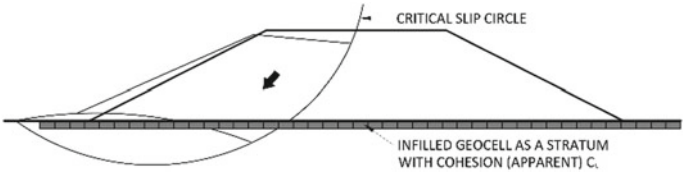

Fig. 6 Geocell as basal reinforcement, considered as a stratum with shear strength c_τ

where

$\Delta\sigma_3$ is the lateral pressure under "at rest" condition acting on the geocell cell and is equal to $\sigma_1(1 - \sin\varphi)$;
σ_1 is the vertical stress on the infill within the cell;
φ is the angle of internal friction of the infilled (non-plastic) soil.

Global stability analysis is then carried out considering the total geocell layer as a stratum with an apparent cohesion value of c_τ, as shown in Fig. 6.

2.2 Case Study: Reinforced Soil Structure on Weak Soil (Mane et al. 2015)

The reinforced soil (RS) structures for NH-06 between Dhankuni and Kharagpur in West Bengal are a typical example of earth structures constructed on soft clays (Fig. 7), strengthened through consolidation by prefabricated vertical drains (PVDs). These RS walls are lateral extensions of approaches to rail overbridges (ROBs), and adjoining existing structures for widening the carriageway. The safe height of these structures along the ramp lengths was limited to 2.03 m only from safe-bearing

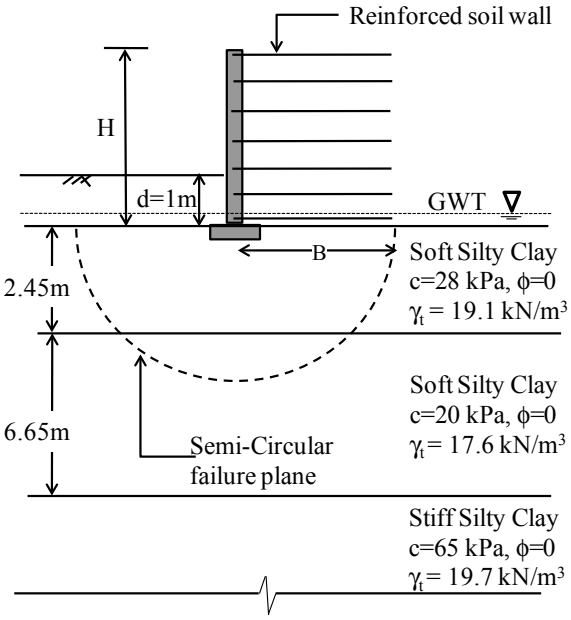

Fig. 7 Sub-surface profile

capacity considerations notwithstanding pond ash, a light material, being used for both reinforced as well as retained backfill.

To treat soft clay below foundation level, ground improvement was carried out with PVDs in triangular array. Surcharging for effectiveness of PVDs was done by progressively increasing the height of the structure itself, while subsoil shear strength progressively developed with consolidation. The subsoil was categorised as plastic; hence, a circular failure surface was assumed (Fig. 7).

Improvement in shear strength was computed for each surcharge increment at 50 and 90% consolidation. Besides foundation bearing capacity computations, global stability analysis was carried out for different heights along the ramp by the standard Mechanically Stabilized Earth Walls Software (MSEW) under static and seismic conditions. Since the structure is of reinforced soil, check for failure due to lateral sliding did not arise. PVDs installed for the new structure adjoining the existing structure are shown in Fig. 8.

Figure 9 graphically highlights the stages of loading and the settlements that occurred at the abutment, the highest section at 7 m. It must be noted that no construction time was lost during the "plateaux" in Fig. 9, since pond-ash filling was planned to be carried out from the abutment end to the commencement of the ramp, then back to the abutment end.

Both analysis and execution in the field demonstrated that PVDs with incremental RS wall surcharge were effective in progressive development of shear strength of the plastic subsoils. With the help of this technique, flexible RS systems could be

Fig. 8 PVDs for extension adjoining the existing structure

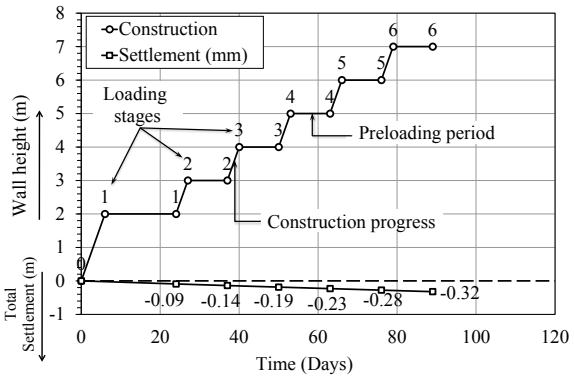

Fig. 9 Load increments and associated settlements

constructed up to desired heights without failure, within the construction time frame. No distress was observed in the adjoining existing structure.

It must be highlighted to the merit of this project that pond ash from the National Thermal Power Station at Kolaghat was used for constructing the reinforced soil structures. Material which otherwise was deemed as marginal and otherwise waste of nuisance value was put to use as engineered fill. The added advantage is that the specific gravity of pond ash is as low as 2.31 and the drained angle of internal friction as determined in the laboratory was as high as 42° (the design value was taken as 32° under advice of the principle client). Further savings were incurred by minimising

the width of right of way through the reinforced soil concept. Area to be consolidated by PVDs was also less than that for a conventional trapezoidal embankment section.

3 Pavement Component of the Road

The pavement is a structural entity which safely transfers cyclic stresses from various types of vehicles from the surface to the subgrade over its designated life, with vertical and horizontal deformations within defined limits. The pavement surface is subject to vertical and horizontal stresses and these stresses develop strains in the various components of the pavement, which, when exceeded beyond certain magnitudes, can cause rutting, and surface fatigue cracks (Fig. 10). Horizontal stresses and corresponding strains are also generated by vehicle traction and other factors including temperature variations. The quality of the riding surface is a key factor to give comfort to the driver and the passengers, and the pavement is designed to cater to these stresses and minimise strains over the designated life—Bagli (2017a, b).

Considering that this Paper addresses both pavements and (flexible) embankments bearing the pavements, it is appropriate to discuss flexible pavements only. At the ultimate stage of the design, the pavement and the embankment need to be holistically deliberated. However, it is quite often that pavements need to be supported directly on natural but dressed subgrade rather than an engineered embankment.

Fig. 10 Rutting and fatigue cracks—the Internet

3.1 Challenges in Designing and Constructing a Pavement

The concept of sequential components that form flexible pavements has been followed since the days of Thomas Telford and John McAdam almost two centuries ago, with modifications. However, in the current day scenario, sound natural material is scarce, costly and its availability is much constrained owing to indisputably and justifiable strict environmental norms.

The flexible pavement often necessitates to be constructed from marginal materials. Besides this, considering the high cost of ground treatment, for pavements directly supported on weak soils with a low California-bearing ratio (*CBR*) would require further engineering beyond the established and standardised norms. There are cases highlighted herein where marginal material is required to be used even where the *CBR* value is very low. These conditions require a paradigm change in the design of the pavement section using geosynthetics.

3.2 Conventional Pavement Section

The conventional concept of the pavement is shown in Fig. 11—Zornberg (2012).

There are two common philosophies of design:

1. The "mechanistic-empirical" method, developed by the National Cooperative Highway Research Program (NCHRP), and also advocated by the Indian Roads Congress (IRC), IRC: 37-2012 "Guidelines for the design of flexible pavements";
2. The American Association of State Highway and Transportation Officials (AASHTO) flexible pavement structural design.

The AASHTO method of design is based on pavement performance incorporating road-user's definition of pavement failure, as well as the effect of structural parameters (such as component material properties and thicknesses) and the magnitude and frequency of the axle loads. The method uses empirical equations developed from road tests.

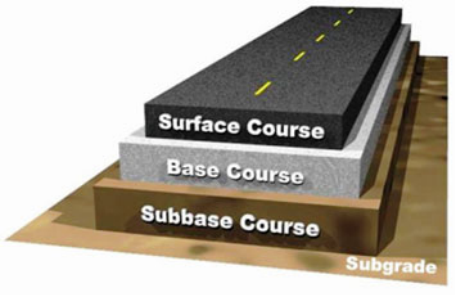

Fig. 11 Conceptual sketch of a conventional pavement

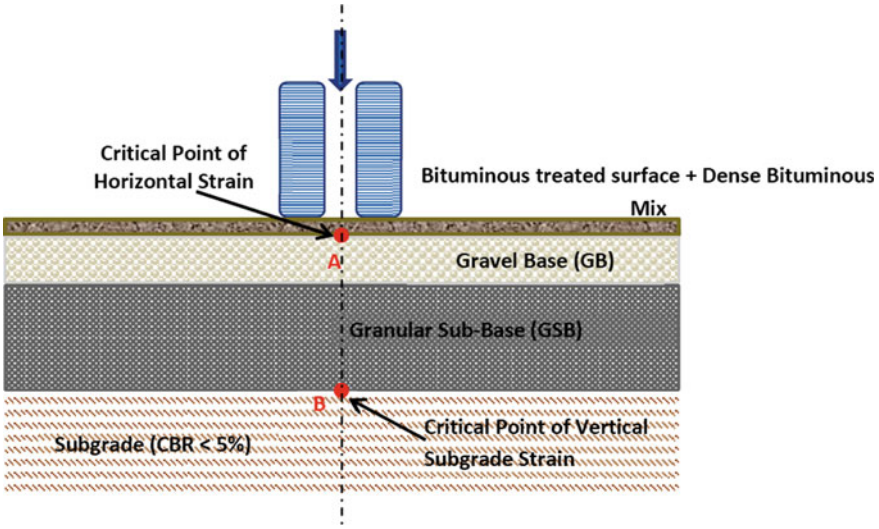

Fig. 12 Critical strain points in a pavement section—Bagli (2017a, b)

The mechanistic-empirical method considers the resilient modulus M_R of each component in the analysis, which is based strictly on structural stress–strain concepts. The method uses mechanistic principles and detailed input data to minimise reliance on empirical observations and correlations. It improves design reliability, allows flexibility to reduce life-cycle costs and provides economic solutions.

Determining the stresses and strains within the pavement components by the finite element method (FEM) is trending. The advantage is that the modelling can consider boundaries between pavement components as elements and corresponding stresses and strains are compared with limits set for fatigue cracking or rutting. However, owing to high cost of such software, this method is not accessible for common usage as compared to the software commonly used for pavement analysis and design in India, viz. IITPAVE.

3.3 Pavement Section Incorporating Geosynthetics

The essence of pavement design incorporating geosynthetics is to ensure that:

(1) horizontal strain at the junction of the bituminous layers and the underlying granular component (Point A in Fig. 12) is within defined limits;
(2) vertical strain at the top of the subgrade (Point B in Fig. 12) is also within defined limits.

On incorporating geosynthetics, the following one, or a combination of the following can be achieved:

(1) Reduce the thickness of costlier pavement section component(s), particularly where the CBR is as low as 1%;
(2) Use marginal soils within the pavement section without compromising on the performance or its life in terms of traffic;
(3) Extend the life of the pavement in terms of number of standard (msa)/equivalent single axle loads (ESAL), and also increase the time between maintenances.

Geosynthetics often considered for pavements are HDPE geocells and polyester or polypropylene biaxial geogrids, flexible or rigid.

Geosynthetics are generally placed nearest to the level of imposed load. This is often at the interface between the bituminous layers and the granular layers. Where poor *CBR* value of the subgrade is the prime concern, the geosynthetic is laid above the dressed and compacted subgrade. Figure 13a, b shows HDPE geocells and geogrids/geogrid composites in the pavement section below the bituminous layer.

The philosophies of design outlined above differ while designing for geocells and for geogrids. As a practice, pavements incorporating geocells are designed by the mechanistic-empirical method, whereas designs of pavements incorporating geogrids follow the AASHTO method.

Components of the pavement section are modified if economies are to be affected. Thickness of the most expensive section is reduced first. Analysis is carried out with the geosynthetic in position and M_R of the relevant pavement component, appropriately and judiciously modified considering the influence of the geosynthetic over the relevant portion. Horizontal tensile strains at Point A and vertical strains at Point B are thus evaluated and compared with the corresponding values at A and B in the conventional section. The levels of strains in the modified section reinforced with the geosynthetic must be less than or just equal to those for the conventional section, for the new section to be acceptable. The entire process would be by trial and error.

If the life of the pavement is to be extended and the time to the next maintenance is to be prolonged, thicknesses of the various components are retained and the new life in terms of increased standard/equivalent axles is evaluated.

In the case of geocells in pavement sections, it is significant to note that weld seam strength does not play any role. Unlike the case of geocells as basal reinforcement for embankments, in this case, the external force is perpendicular to the plane of the geocell panel. All cells of the geocell system are infilled, and the infills of each congruent exert (almost) equal and opposite reactions, which is the essence of spread of normal force over larger areas by geocells.

3.3.1 Mechanistic-Empirical Method

It is fairly direct to evaluate the strains at the two critical Points A and B in Figs. 13 and 14, by the basic first principles mechanistic-elastic method. The new resilient modulus of that component of the pavement, within which the geosynthetic is integrated, must be evaluated and judiciously used in the analysis.

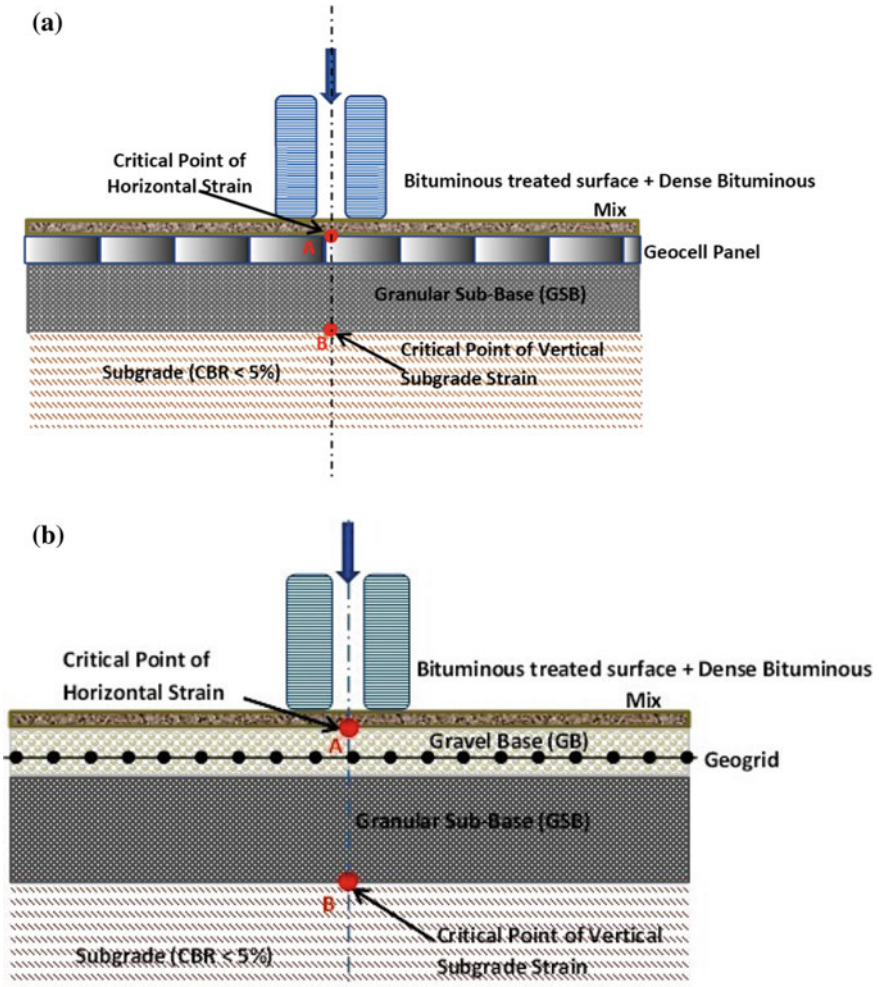

Fig. 13 **a** Geocells in pavement section, **b** geogrids in pavement section

3.3.2 Mechanistic-Empirical Method—Geocells

Adequate information is available on the improvement of the resilient modulus M_R of the pavement component with the inclusion of geocells that component. The ratio of the improved resilient modulus as against the original resilient modulus is known as the modulus improvement factor (*MIF*). While it is necessary to conduct field and/or laboratory tests to determine the *MIF* for a particular style of geocell and the classification of infill, extensive research has shown *MIF* to range anywhere between 2 and 3 and higher, depending essentially on the type of infill. According to Rajagopal et al. (2011), the value may be of the order of 2.75 and Basu and Soni (2013) have

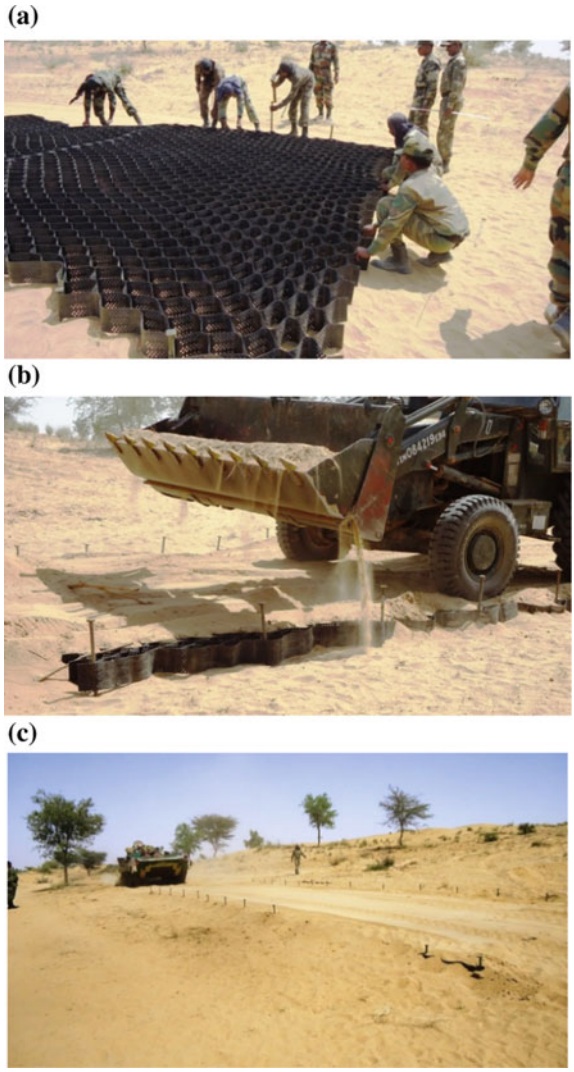

Fig. 14 **a** Laying the geocell panel, **b** infilling the geocell panels with local sand, **c** unpaved track through several trial runs

stipulated MIF to be of the order of 2.5. The *MIF* is to be considered for the thickness equivalent to the depth of the geocell. Basu and Soni (2013) have highlighted that owing to the confining effect of the geocells, there is further interlocking of the granular material above and below the geocell. Hence, the *MIF* is effective 25 mm above the geocell and 20 mm below the geocell within the granular material. These additional thicknesses above and below the geocell layer may be left to the discretion of the designer. Rajagopal et al. (2011) have also stated, based on tests that the aspect ratio, i.e. depth to average diameter ratio of the geocell should be as close as possible to 1.

3.3.3 Mechanistic-Empirical Method—Geogrids

In the case of geogrids, the *MIF* may similarly be determined by field and/or laboratory tests. The "zone of influence" of the geogrid reinforcement depends on the stiffness of the geogrid, the aperture size and interlocking of the base/sub-base granular material with the geogrid. Tests with granular base course with geogrids demonstrated reinforcing effects typically approximately 30 mm in thickness on either side of the geogrid—Schuettpelz et al. (2011). The designer may, therefore, apply the *MIF* value to a layer 30 mm above and 30 mm below the geogrid, though judiciously, to the M_R of that component.

Geogrids may be placed in more than one location within the pavement section in the base and sub-base courses. There is also an opinion that the modified M_R would apply to the entire pavement component within which the geogrid is placed, a debatable point according to the Author's opinion, unless multiple layers of geogrid are judiciously placed in position. Due consideration needs to be given to parameters, viz. geogrid flexibility/stiffness and aperture size, and particle size of the material being reinforced while considering the effective reinforced layer thickness.

Analysis to determine the critical strains at Points A and B is carried out by the KENPAVE software, or IITPAVE which is preferably used in India.

3.4 Mechanistic-Empirical Method Considering Geosynthetic Layer Coefficient Ratio

Conventionally, pavement design in India has been carried out by the mechanistic-empirical method, the procedure recommended by Indian Roads Congress (IRC), IRC: 37-2012 "Guidelines for the design of flexible pavements". Two of the inputs are M_R for the pavement component and *MIF* for the geosynthetic. A lot of work has been done in India to determine *MIF* for geocells infilled with various types of soil. However, *MIF* is not commonly stated for geogrids in pavement design and globally *LCR* for the respective style and branding of the geogrids are considered, appropriate for the AASHTO method of pavement design.

The AASHTO method considers the pavement section as a multi-layered elastic system. It introduces an empirical parameter, "Structure Number (*SN*)" which throws light on the total pavement thickness and its resilience to repeated traffic loads. *SN* is defined as:

$$\mathrm{SN} = (a_1 d_1) + (a_2 d_2 m_2) + (a_3 d_3 m_3) \tag{5}$$

where

a_1, a_2, a_3 are structural layer coefficients reflecting resilient moduli of the bitumen layer, base course and sub-base course, respectively; determined from

AASHTO empirical or nomographs from AASHTO Guide for Design of Pavement Structures;

d_1, d_2, d_3 are thicknesses of the bitumen layer, base course and sub-base course, respectively;

m_2, m_3 are moisture modifiers for base course and sub-base course, respectively, and reflect the quality of drainage and the percentage of time that the pavement is exposed to near-saturation moisture levels

SN is used in Eq. (6) below, a standard empirical relationship which determines the anticipated cumulative 18 kip Equivalent Single Axle Loads (ESALs):

$$\log W_{18} = Z_R * S_O + 9.36 * \log(SN + 1) - 0.2 + \frac{\log \frac{\Delta_{PSI}}{2.7}}{0.4 + \frac{1094}{(SN+1)^{5.19}}} + 2.32 \log M_R - 8.07 \quad (6)$$

where

Z_R is the standard normal deviate reliability level;
S_O is the overall standard deviation;
Δ_{PSI} is the allowable loss in serviceability;
M_R is the resilient modulus of the underlying subgrade.

SN is determined from Eq. (6), and the thicknesses of individual layers are determined through several iterations with due consideration to the relative costs of each layer and the minimum specified thickness, particularly of the surface bituminous course.

For designing with geogrids, a unique empirical number called the layer coefficient ratio (*LCR*) is defined for a specific geogrid by the manufacturer. This number is a multiplier in Eq. (5) and is applicable for the pavement component within which the geogrid is placed. Hence, Eq. (5) would be modified as:

$$SN_{GS} = (a_1 d_1) + (LCR_2 a_2 d_2 m_2) + (LCR_3 a_3 d_3 m_3) \quad (7)$$

where

SN_{GS} is the new structural number for the pavement incorporating the geogrid;
LCR_2 is the layer coefficient ratio for the specific geogrid located in the base course, invariably greater than 1;
LCR_3 is the layer coefficient ratio for the specific geogrid located in the sub-base course, invariably greater than 1;
SN_{GS} thus obtained is substituted for *SN* in Eq. (6).

LCR values are provided by the geosynthetic manufacturer based on exhaustive tests carried out through accredited laboratories.

Where it is essential to carry out analysis of a pavement section reinforced with geogrids, but by the mechanistic-empirical method, the Author recommends the following procedure for designing with geogrids whose *LCR* is specified—Bagli (2017a, b):

(1) Resilient moduli M_{R2} and M_{R3} are evaluated for the base and sub-base. The units are converted from kPa to psi (to be considered as E_{BS} and E_{SB} in the AASHTO process as per Eqs. (7) and (8) below.
(2) The tensile horizontal and vertical strains are evaluated for the conventional section at critical Points A and B for the given subgrade *CBR* and traffic/pavement life in terms of msa as per IRC: 37-2012.
(3) Structural layer coefficients are derived from the resilient moduli (in psi) using the following AASHTO equations:

$$a_2 = 0.249\left(\log_{10} E_{BS}\right) - 0.977 \tag{7}$$

$$a_3 = 0.227\left(\log_{10} E_{SB}\right) - 0.839 \tag{8}$$

(4) Consider the layer within which the geogrid is placed, base or sub-base, or both. Accordingly, the corresponding structural layer coefficient(s) is/are modified by multiplying by the corresponding layer coefficient ratios. Hence:

$$\mathrm{LCR}_2 a_2 = 0.249\left(\log_{10} E_{BSGS}\right) - 0.977$$

or

$$E_{BSGS} = 10^{\frac{(\mathrm{LCR}_2 a_2)+0.977}{0.249}}$$

$$\mathrm{LCR}_3 a_3 = 0.227\left(\log_{10} E_{SBGS}\right) - 0.839 \tag{9}$$

or

$$E_{SBGS} = 10^{\frac{(\mathrm{LCR}_3 a_3)+0.839}{0.227}} \tag{10}$$

(5) From Eq. (9) and/or Eq. (10), E_{BSGS} and/or E_{SBGS} are evaluated, and the values are converted from psi units to kPa units to arrive at M_{R2GS} and/or M_{R3GS}.
6) M_{R2GS} and/or M_{R3GS} are then used to determine the reduced thicknesses of the pavement components, or the msa with the geogrids within the pavement component(s) by the mechanistic-empirical method. As in the case of geocells, the increased modulus is applicable only to the reinforced zone of the geogrid. The confinement action due to the geogrid would be extended to 30 mm above and below the reinforcing layer as discussed earlier, and the effect of M_{R2GS} and/or M_{R3GS} would, therefore, be to the extent of about 60 mm.

4 Marginal Soil Zones Along with Low CBR Subgrades

There can be conditions when roads are required to be constructed through regions where the borrow soils available are marginal, and the subgrade is weak. It is through such areas that roads may have to be constructed on an emergency basis. These roads are often required to carry heavy vehicular loads. There are three cases where geocells have been considered. In all these three cases, the pavements in unpaved conditions carried heavy equipment. Two of these cases were essentially rigorous field trials to check the efficacy of geocells.

4.1 Desert Silty Fine Sands

Trials conducted in the deserts of Rajasthan in silty fine sand, using HDPE perforated and textured geocells of depth 150 mm and weld spacing of 356 mm. Trials were carried out to check out a rapidly constructed track for heavy vehicular track. The soil in the area is silty fine sand which is non-plastic and considered as marginal for the application of an unpaved road. The *CBR* value is low, less than 5%. The material also tends to raise dust due to traction of vehicles.

For the trials, the surface soil was roughly dressed and HDPE geocells were laid out manually as shown in Fig. 14a. Sand from the surrounding area was filled into the expanded geocell layer with a front loader, Fig. 14b. Considering the need for rapid deployment, compaction was done by the bucket of the front loader and the movement of the loader itself. The completed track was rigorously tested with heavy vehicles as shown in Fig. 14c. Speed could also be achieved over the unpaved surface which otherwise was not possible. A notable feature was that despite speed, owing to material confinement, scarcely any dust was raised with tracked vehicle movement.

4.2 Silty Fine Sands with High Ground Water Level

Where there is silty fine sand and the ground water table is high, the subgrade has a low *CBR* value (<3%), rendering it difficult to ply heavy vehicles. In the owner's parlance, the soil was termed "boggy". Pictures in Fig. 15 show how tracks of heavy equipment rutted deep into the material, virtually demonstrating quicksand condition.

As in the previous case, tracks through marshy areas are required impromptu using locally available material. Trials were proposed by the owner considering HDPE geocells. Owing to quicksand conditions and since the track was to be unpaved, geocells of depth 300 mm and weld spacing of 356 mm were proposed. The geocells were perforated and textured. The perforations ensured rapid dissipation of pore water pressures from within the geocells. The unpaved road thus created and as

Fig. 15 Heavy tracked vehicle rutting heavily into the soil; above picture shows depth of ruts

shown in Fig. 16a–c proved that geocells can be reliably deployed where subgrade conditions are difficult, even for heavy traffic.

4.3 Highly Plastic Clay in Subgrade with Low CBR—Bagli (2017a, b)

The Indian National Highway NH-44 near Churaibari on the Assam side of the Assam–Tripura border traverses forested and undulating terrain. The subgrade of the highway is highly plastic, weak clayey soil of low permeability. This region experienced exceptionally heavy rainfall since March 2016 right into September 2016, which completely damaged about 500 m of the stretch and reduced it to a swampy mass as shown in Fig. 17. Conventional repairs were unsuccessful and traffic disruption created a crisis with commodities getting scarce and expensive in Tripura with every passing day.

Both these issues were addressed while designing a pavement section with geocells within the pavement section. The *CBR* value was as low as 0.5% and a traffic intensity of 20 msa. A section was designed and adopted as in Fig. 18. Geocells of depth 150 mm and weld spacing 356 mm were recommended. A *MIF* of 2 was conservatively considered. Granular material was available within reasonable lead and used as infill which ensured drainage of ingressed water.

Fig. 16 **a** Unpaved geocell reinforced path with tracked 50T vehicle after several passes, **b** unpaved geocell reinforced track with wheeled loaded vehicle after several passes, **c** comparison between the unreinforced, unpaved track and reinforced, unpaved track

Fig. 17 NH-44 at Churaibari in July 2016 before rehabilitation

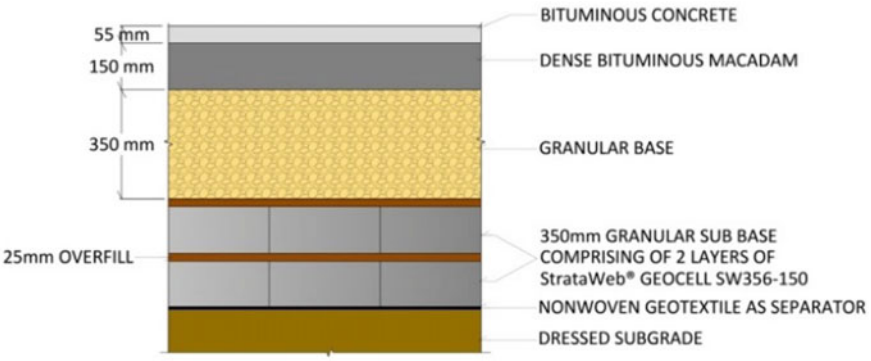

Fig. 18 Proposed section

Fig. 19 Heavy trailers being hauled over the unpaved road in extreme conditions

Fig. 20 Paved pavement in 2017, after the second spell of heavy monsoons

The pavement section was completed up to the 350-mm granular base component by 15 August 2016 in a record time of 15 days from start of work. Traffic was allowed to ply immediately on laying the compacted 350-mm granular base component for several reasons, the major being:

(1) The crisis did not merit any further delay of normal traffic flow;
(2) It was not prudent to lay the top two bitumen components during the continuing rain and wet conditions;
(3) Since the work was done under trying conditions, the behaviour of the road left unpaved was to be reviewed for a short period.

The procedure was successful, and Fig. 19 illustrates heavy vehicular traffic plying the unpaved pavement without any distress, notwithstanding wet conditions. This stretch of NH-44, after being paved has further withstood the heavy brunt of the 2017 monsoons also as shown in Fig. 20.

5 Conclusions

Geosynthetics are important facets of geotechnical engineering. This has been prompted by several inevitable factors that include:

(1) Rapidly depleting resources,
(2) Rigid environmental laws.

Besides, there is a dire need to use materials, which at one point of time were considered as waste. A significant example is pond ash, a waste from coal-fired power plants which is very useful for the construction of embankments and earth structures with steep slopes along with geosynthetics as reinforcement. Pavements can be designed using waste material such as slag and pond ash with appropriate geosynthetic reinforcement.

Construction with geosynthetics does not require any skilled labour and generally do not require any specialised construction equipment.

Geosynthetics and, in particular, geocells can be utilised for rapid construction of emergency roads as well as roads over difficult subgrades and terrain. The *CBR* value of the subgrade may be as low as 1%.

Conventional ground improvement techniques are proving to be time-consuming and costly. Application of appropriate geosynthetics into the system not only reduces time of construction but also prove to be cost-effective as capital costs.

Design of both components of the road, earth structures and pavements which have been designed and constructed with geosynthetics can ensure long life with minimum of maintenance. Geosynthetics per se can have a design life of over 100 years.

Analysis and design of flexible pavements with geogrids can also be carried out by the mechanistic-empirical method.

On considering life-cycle costs, earth structures and pavements with geosynthetic reinforcement score well over conventional designs.

The design and economics of a road with geosynthetics will need a holistic approach, considering the support structure (whether it is an earth embankment or a reinforced soil structure) and the pavement supported by the earth structure. Both design and economics need to consider short-term and long-term performance. In the choice of geosynthetic material, the relative effective performance is the prime consideration. As can be seen from the NH-44 case study, cost was a secondary criterion, whereas getting the highway functional at the earliest was the need of the hour.

References

Almeida MS, Marques MES (2013) Design and performance of embankments on very soft soils. CRC Press/Balkema, Taylor and Francis Group

Bagli SP (2017a) Geosynthetic applications in pavement construction. In: New Building materials & construction world—March 2017, pp 116–126

Bagli SP (2017b) Diverse applications of geocells for highways—two case studies from the North East. In: IGC 2017 GeoNEst, Indian National conference—Dec 2017, IIT, Guwahati

Bathurst RJ, Rajagopal K (1993) Large scale triaxial compression testing of geocell-reinforced granular soils. Geotechn Test J GTJODJ 16(3):296–303

Basu C, Soni JK (2013) Design approach for geocell reinforced pavements. Highw Res J (July–December)

Mane AS, Satav M, Bagli SP (2015) PVDs for progressive development of shear strength of soft plastic soils in foundations for reinforced soil structure—case study. In: 5th Indian young geotechnical engineers conference—March 2015, Vadodara

Rajagopal K, Veeraragavan A, Kief, O, Chandramouli S (2011) Modulus improvement factor for geocell-reinforced bases. In: Geosynthetics India'11, 23–24 Sept 2011, IIT Madras, Chennai

Schuettpelz CC, Fratta D, Edil TB (2011) Evaluation of the zone of influence and stiffness improvement from geogrid reinforcement in granular materials. Transp Res Rec J Transp Res Board. Dec 2009, USA

Zornberg JG (2012) Geosynthetic-reinforced pavement systems. In: Proceedings, keynote lectures & educational sessions, 5th European geosynthetics congress, Valencia

Design Methods for Base Stabilization of Paved Roads

Pietro Rimoldi

Abstract Stabilization is a peculiar function of geosynthetics where the geosynthetics limit the horizontal and vertical deformations of a soil mass by developing lateral confinement through friction and/or interlocking. The stabilization function is widely used for improving the performance of the base and/or subbase of paved and unpaved roads. When installed at the bottom or within a base and/or subbase course, geosynthetics for stabilization afford to (1) increase the service life and/or (2) decrease the required layer thickness. The GMA White Paper (Berg et al. in Geosynthetic reinforcement of the aggregate base/subbase courses of pavement structures; Geosynthetic Materials Association, Roseville, MN, USA, 2000) and AASHTO R50-09 suggest that the improvement to the pavement system provided by geosynthetic can be designed based on modified AASHTO Guide for Design of Pavement Structures (Guide for design of pavement structures; American Association of State Highway and Transportation Officials, Washington, DC, USA, 1993) method by using a traffic benefit ratio (TBR) or base course reduction (BCR), or layer coefficient ratio (LCR) approach. These three approaches may lead to different design for the same road section, applied traffic, and boundary conditions. The latest AASHTO 2008 guidelines call for mechanistic–empirical design of paved roads: Design methods for base stabilization according to AASHTO 2008 are still under development. The paper is aimed to present the four different approaches and to compare the design resulting from their application. The differences in theory and practical results are finally used to provide recommendations for the selection of the most suitable approach and for evaluating the reasons of potential discrepancies when designing with different methods.

Keywords Base stabilization · Geogrids · Design methods

P. Rimoldi (✉)
Consultant, Milano, Italy
e-mail: pietro.rimoldi@gmail.com

R. Sundaram et al. (eds.), *Geotechnics for Transportation Infrastructure*, Lecture Notes in Civil Engineering 28, https://doi.org/10.1007/978-981-13-6701-4_3

1 Introduction

The experience of the last 30 years has shown that geosynthetics used for the stabilization function afford several advantages when compared to traditional materials:

- Material quality control: Geosynthetics are produced in a factory under strictly controlled conditions to minimize material variation and ensure constant properties.
- Cost savings: The overall cost of geosynthetics for purchase, transport, and installation usually affords large saving due to decreased thickness of aggregates.
- Engineered performance: The performance of geosynthetics has been specifically engineered for each specific function and application.
- Fast and easy installation: Installation of geosynthetics is fast and easy, without requiring specialized workers; moreover, geosynthetics can be laid in all seasons and even under bad weather conditions. A single crew can install thousand square meters in one day, while other crews carry out the earthworks.
- Space savings: Geosynthetics are supplied in rolls, usually wrapped in protective film, which can be stacked in limited space even outside at the construction site.
- Quick availability: The fast production rates and the network of local suppliers allow to get on time shipping of geosynthetics to job sites.
- Environmental sustainability: Geosynthetics systems have proven to afford a much lower carbon footprint when compared to traditional materials like soil and concrete.

Road pavements are affected by many factors which can reduce the expected service life: increased heavy traffic, subgrade modifications, water infiltration, increased rainfalls, and post-construction activities. Such factors may require increased maintenance, quicker resurfacing, excavations, and modifications of the original design.

The strategies for improving long-term road and pavement performance include modification of the subgrade, stabilization of road base/subbase, drainage systems, and asphalt reinforcement.

One of the most effective options, which should be considered since the design stage, is the stabilization of base and/or subbase with geosynthetics.

Permanent road pavements include bound layers (wearing course, binder, bituminous base) which shall withstand the stresses produced by traffic and unbound layers (base, subbase) which shall provide the required bearing capacity. When the road is built on weak and soft subgrade, the bearing capacity of the unbound layers and the traffic stress resistance of bound layers can quickly deteriorate due to horizontal and vertical deformations produced by the cyclic and dynamic wheel loads, and the self-weight of all pavement layers.

In these cases, possible solutions consist in excavating and replacing the subgrade to a certain depth, or in modifying the subgrade properties by adding cement, lime, or frictional aggregate. But such solutions are usually expensive and require long working time.

Base stabilization can be considered as the primary function of geosynthetics in paved road applications. The inclusion of one or more stabilizing geosynthetics produces a soil-geosynthetic-aggregate (SGA) which combines the compressive resistance of soil with the strain limitation provided by geosynthetics. The SGA system provides important benefits:

– lateral confinement of the base/subbase aggregate;
– increased stiffness of the base/subbase;
– increased load spreading angle;
– consequent reduction in vertical and shear stresses on the subgrade.

Geosynthetics are commonly used in roadway systems, including geotextiles, geogrids, drainage geocomposite, geomembranes, and erosion control products. Each geosynthetic fulfills one or more specific functions such as separation, filtration, stabilization, drainage, containment, and fluid barrier. Specifically, the three most common functions needed within a flexible pavement cross section are:

Separation: to avoid contamination between adjacent dissimilar soils (i.e., aggregate base layer over fine-grained subgrade soil) and is commonly achieved using geotextiles. Key design aspect is product survivability during installation.

Filtration: The geosynthetic separates two adjacent soils and allows for adequate fluid flow across its plane while limiting soil migration. It is commonly achieved using geotextiles with specifically designed permeability and opening size.

Stabilization: The geosynthetic limits the horizontal and vertical deformations of a soil mass by developing lateral confinement through friction and/or interlocking. By reducing deformations, the geosynthetic will add load-carrying capacity to the pavement system. Woven geotextiles and geogrids are commonly used as stabilization inclusions.

It has to be noted that for a long time, the function of stabilization has been confused with that of reinforcement, but in 2015 ISO 10318-1 (ISO 2015) recognized stabilization as a separate function from reinforcement.

Hence in this paper, reference will be made to stabilization only.

For stabilization purpose, the tensile stiffness and the interface properties (interlocking capacity, surface friction) of the geosynthetic are the most important properties. Since the wheel load is spread in the plane, geosynthetics for stabilization should have high tensile strength at low strains in biaxial or multiaxial directions; moreover, geogrids work mainly by interlocking, while geotextiles work only by surface friction for producing lateral restraint of the aggregate (see Fig. 1).

Biaxial high modulus geogrids are produced by an extrusion or weaving/knitting process characterized by a tensile resistance both in the longitudinal and transversal directions. The biaxial geogrid structure is characterized by sufficiently large apertures to allow positive interlocking with the granular soil. For paved roads, mainly biaxial geogrids are used for reducing the deformations of the road pavement structure which may occur when the subgrade is very weak.

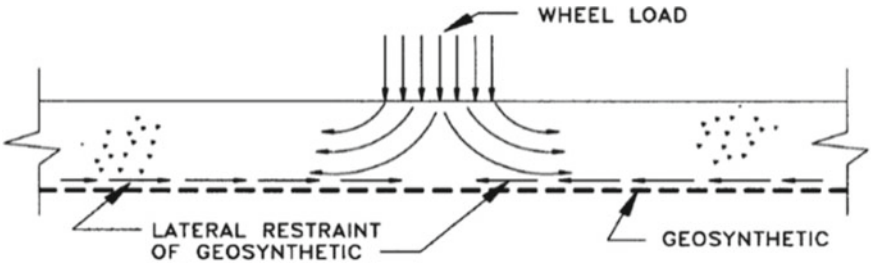

Fig. 1 Base course lateral restraint mechanism

The present paper deals with geosynthetic stabilization of the base and/or subbase of a flexible permanent pavement structure. Base stabilization in low-volume temporary and unpaved roads, commonly designed following empirical design methods, will not be directly discussed in this paper.

Base stabilization occurs when a geosynthetic is placed within the base layer for limiting lateral deformations, with the objective of: (1) increase pavement service life and/or (2) reduce the structural pavement section while keeping equivalent performance.

Base stabilization deeply differs from typical soil reinforcement in earth retention structures: systems are designed for stabilization under service conditions and not failure condition, by minimizing excessive distress, and relevant material properties correspond to small displacement conditions.

The mechanism by which geosynthetics provide base stabilization is historically called base course lateral restraint or shear-resisting interface (Perkins 1999a). Vehicular loading applied to the pavement surface induces a lateral spreading motion of the aggregates away from the wheel path creating tensile lateral and vertical compressive strains within the base, leading to rutting (Fig. 1). By placing a geosynthetic within or at the bottom of the base layer, the lateral tensile stresses are transmitted from the aggregate to the geosynthetic either through friction or interlocking. Thus, inducing tension in the geosynthetic (which, thanks to its relatively high stiffness, creates a tensile- and shear-resisting interface that confines the aggregates interacting with the geosynthetic and therefore retards and reduces the development of lateral tensile strains), the resulting lower lateral strain leads to lower rutting.

The increase in the confinement of the aggregates immediately adjacent to the geosynthetics also leads to an increase in stiffness of the base aggregate layer, which in turn leads to a broader and more uniform distribution of the vertical stress on the subgrade (Perkins and Edens 2003). The benefits of the interaction between the geosynthetic and the base layer are therefore directly reflected on the subgrade, which is subjected to both less lateral strain and less vertical stress, leading to lower rutting in the subgrade.

One more stabilization mechanism is often described in the literature: the tension membrane effect. However, large vertical, out-of-the-plane, deformations are

required to mobilize the geosynthetic strength with such mechanism, and therefore, it is more pertinent to unpaved temporary roads than to permanent paved roads.

Intuitively, understanding the soil–geosynthetic composite behavior mainly under small displacements is essential to properly design a geosynthetic-stabilized base layer. The interaction between the geosynthetic and the soil will therefore govern the performance of geosynthetic-stabilized base layer. Specifically, several studies have been carried out to identify the specific geosynthetic properties with the largest impact on the stabilization performance, such as tensile strength, junction strength and stiffness, geosynthetic geometry (i.e., geogrid aperture size), geosynthetic modulus, and others. However, given the wide variety of geosynthetic products, it is the author's opinion that further research is needed to confidently identify key parameters and minimum values for geosynthetic material properties directly associated with good performance of geosynthetic-stabilized pavement systems.

2 Base Stabilization Design Methods in Paved Road

2.1 Modified AASHTO (1993) Methods

In North America, the state of practice for the design of flexible paved roads with geogrid stabilization in the base layer is according to the AASHTO Guide for Design of Pavement Structures (AASHTO 1993), which has been aligned with the requirements of the AASHTO standard practice document R50-09 (AASHTO 2013). The AASHTO design method was developed in the early sixties based on the AASHO Road Test and later revised multiple times until the final version in 1993.

The AASHTO method uses empirical equations based on multilayer elastic theory to model the pavement cross section. The structure is characterized by a structural number (SN) that reflects the combined structural capacity of the flexible pavement to carry a predefined traffic load. During the design process, the SN value allowing the cross section to support the anticipated traffic load with a loss in serviceability within the project requirements needs to be calculated. The required SN value is determined by solving the following performance equation:

$$\log W_{18} = Z_R S_0 + 9.36 \log(\mathrm{SN}+1) - 0.2 + \frac{\log\left(\frac{\Delta \mathrm{PSI}}{2.7}\right)}{0.4 + \frac{1094}{(\mathrm{SN}+1)^{5.19}}} + 2.32 \log M_R - 8.07 \quad (1)$$

where W_{18} = number of 80 kN single-axle load applications over the design life of the pavement, Z_R = standard normal deviate, S_0 = standard deviation, ΔPSI = allowable loss in Present Serviceability Index, and M_R = resilient modulus of the subgrade.

The required SN shall be obtained by summing up the contribution of all pavement layers, according to Eq. (2):

$$SN = a_1 D_1 + a_2 D_2 m_2 + a_3 D_3 m_3 \tag{2}$$

where a_1, a_2, and a_3 = layer coefficients of surface, base, and subbase, respectively (relative strength of the layer), D_1, D_2, and D_3 = thicknesses of surface, base, and subbase layers, respectively, and m_2 and m_3 = drainage coefficients of base and subbase.

According to the GMA White Paper (Berg et al. 2000), the structural contribution of geosynthetics, intended as geogrids and woven/knitted geotextiles only, to the overall structural capacity of the pavement structure can be included in the design through three factors:

- Traffic bearing ratio (TBR): ratio of number of load applications of the geosynthetic-stabilized section over the number of load applications of the unstabilized section with the same geometry, material, and same defined failure state.
- Base course reduction factor (BCR): percent reduction in the thickness of the geosynthetic-stabilized base layer compared to an unstabilized one.
- Layer coefficient ratio (LCR): ratio of the layer coefficient of the geosynthetic-stabilized base layer over the layer coefficient of the unstabilized one.

Each of these three factors is derived from empirical data specific to each geosynthetic product. It means that each of these parameters needs to be determined from laboratory and field tests carried out by each manufacturer. Specifically, full-scale test trials independently certified are generally required to properly justify the data and to identify the geosynthetic benefits.

As suggested by AASHTO R50-09, when designing a geosynthetic-stabilized pavement structure, one of the first steps is assessing the target benefit of using a geosynthetic in terms of service life, reduction in base thickness or both. This leads the designer to choose whether to apply the traffic benefit ratio (TBR), or the layer coefficient ratio (LCR), or the bearing capacity ratio (BCR) approach.

When using the TBR, Eq. (1) can be modified as shown in Eq. (3) to evaluate the increased total number of equivalent single-axle load (ESAL) due to the beneficial effect of the geosynthetics (Perkins et al. 2012):

$$TBR = W_{18,\,\text{stabilized}} / W_{18,\,\text{unstabilized}} \tag{3}$$

The TBR improvement factors for a given set of pavement design conditions are calculated from regression equations supported by various experimental studies involving the evaluation of laboratory-scale and full-scale test sections. Typical TBR values range from 1.5 to 10 for geotextiles and 1.5–70 for geogrids.

TBR can be used to either extend the performance period of the pavement structure by direct use of Eq. 3 or to reduce the base course thickness for an equivalent performance period as the unstabilized pavement. The latter is accomplished by

solving for the structural benefit of the base giving a particular TBR and using this benefit to reduce the base thickness to yield the same traffic level as the unstabilized pavement.

On the other hand, if the design target is to reduce the base layer thickness, then the BCR approach can be followed. BCR is defined as:

$$\mathrm{BCR} = 1 - \frac{D_{\mathrm{stabilized}}}{D_{\mathrm{unstabilized}}} \tag{4}$$

where $D_{\mathrm{stabilized}}$ and $D_{\mathrm{unstabilized}}$ are the required base/subbase thickness with or without stabilization.

Hence, Eq. (2) can be modified as:

$$\mathrm{SN} = a_1 \cdot D_1 + \frac{1}{1 - \mathrm{BCR}_2} D_{2,\mathrm{BCR}} \cdot a_2 \cdot m_2 + \frac{1}{1 - \mathrm{BCR}_3} D_{3,\mathrm{BCR}} \cdot a_3 \cdot m_3 \tag{5}$$

where $D_{2,\mathrm{BCR}}$ and $D_{3,\mathrm{BCR}}$ are the reduced thicknesses of base and subbase when the BCR_2 and BCR_3 coefficients are applied.

Therefore, when only the base layer is stabilized, the reduced base layer thickness can be calculated as follows:

$$D_{2,\mathrm{BCR}} = \frac{\mathrm{SN} - a_1 \cdot D_1 - a_3 \cdot D_{3,\mathrm{BCR}} \cdot m_3}{\mathrm{BCR}_2 \cdot a_2 \cdot m_2} \tag{6}$$

Typical base course thickness savings range between 20 and 30% for geotextiles and 30–50% for geogrids, resulting in BCR = 0.2–0.3 for geotextiles and BCR = 0.3–0.5 for geogrids.

The design approach of the LCR is afforded when the coefficient is directly applied to Eq. (2) to implement the benefit of the stabilizing geosynthetic into the design method to reduce the base layer thickness. However, LCR is calculated from field test results as the ratio of layer coefficients instead of layer thicknesses. Therefore, it represents the impact that a specific geogrid provides to the layer coefficient of the layer in which the geogrid is placed. The performance benefits are therefore implemented in the design method as follow:

$$\mathrm{SN} = a_1 \cdot D_1 + (\mathrm{LCR}_2 \cdot a_2) \cdot D_2 \cdot m_2 + (\mathrm{LCR}_3 \cdot a_3) \cdot D_3 \cdot m_3 \tag{7}$$

LCR is usually obtained and plotted as a function of the CBR of the layer below, and hence, for the same geogrids, two different LCR values shall be used for base (having subbase below) and subbase (having subgrade below).

Following this method, the designer may quantify the performance benefits of the stabilizing geogrid through both the increase in service life (i.e., number of ESAL) and decrease in layer thickness required.

The standard practice for all these three approaches is very empirical in nature and relies on the experience of the designer and the published data from the manufacturer on full-scale test results to determine the performance benefit coefficients.

By comparing Eq. 5 with Eq. 8, the relationship between LCR and BCR is derived (Perkins et al. 2016):

$$\mathrm{LCR} = \frac{1}{1 - \mathrm{BCR}} \tag{8}$$

Instead, a simple relationship cannot be established between LCR or BCR and TBR.

All the three design methods predict an increase of benefit as the subgrade CBR decreases, and anyway, the three methods predict different levels of benefit, which is partly due to each method having been developed for a particular geosynthetic and partly due to each method being calibrated from different experimental studies.

TBR appears to limit the geosynthetics benefit below a subgrade CBR of 3, whereas the other two methods show this benefit to continue to increase.

There are three principal limitations associated with these methods (Perkins et al. 2016). The first involves the level of documentation associated with establishing the basis for the benefit values used in the methods. BCR and TBR do not provide adequate public documentation to allow the designer to judge the basis for the benefit values reported. LCR provides sufficient documentation, and however, the use of an unrealistic subgrade and the lack of consistency with field test sections raise some questions concerning the appropriateness of the benefit values reported.

A second limitation of LCR and BCR is the suggestion that a single benefit curve for a given geosynthetic product applies, that is a function of the subgrade strength or modulus, which is not dependent on other pavement configuration variables (Perkins et al. 2016). In fact, geosynthetics benefit is known to depend on the thickness of the asphalt concrete, base aggregate, and subbase, if present, the structural quality of these materials and the position of the geosynthetic within the base layer (Berg et al. 2000). TBR accounts for layer thickness, and however, the basis for this accounting could not be established.

The third limitation with these methods concerns the relatively high values of benefit predicted for subgrade strengths approaching and exceeding a CBR of 8. Berg et al. (2000) reviewed available studies and showed conflicting results regarding expected stabilization benefit for pavements on a subgrade with a CBR approaching 8. In general, the majority of studies tended to show diminishing benefit for subgrade strength approaching a CBR of 10. This leads to a recommendation of a subgrade with a CBR of 10 being the typical limit for expected stabilization benefit when the traffic is represented by ESAL. Anyway, experience has shown that important stabilization benefits are achieved even beyond a subgrade CBR of 10 when much higher axle loads than 80 kN are applied on the road structure.

2.2 MEPDG Methods

In 2008, the AASHTO officially adopted the Mechanistic–Empirical Pavement Design Guide (MEPDG). At the core of these methods lies a numerical response model capable of defining key stress and strain parameters for the pavement system. The response model is mechanistic in the sense that it is dependent on the mechanical properties of the individual pavement system constituents. Empirical damage models then use the stress and strain response parameters for defining the short- and long-term performance of the pavement system.

For inclusion of stabilization products within an M-E pavement design framework, mechanistic properties of materials of each pavement layer are input in the design method. Therefore, the M-E platform may be considered as better suited to incorporate the benefits of geosynthetic stabilization. In the presently available models, geosynthetic stabilization is usually incorporated as an equivalent resilient modulus and Poisson's ratio. However, depending on the asphalt layer thickness, the geosynthetic effect could be introduced as a modification of the properties of the base course through an equivalent delay in the development of fatigue cracking. Therefore, the benefits of the stabilizing geosynthetic have not been consistently defined (Perkins et al. 2012). The proper use of the M-E methods with geosynthetics for stabilization would require the definition of rut and fatigue laws for stabilized roads, which would require extensive testing on stabilized sections.

M-E modeling approach (Perkins and Edens 2003) was used to develop a design model based on results from a parametric study using the M-E model (Perkins 2001a, b). The M-E model consisted of a finite-element (FE) response model and empirical damage models and was calibrated from test sections described by Perkins (1999a, b). This facility (Perkins and Edens 2011) consisted of a 2 m by 2 m by 1.5 m deep reinforced concrete box in which the roadway cross section was constructed and loaded by 40 kN applied cyclically at a period of 1.5 s to a 304-mm-diameter steel plate resting on a waffled rubber pad in turn resting on the asphalt concrete surface. A 3D model was used to account for the potential influence of the box's square corners and for the geosynthetic inclusion that has direction-dependent material properties. Symmetry of the box was recognized such that a model of one-quarter of the box was created. Figure 2 illustrates the geometry of the model. Layer thickness was varied for the parametric study performed.

The model used elasto-plastic constitutive models for the majority of the pavement layers. The bounding surface plasticity model described by Dafalias and Hermann (1986) was used to account for the positive effect of aggregate confinement on the increase in stiffness and strength of the base course aggregate. An orthotropic linear elastic model was used for the geosynthetic. Anisotropy was included to account for differences in elastic modulus between machine and cross-machine directions and allowed for specification of the in-plane shear modulus and in-plane Poisson's ratio (Perkins and Edens 2011).

The M-E model was used in a parametric study involving over 465 analyses of various pavement cross sections and properties. The damage models were formulated

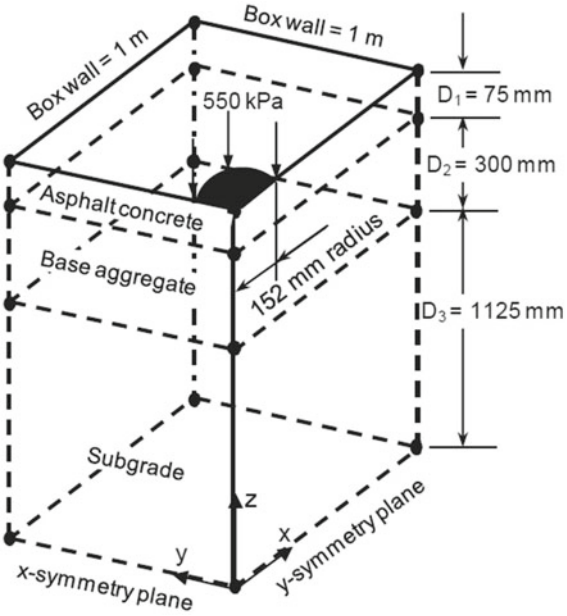

Fig. 2 Finite-element model for the Perkins and Edens (2003) model

to provide a value for extension of roadway service life, defined by a traffic benefit ratio (TBR) for each case analyzed. The model therefore consisted of a series of regression equations used to predict stabilization benefits for a given set of pavement design conditions.

Regression equations were developed between TBR and the variables contained in the parametric study.

Later a more advanced model was developed, which also allowed the comparison between the M-E model and the Modified AASHTO (1993) methods: The mechanistic–empirical model by Perkins et al. (2009) was based on a project reported by Perkins et al. (2004). The model uses features for the conventional pavement layers which include material and damage models for the bound (asphalt concrete) and unbound (base and subgrade) layers and a finite-element response model for the pavement cross section.

The finite-element response model used an elastic perfectly plastic model for the asphalt concrete. An elastic–plastic bounding surface plasticity model was used for the base aggregate and subgrade soil layers. An orthotropic (direction-dependent) linear elastic model was used for the geosynthetic. Anyway, for the geosynthetic, the finite-element response model requires the use of a single isotropic elastic modulus. This property is determined from a method described by Perkins and Eiksund (2005) involving the elastic tensile modulus in the machine and cross-machine directions (by wide-width tensile test according to ASTM D4595 2015 or ISO 10319 2015), in-plane Poisson's ratio from biaxial tests, and an in-plane shear modulus from aperture stability modulus tests (ASTM D7894 2015). The upper and lower surfaces of the

Table 1 Resilient modulus and CBR for subgrade soil

Case	1	2	3	4	5	6
M_R (MPa)	5.3	10	20	42	84	154
CBR	0.5	1	2	4	8	15

geosynthetics were set up to be contact surfaces. Shear interaction along each contact surface was described in terms of a Coulomb friction model having pertinent material properties of the coefficient of friction and an elastic slip parameter, which describes the interface shear stiffness or modulus, which was evaluated from cyclic pullout tests (modified ASTM D6706-01 2013).

The response model was a full three-dimensional model established to match the conditions present in test sections (Perkins 1999a, b) for which the M-E model was calibrated against. The 3D model was also necessary to allow for the inclusion of a direction-dependent material model for the geosynthetic.

The elastic–plastic properties chosen for the asphalt concrete are represented by the resilient modulus of approximately 2500 MPa, which represents a layer coefficient a_1 of 0.40 used in AASHTO (1993) pavement design guide and was based on an average value of resilient modulus from tests performed on asphalt concrete cores from test sections. The elastic–plastic properties of the base aggregate were calibrated from triaxial tests performed on material from test sections. This model and these properties were then used to simulate a resilient modulus test. The resilient modulus, M_R, determined from these simulations was plotted against bulk stress, θ. A commonly used expression in pavement engineering (Eq. 9) was fit to the data.

$$M_R = k_1 \cdot \vartheta^{k_2} \tag{9}$$

Best fit values for constants k_1 and k_2 were 4460 and 0.63 when M_R and θ are in units of psi. According to AASTHO (1993) guide, these values correspond to a typical base aggregate in a damp condition. For a typical value of θ equal to 138 kPa (20 psi), the resilient modulus obtained corresponds to a layer coefficient a_2 of 0.14 used in AASHTO (1993) guide. Six sets of elastic–plastic properties for the subgrade soil were used to represent a subgrade of varying stiffness and strength. The material model and each set of properties were used to simulate a resilient modulus test. Table 1 provides a summary of the resilient modulus determined from these simulations. Equation 10 was used to relate resilient modulus to subgrade CBR strength, where M_R must be in units of psi.

$$M_R = 1500\,\mathrm{CBR} \tag{10}$$

The orthotropic linear elastic model used for the geosynthetic afforded the specification of four properties controlling the mechanical behavior of this component of the pavement system: the elastic tensile modulus in the two principal directions of the material (i.e., machine and cross-machine), the Poisson's ratio between these

two directions, and the shear modulus between these two directions (Perkins et al. 2012). The first two properties can be related to properties determined from existing tension testing methods (i.e., ASTM D4595 2015 or ISO 10319 2015). Existing testing specifications allowing for the determination of the last two properties do not currently exist. As shown below, these properties have an influence on the mechanical behavior of the geosynthetic modeled by this technique and have a moderate impact on predicted pavement performance.

The parametric study involved the variation of tensile modulus in the strong direction of the geosynthetic and the ratio between the tensile modulus in the weak and strong directions.

Given the lack of suitable testing methods for the determination of values for Poisson's ratio and shear modulus, only two extreme values for each parameter were examined. Values of 0 and 0.5 were used for Poisson's ratio. Values of shear modulus were either 0 or values pertaining to an isotropic material. Membrane elements were used for the geosynthetic. These elements are capable of carrying load in tension but have no resistance to bending or compressive stresses. The nodes on the geosynthetic were equivalenced with those of the surrounding base and subgrade. Initially, contact interface surfaces between the aggregate and the geosynthetic and between the subgrade and the geosynthetic were used. Misleading results were possible, however, for the types of response measures extracted from the model. In addition, no suitable method currently exists for the determination of small displacement shear interface stiffness, as is needed in this modeling application. The effect of varying interface properties is therefore accounted for empirically by comparison of model predictions to test section results.

In addition to the variation of subgrade and geosynthetic properties, the thicknesses of the asphalt concrete and base aggregate layers were varied. Variation of these parameters resulted in the analysis of over 465 cases. For each stabilized case, an identical unstabilized pavement was analyzed. For each analysis, the vertical compressive strain in the top of the subgrade and a weighted average of bulk stress for a representative volume of the base aggregate were extracted as response parameters (Perkins and Edens 2011).

Empirical damage models were formulated to use the two response parameters described above. The first damage model is known as a subgrade rutting criterion and is:

$$N_{12.5\,\mathrm{mm}} = A \cdot \varepsilon_{\mathrm{V}}^{-B} \tag{11}$$

where $N_{12.5\,\mathrm{mm}}$ is the number of traffic loads necessary to reach 12.5 mm of pavement deformation, ε_{V} is the vertical compressive strain at the top of the subgrade, and A and B are material parameters (Huang 1993). Parameters A and B were calibrated from test sections and were found to be 1.8×10^{-5} and 4.07, respectively.

The ratio of traffic loads given by Eq. 11 for equivalent stabilized (S) and unstabilized (U) pavement sections provides a direct definition of TBR (Eq. 3). For this

damage model, stabilization results from effects in the subgrade, meaning this TBR is viewed as a partial TBR for subgrade effects (TBR_S):

$$TBR_S = \left(\frac{\varepsilon_{V-S}}{\varepsilon_{V-U}}\right)^{-B} \tag{12}$$

The bulk stress response parameter was determined for comparative stabilized and unstabilized sections. The bulk stress was used in Eq. 9 to calculate a base aggregate resilient modulus for each case. These values were then used in AASHTO (1993) flexible pavement design Eq. (1), with all other parameters being equal, to determine the ratio of traffic loads between the stabilized and unstabilized sections. This TBR was viewed as a partial TBR for stabilization effects in the base layer and is denoted as TBR_B. Total TBR for the stabilized pavement is then computed from Eq. 13:

$$TBR_T = TBR_S \cdot TBR_B \tag{13}$$

These values of TBR correspond to no reduction in base aggregate thickness and are denoted as $TBR_{BCR=0}$ (Perkins and Edens 2011).

Computed values of TBR_S and TBR_B from the M-E model were related to the parametric study variables through a series of regression equations, which form the basis of the design model.

The design model was calibrated from the test section results described by Perkins (1999a, b). This involved the empirical adjustment of the geosynthetic elastic tensile modulus used in the response model from reported values of wide-width tensile modulus measured at 2% axial strain, where the latter is used as an input parameter to the model. Similarly, an empirical reduction factor for interface shear resistance was developed by comparison of design model predictions to test section results. This resulted in a reduction factor of 1.0 for the geogrids used in this study and 0.765 for the geotextile used.

Values of TBR from the design model were then used to compute a base course reduction ratio (BCR) defined as the percentage reduction in base course aggregate for equivalent service life. Computed values of BCR for equivalent service life are denoted as $BCR_{TBR=1}$. Combined values of TBR and BCR were computed based on a selection of either TBR or BCR between the ranges of $1 \leq TBR \leq TBR_{BCR=0}$ and $0 \leq BCR \leq BCR_{TBR=1}$. These selections imply that if values of TBR or BCR less than the full values are used, then there remains a surplus benefit that can be expressed in terms of the other benefit parameter (Perkins and Edens 2011).

These steps necessary to compute BCR were accomplished following the guidelines provided by Berg et al. (2000). This involves the use of TBR to define the increased number of traffic loads that can be applied to a stabilized section of the same structural thickness as an unstabilized section. Within the context of AASHTO (1993) pavement design guide, this is used to define the increased base aggregate structural layer coefficient of the stabilized pavement. This in turn is used in AASHTO (1993) method to determine a reduced stabilized base thickness having this increased

Table 2 Design model input parameters

Parameter	Description
D_1	Asphalt concrete thickness (mm)
D_2	Base aggregate thickness (mm)
CBR	Subgrade CBR (unitless)
$G_{SM\text{-}2\%}$	Geosynthetic secant tensile modulus @ 2% strain (kN/m)
G_{MR}	Geosynthetic secant tensile modulus ratio (unitless)
R_S	Reduction factor for geosynthetic interface shear resistance
R_v	Reduction factor for geosynthetic Poisson's ratio (unitless)
R_G	Reduction factor for geosynthetic shear modulus (unitless)

layer coefficient, or some other base thickness yielding a remaining increase in service life. This method was validated by comparison of predictions made from the M-E model where it was observed that conservative estimates of BCR and combined TBR/BCR benefit values are produced.

The design model contains three principal input parameters describing the unstabilized pavement cross section and five parameters describing the geosynthetic. These parameters are listed along with a brief description in Table 2. Additional details and typical values for these parameters can be found in Perkins (2001a, b). This report also contains information concerning the input of parameters describing the structural and drainage characteristics of the asphalt concrete and base layers and provisions for the inclusion of a subbase layer.

Output from the design model consists of values of TBR_S, TBR_B and TBR_T, and values of BCR for each value of TBR. The design model also computes remaining values of TBR or BCR for specified input values of BCR or TBR, respectively.

The design model has been implemented into a spreadsheet-based program and was used to generate results shown in Fig. 3, which illustrates the effect of subgrade CBR on values of TBR and BCR where it is seen that stabilization benefits are more significant for weaker subgrades and become negligible for subgrade CBR values greater than 8.

The model also predicts decreasing benefit as asphalt concrete and base aggregate thickness increase. These results are consistent with observations from a variety of test sections (Berg et al. 2000).

All results were for an asphalt concrete thickness of 75 mm, a base thickness of 300 mm, and a subgrade CBR of 1.5.

Although this M-E model was complex and used high-level constitutive laws for the various materials, including geosynthetics, yet it did not provide satisfactory results when compared with physical testing.

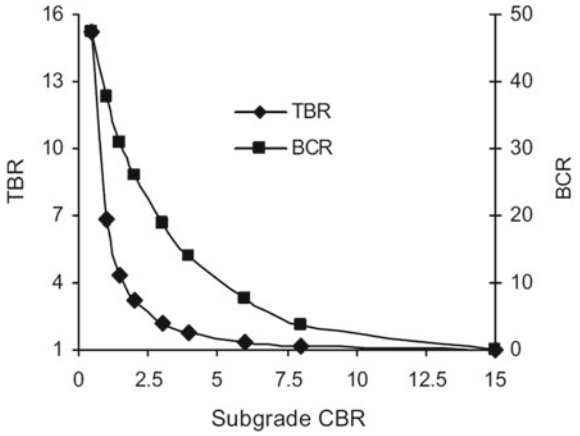

Fig. 3 TBR and BCR versus subgrade CBR

The above-described model was later improved by Perkins et al. (2011): the response model now uses a linear elastic model including temperature and loading rate effects for the asphalt concrete and nonlinear elastic models for the unbound aggregate and subgrade layers. The nonlinear model (Perkins et al. 2012) expresses the resilient or elastic modulus of the material, M_R, as a function of bulk stress, θ, and octahedral shear stress, τ_{oct}, and material parameters k_1, k_2, and k_3 (Eq. 14), where the parameter p_a is taken as atmospheric pressure:

$$M_R = p_a k_1 \left(\frac{\theta}{p_a}\right)^{k_2} \left(\frac{\tau_{oct}}{p_a} + 1\right)^{k_3} \tag{14}$$

The damage model used for definition of pavement permanent surface deformation expresses the accumulated permanent vertical strain, ε_p, at a point in the pavement layer as a function of the vertical resilient strain, ε_r, determined from the response model, the number of load cycles, N, material parameters A and B, and a field calibration factor, β (Eq. 15):

$$\varepsilon_p = \varepsilon_r \beta A N^B \tag{15}$$

The damage model calculations explicitly include seasonal variations of material properties (e.g., temperature influences on asphalt concrete stiffness, freeze/thaw variations in unbound material properties). Traffic loading is modeled using a traffic load spectrum in which the traffic mix and volume may also vary over time. Field calibration of the damage models is still underway.

Several features of the model have been examined to determine how geosynthetic products should be included as structural components in the design procedure. In addition to the model described by Eq. 15, four other material models for the unbound pavement layers have been examined to determine the level of material model complexity needed to illustrate the stabilization effects.

The first model is similar to Eq. 15 but includes anisotropy such that a horizontal modulus of the base aggregate layer that is less than the vertical modulus can be specified. This feature not only has the potential to more accurately model pavement response (Adu-Osei et al. 2001) but may allow for a greater contribution from the geosynthetics.

A nonlinear isotropic hyperelastic model (Hoff et al. 1998) that includes the recoverable dilatancy during each load cycle has been examined. The model has three parameters: Young's modulus, Poisson's ratio, and a dilatancy factor D. The dilatancy effect is proportional to the product of D and the shear strain.

Thus, in agreement with observations from triaxial test results, the dilatancy effect increases at increasing cyclic shear stress.

A Mobilized Friction Model, MFM (Nordal et al. 1989), which is an isotropic elasto-plastic soil model, have been examined. The model allows for full dilatancy control and can model any observed stress–strain curve including the continuous development of dilation.

Finally, Boyce (1980) models have been examined. In this model, the bulk and shear moduli are both functions of the mean normal stress and the shear stress and allow for modeling of dilatant behavior.

Various methods have been examined for how the geosynthetic and its interaction with the surrounding material should be numerically modeled. It was envisioned that the response model would have the added feature of a layer of membrane elements representing the geosynthetic with a contact interface on both sides of the membrane. It was anticipated that the inclusion of a stabilization layer in the numerical response model would result in lateral restraint of the base aggregate and subgrade material, an increase in bulk stress in the aggregate layer leading to an increased stiffness of this layer, a reduction in octahedral shear stress in the subgrade layer leading to an increased resilient modulus, a reduction of vertical stress on the subgrade, and a reduction of vertical resilient strain in the pavement layers. Use of this reduced resilient strain in the damage model given by Eq. 15 resulted in less permanent deformation for the pavement section for a given number of applied traffic loads.

Large-scale cyclic triaxial tests were performed on unstabilized and stabilized aggregate specimens to assess the effect of geosynthetics on the parameters contained in Eqs. 14 and 15. It was anticipated that geosynthetics have the effect of reducing the development of permanent strain for a given number of load cycles and hence affecting the values of parameters A and B in Eq. 15. Geosynthetics may also have the effect of increasing the resilient modulus through a shift in the k_1, k_2, and k_3 parameters contained in Eq. 14.

Various laboratory tests were performed on geosynthetics and geosynthetic–aggregate systems to define material properties appropriate for use in this application. These tests include wide-width and uniaxial tension tests under various loading rates and cyclic loading regimes, cyclic pullout tests to define a resilient shear interaction modulus, and confined tension tests to examine the dependency of geosynthetic tension modulus on normal stress confinement. These tests have been designed to provide material properties pertinent to small strain/small displacement conditions. The cyclic tension and cyclic pullout tests are designed to provide stress conditioning

prior to the measurement of material properties. Stress conditioning is a feature also inherent in resilient modulus testing of pavement and unbound aggregate materials where small strain stiffness parameters are sought.

Results from the design method have been compared to results from previously constructed test sections (Perkins et al. 2012) and new test sections. A complete set of laboratory pavement material tests were performed on the materials used in these test sections to provide the necessary input into response and damage models and other material models being used in the project.

The stabilized model showed only a modest (8.4%) increase in the number of traffic passes carried at a surface deformation of 25 mm (53,850 vs. 58,400 traffic passes). For this test section with this particular geosynthetic product, the stabilized test section was seen to carry approximately 600,000 load passes necessary to reach 25 mm of surface deformation (Perkins et al. 2005).

These results (Perkins et al. 2005) show the inability of simple and conventional methods for modeling stabilized sections and points to the need for additional considerations for stabilized response models that account for the effect of lateral restraint created during compaction and traffic loading of the pavement.

Previous work (Perkins et al. 2005) has shown that modeling the elastic response of a stabilized pavement simply using the components described above does not sufficiently account for the beneficial influence of the stabilizing geosynthetics on pavement response. It is commonly accepted that geosynthetic base stabilization results from confinement and restraint of the aggregate adjacent to the geosynthetics, which has recently been demonstrated experimentally (White et al. 2011). To account for this, response model modules were developed that simulate certain construction and traffic loading effects that the geosynthetics have on the pavement system.

2.2.1 Response Model Modules

Response model modules were developed that simulate certain construction and traffic loading effects that the geosynthetics have on the pavement system (Perkins et al. 2012). The nonlinear elastic material model used for the base aggregate and subgrade imposes certain limitations in rigorously modeling the effects of the geosynthetics.

This relatively simple constitutive model is insufficient for exactly describing the full sequential process of construction followed by the application of many repetitions of vehicular traffic (Perkins et al. 2012). Since the material model for the base aggregate shows improved performance through an increased elastic modulus arising from an increase in mean stress, the response model modules were developed to yield an increase in aggregate confinement during compaction and traffic loading. Hence, the response model modules show an increase in horizontal stress in the aggregate, which has a reasonable physical basis as supported by research (Perkins et al. 2012), yet the modeling methods for doing so are partially physically artificial but necessary given the limitations of the material models used.

The response model modules include a model describing effects during compaction and three response models used in succession and in an iterative manner

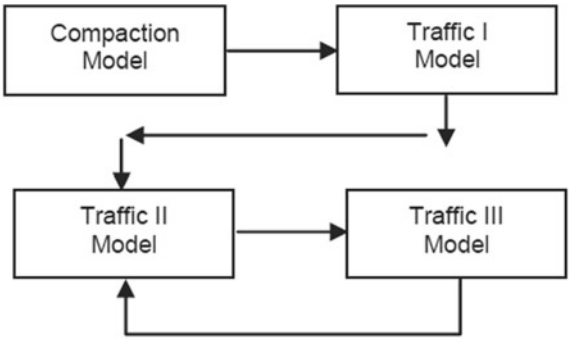

Fig. 4 Flowchart of response model modules. From Perkins et al. (2010)

to describe the effects of geosynthetics during traffic loading (Perkins and Cuelho 2008). Figure 4 provides a flow chart of these response models. The compaction and Traffic I response model modules are analyzed once for a given pavement cross section. The Traffic II and III models are analyzed a number of times to describe pavement response during different periods of the pavement life as the permanent strain is developed in the geosynthetics.

2.2.2 Compaction Model

Material presented above showed that locked-in horizontal stresses exist in aggregate layers compacted on top of a geosynthetic. From a response modeling perspective, greater lateral stresses at the beginning of analysis will mean that modulus of the material will be initially higher when nonlinear stress-dependent elastic material models are used (Perkins et al. 2012).

The principal effect of the geosynthetics during compaction is to limit lateral movement of the aggregate as compaction tends to compress and shove material vertically and laterally. On a local level, restraint is provided by aggregate interacting with and transferring load to the geosynthetics (Perkins et al. 2012). As compaction equipment is worked around on the aggregate layer, aggregate never assumes a predominant direction of motion, meaning that the creation of tensile strains in the geosynthetics may be negated and reversed when equipment operates in another location. The effect of this random process is to leave the aggregate with possibly a greater density but more importantly with locked-in horizontal stresses and the geosynthetic in a relatively strain-free state (Perkins et al. 2012). As such, the process should not be viewed as a geosynthetics pretensioning effect, which experimentally has not been shown to be effective. The tensile modulus of the geosynthetics is, however, important in this process in that it will contribute to the reduction in lateral movement of the aggregate during each pass of compaction equipment and will contribute to the buildup of locked-in horizontal stresses (Perkins et al. 2012). In addition, the contact properties between the aggregate and the geosynthetics are of

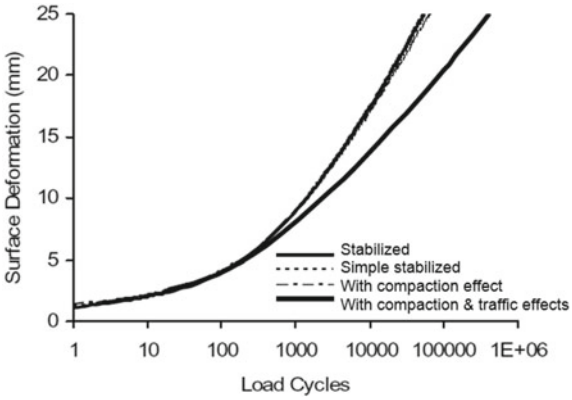

Fig. 5 Surface deformation versus load cycles for stabilized model with compaction- and traffic-induced initial stresses. Modified from Perkins et al. (2010)

importance with interfaces showing less shear stiffness leading to lower values of locked-in horizontal stresses (Perkins et al. 2012).

A simple procedure was sought to model this process within the context of a finite-element pavement response model (Perkins et al. 2012). Exact replication of this random and complex process is extremely difficult and unwarranted. The procedure developed involves assigning thermal contractive properties to the geosynthetic sheet and creating shrinkage of the material by applying a temperature decrease. This produces relative motion between the geosynthetic and the aggregate and essentially models in reverse and in a simplified way the complex effect of aggregate being shoved laterally back and forth during compaction. Once the temperature decrease has been applied, horizontal stresses at the element centroid are extracted from the model for a column of elements in the base along the model centerline (Perkins et al. 2012). These horizontal stresses, along with the geostatic vertical stresses due to material self-weight, are then used as the initial stresses for the entire base layer in a subsequent stabilized response model (i.e., the Traffic I model).

These steps provide a means of describing the locked-in horizontal stresses in the aggregate due to relative motion between the aggregate and the geosynthetics during compaction (Perkins et al. 2012).

To illustrate the effect of this step, a third analysis was performed by taking the stabilized model described previously and using the initial stress state for the base from the compaction model described above before applying pavement load (Perkins et al. 2005). Figure 5 shows the results from this analysis as compared to the previous two analyses. The stabilized model with the compaction-induced stresses results in 23% more traffic passes necessary to reach 25 mm of surface deformation (Perkins et al. 2005). While this is an improvement over the simple stabilized model, the result is still far below the benefit seen in this test section, indicating that additional considerations are needed.

2.2.3 Traffic I Model

In addition to an increased horizontal stress due to compaction of aggregate on top of a layer of geosynthetic, lateral confinement of the aggregate base layer develops during vehicular loading of the roadway (Perkins et al. 2005).

Additional lateral confinement is due to the development of interface shear stress between the aggregate and the geosynthetics, which in turn transfers load to the geosynthetics. As a cycle of traffic load is applied, there is both a transient or cyclic shear stress and residual shear stress that exists when the traffic load is removed. The residual interface shear stress continues to grow as repeated traffic loads are applied, meaning that the lateral confinement of the aggregate base layer becomes greater with increasing traffic load repetitions. The Traffic I response model module is used to provide data for the transient interface shear stress distribution between the geosynthetics and the surrounding materials (Perkins et al. 2005).

Experimental data from test sections where geosynthetics were instrumented show the development of permanent radial strain in the geosynthetics with traffic load applications. Experimental data and theoretical considerations with simplifying approximations have been made to show the equality between the ratio of permanent to resilient strain in the geosynthetics to the ratio of residual to transient shear stress on the geosynthetic–aggregate interface (Perkins and Svanø 2006). This leads to Eqs. 16 and 17 describing the residual shear stress on the interface as a function of traffic passes (Perkins et al. 2005).

$$\tau_r = \tau_t \frac{\varepsilon_p}{\varepsilon_r} \tag{16}$$

$$\log\left(\frac{\varepsilon_p}{\varepsilon_r}\right) = \log(A) + B \log\left(\frac{N}{N_{25\,mm}}\right) \tag{17}$$

where

τ_r	residual shear stress on interface
τ_t	transient shear stress on interface
ε_p	permanent strain in the geosynthetic
ε_r	resilient strain in the geosynthetic
$N/N_{25\,mm}$	ratio of actual traffic passes to passes necessary for 25 mm permanent deformation
A, B	interface shear stress growth parameters. Parameters A and B are currently calibrated from geosynthetic strain measurements in test sections.

The Traffic I module provides a means of determining the transient interface shear stress (τ_t) for use in Eq. 16. From this model, the interface shear stresses are extracted when full pavement load is applied (Perkins et al. 2012).

This interface shear stress distribution is taken as the values for τ_t as a function of model radius. The resulting shear stress distribution is then scaled by selected values of $\varepsilon_p/\varepsilon_r$, leading to new shear stress distribution curves representing different periods in the life of the pavement. Equivalent nodal forces are then calculated by

distributing the shear stresses over the contributory area of each node and used in the subsequent Traffic II model to examine the effects of this shear stress distribution (Perkins et al. 2012).

2.2.4 Traffic II Model

The Traffic II response model module gives the elevated horizontal stresses in the base due to compaction effects and for the additional locked-in stresses due to the increasing tensile strains in the geosynthetics with increasing traffic. This is accomplished by applying the nodal forces due to the residual interface shear stresses for a particular pavement life period from the Traffic I model to an unstabilized model having an identical cross section and pavement layer properties (Perkins et al. 2012).

The Traffic II model starts with an initial state of stress that comes from that determined in the compaction model. Nodal forces calculated from the Traffic I model analysis are then applied to nodes in the base at the same level where the geosynthetic was present. Once these nodal forces have been applied, the horizontal stresses at element centroids for the column of base aggregate elements along the model centerline are extracted (Perkins et al. 2012). These horizontal stresses along with the geostatic vertical stresses are then taken as initial stresses in a subsequent and final response model (i.e., Traffic III module).

The analysis using the Traffic II model is repeated for the number of $\varepsilon_p/\varepsilon_r$ ratios selected to determine equivalent nodal forces. Thus, the Traffic II analysis provides a means of assessing the effect of residual interface shear stresses on lateral stresses developed in the base aggregate layer for different periods in the life of the pavement within the context of a finite-element response model (Perkins et al. 2005).

2.2.5 Traffic III Model

The Traffic III model uses the same pavement response model as the Traffic I model but uses the horizontal stresses determined from the Traffic II model along with the geostatic vertical stresses as initial stresses. This model is run for the same number of Traffic II models evaluated. From each model, the distribution of vertical strain versus depth along the model centerline is extracted and used in conjunction with the damage models for permanent deformation to determine permanent surface deformation for the load cycles that apply to the period for which the $\varepsilon_p/\varepsilon_r$ ratios apply (Perkins et al. 2005).

For each data set of vertical resilient strain versus depth, the damage models for permanent deformation are used to determine a curve of permanent surface deformation versus traffic load applications (Perkins et al. 2005).

This curve is taken to apply to the load cycles ranging from the previous $\varepsilon_p/\varepsilon_r$ ratio to the current $\varepsilon_p/\varepsilon_r$ ratio (Perkins et al. 2005). A cumulative surface deformation curve is then computed by taking deformation that occurs for each period and accumulating it over the number of analysis periods. Figure 5 (Perkins et al. 2012) shows the

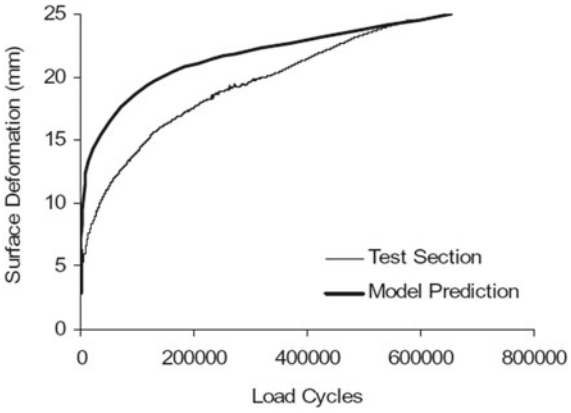

Fig. 6 Permanent surface deformation versus load cycles for procedure including reduced permanent strain in the stabilized base aggregate. From Perkins et al. (2010)

resulting curve as compared to the previous analyses where it is seen that the model with compaction and traffic effects offers considerable improvement.

2.2.6 Other Considerations

The above procedure resulted in a significant improvement in predicting stabilized pavement performance as compared to conventional procedures (Perkins et al. 2005).

Additional work involving large-scale cyclic triaxial testing of stabilized aggregate (Perkins et al. 2004) has shown that geosynthetics reduces the development of vertical permanent strain under repetitive loading. These tests were used to develop damage laws for the permanent strain for stabilized aggregate (Perkins et al. 2012).

This work also showed that the modified damage law should be only applied for a zone of aggregate adjacent to the geosynthetics of 150 mm in thickness or where the degree of stress mobilization exceeds a threshold value corresponding to an angle of 30° (Perkins et al. 2005). When these equations and considerations are applied to the aggregate in the test section modeled, the resulting predicted surface deformation versus load cycle curve is shown in Fig. 6 (Perkins et al. 2005); the measured response from the test section is also reported, showing a reasonable correspondence between the mechanistic-empirical prediction and results physically measured from a test section.

2.2.7 Considerations on M-E Models

The mechanistic–empirical models described above are surely among the best and more complete models available so far for geosynthetic-stabilized paved road.

They clearly show that including geosynthetics (intended as geogrids or woven/knitted geotextiles) for stabilization of paved road in M-E models is not a simple exercise, since all contributions of geosynthetics (on compaction, dilatancy,

shear stresses, permanent and resilient strains, number of traffic passes, etc.) shall be properly modeled, which requires a high number of parameters to be determined by laboratory- and/or full-scale testing. Moreover, the parameters of rutting and traffic laws need to be determined for the stabilized road sections, which still requires empirical values and formulas to be introduced.

To the author's knowledge, such sophisticated models are presently available mainly for geogrids and, with some restrictions, for woven/knitted geotextiles, while they are not available for geocells or other geosynthetics which may have stabilizing effects.

It is also evident that modeling the effect of stabilizing geosynthetics through a simple modulus improvement factor (MIF), like in some models developed mainly for geocell stabilization, is a banal simplification which may well lead to distorted results.

Hence, there is still a long way for arriving at a standardized M-E model of stabilized paved roads.

2.3 Use of LCR with Indian Norm IRC 37(2012)

IRC 37(2012) is a type of M-E design method for paved roads based on limitation of strains at the interface with subgrade, which, at present, does not provide any criteria for incorporating geogrids or other geosynthetics into base and/or subbase.

Unfortunately, the enforcement of this method has prevented for long time the use of geogrids for base stabilization in India; instead in all other Countries (including USA), while proper M-E models of geosynthetic-stabilized paved road are developed, modified AASHTO (1993) continues to be used for designing granular bases stabilized with geogrids, thus saving millions $ in highly expensive granular materials.

IRC37-2012 provides equations for unstabilized sections. As many of the parameters used are still empirical, the equations would require modification to include the benefit of stabilizing geosynthetics in the pavement layers, which would call for extensive research by laboratory and field testing, as shown for the M-E models above described.

While the M-E method for geosynthetic-stabilized paved roads will be developed, at present the advantage of both empirical and mechanistic–empirical methods for stabilized pavement design may be afforded by carrying out design according to both IRC: 37-2012 and modified AASHTO (1993) method based on LCR approach, by the following simplified procedure:

- Determine the subgrade CBR and modulus, and the design traffic load;
- Determine the road section from IRC: 37-2012 for given subgrade CBR and design traffic;
- Determine the layer coefficients a_1, a_2, a_3 for AASHTO (1993) method, in such a way that they correspond to the same elastic modulus of each layer of the unstabi-

lized section from IRC: 37(2012) calculation. Graph shown in Figs. 2.6 and 2.7 of AASHTO (1993) guidelines may be used to estimate the layer coefficients a_2, a_3 for a granular base and subbase material from its elastic (resilient) modulus, E_{BC} and E_{SB}, or the following formulas may be used:

$$a_2 = 0.249\left(\log_{10} E_{BC}\right) - 0.977 \tag{18}$$

$$a_3 = 0.227\left(\log_{10} E_{SB}\right) - 0.839 \tag{19}$$

where

E_{BC} elastic modulus of base layer
E_{SB} elastic modulus of subbase layer.

– Since the base and/or subbase layer is being stabilized with geogrids, corresponding layer elastic modulus will increase; the increased elastic modulus of the stabilized layers shall be determined by applying layer coefficient ratio (LCR) to the unstabilized layer coefficient; hence, the improved layer coefficients will be obtained as:

$$a_i' = \mathrm{LCR}_i \times a_i \tag{20}$$

where

a_i layer coefficient of ith layer
LCR_i layer coefficient ratio of ith layer.

LCR values should be obtained from the geogrid manufacturers based on their field and laboratory testing.

– Using the improved layer coefficients a_i', corresponding improved elastic modulus for stabilized layers shall be determined using Eqs. 18 and 19;
– Design the stabilized section from modified AASTHO (1993) with the LCR approach;
– Check the stabilized section for fatigue and rutting failure criterion by inputting the improved elastic modulus into IRC: 37-2012 formulas;
– By using critical tensile strain and compressive strain induced at the bottom of the bituminous course and at top of the subgrade, respectively, the allowable traffic should be determined for fatigue and rutting failures using equations from IRC: 37-2012: obtained traffic value from critical strains shall exceed the design traffic load.

In this way, the advantages of both the M-E method from IRC: 37-2012 (for unstabilized road design) and modified AASHTO (1993) method (for stabilized road design) are taken into consideration in designing stabilized sections. Since the LCR values are obtained through extensive laboratory and field tests, with the application

of hundred thousand or even million ESAL load cycles, the above procedure allows taking the benefit of the LCR for each specific geogrid and CBR value of the layer below.

3 Numerical Comparison

The numerical comparison between LCR, BCR, and TBR methods can be carried out as follows:

- Using specific software (Maccaferri MacRead 2.0 has been used in the present paper), the road design is carried out based on LCR method, for a given traffic (e.g., 20M ESAL).
- The same software provides also the TBR for the geogrid stabilized section having the same thickness of base course BC and/or subbase SB of the unstabilized section and the BCR of the geogrid stabilized section with reduced thickness of BC and/or SB, having the same traffic W_{18}.
- It is evident that, by using Eq. 8, the same reduced thickness for BC and/or SB can be obtained by applying congruent values of either LCR or BCR coefficients.
- Comparison between LCR and TBR can be achieved by using TBR for calculating the reduced thickness of base and/or subbase: This can be done by rerunning the calculation with the software, using the same input data, except that (from Eq. 3) traffic is now reduced as $W_{18\text{-TBR}} = W_{18}/\text{TBR}$; the resulting unstabilized cross section represents the TBR design of the reduced thickness, which can be compared with the LCR design.

The procedure is illustrated in Figs. 7, 8, and 9 with both BC and SB stabilized:

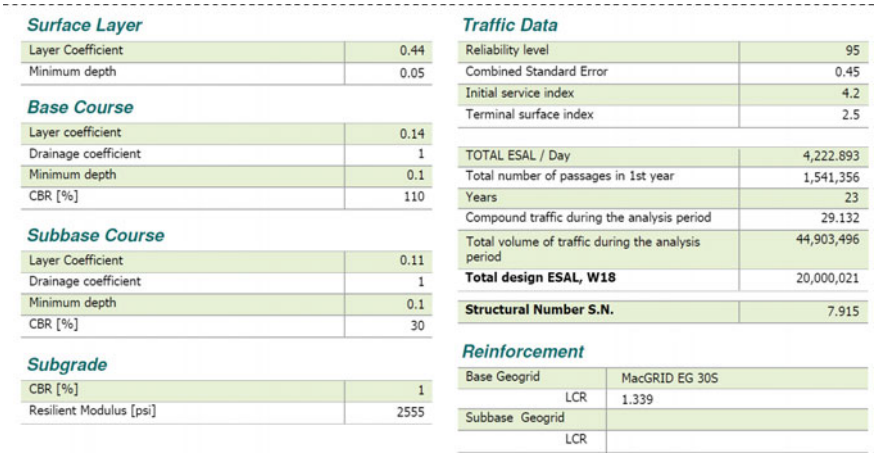

Surface Layer

Layer Coefficient	0.44
Minimum depth	0.05

Base Course

Layer coefficient	0.14
Drainage coefficient	1
Minimum depth	0.1
CBR [%]	110

Subbase Course

Layer Coefficient	0.11
Drainage coefficient	1
Minimum depth	0.1
CBR [%]	30

Subgrade

CBR [%]	1
Resilient Modulus [psi]	2555

Traffic Data

Reliability level	95
Combined Standard Error	0.45
Initial service index	4.2
Terminal surface index	2.5

TOTAL ESAL / Day	4,222.893
Total number of passages in 1st year	1,541,356
Years	23
Compound traffic during the analysis period	29.132
Total volume of traffic during the analysis period	44,903,496
Total design ESAL, W18	20,000,021

Structural Number S.N.	7.915

Reinforcement

Base Geogrid	MacGRID EG 30S
LCR	1.339
Subbase Geogrid	
LCR	

Fig. 7 Input data for the numerical comparison

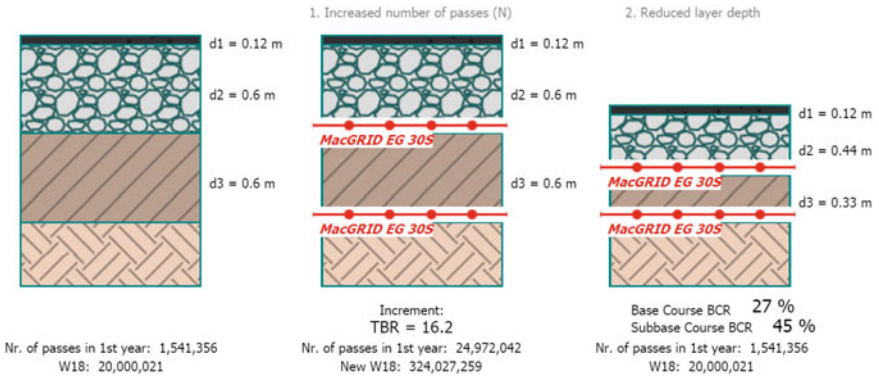

Fig. 8 Results of LCR calculation with both BC and SB stabilized

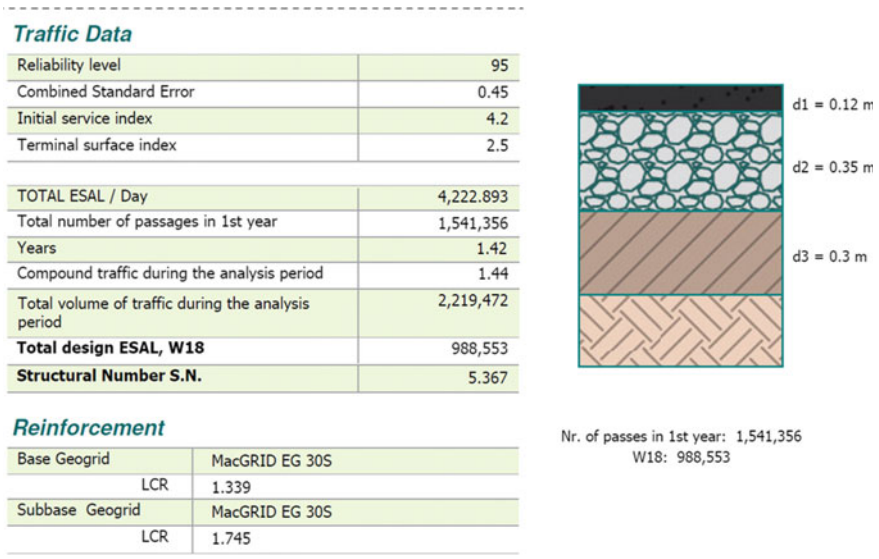

Traffic Data

Reliability level	95
Combined Standard Error	0.45
Initial service index	4.2
Terminal surface index	2.5
TOTAL ESAL / Day	4,222.893
Total number of passages in 1st year	1,541,356
Years	1.42
Compound traffic during the analysis period	1.44
Total volume of traffic during the analysis period	2,219,472
Total design ESAL, W18	988,553
Structural Number S.N.	5.367

Reinforcement

Base Geogrid	MacGRID EG 30S
LCR	1.339
Subbase Geogrid	MacGRID EG 30S
LCR	1.745

Fig. 9 Results of TBR calculation with both BC and SB stabilized

– Figure 7 shows the input data for the LCR calculation;
– Figure 8 shows the result of the LCR calculation: at left the unstabilized section, at center the stabilized section with same thicknesses of the unstabilized one and the related TBR value, at right the stabilized section, with related BCR;
– Figure 9 shows the results of the TBR calculation of reduced thicknesses.

From this numerical comparison the following conclusions can be drawn:

– LCR and BCR methods provide the same results if coherent input data are used.
– TBR method affords lower stabilized thicknesses than LCR method, for both BC and SB stabilized.

Table 3 Input for the Perkins et al. (2016) numerical comparison

Property	Value
Asphalt concrete thickness, D_1 (mm)	75
Asphalt concrete layer coefficient, a_1	0.40
Base thickness, D_2 (mm)	300
Base layer coefficient, a_2	0.14
Base layer drainage coefficient, m_2	1.0
Subgrade CBR	2
Geosynthetic modulus, $G_{\text{SM-2\%}}$ (kN/m)	1140
Geosynthetic modulus ratio, G_{MR}	0.995
Reduction factor for interface shear	1.0
Reduction for Poisson's ratio	Checked
Reduction for shear modulus	Unchecked

Hence, it appears that LCR and BCR methods are more conservative than TBR method.

Perkins et al. (2016) used the Perkins et al. (2011) model for comparing the results of the M-E model with the results of the LCR model, for a single pavement cross section having the geometry as shown in Table 3. Perkins et al. (2011) model was used to analyze a pavement with and without stabilization. The number of load cycles necessary to achieve a rut depth of 25 mm was determined for each model, which allowed the TBR to be determined, which had a value of 5.3. The AASHTO'93 pavement design Eq. (1) was then used to solve for the structural number of the pavement producing the number of traffic passes to reach a rut depth of 25 mm for the stabilized pavement. Equation 21 was then used to solve for LCR where values of a_1, a_2, and m_2 were the same as those shown in Table 3 and D_{2R} was 300 mm. This resulted in an LCR value of 1.51.

$$\text{LCR} = \frac{\text{SN} - a_1 D_1}{a_2 D_{2R} m_2} \tag{21}$$

Such LCR value is consistent with the published LCR value for the geogrid used in the model.

This clearly shows that the LCR method, if properly applied, can produce results that are consistent with the far more complicated M-E models.

4 Conclusions

The analysis of currently available empirical design methods and mechanistic–empirical design methods for unstabilized and geosynthetics stabilized paved roads has been carried out in the present paper.

The use of mechanistic–empirical pavement design methods represents a significant step in pavement engineering that is being embraced in the USA through the development of the 2008 AASHTO Pavement Design Guide.

It appears that there are several advantages of M-E methods (Perkins and Edens 2003):

- They can be used for both existing pavement rehabilitation and new pavement construction.
- They can accommodate changing load types.
- They can better characterize materials.
- They use material properties that relate better with actual pavement performance.
- They provide more reliable performance predictions.
- They define the role of construction in a better way.
- They accommodate environment and aging effect of materials in the pavement.

But there are also some disadvantages:

- M-E methods require a very high number of parameters and very complex traffic data; it is highly questionable if standard traffic data are suitable as input.
- Many of the parameters used in M-E methods are still empirical and/or need to be obtained by laboratory and field testing.
- The presently available M-E methods do not provide any criteria for incorporating geogrids or other geosynthetics into base/subbase.

The effect of geogrids into base/subbase should be evaluated in terms of an increase in performance of the related stabilized layer; but in M-E methods each layer is characterized by a long list of properties and parameters (many of them empirical or by testing): Hence, a very long work is required to characterize geogrid stabilized layers in M-E methods; this work is just at the beginning.

Therefore, at present there is no standard method for designing stabilized roads with M-E models.

On the other hand, the empirical method based on modified AASHTO (1993) guidelines with the LCR approach still provides reasonable results with a limited number of input data. In the LCR method, the layer thickness is designed with AASHTO (1993) method, which allows to take into account the dynamic loads from traffic, the materials characteristics through the layer coefficients, the rain and drainage characteristics through the m factors (see Eqs. 2, 5, and 7), and the inclusion of specific geogrids through their LCR. Then, geogrids are designed through a multilayer elastic analysis. Hence, it is a simplified method, compared to M-E methods, yet it follows the same principles.

Layer thickness may be designed using M-E methods rather than using empirical methods derived from modified AASHTO (1993) guidelines, but only for unstabilized roads. Using such sophisticated M-E methods to obtain unstabilized thicknesses and then apply questionable empirical factors for obtaining the stabilized thicknesses is not a suitable engineering option.

Moreover, there is still the need to design the geogrids within these reduced thicknesses, which at present is not possible with M-E methods.

Therefore,

– M-E methods are surely the future of road design.
– But at present, it is not possible to use M-E methods for stabilized roads.

Engineers and researchers familiar with geosynthetics have recognized for many years the ability of specific types of geosynthetics to provide stabilization to paved roads.

Broad-based acceptance and usage of geosynthetics for this application has been hindered, however, by the lack of appropriate M-E design methods. As transportation agencies move toward the adoption of M-E methods, it is imperative that methods be developed for the inclusion of stabilizing geosynthetics within the framework of M-E design methods.

Yet, until M-E methods will be developed also for stabilized roads, modified AASHTO (1993) methods are still a valid option, considering that they were validated by thousands of successful projects of geosynthetic-stabilized paved roads all around the world.

References

AASHTO (1993) Guide for design of pavement structures. American Association of State Highway and Transportation Officials, Washington, DC

AASHTO (2008) Mechanistic-empirical pavement design guide. American Association of State Highway and Transportation Officials, Washington, DC

AASHTO R 50-09 (2013) Recommended practice for geosynthetic reinforcement of the aggregate base course of flexible pavement structures. American Association of State Highway and Transportation Officials, Washington, DC

ASTM D6706-01 (2013) Standard test method for measuring geosynthetic pullout resistance in soil. ASTM International, West Conshohocken, PA

ASTM D7864 (2015) Standard test method for determining the aperture stability modulus of geogrids. ASTM International, West Conshohocken, PA

Adu-Osei A, Little DN, Lytton RL (2001) Cross-anisotropic characterization of unbound granular materials. Transp Res Rec 1757

Berg RR, Christopher BR, Perkins SW (2000) Geosynthetic reinforcement of the aggregate base course of flexible pavement structures. GMA White Paper II, Geosynthetic Materials Association, Roseville, MN

Boyce HR (1980) A non-linear model for the elastic behaviour of granular materials under repeated loading. In: Proceedings international symposium on soils under cyclic and transient loading, Swansea, UK, pp 285–294

Dafalias YF, Hermann LR (1986) Bounding surface plasticity. II: application to isotropic cohesive soil. J Eng Mech ASCE, 112(12):1263–1291

Hoff I, Nordal S, Nordal RS (1998) New hyperelastic material model for granular materials in pavement structures. In: 5th international conference on bearing capacity of roads and airfields. Trondheim, Norway

Huang YH (1993) Pavement analysis and design. Prentice Hall, Englewood Cliffs, NJ

ISO 10318-1 (2015) Geosynthetics—part 1: terms and definitions. International Organization for Standardization, Geneva, Switzerland

ISO 10319 (2015) Geosynthetics—wide-width tensile test. International Organization for Standardization, Geneva, Switzerland

Nordal S, Jostad HP, Kavli A, Grande L (1989) A Coulombian soil model applied to an offshore platform. Soil mechanics and foundation engineering. In: Proceedings 12th international conference, Rio de Janeiro, Brazil

Perkins SW (1999a) Mechanical response of geosynthetic reinforced pavements. Geosynth Int 6(5):347–382

Perkins SW (1999b) Geosynthetic reinforcement of flexible pavements: laboratory based pavement test sections. Report No. FHWA/MT-99/8106-1. U.S., Department of Transportation, Federal Highway Administration, Washington, DC, 140 p

Perkins SW (2001a) Mechanistic-empirical modeling and design model development of geosynthetic reinforced flexible pavements, Final Report, Report No. FHWA/MT-01/002/99160-1A. Montana Department of Transportation, Helena, Montana, USA

Perkins SW (2001b) Numerical modeling of geosynthetic reinforced flexible pavements, Report No. FHWA/MT-01-003/99160-2. U.S., Department of Transportation, Federal Highway Administration, Washington, DC, 97 p

Perkins SW, Cuelho EL (2008) Mechanistic–empirical design model predictions for base-reinforced pavements. Transp Res Rec: J Transp Res Board. 2018

Perkins SW, Edens MQ (2003) A design model for geosynthetic-reinforced pavements. Int J Pavement Eng

Perkins SW, Edens MQ (2011) Finite element and distress models for geosynthetic-reinforced pavements. Int J Pavement Eng 3(4):239–250

Perkins SW, Eiksund GR (2005) Geosynthetic material properties for use in 2-D finite element pavement response models. In: Proceedings of the seventh international conference on the bearing capacity of roads, Railways and Airfields, Trondheim, Norway

Perkins SW, Svanø G (2006) Assessment of interface shear growth from measured geosynthetic strains in a reinforced pavement subject to repeated loads. Eighth International Conference on Geosynthetics, Yokohama, Japan

Perkins SW, Christopher BR, Cuelho EL, Eiksund GR, Hoff I, Schwartz CW, Svanø G, Watn A (2002) Mechanistic-empirical models for reinforced pavements. In: Proceedings 7th international conference on geosynthetics. Nice, France

Perkins SW, Christopher BR, Cuelho EL, Eiksund GR, Hoff I, Schwartz CW, Svanø G, Watn A (2004) Development of design methods for geosynthetic reinforced flexible pavements, FHWA Report Reference Number DTFH61-01-X-00068. U.S. Department of Transportation, Federal Highway Administration, Washington, DC, p 263

Perkins SW, Christopher BR, Eiksund GR, Schwartz CS, Svanø G (2005) Modeling effects of reinforcement on lateral confinement of roadway aggregate. In: Proceedings of the conference geofrontiers, Geotechnical Special Publication 130, Advances in Pavement Engineering, ASCE, Austin, Texas

Perkins SW, Christopher BR, Cuelho EV, Eiksund GR, Schwartz CS, Svanø G (2009) A mechanistic-empirical model for base-reinforced flexible pavements. Int J Pavement Eng 10(2):101–114

Perkins SW, Christopher BR, Lacina BA, Klompmaker J (2012) Mechanistic-empirical modeling of geosynthetic-reinforced unpaved roads. Int J Geomech

Perkins SW, Christopher BR, Klompmaker J (2016) Reinforced flexible pavement layer coefficients determined by mechanistic-empirical modeling. In: Proceedings 6th European conference on geosynthetics, Ljubliana, Slovenia

White DJ, Vennapusa PKR, Gieselman HH, Douglas SC, Zhang J, Wayne MH (2011) In-ground dynamic stress measurements for geosynthetic reinforced subgrade/subbase. In: Proceedings conference geo-frontiers 2011, Dallas, Texas, USA

Challenges in Renovation of Existing Runway and Its Extension—A Case Study

Satyajit Roy, Dr. Rajesh Khanna and Mahabir Dixit

Abstract The study involves challenges faced in construction of runway pavements in the Northeastern part of India. These runways are very much important from strategic point of view. Most of these runways constructed during the Second World War were either renovated or extended many times. These runways though renovated and extended many times still require upgrading for easy and quick access to remote areas and to facilitate the movement of modern different types of aircraft as per PCN (Pavement Classification No.) and ICAO norms. Construction/renovation of these runways to keep them active for flying in all seasons is a major challenge especially during prolong heavy rainy seasons, floods, scarcity/non-availability of construction materials, skilled man power, etc. Apart from these problems, the other challenges faced are generation of actual profile of runway as per ICAO norm, laying of DBM as grade correction layer, laying of PQC layers without development of surface cracks, cutting of concrete joints, repair of cracks/broken slabs, and making of earthen shoulders/embankments before monsoon season. This paper attempts to present the issues related to quality control, quality assurance, and quality audit works carried out during the execution of the project.

Keywords PCN · ICAO norms · DBM · PQC · FOD

1 Introduction

Airfield pavements are constructed/resurfaced to provide operational surfaces for aircraft ground movements. Suitability of these infrastructures for traffic depends on geometric and operational quality attributes. Geometric standards for lengths,

S. Roy (✉) · Dr. R. Khanna · M. Dixit
Central Soil and Materials Research Station, New Delhi 110016, Delhi, India
e-mail: satyajit_wow@yahoo.com

Dr. R. Khanna
e-mail: rajesh12khanna@yahoo.com

M. Dixit
e-mail: mdixit64@gmail.com

R. Sundaram et al. (eds.), *Geotechnics for Transportation Infrastructure*, Lecture Notes in Civil Engineering 28, https://doi.org/10.1007/978-981-13-6701-4_4

widths, gradients, and clearances are as per aircraft characteristics and are based on prevalent ICAO norms, codal provisions, and technical instructions. Most of the runways in the Northeastern part of India constructed during the Second World War were gradually upgraded post-independence. Extensive expansion of these airfields continued after the Indo-China war. These runways are constructed and maintained by Military Engineering Services (MES). Number of technologies emerged over a period of time. Out of these, one of the economically viable options for upgradation is resurfacing by the combination of rigid and flexible overlays. Resurfacing of runway is a very challenging task considering the quality attributes involved and implications in terms of operational requirements. Successful implementation of such specialized work requires previous experiences and inputs by the diligent users from functional point of view. There is a need to document various resurfacing aspects so as to enable quality control and quality assurance measures of the runways to have standing guidance for future improvements. This paper presents technical challenges faced during construction of runway along with some local Northeast problem.

2 Parameters Necessary for Resurfacing

As per Khanna and Justo (1992), Khanna and Arora (1999), Saxena (1999), and Rangwala and Rangwala (2012), main parameters for resurfacing of airfield to achieve operational quality of pavement are:

i. Bearing strength (ability to support traffic loads controlled by structural design).
ii. Skid resistance (level of friction available for braking and directional control) airfield pavements should have a good level of micro- and macro-texture and be resistant to near and polishing under braking tire.
iii. Ride quality (effect of surface roughness on ride comfort and safety and is a function of paving methods and quality of construction of workmanship. Ride quality is of particular importance for runways serving large fighter aircraft with high takeoff and landing speeds).
iv. Structural integrity (surface intactness and potential for foreign object disposal (FOD) hazard to aircraft from loose materials).

Proper quality control and quality assurance for resurfacing of the runway are not only a specialized but also a challenging task. Importance of proper planning and execution at every stage with strict quality assurance as well as quality audit cannot be overemphasized.

2.1 General Cross Section of Pavement

General cross sections of various types of overlays for resurfacing are presented in Fig. 1.

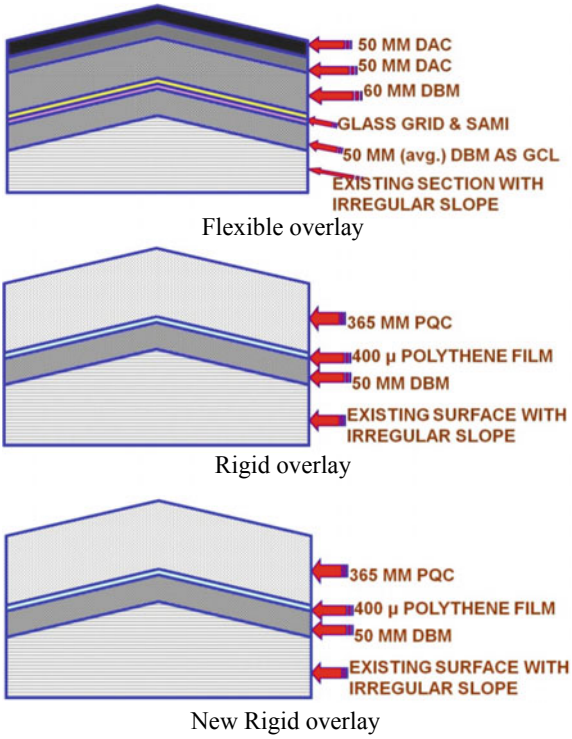

Fig. 1 Various cross section of pavement

The cross sections vary depending upon the value of PCN and project conditions.

3 Typical Challenges of Northeastern Region

Northeast region of India has got certain inbuilt peculiar challenges which need to be considered well in advance to expedite the construction of runway in time. Certain challenges specific to the Northeast region are enumerated below:

i. Plain area with heavy rainfall.
ii. Hot and humid climatic conditions.
iii. Zone V of seismic zone.
iv. Flat and clay area with thick vegetation.
v. Very high water table.
vi. Prolonged monsoon season from April to September.
vii. Scarcity of quarries and zone II sand.
viii. Scarcity of skilled labor.
ix. Reluctance of national-level agencies to work in this belt.
x. Frequent power cutoff.

xi. Distance Factor:

   a. Bitumen 60/70 grade from Haldia.
   b. Glass grid and PMB-70 from Gurgaon.
   c. Steel from Kolkata.
   d. Cement from Chhattisgarh.

Notwithstanding, the above-mentioned challenges certain precautionary measures can be adopted well in advance to expedite the work in time such as

i. Installation of two ready-mix concrete plants (RMC) such that plant capacity shall be matching with paver capacity.
ii. Standby power backup with adequate DG sets.
iii. Labor camp for skilled man power coming from outside Northeastern states.
iv. Mix design approval for three brands of cement to avoid shortage of any particular brand of cement.
v. Contractor shall be bound in the contract to store some vital spare parts so as to ensure serviceability of plants.
vi. Subsurface drains at the junction of links and runway to avoid even smallest of stagnation of water at these junctions.
vii. Holistic drainage system shall be planned along with the resurfacing.

4 Challenges Occurs and Their Solution During Resurfacing

Various challenges that erupt during resurfacing of airfields may cause considerable delay in projects. Following solutions are to be implemented for overcoming challenges and smooth execution of work.

4.1 Profile Correction

With passage of time due to extensive use of runway, severe distresses like spalling of joints/edges, localized depressions, dislodging of aggregates, and extensive cracks develop in pavement, which results in poor riding quality and severe FOD hazards. In addition, longitudinal and transverse gradient of runway get disturbed badly to the extent beyond the limit of ICAO norms. Also sometimes, there are portions in runway where only one-sided slope in transverse direction exists. These slopes require modification. Correction of old profile requires initial levels of runway with a grid size of 3 m $\times$ 2 m in the field. These levels are plotted, and necessary corrections are made. It should be noted that even extra variation of 1–2 mm in levels can lead to an increase in quantities of layers causing financial burden for projects.

4.2 Process for Generation of Profile

As per ICAO (International Civil Aviation Organization) manual and guidelines (1999), finished runway levels are usually designed.

4.2.1 Longitudinal Slope and Transverse Slope

The longitudinal slope is computed by dividing the difference between the maximum and minimum elevation along the runway centerline by the runway length. It shall not exceed 1–2%. Where slope changes cannot be avoided, a slope change between two consecutive slopes shall not exceed 1.5–2%. The transition from one slope to another shall be accomplished by a curved surface in such a way that the rate of change shall not exceed 0.1–0.4% for every 30 m length. Figure 2 depicts the longitudinal gradient correction based on data recorded during execution of one of the airfields in the NE region.

The recommended transverse slope gradient as per ICAO norms is 1–1.25% of runway width at runway and links. The transverse gradient correction based on data recorded during execution of project is presented in Fig. 3.

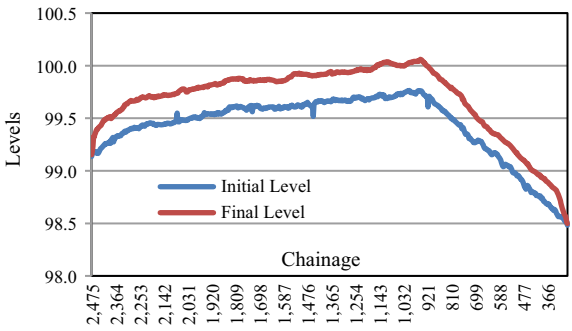

Fig. 2 Longitudinal gradient correction

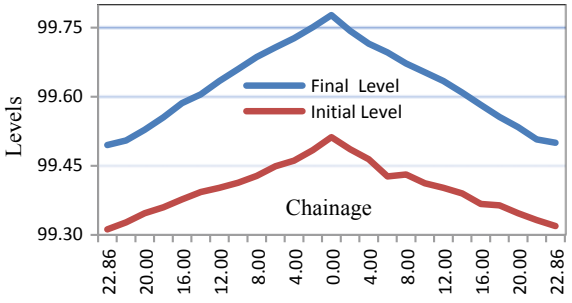

Fig. 3 Transverse gradient correction

Fig. 4 Repair of broken slab

4.3 Repair of Broken Slab

At first, cracks existing in old surface should be marked so that adjacent area/slabs do not get affected during repair work. It is necessary that slabs having minimum cracks should be repaired with epoxy mortar, and slabs having multiple cracks should be dismantled and recasted before laying new layer. It is very difficult to compact subgrade of the individual slab to be demolished because roller entry at this particular point is not possible. Therefore, a contraption fabricates at site, install on JCB boom for compacting. Figure 4 depicts repair of broken slab.

4.4 Laying of Correction Layer as Dense Bituminous Macadam (DBM)

DBM layers are designed and laid as per guidelines of IRC 94 (1986). In case of airfield, general requirement of Marshall Stability value to satisfy PCN 70 is 9 KN at 60 °C. It is generally used as grade correction layer in flexible pavement. The depth of correction layer varies longitudinally/transversely along the runway. The real challenge is to decide the thickness of each layer since as per IRC guidelines the thickness of DBM shall not be more than 75/100 mm for GdeI/GdeII type DBM. The deciding level/thickness to be laid of each layer needs prediction and to be checked at every layer. Hence, strict supervision and control are very important. The challenge of laying various correction layers with varying width can be overcome by using sensor paver moved on prefixed string lines for proper thickness as decided. The next challenge which comes during execution is to cut the uncompacted DBM layer on edges before laying adjacent layer as it is mandatory as per IRC/MORTH (2005) guidelines. This can be achieved by mounting a locally fabricated cutter to rear wheel of tandem vibratory roller so that the same can be cut while rolling only. The laying of DBM is presented in Fig. 5.

Fig. 5 Laying of DBM

4.5 Laying of Pavement Quality Concrete (PQC)

Pavement quality concrete layers are designed and laid as per guidelines of IRC15 (2011) and MORTH (2005). Airfield requirement of minimum field flexural strength to satisfy PCN 70 is 45 kg/cm^2. It is used as top layer in rigid pavement. It is seen that sand used in PQC sometimes carries lumps, which ultimately leads to formation of potholes in PQC surface. Therefore, sand screener can be fabricated at site with conveyor belt to avoid lumps in sand. Laying PQC is challenging job as it develops initial cracks on surface within curing period or within few months of construction of new slabs. Improvements can be done to avoid/minimize any such cracking by using following methods.

i. Design of PQC with less water/cement ratio, using appropriate admixture, having slump as 0–10.
ii. Using curing compound sprinkling for initial 48 h for curing during cutting operation.
iii. Using PVC fibers for avoiding surface cracks.
iv. Continuous laying of PQC without putting expansion pads for providing expansion joints at predecided intervals, otherwise level difference between two adjacent slabs occurs.
v. Always aim should be to finish the days work at dummy joint position.

One more important aspect is joint mapping. Joints which are to be provided in new surface should be such that, they are replica of old surface, otherwise reflection cracks will propagate to new surfaces within few years. Figure 6 depicts laying of PQC.

4.6 Joints

As per IRC15 (2011), MORTH (2005), and MES Standard Schedule of Rates Part I (2010), there are three general types of joints that are to be provided in PQC. These are

Fig. 6 Laying of PQC

i. Expansion joint: Such joint provides the space into which pavement can expand, thus relieving compressive stresses due to expansion and inhibiting any tendency toward buckling of concrete slabs.
ii. Contraction joint: Such joint relieves tensile stresses in the concrete and prevents formation of irregular cracks due to restraint in free contraction of concrete. Contraction joints also relieve stresses due to warping.
iii. Warping joint: Such joint relieves stresses due to warping. These are commonly used for longitudinal joints dividing the pavement into lanes.

4.6.1 General Pattern of Joints

The general patterns of joint that are generally maintained in airfield of NE region are given below.

Construction joint: Construction joint of size 8 mm wide and 30 mm deep is provided at all locations where joints are due to construction sequence, and full-depth joint is automatically created by applying epoxy primer between the two concrete slabs. Figure 7 depicts details of construction joint.

Dummy/contraction joint: Dummy joint is of size 8 mm wide and 100–125 mm deep and filled with polyurethane joint sealant over 12-mm-thick backup rod after application of primer. Contraction/construction joint is provided at every 3.81 in transverse direction, i.e., half of the width of PQC laid and 4.5 m in longitudinal direction. The details of dummy joint are depicted in Fig. 8.

Expansion joint: In case of expansion joints, initial cuts of 3 mm wide and 10 mm depth are made in concrete surface within 48 h of concreting to avoid any surface cracks in concrete. After 28 days of curing, expansion joints are developed by cutting full depth, twice 14 mm apart and 4 mm wide later widening to 6 mm wide, and removing the middle concrete by breaking it. Finally, a 25-mm-thick joint is created. Figure 9 depicts initial cut and final shape of expansion joint.

The filler board and backup rod are inserted after applying primer. After this, joints are filled with polyurethane sealant with the help of masking tape to avoid spilling of sealant. Figure 10 depicts details of expansion joint.

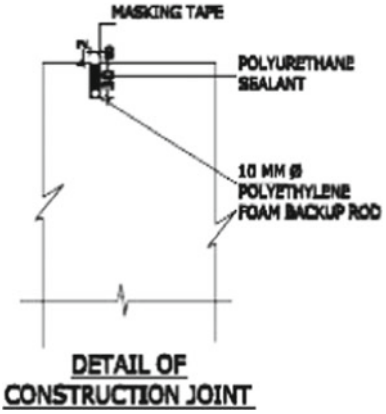

Fig. 7 Details of construction joint

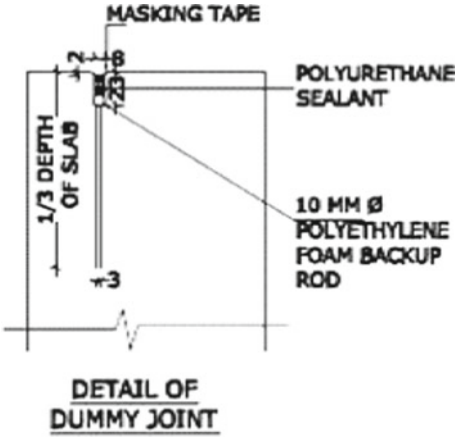

Fig. 8 Details of dummy joint

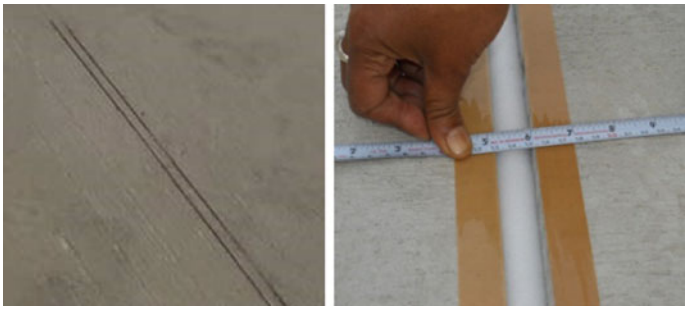

Fig. 9 Initial cut and final shape of expansion joint

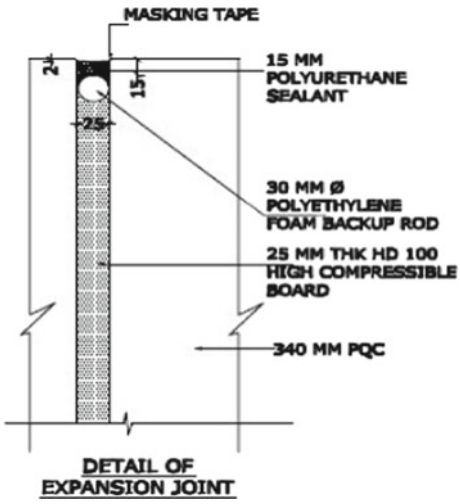

Fig. 10 Details of expansion joint

Table 1 Spacing of expansion joint

Thickness of slab (in meter)	Spacing of expansion joint (in meter)
0.2 and above	36.0
0.15	27.0
0.1	27.0

As per IS 6509 (1985), Table 1 depicts spacing of expansion joint.

During summer due to extreme climatic temperature variation in Northeast, slabs tend to come closer to each other at many places reducing the 20 mm gap of expansion joint to minimum or zero. This results in spilling of joint filling material, breaking of edges of concrete slab, and sliding of one slab on another. Therefore, from the practical practice at site spacing of expansion joint is reduced from 36.0 to 18.0 m to counter attack the expansion and contraction of slabs during summer.

4.7 Shoulder/Embankment Construction

Construction of earthen shoulder/embankment is very much important activity for draining out of rainwater from runway into monsoon drain. As the level of runway goes up for resurfacing, there is need of laying of earthen shoulder along the edges of runway. The width of shoulder should be 45 m in both sides of runway laid at slope of 1:80. Generally, filling of earth in shoulder should be carried out in non-monsoon period (Oct–March) as in rainy season there is a chance of washing out of soil with water. Further, growing of grass on the shoulder will provide additional stability against erosion. Shoulders can be also used in case of emergency if aircraft slips out

Fig. 11 Finished surface of runway

from runway. Construction of shoulder free from FOD is challenging job. Manual screening of material at the time of shoulder preparation is the only option.

5 Conclusions

The functional requirement of the airfield pavements is much more stringent because of the aircraft characteristics and consequences involved. Over the years, there have been a lot of emphases laid on education, research, training, and documentation of highway pavements. Although a great deal of guidance is available from the documents of Internal Civil Aviation Organization (ICAO), Central Road Research Institute (CRRI) India, Indian Road Congress (IRC), Indian Standards (IS), etc. Runway resurfacing has to satisfy the functional and structural requirements according to its local climatic conditions, materials of construction, and construction technologies. Therefore, challenges and their solution discussed in this paper will lead to complete the project in stipulated time with high factor of quality assurance. The finished surface of runway is presented in Fig. 11.

Acknowledgements I would like to express my thanks and deep sense of gratitude to engineers of Military Engineering Services and Col Sudeep Mishra in particular who shared their experiences about challenges faced in resurfacing of runway in Northeast region and helped me in writing this paper.

References

ICAO (1999) Aerodrome design and operations. Annex 14, 3rd edn., 999 University Street, Montréal, Quebec, Canada H3C 5H7

IRC 94 (1986) Specification for Dense Bituminous Macadam. New Delhi, India

IRC 15 (2011) Standard specifications and code of practice for construction of concrete roads. New Delhi, India

IS 6509 (1985) Code of practice for installation of joints in concrete pavement, BIS, New Delhi, India

Khanna SK, Arora MG (1999) Manual of airport planning and design. Nem Chand & Brothers, Roorkee
Khanna SK, Justo CEG (1992) Manual of highway engineering. Nem Chand & Brothers, Roorkee
Military Engineering Services (2010) Manual on standard schedule of rates (part-1)
MORT&H (2005) Road and bridge works. In: Specification, Indian roads congress
Rangwala SC, Rangwala PS (2012) Manual of airport planning and design. Charotar
Saxena SC (1999) Manual of airport engineering. Charotar

A Critical Review on Evaluation of Pavement Drainage Systems

Mustafa A. Ghasia, Yogesh U. Shah and Veerabhadra Rotte

Abstract Pavement distresses decline the pavement surface condition and affect the structure resulting in declination of load-carrying capacity. Generally, paved and unpaved roads in India are subjected to problems in relation to excessive percolation of water in foundation structure due to improper drainage. Unwanted amount of water in pavement layers contributes to many problems which may result in premature failure of pavement. The infiltration of water either from top surface of pavement or intrusion by groundwater, i.e., subgrade soil when exposed to water, results in reduction in its shear strength. Moreover, robustness of base/subbase dependency is chiefly on strain, and if these layers get degraded, it will ultimately result in poor performance of top granular layers, i.e., structural distresses. It is necessary to drain the excessive moisture from the pavement layers so as to prevent the reduction in load transfer mechanism through aggregate interlock. This paper presents a review of about several techniques like use of ground-penetrating radar (GPR), time-domain reflectometry (TDR), and computational analysis using finite element modeling (FEM) pertaining to the evaluation of pavement drainage systems for efficacy of pavement performance. It also describes various studies related to the effect of pavement drainage on pavement performances.

Keywords Pavement drainage · Ground-penetrating radar (GPR) · Time-domain reflectometry (TDR) · Pavement performance

M. A. Ghasia · Y. U. Shah (✉) · V. Rotte
Department of Civil Engineering, Institute of Infrastructure Technology Research and Management, Ahmedabad 380026, India
e-mail: yogeshshah@iitram.ac.in

M. A. Ghasia
e-mail: ermustafaghasia23@gmail.com

V. Rotte
e-mail: vmrotte@iitram.ac.in

R. Sundaram et al. (eds.), *Geotechnics for Transportation Infrastructure*, Lecture Notes in Civil Engineering 28, https://doi.org/10.1007/978-981-13-6701-4_5

1 Introduction

Road infrastructure facilities hold a major role in all-round development of a country by providing connectivity of places for humans as well as goods. Since independence, all government policymaker accorded topmost importance to build roads of quality and to reduce road maintenance. With economic prosperity, there is an increase in vehicular usage resulting in pavement distresses and failures due to improper designing and construction of pavement. Pavement distresses decline the pavement surface conditions and also reduce structural strength. Water is a major evil affecting the pavement condition and its structure resulting in declination of load-carrying capacity. The bearing capacity of a pavement majorly depends on bearing capacity of the sublayers which will be majorly affected by the presence of free water and soil suction (Hicks 1970; Fang 1991). Also, if there is an increase in water in sublayers of pavement, it will majorly affect the pavement stiffness and will result in greater deflections (Scullion et al. 1995). Also excessive water shall be drained off by any means, if not premature failure in pavements will be noticed.

Researchers have stated that the presence of moisture in asphalt layer and the layers underlying it can make a bond between asphalt cement and aggregates to fail in result to which 'stripping' phenomenon is observed. This greatly affects the service life of the pavement layers (Scullion et al. 1994; Maser 1996).

In construction technique of a conventional pavement, a typical layer of asphalt is laid which acts as surface coating which is laid on top of thick gravel layer which may be bound or unbound which functions as a drainage layer and protects the subgrade which is of native soil against the frost action.

For designing of these layers, the designer has to check the conditions under which the pavement has to function. For this purpose, design engineer must collect the data regarding the annual vehicular traffic, regional precipitation, soil properties, pavement geometrics, and surface and subsurface drainage properties.

2 Aim of Review

The current paper mainly focuses on reviewing an existing literature on the pavement drainage assessment techniques and the effect of the drainage systems on pavement performance. The review is presented in following three categories:

a. Design of pavement drainage systems
b. Evaluation of pavement drainage system
c. Effect of drainage on pavement performance.

3 Studies Related to Design of Pavement Drainage Systems

Drainage of unwanted water from the pavement system is an important factor in designing of pavement. Theoretically, if the drainage capacity of base and subbase is higher than the infiltration rate, requirement of internal drainage system is not necessary. For every segment of road, it is very difficult to check whether the above-mentioned criteria are being satisfied or not. Hence, the need of designing and providing drainage system arises. In early times, the methodology adopted for drainage system was simply a provision of trench, backfilling with freely draining aggregates to which an outlet used to be provided for water to exit the system. Later, to increase the discharge rate of the system, perforated pipes were introduced to the backfill. The concept of provision of edge drains was introduced in mid-1980s (Fleckenstein et al. 1996).

Now, generally base and subbase layers act as a drainage layer in pavements. If the base layer is properly designed and constructed, it may also function as a conventional dense graded base which can support the pavement by load distribution. This will reduce the time to drain cost-effectively. As per M-E design manual recommendation, minimum value for laboratory permeability value should be around 1000 ft/day for permeable bases (Apul et al. 2002).

Further, for improvising the pavement subsurface drainage efficiency, geocomposite membrane can be placed beneath drainage layer (open graded drainage layer, OGDL). By adopting this method, Al-Qadi et al. (2004) observed that the moisture content in the layers beneath the geocomposite membrane is comparatively less than that of the pavement section without it. Hence, the application of geomembrane is fruitful for preventing the intrusion of water in the sublayers of pavement and assists the drainage layers for disposal of the water out from the pavement. As per the FHWA guidelines for subsurface drainage systems for highway pavement structural sections, provision of collector pipes with open graded drainage layer should be made to satisfy the need of generating positive drainage for continuous free flow of water.

4 Studies Related to Pavement Drainage Systems

4.1 Evaluation of Drainage Systems Using Ground-Penetrating Radar (GPR)

Advancement in technology has created a remarkable approach to store more data than before. Ground-penetrating radar (GPR) is a nondestructive technology majorly associated with archeological studies, but nowadays this technology can significantly be used in civil engineering works such as subsurface investigations and structural assessments.

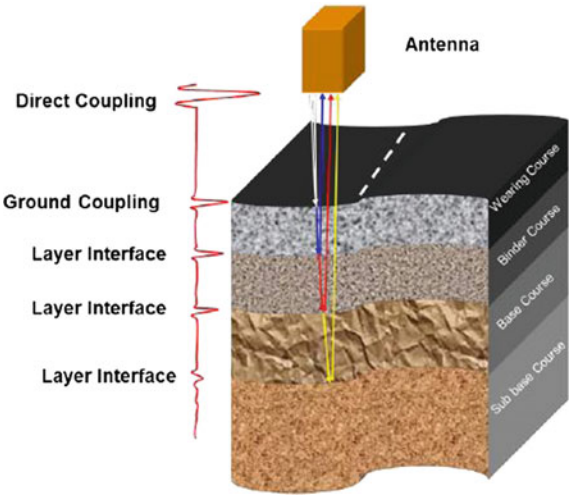

Fig. 1 Functioning principle of GPR system (after Korczak et al.)

Scientists have been using this technique from early 1990 for variety of investigations and have even started using in highway and transport engineering investigations such as measuring the pavement layer thickness (Cuvillier et al. 1987; Eckrose 1989), evaluating the bridge decks (Clemena 1983), detecting the voids in the pavement structure (Clemena et al. 1986; Saarenketo et al. 1994).

Fundamental of this technology is based on the reflection/transmission of microwave electromagnetic energy and capturing its response over various materials as shown in Fig. 1.

Electromagnetic wave is transmitted from the GPR device which travels vertically through the pavement layers at certain velocity (u) which is a function of permittivity and speed of light in vacuum $c = 0.3$ m/ns

$$u = c \div \left(\sqrt{\varepsilon}\right) \tag{1}$$

The wave further travels in downward direction until it touches a stratigraphic layer having different electrical properties than the host layer (propagation of wave from a dry gravelly medium to wet sand layer) (Daniels 2000).

Hence, by means of GPR technique, one can know the subgrade depth to which the water has percolated the need to provide even better subsurface drainage system as the permittivity (ε) and dielectric constant (K) of subsurface material will vary hysterically, notably in the existence of free water ($\varepsilon_{air} = 1$, $\varepsilon_{granite(dry)} = 5$, $\varepsilon_{clay} = 5$–40, $\varepsilon_{water} = 81$) (Saarenketo 2006).

Dielectric constant (K) can be obtained from the following relationship:

$$K \approx \left(\frac{c}{v}\right)^2 \tag{2}$$

where

c Plane wave propagation velocity of EM waves in free space (Davis and Annan 1989),
v Velocity of EM wave to an interface.

For the estimation of water content in pavement layers, Saarenketo et al. (1994) processed GPR-collected data to qualitatively observe the infiltration of saline water injected on the side of high. Scullion et al. (1995) used GPR data for quantitative assessment of water content in pavement aggregates which were tested under controlled conditions in laboratory over four samples.

In the research studies for obtaining an effective approach for improving pavement drainage layers by Al-Qadi et al. (2004), GPR was used for the estimation of moisture content of an unbound aggregate subbase layer in two different pavement sections, one without a geocomposite membrane and one having it placed underneath an open graded drainage layer (OGDL). From GPR data, it was seen that moisture accumulation under the geocomposite membrane remains always lower than that in section of pavement without it. Major outcomes of the study were presented:

a. A nondestructive method for measuring the quantity of moisture content in granular material
b. The perks of adding a moisture barrier which should be impervious in nature underneath OGDL and is validated using GPR data and falling weight deflectometer (FWD) method for measurement of deflection.

A detailed study of physical and chemical properties of rock and their interaction with fluids can generate a relationship which can be used to convert dielectric constant (K) to volumetric water content (θ_u) developed by Roth et al. (1990)

$$\theta_u = \frac{\left(K_{\text{effective - mixing}}^{1/2}\right) - (1-\eta)K_{\text{solid}}^{1/2} - \eta K_{\text{air}}^{1/2}}{K_{\text{water}}^{1/2} - K_{\text{air}}^{1/2}} \tag{3}$$

where

η	Porosity,
K_{air}, K_{solid}, and K_{water}	Dielectric constants of air, solid, and water components of mixture,
$K_{\text{effective}}$	Mixing is the estimate of dielectric constant obtained from EM measurement.

By using GPR signals in finite difference time domain (FDTD), it was seen that the prediction of subsurface drainage pipe can be made, i.e., whether the pipes are clogged with soil or any other material or are filled with water or they are empty and are able to drain out the subsurface water efficiently (Zhao and Al-Qadi 2017).

4.2 Evaluation of Drainage Systems Using Time-Domain Reflectometry (TDR)

Generally, water in unbound granular asphalts significantly affects the asphalt's execution, especially its quality and groove protection. Along these lines, estimation of the dampness substance of these asphalts gives important data to assess street conditions and development quality, including the possibility to help in overseeing surge occasions and related street terminations (Horey-Lacy et al. 2014). TDR determines the moisture content by measuring the waveforms reflected.

Previously, TDR was majorly used to detect breaks in communication lines, but nowadays there has been an extensive use of this system for measuring the change in moisture content of granular materials in pavement engineering by observing the change in dielectric permittivity of soil nearer to the TDR probe.

As per FHWA guidelines for determining soil volumetric moisture content $V_w(\%)$ using TDR—1998, as given by Eq. (2)

$$V_w(\%) = \frac{(5L_a - 1) - B_0 \frac{\gamma_d}{G_s \gamma_w}}{B_1} \tag{4}$$

where

L_a	Apparent depth of TDR response,
γ_d and γ_w	Unit wt. of soil and water,
G_s	Specific gravity of soil,
B_0 and B_1	Regression coefficients.

L_a can be obtained from several methods like method of tangents, method of peaks, method of diverging lines, alternate method of tangents, and Campbell scientific method. Most of the researchers adopt method of tangents and method of peaks (Topp et al. 1980).

A generalized cubic relationship with permittivity was formed, but the Topp equation is majorly considered as standard equation for obtaining the volumetric content of water.

$$\theta = a_0 + a_1\varepsilon + a_2\varepsilon^2 + a_3\varepsilon^3 \tag{3}$$

where

θ	Volumetric water content,
ε	Permittivity.

However, it was seen that the Topp equation was appropriate for loosely compacted crushed rock (1.5 g/cm^3) and for subgrade clay with dry density (1.85 g/cm^3) and the relationship was not suitable for rocks crushed and compacted to 2.0 g/cm^3.

Horey-Lacy et al. (2014) presented TDR-based monitoring of moisture for unbound granular pavements in materials from the permittivity of the materials.

5 Effect of Pavement Drainage on Pavement Performance

Initially in 1930s, pavement surface drainage was given more significance while designing road. Now from past few decades, not only surface drainage but even subsurface drainage systems are taken in account while designing a road. Subsurface drainage is essential for maintaining the service life of pavements.

In research work of Fleckenstein et al. (1996), provision of edge drains in drainage system showed reduction in moisture content in subgrade as much as to 28%, and falling weight deflectometer (FWD) results showed significant increase in the shear strength of subgrade. Thus, increase in subgrade strength should increase the pavement life. Also change in riding index (RI) was studied using FWD. The results indicate an increment of 7 years to reach a critical RI by providing edge drain system. A critical RI of 2.7 was assumed for pavements with an annual ADT of 8000 or greater.

Harvey et al. (1998) in his research work tested the asphalt-treated permeable base materials (ATPB) which contained 2–3% of asphalt. Soaking for few days, there was a reduction in stiffness which was measured from resilient modulus. This reduction in stiffness was due to stripping of asphalt. It was found that dry samples under repetitive loading did not face much of strain as compared to saturated samples. From their estimation, fatigue life of typical California pavement of soaked samples was reduced by 2–3 times.

Zaghloul et al. (2004) in their studies for analyzing the effect of positive drainage over flexible pavement life cycle and cost analyzed the pavement response over the effect of moisture content in terms of FWD deflection by using TDR for recording only moisture content data. The data collected by FWD and TDR probes from test sections were used for developing a relationship among moisture content and pavement structural capacity which was expressed as structural adequacy index (SAI). The analysis resulted in decrease in service life on increase in moisture content in base course due to poor subsurface drainage. A good provision of subsurface drainage system when applied to pavement structure will result in lowering retaining moisture content within the pavement layers, and also life cycle cost can further more be reduced to more than 50% compared to pavement sections with poor drainage. Hence, a significant long-term savings can be obtained by improving the quality of subsurface drainage system of pavements.

Mahboub et al. (2003) carried out research for evaluation and analysis of highway pavement drainage in Kentucky using SEEP/W; a 2D finite element software obtained that if longitudinal drain is placed in center of pavement, it can change the flux distribution in pavement and thus pavement drainage efficiency can be improved. Also from his analysis, it was proved that increase in cross slope of the drainage blanket, increases the ability of the pavement to drain water more efficiently.

Stormont et al. (2005) in his research work for edge drain performance for unsaturated flow of water suggested the significance of trench backfill material over drainage efficiency. If in backfill material gravels are used, it will create an opposite effect than intended; i.e., it will not assist the drainage of water. Other than the drainage material,

partial trench system beneath the base layer will always provide less drainage with respect to the full trench configuration extending through the base course. Water in pavement affects majorly its stiffness, load-carrying capacity, modulus of resilient, and other such properties. Thus, the performance of the pavement is hampered.

6 Concluding Remarks

On the basis of literature review presented in this paper, it can be rightly justified that the design of drainage layer is an important component in designing of pavement. Water in pavement will result in structural and functional pavement distresses and increase in the maintenance cost. For improving the drainage efficiency of pavement, provision of collector pipe with OGDL will satisfy the need of generating positive flow toward the outlet and support the drainage of water out from the pavement. Ground-penetrating radar and time-domain reflectometry can rightly be associated for subsurface water estimation and can be an effective approach for quantifying the quantity of water as well as the depth to which the water has infiltrated in pavement section. Also it can be used for investigating the efficiency of drainage materials. It has also been reviewed that providing the effective drainage system either in terms of side drains or subsurface drainage layer, the performance parameters of pavement like riding index and structural adequacy are improved.

References

Al-Qadi IL, ASCE F, Lahouar S, Loulizi A, Elseifi MA, Wilkes JA (2004), Effective approach to improve pavement drainage layers. J Transp Eng, ASCE 130(5)

Apul D, Gardner K, Eighmy T, Benoit J, Brannaka L (2002) A review of water movement in the highway environment: implications for recycled materials use. Recycled Materials Resource Center, University of New Hampshire, Durham, New Hampshire

Clemena G (1983) Nondestructive inspection of overlaid bridge decks with ground-penetrating radar. Transportation Research Record Journal of the Transportation Research Board, Washington, DC

Clemena G, Sprinkel M, Long R (1986) Use of ground penetrating radar for detecting voids underneath a jointed concrete pavement. Final Rep. Virginia Highway and Transportation. Council, Charlottesville, VA

Cuvillier M, Boaddard JF, Retour P (1987). New methods developed in France for road network survey and maintenance. In: Proceedings of 6th conference structural design of asphalt pavements, 1. University of Michigan, Ann Arbor, MI

Daniels J (2000) Ground penetrating radar fundamentals, s.l.: Prepared as an appendix to a report to the US EPA, Region V 1-21

Davis JL, Annan AP (1989) Ground-penetrating radar for high-resolution mapping of soil and rock stratigraphy. Geophys Prospect 37:531–551

Eckrose R (1989) Ground penetrating radar supplements deflection testing to improve airport pavement evaluations, non-destructive testing of pavements and back calculation of moduli. ASTM Special Technical Publication, Philadelphia, PA, p 1026

Fang H-Y (1991) Foundation engineering handbook. Van Nostrand Reinhold, New York
Fleckenstein LJ (1996) Evaluation of pavement edge drains and their effect on pavement performance. J Transp Res Board 2465:28–35
Harvey J, Tsai B, Long F, Hung D (1998) Asphalt-treated permeable base: laboratory testing, performance and predictions. Transportation Research Record 1629, TRB, National Research Council, Washington, DC, pp 127–136
Hicks RG (1970) Factors influencing the resilient properties of granular materials. Ph.D. dissertation, University of California, Berkeley
Horey-Lacy W, Bodin D, Scheuermann A (2014) Time domain reflectometry (TDR) based moisture monitoring system for unbound granular pavements. In: ARRB conference, research driving efficiency, Sydney, New South Wales
Mahboub KC, Lui Y (2003) Evaluation and analysis of highway pavement drainage research report. KTC-03-32/SPR207-00-1F, Kentucky Transportation Center
Maser KR (1996) Condition assessment of transportation infrastructure using ground-penetrating radar. J Infrastruct Syst 2(2):94–101
Roth K, Schulin R, Fluhler H, Attinger W (1990) Calibration of time domain reflectometry for water content measurement using a composite dielectric approach. Water Resour Res 26(10):2267–2273
Saarenketo T (2006) Electrical properties of road materials and subgrade soils and the use of ground penetrating radar in traffic infrastructure surveys, s.l.: Oulu University Press
Saarenketo T, Scullion T (1994) Ground penetrating radar applications on roads and highways. Res. Rep., 1923(2F). Texas Transportation Institute, College Station, TX
Scullion T, Lau CL, Chen Y (1994) Pavement evaluations using ground penetrating radar in Texas. In: Proceedings of the 5th International Conference on GPR, Kitchener, Ontario, vol 1, pp 1449–463
Scullion T, Chen Y, Lau CL (1995) Colormap—user's manual with case studies. Texas DOTPD Rep. TX-95-1341-1, Austin, TX
Stornmont JC, Zhou S (2005) Impact of unsaturated flow on pavement edge-drain performance. J Transp Eng, ASCE
Topp GC, Davis JL, Annan AP (1980) Electromagnetic determination of soil water content: measurement of coaxial transmission lines. Water Resour Res 16:574–582
Zaghloul S, Ayed A, Ahmed Z, Henderson B, Springer Z, Vitillo N (2004) Effect of positive drainage on flexible pavement life-cycle cost. Transp Res Rec 1868:135–141
Zhao S, Al-Qadi I (2017) Pavement drainage pipe condition assessment by GPR image reconstruction using FDTD modeling

Behaviour of Cohesive Soil-Flyash Layered Matrix Under Cyclic Loading

M. Junaid Khan, Mehboob Anwer Khan, Kausar Ali and Altaf Usmani

Abstract The present study investigates the effect of cyclic loading conditions on the performance of soil-flyash layered matrix under different intensities of failure load ($I = 25$, 50 and 75%) with varying number of cycles ($N = 100$, 200 and 300). The number of cycles, confining pressures and the intensity of failure loads were varied using triaxial compression testing machine on layered soil-flyash samples. It is observed from the study that nature of stress–strain relationship is initially linear for low stress levels and then turns nonlinear for high stress levels. The experimental results show that the effect of confining pressures of 50, 100 and 150 kPa on deviator stress at failure is significant at higher intensity, *I,* of the load at which loading–unloading is performed for cohesive soil-flyash layered matrix. The study shows that the deviator stress at failure and cohesion continuously increases with increase in the number of cycles *N* at lower values of intensity of load, *I* ($I = 25\%$) in soil-flyash matrix under cyclic loading conditions which signifies good performance of this combination under lower percentages of failure stress levels. The experimental investigation demonstrates the use of flyash in layered combination with cohesive soils under lower number of cycles with high intensity of load *I*, and for higher number of cycles with lower value of intensity of load *I*.

Keywords Cyclic loading · Soil-flyash layers · Deviator stress · Intensity of load · Number of cycles · Confining pressure

M. Junaid Khan · M. A. Khan (✉) · K. Ali
Department of Civil Engineering, AMU, Aligarh, India
e-mail: mehboobcivil@yahoo.co.in

M. Junaid Khan
e-mail: khanjunaid2k13@gmail.com

K. Ali
e-mail: kausarali786@rediffmail.com

A. Usmani
Engineers India Ltd., EIL, New Delhi, India
e-mail: altaf_usmani@rediffmail.com

R. Sundaram et al. (eds.), *Geotechnics for Transportation Infrastructure*, Lecture Notes in Civil Engineering 28, https://doi.org/10.1007/978-981-13-6701-4_6

1 Introduction

Power, being considered as an engine of growth, has always been a focus area for most of the developing countries, including India. The power generation in India has increased from 1362 MW in 1947 to 300,000 MW in 2017. Coal-based power plants produce not only millions of mega-watts of power but also million tons of flyash. About 1000 million tons of ash is estimated as dumped in ash ponds in India, and every year 100 million tons of ash is being added to this quantity (Murthy 1996). As per an estimate of Fly Ash Utilization Programme (FAUP), the annual ash generation figure is expected to reach about 225 million tons by 2017. Large-scale utilization of flyash in geotechnical construction like embankments, road sub-bases, structural land fill as a replacement to the conventional earth material will solve the disposal problems of flyash. When flyash is used in construction of highway and railway embankments, the design life and the maintenance cost of highways/railways may get altered. Theoretically explicit simulation of the response of subsoil under repeated load is preferable. In the past few decades, experimental research has been devoted to the response of soils and pavement materials to traffic-induced cyclic loads. Factors influencing the cyclic performance of soft soils have been investigated, viz. (i) cyclic stress level which determines whether the soil can reach a non-failure equilibrium state or not (Larew and Leonards 1962; Sangrey et al. 1978; Ansal and Erken 1989; Zhou and Gong 2001), (ii) loading frequency which is responsible for the rate of excess pore pressure and axial strains (Procter and Khaffaf 1984; Liu and Xiao 2010), (iii) over-consolidation ratio influencing the effective stress paths and the degradation of the undrained secant shear modulus (Brown et al. 1975), and (iv) static pre-shearing which decreases the cyclic shear strength but increases the total shear strength (Zimmie and Lien 1986; Hyodo et al. 1994). Kutura et al. (1980) proposed a methodology for the design of pavements in which the traffic load was represented by equivalent static load and one-dimensional consolidation theory was used to predict the settlement. A method proposed by Hyodo et al. (1996) combines the two-dimensional dynamic numerical analysis and dynamic triaxial test results to predict the traffic load-induced deformations.

Li et al. (1996) performed undrained cyclic triaxial tests on soft clays, of marine origin, from Wenzhou City, China. The samples of in situ clay were consolidated under K_0 conditions, with an average value of $K_0 \approx 0.55$. Ansal et al. (2001) performed undrained stress-controlled, multistage cyclic triaxial tests to evaluate the changes in the stress–strain and shear strength characteristics. Erken and Ulker (2007) studied the shear strain of the reconstituted soil under different cyclic shear stress, clayey soil. The monotonic undrained shear strength of reconstituted and undisturbed specimens decreased due to the cyclic shear stress history. This decrease depended on the previous number of loading cycles. However, this reduction was significant when the soil specimen exceeded a certain yield strain level under the same shear stress amplitude prior to monotonic undrained test and reached nearly 40% in silty soil. The cyclic shearing behaviour of saturated clays has been addressed in numerous publications (Brown et al. 1975; Castro and Christian 1976). Some investigators have

suggested the relationships between moisture content, dry density and the permanent axial strain accumulation that results from increasing number of load cycles (Li and Selig 1996), but cyclic response of layered soil-flyash system is not available in the literature. Khan et al. (2008) investigated the cyclic load deformation behaviour of soil-flyash layered system by using different intensities of failure load ($I = 25$, 50 and 75%) with varying number of cycles ($N = 10$, 50 and 100). The resilient modulus, permanent strain and cyclic strength factor are evaluated from the test results and compared to show their variation with varying stress levels.

A practical approach of utilization of flyash in embankments is to have alternate layers of soil and flyash for which no study is reported in the literature. In the present research work, a systematic laboratory investigation has been carried out by conducting a series of undrained cyclic triaxial compression tests on layered samples of soil and flyash, under different intensities of deviatoric failure load (I) and varying confining pressures (CP) of 50, 100 and 150 kPa with a view to establish a relationship between stress–strain, shear strength parameters and cyclic loading conditions.

2 Material and Method

The clayey soil used for the study was obtained from the campus of Aligarh Muslim University, Aligarh (UP), India. The flyash was procured from Dadri Thermal Power Plants, Uttar Pradesh, India. The physical, chemical and geotechnical properties of soil and flyash are shown in Tables 1, 2 and 3.

The flyash used in the present study is classified as non-self-cementing, Class F as per ASTM standard. The optimum moisture content (OMC) of flyash and soil was found to be 30 and 17.5%, respectively, using standard proctor compaction test. The morphology and chemical composition of flyash have been examined using optical microscopes, scanning electron microscope (*SEM*) equipped with energy-dispersive X-ray spectroscopy (EDS). The flyash consists of mainly spherical particles. The spherical particles are of varied size ranging from less abundant, 20 μm size down to more abundant, less than 10 μm in size Fig. 1a, b. As determined by EDS, the pre-

Table 1 Physical properties of soil

Physical properties	Value
Specific gravity, G	2.70 at 28 °C
Natural water content, w (%)	5.0
Optimum moisture content, OMC (%)	17.5
Maximum dry density, γ_{dmax} (kN/m^3)	18.2
Liquid limit, W_L (%)	33.0
Plastic limit, W_p (%)	21.0
Plasticity index, I_p (%)	12.0
IS: Soil classification	CL

Table 2 Physical and geotechnical properties of flyash

Properties	Value
Specific gravity, G	2.3
Optimum moisture content, OMC (%)	30.0
Unit weight, γ (kN/m^3)	14.5
Maximum dry density, γ_{dmax} (kN/m^3)	11.5
Liquid limit, W_L (%)	20.0
Plastic limit, W_p (%)	0.0
Plasticity index, I_p (%)	20.0
Co-efficient of permeability, k (m/s)	9.5×10^{-8}
Unit cohesion, c (kN/m^2)	23.0
Angle of shearing resistance, ϕ (degree)	26.0

Table 3 Chemical properties of the flyash

Chemical composition (%)	Value
Silicon dioxide (SiO_2)	59.00
Alumina (Al_2O_3)	29.00
Iron oxide (Fe_2O_3)	6.50
Calcium oxide (CaO)	1.80
Magnesium oxide (MgO)	1.44
Sodium oxide (Na_2O)	0.80
Sulphur trioxide (SO_3)	0.28
Potassium oxide (K_2O)	0.10
Loss on ignition	4.84

dominant elements in the flyash were iron, silicon, sulphur, aluminium and calcium (Fig. 2).

Each triaxial specimen of plain soil, plain flyash and soil-flyash matrix was prepared triaxial metal mould of 85 mm high and 39 mm in diameter. The plain soil, plain flyash specimens were compacted in three equal layers. Each specimen of soil, flyash and soil-flyash layer was prepared at their corresponding OMC which was statically compacted by a mini compactor of 100 g weight under a free fall of 150 mm, imparting approximately 0.123 kg m^2/s^2 of energy. The size of the sample used in triaxial shear test was 84 mm high and 39 mm in diameter. In soil-flyash matrix, two layers of flyash each of thickness 27 mm were sandwiched between 10-mm-thick layers of soil as shown in Fig. 3.

The soil and flyash passing through 425-micron sieve were used in the preparation of the samples. The details of cyclic tests performed on soil-flyash matrix are given in Table 4.

Stress-controlled triaxial shear test was used to assess the shear strength of plain clay, plain flyash under non-cyclic loading and soil-flyash matrix under non-cyclic as well as cyclic loading. The tests were performed under unconsolidated undrained

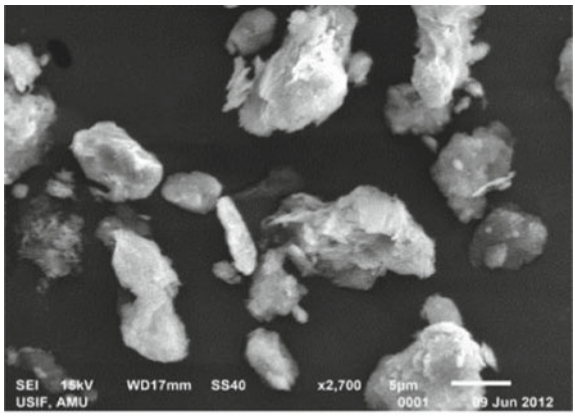

(a) Scanning electron microscope (*SEM*) of soil

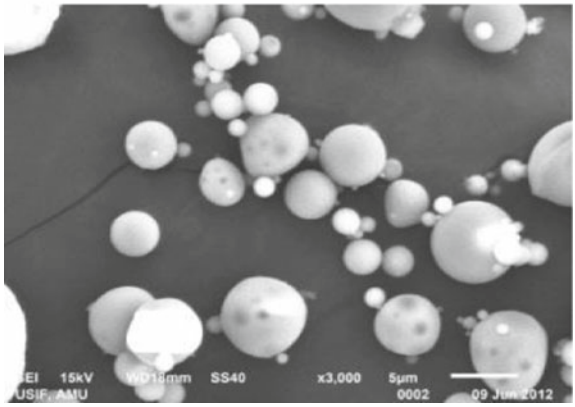

(b) Scanning electron microscope (*SEM*) of flyash

Fig. 1 **a** Scanning electron microscope (*SEM*) of soil, **b** scanning electron microscope (*SEM*) of flyash

Table 4 Number of cycles and intensity of load on soil-flyash matrix

N	I		
	25%	50%	75%
100[a]	√	√	√
200[a]	√	√	√
300[a]	√	√	√

[a]Each set of experiment consists of three tests at confining pressures of 50, 100 and 150 kPa

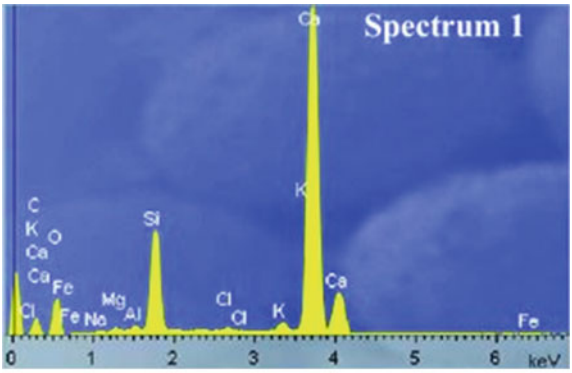

(a) Energy-dispersive *X-ray* spectroscopy (*EDS*) of soil

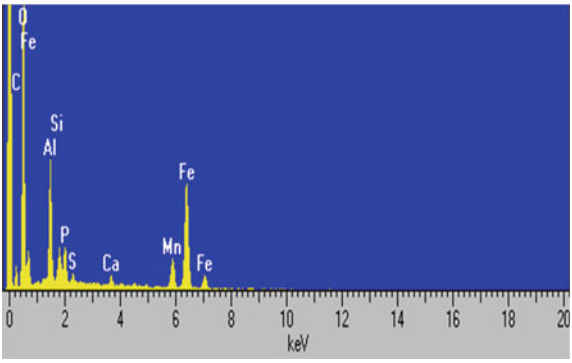

(b) Energy-dispersive *X-ray* spectroscopy (*EDS*) of flyash

Fig. 2 **a** Energy-dispersive *X-ray* spectroscopy (*EDS*) of soil, **b** energy-dispersive *X-ray* spectroscopy (*EDS*) of flyash

conditions. A series of seven sets of stress-controlled cyclic loading condition were tested; each set of triaxial shear test was carried out at three different confining pressures of 50, 100 and 150 kPa. Thus, a total number of thirty triaxial shear tests were performed including non-cyclic tests on plain clay, plain flyash and soil-flyash matrix. The intensity of load (I) at which loading and unloading of cycles were performed is the percentage of the deviator load at failure in non-cyclic loading condition. An equal time for loading and unloading equal to one minute was adopted for all the cycles. After completing the desired cycles, the deviator stress was increased till failure of the specimen. The loading–unloading cycles are shown in Fig. 4.

The vertical axial compression of specimen with the change in the deviator load was recorded.

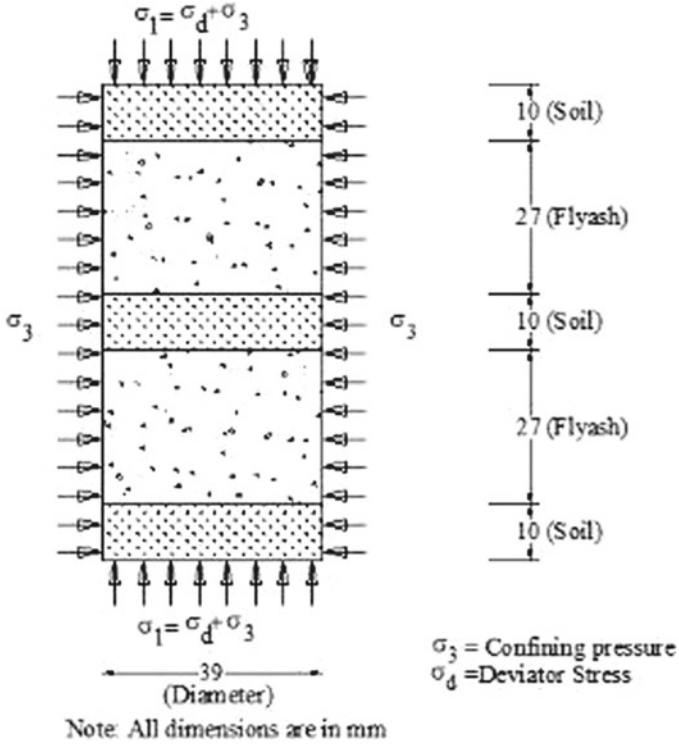

Fig. 3 Free body diagram of soil-flyash layered sample

Fig. 4 Loading and unloading cycles

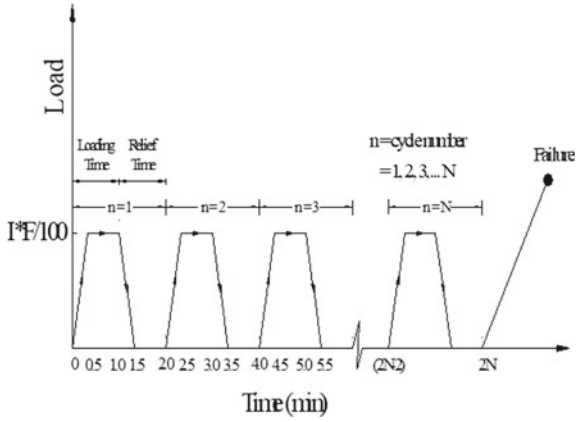

3 Results and Discussion

3.1 Stress–Strain Behaviour for Non-cyclic Loading Conditions

The variation of deviator stress with axial strain for plain soil, plain flyash and soil-flyash layered matrix for non-cyclic loading conditions is presented in Figs. 5, 6 and 7, respectively.

These figures show the stress–strain behaviour with different values of confining pressures of 50, 100 and 150 kPa. It was observed that the stress–strain behaviour

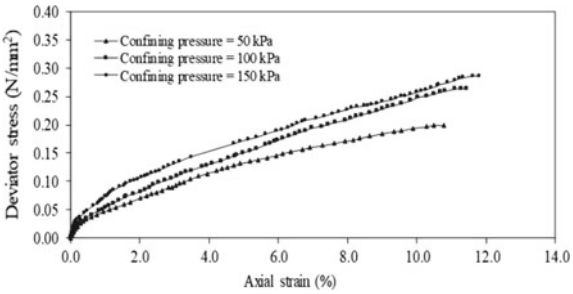

Fig. 5 Deviator stress versus axial strain curves of non-cyclic loading for plain flyash

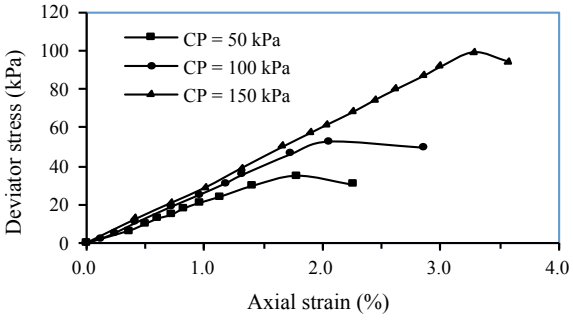

Fig. 6 Deviator stress versus axial strain curves of non-cyclic loading for plain clayey soil

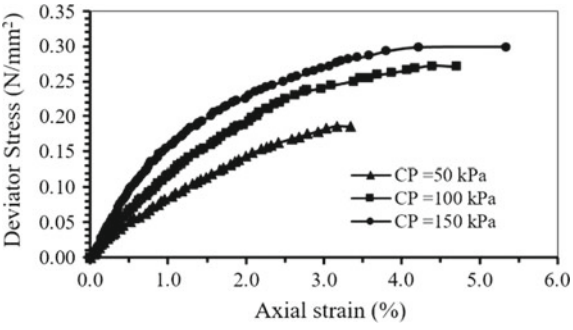

Fig. 7 Deviator stress versus axial strain curves of non-cyclic loading for soil-flyash matrix

of soil-flyash layered matrix is similar to that of plain soil under non-cyclic loading conditions. It is also observed that the increase in confining pressure results in increase in ultimate deviator stress and ultimate strain of soil, flyash and soil-flyash layered matrix. However, magnitude of deviator stress is considerably higher for plain flyash as compared to plain soil which shows significant effect of confining pressures in flyash. Further ultimate deviator stress and ultimate axial strain of plain flyash are considerably less than the plain soil at the same magnitude of confining pressure. It is also observed that the deviator stress at failure of soil-flyash matrix at confining pressure of 50 kPa is slightly less (~6.0%) than the corresponding value of plain soil, whereas at higher confining pressure of 150 kPa, the deviator stress at failure of soil-flyash matrix is slightly more (~3.0%) than their corresponding values of plain soil. The failure strain of soil-flyash matrix is slightly more than the corresponding values of plain flyash.

3.2 Effect of Intensity of Load (I) and Number of Cycles (N)

The variation of deviator stress at failure of soil-flyash matrix with intensity of load ($I = 25$, 50 and 75%) and confining pressures (CP) of 50, 100 and 150 kPa is shown in Figs. 8, 9, 10, 11, 12, 13, 14, 15 and 16.

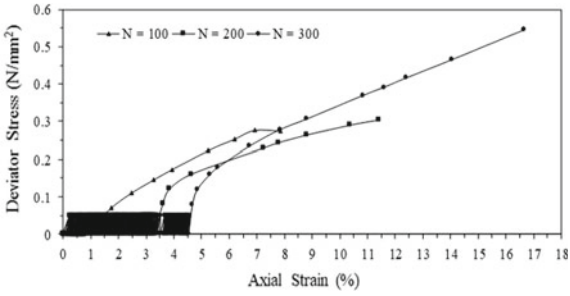

Fig. 8 Deviator stress versus axial strain curves for confining pressure, $\sigma_3 =$ 50 kPa and $I = 25\%$

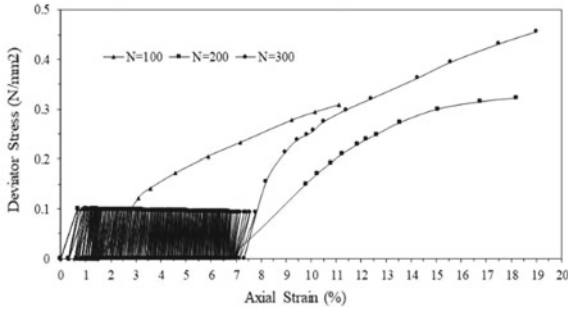

Fig. 9 Deviator stress versus axial strain curves for confining pressure, $\sigma_3 =$ 50 kPa and $I = 50\%$

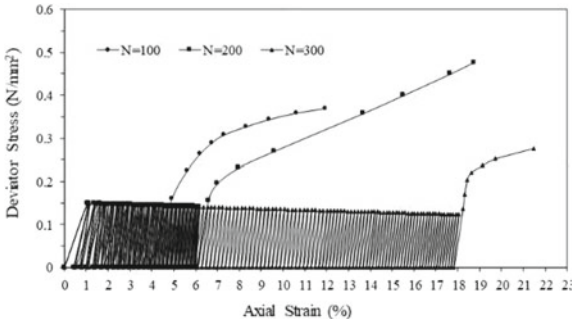

Fig. 10 Deviator stress versus axial strain curves for confining pressure, $\sigma_3 =$ 50 kPa and $I = 75\%$

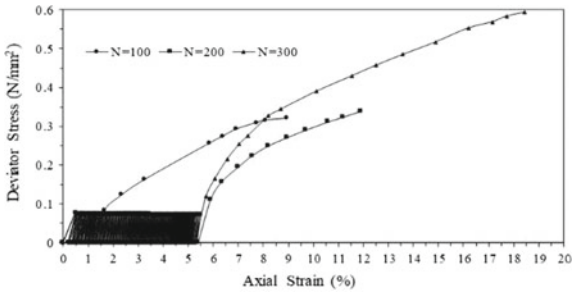

Fig. 11 Deviator stress versus axial strain curves for confining pressure, $\sigma_3 =$ 100 kPa and $I = 25\%$

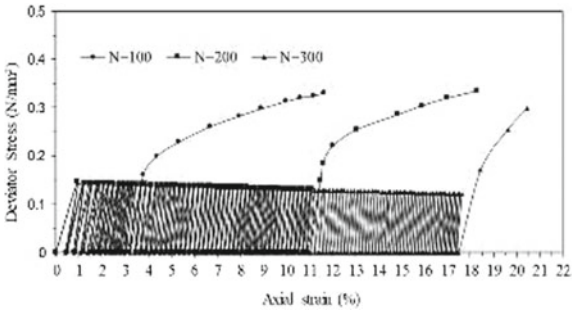

Fig. 12 Deviator stress versus axial strain curves for confining pressure, $\sigma_3 =$ 100 kPa and $I = 50\%$

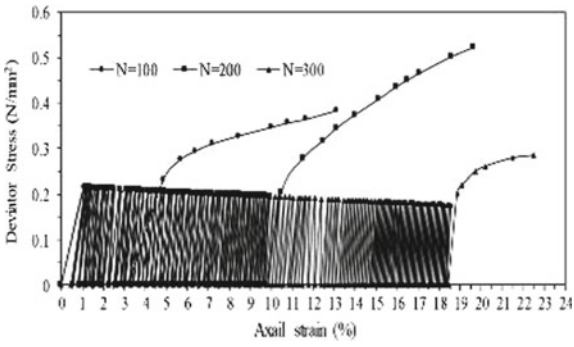

Fig. 13 Deviator stress versus axial strain curves for confining pressure, $\sigma_3 =$ 100 kPa and $I = 75\%$

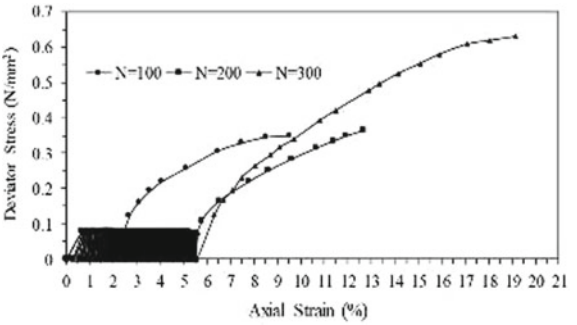

Fig. 14 Deviator stress versus axial strain curves for confining pressure, $\sigma_3 =$ 150 kPa and $I = 25\%$

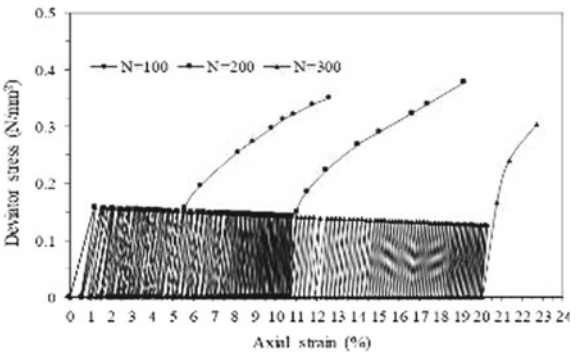

Fig. 15 Deviator stress versus axial strain curves for confining pressure, $\sigma_3 =$ 150 kPa and $I = 50\%$

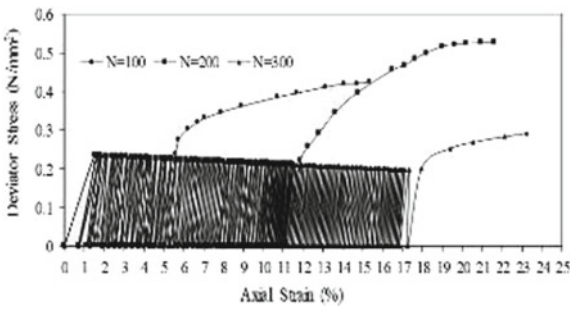

Fig. 16 Deviator stress versus axial strain curves for confining pressure, $\sigma_3 =$ 150 kPa and $I = 75\%$

It is observed that for $N = 100$ and 200, deviator stress at failure increases with increase in value of I, whereas for $N = 300$, it increases initially and then decreases. It is also observed that the deviator stress at failure for a given number of cycles (N) and intensity of load (I) increases with increase in confining pressure. The deviator stress at failure increases with increase in N for low values of I ($I \leq 50\%$), whereas at higher value of I ($I = 75\%$), it increases up to $N = 100$ and then decreases. Maximum value of deviator stress at failure of soil-flyash matrix is obtained for $N = 300$ at $I = 25\%$ and under a confining pressure of 150 kPa which is 113% more as compared to that of non-cyclic condition ($N = 0$). This increase is only 17 and 23.3% for number of

cycles $N = 100$ and $N = 200$, respectively. The experimental results indicate that the effect of confining pressure on deviatoric stress at failure is significant at higher value of I for soil-flyash matrix, which indicates the greater stability for soil-flyash layered combination even at larger values of I. The experimental investigation carried out also shows that the increase in the number of cycles, N, and the parameter, I, leads to the degradation of stress–strain and shear strength properties of the soil-flyash matrix, but the intensity of load (I) has more significant effect.

3.3 Shear Strength Parameters and Shear Strength

The shear strength parameters of soil, flyash and soil-flyash matrix under non-cyclic and cyclic condition have been evaluated by using the following relation

$$\sigma_1 = \sigma_3 \tan^2(45 + \phi/2) + 2c \tan(45 + \phi/2)$$

where $\sigma_1 = \sigma_3 + \sigma_d$, σ_3 = confining pressure, σ_d = deviator stress, c = cohesion and ϕ = angle of shearing resistance.

Shear strength of the samples was obtained using the relation, $\tau_f = c + \sigma_n \tan\phi$ where τ_f = shear strength and σ_n = normal stress.

The values of shear strength parameters and shear strength of soil, flyash and soil-flyash matrix under non-cyclic and cyclic conditions are presented in Tables 5 and 6.

Table 5 Shear strength parameters for non-cyclic loading conditions

CP	τ_f	N	σ_d	c	(ϕ)
(kPa)	(kPa)		(kPa)	(kPa)	(Degree)
Plain soil					
50		–	30		
100	35.8	–	50	30.0	15
150		–	100		
Plain flyash					
50	12.0	–	190	5.2	25
100		–	260		
150		–	280		
Soil-flyash layers					
50		–	180	35	20
100	41.0	–	270		
150		–	300		

where *CP* = Confining pressure

Table 6 Shear strength parameter of soil-flyash layered matrix for cyclic loading conditions

CP	I	N	c	(ϕ)
(kPa)	(%)		(kPa)	(Degree)
50	25	100		
100	25	100	41.0	15.4
150	25	100		
50	25	200		
100	25	200	50.0	13.5
150	25	200		
50	25	300		
100	25	300	65.0	14.0
150	25	300		
50	50	100		
100	50	100	45.0	15.0
150	50	100		
50	50	200		
100	50	200	53.0	13.8
150	50	200		
50	50	300		
100	50	300	68.0	17.6
150	50	300		
50	75	100		
100	75	100	50.0	15.0
150	75	100		
50	75	200		
100	75	200	59.0	13.9
150	75	200		
50	75	300		
100	75	300	73.0	18.6
150	75	300		

For $N = 100$, there is hardly any significant influence of the parameter, I. The shear strength parameters are: $c = 41.0$ kPa, $\phi = 15.4°$. For $N = 200$, the shear strength parameters for $I = 25\%$ and $I = 50\%$ are almost the same, whereas for $I = 75\%$, shear strength parameters are

$$c = 50.0\,\text{kPa},\ \phi = 14° \text{ for } I \leq 50\%$$
$$c = 59.0\,\text{kPa},\ \phi = 13.7° \text{ for } I > 50\%$$

For $N = 300$, the shear strength parameters considered are for $I = 25\%$ and another combined value for $I = 50\%$ and 75% whose values are close to each other. The shear strength parameters are:

$$c = 65.0\,\text{kPa},\ \phi = 14.0^\circ \text{ for } I < 50\%$$
$$c = 73.0\,\text{kPa},\ \phi = 18.6^\circ \text{ for } I \geq 50\%$$

The maximum binding effect, i.e. cohesion (73 kPa) and maximum shear strength for soil-flyash matrix (79 kPa), is obtained at $N = 300$ and $I \geq 50\%$ which is approximately two times as compared to non-cyclic condition of soil-flyash matrix ($N = 0$).

4 Conclusion

The experimental results indicate that the effect of confining pressure on deviatoric stress at failure is significant at higher value of intensity of load (I) at which loading–unloading is done for soil-flyash matrix. It is also observed that the increase in the number of cycles, N, and the parameter, I, leads to the degradation of stress–strain and shear strength properties of the soil-flyash matrix, but the later has more significant effect. The experimental investigation substantiates the use of flyash in layered combination with clayey-type soil under lower number of cycles with high value of intensity of load, I, and for higher number of cycles with lower value of parameter I. The study shows that the value of deviator stress at failure and cohesion continuously increases with the increase in the number of cycles N for lower values of I ($I = 25\%$) in soil-flyash matrix under cyclic loading conditions which signifies the good performance of this combination under lower percentages of failure stress levels. From this study, it can be inferred that more than 50% of flyash can be utilized in place of conventional material for the construction of highway and railway embankment.

References

Ansal AM, Erken A (1989) Undrained hehavior of clay under cyclic shear stresses. J Geotech Eng 115(7):968–983

Ansal AM, Iyisan R, Yildirim H (2001) The cyclic behaviour of soils and effects of geotechnical factors in microzonation. Soil Dyn Earthq Eng 21:445–452

Brown SF, Lashine AKF, Hyde AFL (1975) Repeated load triaxial testing of silty clay. Geotechnique 25(1):95–114

Castro G, Christian JT (1976) Shear strength of soils and cyclic loading. J Geotech Eng, ASCE 102:887–894

Erken A, Ulker BMC (2007) Effect of cyclic loading on monotonic shear strength of fine-grained soils. Eng Geol 89:243–257

Hyodo M, Yamamoto Y, and Sugiyama M (1994) Undrained cyclic shear behaviour of normally consolidated clay subjected to initial static shear stress. Soils Found 34(4):1–11

Hyodo M, Yashura K, Murata H (1996) Deformation analysis of soft-clay foundation of low embankment road under traffic loading. In: Proceedings of 31st symposium of Japanese society of soil mechanics and foundation engineering, pp 27–32 (in Japanese)

Khan MA, Usmani A, Shah SS, Abbas H (2008) A study of multilayer soil-fly ash layered system under cyclic loading. Int J Civ Eng 6(2):73–89

Kutura K, Miki H, Mashita Y, Seki K (1980) Settlement and counter measures of the road with low embankment on soft ground. Tech Rep Civ Eng JSCE 22(8):13–16 (in Japanese)

Larew HG, Leonards GA (1962) A strength criterion for repeated loads. Highw Res Board Proc 41:529–556

Li LL, Dan HB, Wang LZ (1996) Undrained behavior of natural marine clay under cyclic loading. Ocean Eng 38(16):1792–1805

Li D, Selig ET (1996) Cumulative plastic deformation for fine-grained subgrade soils. J Geotech Eng 122(12):1006–1013

Liu JK, Xiao JH (2010) Experimental study on the stability of railroad silt subgrade with increasing train speed. J Geotech Geoenviron Eng 136(6):833–841

Murthy AVSR (1996) Fly ash in construction of roads and embankments, Central Road Research Institute India

Procter DC, Khaffaf JH (1984) Cyclic triaxial tests on remoulded clays. J Geotech Engrg 110(10):1431–1445

Sangrey DA, Polard WS, Egan JA (1978) Errors associated with rate of undrained cyclic testing of clay soils. In: Cyclic geotechnical testing. ASCE, Special Technical Publication STP 654, pp 280–294

Zimmie TF, Lien CY (1986) Response of clay subjected to combined cyclic and initial static shear stress. In: Proceedings of 3rd Canadian conference on marine geotechnical engineering, pp 655–675

Zhou J, Gong XN (2001) Strain degradation of saturated clay under cyclic loading. Can Geotech J 38:208–212

Challenges of Embankment Design to Comply with Statutory Requirements for Environment Protection

Vimal Kumar, K. N. Agrawal and A. Sridharan

Abstract A large number of big and small embankments are constructed in India with soil for road infrastructure. The Government of India, with an objective to curtail this unsustainable practice issued its First Notification [S.O.763(E) dated 14 September 1999] under Environment Protection Rules 1986 and issued amendment [S.O.979 (E) dated 27 August 2003] forbidding the design or construction of road and flyover embankment located within 100 km of a coal-based thermal power plant with soil and mandating that such embankments shall be designed and constructed with fly ash. The amendment [S.O.254 (E) dated 25 January 2016] has increased the above-said lead distance of 100–300 km. With increased knowledge of benevolent fly ash engineering properties, a large number of road and flyover embankments have been constructed in India with fly ash, including 8–10-m-high road embankment in flood zone area, road and flyover embankments in marshy and wetlands and reinforced fly ash walls (in place of reinforced soil/ RE walls). All fly ash embankments have performed very well for more than two decades. No signs of distress or settlement have been reported. In spite of the above, a number of road embankments are still being designed and constructed with topsoil within the forbidden lead distance of 300 km from coal-based thermal power plants. Geotechnical design engineers have the challenging moral and professional duty to abide by the legal and statutory framework even though their clientele may be ignorant.

V. Kumar (✉)
Fly Ash, DST, GoI, New Delhi, India
e-mail: info@c-farm.org

V. Kumar · K. N. Agrawal
Centre for Fly Ash Research and Management (C-FARM), F-39, LGF, Kalkaji, New Delhi 110019, India

K. N. Agrawal
CPWD, New Delhi, India

A. Sridharan
IISc, Bangalore, Bengaluru, India

Indian National Academy of Science, New Delhi, India

R. Sundaram et al. (eds.), *Geotechnics for Transportation Infrastructure*, Lecture Notes in Civil Engineering 28, https://doi.org/10.1007/978-981-13-6701-4_7

Keywords Fly ash · Embankments · Environment protection · Fly ash notifications

1 Genesis

In India, electricity generation primarily depends on coal as the source of energy. During the initial years after independence, the share of coal-based electricity generation was higher than 80%. The continued efforts to increase the share of nuclear power, hydropower, solar power and wind power have succeeded to the extent that the share of coal-based power generation has come down to about 65%. The projections made about four years back by the then Planning Commission and the Ministry of Power indicate that this share of coal as an energy source for electricity generation would continue at least up to 2031–32. The current thrust and emphasis on solar and wind energy may have some impact on this projection.

With large quantity of coal being burnt in thermal power stations, a huge quantity of fly ash, the residue of burning of coal is generated. This magnitude of ash generation takes a mammoth size due to a high ash content in Indian coals made available to coal-based thermal power stations. The fly ash generation in the country during 1994 was about 40 million tonne, and its utilization was only about 1 million tonne. The unutilized fly ash is put into ash ponds as slurry, and in some cases, it was allowed, during the early years, to flow into water bodies causing water pollution. Non-maintenance of ash ponds results in air pollution as fly ash being a light material gets airborne easily, especially during the summer season. Fly ash even during those years was being utilized gainfully in many other countries. In India, quite a good number of research works were done before that time, the findings of which indicated that fly ash is a suitable material for various applications.

Taking cognizance of these facts, the Government of India through the Department of Science and Technology (DST) commissioned a Fly Ash Mission (FAM) in August, 1994, to take forward the earlier research work done in the area of fly ash to the development of technologies, field demonstration, confidence building and for large scale utilization in the field, *inter alia*, facilitation of development of standards, specifications, code of practices and statutory provisions, etc. The use of fly ash in the construction of road embankment and its utilization in the treatment of problematic soils was among the thrust areas of Fly Ash Mission (FAM).

It has been proved and established that fly ash is a good material for geotechnical applications, besides its suitability for many others. By virtue of its physical and geotechnical properties, fly ash is a good substitute of soil and even moorum when coarser bottom ash is used.

Coinciding with the period of FAM, there was a thrust on development and upgradation of national road network. This provided an opportunity to substitute soil by fly ash for the construction of road embankments including reinforced walls. The field applications proved beyond doubt that the construction of road embankments,

which uses topsoil, resulting in creation of new low-lying areas, can be done using fly ash that is available in plenty.

The annual fly ash generation in the country increased to about 90 million tonne by 2000 and to 190 million tonne by 2010, and currently, it stands at 240 million tonne. The corresponding percentage utilization of fly ash has been 17.78 in 2000, 52.63 in 2010 and 56.25 as of now. In addition to this, more than 2000 million tonne of fly ash is available in the ash ponds. With this background, the Government of India through the Ministry of Environment, Forests and Climate Change (MoEF&CC) brought out notifications at different points of time making it mandatory to use fly ash for the construction of road embankments within a lead distance of 100 km and increased the same to 300 km from coal-based thermal power plants to conserve the topsoil and facilitate utilization of fly ash towards environment protection.

2 Properties of Fly Ash

Properties of fly ash that make it suitable for the construction of road embankments include its gradation, compaction, shear strength, compressibility and permeability. Fly ash has a silty texture, non-plastic in nature and has specific gravity generally in the range of 2.0–2.5. It is less sensitive to variation in moisture content than that of natural soils.

Moisture content–dry density compaction graph of fly ash is generally flatter than that of soils. This is by virtue of higher air voids at MDD in fly ash (10–15%) than soils (that have up to 5%) which tends to limit the build-up of pore water pressure during compaction. The physical and geotechnical properties of fly ash vis-à-vis common soils can be viewed at www.c-farm.org/characterization.html.

Though fly ash is a cohesionless material, it has a higher angle of internal friction (about 30°–40°); in addition, compressibility of fly ash is about half than that of clay loams but with higher consolidation rate (Sridharan et al. 2001).

Subsequent settlement in fly ash embankment is practically nil. However, these embankments need to be protected with soil cover and appropriate pitching on the sides.

The soil material required for the protection cover can be excavated from the alignment itself. If the alignment soil is not suitable as a cover material, it can be borrowed from nearby area. The pit created in the process should be filled/ reclaimed by fly ash with a soil cover.

3 The Need to Use Fly Ash in Embankment Construction

The large quantity of fly ash generation in the country and its leftover quantities after use in various applications demand huge area for its deposition in the ash ponds. On the other hand, soils excavation for the construction of road embankments consumes

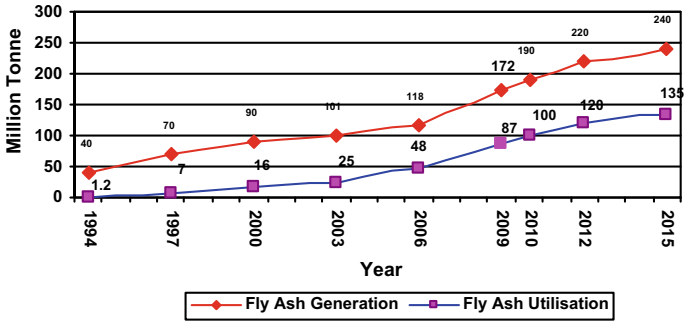

Fig. 1 Fly ash generation and utilization

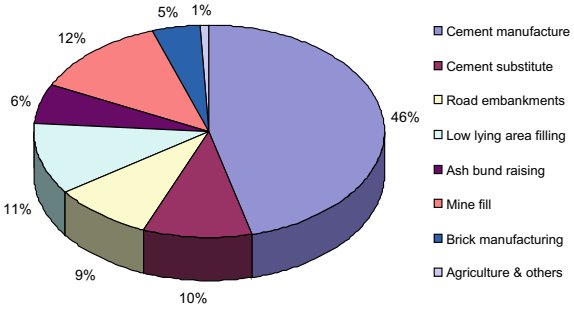

Fig. 2 Fly ash utilization percentage share of different applications of the utilized fly ash

precious topsoil and creates low-lying areas. Figure 1 presents fly ash generation and utilization levels since 1994. Figure 2 depicts the ash utilization scenario for different application areas. The accumulated 2000 MnT of unutilized fly ash has already occupied more than 50,000 ha of precious land in the form of ash ponds. It will grow further if fly ashes are not utilized.

4 Road Embankments with Fly Ash

More than 100 road embankments including reinforced soil walls have been constructed in the country by use of fly ash. A few are listed below:

i. *Vishveshvaraya Setu (Okhla Flyover) Project, New Delhi* (Vimal et al. 2018)

One side of the eastern slip roads adjoining NH2 was very close to the boundary of adjoining private property. The construction of conventional RCC retaining wall would have encroached into private property because of its large foundation base.

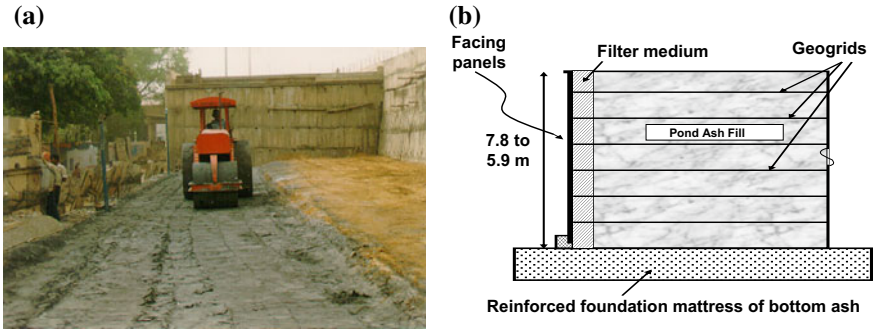

Fig. 3 A & 3B: Vishveshvaraya Setu (Okhla Flyover) Project, New Delhi

This was avoided by the construction of a reinforced fly ash embankment with a RCC facia. It was practically the first application of fly ash in the construction of road embankment in the country, which was made possible by collaborative work of Delhi PWD, CRRI and the Fly Ash Mission. This was the first successful field application of fly ash (pond ash) in road embankment construction in the country. The typical cross section is given in Fig. 3.

ii. *Approach Road Embankment for Second Nizamuddin Bridge Project, New Delhi* (Guru Vittal and Sudhir 2006b)

This is the second and the most important field project of use of fly ash in road embankment construction in the country and may be the only one of its kinds in the world.

The embankment is 1.9 km long and 6–9 m high in a flood zone area a little downstream of the existing Nizamuddin bridge across river Yamuna on NH4 connecting outer ring road of Delhi to Akshardham Temple side. This was a prestigious project for the use of fly ash (pond ash), a cohesionless, lightweight material. The embankment design with filter layers was done by CRRI, logistic support by Fly Ash Mission and execution by PWD-Delhi. The typical cross section of this embankment is in Figs. 4 and 5 shows the work in progress.

Vibratory rollers were used for better compaction. Uniform layers of 25–30 cm thickness (loose) were placed. The road on the embankment was open to traffic in 1998. The post-construction performance was monitored by CRRI through magnetic settlement gauges, pressure cells and piezometers. The success of this project led to the initiative of Indian Road Congress in bringing out a special publication SP 58 for the construction of road embankments with fly ash.

iii. *Yamuna Bazaar Flyover Retaining Wall (Monkey Bridge), Delhi*

The twin approach retaining walls on the river Yamuna side face of this flyover on ring road at Yamuna bazaar near Hanuman Mandir, Delhi, was constructed as fly ash-reinforced wall. Geogrids of mono-oriented HDPE variety was used as the

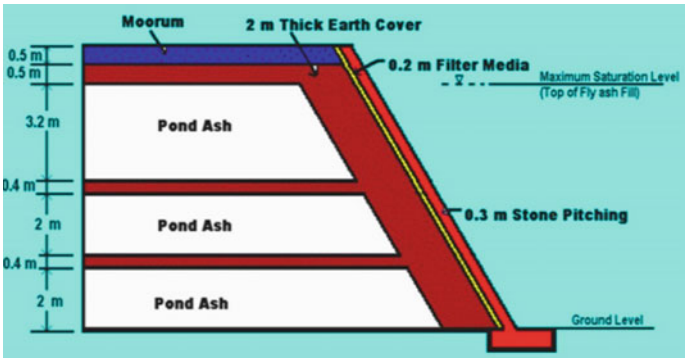

Fig. 4 Road embankment for Nizamuddin Bridge Project, Delhi

Fig. 5 Road embankment for Nizamuddin Bridge Project, Delhi

reinforcing element. The height of the embankment varies up to 4.5 m. Its formation level has an approach gradient of 1 in 25. The embankment was constructed by PWD-Delhi with technical support from CRRI.

iv. *Punjabi Bagh Flyover, New Delhi*

Flyover on the Ring Road at the intersection of Rohtak Road in New Delhi was constructed by PWD-Delhi with geogrid-reinforced fly ash wall. The approach roads to the flyover from Raja Garden side and Azadpur side are 125.5 and 129.5 m, respectively. The maximum height of the embankment is 4.5 m.

v. *Allahabad Bypass*

The project was for four-laning of a length of 84 km of NH2 to provide a bypass of Allahabad. The height of the road embankment is 3–6 m. It utilized about 6,732,000 m^3 of pond ash as the fill material sourced from Unchahar Thermal Power Station. The thickness of soil cover was kept at around 1.5 m, and intermediate layers

of 0.4 m thickness were provided at intervals of 2 m to protect erosion by air/water during construction.

vi. *Use of Pond Ash for Four-Laning Work of NH 6 from Dankuni to Kolaghat, West Bengal* (Guru Vittal and Sudhir 2006a)

Four-laning of NH6 from Dankuni to Kolaghat in West Bengal during 2004–2005 has used 20 million cubic metre of pond ash for embankment construction. The height of the embankment varies from 1.5 to 4 m. Soil cover of 1.5 m thickness was provided. No intermediate layers of soil, bottom ash or moorum were provided. Some stretches of the embankment had waterlogged marshy lands. After dewatering, sand and bottom ash layers of 0.5 m thickness were used (Figs. 6 and 7).

Fig. 6 Four laning work of NH 6 from Dankuni to Kolaghat

Fig. 7 Sarita Vihar Flyover, Delhi

vii. *Sarita Vihar Flyover, Delhi* (Guru Vittal and Sudhir 2006a)

The approach embankment to Sarita Vihar Flyover on Mathura Road, Delhi, has divided carriageway of three lanes on each side. The embankments were constructed with reinforced fly ash wall technology with reinforcement of polymeric ties. The pond ash was sourced from Badarpur Thermal Power Station at about 5 km distance from the project site. The angle of internal friction of pond ash was found to be around 34°. The construction was undertaken by DDA, and proof checking of the design was done by CRRI.

viii. *Rail Over Bridge (ROB) at Chandrapur, Maharashtra*

The ROB constructed at Babupeth, Chandrapur, has a length of 234 m on Chandrapur side and 174 m on Nagpur side. The maximum height of the embankment is 10.5 m. The site, being very near Chandrapur residential area, had space constraint. Hence, it was decided to construct a geogrid-reinforced wall. After due to consideration and keeping in view the space constraints and the fact that the site has poor subsoil strata, it was decided to use fly ash as the fill material in the reinforced wall.

ix. *Rail Over Bridge (ROB) at Raniganj, West Bengal*

The subsoil at the site was of poor engineering quality and was inadequate to carry the loads of the proposed retaining wall. The cost of conventional foundation treatment to improve the bearing capacity was very high. It was decided to improve the local soils' load-bearing capacities by using bi-oriented geogrid/ geocell mattress and to use fly ash, a low weight material, in lieu of soil as fill material for the reinforced wall. The maximum height of embankment is 14 m with a gentle slope up to a distance of 280 km on each side of the ROB.

x. *Widening of Marginal Bund Road at Khajuri, Delhi* (Guru Vittal and Sudhir 2006b)

PWD-Delhi undertook widening of marginal bund road from G.T. Road to Khajuri Chowk, Delhi, using fly ash [pond ash] sourced from Indraprastha Power Station, New Delhi. This section of marginal bund was in a flood zone area of Yamuna River. The embankment height is 6 m with side slopes provided at 1:2 and soil protection layer of about 2 m with two intermediate soil layers of 20 cm. The technical advice was provided by CRRI. The cross section is shown in Fig. 8.

xi. *Use of Fly Ash in the Construction of Kalindi Bypass Embankment on Soft Grounds in New Delhi* (Guru Vittal and Sudhir 2006a)

The embankment is about 4.5 km long from Kalindi Colony to Kalindi Kunj going parallel to river Yamuna. The alignment has soft slushy grounds of 0.5–3 m depth at various locations. CRRI was a consultant to this project of PWD-Delhi. Suitable embankment section using fly ash as construction material was designed by CRRI based on the detailed subsoil investigation using SPT and dynamic cone penetration methods. Fly ash being a light material, no special ground improvement measures were required. Figure 9 shows the work in progress.

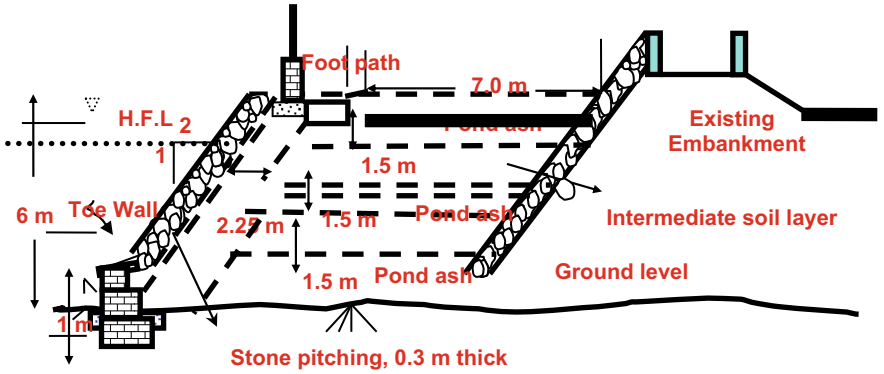

Fig. 8 Widening of Marginal Bund Road at Khajuri, Delhi

Fig. 9 Construction of Kalindi bypass

xii. *Construction of Outer Ring Road, Chennai with Fly Ash*[1]

The Outer Ring Road, Chennai, constructed with fly ash sourced from North Chennai Thermal Power Plant as an embankment material, is a major transport corridor developed along the periphery of Chennai Metropolitan Area (CMA) by the Chennai Metropolitan Development Authority (CMDA). It is 62.3 km long connecting NH 32 (GST Road) at Vandalur, NH 48 (GWT Road) at Nazarethpettai, NH 716 (CTH Road) at Nemilichery to NH 16 (GNT Road) at Nallur and to TPP road at Minjur.

The Phase I of 29.65 km started during August 2010 includes 10 grade separators at major junctions, 50 bus bays and truck lay-byes for parking of around 100 trucks.

Phase II of the project from Nemilicheri to Minjur of 32.65 km length has 143 structures that includes bridges, pedestrian underpasses, vehicular underpasses and

[1]Chennai Outer Ring Road, Tamil Nadu—India, Use of VSoL® retained earth walls for the first phase of a PPP highway.

Fig. 10 Reinforced fly ash wall resting on fly ash-filled area

interchange. The embankments of flyover bridges (Fig. 10) are constructed as fly ash-reinforced walls. Another important feature is that the reinforced fly ash walls are constructed on the fly ash-filled area itself (Sarkar and Ranjana 2012).

A consortium of GMR Group and NAPC India Ltd appointed by Tamil Nadu Road Development Corporation has built the project under a public–private partnership (PPP).

All the fly ash embankments in the country are performing without any failure/ signs of distress, to the best of knowledge of the authors. The annual use of fly ash in the construction of road embankments is currently around 12 million tonne only, but the potential of the use of fly ash is manifold.

5 Statutory Environment Protection: Design Requirements

5.1 Environmental Impact of not Using Fly Ash

It is not difficult to imagine and work out the additional land area that could have been converted into barren land and/ or low-lying area if the fly ash actually used for the construction of road embankments over the last 15–20 years had not have been used for this purpose. In addition, the land area that would have been occupied by the used fly ash, in the form of ash ponds for it's deposition. The estimate works out to about 60,000 acres of land. Thus, the use of fly ash for the construction of road embankments has so far saved about 60,000 acres of land. Land area that has not been saved, by not using fly ash and wherein topsoil has been used is manifold of this.

Moreover, had the fly ash not been used for the construction of road embankments and instead was stored in ash ponds, it would have perpetually demanded maintenance

of ash ponds in terms of water and money and/ or other resources and would have become a source of air and water pollution.

5.2 *Statutory Provisions*[2,3,4,5]

With the above in view and with a foresight, the Government of India through its Ministry of Environment and Forests (MoEF), now known as Ministry of Environment, Forest and Climate Change (MoEF&CC), issued notification no. S.O.979(E) dated 27 August 2003 after about 2 years of publication of SP-58 by IRC, banning the use of soil for design or the construction of road or flyover embankment and filling of low-lying area within a distance of 100 km of a coal-based thermal power plant. An amendment was issued, to bring in more clarity, vide notification no. S.O.2804(E) dated 3 November 2009. The relevant three sub-paragraphs are reproduced here under:

2(5) No agency, person or organization shall within a radius of hundred kilometres of a thermal power plant undertake construction or approve design for the construction of roads or flyover embankments with topsoil; the guidelines or specifications issued by the Indian Road Congress (IRC) as contained in IRC specification No. SP:58 of 2001 as amended from time to time, regarding use of fly ash shall be followed and any deviation from this direction can only be agreed to on technical reasons if the same is approved by Chief Engineer (Design) or Engineer-in-Chief of the concerned agency or organization or on production of a certificate of "fly ash not available from the thermal power plant(s) (TPPs) located within hundred kilometres of the site of construction and this certificate shall be provided by the TPP within two working days from the date of receipt of a request for fly ash if fly ash is not available".

2(6) Soil required for top or side covers of embankments of roads or flyovers shall be excavated from the embankment site, and if it is not possible to do so, only the minimum quantity of soil required for the purpose shall be excavated from soil borrow area. In either case, the topsoil should be kept or stored separately. Voids created at soil borrow area shall be filled up with fly ash with proper compaction and covered with topsoil kept separately as above, and this would be done as an integral part of embankment project.

2(7) No agency, person or organization shall within a radius of hundred kilometres of a coal- or lignite-based thermal power plant undertake or approve or allow reclamation and compaction of low-lying areas with soil; only fly ash shall be used for compaction and reclamation, and they shall also ensure that such reclamation and

[2]MoEF Notification on Fly Ash, No. S.O.763(E) dated 14th September, 1999.

[3]MoEF Notification on Fly Ash, No. S.O.979(E) dated 27th August, 2003.

[4]MoEF Notification on Fly Ash, No. S.O.2804(E) dated 3rd November, 2009.

[5]MoEF&CC Notification on Fly Ash, No. S.O.254(E) dated 25th January, 2016.

compaction are done in accordance with the specifications and guidelines laid down by the authorities mentioned in sub-paragraph (1) of paragraph 3.

5.3 Notification Amendment in 2016

Vide notification no. S.O.254(E) dated 25 January 2016, the Government of India through its Ministry of Environment, Forest and Climate Change (MoEF&CC) increased the mandatory lead distance from thermal power plant for use of fly ash in the construction of road embankments from 100 to 300 km and added the following five additional sub-clauses to facilitate availability of fly ash and reduce the cost burden on road projects:

2(8) Every coal- or lignite-based thermal power plants (including captive and or co-generating stations) shall, within three months from the date of notification, upload on their website the details of stock of each type of ash available with them and thereafter shall update the stock position at least once a month.

2(10) The cost of transportation of ash for road construction projects or for manufacturing of ash-based products or use as soil conditioner in agriculture activity within a radius of hundred kilometres from a coal- or lignite-based thermal power plant shall be borne by such coal- or lignite-based thermal power plant, and the cost of transportation beyond the radius of hundred kilometres and up to three hundred kilometres shall be shared equally between the user and the coal- or lignite-based thermal power plant.

2(13) To ensure that the contractor of road construction utilizes the ash in the road, the authority concerned for road construction shall link the payment of contractor with the certification of ash supply from the thermal power plants.

2(14) The coal- or lignite-based thermal power plants shall within a radius of three hundred kilometres bear the entire cost of transportation of ash to the site of road construction projects under Pradhan Mantri Gramin Sadak Yojana and asset creation programmes of the Government involving the construction of buildings, road, dams and embankments.

3(8) It shall be the responsibility of all state authorities approving various construction projects to ensure that memorandum of understanding or any other arrangement for using fly ash or fly ash-based products is made between the thermal power plants and the construction agency or contractors.

5.4 Facilitation Action by Thermal Power Plants

In pursuance of MoEF&CC notification dated January 2016, most of the thermal power plants have framed policy and guidelines for making available the fly ash for the construction of roads and flyover embankments besides other usages.

6 Way Foreword

It is well established that the use of topsoil for the construction of road and flyover embankments degrades the environment. It is also well established that fly ash, a residue of burning of coal in thermal power plants, generated in large volume, if not utilized, would add to environmental problems. On the other hand, it is also well established and proven that fly ash is a good substitute of topsoil for the construction of road and flyover embankments. Further, recognizing the above-said facts, the Government of India through its MoEF&CC notifications has made it mandatory not to use topsoil but to use fly ash for the construction of road and flyover embankments within a distance of 300 km of a coal-based thermal power plant and has also facilitated the availability of fly ash at the project site delivered by thermal power plant free of cost.

Thus, it becomes the primary duty and mandatory obligation of road and flyover embankment designers, approving authorities as well as contracting agency not to undertake any road projects with the use of soil within 300 km of coal-based thermal power plants.

In most cases, the details covered in this paper may not have reached to the project owners/ authorities, and out of sheer ignorance, there may be requests or demands to design or approve or construct the road or flyover embankments with soil. In such cases, the concerned authorities/ individuals may be made aware of the statutory requirements as mandated by the MoEF&CC notifications in addition to consider it as a societal commitment.

It is important to note that with free delivery of fly ash at project site, the issues of the distance of project site from the thermal power plant and the cartage cost have become irrelevant from the point of view of the road projects.

7 Conclusion

Topsoil needs to be conserved. Fly ash that is a good geotechnical material substitute of soil is mandatory to be used in place of soil for the construction of road and flyover embankments within 300 km of a coal-based thermal power plant. Standards, specifications and guidelines for this use of fly ash are in place. A large number of such projects have successfully used fly ash even in difficult soil conditions including flood zone areas. Cost economic issues have also been resolved. Hence, all need to go in a big way to conserve topsoil and use fly ash.

References

Guru Vittal UK, Sudhir M (2006a) Experiences of fly ash road embankment demonstration projects
Guru Vittal UK, Sudhir M (2006b) Construction of rural roads using fly ash: some case studies

Sarkar SS, Ranjana M (2012) Geo-grid reinforced fly ash technology for construction of approach embankment for ROBs/flyovers in India with case histories
Sridharan A, Pandian NS, Subramanya PP, Srinivas S (2001) Characterization of fly ash. Department of Civil Engineering, Indian Institute of Science, vol 1–8
Vimal K, Mukesh M, Shashank Shekhar S (2018) A case study: manifold increase in fly ash utilisation in India

Comparison of Strength of Recycled Bituminous Pavement in Design and After Execution

Yash Pandey and Atasi Das

Abstract Foam bitumen-treated reclaimed asphalt pavement (RAP) and cement-treated subbase (CTSB) is a widely used technology around the world, but India is still novice in implementing this technology. Although CTSB has found extensive usage recently, RAP has been minimally used for roads of lesser importance. It is a need to perform an exhaustive study on the RAP uses at the place where there is a growing scarcity of proper material for the construction. RAP and CTSB give the benefit of an extensive reduction in material consumption when compared to other pavement options. The current study focuses on the utilization of new technology in rapidly growing infrastructure. RAP preparation could be in-plant or in situ in hot recycling or cold recycling. In this project case, cold in-plant recycling process has been used for RAP generation. In this paper, the laboratory and field evaluation of a newly laid pavement with bituminous concrete (BC), RAP, and CTSB have been done. The design parameters like the Marshall's stability, air voids, density, tensile strength, and elasticity/resilient modulus parameters for BC and RAP are evaluated in laboratory by extracting the cylindrical cores from the newly laid pavement. A field study using falling weight deflectometer (FWD) technique has also been successfully conducted for the same pavement to confirm the most important parameter of elastic/resilient moduli adopted for the various pavement layers in pavement design. The back-calculation is done using KGPBACK software developed by IIT Kharagpur. The laboratory and field findings of the elastic/resilient moduli of the materials corroborate with each other. The study shows that the adoption of RAP and CTSB is a cost-effective option for the construction industry.

Keywords Falling weight deflectometer (FWD) · Reclaimed asphalt pavement (RAP) · Cement-treated subbase (CTSB)

Y. Pandey · A. Das (✉)
G R Infraprojects Limited, 2nd Floor, Novus Tower, Plot 18, Sector 18, Gurugram 122002, Haryana, India
e-mail: atasid@gmail.com

Y. Pandey
e-mail: yashpandey5@gmail.com

R. Sundaram et al. (eds.), *Geotechnics for Transportation Infrastructure*, Lecture Notes in Civil Engineering 28, https://doi.org/10.1007/978-981-13-6701-4_8

1 Introduction

Foam bitumen-treated RAP and CTSB are the latest and less popular technologies in India. These are cost-effective and environmental friendly technologies which not only reduce the scarcity of natural resources but also help in getting the carbon credits. There are very less highways laid using foam bitumen-treated RAP. The growing economy increased the necessity of the highway infrastructure. To increase the awareness about the RAP and CTSB, it is required to evaluate the pavement laid with RAP and CTSB in the Indian condition. In the present study, evaluation of the same has been done using falling weight deflectometer (FWD) technique. FWD is a state-of-the-art equipment used for non-destructive testing of the pavements. It is extensively used equipment to determine the in-service strength parameters of the different pavement layers.

1.1 Literature Review of RAP and CTSB

The foam bitumen-treated RAP is prepared by recycling of existing bituminous pavement. In RAP, the existing milled bituminous material is mixed with some amount of low viscosity bitumen by making foam of it. The CTSB is prepared with the addition of 2% of cement in the GSB material. Adding the cement increases the strength of the GSB by two to three times. The foam bitumen-treated RAP and CTSB is a cost-effective technology which saves the natural resources and also reduces the pavement thickness in comparison to the conventional system due to their high strength. Also, the RAP is produced at a lower temperature which reduces the fume emission.

1.2 Falling Weight Deflectometer

FWD being a non-destructive testing equipment provides easiness in collecting a large number of data with high accuracy. FWD works on the principal of application of dynamic load similar to that applied by a standard axle and then producing a deflection on the different layers of the pavement as shown in Fig. 1 (IRC: 115-2014). The FWD equipment is equipped with highly sophisticated data acquisition system which is responsible for acquiring data from the geophones, stationed at a number of points on the road surface at different radial distance centrally outward from the falling weight, which have recorded the instantaneous deflection caused due to application of instantaneous load impulse similar to the standard load.

FWD offers a number of advantages over the conventional way to structurally evaluate the strength of pavement. In laboratory evaluation, it is required to extract the cores of different layers from site and then test in laboratory under controlled conditions for the strength determination, whereas the FWD test is a non-destructive

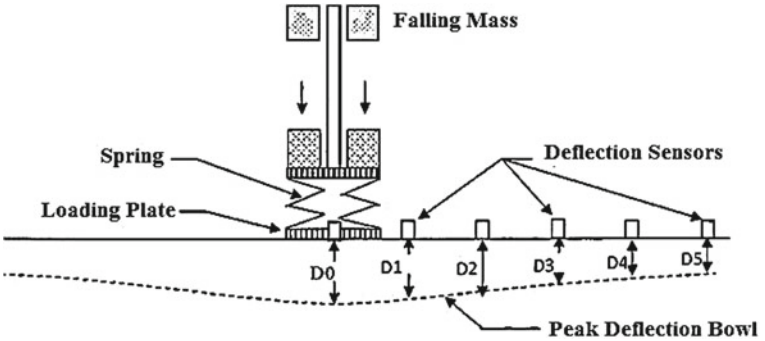

Fig. 1 Working principle of FWD

test in which in a short span of time evaluation of the structural strength of the different layers can be done simultaneously without disturbing the pavement layers.

2 Brief Review of the Project Highway

The present study is done on a 10 km section of National Highway located in Rajasthan state of India having design traffic loading of 15 million standard axle and design period of 15 years. The annual average pavement temperature (AAPT) of the study region is about 33 °C. The design subgrade soil CBR is taken as 12%.

3 Pavement Design Using IITPAVE

The pavement design of the selected region is done based on the mechanistic-empirical design approach as per the Guidelines for the Design of Flexible Pavement (IRC 37:2012) using IITPAVE software.

The schematic details of the combination of layers selected for the pavement section are shown in Fig. 2 (IRC: 37-2012).

3.1 Pavement Thickness Design

The proposed crust thickness and the design input in IITPAVE are shown in Fig. 3, and corresponding allowable strains from fatigue/rutting models and computed strains from IITPAVE are described in Table 1.

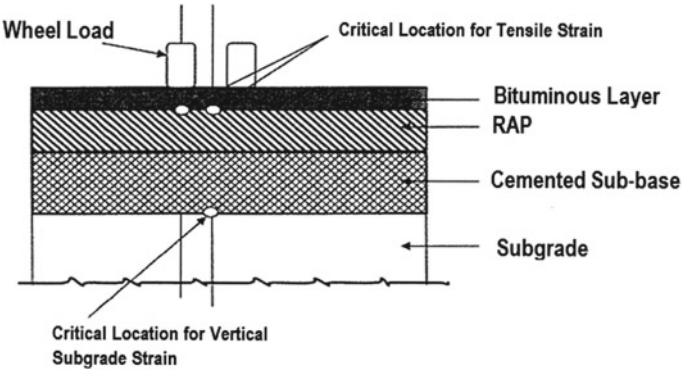

Fig. 2 Schematic details of pavement layers

From Table 1, it is clear that the computed strain values from IITPAVE are less than the allowable strain values. Hence, the design is safe.

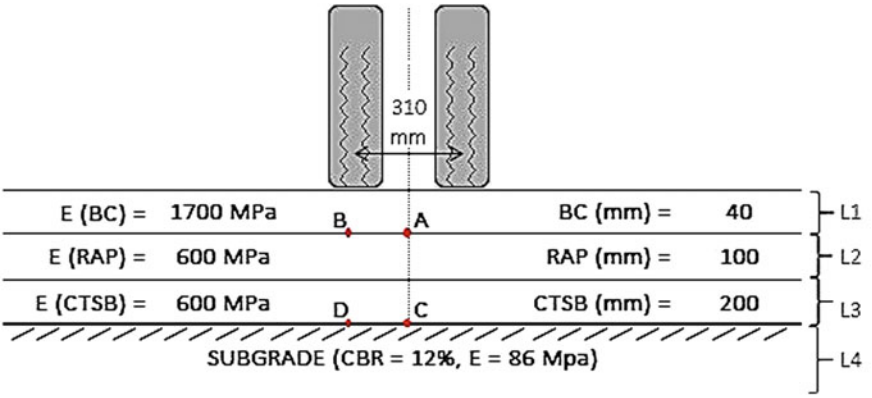

Fig. 3 Pavement composition

Table 1 Tensile and vertical strain calculations

Tensile strain at bottom of bituminous Layer (microns)		Vertical subgrade strain (μ)	
Computed	Allowable	Computed	Allowable
59	320	522	615

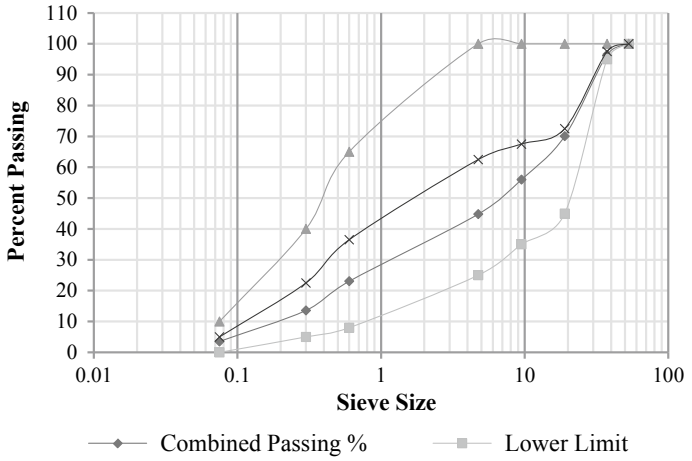

Fig. 4 Gradation curve for CTSB

Fig. 5 A view of KMA 220 plant

4 Objective

The objective of the research work is to verify the strength parameters adopted in design with that obtained in field. The field strength parameters can be obtained using destructive and non-destructive testing. In destructive testing, the cores of bituminous material are extracted from field and then tested for elasticity modulus, and in non-destructive testing, the in situ elasticity modulus is found out using FWD technique.

5 Construction Methodology

The subgrade is prepared prior to the construction of the CTSB in accordance to the MORTH specifications with borrow area soil having CBR in between 14 and 19%.

5.1 Methodology for CTSB

The material used for construction of the CTSB is the granular subbase (GSB) material, stone dust, and cement. Firstly, the firmly mixed GSB and stone dust material are mixed, and then, the 2% of cement is added to it. The water in the desired quantity as per the mix design is added to prepare the CTSB mix. The material is firmly mixed in the Wirtgen KMA 220 plant as shown in Figs. 5 and 6, and the CTSB mix is then loaded to the truck and sent to site for laying. The CTSB material prepared from KMA plant should be laid and compacted within 2 hours of preparation; else, it starts setting. Figure 7 shows the laying, and Fig. 8 shows the properly laid and compacted CTSB layer. The CTSB gradation adopted is shown in Fig. 4 and the mix design parameters achieved at the site is presented in Tables 2 and 3. The freshly laid CTSB layer is cured for a minimum period of 7 days.

5.2 Methodology for Foam Bitumen-Treated RAP

The RAP is laid over the prepared CTSB surface with prime coat, and tack coat of emulsion is laid over it. The foam bitumen-treated RAP is prepared with the existing milled-off bituminous layer material. The existing bituminous milled material is mixed with stone dust (as per suitable gradation in Fig. 9), and then, the material is mixed with foam bitumen. Foam bitumen is the mixture of very hot (about

Fig. 6 Preparation of CTSB mix in KMA plant

Fig. 7 Laying of CTSB

Fig. 8 Prepared CTSB surface

Table 2 Gradation of CTSB

Sieve size (mm)	Material % passing			Combined % passing GSB:dust:cement 83:15:2	Specified % passing	
	GSB	Stone dust	Cement		Lower	Upper
53.000	100.00	100.00	100.00	100.00	100.0	100.0
37.500	95.74	100.00	100.00	96.46	95.0	100.0
19.000	63.93	100.00	100.00	70.06	45.0	100.0
9.500	47.00	100.00	100.00	56.01	35.0	100.0
4.750	33.80	98.32	100.00	44.80	25.0	100.0
0.600	19.33	33.30	100.00	23.04	8.0	65.0
0.300	11.73	12.29	100.00	13.58	5.0	40.0
0.075	1.65	1.55	96.40	3.53	0.0	10.0

Table 3 Physical properties of CTSB

S. no.	Description	Test method	Result	Specified limits
1	Maximum dry density (gm/cc)	IS- 2720 (Part VIII)	2.202	–
2	Optimum moisture content	IS- 2720 (Part VIII)	6.52	–
3	Liquid limit (%)	IS- 2720 (Part V)	21.1	Max. 25
4	Plasticity index (%)	IS- 2720 (Part V)	NP	Min. 6
5	Water absorption (%)	IS- 2386 (Part III)	1.710	Max. 2
6	UCS (MPa) with 2% cement	IS- 2720 (Part X)	1.81 (3 day) 2.3 (7 day)	1.5 to 3.0 for 7 days
7	CBR (%)	IS- 2720 (Part XVI)	97.5	–

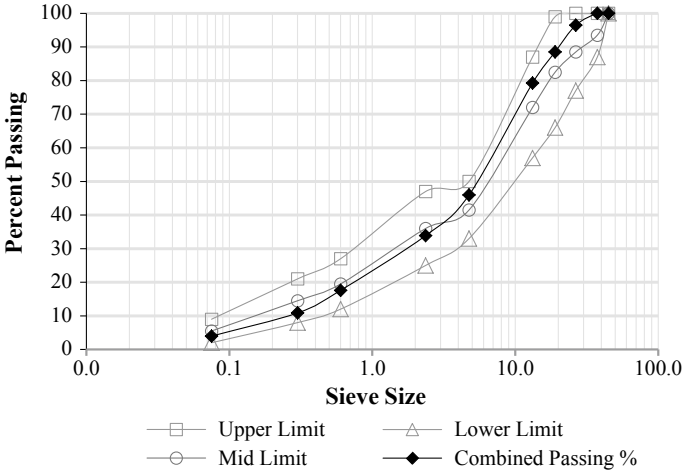

Fig. 9 Gradation curve for RAP

120–130 °C) low viscosity VG10 bitumen with water, due to which the volume of bitumen expands by 8–10 times which is called as foam. This is also prepared in the KMA plant same as that for CTSB. The mix design properties in the current work are shown in Tables 4, 5, and 6 and Fig. 10. After the mix design, the same mix is prepared in KMA plant for the laying of foam bitumen-treated RAP. The paved surface is kept damp for about 3 days with light sprinkle of water during day time till the sealing of surface is done by spraying emulsion. The surface is cured for about 21 days. The operations being carried out at site are shown in Figs. 11, 12, 13, 14, 15, 16, and 17.

Soon after the curing of the RAP, the BC layer is laid and constructed.

Table 4 Gradation of RAP

Sieve size (mm)	Material % passing			Combined % passing RAP:SD:cement 84:15:1	Limits as per IRC 120-2015	
	RAP	Stone dust	Cement		Lower	Upper
45.0	100	100	100	100.00	100	100
37.5	100.00	100	100	100.00	87	100
26.5	95.79	100	100	96.46	77	100
19.00	86.34	100	100	88.53	66	99
13.20	75.28	100	100	79.23	57	87
4.75	35.91	98.73	100	45.97	33	50
2.360	23.21	89.18	100	33.88	25	47
0.600	10.93	49.49	100	17.61	12	27
0.300	6.82	27.63	100	10.87	8	21
0.075	1.77	10.14	96.52	3.98	2	9

Table 5 Determination of water injection

S. no.	Water injected (%)	Temperature (°C)	Half-life (s)	Expansion ratio (times)
1	2	180	18	4
2	3		12	6
3	4		7	10
4	5		4	16

Table 6 Mechanical properties of foam bitumen-treated RAP

S. no.	Name of test	Unit	Test result	Specified limit
1	OMC	%	4.94	–
2	MDD	gm/cc	2.078	–
3	Bulk density	kg/m^3	2171	–
4	OBC, VG10	%	2.5	
5	ITS dry	kPa	338	Min. 225
6	ITS soaked	kPa	313	Min. 100
7	Tensile strength ratio (TSR)	%	92.55	Min. 80

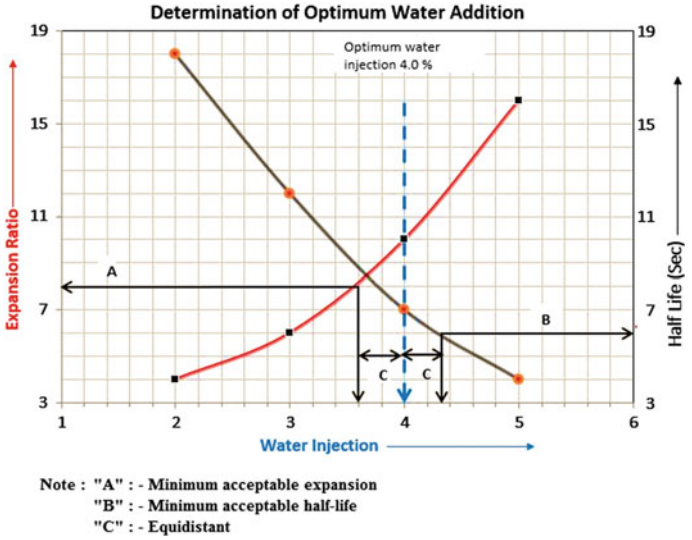

Fig. 10 Determination of optimum water addition

Fig. 11 Milling of the existing bituminous surface for RAP material

Fig. 12 Preparation of foam bitumen RAP in KMA plant

Fig. 13 Loading of RAP mix into dumpers

Fig. 14 Paving of foam bitumen-treated RAP layer using paver

Fig. 15 Compaction operation in progress

Fig. 16 Finished foam bitumen-treated RAP surface

Fig. 17 Sealing of finished surface with Emulsion

6 Methodology Adopted for FWD Test

The 10 km road section is divided into intervals of 500 m in staggered manner. The deflections were measured at the outer lane of each side at a distance of 1 m from the pavement marking. For the testing purpose, the FWD machine used was PaveFWD manufactured by Pave Testing Inc., UK. The FWD machine was first calibrated for the load repeatability at the site. The eight geophones at a radial distance (mm) of 0, 200, 300, 600, 900, 1100, 1350, and 1600 were used to measure pavement response in form of rebound deflections. The deflections were noted using the PaveFWD software provided with the FWD equipment. Also, the pavement and atmospheric temperatures were recorded. The FWD data so obtained is then analyzed using KGP-BACK software developed by IIT Kharagpur for the back-calculation of the elasticity modulus of the different pavement layers.

Inputs required for the back-calculation of data using KGPBACK are as follows:

- The corrected deflections at 40 kN impact load. If the loading impulse differs from the standard load, then the deflection values are then linearly normalized for 40 kN;
- Tyre contact pressure (Adopted 0.56 kPa as per IRC: 115-2014; IRC: 37-2012);
- Geophone positions (0, 200, 300, 600, 900, 1100, 1350, and 1600 in mm);
- Poisson's ratio (adopted 0.35 for bituminous, granular, and subgrade as per IRC: 37-2012 for newly constructed layers);
- Range of moduli (adopted 600–800 for RAP; 600–1000 for CTSB; and 86 for subgrade).

6.1 Corrections Applicable

Calculating the final elasticity modulus requires corrections to be applied to the back-calculated modulus of bituminous, granular, and subgrade layers.

6.1.1 Temperature Correction

Temperature correction is applied for the bituminous layers only as bitumen is a viscoelastic material whose properties vary largely with the temperature variation. So, the back-calculated bituminous modulus is corrected for the standard design temperature (in this case is 35 °C).

6.1.2 Seasonal Correction

Moisture content affects the strength of subgrade and granular subbase/base layers. It is intended that the pavement layer moduli values should pertain when the subgrade is at its weakest condition.

No seasonal correction for the subgrade is applied as the modulus of subgrade is adopted based on the soaked CBR values which automatically denotes its lowest value during the monsoon.

The corrections factors applied to the bituminous and granular are as per IRC 115-2014.

6.2 Relation Between Different Bituminous Layers

The KGPBACK is capable for analyzing the three-layer pavement system only, while in this case we are having four-layer pavement system (Fig. 3). So, it is necessary to combine any two similar layers, so that the back-calculation may be done effectively. As per IRC: 37-2012, the two bituminous mixes of different properties are interrelated by the function below in Eq. 1.

$$\frac{E_1 \times (H_1)^3}{12\left(1-(\mu_1)^2\right)} = \frac{E_2 \times (H_2)^3}{12\left(1-(\mu_2)^2\right)} \tag{1}$$

where E_1, H_1, μ_1, and E_2, H_2, μ_2 are the elastic modulus, thickness, and Poisson's ratio of the two mixes.

Using the above relation as given in Eq. 1, the RAP and BC layers are combined in a single RAP layer. The 40 mm of BC layer comes out to be similar to 55 mm of RAP layer. So, in back-calculation process, the BC and RAP layers are combined together in a single RAP layer having design thickness of 155 mm and having design elasticity modulus as 600 MPa.

7 Results and Analysis

The FWD testing on the project is done during the May month when the air temperature is around 34–36 °C and pavement temperature ranges from 40 to 43 °C. Figure 18 shows the photograph of FWD testing.

Fig. 18 FWD testing equipment

Table 7 Laboratory elasticity modulus values

S. no.	Layer type	Elasticity modulus (MPa) @35 °C	
		Laboratory casted sample	Site core sample
1	BC	1800	1650
2	RAP	950	1000

7.1 Laboratory Test Results

The verification of the design elasticity modulus of BC and RAP has been done by extracting the cylindrical cores from the site and then testing them in the laboratory for elasticity modulus test as per ASTM D4123. The modulus values were found taking the average of three samples of each BC and RAP. The laboratory modulus values of the samples are shown in Table 7.

7.2 Field Data Collection and Analysis

The field data collected in the form of deflection, normalized for standard load, using FWD is tabulated in Table 8, and Fig. 19 shows the graphical representation of the same. The back-calculated modulus values after applying the necessary corrections are shown in Table 9.

Table 8 FWD deflection data collected along the steady stretch

km	Corrected deflection (mm) at 40 kN							
	Geophone no. and position (mm)							
	D1	D2	D3	D4	D5	D6	D7	D8
	0	200	300	600	900	1100	1350	1600
0.0	0.574	0.416	0.239	0.161	0.112	0.068	0.048	0.036
0.6	0.714	0.417	0.322	0.204	0.138	0.073	0.061	0.045
1.1	0.834	0.635	0.368	0.234	0.153	0.078	0.057	0.039
1.5	0.813	0.536	0.389	0.251	0.171	0.092	0.064	0.051
2	0.614	0.391	0.233	0.147	0.097	0.057	0.043	0.034
2.5	0.499	0.336	0.239	0.171	0.124	0.068	0.055	0.042
3	0.584	0.361	0.223	0.136	0.089	0.048	0.038	0.028
3.5	0.758	0.503	0.368	0.244	0.166	0.087	0.065	0.044
4	0.439	0.326	0.206	0.140	0.106	0.053	0.032	0.019
4.5	0.515	0.307	0.232	0.161	0.114	0.066	0.047	0.035
5	0.462	0.318	0.180	0.118	0.082	0.041	0.033	0.022
5.5	0.581	0.420	0.242	0.150	0.095	0.052	0.033	0.031
6	0.312	0.210	0.148	0.110	0.080	0.045	0.032	0.022
6.5	0.504	0.328	0.222	0.156	0.117	0.074	0.061	0.045
7	0.600	0.447	0.262	0.157	0.100	0.053	0.043	0.034
7.5	0.752	0.414	0.316	0.214	0.152	0.086	0.059	0.039
8	0.261	0.194	0.138	0.100	0.077	0.047	0.036	0.026
8.5	0.328	0.215	0.148	0.106	0.080	0.049	0.038	0.028
9	0.257	0.175	0.119	0.090	0.077	0.051	0.044	0.033
9.5	0.627	0.419	0.269	0.169	0.114	0.064	0.048	0.038
10	0.464	0.350	0.197	0.128	0.088	0.051	0.037	0.030
10.5	0.698	0.422	0.258	0.150	0.095	0.052	0.047	0.030

8 Discussions

The elasticity modulus values of the BC material come near to the design value of 1700 MPa with a deviation of $\pm 2\%$. Similarly, the modulus values of RAP and CTSB material come much higher than the adopted value after applying the correction factors. It has been clear that the strength parameters adopted in design are fully incorporated at the field and FWD is a much faster and economical approach toward the verification of the strength parameters.

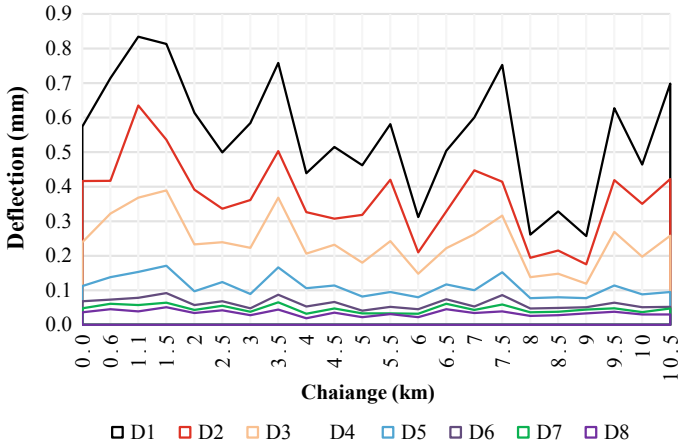

Fig. 19 Graph representing the FWD deflection data along the steady stretch

9 Cost Comparison

The utilization of the foam bitumen-treated RAP and CTSB also imparts a lot of impact on the costing of the project in comparison with the conventional pavement, although the current adopted layer system is preferred for the new alignment or bypasses only. The difference in cost of the conventional and the adopted crust layers is around 24 lacs per km. The cost calculation for both the types of pavement compositions is shown in Tables 10 and 11.

10 Conclusions and Recommendations for Future Work

From the study, it has been concluded that:

- Curing period of foam bitumen-treated RAP is 21 days and non-allowable traffic movement over it till wearing course of BC layer is laid makes it uneconomical for its proposal in the reconstruction or urban areas. This may be proposed only for new alignments or in greenfield areas.
- The FWD is the best-suited equipment for the strength evaluation of the in-service pavements.
- The conversion of the different bituminous layers of different thickness and properties into a single layer of same properties is to be done carefully as the modulus of different types of bituminous layers varies on a large basis.
- The KGPBACK software allows to study a three-layer system only, so to analyze or study a large no of layer system at a moment it is necessary to combine them and make it as three layers.

Table 9 Back-calculated modulus values

km	Pavement temperature (°C)	Back-calculated modulus (MPa)			Final corrected modulus (MPa)		
		Bituminous	Granular	Subgrade	Temperature bituminous	Seasonal granular	Nil correction subgrade
0.0	43	800.0	1000	86	1162	625	86
0.6	42	799.0	1000	86	1113	625	86
1.1	42	800.0	1000	86	1114	625	86
1.5	42	600.0	1000	86	836	625	86
2	42	800.0	1000	86	1114	625	86
2.5	42	800.0	1000	86	1114	625	86
3	42	800.0	1000	86	1114	625	86
3.5	42	600.0	1000	86	836	625	86
4	42	800.0	1000	86	1114	625	86
4.5	41	800.0	1000	86	1059	625	86
5	42	800.0	1000	86	1114	625	86
5.5	41	800.0	1000	86	1059	625	86
6	42	800.0	1000	86	1114	625	86
6.5	41	800.0	1000	86	1059	625	86
7	42	800.0	1000	86	1114	625	86
7.5	41	600.0	1000	86	794	625	86
8	42	800.0	1000	86	1114	625	86
8.5	41	800.0	1000	86	1059	625	86
9	42	800.0	1000	86	1114	625	86
9.5	41	800.0	1000	86	1059	625	86
10	42	800.0	1000	86	1114	625	86
10.5	41	800.0	1000	86	1059	625	86

Table 10 Cost for per km with adopted layers (BC/RAP/CTSB)

Item	Crust (mm)	Width (m)	Length (m)	Quantity[a]	Rate (INR)	Amount (Lacs)
BC	40	10.0	1000	400	7600	30.40
RAP	100	10.0	1000	1000	3300	33.00
CTSB	200	10.3	1000	2060	1100	22.66
Prime coat		10.0	1000	10,000	20	2.00
Tack coat (A)		10.0	1000	10,000	8	0.80
Tack coat (B)		10.0	1000	10,000	10	1.00
Cost of per km section						89.86

[a]Quantity and rate of pavement crust layers is in m^3 while of tack coat and prime coat in m^2

Table 11 Cost for per km with conventional layer (BC/DBM/WMM/GSB)

Item	Crust (mm)	Width (m)	Length (m)	Quantity[a]	Rate (INR)	Amount (Lacs)
BC	40	10.0	1000	400	7600	30.40
DBM	50	10.0	1000	500	7000	35.00
WMM	250	10.3	1000	2575	1100	28.33
GSB	200	10.5	1000	2100	800	16.80
Prime coat		10.0	1000	10,000	20	2.00
Tack coat (A)		10.0	1000	10,000	8	0.80
Tack coat (B)		10.0	1000	10,000	10	1.00
Cost of per km section						114.33

[a]Quantity and rate of pavement crust layers is in m^3 while of tack coat and prime coat in m^2

- The RAP and CTSB layers are very significant in cost and strength point of view.
- The utilization of RAP should be promoted as the good construction material is getting depleted.

Acknowledgements The authors are thankful to the management team of M/s. G R Infraprojects Ltd., especially Mr. Ajendra Agarwal, Director (Technical), for guidance and providing all facilities in carrying out the reported work.

References

IRC: 37 (2012) Guidelines for design of flexible pavement. Indian Road Congress, New Delhi
IRC: 115 (2014) Structural evaluation & strengthening of flexible pavement using falling weight deflectometer (FWD). Indian Road Congress, New Delhi
IRC: 120 (2015) Recommended practice for recycling of bituminous pavements. Indian Road Congress, New Delhi

Design Model for Strength and Location of Geogrids for Road Stabilization

Pietro Rimoldi and Minimol Korulla

Abstract Geogrids are widely used as effective materials for the improvement of soils characterized by low mechanical performances of soil and aggregates for construction of the road and road-related infrastructure. The design methods currently available do not appear capable of accounting for the influence of wide variations in variables such as geogrid type, load magnitude, number of required layers, and mechanical characteristics thereof. A new design method has been developed in order to enable the designer to vary the location of the geogrids as well as the type, the number and the property of it using a multilayered model. Once the base and/or subbase thickness has been defined with one of the available methods in the literature (AASHTO method, Giroud–Han method, Leng–Gabr method, etc.) the proposed design method allows to set the number and the mechanical characteristics of geogrid layers required for absorbing the horizontal forces generated by self-weight, wheel load, and tensioned membrane effect. Case studies of Indian projects are presented where this method was successfully applied.

Keywords Design method · Geogrids · Base and subbase stabilization

1 Introduction

For paved and unpaved roads on soft soil, the design methods usually assume that the road base is stabilized with just one layer of geogrid. However, the actual use of geogrids usually requires further evaluation, design, and specification conformity.

Geogrids inclusion to improve pavement performance is attributed to three stabilizing mechanisms described below.

P. Rimoldi
Officine Maccaferri SpA, Bologna, Italy
e-mail: pietro.rimoldi@gmail.com

M. Korulla (✉)
Maccaferri Environmental Solutions Pvt. Ltd., Gurgaon 122001, India
e-mail: m.korulla@maccaferri.com

R. Sundaram et al. (eds.), *Geotechnics for Transportation Infrastructure*, Lecture Notes in Civil Engineering 28, https://doi.org/10.1007/978-981-13-6701-4_9

1. Lateral restraint mechanism at the base course for horizontal stresses generated by the soil self-weight;
2. Lateral restraint mechanism at the base course for horizontal stresses generated by wheels loading;
3. Tensioned membrane mechanism at the base or subbase–subgrade interface.

Each of these three mechanisms produces tensile forces in the geogrid layers. The tensile forces produced by the horizontal thrust of the pavement structure and by the tensioned membrane mechanism at the base or subbase–subgrade interface are static loads by nature, while the tensile forces produced by traffic load are dynamic/cyclic in nature; however, the critical scenario is when all three mechanisms act on the geogrids, developing the maximum tensile forces, which will be considered in the design model.

For paved or unpaved road design, the dynamic/cyclic effect of wheel loading is always considered in the presently available methods such as AASHTO method, Giroud–Han method (Giroud et al. 1990), and Leng–Gabr method (Leng and Gabr 2006). Hence, the thickness of base and/or subbase afforded by such methods is suitable for providing the structural capacity of the road to resist the design number of wheel passages for the entire design life of the road.

Given this thickness, it is possible to calculate the distribution of the horizontal tensile forces in the whole road structure and the overall tensile forces generated in each layer of geogrid by considering the separate effect of the static loads (soil self-weight and tensioned membrane mechanism) and the dynamic effect of traffic load. Further, it is possible to select the appropriate geogrid for each layer based on a limit state criterion (Korulla et al. 2015).

For a pavement, the limit state criterion is not the failure (which is anyway prevented by the calculation of the thickness according to AASHTO method, Giroud–Han method, Leng–Gabr method, etc.), but rather the operating condition criterion, that is handled by a deformations criteria. Both theory and practical experiences suggest that geogrid strain shall be limited to 5%.

It shall be noted that geogrids in road base and subbase play the function of stabilization and not of reinforcement. Geogrids shall provide lateral confinement in order to limit the deformations of the unbound layers. Moreover, deformations are produced by forces. Hence, tensile strength and strain of geogrids for road stabilization shall be addressed jointly. This is the rational base of the proposed design method.

Indeed, the strain might vary depending on the type of road as well as construction for major roads, like state and national highways, the strain is usually limited to 2%, while for secondary roads, temporary roads and haul roads a higher value of strain might be acceptable. Furthermore, the tension membrane mechanisms, which require a certain deformation to be developed, are only considered for the lowermost geogrid, developed during construction due to the construction of the pavement layer works, is assumed to be “locked in”, without further developments for the entire life of the pavement, that is, with no relaxation phenomena. For upper geogrids, the tension membrane mechanism is not considered because it is assumed that the compacted

and reinforced layers beneath will not deform enough to develop it. Hence, depending on whether the prevailing tensile forces are generated by the static or the dynamic components in the geogrid, the strain limit shall be applied to the short-term tensile strength or to the long-term tensile strength (Korulla et al. 2015).

A practical approach is to limit the short-term tensile strength of the geogrids based on the design strain, measured in a wide width tensile test according to ISO 10319 standard, and then check the longtime elongation produced by the static components of the tensile forces.

After determination of type and number of geogrid layers, the location of geogrids is another important factor while designing and building of reinforced pavement works (Korulla et al. 2015). The most common position for a geogrid in a flexible pavement is at the interface of the subgrade and the unbound subbase or unbound base course. However, this should not be considered the default location, and therefore, the geogrid position should always be determined by estimating where the maximum deformation will occur or where the benefit of increased stiffness can most benefit the performance of a critical or the weakest pavement layer.

The examples reported below will clarify the application of this practical approach.

2 Multilayer Model

The following layers are the general schemes of a pavement structure such a road or a parking deck.

1. Asphalt course AC (wearing course and binder layer are considered as a single layer the thickness of which is the total thickness of the two layers)
2. Base course BC
3. Subbase course SB
4. Subgrade SG.

Therefore, a four-layer model has been developed for the geogrid design. Figure 1 depicts general scheme of the model and all symbols that will be used for subsequent calculations.

The model assumes that the wheel load is applied as a uniform vertical pressure $\sigma_{v0} = p$ (tire inflation pressure) on a circular area with equivalent radius r_0; this load spreads in three layers of the road structure (AC, BC, and SB) with their load spreading angles α_1, α_2, α_3, respectively. At least, the base course shall be present and shall be stabilized with geogrids; the asphalt course may not be present (in case of an unpaved road) and, if present, it is not reinforced (asphalt reinforcement is dealt with by a different design method); the subbase course may be present or not; when it is present, it may be either stabilized with geogrids or unstabilized.

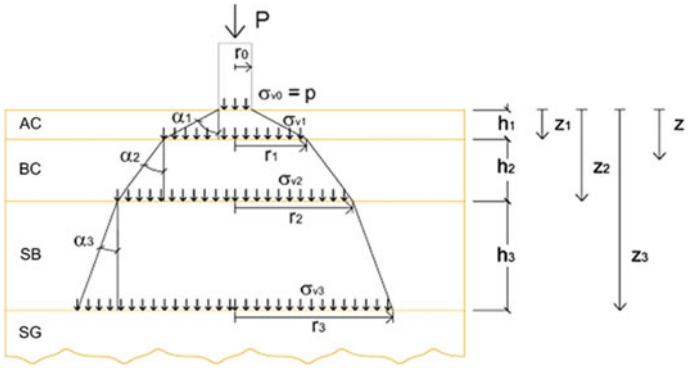

Fig. 1 General scheme of the three layers model

2.1 Force Due to Horizontal Soil Thrust

The tensile force T_{Zi} generated in ith geogrid layer by the horizontal thrust of soil above can be easily calculated on the basis of classic geotechnical theory.

The vertical stress at depth Z_1 due to self-weight of asphalt is:

$$\sigma_{vi} = \gamma_1 Z_1 \tag{1}$$

where

γ_1 unit weight of asphalt layer (kN/m^3).

For $Z_1 < Z < Z_2$:

$$\sigma_v = \gamma_1 Z_1 + \gamma_2 (Z - Z_1) \tag{2}$$

The related horizontal stress is:

$$\sigma_h = K_2 \sigma_v \tag{3}$$

$$K_2 = \tan^2(45^\circ - \phi_2/2) \tag{4}$$

where

K_2 active soil thrust parameter for the base BC
ϕ_2 angle of internal friction of BC (degrees).

Then, it can be assumed that the tensile force T_{zi} generated in ith geogrid layer in the base course is the integral of horizontal soil stresses between ith geogrid layer and $(i - 1)$th geogrid layer,

$$T_{zi} = 0.5K_2 \cdot [2\gamma_1 Z_1 + \gamma_2(Z_i + Z_{i-1} - 2Z_1)].(Z_i - Z_{i-1}) \quad (5)$$

For $Z_2 < Z < Z_3$:

$$\sigma_v = \gamma_1 Z_1 + \gamma_2(Z_2 - Z_1) + \gamma_3(Z - Z_2) \quad (6)$$

The related horizontal stress is:

$$\sigma_h = K_3 \sigma_v \quad (7)$$

$$K_3 = \tan^2(45^\circ - \phi_3/2) \quad (8)$$

where

K_3 active soil thrust parameter for the subbase SB
ϕ_3 angle of internal friction of SB (degrees)

The tensile force T_{Zi} generated in ith geogrid in the subbase course is:

$$T_{Zi} = 0.5K_3 \cdot [2(\gamma_1 Z_1 + \gamma_2 Z_2 - \gamma_2 Z_1) + \gamma_3(Z_i + Z_{i-1} - 2Z_2)] \cdot (Z_i - Z_{i-1}) \quad (9)$$

2.2 Force Due to Horizontal Stresses Created by Wheels Loading

Assumptions

- Wheel load is applied on a circular area of equivalent radius r_0,
- The load spreads in layers below as a cone whose generatrix is inclined of the load spreading angle α_i,

Then, the radius r at depth Z below the top surface is given below.

For $0 < Z < Z_1$:

$$r = r_0 + Z \tan \alpha_1 \quad (10)$$

Since it must be:

$$\pi r_0^2 \sigma_{v0} = \pi r_i^2 \sigma_{vi} \quad (11)$$

Then, the vertical stress produced by the wheel load at depth Z is:

$$\sigma_v = \sigma_{vo} r_0^2 / r_i^2 \quad (12)$$

For $Z_1 < Z < Z_2$:

$$r = r_1 + (Z - Z_1)\tan\alpha_2 \tag{13}$$

$$\sigma_{\mathrm{v}} = \sigma_{\mathrm{v}1} r_1^2 / r_i^2 \tag{14}$$

$$\sigma_{\mathrm{h}} = K_2 \sigma_{\mathrm{v}} \tag{15}$$

For $Z_2 < Z < Z_3$:

$$r = r_2 + (Z - Z_2)\tan\alpha_2 \tag{16}$$

$$\sigma_{\mathrm{v}} = \sigma_{\mathrm{v}2} r_2^2 / r_i^2 \tag{17}$$

$$\sigma_{\mathrm{h}} = K_3 \sigma_{\mathrm{v}} \tag{18}$$

$\mathrm{T}_{\mathrm{P}i}$ = Tensile force generated in *i*th geogrid layer in the base or subbase course by the wheel load, it is the integral of horizontal soil stresses between *i*th geogrid layer and $(i - 1)$th geogrid layer,

$$T_{\mathrm{P}i} = 0.5(\sigma_{\mathrm{h}i} + \sigma_{\mathrm{h}i-1})(Z_i - Z_{i-1}) \tag{19}$$

2.3 *Force Created Due to Tensioned Membrane Mechanism at the Interface with Subgrade*

The tensioned membrane mechanism occurs only when out-of-the-plane deformations are produced. Since geosynthetics for road stabilization are placed horizontally, then vertical deformations shall occur to generate the tensioned membrane mechanism.

When the first soil lift gets spread and compacted, the lowest geosynthetics layer at the interface with subgrade is subjected to the highest vertical deformations, due to the settlement of the soft subgrade. The next geogrid layers are far less subject to vertical displacements. Hence, it can be reasonably assumed that the lowermost geogrid layer is subjected to the tensioned membrane mechanism, while for the upper layers such mechanism is negligible. In contrary, no tensioned membrane mechanism can occur if the bearing capacity of the subgrade is enough to support the weight of the first lift of fill and the wheel load.

We will refer to the scheme shown in Fig. 2.

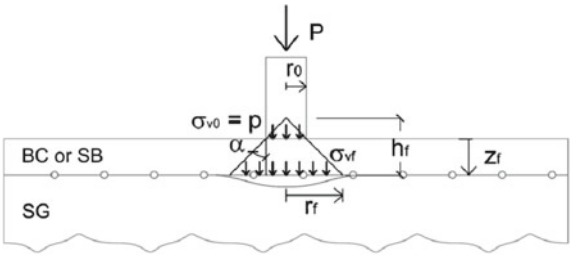

Fig. 2 Scheme of the first geogrid layer subject to tensioned membrane mechanism

2.3.1 Case 1: When the Subbase Is Not Present

As per the tensioned membrane theory (Giroud et al. 1990), the uniform vertical load W_{TC} on the catenary layer of geogrid is given below.

W_{TC} = [(volume (V) of load cone below the wheel) · (fill density (γ)) + wheel load (P) − subgrade reaction (R)]/(area at reinforcement catenary layer (A)).

For the geogrid layer at the base course bottom V and A become:

$$V = 1/3\pi\, r_f^2 h_f - 1/3\,\pi\, r_0^2 (h_f - Z_f) \tag{20}$$

$$A = \pi\, r_f^2 \tag{21}$$

where Z_f is the depth of the first base course lift (m), h_f is the height of the load cone (m)

The wheel load P and the tire pressure p in this case are referred to a truck or dumper which is used at the job site for carrying the soil. As we are dealing with the first lift of aggregate placed on a soft soil, very heavy vehicles shall not be used. Henceforth, for tensioned membrane mechanism calculations wheel load P and tire pressure p shall be referred to the truck or dumper which is used at the job site for carrying the soil.

Also an assumption can be made that the subgrade reaction R is equal to the allowable bearing capacity of a cohesive soil layer with geogrid reinforcement (Rodin 1965), that is:

$$R = 2\pi c_u A/\mathrm{FS} = 2\pi (30\,\mathrm{CBR_{SG}}) A/\mathrm{FS} = 60\pi\ \mathrm{CBR_{SG}} A/\mathrm{FS} \tag{22}$$

where FS is the factor of safety for subgrade bearing capacity, c_u is the undrained cohesion of subgrade (kPa), $\mathrm{CBR_{SG}}$ is the California bearing ratio of subgrade.

Since it is:

$$r_f = r_0 + Z_f \tan\alpha_2 \tag{23}$$

$$h_f = r_f / \tan\alpha_2 \tag{24}$$

Table 1 Values of dimensionless factor Ω

ε_r (%)	1	2	3	4	5
Ω	2.07	1.47	1.23	1.08	0.97

$$(h_f - Z_f) = r_0 / \tan \alpha_2 \tag{25}$$

$$P = \pi r_0^2 p \tag{26}$$

For the first lift of the base course:

$$W_{TC2} = \left[(\gamma_2/3)\left(r_f^3 - r_0^3\right)/\left(r_f^2 \tan \alpha_2\right)\right] + p\left(r_0^2/r_f^2\right) + 60\,\pi\,\mathrm{CBR_{SG}}A/\mathrm{FS} \tag{27}$$

The tensile load in the catenary geogrid at base course bottom is calculated based on tensioned membrane theory which is a function of the amount of strain in the geogrid. The tension in the geogrid is determined from the following equation:

$$T_{m2} = W_{TC2}\Omega\, r_f \tag{28}$$

where Ω is the dimensionless factor from tensioned membrane theory, as a function of geogrid strain ε_r (refer Table 1).

If the bearing capacity of the subgrade is enough to support the first lift of the base course and the wheel load, W_{TC2} becomes negative. In such case, no tensioned membrane mechanism occurs, hence

$$T_{m2} = 0 \tag{29}$$

2.3.2 Case 2: When the Subbase Is Present

In this case, the geogrid at base course bottom is not subject to the tensioned membrane mechanism, hence

$$T_{m2} = 0 \tag{30}$$

The geogrid layer at subbase bottom instead is subject to the tensioned membrane mechanism; hence, considering the first lift of subbase course, Hence

$$r_f = r_0 + Z_f \tan \alpha_3 \tag{31}$$

$$h_f = r_f / \tan \alpha_3 \tag{32}$$

$$(h_f - Z_1) = r_0 / \tan \alpha_3 \tag{33}$$

$$W_{TC3} = [(\gamma_3/3)\left(r_f^3 - r_0^3\right)/(r_f^2 \tan\alpha_3)] + p\left(r_0^2/r_f\right) + 60\pi\ \mathrm{CBR}_{SG} A/\mathrm{FS} \quad (34)$$

$$T_{m3} = W_{TC3}\Omega\, r_f \quad (35)$$

In this situation, if the bearing capacity of the subgrade is enough to support the first lift of the subbase course and the wheel load, W_{TC3} becomes negative; in such case, no tensioned membrane mechanism occurs, hence

$$T_{m3} = 0 \quad (36)$$

2.4 Total Horizontal Force

The total horizontal force in the *i*th geogrid layer is given below.

$$T_{tot-i} = T_{Zi} + T_{Pi} + T_m \quad (37)$$

where T_m applies only to the lowest geogrid layer at the interface with the subgrade, either of the base course or of the subbase course.

3 Geogrids Design—Indian Case Histories

3.1 Pavement Stabilization Works for Creek KalatalavSanesh Road, Bhavnagar, Gujarat

The paper presents a road project in Bhavnagar Old Port (Korulla et al. 2015). Tables 2 and 3 depict the pavement and traffic data.

For both reinforced and unreinforced cases, design has been checked as per the AASHTO method. The cross sections for unreinforced and reinforced cases are illustrated in Fig. 3 (Korulla et al. 2015).

For the design of reinforced road, extruded biaxial geogrids having 40 × 40 kN/m tensile strength (type Maccaferri MacGrid EG40) was selected as a base reinforcement. For these geogrids, layer coefficient ratio (LCR) is considered from the manufacturer's technical data sheet report which is $\mathrm{LCR}_{GG40} = 1.906$.

LCR is the layer coefficient ratio, with a value higher than one, which is determined on the basis of results from the field and laboratory testing on flexible pavement system with and without geogrid, which represents the improvement to the layer coefficient of base and/or subbase provided by the presence of the geogrid (Korulla et al. 2015).

Table 2 Pavement data for the Sanesh road (Korulla et al. 2015)

Surface layer	Value
Layer coefficient (a_1)	0.40
Minimum depth (m)	0.10
Base course	
Layer coefficient (a_2)	0.14
Drainage coefficient (m_2)	1.15
Minimum depth (m)	0.25
Subbase course	
Layer coefficient (a_3)	0.11
Drainage coefficient (m_3)	1.00
Minimum depth (m)	0.25
Subgrade course	
CBR (%)	5
Effective subgrade resilient modulus, M_r (kPa)	7157

Table 3 Traffic data for Sanesh road (Korulla et al. 2015)

Traffic data	Value
Reliability level, R (%)	95
Combined standard error (S_o)	0.45
Initial service index (p_o)	4.2
Terminal surface index (p_t)	2.5
Total ESAL/day	8800.369
Total number of passes	3,212,134
Compound traffic growth factor	27.086
Total volume of traffic during the analysis period	87,003,878
Design ESAL (W18)	65,000,000
Structural number, SN (inches)	6.805

The structural number (SN) is calculated by the following formula (AASHTO 1993)

$$\log W_{t18} = Z_R \cdot x \cdot S_0 + 9.36 \log(\mathrm{SN}+1) - 0.20 + \frac{\log[(4.2-p_t)/(4.2-1.5)]}{0.4+1094/(\mathrm{SN}+1)^{5.19}} + 2.32 \log M_R - 8.07 \quad (39)$$

where W_{t18} = number of 80 kN equivalent single axle load (ESAL) applications; Z_R = standard normal deviate; S_0 = combined standard error of the traffic prediction and performance prediction; ΔPSI = difference between the initial design serviceability

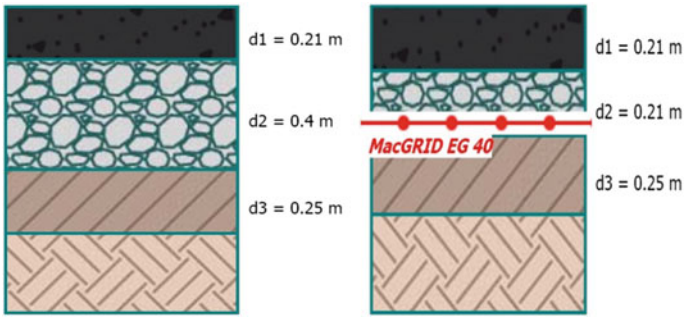

Fig. 3 Unstabilized pavement section resulting from calculation with AASHTO 1993 method and stabilized pavement resulting from calculation with modified AASHTO 1993 method with the inclusion of a geogrid for the base stabilization

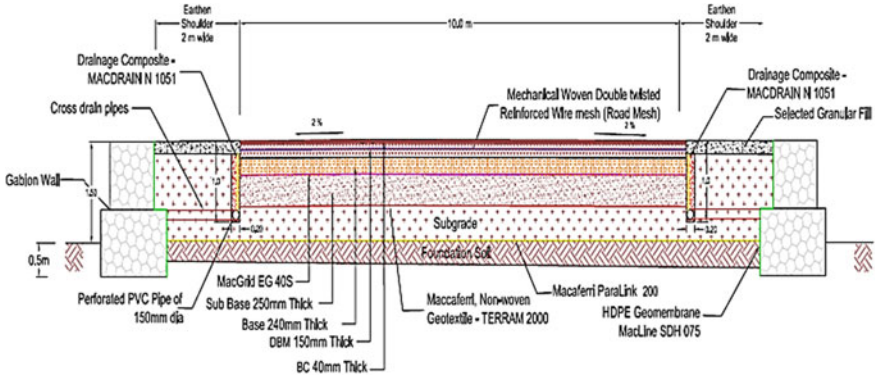

Fig. 4 Final design layout

index p_o, and the design terminal serviceability index p_t; M_R = resilient modulus (kPa).

Figure 4 depicts the final design layout.

3.2 Widening and Strengthening of Kuragalu–Malkapuram Road at Velgapudi, Andhra Pradesh

The project is a part of construction and rehabilitation of AP new secretariat road from Velgapudi situated in Guntur district, which is a part of urban notified area of Amaravati, state capital for Andhra Pradesh. The major portion of soil condition in Guntur district is poor due to the presence of silty clay with CBR < 3%. The weak subgrade condition calls for heavy pavement sections even with low design traffic resulting in high cost. Also, water table is at a shallow depth which continuously

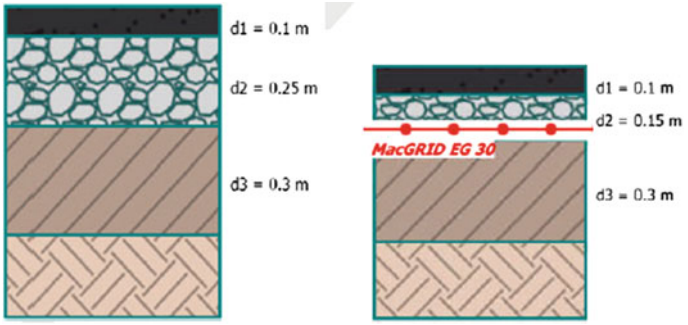

Fig. 5 Unstabilized and stabilized sections

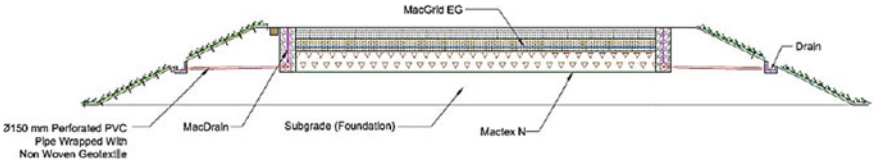

Fig. 6 Cross section of pavement stabilization

degrades the structural functioning of the pavement section. With low CBR and shallow water depth, time required for construction of road was high, while the client was looking for solution that helps in the faster construction of pavement. As the subgrade is soft, base/subbase laid over it will intrude and may not work to its intended function effectively; hence, a nonwoven needle punched polyester geotextile (Mactex N) separator is used between subgrade and subbase. Using biaxial extruded geogrid (Macgrid EG), it was possible to reduce the thickness of the base course by 40% thereby reducing the quantity and time of construction. Thickness of conventional pavement section and stabilized pavement section determined as per the approach given in the paper is shown in Fig. 5, where $d1$, $d2$, $d3$ represent the thickness of surface, base and subbase courses of the pavement, respectively.

To take care of the drainage, a geocomposite drain (Macdrain) with the required long-term flow capacity was installed as edge drain system on either side of the pavement section.

The final layout of the pavement section with geogrid and geocomposite drain adopted for the project is shown in Fig. 6.

4 Conclusions

The conclusions drawn from the design model for strength and location of geogrids for road stabilization are the following.

- Pavement design methods such as AASHTO 1993 or Giroud–Han or Leng–Gabr consider only one geogrid layer in the pavement.
- Anyway, geosynthetics can perform not only the stabilization function but filtration, separation, and drainage as well, which are not taken into account in the aforementioned methods resulting in a requirement for geotextiles and geocomposite for drainage which can be taken into account in the design of the pavement.
- The geogrid design method here presented allows using multilayered geogrids for stabilization of base and subbase, depending upon design requirements.
- Additional geosynthetics for filtration, separation, and drainage can be added at design stage, depending on project conditions.
- Successful projects were herein reported as demonstration of the validity of the design model.

References

American Association of State Highway and Transportation Officials (AASHTO) (1993) Guide for design of pavement structures

Giroud JP, Bonaparte R, Beech JF, Gross BA (1990) Design of soil layer-geosynthetic systems overlying voids. Geotextiles Geomembrane 9(1)

Korulla M, Gharpure A, Rimoldi P (2015) Design of geogrids for road base stabilization. Ind Geotech J

Leng J, Gabr MA (2006) Deformation-resistance model for geogrid-reinforced unpaved road. J Transport Res Board 1975, 146–154

Rodin S (1965) Ability of a clay fill to support construction plant. J Terrramech 2:51–68

Evaluation of Flexible Pavement Distress Using Nonlinear Regression Analysis

Pranav R. T. Peddinti, B. Munwar Basha and Sireesh Saride

Abstract The current study aims at developing well-predicting regression equations for evaluating the fatigue and rutting strains at critical locations within the flexible pavement layers. With an objective to develop unified regression models, the practical on-field ranges for thickness and layer moduli of various pavement layers are used in the analysis. These design input combinations are fed into a multilayer elastic analysis program using an automation technique to reduce a lot of human effort and evaluation time. The output obtained from the program is used to develop equations for fatigue and rutting strains by nonlinear regression analysis. The outcomes of this study will aid the design engineers as well as researchers in multiple ways. In addition to the advantages in pavement design, the automation procedure combined with regression would also aid the researchers in simulation studies, reliability analysis, etc.

Keywords Flexible pavement · Fatigue · Rutting · Regression

1 Introduction

The design of flexible pavement requires an evaluation of multiple combinations of layers with different thicknesses and material properties before finalizing a well-performing and economical pavement section. Such an evaluation is tedious and time-consuming in case of multilayered systems in view of the high computational effort involved in the computation. The availability of programs like KENPAVE, ILLIPAVE, and IITPAVE reduces the human effort to a certain extent. However, repeated manual data entry of various combinations into these programs is still time-

P. R. T. Peddinti · B. Munwar Basha · S. Saride (✉)
Department of Civil Engineering, Indian Institute of Technology Hyderabad, Kandi, Sangareddy, Hyderabad 502285, India
e-mail: sireesh@iith.ac.in

P. R. T. Peddinti
e-mail: ce14resch11005@iith.ac.in

B. Munwar Basha
e-mail: basha@iith.ac.in

R. Sundaram et al. (eds.), *Geotechnics for Transportation Infrastructure*, Lecture Notes in Civil Engineering 28, https://doi.org/10.1007/978-981-13-6701-4_10

consuming and may lead to erratic data entry. In this regard, a simplified solution for evaluating flexible pavements would be beneficial.

Developing distress models has been proposed as a viable solution to this problem. These models reduce the run time and aid in quick calculation of distress for a given pavement geometry, climate, and materials used. These models serve as the basis for generating the performance functions required for reliability-based designs. Hence, it is to be noted that the accuracy and applicability of these models are highly important for the success of design methods. It is necessary either to obtain sufficient field data from various locations or to perform a reasonable number of laboratory investigations for developing these models. Several researchers have developed distress models to evaluate fatigue and rutting strains as discussed in the following section. However, research scope is still open for developing unified and well-predicting distress models. Hence, the current study focuses on developing unified regression models for predicting pavement distresses, viz. fatigue and rutting.

2 Background

Kim et al. (2000) proposed a nonlinear rut prediction model by collecting data from 39 in-service pavements in Michigan, USA. The model is based on the in situ pavement geometry, layer moduli, climate, and surface deflection. Timm and Newcomb (2003) calibrated the existing distress models to suit the fatigue and rutting levels in Minnesota, USA. The process involved iteration of fatigue and rutting limiting constants until the distress levels match with the in situ distress levels of Minnesota.

Wu et al. (2011) presented a finite element model for rut prediction in cementitious base/sub-bases to improve the existing models. The models have been developed from ABAQUS program using data obtained from six accelerated pavement test sections.

Hall et al. (2012) developed surrogate models for alligator cracking and rutting using central composite response surface methodology. The equations are based on the data obtained from 38 flexible pavement sections from Arkansas, USA, and the variables include pavement geometry, material properties, climate, Asphalt binder grade, traffic, and annual temperature. However, climate, operational speed, binder, and asphalt gradation showed a nominal impact on the models.

Dilip et al. (2013) and Dilip and Babu (2013) developed fatigue and rutting models as functions of the geometrical and material properties of the pavement using KENPAVE software. The linear response surface models were developed for a given geometry of flexible pavement considered in the studies. Bhattacharjee (2016) developed nonlinear response surface models to develop limit state fatigue cracking models using central composite design methodology. The variables used are layer thicknesses, layer moduli, percentage air voids in HMA, and design traffic.

Apart from these studies, several researchers studied the rutting behavior of unbound granular materials (UGM) for use in pavement design procedures. Studies by Uzan (1999), Chazallon et al. (2006), and Chen et al. (2010) are based on elasto-plastic theory by considering the influence of stress level on rutting of UGMs. Other

studies based on mechanistic-empirical models are presented by Gabr and Cameron (2013) and Gu et al. (2016). These models are based on laboratory repeated load tests which can be calibrated and used for the evaluation of flexible pavements.

The above-mentioned studies were performed on limited datasets confining to a specific geographical location or a project. The necessity for globally acceptable and well-predicting distress models for fatigue and rutting still persists, paving a reasonable scope for the current study.

3 Methodology

3.1 Input Data Generation

Among the available pavement analysis programs, KENPAVE program enables the user to feed the whole input data in the form of a single .DAT file. In this regard, the present study uses KENPAVE program for evaluating the input combinations. To handle the huge queue of input files, an algorithm was written in MATLAB (2015) to generate the input files. The random and deterministic variables used in the study are mentioned in Table 1. A total of 161,051 files were generated for the specified range of values. To develop a regression model that can be accepted globally, the commonly used practical range of random variables was considered.

An image identification technique was used to automate the process and reduce the time of evaluation. The program called Sikuli developed by Yeh et al. (2009), which runs on Java or Python script, was used for this purpose. The resulting output files were processed through a MATLAB algorithm to store the required fatigue values from the .TXT files into easily workable data sheets. The obtained data was used for further regression and reliability analysis.

Table 1 Range of parameters considered in the study

Random variables	
Variable	Range
Surface layer thickness, h_1 (cm)	4–15
Base layer thickness, h_2 (cm)	20–80
M_r of surface layer, M_{r1} (kPa)	2×10^6–5×10^6
M_r of base layer, M_{r2} (kPa)	1×10^5–6×10^5
M_r of subgrade layer, M_{r3} (kPa)	1×10^4–1×10^5
Poisson's ratio of surface layer, υ_1	0.30
Poisson's ratio of base layer, υ_2	0.35
Poisson's ratio of subgrade, υ_3	0.40

3.2 Regression Analysis

Regression analysis is performed to develop an equation for fatigue strain in terms of layer thickness and layer moduli. An initial first-order linear regression analysis yielded a poor fit with a coefficient of determination (R^2) of 0.5. The reason for poor regression coefficient may be attributed to the inclusion of non-contributing terms and insufficiency of linear terms to explain the data trend. In order to identify the level of influence of random variables, sensitivity analysis was performed using Minitab (2000) statistical software as shown in Fig. 1. The sensitivity plots were drawn between the mean of the response variable and means of individual variables. They consider the variability of each individual variable over their range and then assess the influence of that parameter keeping the others at a constant value.

As the fatigue is measured at the bottom of the surface layer, it is mechanistically reasonable that the impact of resilient modulus of the subgrade layer (M_{r3}) is minimum, which can be understood from its near horizontal trend in Fig. 1. On the other hand, resilient modulus of base layer (M_{r2}) and height of the surface layer (h_1) show a notable influence on the fatigue strain. Linear regression was performed without considering the minimum influencing parameters. However, removing the minimum influencing inputs did not improve the regression coefficient. The prediction of data as compared to KENPAVE was found unsatisfactory. Hence, it can be summarized that linear regression could not completely accommodate the variation in the fatigue strain.

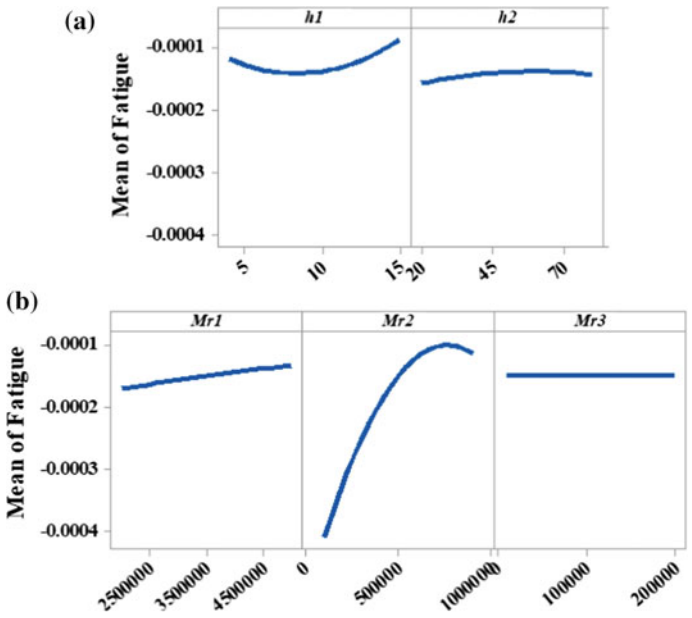

Fig. 1 Sensitivity of design variables for fatigue strain

3.2.1 Nonlinear Regression Analysis

To improve the accuracy of regression, nonlinear models have to be adopted by addition of higher-order terms. As the number of random variables is five (Table 1), there will be several higher-order combinations such as h_1h_2, $h_1M_{r1}M_{r2}$, and $M_{r1}M_{r2}^2$. In order to investigate the influence of each input combination, interaction plots presented in Fig. 2 are helpful. The interaction plots verify the suitability of a particular mathematical combination of the variables for inclusion in the regression. For the present problem, fatigue strains are evaluated at selected fixed values of input parameters considered for suitability in the model. The second-order products were verified for their suitable inclusion in the fatigue model as shown in Fig. 2. Single/multiple intersections or complete overlap between the lines denotes the considerable contribution of that particular term to the regression model. Non-intersecting nature of the lines as shown in Fig. 2 denotes that the respective term does not contribute to the model (as highlighted in gray background in Fig. 2b). The term h_2M_{r2} can be opted out of regression considerations. The sensitivity analysis presented in Fig. 1 is helpful to add the nonlinear terms to the model. The similar procedure can be repeated to verify the influence of higher-order terms. The regression analysis was further performed on the finalized terms. Addition of third order terms was found inevitable to obtain a reasonable fit. The final regression equation to predict fatigue strain is presented in Eq. 1. The R^2 and R_{adj}^2 values were found to be 0.9621 and 0.9620, respectively. R_{adj}^2 is a more authentic measure of goodness of regression fit. Unlike R^2, R_{adj}^2 value increases only if the regression model contains suitable terms. The higher and nearly close values of R^2 and R_{adj}^2 depict a well-built regression model.

$$\varepsilon_t = \begin{bmatrix} -7.075 \times 10^{-5} h_1 + 4.471 \times 10^{-9} M_{r2} \\ -1.368 \times 10^{-10} M_{r3} + 3.303 \times 10^{-8} h_1 h_2 \\ -1.699 \times 10^{-10} h_1 M_{r2} + 9.326 \times 10^{-6} h_1^2 \\ -6.765 \times 10^{-15} (M_{r2})^2 + 1.850 \times 10^{-11} h_1 M_{r3} \\ +5.373 \times 10^{-12} h_1 M_{r1} - 2.794 \times 10^{-7} h_1^3 \\ +3.335 \times 10^{-21} (M_{r2})^3 + 2.045 \times 10^{-16} h_1 (M_{r2})^2 \\ -9.423 \times 10^{-18} h_1 M_{r1} M_{r2} - 7.695 \times 10^{-4} \end{bmatrix} \quad (1)$$

3.3 *Validation of Fatigue Regression Equation*

Though the R^2 and R_{adj}^2 values are higher, there is always a chance for the equations to have higher curvature within the range of inputs which may result in overfitting models. To verify the same, fatigue strains obtained from the regression analysis are validated by comparing the same with KENPAVE program. About 10,000 input–output combinations for the range of parameters mentioned in Table 1 are used to validate the regression equation. The results as shown in Fig. 3a are in good agreement with

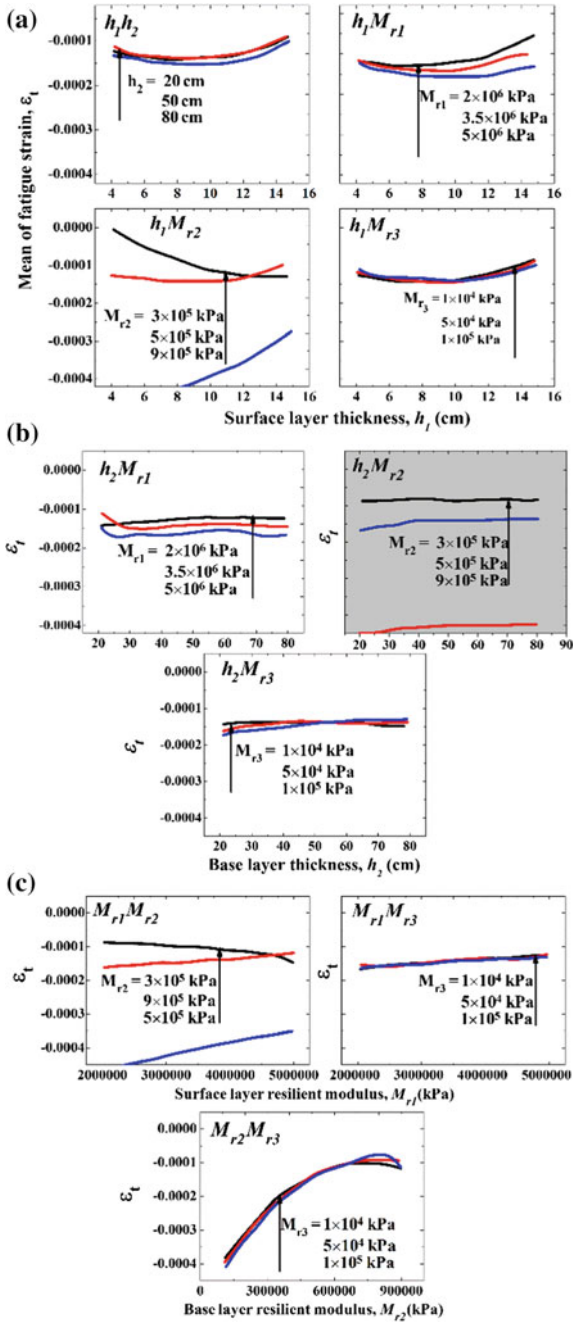

Fig. 2 Interaction plots to verify second-order terms in the regression model

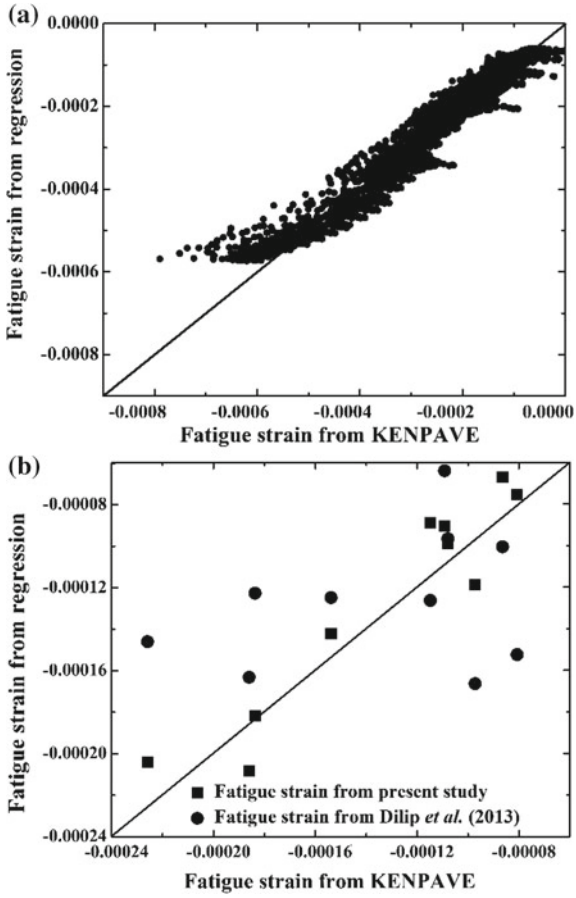

Fig. 3 Validation charts for fatigue regression model

the KENPAVE results. In addition, the present results are also validated with those obtained from the linear regression equation developed using KENPAVE by Dilip et al. (2013) as shown in Fig. 3b. It was observed that inclusion of higher-order non-linear terms and considering the practical range for the random variables (Table 1) yielded a superior fatigue model which has predicted the strains with high accuracy.

Hence, the nonlinear regression equation for predicting the fatigue strain (ε_t) proposed in this study is valid across the practical range of values of inputs considered.

4 Regression Analysis for Rutting Strain

Similar analysis was performed to evaluate the rutting strains at the top of subgrade layer. The initial linear regression analysis resulted in a low R^2 value of 0.68. Hence,

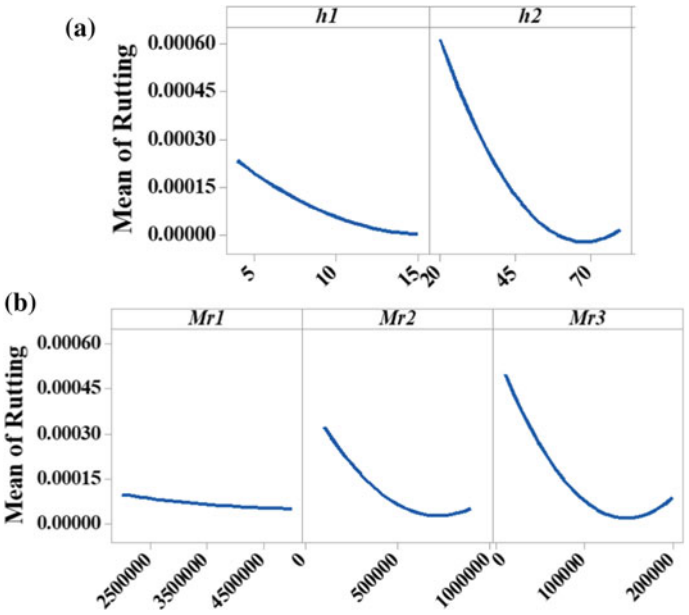

Fig. 4 Sensitivity of design variables for rutting strain

sensitivity analysis and interaction plots are studied for the prediction of rutting strain as well. The sensitivity curves corresponding to rutting are presented in Fig. 4. It can be observed that the rutting strain is influenced by all the design inputs. This is due to the fact that rutting is a result of accumulated vertical strains in all the pavement layers above subgrade. Hence, all design parameters show a significant influence on the rutting. The nonlinear regression equation obtained for rutting (ε_z) is shown in Eq. 2. The R^2 and R^2_{adj} values are found to be 0.9712 and 0.9711, respectively, for rutting.

$$\varepsilon_z = \begin{bmatrix} -0.1461h_1 - 0.06332h_2 \\ -5.541 \times 10^{-8} M_{r1} - 1.688 \times 10^{-6} M_{r2} \\ +1.532 \times 10^{-8} h_2 M_{r2} + 4.399 \times 10^{-11} (M_{r2})^2 \\ -1.685 \times 10^{-5} M_{r3} + 2.255 \times 10^{-4} h_2^2 \\ +1.180 \times 10^{-3} h_1^2 + 1.287 \times 10^{-3} h_1 h_2 - 3.225 \end{bmatrix} \quad (2)$$

The validation with KENPAVE and Dilip et al. (2013) are presented in Fig. 5. As observed in Fig. 5a, the rutting strains are well predicted by the proposed regression model.

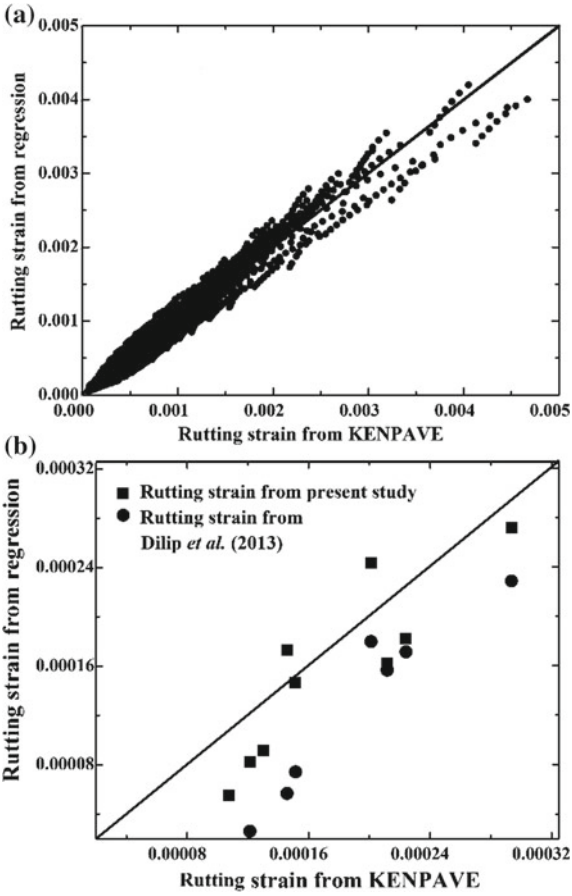

Fig. 5 Validation charts for rutting regression model

5 Discussion

- Nonlinear regression equations are developed for fatigue and rutting strains based on their sensitivity to practical geometrical and resilient modulus properties of three-layered flexible pavement systems.
- The performance of these models was found to closely match with the results obtained from KENPAVE software.
- From the sensitivity analysis, fatigue was found to be predominantly influenced by the magnitude and variability of h_1 and M_{r2}. On the other hand, rutting was considerably influenced by all the variables.
- Interaction plots give the user an insight into the role of higher-order terms to be used in the model. Proper sensitivity and interaction analysis are a definite prerequisite for developing well-performing models.

- Base resilient modulus (M_{r2}) was found to be the influencing factor in common for both fatigue and rutting. This is attributed to the fact that fatigue and rutting are measured just above and just below the base layer in case of three-layered flexible pavements. Also, in view of the variety of materials used in base course, the associated variability is as high as 50%.
- The proposed nonlinear regression procedure coupled with automatic data generation and processing serves as a powerful tool for researchers and field practitioners in various ways.
- The present study considers the pavement geometrical and material properties as inputs, because there is a scope for unaccountable uncertainty in these parameters. If such parameters are grouped in a single regression model, other parameters like traffic and climate, whose uncertainty is accountable, can be explicitly used at relevant places during design.

References

Bhattacharjee S (2016) Assessment of reliability and load factor design approach against fatigue cracking in flexible pavements. J Transp Res Board 2368, 56–65

Chazallon C, Hornych P, Mouhoubi S (2006) Elastoplastic model for the long-term behavior modeling of unbound granular materials in flexible pavements. Int J Geomechanics 6(4):279–289

Chen C, Ge L, Zhang J (2010) Modeling permanent deformation of unbound granular materials under repeated loads. Int. J. Geomechanics 10(6):236–241

Dilip D, Ravi P, Babu GLS (2013) System reliability analysis of flexible pavements. J Transport Eng 139(10):1001–1009

Dilip DM, Babu GLS (2013) Methodology for pavement design reliability and back analysis using Markov chain Monte Carlo simulation. J. Transport Eng 139(1):65–74

Gabr A, Cameron D (2013) Permanent strain modeling of recycled concrete aggregate for unbound pavement construction. J Mater Civil Eng 25(10):1394–1402

Gu F, Zhang Y, Droddy CV, Luo R, Lytton RL (2016) Development of new mechanistic empirical rutting model for unbound granular material. J Mater Civil Eng 28(8):1–10

Hall KD, Xiao DX, Pohl EA, Wang KCP (2012) Reliability-based mechanistic–empirical pavement design with statistical methods. J. Transport Res Board 2305:121–130

Kim H, Buch N, Park DY (2000) Mechanistic-empirical rut prediction model for in-service pavements. J Transport Res Board 1730:99–109

MathWorks (2015) *MATLAB 2015b*. Natick, MA

MINITAB User's Guide 2 (2000) Data analysis and quality tools. Minitab, State College, PA, pp 27–52

Timm DH, Newcomb DE (2003) Calibration of flexible pavement performance equations for Minnesota road research project. J Transport Res Board 1853:134–142

Uzan J (1999) Permanent deformation of a granular base material. J Transport Res Board 1673:89–94

Wu Z, Chen X, Yang X, Zhang Z (2011) Finite element model for rutting prediction of flexible pavement with cementitiously stabilized base–subbase. J Transport Res Board 2226:104–110

Yeh T, Chang TH, Miller R (2009) Sikuli: using GUI screenshots for search and automation. In: Proceedings of 22nd annual ACM symposium on user interface software and technology, Victoria, BC, Canada, pp 183–192

Laboratory and FEM Study on Construction and Demolition Waste and Fly Ash for Use as Pavement Material

Rohan Deshmukh, S. Patel and Jagdish Telangrao Shahu

Abstract The basic aim of this research is to evaluate the feasibility of using geogrid incorporated C&D wastes and fly ash as road base or subbase material by conducting laboratory tests and finite element analysis. Various laboratory tests were conducted on C&D waste to check its suitability in base/sub-base course, and finite element analysis was done by using PLAXIS 2D to check the effectiveness of geosynthetic reinforcement. Fly ash was used for the stabilization of subgrade soil (BC soil) and also used in the form of a compacted layer over a stabilized subgrade to improve the bearing ratio. Geogrid reinforcement was used to reduce the critical strains in the pavement. It is concluded that Geosynthetic at middle of base course shows the least settlement of pavement and reducing critical strain.

Keywords Construction and demolition waste (C&D) · Fly ash · Black cotton soil · Geosynthetic · Base and sub-base course · FEM · Plaxis 2D

1 Introduction

For construction, maintenance, and widening of roads, a large quantum of construction material is required. On the other hand, demand for electricity in India is increasing rapidly and its production largely depends on thermal power plant which is responsible for massive fly ash generation. Also, construction and demolition activity is responsible for the generation of a huge quantity of waste which creating a tremendous threat to public health and ecology.

R. Deshmukh (✉) · S. Patel
Applied Mechanics Department, SVNIT, Surat 395007, Gujarat, India
e-mail: rohandeshmukh520@gmail.com

S. Patel
e-mail: spatel@amd.svnit.ac.in

J. T. Shahu
Civil Engineering Department, IIT, Hauz Khas 110016, New Delhi, India
e-mail: shahu@civil.iitd.ac.in

R. Sundaram et al. (eds.), *Geotechnics for Transportation Infrastructure*, Lecture Notes in Civil Engineering 28, https://doi.org/10.1007/978-981-13-6701-4_11

1.1 Necessity of study

Bulk utilization of solid wastes coupled with geosynthetics in road construction can solve the following three problems with one effort:

(a) Disposal of solid waste. (b) Depletion of natural aggregate resources. (c) Excessive rutting and fatigue cracking in the pavement.

1.2 Fly ash

In India, one of the major sources of electric power is through thermal power plants. Thermal power station using pulverized coal as fuel generates large quantities of ash as a by-product. The production of coal ash in India has increased phenomenally to about 112 million tons per year, but hardly about 37.5% of the total production of coal ash is utilized for the gainful application (Dhadse et al. 2008).

1.3 Construction and Demolition Waste

Means "the waste comprising of building materials, debris and rubble resulting from construction, remodeling, repair and demolition of any civil structure." The volume of construction and demolition waste (C&D waste) generated in Delhi has increased considerably in recent years due to the rapid pace of development in the city, and it is increasing day by day. As per section 42 of Delhi Municipal Corporation Act, 1957 (amended to date), disposal of unclaimed C&D waste from its jurisdiction is the obligatory function of North Delhi Municipal Corporation. It is estimated on a conservative basis that over 25–30 million tons of C&D waste are generated annually that clogs rivers, blocks traffic, and occupies dumping space.

2 Methodology

The study is divided into three parts. The methodology worked out to achieve the above-mentioned objectives is as follows.

(1) In the first part, the emphasis was given to laboratory evaluation of construction and demolition waste. The properties like crushing value, impact value, specific gravity, and Los-Angeles abrasion are compared with the properties of natural aggregate as mentioned above and according to that suitability of replacement of natural aggregate with construction and demolition waste is decided. Similarly, some laboratory tests were carried out to check the feasibility of fly ash for use as a stronger subgrade layer.

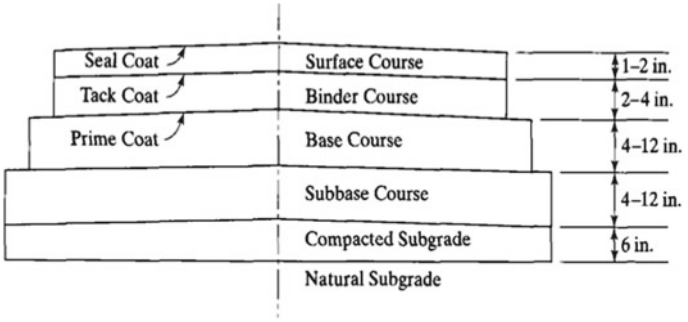

Fig. 1 Typical cross-section of conventional flexible road pavement (Huang 2004)

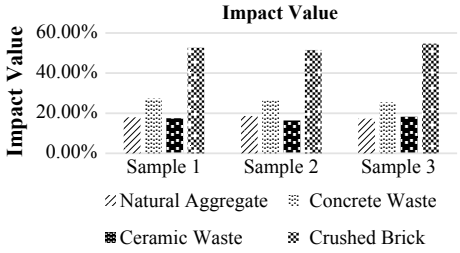

Fig. 2 Graphical representation of impact value test

(2) The second part is devoted to the stabilization of black cotton soil using fly ash. As black cotton soil is not suitable for road construction due to its expansive nature, there is a need to improve its properties by addition of fly ash.
(3) In the third part, finite element analysis was done on the road section constructed of solid waste and different combinations of geosynthetic location to find out the exact location for their effective utilization (Fig. 1).

3 Results and Discussion

As the impact value of the natural aggregate lies between 10 and 20%, it is classified as strong. The impact value of concrete waste lies between 10 and 20%; hence, it is classified as strong. The impact value of ceramic waste lies between 10 and 20%; hence, it is classified as strong. The impact value of brick waste is more than 35% (50–53%); it is very weak for road surfaces, and hence it cannot consider brick waste as sub-base material. According to Indian Road Congress (IRC), the maximum impact value is up to 30% is considered for bituminous surface dressing penetration macadam, bituminous carpet concrete and cement concrete wearing course (Figs. 2, 3, and 4; Tables 1, 2, and 3).

As the crushing value of the natural aggregate is less than 30%, it is suitable for surface or wearing course. The crushing value of concrete waste lies between 20

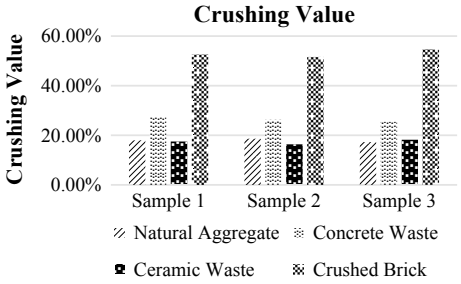

Fig. 3 Graphical representation of crushing value test

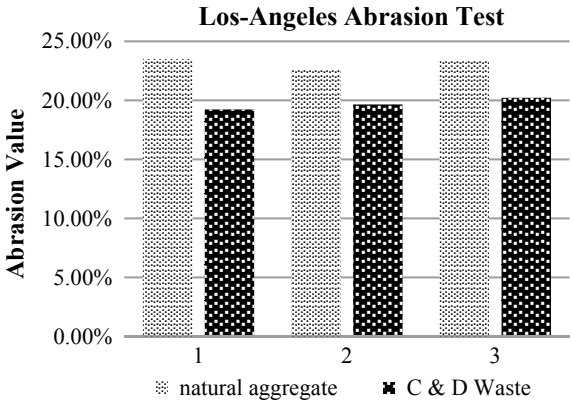

Fig. 4 Graphical representation of Los-Angeles abrasion test

Table 1 Impact value test results

Sample	Natural aggregate (%)	C&D waste		
		Concrete waste (%)	Ceramic waste (%)	Crushed brick (%)
1	11.04	14.75	10.31	52.52
2	10.11	18.67	14.49	51.32
3	10.00	13.17	12.38	53.22

Table 2 Impact value test reference

Aggregate impact value (%)	Classification
<10	Exceptionally strong
10–20	Strong
10–30	Satisfactory for road surfacing
>35	Weak for road surfacing

Table 3 Crushing value test

Sample	Natural aggregate (%)	C&D waste		
		Concrete waste (%)	Ceramic waste (%)	Crushed brick (%)
1	17.99	27.30 5	17.50	52.64
2	18.65	26.25	16.39	51.58
3	17.29	25.49	18.25	54.68

Table 4 Crushing value test reference

Type of road construction	ACV not more than (%)
Flexible pavements	
(A) soiling	50
(B) water bound macadam	40
(C) bituminous macadam	40
(D) bituminous surface dressing or thin premix carpet	30
(E) dense mix carpet	30
Rigid pavements	
(A) other than wearing course	45
(B) surface or wearing course	30

Table 5 Los-Angeles abrasion test result

Sample	Natural aggregate (%)	C&D waste (%)
1	23.50	19.24
2	22.65	19.66
3	23.41	20.24

and 30%; hence, it is suitable for both rigid and flexible pavements. The crushing value of ceramic waste lies between 10 and 20%; hence, it is suitable for surface or wearing course. The crushing value of brick waste is more than 30% (50–55%); it is very weak for road surfaces, and hence it cannot consider brick waste as surface or wearing course. However, concrete and ceramic waste fulfill the criteria given by IRC for use in surface or wearing course (Tables 4, 5, and 6).

As the abrasion value of the natural aggregate is less than 30%, it is suitable for the bituminous concrete surface course. The abrasion value of concrete waste lies between 15 and 30%; hence, it is suitable for the bituminous concrete surface course. According to IRC, the maximum abrasion value is up to 30%, and hence C&D waste can consider as a bituminous concrete surface course.

Table 6 Los-Angeles Abrasion Test Reference

Sr. No.	Type of pavement	Limiting value
1	W.B.M sub-surface course	60
2	W.B.M base course with bituminous surfacing	50
3	Bituminous bound macadam	50
4	W.B.M surface course	40
5	Bituminous penetration macadam	40
6	Bituminous surface dressing, cement concrete surface course	35
7	Bituminous concrete surface course	30

3.1 Physical Properties of Black Cotton Soil and Fly ash

Different physical properties for BC soil and fly ash were found out from laboratory testing (following IS code) and summarized in Tables 7 and 8.

3.1.1 Fly ash for Stabilization

Fly ash with different proportions is used in BC soil for stabilization purpose. Fly ash possesses pozzolanic property due to which it can stabilize the expansive type of soil (Sharma et al. 2012). Pozzolans are natural or artificial siliceous and aluminous substances which react with lime in the presence of water at atmospheric pressure and temperature to form a cementitious compound. As stated in methodology, there is a need to stabilize expansive BC soil.

From Table 8, it is concluded that black cotton (BC) soil comes under the category of the expansive type of soil due to its high value of liquid limit (>50%) and low values of shrinkage limit.

Table 7 Physical properties of Fly ash

Physical properties	Fly ash
Coefficient of uniformity	2.22
Coefficient of curvature	4.54
Specific gravity	2.11
Liquid limit	NP
Plastic limit	NP
Permeability (cm/s)	$4.122 * 10^{-4}$
OMC (%)	28
MDD (kN/m^3)	11.40

Table 8 Test result of black cotton soil

Sr. No.	Name of test	Black cotton soil
1	Specific gravity	2.67
2	Liquid limit	58.40%
3	Plastic limit	30.37%
4	Plasticity Index	28.03%
5	Shrinkage limit	8.93%
6	IS classification	CH
7	Free swell index	103%
8	OMC	24.5%
9	MDD	1.53gm/cm^3
10	UCS	0.291 kg/cm^2
11	Fine sand	31.5%
12	Silt and clay	68.5%

Table 9 Test results of BC Soil + Fly ash

Sr. No.	Name of test	%Fly ash			
		5%	10%	15%	20%
1	Liquid limit %	57.61	56.25	55.7	53.2
2	Plastic limit %	30.15	29.79	29.64	28.96
3	Plasticity index %	27.46	26.46	26.06	24.24
4	Shrinkage limit %	20.69	25.92	27.7	27.91
5	Free swell index %	88	79	71	62
6	OMC%	23.84	22.34	22.59	22.86
7	MDD gm/cm^3	1.56	1.64	1.61	1.59
8	UCS kg/cm^2	0.327	0.391	0.348	0.306

3.1.2 Compacted Fly ash Layer

In case the subgrade soil is of poor quality, it can be improved in respect of its bearing ratio (CBR) by replacing the top part of the soil with fly ash (Ashimanta Sengupta et al. 2017). In order to increase the bearing ratio of weak subgrade soil, compacted fly ash layer with a 250-mm thickness is utilized above stabilized and unstabilized subgrade soil.

By comparing Tables 8 and 9, it is concluded that due to the addition of fly ash (in varying %) in BC soil liquid limit decreases and shrinkage limit increases. Compressive strength increased by 12.37% for 5% fly ash (FA) and 34.36% for 10% FA. As further addition of FA lead to a decrease in the UCS value, 10% FA is chosen as optimum.

Table 10 Physical properties for FEM model

Soil	E kN/m^2	γ kN/m^3	c, ϕ kN/m^2	Material model
Subgrade (15%FA)	4×10^4	17.9	1×10^{-4}, 30°	Mohr-Columb
Fly ash	6×10^4	11.4	0, 41°	Mohr-Columb
Sub-base (C&D)	1×10^5	21.4	1×10^{-4}, 49°	Mohr-Columb
Base	1.2×10^5	21.8	1×10^{-4}, 48°	Mohr-Columb
DBM	2×10^6	22.6	–	Linear elastic
BC	2×10^6	23.3	–	Linear elastic

(E—Modulus of Elasticity, γ—Unitweight, C—Cohesion)

4 Finite Element Analysis by PLAXIS 2D for Effective Geosynthetic Inclusion

Three locations of the geosynthetic reinforcement are studied by (Bassam Saad et al. 2006), namely the base–asphalt concrete interface, the base–subgrade interface, and inside the base layer at a height of 1/3 of its thickness from the bottom. In the current study, finite element analysis is done on different road sections constructed of solid waste in sub-base layer and different combinations of geosynthetic location to find out the exact location for their effective utilization. The loading (tire pressure) is 575 kPa and radius of loading is 150 mm consider for the study. Boundary conditions of the model were chosen in such a way that, the influence of stress distribution would be minimized. A fixed support was used at the horizontal base for no movement. Vertical displacement allowed for both vertical sides of the model and no horizontal movement allowed at sides of the mesh. Unreinforced and reinforced models used for the study the effect of reinforcement on the pavement section (Table 10).

To check the performance of this geogrid-reinforced C&D waste in pavement against rutting and fatigue cracking, critical strains were measured such as ϵ_{xx} and ϵ_{ZZ} at bottom of DBM and top of the subgrade.

In Table 11, horizontal tensile strains (ϵ_{xx}) at the bottom of DBM layer and vertical compressive strains (ϵ_{ZZ}) at top of the subgrade are given. Traffic intensity considers for this FEM analysis is 150 MSA as per IRC: 37-2012. It is concluded that due to the installation of 250-mm compacted fly ash layer horizontal strain at bottom of DBM is reduced by 66.05% and vertical strain at top subgrade reduced by 4.43%. It is concluded that among all the combination of geosynthetic inclusion in base and sub-base layer, geosynthetics in middle of base course gives good results, and it reduces down horizontal strains by 168% and vertical strains by 101% (Figs. 5 and 6).

There is no significant change observed for geogrid in sub-base due to less tension in geogrid. The performance of C&D waste in base/sub-base layer is improved due to this geogrid inclusion which helps to minimize the pavement failure such as rutting and fatigue cracking by reducing critical strains. The improvement in performance of

Table 11 Strain value in the pavement from FEM analysis

Strains in micron	250-mm compacted Fly ash		250-mm compacted Fly ash + Geogrid (EA = 40 kN/m)	
	Without	With	In base	In sub-base
ϵ_{xx}	36	21.68	13.41	21
ϵ_{ZZ}	180	172.3	89.19	165

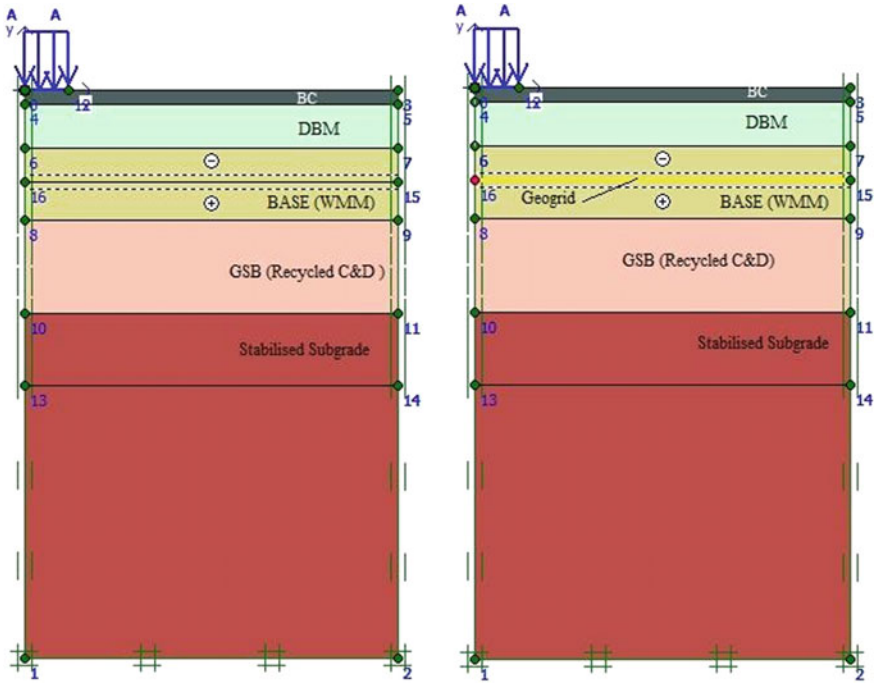

(a) Without Geogrid (b) With Geogrid (EA = 1000 kN/m)

Fig. 5 FEM model for recycled C&D waste GSB and Fly ash stabilized subgrade

geogrid-reinforced C&D waste material is mainly due to the tensile effect of geogrid, friction between recycled aggregate and geogrid.

5 Conclusions

1. The C&D waste impact value is between 10 and 20%. Hence, classified as strong for flexible pavement and the brick waste cannot be used for sub-base due to high impact value.

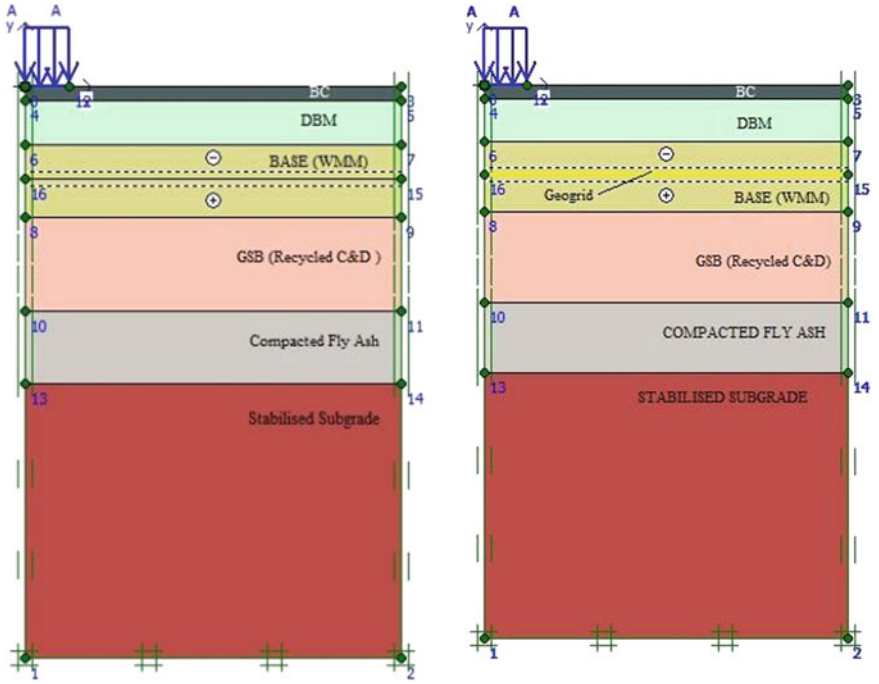

(a) Without Geogrid (b) With Geogrid (EA = 1000 kN/m)

Fig. 6 FEM model for recycled C&D waste GSB, compacted Fly ash, and Fly ash stabilized subgrade

2. The C&D waste crushing value is between 20 and 30%. Hence, classified as strong for flexible as well as rigid pavement and the brick waste cannot be used for sub-base due to high crushing value.
3. The C&D waste abrasion value is between 15 and 30%. Hence, classified as strong for the bituminous concrete surface course.
4. In the second part, fly ash is used as an additive with 10% contribution shows comparatively strong results with reduced OMC (8.82%) and increased MDD (7.18%) and UCS (34.36%).
5. It is concluded that due to the installation of 250-mm compacted fly ash layer, horizontal strain at bottom of DBM is reduced by 66.05% and vertical strain at top of subgrade is reduced by 4.43%.
6. FEM results show that geosynthetics (Geogrid, EA = 40 kN/m) at the middle of the base gives good result among all the combinations of geosynthetic location. It reduces or minimizes the chance of rutting and fatigue cracking by reducing vertical compressive strain at top of subgrade by 101% and horizontal tensile strain at bottom of DBM by 168%.

References

Huang YH (2004) Pavement analysis and design. Pearson Education, Inc

Dhadse S, Kumari P, Bhagia JL (2008) Fly ash characterization, utilization and government initiatives in India—A review. J Sci Ind Res 67:11–18

IRC (Indian Roads Congress) (2012) Tentative guidelines for the design of flexible pavements. IRC 37, New Delhi, India

Saad B, Mitri H, Poorooshasb H (2006) 3D FE analysis of flexible pavement with geosynthetic reinforcement. J Transp Eng ASCE 132(5):402–415

Sengupta A, Mukherjee S, Ghosh A (2017) Improvement of bearing ratio of clayey subgrade using compacted flyash layer. Geotech Geol Eng (Springer). https://doi.org/10.1007/s10706-017-0179-y

Sharma NK, Swain SK, Sahoo UC (2012) Stabilization of a clayey soil with fly ash and lime: a micro level investigation. Geotech Geol Eng 30:1197–1205 (Springer)

Potential of Marble Dust to Improve the Physical Behavior of Soil

Arvind Kumar Jha, Ankush Kumar Jain and Shivanshi

Abstract The production of huge amount of waste by-products from commercial industries possesses an adverse effect on environment due to lack of proper disposal and utilization. In Rajasthan state of India, 15–20 lakh tons of marble waste is producing each year by marble processing units which is indestructible and harm to general public. Hence, the bulk utilization of marble quarry waste needs to be done to embrace sustainable development and safe ecosystem, and mostly for environmental friendly construction operations. Highway construction is an area where marble quarry waste can be utilized in the bulk amount with an advantage. In the present study, various experimental and physico-chemical studies have been carried out to characterize the materials used and to understand the potential of marble dust in improving the physical behavior of poorly graded sand (SP). The liquid limit of soil reduces significantly with an increase in marble dust. Further, it is observed that marble dust leads to increase the maximum dry density and optimum water content. The increase in specific gravity of soil, reduction in voids within the soil matrix, and ionic reactions between aluminium, silica and calcium present in soil and marble dust are the key factors to control the physical behavior of SP.

Keywords Compaction · Marble dust · Microanalysis

A. K. Jha (✉) · A. K. Jain · Shivanshi
Department of Civil Engineering, Manipal University Jaipur (MUJ), Jaipur 302026, India
e-mail: arvindkumar.jha@jaipur.manipal.edu

A. K. Jain
e-mail: anksjain007@gmail.com

Shivanshi
e-mail: shivanshi57@yahoo.in

R. Sundaram et al. (eds.), *Geotechnics for Transportation Infrastructure*, Lecture Notes in Civil Engineering 28, https://doi.org/10.1007/978-981-13-6701-4_12

1 Introduction

Soil stabilization is the process of altering the properties of a soil by applying some additives to meet specific engineering requirement (Jha and Sivapullaiah 2015). In road construction, all the naturally available materials cannot be utilized as construction materials. The problematic nature and limitations of such soils can be improved by application of stabilizing agents such as chemical stabilizers and waste materials. It has been believed that the application of stabilizing agents can improve the strength, durability, and resistance of pavement layer. Various techniques like; mechanical stabilization, chemical stabilization, columnar injection, preloading, asphalt stabilization, and use of reinforcing materials have frequently used to suppress the susceptible behavior of these soils (Soosan et al. 2005). However, the most viable option to stabilize the soil is observed with chemical additives alone or, in combination with waste materials. Bulk utilization of waste materials such as fly ash, ground-granulated blast-furnace slag (GGBS), rice husk, stone quarry dust, and marble dust are used to improve the properties of expansive soils economically and also fruitful to embrace sustainable development and safe ecosystem for environmental friendly construction operations (Jha and Sivapullaiah 2017).

Around 90% of the world's production of marble comes from India and approximately 85% of India's production is received from Rajasthan (Pappu et al. 2006). Rajasthan has more than 4000 marble mines and about 1100 marble gang saws (processing units) which are producing 15–20 lakh tons of marble slurry waste which is indestructible waste and harm to general public such as air and water pollution, contamination of surface and groundwater, visual impacts, accidents due to unscientific dumping, dry slippery road, wet slippery road, and loss to flora and fauna (Celik and Sabah 2008).

The formation of marble is due to the exposure of limestone to high temperatures and pressure. The waste marble dust is utilized generally in the production of concrete mix, as filler materials for roads and embankments, manufacture of bricks and Portland cement, ceramic tiles, lime, activated calcium carbonate, hollow blocks and wall tiles, and in decorative plastic coating. Further, it has been reported that utilization of marble dust leads to the reduction of its environmental impact and is economically beneficial (Singh et al. 2017). However, the environmental impact of using marble dust as construction material needs to be reviewed for its longevity and sustainable utilization.

The marble waste/slurry is predominated with calcium carbonate ($CaCO_3$), magnesium carbonate ($MgCO_3$), calcium oxide (CaO), and magnesium oxide (MgO) and usually contains other impurities such as: clay minerals, micas, quartz, pyrite, iron oxide, and graphite (Segadães et al. 2005). The presence of calcium in marble dust is the key component for soil modification and stabilization. The reactions between soil and calcium in the presence of water proceed through a combination of four basic mechanisms: (i) cation exchange or ion exchange; (ii) flocculation and agglomeration; (iii) pozzolanic reaction, and (iv) carbonation. The first two (cation exchange and flocculation) are known as short-term reactions which result an increase in the

soil workability, shear strength, and plasticity (Bell 1996). The second two reactions are well known as stabilization reactions which are responsible for increase in the strength of soil. Hence, it has been aimed in the proposed work to take advantage of free calcium predominated in the marble waste to improve the properties of different problematic soils for highway construction.

Most of the previous researches carried out, particularly in India, are focused on the utilization of waste materials like fly ash, GGBS, rice husk, and stone quarry dust alone or in combination with calcium-based stabilizers. However, relatively less research has been done for the effective and bulk utilization of marble waste products (dust and slurry) to stabilize the problematic soils for sustainable and eco-friendly construction. Misra et al. (2009) mentioned that marble slurry waste can be effectively used for sub-grade preparation. The plasticity and California-bearing ratio (CBR) of red tropical soils are improved with marble dust; however, strength development is not enough to suit as base materials (Okagbue and Onyeobi 1999). Tozsin et al. (2014) suggested that marble waste can be used as soil amendments for the neutralization of acid soils. The fly ash, marble dust, and waste sand are fairly good additive materials in road subbase fill and reaction substantially improves their CBR, swelling ratio, and water conductivity (Firat et al. 2012). The previous research is focused on the particular type of soils with inconsistency in outcomes. Hence, the potential of marble quarry dust to improve the properties of soils needs to be study considering all factors such as environmental, physical, and chemical.

The present study is aimed to examine the potential of marble dust to modify the physical behavior of soil for further investigation of its engineering behavior and to develop the protocol. To achieve the objectives, the characterization of soil and marble dust is done in detail by performing various experimental tests such as Atterberg's limits, particle-size analysis, compaction characteristics, and microanalyses (mineralogical and microstructure). Further, the effects of varying marble dust on the physical behaviors (specific gravity, liquid limit, compaction characteristics, and void ratio) are examined thoroughly.

2 Materials Used and Methodologies Followed

2.1 Soil and Its Characterization

Soil used in the present study was collected from Dahmi Kalan, Rajasthan-303026, India. The soil was obtained from a depth of approximately 1–1.5 m below the natural ground level by open excavation. The particle-size analysis (IS 2720 Part 4) of soil confirmed the presence of predominant amount of sand-sized particle (i.e., 98.4%) as shown in Fig. 1.

As per the classification charts of Indian Road Congress (IRC) and Unified Soil Classification System (USCS), soil is classified as a poorly graded sand (SP) having non-plastic behavior. The liquid limit (LL) (IS 2720 Part 5) and specific gravity (IS

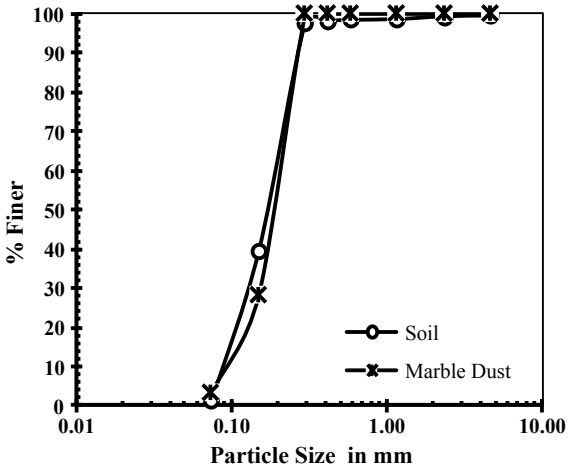

Fig. 1 Particle-size analysis of soil

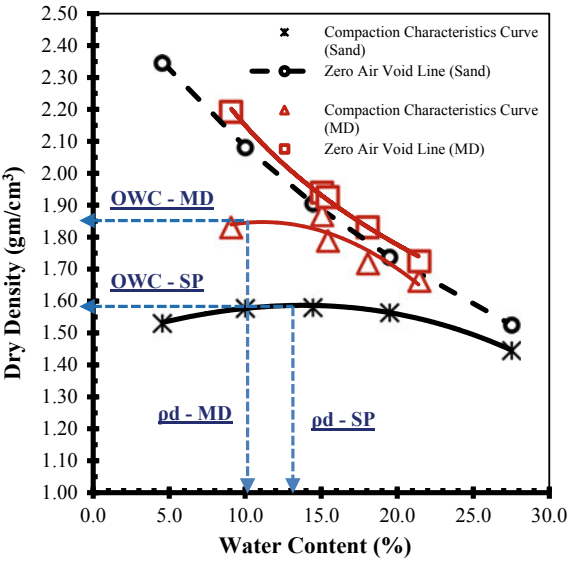

Fig. 2 Compaction characteristic curve of soil and marble dust

2720 Part 3) of soil are obtained to be 44.60% and 2.630, respectively. The optimum water content (OWC) and dry density of soil is 13% and 1.58 gm/cm^3, respectively (Fig. 2). The pH test of soil (IS 2720 Part 26) was also obtained 9.71 which shows an alkaline nature.

The mineralogical composition of the sand is determined by performing an X-ray diffraction (XRD) spectrometer by using graphite monochromator and Cu-Kα radiation. The sample is scanned for 2θ ranging from 3° to 90°. The presence of various minerals in the sample is identified with the help of the data files developed by the Joint Committee on Powder Diffraction Standards (JCPDS 1999). The X-ray

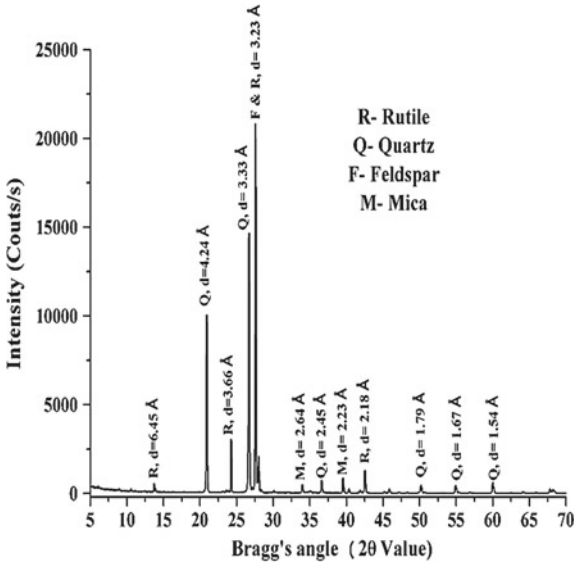

Fig. 3 XRD analysis of sand

diffractogram, refer to Fig. 3, confirmed the crystalline nature of the sand. With the help of JCPDS data files, the presence of quartz, rutile, and mica minerals are confirmed as predominant minerals.

The microstructural examination and chemical composition of soil are performed with field emission scanning electron microscope (FESEM) coupled with energy dispersive X-ray spectroscopy (EDAX). A small amount of oven-dried soils are mounted on the aluminum mounting disk (also called SEM stubs) with the help of carbon tape. Prior to SEM examination, the sample was coated with 100-Å-thin layer of gold-palladium for 38 s using a sputter coater, polaron E5100 at 10^{-3} Torr Vacuum. The gold coating is done in order to avoid charging problem during imaging.

SEM image of sand (Fig. 4a) illustrate the irregular shape having different size of sand particles. Further, SEM image (Fig. 4b) is also captured at higher magnification to observe the texture of sand particle. The texture of sand particle is observed to be rough and the presence of small cavities. Chemical composition of soil is performed by using EDAX to observe the element present in sand and is shown in Fig. 5. It is observed that sand is predominated with Silica (Si) and Aluminum (Al) with minor amount of Calcium (Ca) and Sodium (Na) (Table 1).

2.2 Marble Dust

Marble dust is collected from the quarry of marble industry, Kishangarh, Rajasthan. The marble dust passing through 425-μm IS sieve is used for experimental purpose. The particle-size analysis (IS 2720 Part 4) of marble dust confirmed the presence

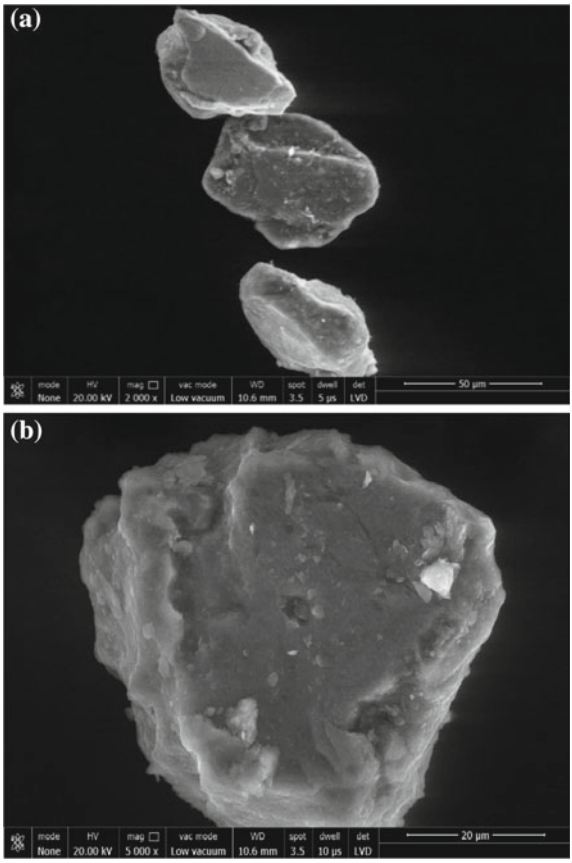

Fig. 4 SEM images of sand **a** showing different size of particles; **b** shape of the particles

of predominant amount of sand-sized particle (i.e., 96.5%) as shown in Fig. 1. The specific gravity and liquid limit of marble dust are found to be 2.74 and 17.5%, respectively. The compaction characteristic curve of marble dust (Fig. 2) shows the reduction in optimum water content (OWC) to 10% and increase in maximum dry density to 1.85 gm/cm^3 with respect to the OWC (i.e., 13%) and dry density (i.e., 1.58 gm/cm^3) of soil.

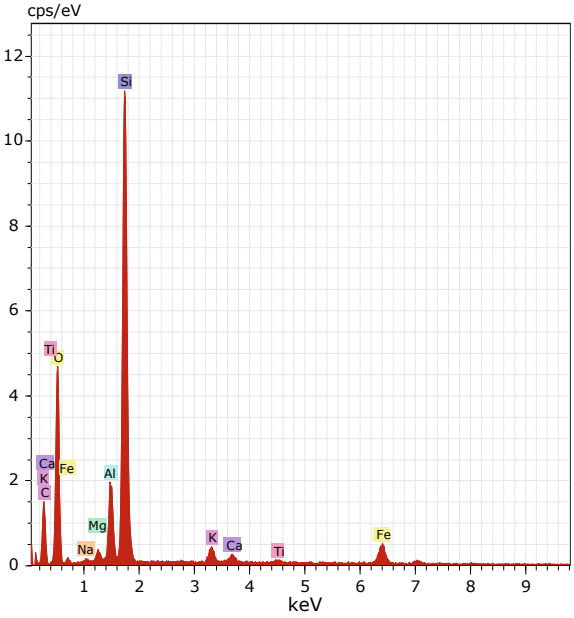

Fig. 5 Chemical composition analysis of sand

Table 1 Chemical composition analyses of sands

Element	Atomic (%)
O	71.28
Si	21.24
Al	3.99
Fe	1.01
K	0.72
Mg	0.81
Ca	0.31
Na	0.50
Ti	0.15
C	0.00
Total	100.00

3 Results and Discussion

3.1 Effect of Marble Dust on the Specific Gravity of Sand

Figure 6 shows the effect of varying marble dust content on the specific gravity of sand.

It is observed that the specific gravity increases continuously after the replacement of sand with different amount of marble dust up to 20%. The increase in specific gravity with the addition of marble dust is attributed to the higher specific gravity value of marble dust (i.e., 2.74) than that of sand (i.e., 2.63).

3.2 Effect of Marble Dust on the Liquid Limit of Sand

The effect of replacement of sand percentage with varying marble dust on the liquid limit is shown in Fig. 7.

It is observed that there is a drastic reduction in the liquid limit of sand with increase in the percentage of marble dust. It is reported that liquid limit of soil is ascribed to the void water present both within floccules and between the clay particles comprising the floccules (Terzaghi and Peck 1967). However, this is insignificant for sandy and kaolinite soils (Sridharan and Rao 1975). For sandy soil, the liquid limit is mainly controlled by shearing resistance between the particles. Hence, in the present

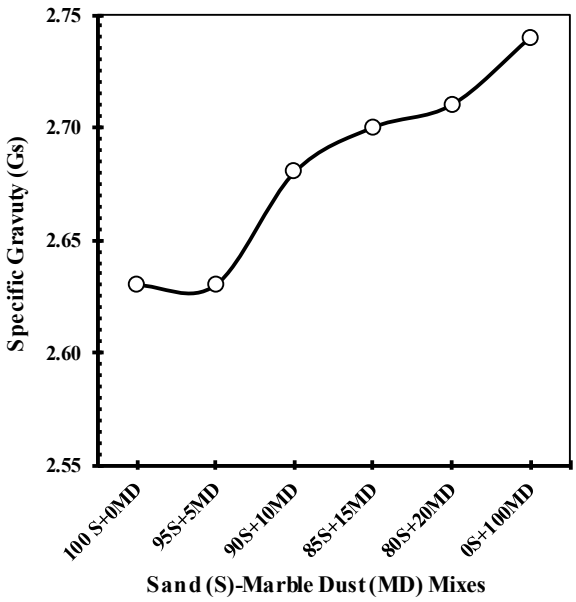

Fig. 6 Variation of specific gravity of sand (S) with the addition of marble dust (MD)

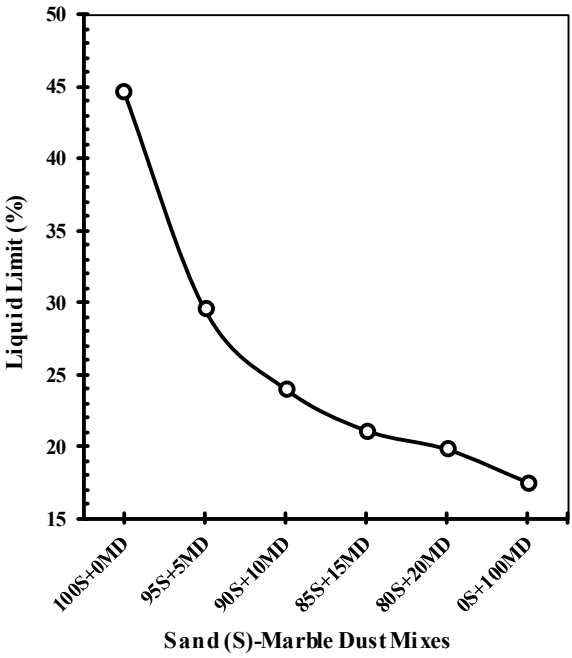

Fig. 7 Variation of liquid limit of sand (S) with the addition of marble dust (MD)

case, the reduction in liquid limit of soil with addition of marble dust may be due to (i) the aggregation of soil particles at microlevel due to reaction between aluminum and silica present in soil (Table 1) and calcium present in marble dust, (ii) lower liquid limit value of marble dust compared to soil, and (iii) increase in specific gravity of sand with addition of marble dust.

3.3 Effect of Marble Dust on the Compaction Characteristics (Maximum Dry Density and Optimum Water Content of Sand)

Influence of marble dust on the maximum dry density (MDD) and optimum water content (OWC) of sand is shown in Figs. 8 and 9.

It is observed that the marble quarry dust shows the higher value of MDD and lower OWC compared to sand. This is primarily due to coarser solid particles and high specific gravity of marble dust than sand. The initial drop in dry density is observed with the addition of MD up to 10% to sand (Fig. 8). The void ratio of within the sand matrix increases initially with lower marble content, whereas significant reduction is observed with higher MD content. Hence, reduction in dry density may be due to the disturbance in initial soil matrix and increase in pore volume (Fig. 10) with

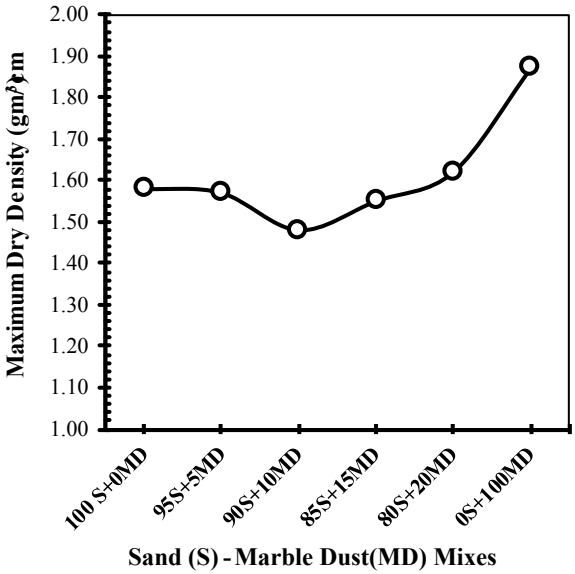

Fig. 8 Variation of maximum dry density of sand (S) with the addition of marble dust (MD)

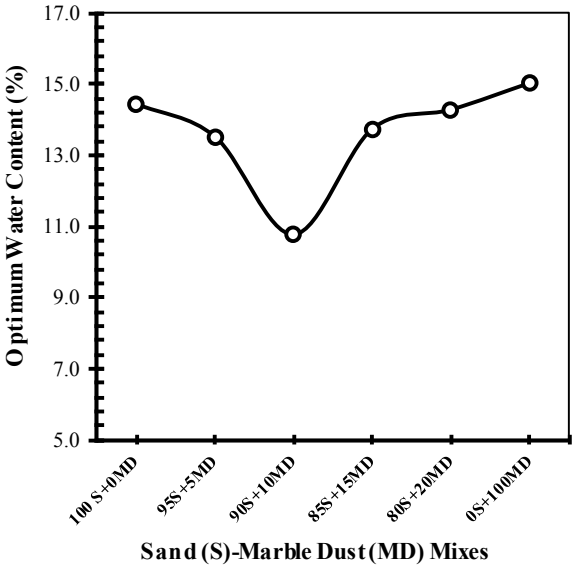

Fig. 9 Variation of optimum water content of sand (S) with the addition of marble dust (MD)

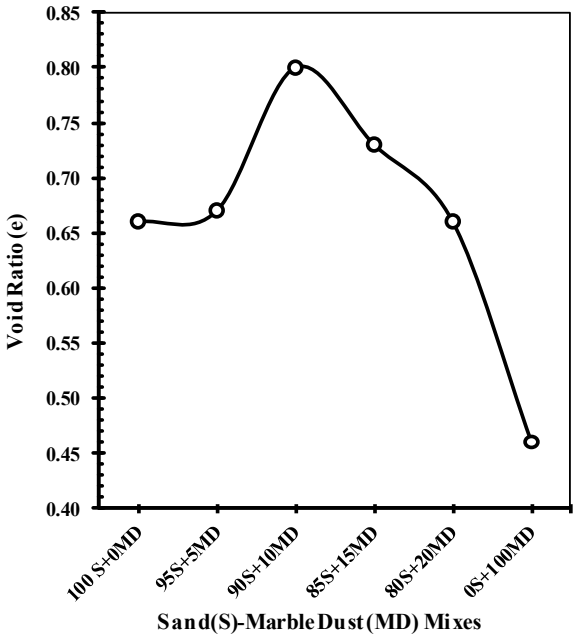

Fig. 10 Variation of void ratio of sand (S) with the addition of marble dust (MD)

the formation of weak agglomerated soil matrix. Further increase in dry density with MD content is attributed to the improvement in gradation of soil and formation of cementitious such as calcium silicate hydrate (C–S–H) and calcium aluminum silicate hydrate (C–A–S–H) gel by reactions between calcium and aluminum and silica present in soil.

Similar trend with an increase in optimum water content beyond 10% marble dust is observed for different sand–marble dust mixtures as shown in Fig. 8. The OWC of sand reduces with an addition of 10% marble dust but increases thereafter with an increase in amount of marbled dust up to 20%. The reduction in OWC at 10% MD may be attributed to the improvement in the gradation of soil. However, increase in OWC beyond 10% addition of marble dust is due to the requirement of additional water to complete the reactions between calcium and ions (Al and Si).

4 Conclusions

The effect of varying amount of marble dust on the physical behavior of sand is studied in detail. The major conclusions that can be drawn from the present study are as follows:

1. The detailed characterization of materials is essential to elucidate the mechanism of behavior change in the soil–marble dust mixtures.

2. The specific gravity of sand increases with the amount of percentage of marble dust to sand, whereas the reduction in liquid limit of sand is observed with the addition of marble dust. This may be mainly due to the increase in shear resistance of sand with the addition of marble dust.
3. The dry density of sand reduces initially up to lower marble dust content of 10%. However, increase in dry density is observed with the further addition of MD. Similar behavior is observed for OWC of sand–marble dust mixes. The alteration in gradation and formation of cementitious compounds with reaction among silica–aluminum–calcium–water are the key factors to control the compaction characteristics of sand–marble dust mixtures.
4. Void ratio of within the sand matrix increases initially with lower marble content, whereas significant reduction is observed with higher MD content.

The present study provides a base to perform further research on engineering behavior the soil–marble dust mixtures and examine its effectiveness in the highway construction.

Acknowledgements This study is supported financially by the Research and Development (R&D) division of Manipal University Jaipur (MUJ) under SEED grant. The authors would like to acknowledge this support. Authors thank to the reviewer for their critical review which supports to improve the content and quality of the paper.

References

Bell FG (1996) Lime stabilization of clay minerals and soils. Eng Geol 42(4):223–237

Celik MY, Sabah E (2008) Geological and technical characterization of Iscehisar (Afyon-Turkey) marble deposits and the impact of marble waste on environmental pollution. J Environ Manage 87:106–116

Flrat S, Yılmaz G, Cömert AT, Sümer M (2012) Utilization of marble dust, fly ash and waste sand (Silt-Quartz) in road subbase filling materials. KSCE J Civ Eng 1–9

JCPDS (Joint Committee on Powder Diffraction Standards) (1999) Index to the powder diffraction file. International Centre for Diffraction Data, Newtown Square, PA

Jha AK, Sivapullaiah PV (2015) Mechanism of improvement in the strength and volume change behavior of lime stabilized soil. Eng Geol 198:53–64

Jha AK, Sivapullaiah PV (2017) Physical and strength behavior of lime treated gypseous soil with fly ash—micro-analyses. Appl Clay Sci 145:17–27

Misra et al (2009) A new technology of marble waste utilization in roads. J Sci Ind Res 69:67–72

Okagbue CO, Onyeobi TUS (1999) Potential of marble dust to stabilise red tropical soils for road construction. Eng Geol 53(3):371–380

Pappu A, Saxena M, Asolekar SR (2006) Solid wastes generation in India and their recycling potential in building materials. Build Environ 42:2311–2320

Segadães AM, Carvalho MA, Acchar W (2005) Using marble and granite rejects to enhance the processing of clay products. Appl Clay Sci 30:42–52

Singh M, Choudhary K, Srivastava A, Sangwan KS, Bhunia D (2017) A study on environmental and economic impacts of using waste marble powder in concrete. J Build Eng 13:87–95

Soosan TG, Sridharan A, Jose BT, Abraham BM (2005) Utilization of quarry dust to improve the geotechnical properties of soils in highway construction. Geotech Test J 28(4):391–400

Sridharan A, Rao GV (1975) Mechanism of controlling liquid limit of clays. In: Proceedings of Istanbul conference on soil mechanics and foundation engineering, vol 1, pp 75–84
Terzaghi K, Peck RB (1967) Soil mechanics in engineering practice, 2nd edn. Wiley, New York, p 729
Tozsin G, Arol AI, Oztas T, Kalkan E (2014) Using marble wastes as a soil amendment for acidic soil neutralization. J Environ Manage 133:374–377

Soil Treatment with Lime for Earthworks: An Economical and Sustainable Solution

Christophe Joseph Esther Denayer, Amit Kumar and Larisa Cristina Soporan

Abstract Fine clayey soils with a poor rating have the tendency to swell and shrink due to the absorption of water and drying out effect. Mixing those marginal soils with lime will immediately dry out and modify the soil by flocculation, resulting in a reduction in the plasticity index and switching fine clayey soils, which are difficult to handle, into friable and granular particles which are much easier to work and compact. Pozzolanic reactions between clay, soil water and lime will increase the bearing capacity of compacted layers gradually, and result in flexible structural layers situated in subgrade till top of capping layer for large-sized earthworks of civil engineering projects. This technology of soil recycling in situ is recognized as an economical and sustainable methodology.

Keywords Soil treatment · Soil stabilization · Lime · Fine soils · Marginal soils · Earthworks · Subgrade · Capping layer

1 Introduction

Soil treatment with lime is a technique where fine soils are mixed in situ, in order to obtain flexible, permanent structural layers like subgrade, subbases, bases and capping layers for all types of roads, highways and railways construction and also unpaved country road and temporary service roads.

C. J. E. Denayer (✉)
Carmeuse Europe, Boulevard de Lauzelle 65, 1348 Louvain-la-Neuve, Belgium
e-mail: christophe.denayer@carmeuse.com

A. Kumar
Carmeuse Middle East & Asia, Building no 6WA, Office no 116,
Dubai Airport free zone, Po Box no 371748, Dubai, UAE
e-mail: amit.kumar@carmeuse.com

L. C. Soporan
Carmeuse Holding, 127A Carierei Street, Brasov, Romania
e-mail: larisa.soporan@carmeuse.ro

R. Sundaram et al. (eds.), *Geotechnics for Transportation Infrastructure*, Lecture Notes in Civil Engineering 28, https://doi.org/10.1007/978-981-13-6701-4_13

Lime addition to fine soils creates different effects. The first effect, soil drying, is a rapid decrease in soil moisture content due to the chemical reaction between water and quicklime (calcium oxide) into a moist soil by the formation of calcium hydroxide. The second effect, soil modification, includes the reduction in soil plasticity, increase in optimum moisture content, decrease in maximum dry density, improved compactability, reduction in the soil's capacity to swell and shrink and improved strength and stability after compaction. These effects generally take place within 1–48 h. The third and last effect, soil stabilization, is due to the clay flocculation made by the physical–chemical reaction among clay components and calcium—induced by the pH increase—changing soil particles size and making a heterogeneous size distribution.

The quantity of lime addition—expressed as a percentage of dry soil—is determined in the laboratory after soil analysis and is in function of the required performances. Soil treatment with lime produces long-term strength and as well as a permanent reduction in shrinking, swelling and soil plasticity, resulting in durable, flexible basement materials.

2 Assessment of Suitability for Lime Stabilization

2.1 Soil Classification

Not all types of fine soils are suitable for soil stabilization. AASHTO M 145 or ASTM D3282 classifies soils in different classes, based on particle size distribution, liquid limit and plasticity index.

Soil stabilization with lime is suitable in very cohesive soils with a "fair to poor" subgrade rating like soils of class A2-6, A2-7, A6 and A7. In addition, class A5 is suitable, having a plasticity index above 8%. All suitable soil categories are based on Italian procedures according Quaderni Tecnici A.L.I.G. n°3 and in line with Mixture Design and Testing Procedures for Lime Stabilized Soils from the American National Lime Association.

2.2 Limited Quantity of Organic Materials

Different test methods can be used to determine the organic content of in situ soils. The method prescribed in AFNORNF 94-055—used in Italy and France—evaluating organic substances by oxidation using potassium dichromate. Soil treatment with lime is suitable as the results are below 2% of organic content. The limit of 2% can be exceeded—it differs from country to country—in general 4% being the maximum acceptable amount—as long as the requirements of resistance are satisfied.

Soils with organic materials exceeding the limits are difficult to stabilize or may require uneconomical quantities of lime.

2.3 Limited Content of Sulphur Salts

This is recommended for areas where sulphate contamination in soils is known. Lime addition is still feasible, however, only in case of limited content of sulphur salts (sulphates and sulphides).

The total content of sulphur salts can be evaluated according UNI 8520 part 11. Results must be lower than 0.25%. Some soils with a content of sulphates between 0.25% and 1% can be accepted only after a detailed soil study in the laboratory. The soils with sulphate content higher than 1% should be replaced by soils with lower sulphur salts or local suitable quarry materials.

High sulphate concentrations can cause deleterious reactions, similar to sulphate attack in concrete, that can lead to loss of stability and heave.

3 Immediate Lime Consumption

3.1 Lime–Soil Interactions

Clay at this natural moisture content forms a colloidal solution. A colloid is a substance at a fine-grained dispersed state between a homogeneous solution and a heterogeneous suspension. This "micro-heterogeneous" state consists of two phases: a microscopic dimensioned substance (diameter between 10-9 m and 10-6 m) dispersed in a continuous phase (Table 1).

Chemical reactions are described according Little DN, stabilization of pavement sugrades and base courses with lime. By adding quicklime (calcium oxide) into the soil at natural moisture content, soil will dry out due to the reaction between calcium oxide and water, resulting in calcium hydroxide (hydrated lime). This is an exothermic reaction:

$$CaO + H_2O \rightarrow Ca(OH)_2 + 15.5\,kCal \quad (1)$$

Table 1 Dimensions of particles in solution

$<10^{-9}$ m	10^{-9} to 10^{-6} m	$>10^{-6}$ m
Homogeneous solution	Colloidal solution	Heterogeneous suspension

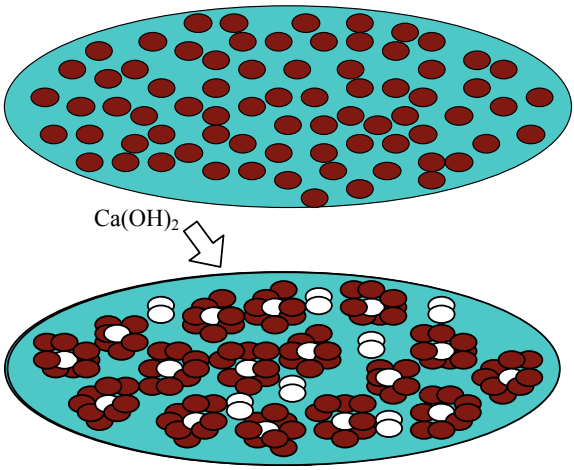

Fig. 1 Colloidal solution of clayey soil (top) and clay flocculation due to Ca^{2+} (below)

Calcium hydroxide, in the presence of water, will be split into Ca^{2+} and OH^- ions, which are increasing the pH of the solution. In these conditions, Ca^{2+} ions will fix the clay particles around them creating macro-particles which are very stable. This process is called clay flocculation (Fig. 1).

At this stage, the plasticity index is highly reduced, and the soil becomes friable and granular, making it easier to work and compact. Due to increased pH of soil mixture, alumina and silica present in clay particles are solubilized. After compaction, pozzolanic reactions are starting, between calcium ions, hydroxide ions, soluble silicates and alumina, resulting in gradual hardening, by the creation of calcium silicate hydrate (CSH) and calcium aluminate hydrate (CAH). Those reactions are similar to the hydration process of Portland cement:

$$Ca^{2+} + OH^- + SiO_2 \rightarrow CSH \tag{2}$$

$$Ca^{2+} + OH^- + Al_2O_3 \rightarrow CAH \tag{3}$$

3.2 Lime Specifications

Building limes for soil treatment are classified according to EN 459-1 with CE marking for the products within the European Union. Only limes of category CL 90 and CL 80 are suitable for soil treatment (Table 2).

In case of quicklime, some additional requirements have to be performed on particle size distribution and reactivity according to EN 14227-11 (Table 3).

Concerning reactivity, quicklime shall attain a temperature of 60 °C within 25 min.

Table 2 Chemical requirements for lime for soil treatment (according to EN 459-1) and test methods described according to EN 459-2

Constit. %	CaO + MgO	MgO	CO_2	SO_3	Av. lime[a]
CL 90	≥90	≤5	≤4	≤2	≥80
CL 80	≥80	≤5	≤7	≤2	≥65

[a]Av. lime: available lime. These are minimum requirements because the designer may request higher values to optimize the lime consumption for the projects (see paragraph 4)

Table 3 Physical requirements, concerning particle size distribution for quicklime

Passing on sieve (mm)	(%)
5	100
2	≥95
0.2	≥70
0.09	≥50

3.3 Immediate Lime Consumption

The test consists of measuring pH of a soil–lime mixture, starting at 2% by mass addition of lime. Lime addition is increased in steps of 0.5% until a value superior to 12.4 at 25 °C is obtained. The minimum lime content, reaching the threshold of 12.4, is defined as the immediate lime consumption.

The procedures are prescribed in ASTM D 6276—Eades and Grim pH test. The reason for high pH is linked to satisfy immediate lime–soil reactions and still provide significant residual calcium to provide proper conditions for the long-term pozzolanic reactions.

4 Lime Optimization

During the soil analysis in the laboratory, additional information on the density of soil in function of the moisture content and in relation to the quantity of lime added has to be measured, to ensure bearing capacity performances on compacted soils in practice.

4.1 Maximum Dry Density and Optimum Moisture Content

Manufacture natural soil and soil-mixed specimens in accordance with EN 13286-50 at standard Proctor compaction. Determine first the maximum dry density and optimum moisture content according to EN 13286-2 for five soil specimens at different moisture content, followed by five specimens with lime added to the soil, also

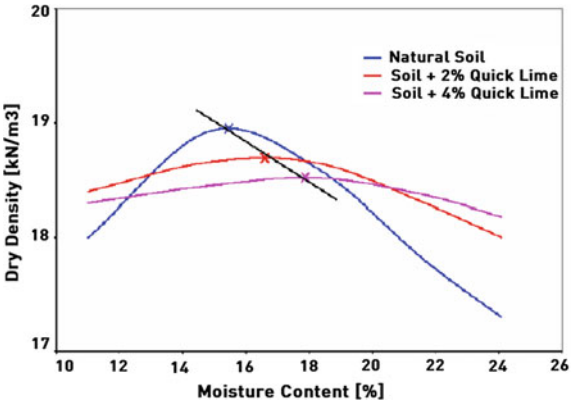

Fig. 2 Maximum dry density for natural soil and soil added with lime, at different moisture content

Table 4 AASHTO-DoT (USA) compressive strength specifications for soil mixtures with lime in relation to the application (subbase, base) and climate conditions

Min. CS (N/mm^2)	8 days soaked	3 FT cycles	7 FT cycles	10 FT cycles
Subbase				
Rigid pavement/floor slab/foundations	0.35	0.35	0.62	0.82
Flexible pavement (>25 cm)	0.42	0.42	0.69	0.90
Flexible pavement (20–25 cm)	0.48	0.48	0.69	0.97
Flexible pavement (13–20 cm)	0.62	0.62	0.90	1.10
Base				
	0.90	0.90	1.17	1.40

at different moisture contents. By extrapolation, the maximum dry density can be visualized in graph form (Fig. 2).

4.2 Compressive Strength on Proctor Specimens

Manufacture natural soil and soil-mixed specimens in accordance with EN 13286-50 at standard Proctor compaction. Determine compressive strength—after a conditioning period of 28 days—that ensures adequate field performance in a cyclic freezing and thawing and an extended soaking environment.

Tables 4 and 5 give information about USA requirements in function of the application and classes for designers according to European standards.

Table 5 Compressive strength measured on Proctor samples according EN 13286-41 and also specified in EN 14227-11

Compressive strength (MPa)	Class
≥0.2	Rc 0.2
≥0.5	Rc 0.5
≥1.0	Rc 1.0
Other declared value but not less than 0.2 MPa	Rc DV

Table 6 Californian bearing ratio according to EN 14227-11

CBR after 4-day soaking (or other longer specified)	Class
≥15	CBR15
≥20 and not less than the immediate bearing index	CBR20
≥30 and not less than the immediate bearing index	CBR30
≥40 and not less than the immediate bearing index	CBR40
≥50 and not less than the immediate bearing index	CBR50
Declared value (but not less than 15)	CBRDV

4.3 Mechanical Performance

The California bearing ratio (CBR) is a penetration test for evaluation of the mechanical strength of road subgrades and base courses. It was developed by the California Department of Transportation.

The test is performed by measuring the pressure required to penetrate a soil sample with a plunger of standard surface area. The measured pressure is then divided by the pressure required to achieve an equal penetration on a standard crushed rock material. The CBR test is described in EN 13286-47.

The harder the surface, the higher the CBR value. A CBR of 5 equates to moist clay, while moist sand may have a CBR of 10. High quality crushed rock has a CBR over 80. The standard material for this test is crushed Californian limestone which has a value of 100. It is not excluded to achieve CBR values higher than 100, on samples of fine clayey soils, treated with lime.

It is acknowledged as a good practice, to measure CBR after 11 days, this means after 7 days (air conditioning), followed by 4-day soaking. During the first 7 days, specimens shall be prevented from drying out, and temperature shall be maintained at (20 ± 2) °C. The reason for this is related to pozzolanic reactions between soil and lime that should be completed. After that period, the test specimens shall undergo soaking for 4 days at a temperature of (20 ± 2) °C (Table 6).

4.4 Volumetric Swelling After 4-Day Soaking

Volumetric swelling, determined on fully soaked (immersed) CBR specimens in accordance with EN 13286-47—using water that is continuously aerated—is rec-

ommended to be below 1%. This information gives us an idea of how the quantity of lime in the mix design is sufficient to stabilize the clay particles. In some situations, max. 2% can be allowed and even higher. However, a complementary study should be made, according to experience at the place of use.

5 Execution

The construction steps involved in soil treatment for road in place mixing are similar for stabilization and modification. Fediex, Section Lime or the Belgian Lime Association as well as SETRA, the French Ministry of Transportation document very well the different steps for the execution. Generally, stabilization requires more lime and job control than modification. Basic steps include

1. preparation of soil,
2. spreading of lime,
3. eventually adding water and mixing,
4. compacting to maximum (practical) density and
5. curing prior to placing the next layer or wearing course.

5.1 Preparation of the Soil

This operation is not always necessary. It may be carried out with a ripper, a harrow or a plough. Part of the aim of ploughing is to remove larger stones or gravel (>10 cm) present in the soil which might harm the mixing unit. Additionally, it helps to modify the humidity of the soil by ventilating or moistening it.

5.2 Lime Spreading

Lime is supplied pneumatically to the spreader, either directly from the silo vehicle or by using buffer silos.

Lime is dispersed using a spreader fitted with a weighing device. This operation should be carried out with a maximum of precision and regularity. The type of lime dispersed, quicklime or hydrated lime, should be based on multiple considerations, such as contractor experience, equipment availability and soil moisture.

Quicklime, or calcium oxide, is a more concentrated form of lime than hydrated lime, containing 20–24% more "available" lime oxide content. Thus, about 3% quicklime is equivalent to 4% hydrated lime when conditions allow full hydration of the quicklime with enough moisture. Quicklime has also a greater bulk density, requiring smaller storage facilities. The construction season may be extended because the

exothermic reaction caused by water and quicklime can heat up the soil. Quicklime is also excellent for drying wet soils. Quick lime is the most common product used for soil treatment in Europe and North-America.

Hydrated lime can be used for in case of soils with a moisture content below its optimum, but it is not as effective as quicklime. Hydrated lime particles are very fine so that dust can be a problem, rendering this type of application generally unsuitable for populated areas. For populated areas, a coarser milled quicklime or lime slurry (mix of lime and water) can become an option.

5.3 Mixing

If quicklime is used, it is essential that all particles have hydrated and well-mixed into the soil. Additional water may be required during final mixing (prior to compaction) to bring the soil to 3% above optimum moisture content of the treated material.

5.4 Compaction

Initial compaction is usually performed as soon as possible after mixing, using a sheep-foot-type roller or a vibratory pad-foot roller. After the section is shaped, final compaction can be accomplished using a smooth drum roller or pneumatic roller compactor. The equipment should be appropriate for the depth of the section being constructed.

In warm weather and when the soil is wet, it is advisable to carry out the compaction 2–4 h after mixing, to give the unslaked lime ample time to bind with water and evaporate. If risk of rain, the compaction of the soil should be done before any water can again penetrate the treated layers.

5.5 Curing and Protection

The surface of the subgrade, subbase or base should be kept moist until loaded construction equipment can drive over it without rutting formation. Drying time is about 1 h to 1 day, depending on outside temperatures and quantity of lime, to achieve enough bearing capacity for temporary access construction haulage roads, or next layer of the basement.

6 Control on Site

6.1 Quantity of Moisture Content in the Soil

It is recommended—before starting the working day—to measure the moisture content of the soil. This gives additional data to the contractor to determine this daily lime consumption.

If moisture is above optimum moisture content, quicklime shall be used. If moisture content is below optimum moisture content, eventually hydrated lime, or quick lime by adding additional water to the soil will be used.

6.2 Quantity of Lime Dispersed by Spreader

It is recommended to execute every day quality control on the quantity of lime dispersed by the spreader. This quantity of lime can easily be measured by a weight balance and using a metal plate of 0.5 m $\times$ 0.5 m, on which the lime falls by passing over by the spreader.

6.3 Static Plate Load Test on Compacted Soil

To control the quality of executed compaction, a static plate load test is an easy and quick method to have an idea about the bearing capacity of the compacted layer in situ.

The plate load test—plate of approx. 200 cm^2—is used to measure the deflection or deformation modulus (in USA: modulus of subgrade reaction) of compacted soil in situ. The vertical load on the plate is applied in steps through a hydraulic jack and a counterweight. The resulting surface deflection or penetration of the plate is read after stabilization at three points spread over 120° from a fixed frame. The average deflection is calculated, and this allows the determination of the deflection or deformation modulus.

The requested performances depend on the application (subgrade, subbase, base) and are in function of the compaction of soil–lime mixtures. However, similar values as compacted quarry aggregates can be achieved with lime treatment. An example of procedures concerning the static plate load test can be found in AASHTO T 222 and ASTM D 1196.

7 Economical Solution

7.1 Time Savings

Soil treatment with lime is reducing the construction time considerably compared to the traditional method, named dig and dump. In the traditional method, soil has to be excavated and transported—truck by truck—to a landfill, as well as truck by truck of new aggregates, has to be placed on the embankment and compacted as well. Those operations are not only expensive (see paragraph 7.2.) but they are also time-consuming.

7.2 Environmental Friendly Solution

The technique of soil treatment with lime is an environmental friendly solution because one truck movement of lime (=delivery of 30 T of lime by silo truck) is replacing 100 movements of trucks:

- 35 trucks to remove soil to landfill
- 35 trucks bringing new aggregates to the yard.

The taxes for landfilling of excavated soils can be avoided.

7.3 Important Cost Savings

The use of soil treatment in road construction is a very economical solution, compared to the traditional method where existing soil is removed and replaced by local quarry aggregates.

In the example below, based on FEDIEX, Section Lime, the following assumptions are made in the benchmarking for cost calculations:

- quarry at a distance of 20 km
- disposal site for landfill at 20 km
- 300 m between excavation and embankment
- landfill taxes at 6 €/T (Table 7).

This type of cost calculation should be made for each individual project or road construction. Savings of more than 60%—compared to the traditional method—are usual and common.

Table 7 Costs traditional method compared to soil treatment (Belgian reference prices 2017, based on data Fediex, Section Lime)

Replacement of soil by aggregates	
	€/m^3
Excavation of soil	2.00
Transport to landfill site	6.00
Tax landfill (1.7 T/m^3 × 6€/T)	10.20
Purchase aggregates (2 T/m^3 × 6€/T)	12.00
Transport aggregates to yard (7€/T × 2T)	14.00
Grading and compacting aggregates	2.00
Total	**46.20**
Soil treatment with lime	
	€/m^3
Excavation of soil	2.00
Transport soil to embankment	2.00
Disposal of soil in embankment	0.50
Purchase lime (3% × 1.7T/m^3 × 120€/T)	6.12
Mixing and spreading	2.50
Grading and compacting soil	2.00
Total	**15.12**

8 Conclusions

The use of lime in soil treatment in road construction is a proven method. The concept to mix clayey soils, resulting in durable basement materials, is recognized all over the world.

This concept can also be used to mix soils and dirty aggregates in a stationary mixing plant and to produce a building material that can be compacted for road construction or filling material.

Acknowledgements We would like to thank Prof. Gabriele Tebaldi, P.E, Ph.D., University of Parma (Italy), Department of Civil and Environmental Engineering and Architecture Road & Transport Section, for support to realize this paper.

References

AASHTO M 145: Standard specifications for classification of soils and soil-aggregate mixtures for highway construction purposes

AASHTO T 222 and ASTM D 1196: standard method of test for nonrepetitive static plate load test of soils and flexible pavement components, for use in evaluation and design of airport and highway pavements

AFNOR NF 94-055: Détermination de la teneur pondérale en matières organiques d'un sol - méthode chimique
AssociazioneLaboratori di Ingegneria e Geotecnica (Italy) (2013) QuaderniTecnici A.L.I.G. n°3, October 2013
ASTM D3282: Standard practice for classification of soils and soil-aggregate mixtures for highway construction purposes
ASTM D6276 - 99a(2006)e1: Standard test method for using ph to estimate the soil-lime proportion requirement for soil stabilization
EN 459-1: building lime
EN 459-2: building lime—test methods
EN14227-11: Hydraulically bound mixtures—specifications—Part 11: soil treated by lime
EN 13286-2: Unbound and hydraulically bound mixtures—Part 2: test method for the determination of the laboratory reference density and water content—proctor compaction
EN 13286-41: Unbound and hydraulically bound mixtures—Part 41: test method for the determination of the compressive strength of hydraulically bound mixtures
EN 13286-47: Unbound and hydraulically bound mixtures. Test method for the determination of California bearing ratio, immediate bearing index and linear swelling
EN 13286-50: Unbound and hydraulically bound mixtures—Part 50: Methods for making test specimens using proctor equipment or vibrating table compaction
Fediex, Section Lime, Soil treatment using lime. www.chauxflash.be
Little DN (1995) Stabilization of pavement subgrades and base courses with lime. Kendall/Hunt Publishing Company, Dubuque, Iowa 52002
Little DN, Shafee Yusuf FAM (2001) Example problem illustrating the application of the National Lime Association Mixture Design and Testing Protocol (MDTP). www.lime.org. September 2001
National Lime Association, Lime Treated Soils save Money & Time. www.lime.org (2005)
National Lime Association, Mixture Design and Testing Procedures, for Lime Stabilized Soil. www.lime.org. October 2006
Service d'Etudes techniques des routes et autoroutes SETRA - Guide Technique – Traitement des sols à la chaux et/ou aux liants hydrauliques, République Française, Ministère de l'Ecologie du Développement et de l'Aménagement, septembre 2007
UNI 8520 Parte 11: Determinazione del contenuto in Solfati

Part II
Design and Construction of High Speed Railway and Metro Track Substructures

Concepts and Methodologies for Track Improvement and Associated Physical Modelling and Field Monitoring

Buddhima Indraratna, Ngoc Trung Ngo, Qideng Sun, Cholachat Rujikiatkamjorn and Fernanda Bessa Ferreira

Abstract As the heavy haul freight trains become longer and heavier, ballast grain experience pronounced breakage and deformation, resulting in the deterioration of the ballasted track substructure. Suitable soil stabilisation approaches using geosynthetics and/or energy-absorbing rubber mats are commonly employed to enhance the stability and longevity of ballasted tracks. This paper reviews the research studies that have been conducted at the University of Wollongong on track technology using advanced laboratory and computational modelling, as well as real-life health monitoring of selected track sections. Full-scale instrumented field monitoring supported by Australian rail organisations has been carried out to obtain measurements of actual stresses and displacements and thereby evaluate track performance supplemented by computational models. In the past decade, the authors have tested varied types of geosynthetics and rubber mats both in the laboratory and in the field where these geoinclusions were put underneath the ballast layer in tracks built on various subgrade types (i.e. soft and hard subgrades). Stresses induced by traffic, ballast degradation, vertical and lateral displacements of the ballast aggregates were routinely recorded using extensive instrumentation systems. These results provide suitable approaches that can be considered into current track design for future heavy and long freight train travelling at higher speeds.

B. Indraratna (✉) · N. T. Ngo · Q. Sun · C. Rujikiatkamjorn · F. B. Ferreira
Centre for Geomechanics and Railway Engineering (CGRE) and ARC Training Centre for Advanced Technologies in Rail Track Infrastructure (ITTC-Rail), University of Wollongong, Wollongong, NSW 2522, Australia
e-mail: indra@uow.edu.au

N. T. Ngo
e-mail: trung@uow.edu.au

Q. Sun
e-mail: qideng@uow.edu.au

C. Rujikiatkamjorn
e-mail: cholacha@uow.edu.au

F. B. Ferreira
e-mail: fernanda@uow.edu.au

R. Sundaram et al. (eds.), *Geotechnics for Transportation Infrastructure*, Lecture Notes in Civil Engineering 28, https://doi.org/10.1007/978-981-13-6701-4_14

Keywords Ballast · Rail transportation · Synthetic inclusions · Finite element modelling

1 Introduction

Rail network forms an important part of the transport system in Australia and many other countries in the world. Railways play a vital role in its economy through transporting freight and bulk commodities between major cities and ports, apart from carrying passengers in commuter trains using the same rail networks, particularly in urban areas. The need to maintain competitive advantages over other transportation modes has increased stresses on the railway industry to enhance its efficiency and decrease maintenance and infrastructure costs (Indraratna et al. 2011a). In the case of ballasted tracks, the cost of maintenance can be decreased if a better understanding of the engineering concepts and mechanisms is obtained in relation to physical and mechanical characteristics of the rail substructure and of the ballast layer in particular.

The ballasted rail track network offers the most demanded and widely used mode of freight transportation in Australia. In order to support track superstructure, the use of a ballast layer is prioritised for several reasons, including construction economics (availability and abundance of materials), ensuring rapid drainage, sufficient bearing capacity, and resiliency to withstand repeated wheel loads (Indraratna et al. 2011a). Upon train loading, ballast grains become degraded by cyclic train loading. The adverse consequences can be the fouling of ballast, causing reduced friction and shear strength (Indraratna et al. 2012, Selig and Waters 1994, Rujikiatkamjorn et al. 2012). The number of studies carried out to assess the adverse effects that fouling has on the shear behaviour of ballast is very limited (Ngo et al. 2014, 2016a, 2017; Budiono et al. 2004, Tutumluer and Dombrow 2008, Indraratna et al. 2013; Rujikiatkamjorn et al. 2013). Upon fouling, the accumulation of fine particles (e.g. coal, subgrade silt, and clay) influences ballast behaviour to make tracks become unstable and misaligned (e.g. differential settlement and localised undrained failure). It is noteworthy that the Australian rail industry spends over hundred millions of dollars in track maintenance and ballast replacement every year.

Since ballasted tracks have minimum transverse lateral support (confinement), the confining pressure must be increased to control lateral deformation (Lackenby et al. 2007, Indraratna et al. 2012, Sun et al. 2016). The mechanical behaviour of ballast is governed by several properties of this granular material such as the particle size distribution (PSD), void ratio, and the corresponding relative density (Indraratna et al. 2011a). It is noted that while the properties of each ballast particle such as size, shape, and angularity affect its degradation response under traffic loading, the deformation is also influenced by the magnitude of axle loads, number of loading cycles, and frequency (Sun and Indraratna 2014; Sun et al. 2016; Selig and Waters 1994, Indraratna et al. 2014b). The magnitudes of the impact forces are dependent on the imperfections on the wheels (long-term wear) and rails (corrugations), as well as on the dynamic responses of the track (Powrie et al. 2007; LePen 2008).

The use of polymeric geosynthetics (geogrids, geotextiles, and geocomposites), shock mats (under ballast mats and under sleeper pads), and recycled rubber tyres can improve the stability and longevity of track, while reducing the annual maintenance costs (Indraratna et al. 2017a). Geogrids have been widely used to reinforce ballasted tracks and also increase the duration of track serviceability (e.g. Bathurst and Raymond 1987; McDowell et al. 2006; Brown et al. 2006; Ngo et al. 2017; Tutumluer et al. 2012). It has been reported that, once have they been placed, the mechanical interlock by geogrids with the surrounding ballast assembly can decrease the lateral displacement and particle degradation (Bathurst and Raymond 1987; Indraratna et al. 2017). In order to obtain greater insight into the performance of geosynthetic inclusions, extensive field trials have been implemented on two specific rail lines in the towns of Singleton, Bulli, located in NSW, Australia, with the support from Australian Rail Track Corporation (ARTC) and Sydney Trains (previously RailCorp) (Indraratna et al. 2010, 2017c). The beneficial effects of geosynthetics and rubber mats were also examined using large-scale laboratory tests subjected to both cyclic and impact loadings. Details of instrumentations, the process of field monitoring, and results measured from these field studies and laboratory tests are presented in the following sections.

With these obvious profits, available research on the geogrid–ballast interface response is limited, albeit some laboratory studies and computational simulations, especially when ballast gets degraded (Indraratna et al. 2011b). Past research has also attempted to use cellular reinforcement to provide additional lateral confinement to the substructure or capping layer with geocell-infilled aggregates (Biabani et al. 2016a). Under the induced loads, additional confinement by the geocell helps to prevent the enclosed aggregates from spreading laterally (Ngo et al. 2016). Also, by increasing the infill rigidity, the geocell could enhance the load-bearing capacity of the track, which in turn enhances its performance in view of load–deformation response (Biabani et al. 2016b; Ngo et al. 2016b). In this paper, the role of geosynthetics and rubber energy-absorbing layers in rail track stabilisation is described based on a series of large-scale laboratory tests involving fresh and fouled ballast, finite element modelling (Indraratna et al. 2011b, 2017a, 2018; Tennakoon et al. 2012; Sun et al. 2016), and data obtained from comprehensive field trials conducted on a instrumented ballasted embankment at Singleton (Nimbalkar and Indraratna 2016).

2 Laboratory Tests on Ballast

2.1 Ballast Fouling

During train operations, fine particles may fill the voids of ballast aggregates. This can be due to: (i) breakage of ballast sharp edges, (ii) fines infiltrating from the track surfaces, and (iii) fluidisation of soft subgrades (i.e. mud pumping) under extremely high hydraulic gradients caused by cyclic loads (Tennakoon et al. 2012).

As the fouling material occupies the free voids of ballast, it slowly impedes the track drainage capacity. Most ballast fouling (nearly 75%) stems from the breakage and abrasion of the rock grains, 13% due to infiltration from the sub-ballast, 7% migration from the top surfaces, followed by 3% intrusion of subgrade, and 1% comes from sleeper wear (Selig and Waters 1994). In Australia, coal fouling and degradation of ballast are the main sources of fouling materials and they account for about 70–95 and 5–30% (Feldman and Nissen 2002). In coastal track lines, fine silts and clays can be fluidised and pumped up into the ballast aggregates. However, this problem can be eliminated if a properly graded filtration layer or an appropriate geosynthetic filter is placed underneath the ballast layer (Trani and Indraratna 2010; Indraratna et al. 2011a).

2.2 Assessment of Ballast Fouling

There are a number of fouling indices available for evaluating the ballast fouling. Selig and Waters (1994) introduced a fouling index (FI) that is the total by mass of fouled ballast passing a 4.75 mm (i.e. No. 4) sieve and 0.075 mm (i.e. No. 200) sieve. Later, Feldman and Nissen (2002) suggested a percentage void contamination (PVC) to overcome some of the limitations associated with FI; PVC is given by the ratio of volume of fines to the void volume of fresh ballast. Since the mass-based index could give an inaccurate estimation of fouling when the contaminating materials (e.g. coal fines) have a relatively small specific gravities, this fouling index has become questionable in certain coal networks. Tennakoon et al. (2012) modified this fouling index by introducing a new fouling index called the Void Contaminant Index (VCI):

$$\mathrm{VCI} = \frac{(1 + e_\mathrm{f})}{e_\mathrm{b}} \times \frac{G_\mathrm{sb}}{G_\mathrm{sf}} \times \frac{M_\mathrm{f}}{M_\mathrm{b}} \times 100 \tag{1}$$

in which e_f is void ratio of fouled materials; G_sf is specific gravity of the fouling materials; e_b is void ratio of ballast; G_sb is specific gravity of ballast; M_b is weight of ballast; and M_f is weight of fouling agent. It is noted that there can be a considerable change in the void ratio, but the *VCI* can include all of these variations to an acceptable level.

2.3 Influence of Ballast Fouling on Track Drainage

Constant head permeability tests were conducted by Tennakoon et al. (2012) at the University of Wollongong (Fig. 1). They measured the hydraulic conductivity for ballast at different amounts of fouling to analyse the relationship between the VCI and the permeability. This permeability equipment is 500 mm diameter and 1000 mm height. A geotextile membrane (i.e. filter) was put above a bottom coarse granular

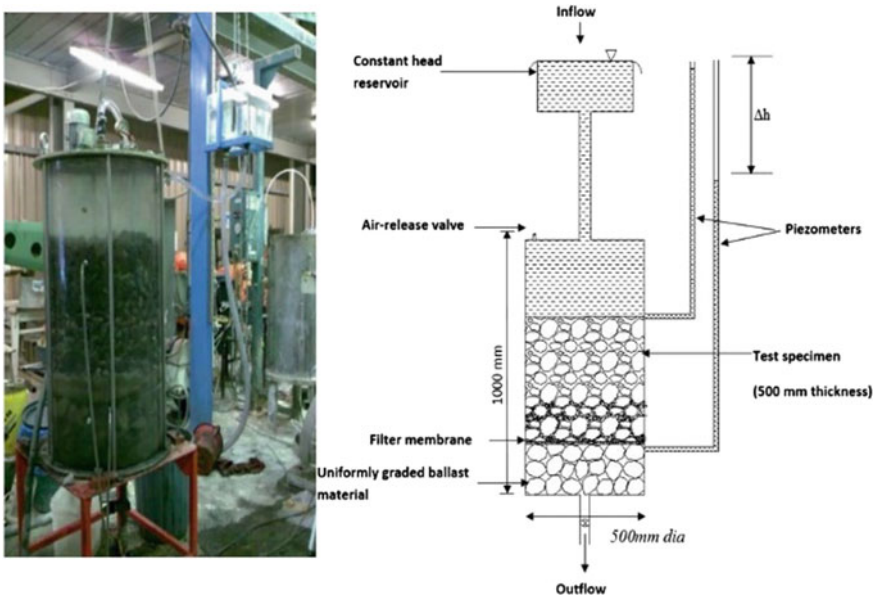

Fig. 1 Permeability test facility used in laboratory

layer while still maintaining a free drainage boundary to prevent fouling material flowing out. The ballast thickness in most rail tracks is commonly between 300 and 500 mm, so a 500-mm-thick ballast layer was used to determine the permeability of fouled ballast. The fouled ballast was placed into the apparatus and compacted in several layers (i.e. equal thickness) to represent a desired density of 15.5 kN/m^3. Fouling materials having different gradation curves such as coal fines, commercial kaolin, and clay-fine sand were used to simulate fouled ballast. To mimic a real ballast fouling scenario, the ballast aggregates were compacted and the fouling agents were let to infiltrate downwards by water. For the case of uniformly distributed fouling, predetermined amounts of kaolin corresponding to different degrees of fouling were mixed with ballast and compacted to obtain similar initial density of ballast.

Figure 2 shows that the hydraulic conductivity decreases with increased *VCI*. The laboratory test data reveal that around 5% increased *VCIs* results in a reduction of hydraulic conductivity of at least 200 times and up to 1500 times when ballast is fouled by coal fines and fine silty sands, respectively. It is also observed that the reduced permeability did not influence the required drainage capacity for safe track operations. Once the *VCI* is higher than 75%, a further decrease in hydraulic conductivity is less pronounced as it gets closer to the hydraulic conductivity of the fouling agent.

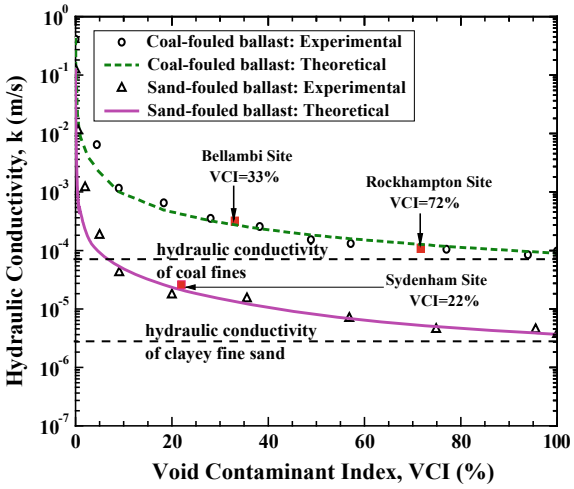

Fig. 2 Evolution of hydraulic conductivity (k) at different VCIs. *Data source* Tennakoon et al. (2012)

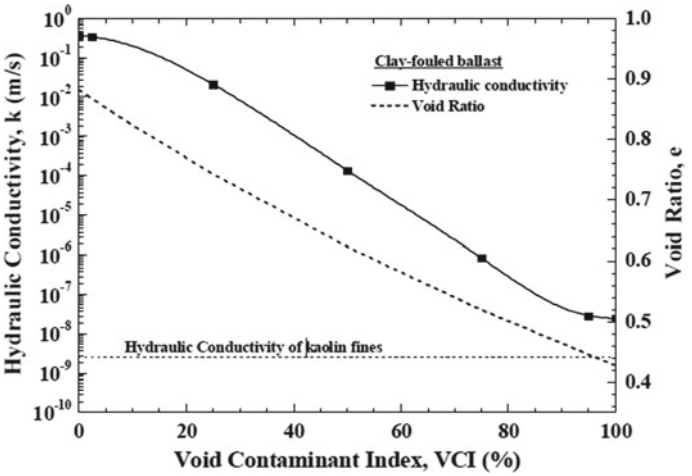

Fig. 3 Changes of hydraulic conductivity with varying VCIs for uniform clay-fouled ballast. *Data source* Tennakoon et al. (2012)

Figure 3 shows the evolution of hydraulic conductivity with increasing *VCI* values for clay-fouled ballast. At a small amount of *VCI*, hydraulic conductivities of fouled ballast are almost unaffected, but when the *VCI* is higher than 90%, the permeability of fouled ballast is significantly reduced and approaches that of pure kaolin.

2.4 Large-Scale Direct Shear Tests

A large-scale direct shear box utilised in this study has a plan area of 300 mm × 300 mm^2 and a height of 200 mm (Fig. 4). The ballast obtained from a quarry near Wollongong was cleaned and mixed in required proportions following the Australian Standards AS 2758.7 (1996). Coal fouling was selected as fouling agents, while the Void Contaminant Index was used to measure the fouling level. Direct shear tests were carried out for both fouled ballast and fresh ballast stabilised by 40 mm × 40 mm aperture geogrid to a shear deformation of $\Delta h = 37$ mm; and the detailed results were discussed elsewhere by Indraratna et al. (2011b). These test results show that the shear strength of ballast increases with increased normal stresses, while it decreases with increased amount of fouling. Strain softening has also been recorded for all the tests. For a higher normal stress σ_n, a greater peak shear stress and reduced dilation were observed.

Figure 5 shows that fouling agents decrease the shear strength of unreinforced and reinforced ballast specimens by coating the aggregates surfaces, thus reducing the interparticle friction while inhibiting the shearing constraint of the composite assemblies. Tutumluer et al. (2008) found that the ballast aggregates they tested in the laboratory had alike stress–strain responses. The evolutions of normalised maximum shear stress (τ_p/σ_n)(a friction angle, ϕ (apparent angle) versus *VCI* for fouled/fresh ballast specimens considering the role of geogrid reinforcement are shown in Fig. 5. Note that the coal fines considerably reduce the maximum shear stress and decrease the friction angle of the fouled ballast. When the *VCI* is smaller than 70%, the reduction of (τ_p/σ_n) due to the fines is significant, but it has marginal effect when the *VCI* is greater. The measured apparent friction angles of the unreinforced ballast varied from 46° to 65° depending on the applied normal stress. It is believed that the friction of ballast decreases with increased confining pressure, and this trend is similar to that of unreinforced/reinforced ballast.

2.5 Geogrid–Ballast Interface Behaviour

The influence of the grid geometry, opening size of geogrid, and the confining pressure on the interface behaviour of a geogrid-reinforced ballast assembly was evaluated by Indraratna et al. (2012). In this study, seven geogrids (*G*1–*G*7, Table 1), having rectangular, square, and triangular opening aperture (i.e. 36–70 mm), were tested under various normal stresses (15–75 kPa). All the specimens were subjected to a lateral deformation of 36 mm, corresponding to a horizontal shearing strain of 12%.

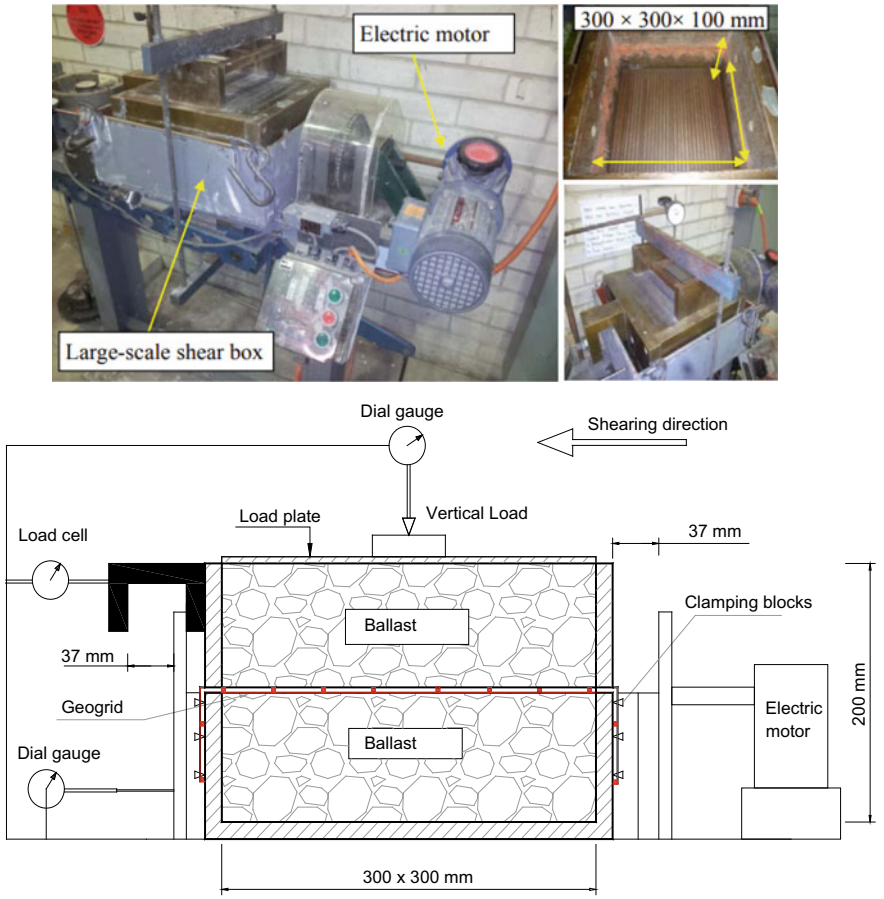

Fig. 4 Large-scale direct shear box

The actual effectiveness of the ballast–geogrid interaction can be quantified via an interface efficiency factor (α). This factor can be computed as:

$$\sigma = \frac{\tan \delta}{\tan \phi} \tag{2}$$

where ϕ is ballast friction angle and δ is ballast–geogrid interface friction angle.

The effect of the geogrid opening size (A) on the shear strength of geogrid-reinforced ballast specimens is presented in Fig. 6, where α values are plotted as a function of the A/D_{50} ratio. It is observed that α raises with increased A/D_{50} until it reaches a highest value of 1.16 when A/D_{50} is 1.21. The α value decreases as A/D_{50} comes close to 2.5. When $\alpha < 1$ shows a reduced interlocking among aggregates, whereas $\alpha > 1$ implies a reasonable interlocking, which contributes to an increase

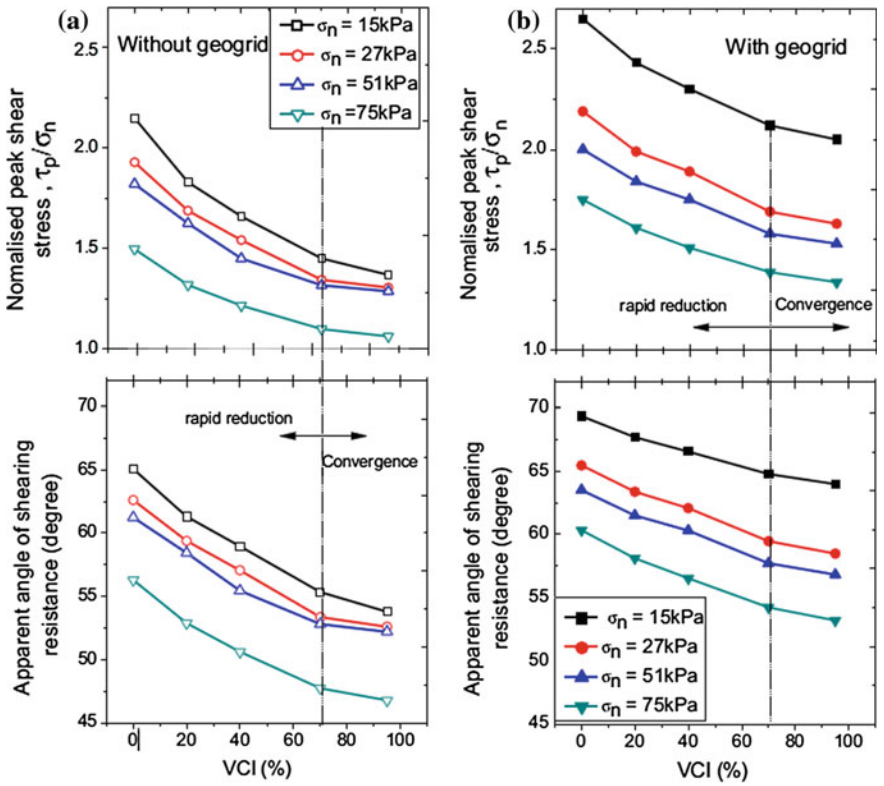

Fig. 5 Influence of *VCI* on shear strength and frictions of ballast specimens: **a** no geogrid; **b** with geogrid. *Data source* Indraratna et al. (2011b)

Table 1 Physical data of the various geogrids tested

Geogrid type	Aperture shape	Aperture size (mm)	Tensile strength (kN/m)
Grid 1	Square	38 × 38	30
Grid 2	Triangle	36	19
Grid 3	Square	65 × 65	30
Grid 4	Rectangle	44 × 42	30
Grid 5	Rectangle	36 × 24	30
Grid 6	Square	33 × 33	40
Grid 7	Rectangle	70 × 110	20

Data source Indraratna et al. (2012)

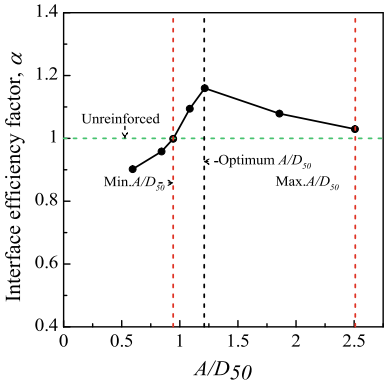

Fig. 6 Interface efficiency factor (α) versus A/D_{50}. *Data source* Indraratna et al. (2012)

of peak shear stresses. This study implies that the geogrid opening aperture sizes to optimise the shear strength are $0.95D_{50}$ and $2.50D_{50}$, respectively, and the optimum aperture size is approximately 1.2–1.3 times the value of D_{50}.

2.6 Large-Scale Triaxial Tests for Ballast Subject to Various Frequencies

The effect of varied frequencies (i.e. train speeds) on the ballast degradation and deformation when subjected to dynamic train loads has been examined using a novel large-scale cylindrical triaxial test facility (Fig. 7). The ballast specimens have been consolidated under lateral confinements (σ_3') of 10, 30, and 60 kPa. Frequencies (f) ranging from 5 to 60 Hz were tested to resemble train speeds of 40–400 km/h. Maximum cyclic deviatoric stresses ($q_{\max,cyc}$) of 230–370 kPa were applied to simulate axle train loading of 25–40 tonnes.

Figure 8 shows the evolution of axial strains (ε_a) with increased load cycles (N) under varying loading amplitudes ($q_{\max,cyc}$) and varying frequencies (f). It is seen that for a given value of f, the value of ε_a increases with N. Also, for varying values of f, ε_a increases with the increase of f at any given N. Laboratory test data indicate that four stages of deformation exist under cyclic loads: (i) elastic shakedown; (ii) plastic shakedown with some accumulation of permanent strains; (iii) ratcheting zone where significant accumulation of plastic strains is observed; and (iv) plastic collapse, as described by Sun et al. 2016. Correspondingly, three stages deformation were identified with the variation of frequency of loading, including Range I, at $f \leq$ 20 Hz—plastic shakedown; Range II, for 30 Hz $\leq f \leq$ 50 Hz—plastic shakedown and ratcheting; and Range III, for $f \geq$ 60 Hz—plastic collapse, as illustrated in Fig. 5a, b. The frequency f applied in these triaxial tests could be converted to equivalent train speed V based on standard gauge track geometry (Indraratna et al. 2011a). Cyclic testing data reported by Lackenby et al. (2007) also emphasized the

Fig. 7 Large-scale triaxial test facility at UOW

coexist of identical stages of ballast deformation behaviour based on the stress ratio ($q_{\max,cyc}/p'$).

Different ballast degradation characteristics were identified according to varying deformation stages during loading tests (Fig. 9). In Range I, $f \leq 30$ Hz, corner breakage and attrition of asperities were the major forms of particle degradation. In Range II, 30 Hz $< f <$ 60 Hz, particle splitting due to fatigue and particle attrition associated with increased vibration were predominant. In Range III, $f \geq 60$ Hz, particle splitting occurred due to decreased coordination number.

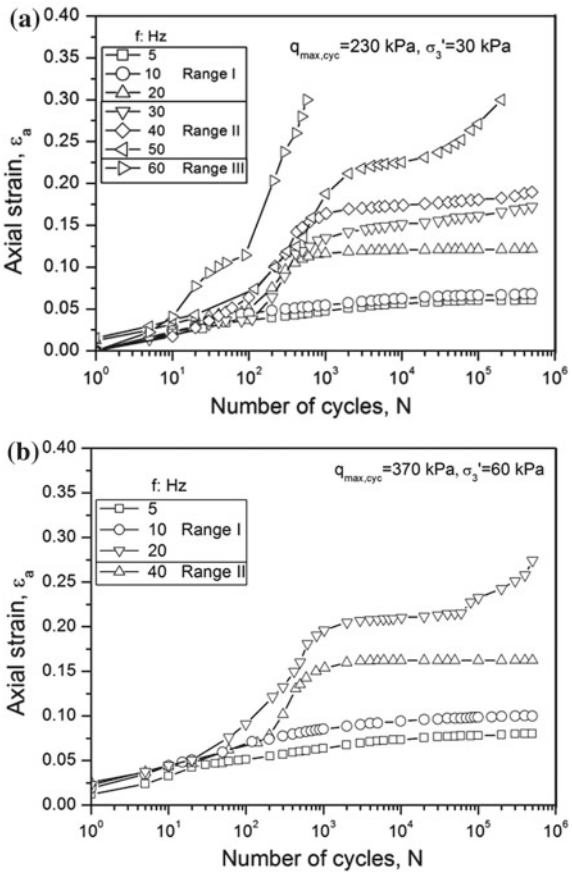

Fig. 8 Evolutions of axial strains versus load cycles: **a** $q_{max,cyc} = 230$ kPa and **b** $q_{max,cyc} = 370$ kPa (modified after Sun et al. 2016)

3 Performance of Rubber Tyre-Confined Capping Layer for Railroad Conditions

3.1 Description of Testing Materials and Test Procedure

Cyclic triaxial tests were done using a prototype process simulation prismoidal triaxial apparatus (PSPTA—Fig. 10). The bottom layer was compacted by a 50-mm-thick rockfill, followed by a 200-mm-thick sub-ballast layer was filled. Two types of ballast including fresh crushed basalt and recycled aggregates were tested with and without the inclusion of recycled tyres. A woven geomembrane was put under the rubber tyres as a separator. Strain gauges were installed on interior walls of the scrap tyres to record mobilised strains in axial and circumferential directions. The upper segment consisted of fresh ballast. A concrete tie (sleeper) and rail assembly was installed above the ballast layer, and then, the gaps between sleeper and walls were

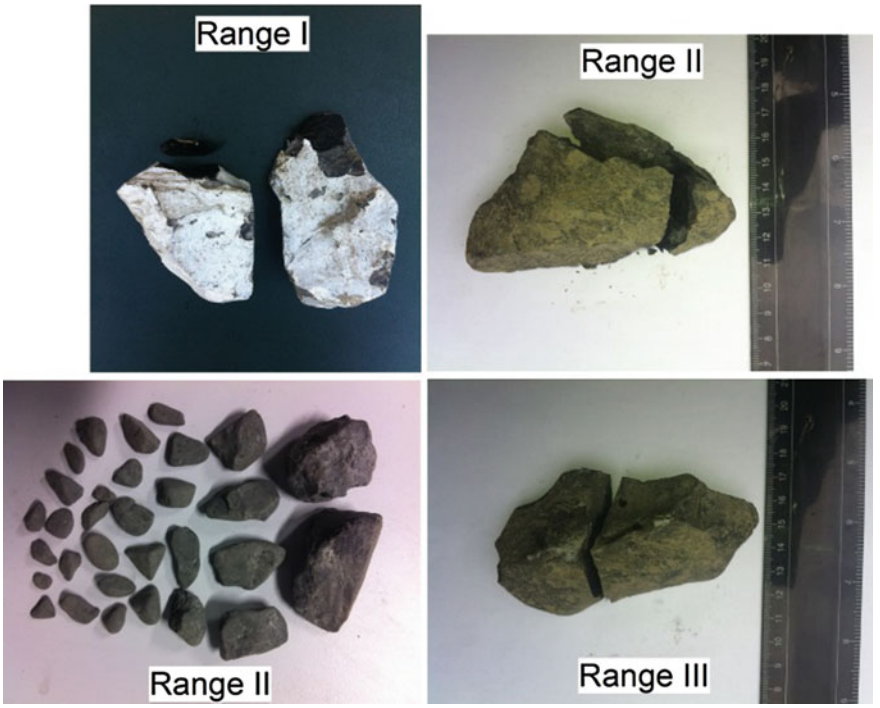

Fig. 9 Typical images of particle breakage (modified after Sun et al. 2016)

placed by additional aggregates. Whereas the 200-mm-thick sub-ballast layer was compacted in two layers of 100 mm thickness, the 300-mm-thick ballast stratum was compressed in every 75-mm-thick layers to attain their representative unit weight in the field. These materials were compacted using a vibratory hammer. The set-up for this specimen is shown in Fig. 11.

The above tests utilised σ'_{1cyc} 370 kPa to simulate the vertical stress generated from a static heavy haul train having a maximum axle load of 40 tonnes. The load frequency is generally described by $f = V/L$, in which V is train speed and L is length between the closest sets of axles in a given freight train. Therefore, for the smallest distance between axles of 2.02 m between an adjacent set of bogies, the frequency is around 0.138 V; hence, a value of $f = 15$ Hz represents a maximum train speed of approximately 110 km/h.

To mimic actual track conditions, a relatively small lateral pressure $\sigma'_3 (= \text{kPa})$ was applied to the assembly by hydraulic jacks. Every test was carried out to $N = 500{,}000$ cycles. After completing each test, the ballast was then sieved to calculate the amount of breakage according to the BBI—ballast breakage index proposed by Indraratna et al. 2005.

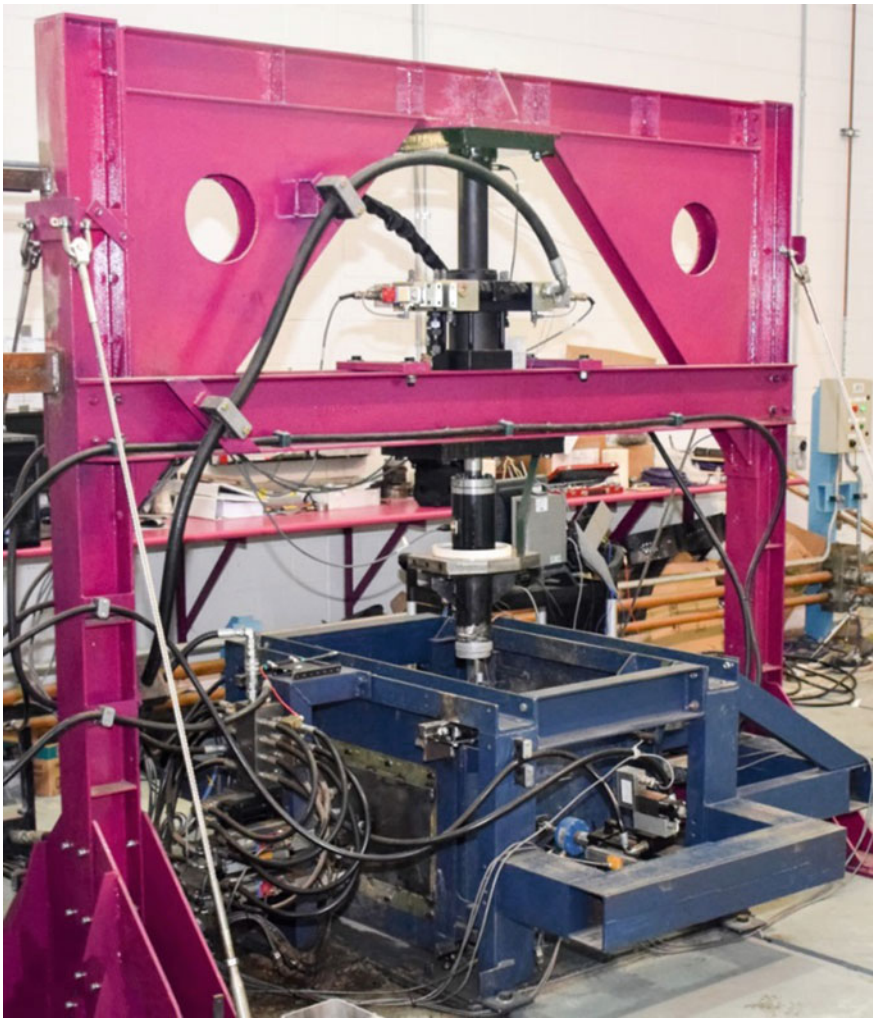

Fig. 10 Process simulation prismoidal triaxial apparatus (photograph taken at SMART Rail lab-UOW)

3.2 Results and Discussion

Figure 12 shows the evolution of the lateral displacements of the specimens with the number of cycles. As expected, the lateral movement of the specimens tested without tyre confinement increased rapidly for a small number of loading cycles and then stabilised at $N = 100{,}000$ cycles. Furthermore, the specimens confined with the rubber tyre cell infilled with spent ballast exhibited a substantial reduction in the lateral spreading (approximately 60%), whereas the tyre cell specimens infilled

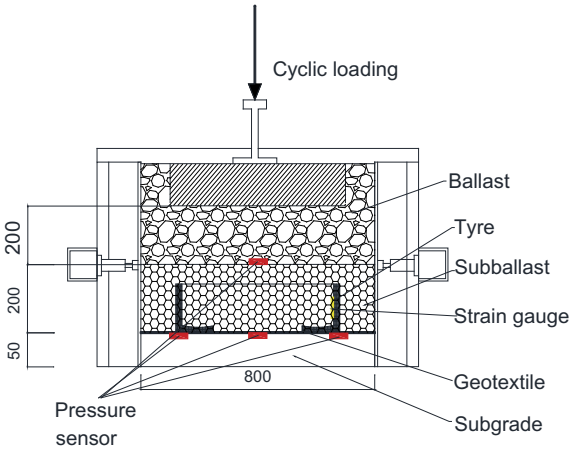

Fig. 11 Schematic illustration of process simulation prismoidal triaxial apparatus (dimensions in mm)

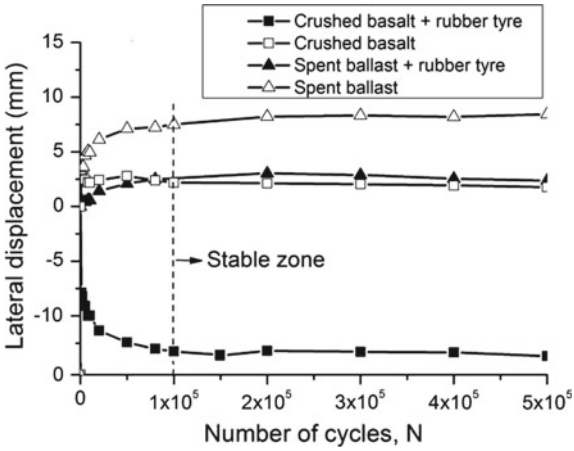

Fig. 12 Variation of lateral displacement of specimens versus load cycle. *Data source* Indraratna et al. (2018) with permission from ASCE

with a finer (crushed) basalt mainly compressed laterally. This is not surprising as under cyclic loads granular materials are compressed vertically and are expected to spread laterally; however, the rubber tyre cell can provide additional confinement to the infilled materials, thus minimising their lateral displacement. In addition, visual inspection during the tests showed that the ballast particles around the sleeper (Fig. 11) moved upwards under vibration loading, and the vertical boundaries of the specimen were pushed inwards by the constant lateral pressure σ_3'(=kPa) applied by the hydraulic jacks.

During service, railway ballast undergoes significant changes in stress because of repeated cyclic and impact loading and also experiences considerable particle breakage (Indraratna et al. 2011a). The fresh ballast directly under the tie (sleeper) was painted white (Fig. 13a) to conveniently determine the BBI after each test. Various ballast breakage modes such as the attritions and corner breaks

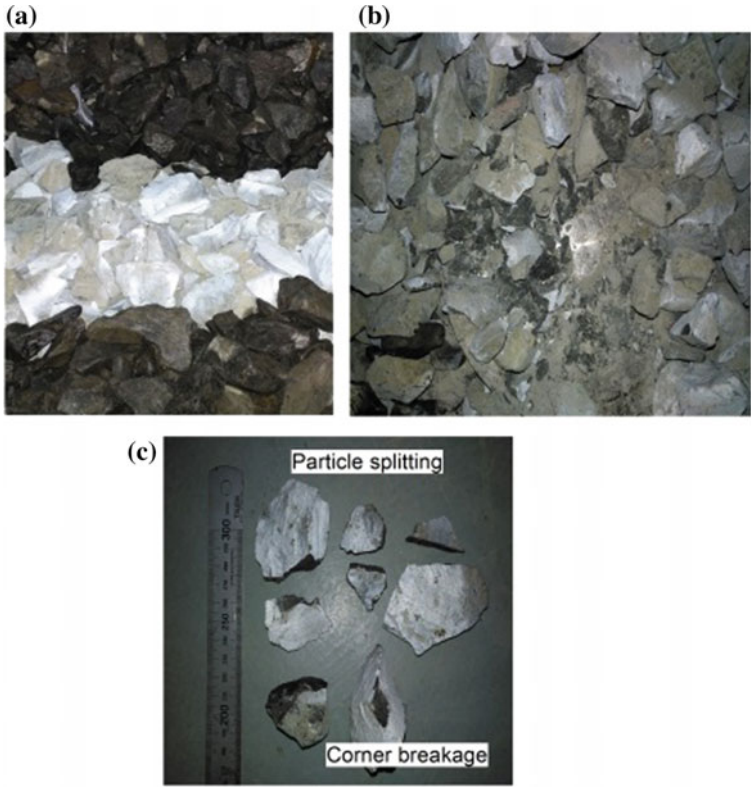

Fig. 13 **a** Fresh ballast before test; **b** degraded ballast after test, and **c** examples of particle degradation modes (after Indraratna et al. 2018)

(Fig. 13b, c) and particle splitting (Fig. 13c) occurred after cyclic loading. Figure 14 compares the PSD curves of the samples before and after each test, whereby the values of BBI are smaller for the specimens having a rubber tyre cell. This indicates that the use of a rubber tyre cell to confine the capping layer can effectively reduce ballast degradation, as such a system has a higher capacity to attenuate the energy which in turn could improve the overall track longevity.

4 FEM Modelling for Tracks with Tyres

4.1 Description of the FEM Model

A plane strain (transverse) cross section of a rail track was simulated by FEM to evaluate the ballast lateral deformation and the subgrade (natural soil foundation)

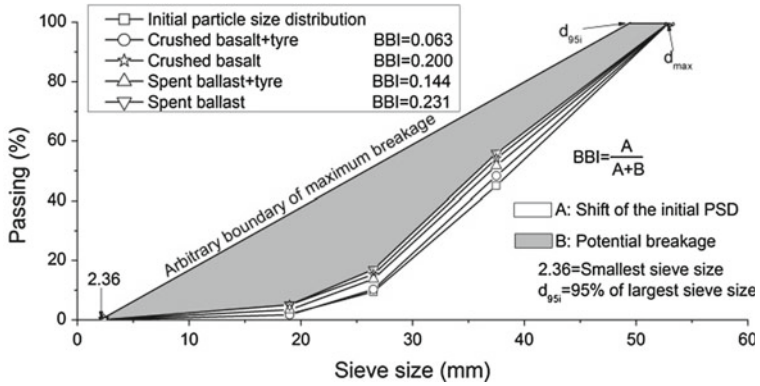

Fig. 14 PSD curves before and after cyclic loading. *Data source* Indraratna et al. (2018)-with permission from ASCE

stress with and without rubber tyres reinforcing the capping layer. The FEM model with the inclusion of rubber tyres is shown in Fig. 15.

The ballast, sub-ballast (capping), and subgrade were considered as elastoplastic following to Mohr Coulomb failure criterions. The scrap tyres were simulated as a cylinder. The rails and sleepers were taken as linear elastic materials, whose considerably higher stiffness in comparison to the rubber tyres, ballast, and subgrade

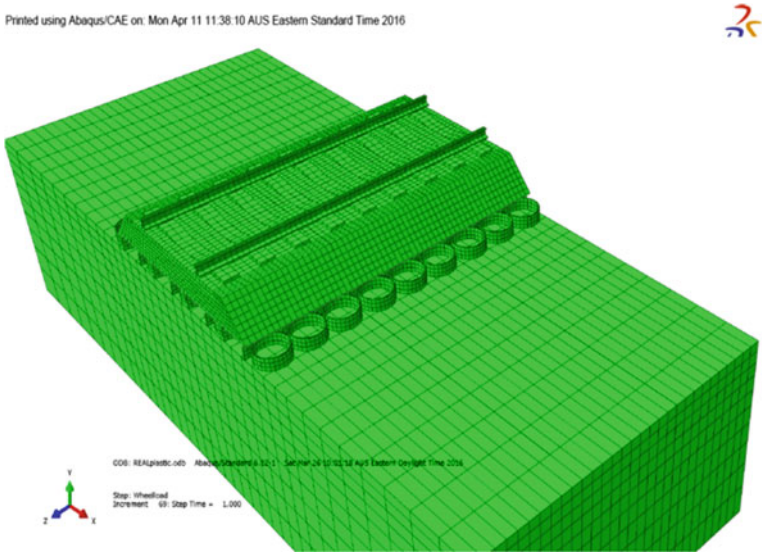

Fig. 15 FE mesh of a ballasted rail track with inclusion of rubber tyres

mimicked a composite layered structure of varied stiffness with depth. The values of model parameters used in the FEM simulation are shown in Table 2.

It may be argued that to simulate a track substructure, a true 3D-FEM would be more appropriate, but the track is very long, and therefore, it can be assumed as plane strain conditions that could be done by applying correct boundary constraints. In the current analysis, the width of the model was simulated as 1.9 m, and given the symmetry of its geometry, only half of typical tracks were considered. Ballast and subgrade layers were simulated by meshes composed of C3D8R, as described by Abaqus manual. In order to resemble the conditions prevailing in the field, the plane strain criterion was imposed, where the longitudinal deformations were considered insignificant when compared to the transverse strains. The outside vertical planes of the model were fixed from any horizontal movements (i.e. transverse directions), and the same conditions were applied to the *xy*-planes to restrict horizontal movement in *z*-directions. The bottom of the track was fixed (non-displacement boundary), as typically needed for a FEM model.

4.2 Model Predictions

Railway design often ensures that the traffic load acting on the subgrade is kept within limits that can avoid excessive shear failure and/or significant plastic deformations of the subgrade (Li and Selig 1998), as well as reducing the degradation and dilation of the track substructure materials including ballast and subballast (Indraratna et al. 2011a). To keep track alignment, ballast horizontal strains should be kept within specific ranges. It is therefore important to understand how the ballast lateral spreading and subgrade stress can be affected by the inclusion of rubber tyres in the capping layer, as opposed to the unreinforced case.

Figure 16 shows that the lateral strains along the slope of the track embankment could be significantly reduced by the use of tyre reinforcement. The lateral displacement contours for tyre-reinforced and unreinforced layers of subballast are presented in Fig. 17. It can be seen that for the reinforced case, the largest lateral displacement occurs underneath the sleeper edge. This analysis also indicates that the highest horizontal movements for the unreinforced subballast layer (0.1 m) was significantly larger than that of the reinforced sub-ballast (0.01 m) subjected to the same loading conditions.

The influence of the reinforcement provided by end-of-life tyre on the stresses acting at the interface between the subballast and the subgrade is illustrated in Fig. 18. As expected, the largest deviatoric stresses develop close to sleeper edges and then they decrease to the centre of the sleepers. This is in agreement with data measured in the field where the highest settlements typically take place near the sleeper edges (Li and Selig 1998). In the presence of waste tyres, a train with a given axle load operating at a certain speed induces a maximum deviator stress on the subgrade that is almost 12% less than that in the absence of the reinforcement. Intuitively, the confining effect provided by the recycled tyres causes the tyre-infilled gravel composites acting as

Table 2 Values of model parameters used in the FEM analysis (after Indraratna et al. 2017a)

Track parameters	Values
Parameters for rails	
Density	2000 (kg/m^3)
Young's modulus E	500,000 (MPa)
Poisson's ratio, ν	0.30
Parameters for sleepers	
Density	2000 (kg/m^3)
Young's modulus E	30,000 (MPa)
Poisson's ratio, ν	0.25
Parameters for ballast aggregates	
Density	1530 (kg/m^3)
Young's modulus E	200 (MPa)
Poisson's ratio, ν	0.30
Friction angle, ϕ	45°
Dilation angle, ψ	15°
Cohesion	1 (kPa)
Thickness of ballast	350 mm
Parameters for sub-ballast	
Density	2100 (kg/m^3)
Young's modulus E	2000 (kPa)
Poisson's ratio, ν	0.3
Friction angle, ϕ	39°
Dilation angle, ψ	15°
Cohesion, c	1.0 (kPa)
Parameters for subgrade	
Density	1700 (kg/m^3)
Young's modulus, E	2000 (kPa)
Poisson's ratio, ν	0.30
Friction angle, ϕ	40°
Dilation angle, ψ	15°
Cohesion, c	5.0 (kPa)
Parameters for scrap tyres	
Density	1500 (kg/m^3)
Young's modulus, E	750 (MPa)
Poisson's ratio, ν	0.35

(continued)

Table 2 (continued)

Track parameters	Values
Parameters for wheel loads	
Static loads	122.5(kN)
Train velocity	100 (km/hour)
Dynamic amplification factors (DAFs)	1.540
Dynamic wheel loads	188.2 (kN)
Parameters for interface	
Normal properties	Hard contact
Tangential coefficients	0.450

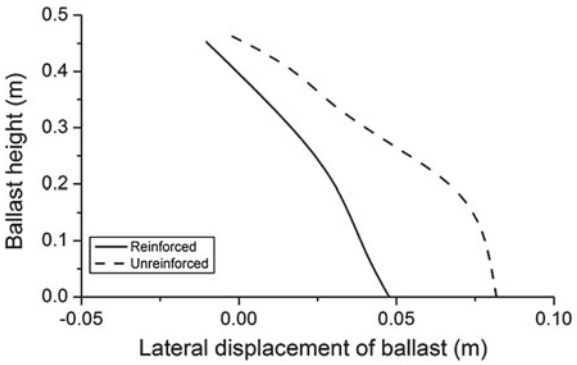

Fig. 16 Horizontal movements of ballast. *Data source* Indraratna et al. (2017b)

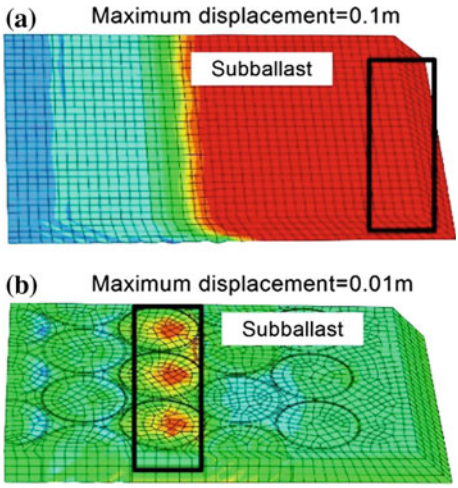

Fig. 17 Maximum lateral displacement in the subballast layer: **a** without rubber tyres and **b** with rubber tyres (after Indraratna et al. 2017b)

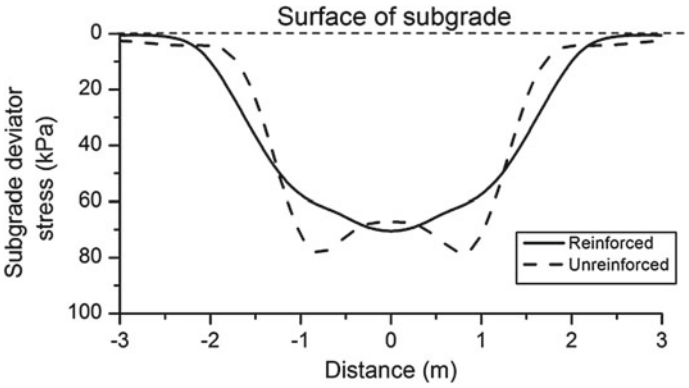

Fig. 18 Stress distributions on subgrade (after Indraratna et al. 2017b)

a stiffer layer that enables more uniform stress distribution to be transferred to the underlying subgrade layer. Figure 18 also suggests that the induced subgrade stresses can be distributed over a wider area when the tyre reinforcement is included.

5 Use of Geogrids and Shock Mats

5.1 Field Study: Singleton Track

To assess the benefits of using geogrids and rubber mats in rail tracks, a field test was implemented in the town of Singleton, located at about 200 km from Sydney (Nimbalkar and Indraratna 2016; Indraratna et al. 2016).

5.2 Construction of Singleton Tracks

The track substructure was composed of a 300-mm-thick ballast layer underlain by a sub-ballast having 150–300 mm thickness. A 400–600-mm-thick structural fill was placed below the capping layer. Eight instrumented sections were constructed and monitored for a period of 5 years. The locations of the experimental sections along the track are illustrated in Fig. 19. In order to examine the effect of the subgrade type on the overall performance of geogrid reinforcement, these experimental sections were built on distinct subgrade types, namely (i) Section B—stiff bridge deck with reinforcement; (ii) Sections C and 5—intermediate siltstones; and (iii) Sections A and 1 to 4—soft alluvial with silty-clay deposits.

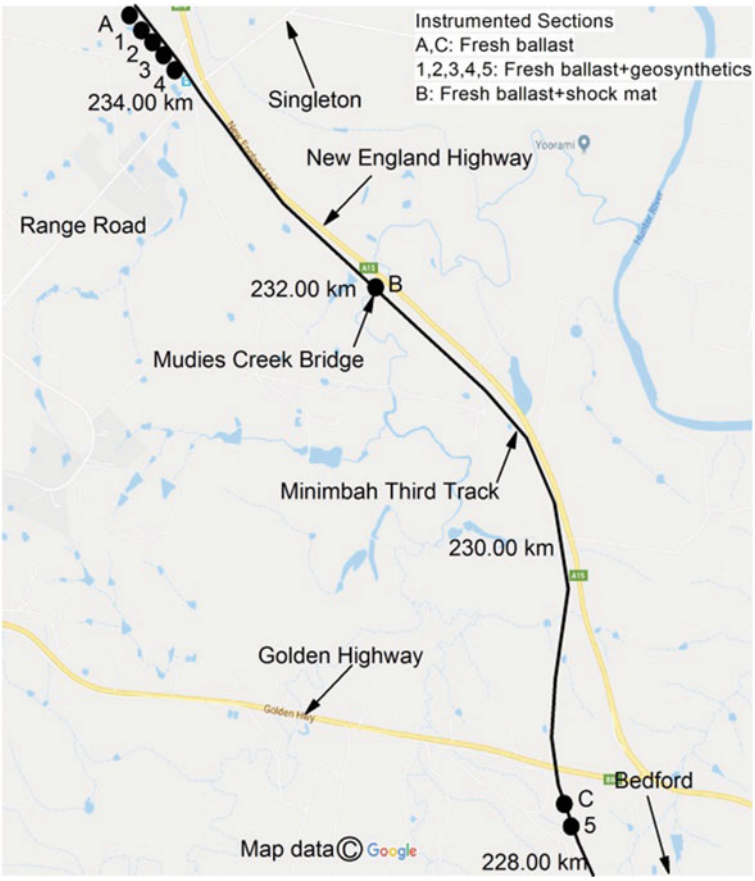

Fig. 19 Map of the Singleton tracks (after Indraratna et al. 2014a)

Three different geogrids were used for Sections 1, 3, 5. In addition, a layer of under ballast mat (UBM) was placed for Section B—ballast deck bridge. The physical and mechanical properties of the used geogrids and UBM can be found in Nimbalkar and Indraratna (2016).

5.3 Deformation of Ballast

The permanent vertical deformations of the ballast layer were estimated by subtracting the settlements at the ballast–sub-ballast from that at the top surface of ballast layer. A comparison of the vertical settlements measured at experimental sections without reinforcement and under different subgrade conditions is given in Fig. 20. It

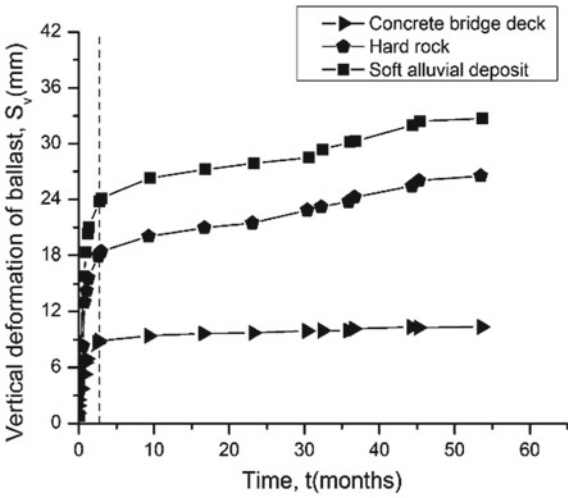

Fig. 20 Vertical deformations of ballast layer for varying subgrade types. *Data source* from Nimbalkar and Indraratna (2016)

is observed that the vertical settlement increased rapidly and was more pronounced under softer subgrade conditions; i.e., the lowest ballast deformations were obtained on the concrete bridge, whereas the largest deformations were measured at track sections involving a silty-clay foundation. The low deformation at the bridge (Muddies Creek) may result from the confinement provided to the ballast by the bridge barriers and from the use of rubber mat, which led to reduced lateral movements of ballast. However, at other places, ballast particles could move freely in the lateral directions, which in turn caused larger vertical deformations.

The permanent vertical deformations of geogrid-reinforced ballast were 5–35% smaller than those in the absence of reinforcement, as shown in Fig. 21. This behaviour was also seen by laboratory studies (Ngo et al. 2017b; Indraratna and Salim 2003; Indraratna and Nimbalkar 2013; Göbel et al. 1994; Indraratna et al. 2016) and others (Fernandes et al. 2008) and can be justified by the additional internal confinement resulting from ballast–geogrid interlocking. It was also noticed that the effectiveness of the geogrid reinforcements in reducing ballast deformations was higher under softer subgrade conditions. This finding is consistent with the test data presented by Ashmawy (1995). Moreover, the geogrid (GG-3) usually exhibited the most effectively with respect to the attenuation of ballast strains associated with its aperture ($D_{50} = 40$ mm) that promoted strong interlock among the ballast grains and geogrids, i.e. increased the interface friction (Indraratna et al. 2014b). Conversely, the aperture size of GG-2 ($1.8D_{50} = 65$ mm) was too large to enable effective interlock with the ballast commonly adopted in Australian tracks.

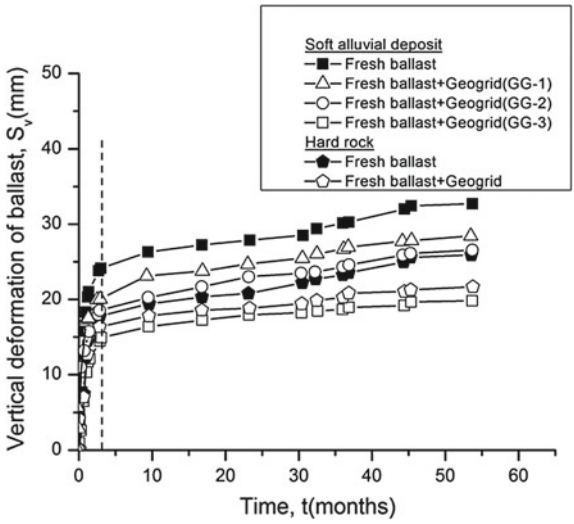

Fig. 21 Vertical deformations of ballast layer for varying reinforcement types *Data source* from Nimbalkar and Indraratna (2016)

5.4 Ballast Breakage

To analyse the extent of particle breakage upon repetitive train loading, ballast samples were collected from various places along the tracks during the intermittent periods of closure. A sampling pit (1.80 × 1.30 m) was obtained by excavating ballast particles from the load-bearing, cribs, and shoulders of the track. The ballast was obtained from three identical locations between the base of sleepers and formation levels and was recovered based on recommendations of AS 1141.3.1 (2012). The ballast profile was subsequently restored by installing fresh ballast which was compacted by tamping heads.

The particle breakage was assessed using the BBI and presented in Fig. 22. The value of BBI for ballast layers stabilised with the geogrid GG-3 was approximately 35% lower than one for non-reinforced sections, indicating geogrids could attenuate the ballast degradation. Even though the train velocities for all sections were nearly the same, the presence of under ballast mat at the concrete bridge deck resulted probably in a reduced amount of breakage (BBI < 5%). As expected, particle breakage was more significant for the hard subgrade when compared to one measured for soft subgrade.

6 Conclusions

This paper encapsulates the research works conducted on railroad geomechanics that obtained from advanced large-scale testing and field studies carried out at UOW over the past twenty years. The application of geogrids and recycled rubber mats

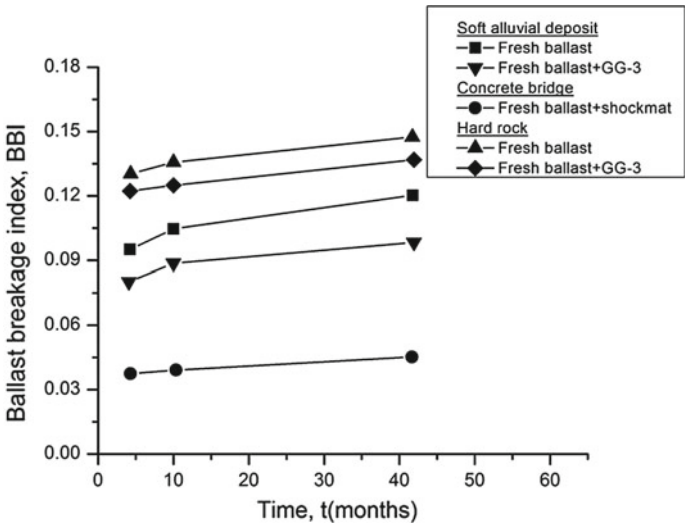

Fig. 22 Variation of BBI with time for different subgrade conditions. *Data source* from Nimbalkar and Indraratna (2016)

to enhance rail track performance has been analysed together with numerical modelling. Large-scale permeability tests were carried out under varying levels of ballast contamination to establish the relationship between the VCIs and the corresponding hydraulic conductivities. The results showed a decrease in the hydraulic conductivities associated with an increase in the VCI. A serious condition with respect to track maintenance would be reached when VCI was higher than 40% for clay-fouled ballast and 60% for coal fouling.

Large-scale direct shear test for fresh/fouled ballast, both with and without geogrid reinforcement, was implemented to evaluate the shear stress–strain responses and volumetric changes. The test data indicated that the geogrid increased shear strengths and friction angles, while only marginally reducing the vertical deformation of the geogrid-stabilised ballast specimens. When the ballast was fouled, the efficiency of the geogrids reduced in proportion to the amount of fouling. Based on these tests, the optimum opening aperture of grids to provide a maximum interface shear strength was about $1.20D_{50}$.

The use of rubber tyre cells for capping (sub-ballast) layer provides considerable lateral confinement to the infilled materials, thus contributing to a reduction in the lateral spreading of particles, hence overall dilation of subballast. In addition, the results of the study showed that a sub-ballast layer stabilised with scrap tyres could effectively eliminate the degradation and vertical movement of the overlying ballast layer.

The improved field performance of a ballasted track in Singleton using geogrids and rubber shock mats was most encouraging. The track performance was examined through a fully instrumented track section employing different types of geogrids

and rubber mats. The field results indicated that the geogrids decreased the ballast settlement by approximately 35%. This would have a considerable reduction of the maintenance costs. The reduction in vertical strains was observed to be higher under softer subgrade conditions. Ballast aggregates experienced considerable breakage due to more intensive train loadings, especially over concrete bridge decks where the placing of rubber shock absorbing mats is highly recommended. The enhanced geogrid-stabilised ballast interactions increased lateral confinements of sub-ballast by tyre cells or geocells, and the placing of rubber mats resulted in more stable tracks with enhanced longevity and stability.

Acknowledgements Research projects on ballasted rail tracks as presented in this keynote paper were supported by the Australian Research Council (ARC) and three consecutive Cooperative Research Centres (CRCs) for railways over the past two decades. The authors gratefully acknowledge the efforts of Dr. Syed K. Hussaini, Dr. Nayoma Tennakoon, Dr. Mahdi Biabani, Dr. Joanne Lackenby, and Dr. Sanjay Nimbalkar that have contributed to the contents of this paper. The support and efforts of colleague A/Prof Jayan Vinod and Dr. Ana Heitor over the past years are also appreciated.

The authors greatly appreciate the financial support from the Rail Manufacturing Cooperative Research Centre (funded jointly by participating rail organisations and the Australian Federal Government's Business Cooperative Research Centres Programme) through Project R2.5.1—*Performance of recycled rubber inclusions for improved stability of railways* and Project R2.5.2—*Application of geogrids for minimising track deformation and degradation under high frequency cyclic and heavy haul loading*. The authors wish to thank the Australasian Centre for Rail Innovation (ACRI), Tyre Stewardship Australia (TSA), Global Synthetics Pty Ltd., Naue GmbH & Co. KG, Foundation Specialists Group, Sydney Trains (formerly RailCorp), and Australian Rail Track Corporation for the financial support. The cooperation of David Christie (formerly Senior Geotechnical Consultant, RailCorp), Tim Neville (ARTC), and Michael Martin (Aurizon/QLD Rail) during these industry linkages is gratefully acknowledged. Salient contents from these previous studies are reproduced herein with kind permission from the original sources, including ASCE, CGJ, Geotextiles and Geomembranes, Geotechnical Testing Journal, among others. The authors are also grateful to UOW technical staff, namely Alan Grant, Cameron Neilson, Duncan Best, and Ritchie McLean for their assistance during laboratory and field studies.

References

AS 2758.7 (1996) Aggregates and rock for engineering purposes—Part 7: Railway Ballast, Standard Australia, Sydney, NSW, Australia

AS 1141.3.1 (2012) Methods for sampling and testing aggregates—Method 3.1: sampling-aggregates, Sydney, NSW, Australia

Ashmawy B (1995) Geosynthetic-reinforced soils under repeated loading: a review and comparative design study. Geosynthetics Int 2(4):643–678

Bathurst RJ, Raymond GP (1987) Geogrid reinforcement of ballasted track. Transp Res Rec 1153:8–14

Biabani MM, Indraratna B, Ngo NT (2016a) Modelling of geocell-reinforced subballast subjected to cyclic loading. Geotext Geomembr 44(4):489–503

Biabani MM, Ngo NT, Indraratna B (2016b) Performance evaluation of railway subballast stabilised with geocell based on pull-out testing. Geotext Geomembr 44(4):579–591

Brown SF, Thom NH, Kwan J (2006) Optimising the geogrid reinforcement of rail track ballast. In: Railfound conference, Birmingham

Budiono DS, McSweeney T, Dhanasekar M, Gurung N (2004) The effect of coal dust fouling on the cyclic behaviour of railtrack ballast. In: Cyclic behaviour of soils and liquefaction phenomena. Taylor & Francis Group, London

Feldman F, Nissen D (2002) Alternative testing method for the measurement of ballast fouling. In: Conference on Railway Engineering, Wollongong, RTSA

Fernandes G, Palmeira M, Gomes RC (2008) Performance of geosynthetic-reinforced alternative subballast material in a railway track. Geosynthetics Int 15(5):311–321

Göbel W, Kirschner RA (1994) Effectiveness of a reinforced geogrid in a railway subbase under dynamic loads. Geotext Geomembr 13(2):91–99

Indraratna B, Salim W (2003) Deformation and degradation mechanics of recycled ballast stabilised with geosynthetics. Soils Found 43(4):35–46

Indraratna B, Lackenby J, Christie D (2005) Effect of confining pressure on the degradation of ballast under cyclic loading. Géotechnique 55(4):325–328

Indraratna B, Hussaini SKK, Vinod JS (2012) On the shear behaviour of ballast-geosynthetic interfaces. Geotech Test J 35(2):1–8

Indraratna B, Salim W, Rujikiatkamjorn C (2011a) Advanced rail geotechnology—ballasted track. CRC Press, Taylor & Francis Group, London, UK

Indraratna B, Ngo NT, Rujikiatkamjorn C (2011b) Behavior of geogrid-reinforced ballast under various levels of fouling. Geotext Geomembr 29(3):313–322

Indraratna B, Ngo NT, Rujikiatkamjorn C (2013) Deformation of coal fouled ballast stabilized with geogrid under cyclic load. J Geotech Geoenviron Eng 139(8):1275–1289

Indraratna B, Nimbalkar S, Christie D, Rujikiatkamjorn C, Vinod JS (2010) Field assessment of the performance of a ballasted rail track with and without geosynthetics. J Geotech Geoenviron Eng ASCE 136(7):907–917

Indraratna B, Nimbalkar S (2013) Stress-strain degradation response of railway ballast stabilized with geosynthetics. J Geotech Geoenviron Eng 139(5):684–700

Indraratna B, Nimbalkar S, Neville T (2014a) Performance assessment of reinforced ballasted rail track. In: Proceedings of the ICE—ground improvement, vol 167, pp 24–34

Indraratna B, Ngo NT, Rujikiatkamjorn C, Vinod J (2014b) Behaviour of fresh and fouled railway ballast subjected to direct shear testing—a discrete element simulation. Int J Geomech ASCE 14(1):34–44

Indraratna B, Sun Q, Ngo NT, Rujikiatkamjorn C (2017a) Current research into ballasted rail tracks: model tests and their practical implications. Aust J Struct Eng, 1–17

Indraratna B, Nimbalkar S, Ngo NT, Neville T (2016) Performance improvement of rail track substructure using artificial inclusions—experimental and numerical studies. Transp Geotech 8:69–85

Indraratna B, Sun Q, Grant J (2017b) Behaviour of subballast reinforced with used tyre and potential application in rail tracks. Transp Geotech 12:26–36

Indraratna B, Ngo NT, Rujikiatkamjorn C (2017c) Improved performance of ballasted rail tracks using plastics and rubber inclusions. Procedia Eng 189:207–214

Indraratna B, Sun Q, Heitor A, Grant J (2018) Performance of a rubber tyre-confined capping layer under cyclic loading for railroad conditions. J Mater Civ Eng ASCE 30(3):06017021

Lackenby J, Indraratna B, McDowell GR, Christie D (2007) Effect of confining pressure on ballast degradation and deformation under cyclic triaxial loading. Géotechnique 57(6):527–536

LePen L (2008) Track behaviour: the importance of the sleeper to ballast interface. Ph.D. Thesis, University of Southamton, UK

Li D, Selig ET (1998) Method for railroad track foundation design. I: Development. J Geotech Geoenviron Eng 124(4):316–322

McDowell GR, Harireche O, Konietzky H, Brown SF, Thom NH (2006) Discrete element modelling of geogrid-reinforced aggregates. In: Proceedings of the ICE—Geotechnical Engineering, vol 159, Issue 1, pp 35–48

Ngo NT, Indraratna B, Rujikiatkamjorn C (2014) DEM simulation of the behaviour of geogrid stabilised ballast fouled with coal. Comput Geotech 55:224–231

Ngo T, Indraratna, Rujikiatkamjorn C (2016a) Modelling geogrid-reinforced railway ballast using the discrete element method. Transp Geotech 8:86–102
Ngo NT, Indraratna B, Rujikiatkamjorn C (2017a) A study of the geogrid–subballast interface via experimental evaluation and discrete element modelling. Granular Matter 19(3):54–70
Ngo NT, Indraratna B, Rujikiatkamjorn C (2017b) Stabilisation of track substructure with geo-inclusions—experimental evidence and DEM simulation. Int J Rail Transp 5(2):63–86
Ngo NT, Indraratna B, Rujikiatkamjorn C, Biabani MM (2016b) Experimental and discrete element modeling of geocell-stabilised subballast subjected to cyclic loading. J Geotech Geoenviron Eng 142(4):04015100
Nimbalkar S, Indraratna B (2016) Improved performance of ballasted rail track using geosynthetics and rubber shockmat. J Geotech Geoenviron Eng 142(8):04016031
Powrie W, Yang LA, Clayton CRI (2007) Stress changes in the ground below ballasted railway track during train passage. In: Proceedings of the Institution of Mechanical Engineers, Part F: Journal of Rail and Rapid Transit, pp 247–261
Rujikiatkamjorn C, Indraratna B, Ngo NT, Coop M (2012) A laboratory study of railway ballast behaviour under various fouling degree. In: The 5th Asian regional conference on geosynthetics, pp 507–514
Rujikiatkamjorn C, Ngo NT, Indraratna B, Vinod JS, Coop M (2013) Simulation of fresh and fouled ballast behaviour using discrete element method. In: International Conference on Ground Improvement & Ground Control (ICGI 2012), pp 1585–1591
Selig ET, Waters JM (1994) Track geotechnology and substructure management. Thomas Telford, London
Sun Q, Indraratna B, Nimbalkar S (2016) Deformation and degradation mechanisms of railway ballast under high frequency cyclic loading. J Geotech Geoenviron Eng 142(1):04015056
Sun Q, Indraratna N (2014) Effect of cyclic loading frequency on the permanent deformation and degradation of railway ballast. Géotechnique 64(9):746–751
Tennakoon N, Indraratna B, Rujikiatkamjorn C, Nimbalkar S, Neville T (2012) The role of ballast-fouling characteristics on the drainage capacity of rail substructure. Geotech Test J 35(4):1–11
Trani LD, Indraratna B (2010) Assessment of subballast filtration under cyclic loading. J Geotech Geoenviron Eng 136(11):1519–1528
Tutumluer, Dombrow (2008) Laboratory characterization of coal dust fouled ballast behaviour. In: AREMA 2008 annual conference & exposition. Salt Lake City, UT, USA
Tutumluer E, Huang H, Bian X (2012) Geogrid-aggregate interlock mechanism investigated through aggregate imaging-based discrete element modeling approach. Int J Geomech 12(4):391–398

Damage of Heavy Rain on Local Transportation Line

Ikuo Towhata

Abstract The slope instability in mountain terrain induces many kinds of disasters. One of the problems to the human community is that transportation line is a linear infrastructure and is easily stopped by slope disaster at a single point along the route. This situation is particularly serious after big earthquakes or heavy rains when emergency activity is important. This paper addresses slope monitoring and an early warning that facilitate emergency traffic control. It can capture the minor slope movement and allow an early warning to be issued. Further, a recent development of very inexpensive sensor is introduced and a future scope toward the multi-sensor monitoring is described.

Keywords Rainfall · Landslide · Monitoring · Safety of transportation line

1 Introduction

This paper addresses the resilience of transportation routes that undergoes the risk of natural disasters. Transportation route is a typical linear infrastructure in which damage at one point affects the operation of the entire route. Because the route is located often upon many vulnerable geomorphologies such as unstable sloping ground and soft alluvium, the risk of a natural disaster deserves engineering attention.

The 2011 Tohoku earthquake in Japan showed the importance of resilience of transportation routes during the post-earthquake emergency. Sendai City with more than one million populations was located in the center of the affected area, and all the transportation routes connected to the city lost operation. Railway tracks stopped operation due to heavy distortion failure of the embankment, express motorways stopped due to the embankment distortion as well, the Sendai Airport was destroyed by tsunami, and harbors were affected by tsunami. Consequently, cargo transportation stopped for days and fuel shortage, in particular, was very serious in Sendai area.

I. Towhata (✉)
Department of Civil Engineering, Kanto Gakuin University,
Mutsu-ura-Higashi, Kanazawa-Ku, Yokohama 236-8501, Japan
e-mail: towhata.ikuo.ikuo@gmail.com

R. Sundaram et al. (eds.), *Geotechnics for Transportation Infrastructure*, Lecture Notes in Civil Engineering 28, https://doi.org/10.1007/978-981-13-6701-4_15

Heavy rain is another important natural disaster that threats transportation routes. Many roads in mountainous regions are prone to the instability of both natural and artificial slopes, and the local communities in mountainous terrain are insulated from the outer world if transportation stops during heavy rain. Noteworthy is that the risk of heavy rain may be increasing due to the global climate change, although verification of this idea needs more scientific investigation.

With these in mind, the present paper addresses the risk of natural disasters on the resilience and serviceability of transportation routes as well as their possible mitigations. The related problems are so vast, and the content of this paper is limited due to the ability of the author.

2 Findings During Recent Natural Disasters

The 2004 Chuetsu earthquake in Japan registered the magnitude of Mw = 6.6 (Fig. 1). Because this earthquake hit a mountainous region that was composed of soft rock, many slopes failed. Figure 2 shows a slope failure that closed the entrance of a road tunnel. Figure 3 indicates the distortion of the same tunnel that was probably caused by the deformation and dynamic earth pressure in the surrounding soft rock mass. Noteworthy is that many road embankments were destroyed by this earthquake and land transportation stopped operation (Fig. 4). Consequently, the road network in this region stopped operation and the emergency rescue for the local people became impossible. The public sector decided to let people be evacuated to the outer world, sometimes by helicopters.

The northern part of Kyushu Island of Japan experienced a heavy rainfall in early July 2017. The total precipitation reached at maximum 660 mm during the entire

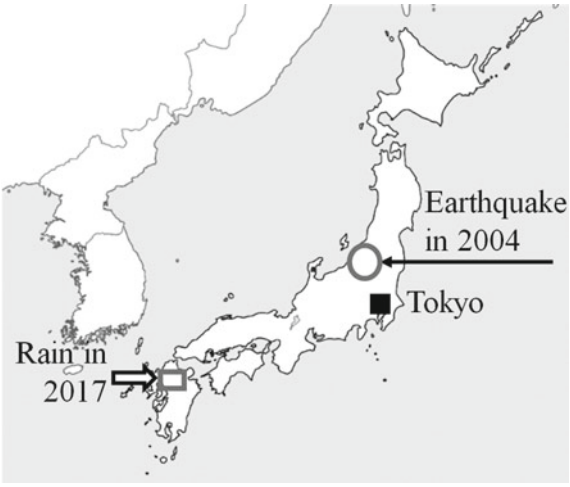

Fig. 1 Location of areas affected by 2004 Chuetsu earthquake and 2017 heavy rain

Fig. 2 Slope failure that closed the portal of Haguro Tunnel during the Chuetsu earthquake in 2004

Fig. 3 Distortion of Haguro Tunnel during the earthquake

Fig. 4 Collapse of road embankment that was made of local mudstone prone to hydration and deterioration

Fig. 5 Site of a natural dam in Ono of Hita City (this picture was taken on November 14, 2017)

rainfall period (Meteorological Agency of Japan 2017). Consequently, many slope failures occurred in the affected region. Some of the landslides stopped river flow, and natural dams were formed. Figure 5 shows one of the sites of the natural dams.

Slope failures and debris flows affected the local railway network. Figure 6 illustrates the Chikuzen-Iwaya Station of Hita-Hikosan Line. According to Yamamoto et al. (2017), the one-day precipitation on the day of disaster (July 5) was 500–600 mm. Consequently, a debris flow occurred near the station and the railway operation stopped. The significant problem therein is that the business of this part of the railway had been very low for many years (insufficient number of passengers) and the reconstruction of the railway is not preferable to the railway company.

The underlying situation is that the railway company is responsible for both maintenance of railway infrastructure, inclusive of the protection from natural disasters, and safe operation of trains. In contrast, the competitor, which is road traffic, does not have to take care of the road maintenance. Therefore, the railway business in regions of low traffic demand (less population) is critical and the railway company wishes to convert the railway service to bus service. In such a situation, damage by a natural disaster is a good reason for stopping railway service and conversion. However, the local communities do not like this idea. Because many rainfall disasters are occurring in the recent decade, the same situation will occur at many places. Therefore, it is now essential to seriously discuss the future direction, whether or not the railway shall be maintained with more public supports. Without reasonable support, many railway lines will disappear. If the public provides support, the most likely way is that the railway track is owned and maintained by local municipalities and the railway companies take care only of train operation. Since the public sector in the rural area is not wealthy, the railway maintenance and, particularly, prevention of a natural disaster have to be made inexpensive.

(a) Platform of the station

(b) Deposit of debris flow in the very vicinity of the station

Fig. 6 Site of debris flow that affected the Chikuzen-Iwaya Railway Station of Hita-Hikosan Line

3 On Rainfall Criterion for an Early Warning of Slope Failure

Safe operation of traffics during rainy seasons needs many expensive structures such as slope stabilizations and flood channels. To avoid such costly measures, the present paper introduces an early warning of slope instability which aims to stop traffics before disaster.

An early warning combined with resuming of emergency action in advance is an efficient way to mitigate rainfall-induced disasters. The point of discussion is the logic by which warning is issued. A common practice nowadays is called rainfall criterion for which local rainfall is monitored, and if the observed data reach a critical level, warning is issued. Because rainfall monitoring is widely practiced in many countries and data are easily available, rainfall criterion is popular.

Obviously, rainfall plays the most important role in triggering of slope failure because infiltration of rainwater into a slope increases the moisture content and weight of subsoil and reduces the effective stress, thus making the slope unstable. Practice employs the total precipitation data since the beginning of one rainfall event (in other words, rainfall intensity and its duration time) as well as current rainfall intensity (during the recent one hour or 10 min, for example); refer to Baum and Godt (2010), Lazzari et al. (2013), Moriwaki et al. (2004), Nakai et al. (2007), Osanai et al. (2010) and Terlien (1998) among many others. Furthermore, the Japanese Railway Central Company (2014) employs a rainfall-based criterion for decision making whether or not the high-speed train service is stopped. However, there is not yet a criterion to resume train operation after heavy rain; empiricism based on human observation is still important.

The rainfall-based approach has been adopted by many public sectors, and an early warning has been issued on a regional basis. The limitation of the rainfall criterion is the lack of geological, topographical and geotechnical consideration. Therefore, it is not possible to judge whether or not a particular slope is unstable during heavy rain. Monitoring of moisture content may foresee the incipient slope failure because increased moisture content reduces the shear strength of soil. For this purpose, however, the moisture content within the slip surface has to be monitored. This is not very easy without conducting field investigation at many places of numerous mountain slopes and knowing the strength properties of the subsoil.

4 On Displacement Criterion for an Early Warning of Slope Failure

It has been traditionally known that slope failure is preceded by surface cracks which is induced by minor slope deformation. In this regard, an alternative methodology of slope monitoring aiming at an early warning is to monitor the displacement/deformation of slopes. The advantage is that the instability of any particular slope could be predicted in contrast to a regional warning as was the case of rainfall criterion. The early example of this approach is found in Saito (1965, 1969, 1987), Saito and Uezawa (1961) and Saito and Yamada (1973) who introduced creep model for prediction of the failure time of an unstable slope. They supposed that monitoring minor slope displacement (precursor) is able to predict the incipient slope failure within a short time. This idea is correct, and scheduled inspection is widely carried out along roads and railway lines in mountainous regions in order to detect any abnormal deformation of slopes, retaining walls and road pavements. Note that the target of their study was a landslide that is induced by gravity and takes weeks or months or longer until failure. Rainfall-induced slope failure was not their target. The required instrument for slope monitoring is typically an extensometer that can monitor the change of distance between stable and moving soil masses. The installation of instrument needs knowledge on which part of slope is moving. Such information

is hardly available in case of rainfall-induced landslide, because it occurs suddenly during rain in a slope that has been stable for years.

Efforts have been made to mitigate landslide disasters of transportation lines in mountainous regions by inspecting possible displacement and deformation of slopes, pavements, nearby retaining walls, etc., and, in case that any abnormal situation is detected, traffics are stopped and emergency actions are resumed. The idea underlying this common practice is that slope failure is preceded by minor displacement and deformation which is called precursor in this paper. Ochiai et al. (2004) induced slope failure by artificial rainfall. They monitored the development of slope deformation during rain and demonstrated that minor deformation had started more than one hour before the final failure. This finding supports the idea of displacement criterion for slope monitoring by which the warning of slope failure is issued. Note that the displacement criterion is useful even during the post-rainfall stage when a decision has to be made on resuming traffic operation again.

5 Slope Monitoring by Tilting Angle Sensor

The author and his colleagues (Uchimura et al. 2015; Towhata et al. 2015) have been developing an early warning technology by which the precursing minor slope displacement is detected and interpreted. The basic principles therein are summarized as what follows:

1. The target of the monitoring is a shallow failure in which the soft surface layer becomes unstable during heavy rain.
2. The typical thickness of the surface unstable layer is 1–1.5 m.
3. Upon installation of monitoring sensors, it is difficult to know which part of a slope will fall down during the next heavy rain.
4. Therefore, as many sensors as possible should be installed over the entire suspected slope.
5. To install many sensors within a given financial limitation, less expensive and appropriately accurate sensors are more useful than very accurate but expensive sensors.
6. For successful early warning, the displacement of 1 cm or less has to be captured.
7. The monitored data should be transmitted through wireless communication to the data interpreter for quick emergency action, if necessary.

The recent development of **m**icro**e**lectro**m**echanical **s**ystems (MEMS) technology provides a very accurate tilting angle sensor (sensitivity being less than 0.01 deg.) at low cost (typically US 20 $/piece or less). When monitored slope displaces 1 cm or less well prior to failure, the MEMS sensor can capture the small tilting angle of the field equipment much easier than directly measuring the slope displacement. The low price of MEMS is very important because the GPS displacement monitoring, which is a competitor, with the accuracy of 1 cm or less is approximately one hundred times more expensive than the MEMS monitoring of tilting.

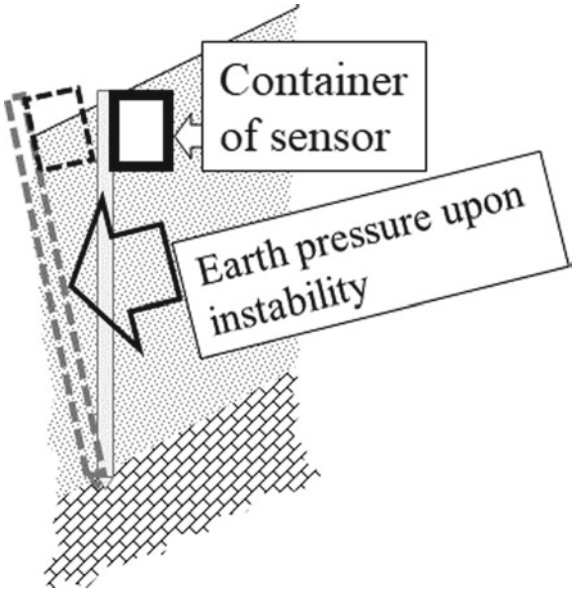

Fig. 7 Working principle of the MEMS tilting sensor

Figure 7 illustrates the working principle of the MEMS tilting sensor. First, a vertical steel rod is manually driven into slope until it hits a hard base layer. Second, a unit of tilting sensor and batteries (with a moisture sensor, if desired) is attached to the top and is connected to a wireless communication kit. When the surface layer becomes unstable and translates slightly, the lateral earth pressure on the rod increases and the rod rotates around the bottom that is fixed in the stable base. This rotation angle is monitored by a MEMS tiltometer.

The maximum distance of the wireless communication is hundreds of meters. Several units of this kind are installed in a suspected slope together with one main station (Fig. 8) through which all the data are transmitted into LAN network. For cost reduction, the following efforts have been made.

Tilting sensors are operated by four dry cell batteries that are substantially cheaper than solar batteries.

1. The monitoring is switched on once every 10 min in order to save the battery energy; four batteries can work for one year according to the experience.
2. Monitoring of moisture content is not necessary in order to save energy. Moisture content data are useful if only the location of the slip plane is known in advance during installation of sensor. This is hardly the case in reality because the determination of a slip plane requires expensive field investigation on shear strength parameters of subsoil.

The developed tiltometer has been installed for slope monitoring at more than 80 sites in Japan as well as in such countries as China, Taiwan, India and Australia.

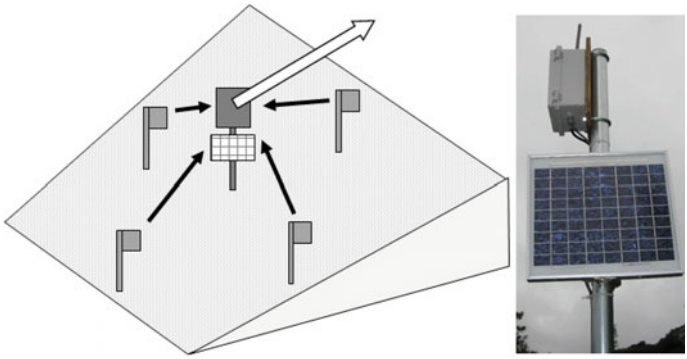

Fig. 8 Main station for data transmission (operated by a solar battery)

Fig. 9 Monitored slope in the Three Gorges Dam area in China

6 Validation of Employed Criterion

An early warning is issued based on the monitored tilting angle if the rate of tilting exceeds 0.1 degree/hour. This criterion was decided by experience. Figure 9 shows the Three Gorges Reservoir site in China. During the first filling of the reservoir, minor slope failure happened at many places and one of them was chosen for the validation of the monitoring (Fig. 9). As anticipated, the selected slope fell down on June 7 to 8, 2009, and time history of tilting angle was recorded. As Fig. 10 illustrates, the rate of the recorded tilting angle was 0.11 deg/hour before the final failure, thus being greater than and validating the proposed threshold value of 0.1 deg/hour. Obviously, the significant precipitations on June 7 and 8 triggered the final failure.

Figure 11 is a two-dimensional plot of the monitored tilting angles. On June 8, the equipment tilted toward the upslope direction. This suggests rotational slope movement of the slope.

Figure 12 compares the time changes of tilting angle and the moisture content. Because the moisture was measured near the surface (adjacent to the tiltometer),

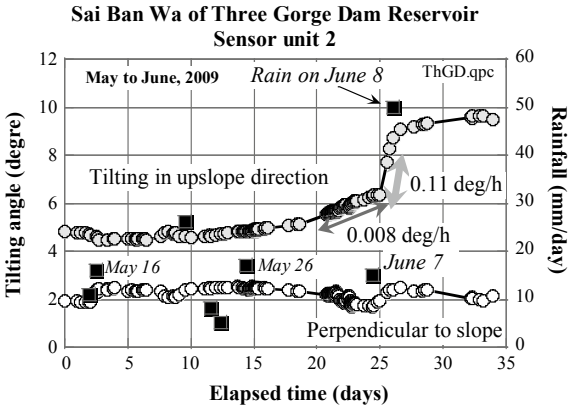

Fig. 10 Time history of tilting angle and rainfall at the Three Gorges Dam site in China

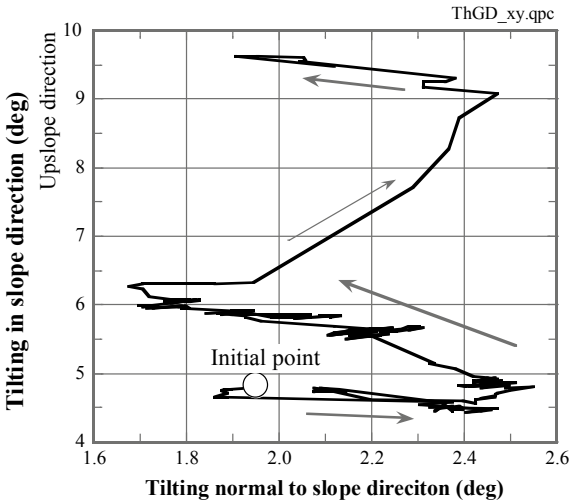

Fig. 11 Two-dimensional plot of tilting angle at the Three Gorges Dam site in China

information exactly in the slip plane is unknown. There is, however, some correlation between the increase of the moisture content and the progress of tilting.

An artificial rainfall test was carried out in Sichuan Province of China (Uchimura et al. 2015) in order to investigate the rainfall-induced slope failure under controlled environment (Fig. 13). One part of a natural slope, which was originally formed by deposition of gravelly debris flow, was cut and was subject to rain (Fig. 14). Care was taken to leave the original slope on the downslope side of the site (to the left of Fig. 13) in order to stop the failed soil mass and avoid slope disaster in the village at the bottom of the slope. The time histories of recorded tilting angle are indicated in Fig. 15. It is important herein that the data of K-50 Upper achieved the rate of 0.15 deg/hour prior to failure, thus validating the proposed warning threshold value of 0.1 deg/hour. It is interesting in Fig. 16 that the displacement measured by an extensometer during this test and the displacement assessed by the newly developed tiltometer (tilting angle

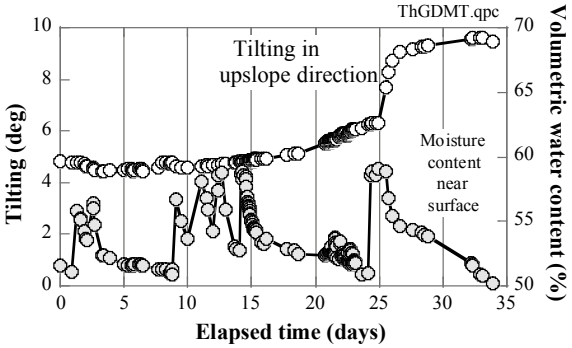

Fig. 12 Relationship between tilting angle and volumetric water content in subsoil

Fig. 13 Artificial rainfall test on slope instability

sensor) are equivalent to each other. Note that the latter displacement was assessed by (length of rod) × tan(tilting angle). This implies that tiltometer is a reasonable replacement of the traditional extensometer. For the same budget, more number of tiltometers can be installed in place of an expensive extensometer.

For practice, it is always important to compare the developed tiltometer and the conventional extensometer. Figure 17 is a site in Northern Kyushu Island of Japan where two kinds of monitoring were compared. As illustrated in Fig. 18a, all the time histories respond to the slope movement equally. However, in more detail, Figs. 18b and 19 compare the variation of these records and it is herein interesting that, upon all the events of slope movement, the tiltometer responds first and is followed by the extensometer. This suggests that the precursing movement is detected by the tiltometer earlier than the extensometer. Hence, there is more time to evacuate if a tiltometer is installed than in the case of extensometer. Moreover, there is no need to mention the significant difference in the price of these sensors.

(a) Total time history
(b) Details in narrow time range.

Fig. 14 Cut slope subject to artificially induced rainfall–slope failure

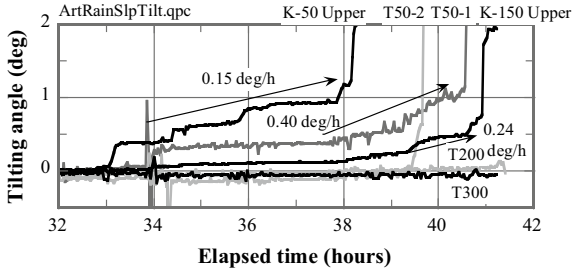

Fig. 15 Time history of tilting angle during artificial rain test

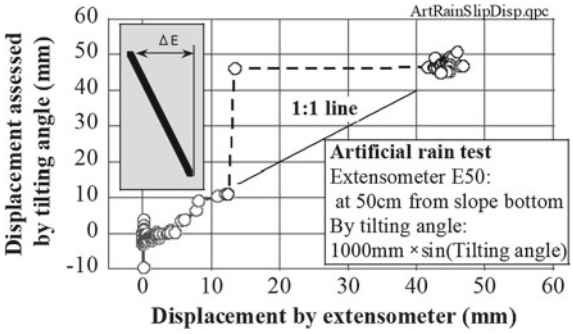

Fig. 16 Comparison of displacement data by extensometer and tiltometer

7 Safety Control During Construction Project

Slope monitoring is useful in safety control during construction project. Figure 20 is a slope that failed during heavy rain. During the restoration, it was feared that further slope failure might occur. To protect the safety of the site engineers and workers, three tiltometers were installed at the top of the failed slope. A few months later, a secondary failure occurred as expected and the monitored time history of tilting angle

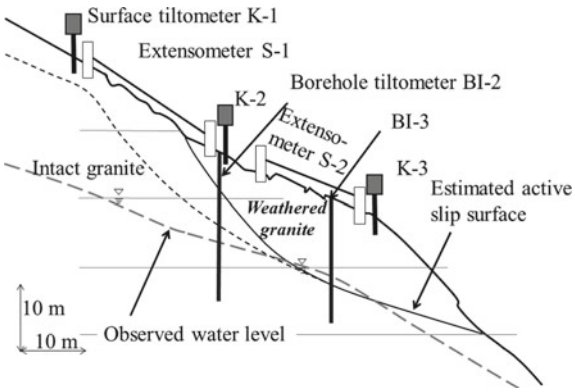

Fig. 17 Comparative study of tiltometer and extensometer

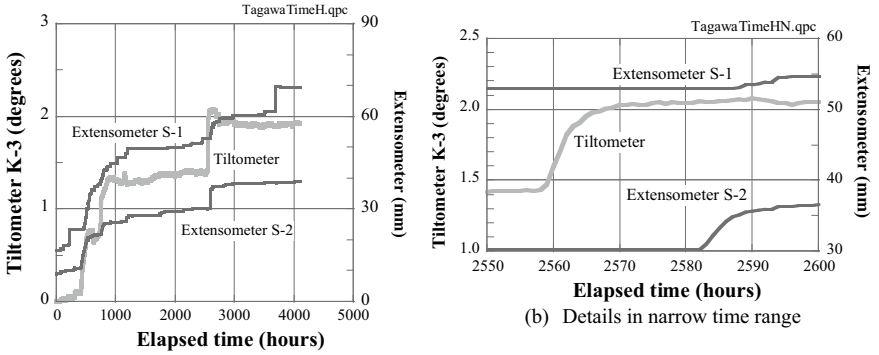

(a) Total time history

(b) Details in narrow time range

Fig. 18 Time histories of data by tiltometer and extensometers

is plotted in Fig. 21. Note again that the rate of tilting exceeded 0.1 degree/hour one hour before failure. It is thus recommendable to continuously monitor the behavior of a slope during construction and control the safe environment of people on site.

Figure 22 is a two-dimensional plot of tilting angles. In this case, tilting perpendicular to the slope gradient was predominant. This suggests that the slope soil mass was disrupted during the final failure.

Another example of safety control deserves attention. During construction of an expressway by cut-and-fill of a slope, a crack was detected at the top of the slope. A tiltometer was installed there, and slope stabilization was resumed by placing a counterweight fill at the slope bottom (Fig. 23). This mitigation was successful, and the slope movement ceased. Note that the entire stabilization procedure was carried out while monitoring the slope movement until completion of the project. Figure 24 illustrates that the rate of tilting was kept very low. Note here that the rate of tilting was as low as of the order of 0.001 deg/hour.

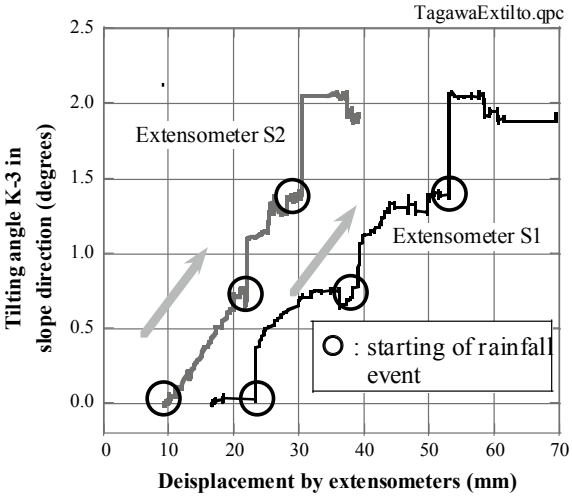

Fig. 19 Comparison of time change of data from extensometer and tiltometer

Fig. 20 Failed slope along a national highway (failure in 2009)

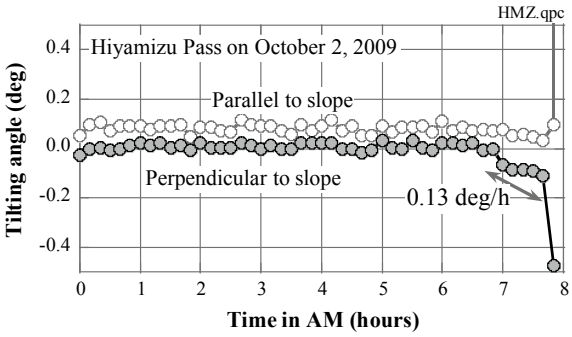

Fig. 21 Time history of tilting angle of a slope in a restoration site

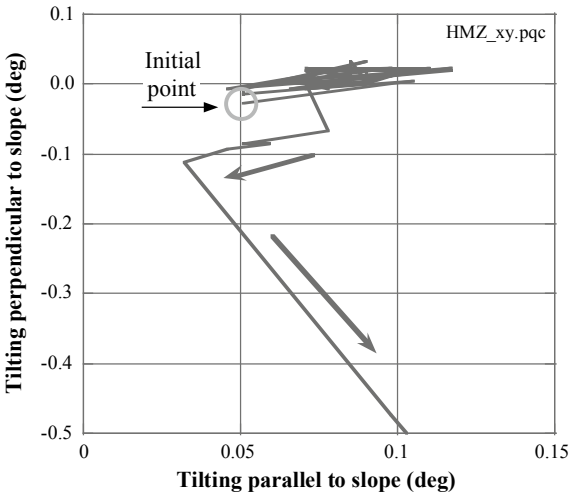

Fig. 22 Two-dimensional history of tilting angle

Fig. 23 Stabilization of an express motorway construction by counterweight

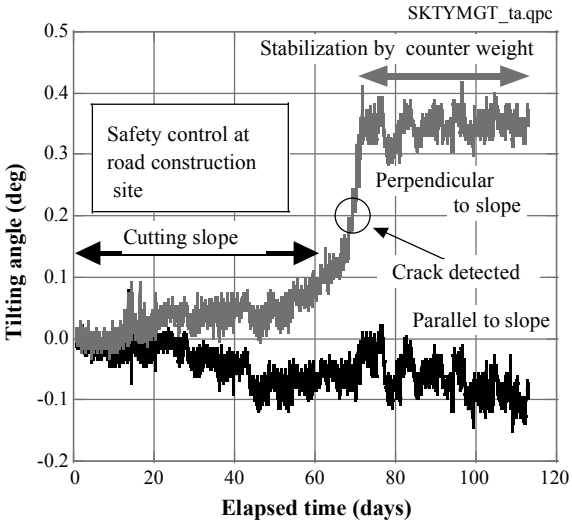

Fig. 24 Time history of tilting angle during installation of counterweight and slope stabilization

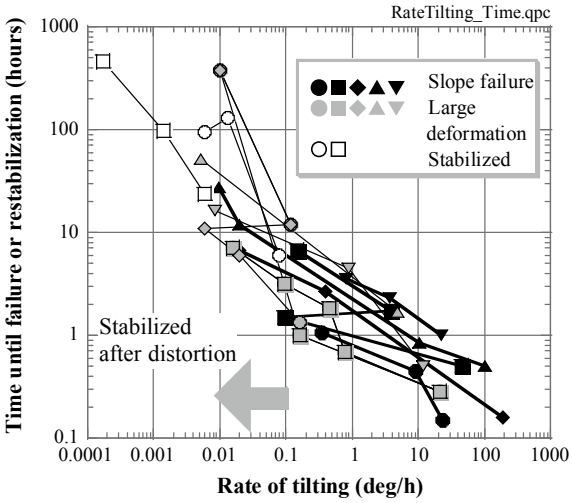

Fig. 25 Empirical relationship between rate of tilting and time until failure/stabilization of monitored slopes

Finally, Fig. 25 illustrates the relationship between the observed rate of tilting angle and the time until final failure, large deformation or stabilization. These data were obtained by either field monitoring or model tests. It is interesting that data from failed cases and stabilized cases suggest together a consistent trend. From this figure, it is reasonably stated that more than one hour or possibly 3 h is available until slope failure if evacuation order is issued when the rate of tilting exceeds 0.1-deg/h. Note that this empirical rule was obtained from many different kinds of geology, slope size and rate of rainfall. So, it is robust.

8 Development Toward High-Density Multi-sensor Monitoring

Recently, efforts have been made to develop less expensive sensors of tilting angle and deploy more sensors in a suspected slope. This idea is in line with the reality in which local geology under a slope is not uniform and the displacement/deformation is different from place to place. Because of the reduced cost, the new inexpensive sensor has even shorter distance of wireless data transmission. Hence, the general hierarchy of sensors on site is as illustrated in Fig. 26. The recent decrease in price of sensors and batteries helps develop the multi-sensor strategy in recent times.

The development of very inexpensive sensors opened a horizon toward multi-sensor monitoring of a slope in which slope angle, geology/soil conditions and displacement are heterogeneous. Figure 27 shows a site of a multi-sensor project that was supported by the SIP Project of the government. One typical result of multi-

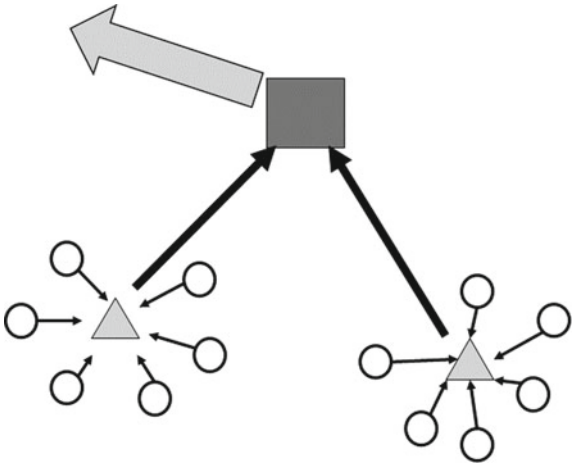

Fig. 26 Structure of sensor hierarchy and flow of monitored data

Fig. 27 Site of multi-point slope monitoring along a national highway

sensor monitoring is presented in Fig. 28. Because the entire slope is monitored, the risk of missing slope instability is reduced.

9 Conclusion

This paper is concerned first with the vulnerability of traffic lines in mountainous regions where the vulnerability of heavy rain is high and slope disaster is likely. The recent financial difficulty for maintaining traffic routes in vulnerable regions makes the reconstruction of damaged routes very difficult. Under this situation, the local municipality is expected to be involved in the maintenance of the routes in spite of its own financial limitation. In this regard, safe operation of traffics during a natural disaster is a very difficult problem. In relation to this viewpoint, the second half of

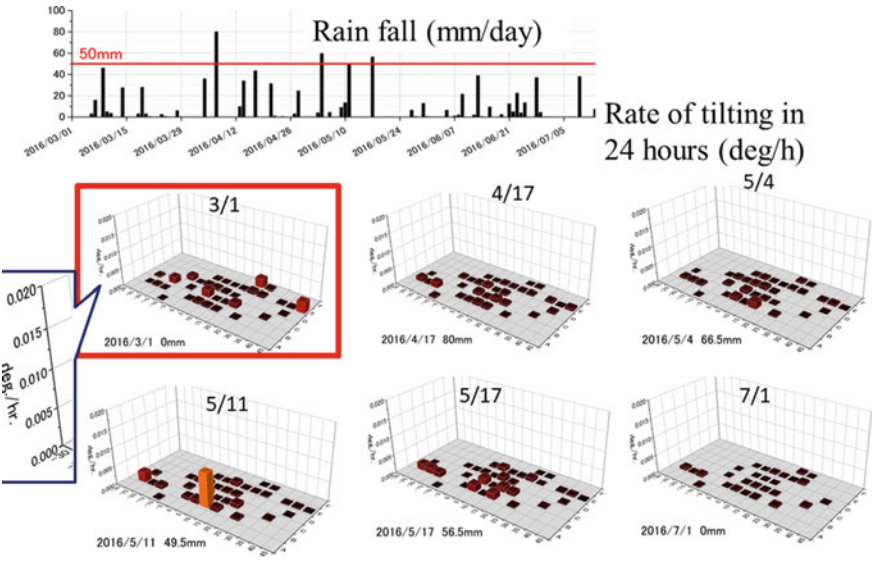

Fig. 28 Example of multi-sensor monitoring (distribution of rate of tilting) (SIP in 2016)

the paper introduced the use of inexpensive slope monitoring for issuing an early warning. Several achievements to date and new development of inexpensive sensors were described, and a future direction toward multi-sensor monitoring was presented.

Acknowledgements Many on-site projects have been conducted as a collaboration work between the Chuo Kaihatsu Corporation in Tokyo and the Institute of Mountain Hazards and Environment in Chengdu, China. The multi-sensor monitoring was carried out with a financial support by the Cross-ministerial Strategic Innovation Promotion Program supported by the Japanese Government. Dr. Taro Uchimura of Saitama University made significant contributions to the development of equipments. These supports and collaborations are deeply appreciated.

References

Baum RL, Godt W (2010) Early warning of rainfall-induced shallow landslides and debris flows in the USA. Landslides 7(3):259–272

Lazzari M, Piccarreta M, Capolongo D (2013) Landslide triggering and local rainfall thresholds in Bradanic Foredeep, Basilicata region (southern Italy). Early warning, instrumentation and modeling. In: Margottini et al. (eds) Landslide science and practice, Proceedings of the Second World Landslide Forum, Springer Series, Rome, vol 2, pp 671–678

Meteorological Agency of Japan (2017) On storm and heavy rain during June 30 to July 10, 2017, Quick information (in Japanese)

Moriwaki H, Inokuchi T, Hattanji T, Sassa K, Ochiai H, Wang G (2004) Failure process in a full-scale landslide experiment using a rainfall simulator. Landslides 1(4):277–288

Nakai S, Kaibori M, Sasaki Y, Moriwaki T (2007) Applicability of a new rainfall index R' for recent cases and proposal of the method for warning against sediment-related disaster. J Jpn Soc Erosion Control Eng 60(1):37–42 (in Japanese)

Ochiai H, Okada Y, Furuya G, Okura Y, Matsui T, Sammori T, Terajima T, Sassa K (2004) A fluidized landslide on a natural slope by artificial rainfall. Landslides 3(1):211–219

Osanai N, Shimizu T, Kuramoto K, Kojima S, Noro T (2010) Japanese early-warning for debris flows and slope failure using rainfall indices with radial basis function network. Landslides 7(3):325–338

Saito M (1965) Forecasting the time of occurrence of a slope failure. In: Proceedings of the 6th ICSMGE, vol II, pp 537–541

Saito M (1969) Forecasting time of slope failure by tertiary creep. In: Proceedings of the 7th ICSMGE, Mexico City, vol 2, pp 677–683

Saito M (1987) On application of creep curves to forecast the time of slope failure—in answer to comments upon failure forecasting. J Jpn Landslide Soc 24(1):30–38

Saito M, Uezawa H (1961) Failure of soil due to creep. In: Proceedings 5th international conference soil mechanics foundation engineering, Paris, vol 1, pp 315–318

Saito M, Yamada G (1973) Forecasting and result in case of landslide at Takabayama. In: Proceedings of the 8th ICSMGE, Moscow, pp 325–327

Terlien MTJ (1998) The determination of statistical and deterministic hydrological landslide-triggering thresholds. Environ Geol 35(2–3):124–130

Towhata I, Uchimura T, Seko I, Wang L (2015) Monitoring of unstable slopes by MEMS tilting sensors and its application to early warning. In: International symposium on geohazards and geomechanics, IOP Conference Series: earth and environmental science, vol 26, Conference 1. https://doi.org/10.1088/1755-1315/26/1/012049

Uchimura T, Towhata I, Wang L, Nishie S, Yamaguchi H, Seko S, Qiao J-P (2015) Precaution and early warning of surface failure of slopes by using tilt sensors. Soils Found 55(5):1086–1099

Yamamoto H, Yamasaki T, Sakamoto K, Yamashita N (2017) Characteristics of heavy rainfall and disaster in northern part of Kyushu on July 5, 2017. Mag Jpn Soc Nat Disaster Sci 36(3):257–279 (in Japanese)

Surfactant Grout and Its Application in CIP for Metro Construction Project

Eun Chul Shin, Bong-Geun Park and Yong-Kwan Rim

Abstract Cast-in-place pile (CIP) has been temporarily or permanently used for the support of the braced cut system during the metro construction project. The function of CIP wall is the purpose of supporting the braced cut wall as well as water barrier system during the construction of underground structures. The construction of CIP wall has a problem of strength loss when it is being installed in the ground where the water table is near the ground level. In this study, a new concept of cast-in-place pile wall is presented to overcome the stress loss problem in the ground with the high water table due to the dilution of cement component and segregation of cement particles. The surfactant grout was developed and called high-performance and multi-functional agent (Hi-FA) for the use in the construction of cast-in-place pile in the high water ground condition. The first part of this paper describes about the material properties and characteristics of Hi-FA grouts as well as the results of laboratory tests for grouts material. The second part of the paper presents the evaluation on the field applicability of cast-in-place pile using surfactant grout (H-CIP) at the metro construction project.

Keywords Cast-in-place pile · Hi-FA grout · Field applicability · Sandy gravel soil

E. C. Shin (✉) · Y.-K. Rim
Department of Civil and Environ Engineering, Incheon National University, Academe Ro 119, Incheon 22012, Republic of Korea
e-mail: ecshin@inu.ac.kr

Y.-K. Rim
e-mail: yk1792@hotmail.com

B.-G. Park
Backyoung ENC, Sadang-Ro 160, Seoul 07030, Republic of Korea
e-mail: busy7080@hanmail.net

R. Sundaram et al. (eds.), *Geotechnics for Transportation Infrastructure*, Lecture Notes in Civil Engineering 28, https://doi.org/10.1007/978-981-13-6701-4_16

1 Introduction

The cast-in-place piles are used in many projects in the world. These piles are normally consisted of steel casing which is driven into the required depth with auger machine and inserted the re-bar case inside the casing. Then, the readymade concrete paste is filled in the steel casing. The steel casing could be pulled out when the soil condition is stiff enough to keep the hole without the caving problem. The advantages of cast-in-place pile are the variations of pile length and pile diameter.

The construction of cast-in-place pile (CIP) wall in the reclaimed land which consisted of granular soil with high ground water table has a facing of leakage problem through the pile wall and strength loss of grouted pile. Several researchers (JSCE 1990; Saric-Coric et al. 2003; Kim et al. 2010) have been studied to solve the leakage and leaching problems when the cast-in-place piles are installed in the high water ground condition. Kim et al. (2010) described that the reduction of long-term durability of grout is a problem for a water glass grout material. Song et al. (2017) indicated that the water leakage in the deep excavated ground with cast-in-place pile wall is a severe problem due to water flow during the grout gel time.

A large-scale land reclamation projects have been implemented in the coastal area in mostly Southeast Asian countries. The lengthy embankments are normally constructed with utilizing a relatively large size of riprap rock and crushed stones at the bottom as well as slope of embankment. The dredged fill soils are mostly consisted of silty sand (SM) and coarse-grained sand (SP) because it is dredged from the seabed by using the pump dredging ship and transported a relatively long distance through the pipeline.

When the deep excavation work like this land reclaimed area is carried out with the construction of cast-in-place pile wall, the leakage is a problem in particularly heavy rainy season due to high hydraulic gradient and high ground water flow. High-performance and multi-functional agent called Hi-FA grouts has been developed and reported the properties of Hi-FA grouts as well as various laboratory test results such as anti-washout test, self-leveling test, bleeding rate test, and uniaxial compression test. The results of field performance on newly developed cast-in-place pile wall (H-CIP) are described with field observation.

2 Engineering Characteristics of Hi-FA Grout and Various Laboratory Test

The admixtures in the high-performance and multi-functional agent (Hi-FA) are formulated by several micelle high-order structures as shown in Fig. 1 (Lee et al. 2017). The micelle structures are clustered molecules and ions which can attribute to form the anti-washout properties. Figure 1 shows the visual observation for dropping the grout mixed into the graduated cylinder which contains the water. Figure 1a shows

(a) Conventional grout

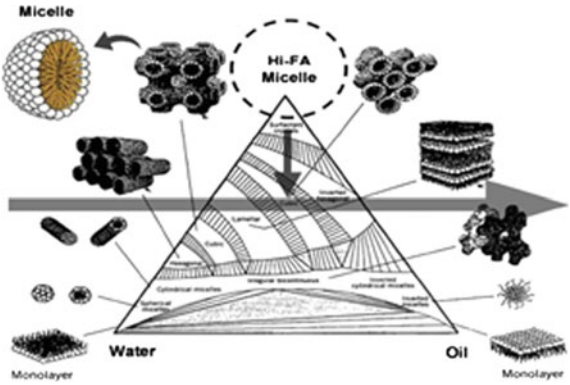

(b) Developing micelle structure

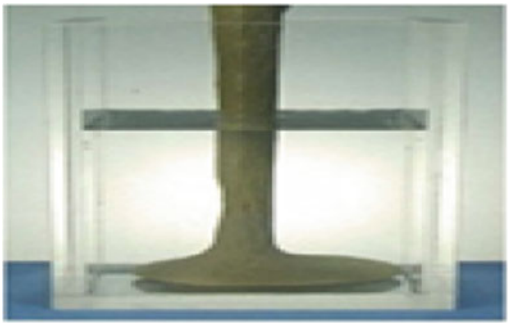

(c) Surfactant grout

Fig. 1 Visual observation of cement grout under water (Lee et al. 2017)

the crumbled grout formulation under the water for conventional cement grout due to dilution and segregation of cement particle.

However, Fig. 1c shows the uniform grout formulation under the water for anti-washout grout due to the surfactant grout mixture and forming the micelle structures as shown in Fig. 1b.

The specific gravity (G_s) of 3% Hi-FA grout with water–cement ratio of 0.5% is approximately the same as water (1.0), and the self-level capacity is about 22 cm/min in average value.

Song et al. (2017) reported the various engineering properties including anti-washout, self-leveling, bleeding, and unconfined compressive strength for the test batch Hi-FA 220. The water–cement ratios are varied as 50, 75, and 100% with the variation of Hi-FA content 0–6%. The engineering properties of surfactant grout named "Hi-FA 200M" are shown in Fig. 2.

The level of anti-washout shown in Fig. 2a gradually increases with increasing the concentration ratio of Hi-FA grout and remains constant after 4–5% concentration of Hi-FA grout. Figure 2b shows the amount of suspended solids (mg/l) which is mostly fallen below 20 mg/l after 3% concentration of Hi-FA grout.

The pH value begins from 12 at the non-Hi-FA mixed specimen, and it is getting decreased rapidly by the concentration 1–3% of Hi-FA; then, it decreases a little bit in the range of pH values 10–9 as shown in Fig. 2c.

The results of self-leveling test and bleeding test for Hi-FA 220L are shown in Fig. 3 (Song et al. 2017).

The flow values shown in Fig. 3a indicate that the higher w/c gives greater flow value. Korea Cement Institute (2010) recommends the standard value of flow is 300 mm at 30 min after mixing the cement grout.

The figure shows that the cement grout for w/c 50% gives around 300 mm, and the rest of Hi-FA grout specimens are much higher values than that of the required value by KCI. The amount of breeding is an important factor to identify the degree of solid particles' separation from the fluid. The required criterion of breeding should be less than 0.01% for the duration of 30–120 min after mixing. Figure 3b shows the amount of bleeding for grout specimen Hi-FA 220L, and it occurs very small amount of breeding. The required criterion of breeding should be less than 0.01% for the duration of 30–120 min after mixing.

3 Construction of H-CIP

The cast-in-place pile by using surfactant grout (H-CIP) can install with utilizing low-pressure grouting system. This method is especially very effective for grouting in sandy gravel soil ground.

There are several advantages to use H-CIP method such as no changing in water–cement ratio, minimum ground disturbance, no cement leaching problem, fast curing speed of grout, not much bleeding, and high mobility in sandy gravel soil.

Figure 4a shows the typical CIP wall construction work in sandy gravel soil ground. In this case, it needs an additional auxiliary insulation method to prevent the water leakage in between CIP piles. While the construction procedures of H-CIP is in Fig. 4b somewhat different from the conventional CIP construction method.

The construction sequence of Steps 1 and 2 shown in Fig. 4c is the same as conventional CIP construction method. The soil excavation is carried out by auger

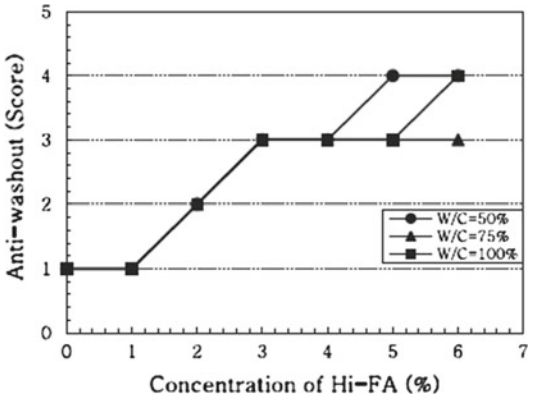

(a) Anti-washout

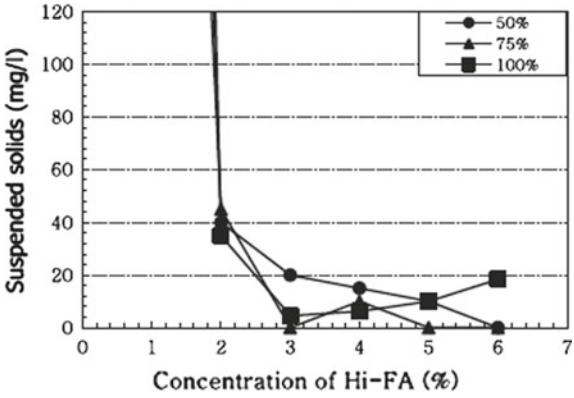

(b) Suspended Solids

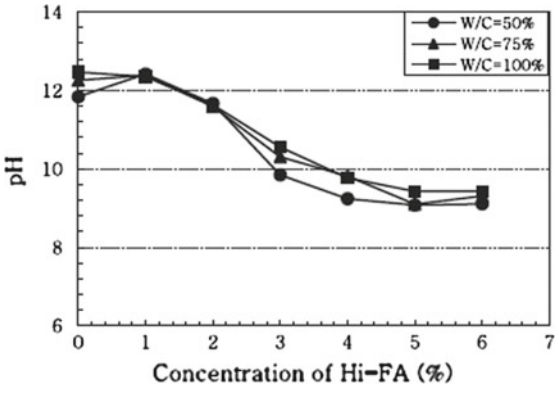

(c) pH test

Fig. 2 Results of anti-washout, suspended solids, and pH tests (Song et al. 2017)

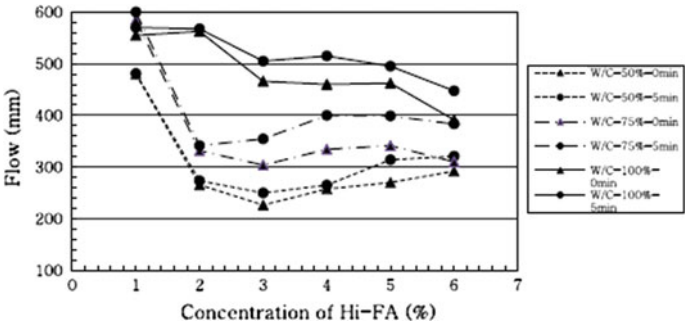

(a) Self-leveling test

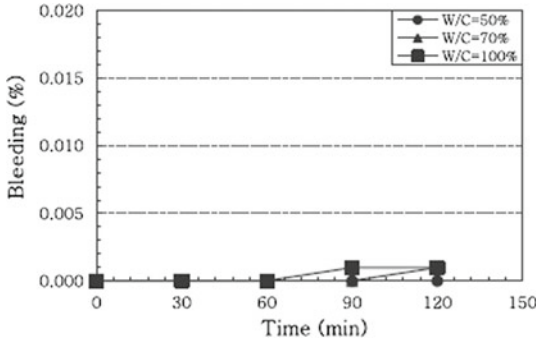

(b) Bleeding test Hi-FA grouts of 3%

Fig. 3 Results of self-leveling and bleeding tests (Korea Cement Institute 2010)

machine with the help of casing pipe and then inserted the re-bar cage inside the casing pipe.

However, the construction method in Steps 3 and 4 is different; that is, in Step 3, a grouting pipe is inserted inside the casing pipe and filled aggregate. In Step 4, high-performance and multi-functional grout is injected through the already installed grout pipe with low pressure and pulled out the steel casing as filling up the grout inside the casing.

There is no slime remaining at the bottom of H-CIP wall because the filling the grout by using an advanced installed pipe at the bottom of casing pipe. The H-CIP installed between conventional CIPS as shown in Fig. 4c gives a good sealant for leakage in between cast-in-place piles.

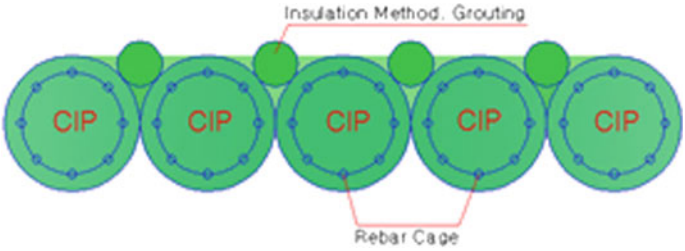

(a) CIP method

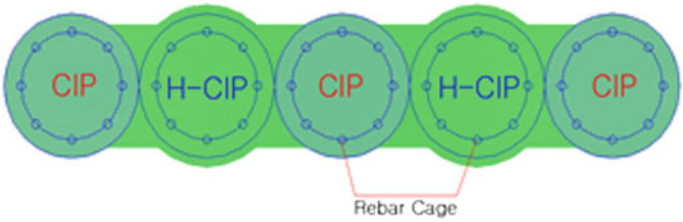

(b) H-CIP method

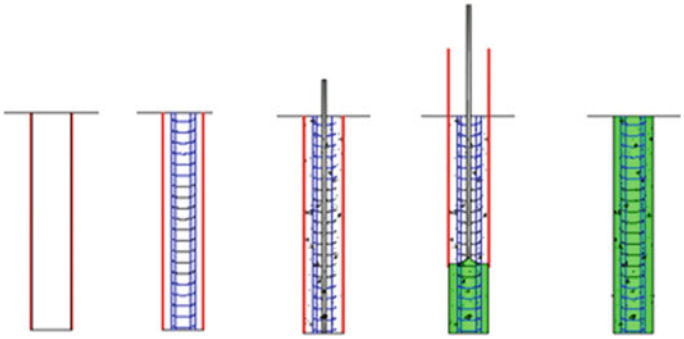

(c) Construction sequence of H-CIP

Fig. 4 Construction of CIP and H-CIP method (Korea Cement Institute 2013)

4 Case Study of Field Applicability

The field pilot tests at the metro construction project site were performed at the sand and sandy gravel deposited soil ground under the high water table, G.L.-3.1m (Lee et al. 2017). The test site of CIP construction is situated in the reclaimed land from the sea. The field visual observation was made to investigate the formation of cast-in-place pile in term of pile diameter and connectivity between completed pipes. The soil stratification at the CIP test site shown in Fig. 5 is typical alluvial deposited soil layers in riverbed.

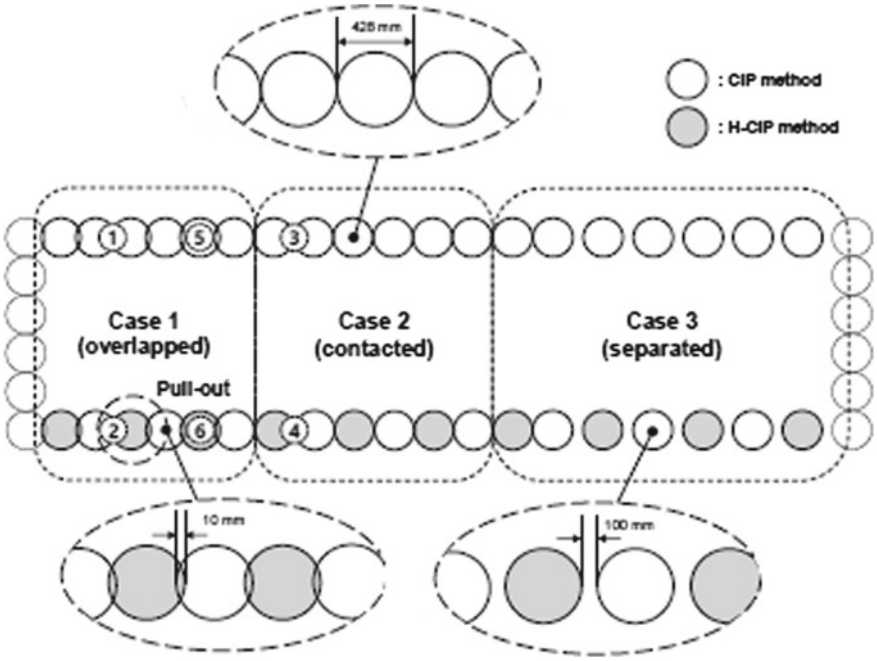

Fig. 5 Layout of CIP construction for field pilot test (Lee et al. 2017)

The soil ground at the pilot test field is composed of 2.5 m thickness of sandy silt soil as a backfill soil with the SPT-N values of 11-25 and the coefficient of permeability of 3.33×10^{-4}cm/sec, and subsequently, 3.5 m thickness of loose silty sand layer is deposited with the SPT-N values of 9–11 and the coefficient of permeability of 3.17×10^{-4} cm/sec. The sandy gravel layers are located at the depth of GL-6m with the SPT-N values of 17–25.

Three different cases of CIP (40 piles with $D = 428$ mm) and H-CIP (10 piles) walls in Fig. 5 were constructed with the variation of pile spacing between CIP piles, that is, 10 mm overlapped (Case 1), contacted (Case 2), and 100 mm separated (Case 3).

The permeability tests were conducted at the joint part of CIP piles and determined the coefficient of permeability to find out the function of cut-off wall for the given site (Lee et al. 2017).

It is turned out to be the permeability values for Cases ② and ④ in Fig. 5 which are the same as the coefficient of permeability of the original ground ($k = 1.15 \times 10^{-3}$–5.49×10^{-4}cm/sec).

It cannot be worked as a water barrier system. However, the permeability at test the center of H-CIP for Case ⑥ ($k = 3.27 \times 10^{-6}$ cm/sec) gives 1/500 of CIP permeability for Case ⑤ ($k = 1.23 \times 10^{-3}$ cm/sec). It is proved that the density of

(a) H-CIP wall

(b) CIP wall

Fig. 6 View of cast-in-place pile walls at the metro construction site

H-CIP wall is much higher than that of CIP wall, and hence, it can use as a cut-off wall system.

Figure 6 shows the construction view of H-CIP walls (a) and CIP walls (b) after excavation of soil around cast-in-place piles at the metro construction site.

Figure 6a for H-CIP method shows much closer contact between piles with comparison of contact view of CIP method in Fig. 6b. The cut-off wall constructed by using H-CIP method does not need an additional auxiliary insulation technique for preventing the leakage through the H-CIP wall. This is proved by the permeability test in field (Lugeon test) for Case ⑥ in Fig. 5 and visual observation made in Fig. 6a. From the observation made by Fig. 6b, the cut-off wall constructed by using CIP only has some problems of connection between piles and has high permeability like Case

Table 1 Results of unconfined compressive strength for grouted pile with permeability

Sampling location	Soil type	k (cm/sec)	Unconfined compressive strength (q_u)		
			CIP (MPa)	H-CIP (MPa)	Δq_u (%)
GL-1.5m	**SM**	**1.17E−5**	**11.89**	14.49	122
GL-3.65m (GWT.GL-3.1m)	**SM**	**1.15E−3**	**6.63**	30.74	464
GL-5.7m	GW-GM	Leakage	N/A	25.75	N/A

5 in Fig. 5. It may need an auxiliary insulation method to control the seepage through the CIP walls. The diameter of cast-in-place pile constructed by using the H-CIP is gradually increased (GL-4m, $D = 509$ mm; GL-5m, $D = 531$ mm; Gl-6.5m, $D = 625$ mm) from the ground level with respect to the soil depth. The lower part of H-CIP takes a higher overburden soil pressure and self-weight of cast-in grout as well. The soil layer at the experimental site is composed of H-CIP. The underground water level is not much influence on the formation of H-CIP because this particular site has a ground water table at 3.1 m below the ground level. The unconfined compression tests were conducted for the core specimens obtained from the CIP and H-CIP piles at the construction site shown in Fig. 6.

The test results of unconfined compressive strength for the grouted specimen of CIP and H-CIP give the integrity of compressive strength for CIP and H-CIP piles. The unconfined compressive strength of core specimen obtained from H-CIP is 122–464% higher than that of CIP due to the effect of surfactant grout and anti-washout performance. The quality of the unconfined compressive strength for H-CIP is remarkable even if it was formed under the ground water level. It is such an excellent performance to be fully worked out in grouting with the sandy gravel soil under the ground water table (GW-GM).

All core specimens obtained from H-CIP show higher unconfined compressive strength than the required q_u (13 MPa) by Korea Concrete Institute (2013). While the core strength obtained from CIP pile does not meet the required unconfined compressive strength of 13 MPa due to the material segregation and dilution with water (Table 1).

5 Concluding Remarks

The construction of cast-in-place pile wall in the sandy gravel soil involves several problems such as leakage control, quality of compressive strength of grouted pile, and formation of grouted pile.

Based on the laboratory test results, the fundamental engineering properties of surfactant mixed grouting paste were evaluated about the self-leveling, anti-washout, breeding, and unconfined compressive strength and compared with the required stan-

dard criterion by KCI. All the engineering properties of surfactant mixed grout are proved to be excellent and recommend highly to use in practice.

The field pilot tests at the metro construction site were conducted to evaluate the applicability of surfactant grout in the sandy gravel soil ground, and the results are compared with the existing CIP method. The field permeability test, unconfined compression test for specimen obtained from field, and visual observation of constructed walls by CIP and H-CIP methods. The integrity of unconfined compression strength both in the laboratory test and field pilot test of H-CIP shows high quality to use in practice even under the ground water level as well as in the sandy gravel soil.

However, the cut-off function of H-CIP wall for deep excavation site and under the ground water should be further studied with consideration various factors such as soil types in ground, condition of ground water, and the quality assurance of field performance.

References

JSCE-D104 (1990) Anti-washout properties under water: degree of separation in water as measured by the mass of suspended substances

KCI-AD102 (2009) Quality specification of antiwashout admixture for concrete

Kim SH, Kim TK, Choi JL, Yim KW (2010) A study on the injection efficiency and strength for grouting method. J Korean Geoenviron Soc 26(9):47–58

Lee JH, Cho JW, Do JU, Park BG (2017) Evaluation of field applicability of cast-in-place piles using surfactant grout. J Key Eng Mater 744:207–213

Saric-Coric M, Khayat KH, Tagnit-Hamou A (2003) Performance characteristics of cement grouts made with various combinations of high-range water reducer and cellulose-based viscosity modifier. Cem Concr Res 33(12):1999–2008

Song BD, Park BG, Choi YK, Kim TH (2017) Determination the engineering characteristics of the Hi-FA series of grout material in an underwater condition. J Constr Build Mater 144:74–85

Evaluation of Geosynthetic-Reinforced Tracks on Clayey Subgrade

Jagdish Telangrao Shahu and Sowmiya Chawla

Abstract In railroad track, geosynthetic is used for multiple functions, namely, reinforcement, separation, filtration, and drainage. In the present study, static and cyclic tests are performed on full-panel railway track models laid on compacted soil subgrades. Tests are performed on model tracks with two different thicknesses of subballast layer and laid on subgrade soil, namely, Dhanaury clay. Model tracks are reinforced with geogrid or geotextile or both at suitable interfaces. Track condition after a heavy rainfall was simulated. The models reinforced with geogrid at ballast—subballast interface were found to be more effective in reducing the tie displacements, ballast and subballast strains, and subgrade displacements as compared to the models reinforced with geotextile at subballast subgrade interface for tracks with Dhanaury clay as subgrade. The present study is also carried out by using a commercially available finite element software code, MIDAS/GTS (Midas manual 2013). Laboratory tests (triaxial tests and interface tests) are being conducted to calculate the constitutive parameters of the different track materials and interfaces which are used in the analyses. Model test results were extended to the field and subgrade modulus (*Esg*) and subballast thickness (*dsb*) as well as shear strength parameters (*c'sg* and ϕ*'sg*) of the subgrade soil, stiffness of geogrid, and coefficient of permeability of the subgrade soil were track parameters.

Keywords Railway tracks · Clayey subgrade · Mud pumping · Geogrid · Geotextile

J. T. Shahu
Department of Civil Engineering, Indian Institute of Technology New Delhi, New Delhi 110025, India
e-mail: shahu@civil.iitd.ac.in.in

S. Chawla (✉)
Department of Civil Engineering, Indian Institute of Technology (ISM), Dhanbad 826004, India
e-mail: sowmiya@iitism.ac.in

R. Sundaram et al. (eds.), *Geotechnics for Transportation Infrastructure*, Lecture Notes in Civil Engineering 28, https://doi.org/10.1007/978-981-13-6701-4_17

1 Introduction

Railways form an important part of the transportation infrastructure of a country and play an important role in sustaining a healthy economy. Indian Railways have now geared up to overhaul and upgrade its infrastructure to meet the future demand of growing traffic. When trains pass over a railway track, the subgrade soil is subjected to a certain cyclic stress. If this stress is greater than a particular stress level, subgrade shear failure occurs (Selig and Waters 1994). On the other hand, after heavy monsoon rains, the subgrade soil beneath a railway track becomes soft, and the overlying ballast causes attrition and erosion of the subgrade soil resulting in the formation of slurry at the subgrade surface. Since a subballast layer consists of free draining granular material (Shahu et al. 2000), this provision becomes uneconomical where the track passes through a long stretch of clayey soil, thereby requiring that the granular material to be brought from long haul distances. Geosynthetics could be an economical solution to bring about the reduction in the subballast depth under such conditions. Geosynthetics also provide an important option to improve the overall track support structure and thereby reduce the track maintenance costs and operation costs due to train delays. Very little work has been done on gainful utilization of geosynthetics by Indian Railways. Therefore, the application of geosynthetics in Indian Railways needs a detailed study under various site-specific conditions, such as type of subgrade soils, track structure, track geometry, material specifications, loading details, and environmental factors. The present study will help in laying out proper specifications for various track materials and geosynthetics, and development of a rational methodology for design of reinforced tracks.

1.1 Application of Geosynthetics in Tracks

Figure 1 shows the main components of a typical geosynthetic-reinforced track structure (Selig and Waters 1994). The components may be grouped into two main categories: superstructure and substructure. Railroad track is one of the few geosynthetic applications where a geosynthetic is used for multiple functions, namely, reinforcement, separation, filtration, and drainage (Koerner 2005). Geogrids are used to reinforce the track and generally provided within or below the ballast layer. Geogrids reduce lateral spreading of the ballast particles increases lateral confinement to the ballast layer (Brown et al. 2007). This increases the stiffness of the ballast layer resulting in better stress distribution and reduction in induced vertical and shear stresses on to the underlying subballast and subgrade (Koerner 2005). Geotextiles can act as a separator preventing the intermixing of a fine-grained subgrade soil with the overlying ballast or subballast materials. They also act as a filter allowing the water to pass through it but retaining the soil within the subgradent. When the subgrade soil is soft, the geotextile can also act as reinforcement and reduce subgrade stresses (Selig and Waters 1994).

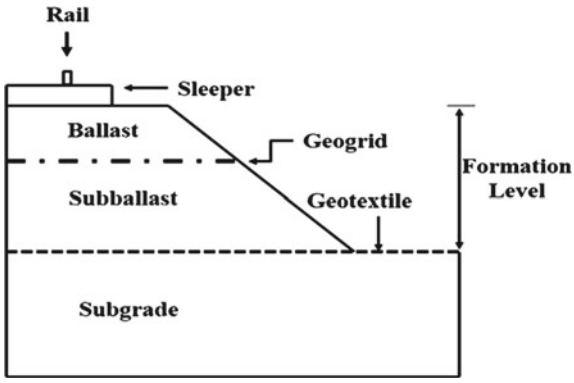

Fig. 1 Cross section of a typical geosynthetic-reinforced railway track

2 Model Testing of Railway Tracks

The present study has investigated the benefits of the use of geosynthetics on tracks laid on fine-grained soils after a heavy monsoon rain in terms of track reinforcement and reduction of mud-pumping. Monotonic and cyclic load tests are performed on model-reinforced tracks with a subballast layer laid on compacted clayey soil subgrades. Track conditions after a heavy monsoon rain are simulated.

2.1 Materials

Tests are performed on model tracks laid at 1:3 scale to the prototype. Grain size distributions of different model track materials are given in Fig. 2 and typical characteristics are listed in Table 1.

2.1.1 Subgrade Soil, Ballast, and Subballast Materials

The ballast was procured from an aggregate crushing plant at Manesar in Haryana state which also supplies ballast to Indian Railways. The range of prototype ballast and subballast materials as specified by the Research Designs and Standards Organization, Indian Railways (RDSO) after their one-third size reduction is presented in Fig. 2. Natural fine-grained soil, namely, Dhanaury clay is used as subgrade soil.

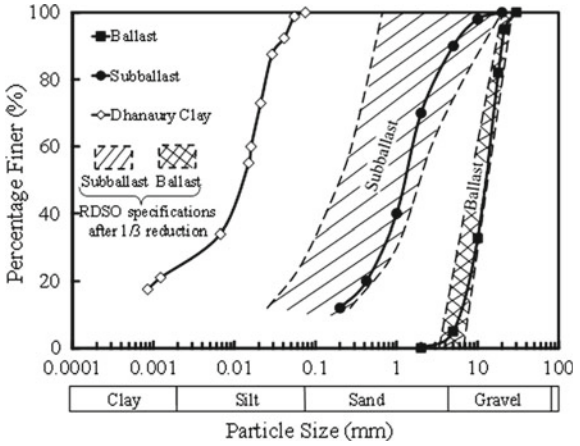

Fig. 2 Grain size distribution of various track layer materials (Chawla and Shahu 2016)

Table 1 Characteristics of different track materials

Item	**Ballast**	**Subballast**	**Dhanaury Clay**
Classification	GW	SW	CI
$\gamma_{d(max)}$ (kN/m^3)	16.4	16.0	17.9
$\gamma_{d(min)}$ (kN/m^3)	14.2	11.7	–
OMC (%)	–	–	16.7
w_L (%)	–	–	36.0
I_P	–	–	15
Fine Sand (%)	–	–	–
Silt (%)	–	–	75.0
Clay (%)	–	–	25.0
Minerals	Quartzite	Quartzite	–
Particle shape	Angular-Subangular	Angular	–
k (m/s)	–	–	3.28×10^{-10}

2.1.2 Geogrid and Geotextile

A non-woven geotextile (GT) and a biaxial geogrid (GG) are used in the model tracks. The geogrid was made up of high-density polyethylene (HDPE) with an aperture size of 30 mm × 30 mm and an initial tensile stiffness of 240 kN/m. The tensile stiffnesses of the geogrid at 2.5 and 5% strain were 120 and 88 kN/m, respectively.

2.2 Modeling Considerations

2.2.1 Similitude Ratio Adopted for Model Testing

Similitude ratio refers to the ratio of any linear dimension of the model to the corresponding dimension of the actual prototype track. Model dimensions were scaled down based on the similitude ratio in such a way that induced stresses in the model remain the same as those in the prototype. The ballast–subballast interface where the geogrid used was subjected to high stresses similar to those in the field. Based on practical consideration, a full-panel model track with a similitude ratio of one-third is used in this study. A comparison of the prototype track and the model track is given in Table 2.

2.2.2 Modeling Rail and Sleepers

It was assumed that the rail transfers stresses on to the sleepers by a beam action and the sleepers then transfer the stresses to the ballast layer mainly by a direct bearing.

Therefore, a square rail section was used in the model such that the flexural rigidity (EI) of the model rail was reduced by 1/81th of that of the actual rail as per the similitude ratio and steel sleepers were used in the model with all the dimensions reduced except thickness as per the similitude ratio in place of prestressed concrete sleepers employed in the prototype.

Table 2 Comparison of model track with prototype track

Parameter	Prototype track	Modeled track	Remark
L_g	1.676 m	0.56 m	1/3
Rail Moment of Inertia, I_r	21,580 cm^4	26.64 cm^4	Reduced by a factor of (1/81)
L_s	2.70 m	0.9 m	1/3
b_s	25 cm	8.3 cm	1/3
t_s	12 cm	3.4 cm	By equating $(EI)_S = (EI)_C$
S	65 cm	21.6 cm	1/3
Sleeper Material	Concrete	Steel	Practical testing considerations
d_{sg}	–	0.5 m	1/3
d_b	350 mm	116.7 mm	1/3
d_{sb}	600 and 1000 mm	200 and 330 mm	1/3

2.2.3 Modeling Geogrid and Geotextile

A geogrid is used at the ballast–subballast interface and/or a geotextile is used at the subballast–subgrade interface. It acts as separator and also helps in settlement reduction which influences load-deformation behavior. Usually, a relatively heavy geotextile of thickness greater than 4 mm is employed in tracks (Martinek 1986); accordingly, an available, heat-bonded, non-woven geotextile of reduced thickness of 2.2 mm was used in the model tests. A 2.2 mm thick geotextile is also considered adequate for the filtration and drainage functions. Based on symmetry, only one-half of the model track was constructed and a smooth boundary was provided along the center line. The load was applied on the top of the rail, and based on the similitude ratio used, this load was equivalent to nine times of that applied on the prototype track.

2.3 Test Setup and Instrumentation

2.3.1 Instrumentation Used

All tests were conducted inside a specially fabricated steel tank with 1.48 m long, 1.3 m wide, and 1 m high. The depth of subballast, ballast and subgrade being 200 and 330 mm, 116.7 mm and 0.5 m respectively. Monotonic and cyclic loadings were applied at the top of the rail by a circular plunger attached to a flat plate, which was, in turn, bolted to the flange plates of the MTS machine. The lower end of the plunger was made to rest on a load cell pedestal through which the load was transmitted to the rail. The instrumentation consisted of displacement transducers, earth pressure cells, and load cells connected to a digital data logger (Fig. 3).

Model tracks were adequately instrumented to record important responses during the tests. The vertical displacement was measured using dual type, strain gauge-based displacement transducers that provide both an electronic signal as well as a digital readout for effective monitoring. Miniature earth pressure cells of 2.5 cm diameter and 0.5 cm thickness of 200, 500, and 1000 kPa capacity were used for measurement of stresses in the subgrade, subballast layer and, ballast layer, respectively, depending upon the expected magnitude of stresses in these layers (Shahu 1993). A load cell of 50 kN capacity was used to measure the vertical load. The whole instrumentation was connected to a 9-channel portable data logger having simultaneous display of measurement of 9 channels for effective monitoring and automatic recording. The actuator of the MTS machine was controlled via a computer operated servo-controlled system.

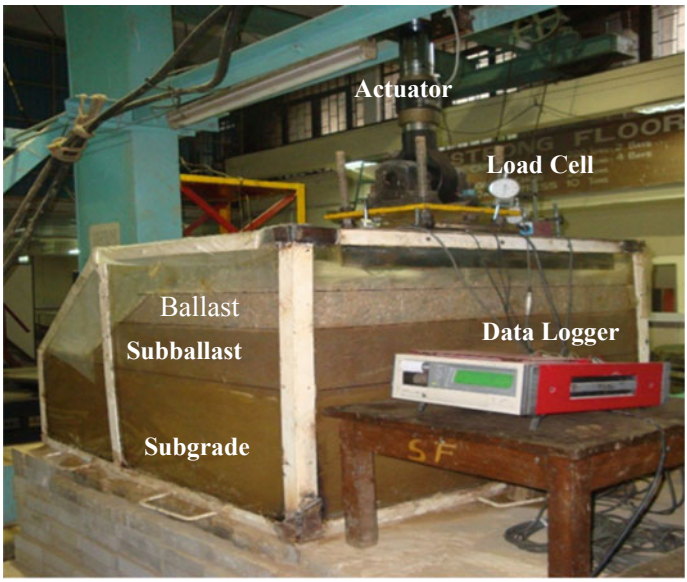

Fig. 3 A schematic view of model test setup

2.4 Test Procedure and Observations

The subgrade soil bed was prepared as follows: first, the dry soil was sieved to remove foreign particles; a required amount of water was then mixed with the soil namely, Dhanaury clay (DC).

To achieve approximately the same target undrained shear strength, Dhanaury clay was mixed with 30% water based on a trial and error procedure. The soil was mixed manually with bare feet in a 30 kg batch each in a large ceramic tub to break up any clods present (Fig. 4a).

The soil was then filled up in separate cylindrical drums and covered up with wet jute bags for 24 h for moisture equalization. At the bottom of the test tank, circular holes were provided at constant interval ensuring a drainage boundary at the bottom of the tank. The test tank was filled up with a required amount of subgrade soil and compacted in three layers to achieve desired dry density. Kneading compaction was carried out using a small specially manufactured sheep foot roller of 22 kg weight as shown in Fig. 4b.

After kneading compaction, the subgrade surface was leveled with a smooth drum roller of 3.5 kg weight (Fig. 4c). After the compaction process, samples were collected from three different locations in plan and from three different depths at each location to monitor water content, dry density, and undrained shear strength (by conducting a laboratory vane shear test). The entire surface area was then covered with wet jute sheets and the soil bed was left in this condition for further 24 h for moisture equalization. An earth pressure cell was then placed exactly below the position of

(a) Through mixing with bare feet

(b) Kneading compaction using sheep foot roller

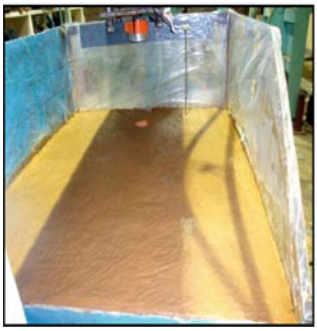

(c) Placing of earth pressure cells and settlement peg

(d) Close view of earth pressure cells arrangement

Fig. 4 Subgrade bed preparation and instrumentation

the load cell and a settlement peg was placed beside it at the top of the subgrade soil (Fig. 4c–d). A complete and continued test procedure is detailed in Sowmiya (2013), Sowmiya et al. (2013).

A total of 10 tests were conducted in two groups. Group 1 tests were termed as DC20 indicating that the models had Dhanaury clay (DC) as the subgrade soil and a subballast thickness (dsb) of 20 cm; group 2 tests as DC33 indicating that the models had Dhanaury clay as the subgrade soil and a subballast thickness of 33 cm; In each group, one monotonic and four cyclic tests were conducted.

2.4.1 Monotonic Tests

For reinforced and unreinforced condition with geosynthetic material for a nearly saturated subgrade soil condition, the cyclic loads which leads to non-terminating deformation in case of the unreinforced track condition was performed. The coupled

analysis was carried out in a single stage wherein a total of 30 kN load was applied over a total time duration of 20 min spread over ten equal steps.

2.4.2 Cyclic Tests

The details of the cyclic test of DC20 group on unreinforced model track (DC20 UR-C) in terms of the number of load cycles with the tie displacement up to initial 100 load cycles with 0.1 Hz frequency are shown in Fig. 5. A threshold stress is defined as a critical level of repeated stress (CLRS) such that when the cyclic stress level is above the CLRS, plastic deformation is non-terminating (Chawla and Shahu 2016). The tie displacement data measured directly by the sensors in MTS machine and the displacement data for all the track layers recorded in the data logger are shown in Fig. 5.

Cyclic test results show that the presence of the geotextile at the subballast–subgrade interface (GT test) or the geogrid at the ballast–subballast interface (GG test) or both the geotextile and the geogrid at their respective interfaces (GT-GG test) reduces the tie displacement δt as well as the subgrade displacement as compared to those for the corresponding unreinforced track(UR test).

For DC20 and DC33 tests, the maximum reduction in the tie displacement at the end of 25,000 load cycles is observed in case of GT-GG test (≅42%), followed by GG test (≅31%) and GT test (≅19%) as expected. The geogrid reinforcement is more effective owing to its nearness to the applied load and its higher stiffness as compared to the geotextile.

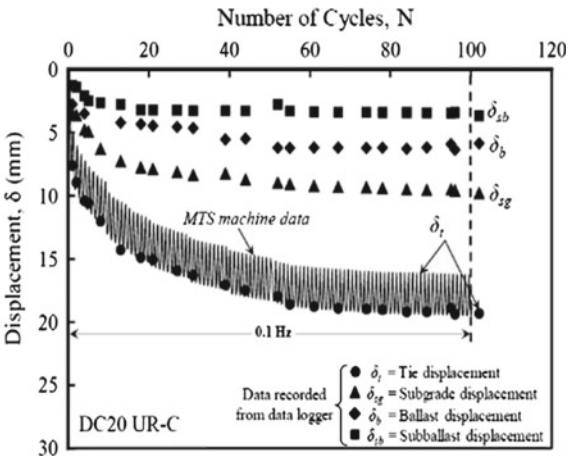

Fig. 5 Variations of tie displacement δt and displacement measured for the track layers beneath the rail seat for initial 100 load cycles N with 0.1 Hz frequency for DC20 UR-C test

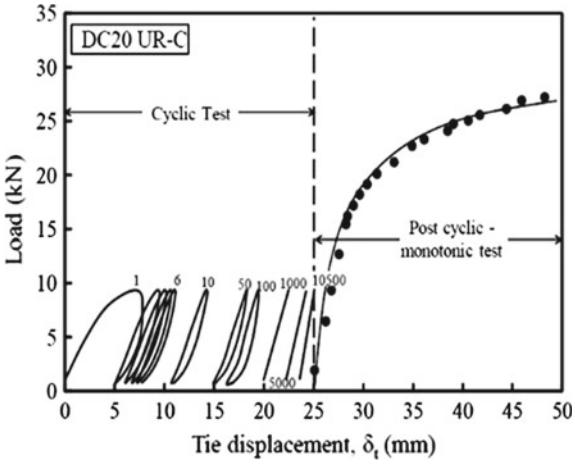

Fig. 6 Typical cyclic and post-cyclic-monotonic test responses of DC20 UR test

2.4.3 Post-Cyclic-Monotonic Load Behavior

After the cyclic loading, post-cyclic-monotonic loading was applied to determine the stiffness and failure load of the model track. Typical cyclic and post-cyclic-monotonic responses for DC20 UR test are shown in Fig. 6. In post-cyclic tests, a higher stiffness and approximately 33% higher failure load was observed for the unreinforced track (UR-C) during the post-cyclic-monotonic test as compared to those observed during the monotonic test on a newly laid model track (UR-M) in case of DC20 group tests. Similarly, in case of GT, GG, and GT-GG tests of DC20 group, the failure load during the post-cyclic-monotonic loading is increased by 42.7, 38.8, and 49%, respectively, as compared to that of the newly laid model track (UR-M).

3 Finite Element Analysis of Model Test Tracks

MIDAS/GTS (Midas manual 2013), a commercially available finite element software code, is used for the finite element analyses of model test tracks. The tests were carried out for three different analyses: first, nonlinear analysis (Duncan and Chang 1970); second, straight analysis; and the third, coupled analysis.

A series model tests conducted for two soil groups DC20 and DC33, within each test group, the following types of model tests were performed: a monotonic test (UR-M) and the first cyclic test (UR-C) were conducted on unreinforced model tracks; the second cyclic test (GT) was conducted on a model track stabilized with geotextile alone present at the subballast–subgrade interface; the third cyclic test (GG) was conducted on a model track reinforced with geogrid alone present at the ballast–subballast interface; and the fourth cyclic test (GT-GG) was conducted on

a model track reinforced with both geotextile and geogrid at their above-mentioned respective interfaces.

3.1 Monotonic Tests

Figures 7 and 8 compare the results predicted by two sets of constitutive relationships with the measured results of monotonic tests for unreinforced tracks (UR-M) for DC20 and DC33, respectively, in terms of load versus tie displacement. Coupled analysis gives better prediction of the measured load-displacement behavior of the model tracks as compared to the nonlinear analysis and straight analysis.

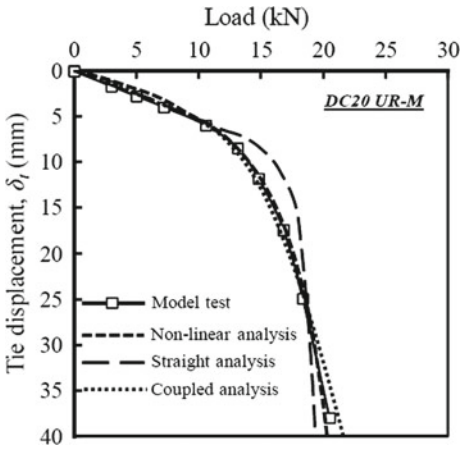

Fig. 7 Model test results compared with the predicted FEM (DC20 UR-M)

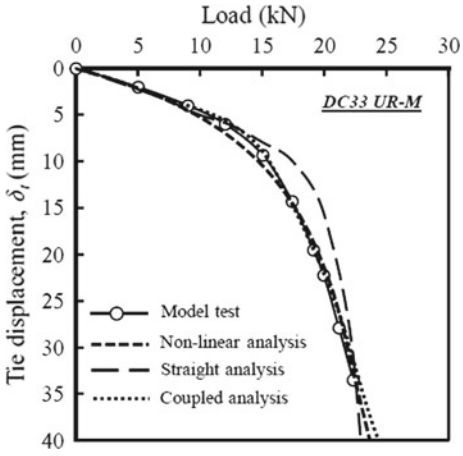

Fig. 8 Model test results compared with the predicted FEM (DC33 UR-M)

The coupled analysis fairly predicts the measured load-displacement behavior of all the three model tracks under monotonic loading (Figs. 7 and 8). The nonlinear analysis gives better results than the straight analysis.

3.2 Cyclic Tests

3.2.1 Tie Displacement

Figure 9 shows typical vertical stress contours for DC20 GT-GG test. The deformed shapes of the track section after failure at wheel load = 13.75 kN along sleeper and rail directions observed through the visible perspex sheet for DC20 UR-M test are compared with the deformed shapes observed in the coupled analysis. The surface profiles and deformed shapes of each layer observed during the model test match well with those obtained by the finite element analysis.

Model test analysis with finite element(coupled) analysis for DC20 and DC33 tests compare the measured load versus tie displacement results during the first loading cycle up to 9 kN load for the cyclic tests of DC20 and DC33 groups with the predicted results by the coupled analysis. The failure loads have been calculated using Vesic's criterion (Vesic 1963) (refer Winterkorn and Fang 1986) as 12.5, 14.25, 15.6, and 16.8 kN, respectively, for UR, GT, GG, and GT-GG tests of DC20 group. The corresponding failure loads are 14.5, 16.2, 17.5, and 19 kN for DC33 group. The geogrid-reinforced track (GG) had a higher stiffness and a higher failure load than the geotextile stabilized track (GT) for both groups.

3.2.2 Vertical Stresses

In general, predicted vertical stresses lie within or at the bottom of the measured scatter values. While the measured stresses were measured during cyclic loading and thus involved some inertial and impact effects, and the predictions were made for the static load.

The coupled analysis consistently predicts higher ballast and subballast top stresses as compared to the nonlinear analysis; however, the reverse is the case for the subgrade stresses. The reason for this is while the ballast and subballast stresses predicted by both coupled and nonlinear analyses are effective stresses, the subgrade top stresses predicted by the coupled analyses are effective stresses and those predicted by the nonlinear analyses are total stresses. It may be noted that the pore water pressures at the subgrade top predicted by the coupled analysis were approximately of the order of 3–5 kPa.

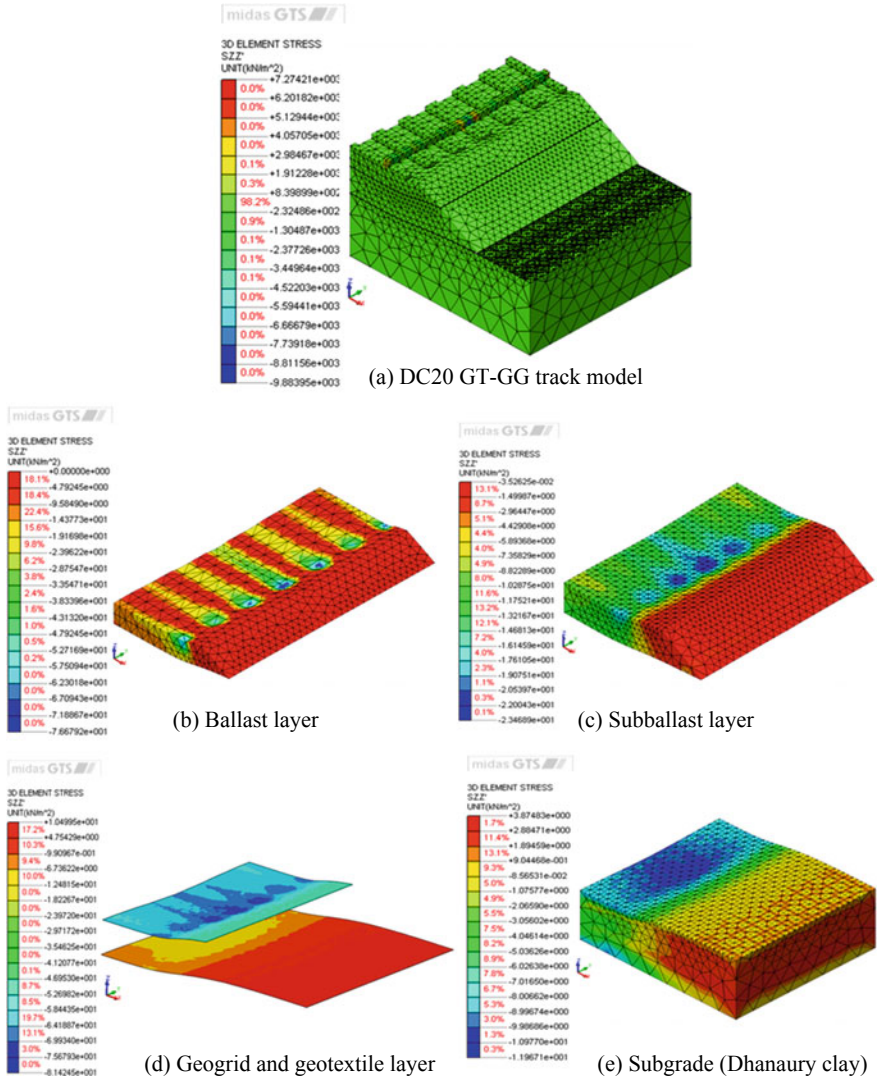

Fig. 9 Vertical stress contour for different components of DC20 GT-GG model (results of coupled analysis)

4 Conclusions

1. Geogrid was found more effective at ballast–subballast interface (GG track) in reducing the vertical stresses at the top of ballast layer and moderately effective in at the top of subballast layer.
2. The geotextile (GT track) is almost equally effective in the reduction of subgrade vertical stresses owing to its closeness to the subgrade surface as the geogrid (GG track).
3. The coupled analysis predicts load versus displacement relationship for the first loading cycle for the cycle tests on both unreinforced and reinforced tracks (UR-C, GT, GG, and GT-GG) for all test groups (DC20 and DC33) accurately.
4. The nonlinear analysis predicts lower vertical stresses at the top of ballast and subballast layers for the test groups (DC20 and DC33) as compared to those predicted by the coupled analysis. However, the total vertical stresses predicted by the nonlinear analyses at the top of subgrade were slightly higher than the effective stresses predicted by the coupled analysis.
5. The deformed shapes generated between the present coupled analysis and of the model track section compare well as they were observed through the perspex sheets of the test tank in both sleeper and rail direction.
6. Geogrid with higher stiffness decreases the tie displacement than the geogrid with lower stiffness. The consumption of subballast materials was reduced approximately by 55–70% with the inclusion of two geogrid layers at proper interfaces. For a long haul distances from which suballast material was procured, in such case it was found economical.
7. Compared to unreinforced section, the dissipation of the pore water pressure becomes faster with installation of geotextile layer between subballast and subgrade.

References

Brown SF, Kwan J, Thom NH (2007) Identifying the key parameters that influence geogrid reinforcement of railway ballast. Geotext Geomembr 25:326–335

Chawla S, Shahu JT (2016) Reinforcement and mud-pumping benefits of geosynthetics in railway tracks: model tests. Geotext Geomembr, Elsevier, 44, pp 366–380

Chen, T-C, Chen R-H, Chen S-S. (2000) A nonlinear homogenized model applicable to reinforced soil analysis, Geotextiles and Geomembranes, 18, pp. 349–366

Duncan JM, Chang YC (1970) Nonlinear analysis of stress and strain in soils. Journal Soil Mechanics and Foundation Engineering Division, ASCE 96(5):1629–1653

Koerner RM (2005) Designing with geosynthetic, 3rd edn. Prentice Hall, Englewood Cliffs, NJ

Martinek K (1986) Geotextiles used by the German Federal Railway—experiences and specifications. Geotext Geomembr 3:175–200

Midas (2013) Midas/GTS (geotechnical and tunnel analysis system) reference manual for modelling. Integrated design and analysis. Midas Corporation

Selig ET, Waters JM (1994) Track geotechnology and substructure management. Thomas Telford, London, UK

Shahu JT (1993) Some analytical and experimental investigations to study the behavior of soils under the railway track, Ph. D. Thesis, Indian Institute of Technology, Kanpur, India
Shahu JT, Yudhbir, Kameswara Rao NSV (2000) A rational method for design of railroad track foundation, Soils Found 40(6): 1–10
Sowmiya LS, Shahu JT, Gupta KK (2013) Stresses and displacements in reinforced tracks. Institution of Civil Engineers, Ground Improvement
Sowmiya LS (2013) Analyses and experimental investigations of railway tracks on clayey subgrades with and without geosynthetic reinforcement, Thesis, Ph. D. Indian Institute of Technology Delhi
Vesic AS (1963) Bearing capacity of deep foundations in sands, National Academy of Science, National Research Council. Highway Res Rec 39:112–153
Winterkorn HF, Fang HY (1986) Foundation engineering handbook. VanNostrand Reinhold Company Inc., New York, USA

A Review on Vibration Generation Due to Subway Train and Mitigation Techniques

Naveen Kumar Kedia and Anil Kumar

Abstract Rapid increase in urban population in India put a lot of pressure on existing transportation systems which results in frequent traffic jams, congestion, and delay. To overcome this problem, governments propose construction of underground metro systems in various cities some of which are either operational or in construction phase. Metro has proved to be safe and efficient mode of transportation in cities. However, passage of trains at certain speed produces vibrations which are uncomfortable and annoying to the people living near the vicinity of the metro systems. In addition to the human annoyance, these vibrations can affect old buildings and sensitive equipment. This paper reviews various vibration issues that are generated due to wheel-track interaction and tunnel-soil interaction in India and other countries. Moreover, track-based countermeasures and ground improvement techniques are summarized and compared. Nonetheless, some issues in numerical modeling of these systems are also discussed.

Keywords Subway metro trains · Vibration issues · Wheel-track interaction · Countermeasures · Numerical modeling

1 Introduction

Traffic jams in big cities have made necessary the use of underground metro trains more than ever. The rapid increase in population of cities and advancement in technology has increased the demand for a comfortable life. The use of underground metro trains as an efficient and safe vehicle could be appropriate alternative for passengers. However, passage of trains with appropriate speed in between stations and

N. K. Kedia (✉)
Center for Transportation Systems, Indian Institute of Technology, 247667 Roorkee, India
e-mail: naveen.kedia@outlook.com; nvkedia.dct2017@iitr.ac.in

A. Kumar
Department of Mechanical and Industrial Engineering, Indian Institute of Technology, 247667 Roorkee, India
e-mail: anikrfme@iitr.ac.in

R. Sundaram et al. (eds.), *Geotechnics for Transportation Infrastructure*, Lecture Notes in Civil Engineering 28, https://doi.org/10.1007/978-981-13-6701-4_18

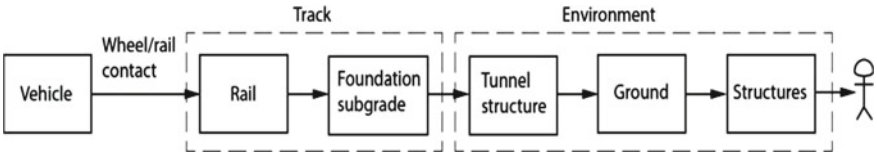

Fig. 1 Vibration transfer mechanism (Fryba 1996)

turnouts (Nielsen 2003) produces vibrations that may sometimes be disturbing to people living in the region close to the transportation systems. The vibrations of this nature cause the buildings to shake and produce the rumbling sound which can be heard inside the building. It can cause fatigue in materials of ground and structure, create differential settlement, crack in the walls, resonance, and other difficulties. Thus, evaluation of vibration due to the movement of train becomes an important factor in selection of the route and the type of rail system to be designed.

The railway traffic induced ground-borne vibrations have become an important environmental issue, which is particularly critical when new rail infrastructure is introduced upon an existing urban environment. These vibrations propagate through the tunnel construction and the surrounding soil into nearby buildings, causing annoyance to people. Control of vibration from trains running in railway tunnels is an important issue and is now receiving increasing attention in research. Figure 1 (Fryba 1996) shows the mechanism of vibration transfer.

In the vicinity of railway traffic, airborne noise and structural vibrations can affect the well-being of humans. Structural vibrations can cause discomfort due to the perceived vibrations or due to noise generated by radiating surfaces affected by the structural vibrations, normally called structure-borne sound. When dealing with railway traffic in tunnels the direct airborne sound, traveling from the train to the receiver (human) is neglected, however, the effect of structural-borne noise must be considered when analyzing the effect of ground vibrations from railway traffic. Especially through a combination effect between annoyance due to vibrations and annoyance due to noise is reported in the literature. The rail vibrations are originated at the wheel-rail interface and propagate through the track support system to the tunnel structure, the ground, and surrounding buildings. Occupants of nearby buildings may detect "rumble" noise during the passage of trains, called ground-borne noise. In some cases, occupants may directly perceive vibration, called ground-borne vibration. The ground-borne vibrations due to railway traffic are mainly generated in the contact zone between the wheel and the rail. It is therefore important that this excitation mechanism is reduced to a minimum. In principle, airborne sound from a train in a tunnel could be transformed into structure-borne sound when affecting the tunnel construction (Fig. 2).

There are several sources of vibration in wheel-rail interaction. Figure 3 provides a list of possible vibration modes and relevant frequency ranges (Connolly et al. 2016). It is clear that the contribution of rail vehicle components such as car body, bogie, and axle is in the lower frequency range, below 10 Hz. However, the frequency range

Fig. 2 Malmö City Tunnel Sweden (COWI 2009)

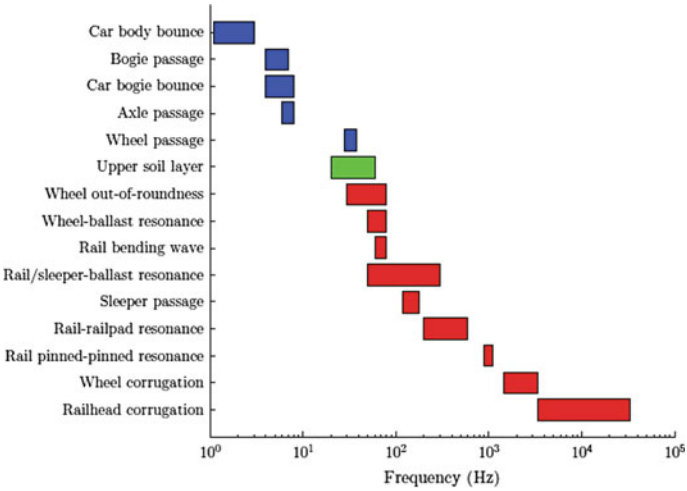

Fig. 3 Main contribution of dynamic vehicle/track and soil interactions (Kouroussis et al. 2014)

above 10 Hz is caused by wheel passage, soil layers, wheel defects, rail bending waves, rail/sleeper-ballast resonance, wheel, and railhead corrugation, etc.

There are five main mechanisms as discussed by Hunt and Hussein (2007) about vibration generation from moving trains. These methods are discussed briefly below.

The **first** method of vibration generation occurs when the continuous axles of the train passes through the fixed observation point. This point shows a peak response

when one of the train wheels comes near to it and a trough response when the point on the rail near to this point lies between two axles. This process can also be referred as the *quasi-static* effect which is modeled by static forces moving along the track at the speed of the train. It significantly contributes to the low-frequency response in the range 0–20 Hz (Jones and Block 1996a).

The **second** method is known as the *parametric excitation* mechanism and is caused by the variation in the stiffness under the moving wheel loads. This process is well illustrated by the rails supported discretely by the sleepers at the regular distance. A moving wheel faces high stiffness at a location of rail—sleeper contact and comparatively low stiffness between two sleepers. The wheel movement over the rail with a constant speed applies a periodic force having the time period equal to the ratio of sleeper spacing and wheel velocity (Heckl et al. 1996).

The **third** mechanism of vibration generation occurs due to the level of differences between rail joints and crossings. A wheel applies an impulsive loading to the rail at these joints as the curvature of the wheel does not follow sudden jump or discontinuities. Moreover, the interaction of wheel with the various joints produces the sound annoying to the passengers of the vehicle. Though it is one of the important sources of vibration generation yet it is obsolete nowadays due to the use of continuously welded rail.

The **fourth** source of vibration arises due to the *wheel and rail unevenness or roughness* present and it includes wheel flats, corrugations, polygonization of wheels, etc. The movement of smooth wheel over a continuous rail having sinusoidal roughness produces the mutual force at the wheel—rail interface having frequency equal to the ratio of train velocity and wavelength. This force is affected by the inertial forces of the train at the same frequency. Some rail roughness has higher amplitude of unevenness for long wavelengths (Frederich 1984), on the other hand, wheel roughness has constant unevenness for wave numbers having the range of frequency produced during the ground vibrations (Degrande et al. 2006). Certain wavelengths of rail roughness at around 25–50 mm is generated by the corrugation (Nielsen 2003), but their frequencies are above 250 Hz. Frequencies of this magnitude are easily attenuated by the ground before its transmission to the nearby buildings.

The **fifth** mechanism of vibration generation is related to the *high-speed train*. In this process, very large amplitudes of vibration can be generated when the speed of the train approach or exceed either Rayleigh wave speed in the ground or the minimal phase velocity of bending waves in the track. Whenever the speed of the train crosses the Rayleigh wave speed, a ground vibration boom occurs. Krylov et al. (2000) taken up the case study of the location near Ledsgard, Sweden where an increase in the train speed from 38 to 50 m/s cause the generated ground vibration to increase by 10 times. If the train speed matches the minimum critical track velocity, large deflection, and derailment of the train might occur.

2 Indian Scenario: Case Study of DMRC

In India, metro subway trains are being constructed in densely populated cities, for example, DMRC has developed metro lines in Delhi. The underground trains pass through tunnels which are strategic elements in transportation and utility networks in any metropolitan city (Singh et al. 2017) and are laid at certain limited depth from the ground surface due to the limitation of the available technology. Moreover, there are several turnouts in the journey that are close to sensitive residential areas. Some preliminary measurements disclose that the dominant vibration frequencies are about above 40 Hz. This shows that the dominant frequency is in the higher range. The main reason for vibration seems to result due to the interaction between wheel and rail. This vibration reaches to nearby buildings and residents on the ground surface through the tunnel and soil layers. There may be concern about the possibility of adverse long-term effects of vibrations on old buildings and historical monuments along metro corridors, especially those in a weak condition (Kishore et al. 2017).

3 International Status

Both theoretical and experimental researches are performed by several researchers worldwide and reported in the literature. Some of the researches done in last decade by some of the prominent authors are summarized below:

Yuan et al. (2009) studied the effectiveness of floating track system as the vibration mitigation measure. They have used the traditional Euler–Bernoulli beam dynamic model to assess the vibration characteristics. The dispersive curves plotted between frequency and wave number revealed that first cutoff frequency is equal to natural frequency of the floating slab and second cutoff frequency equal to natural frequency of rail. They concluded that an increase of slab mass is the most effective way by which the range of vibration isolation can be increased by the track system.

Ming Kuo et al. (2016) set up the experiment of the mass—spring series model to study the property of the slab track as the vibration mitigation measure. They determined that stiff spring use to confront excitation source and using soft spring as the foundation isolator may increase propagation of the vibration and reduce vibrations reflected to the excitation.

Dai et al. (2014) used three-layer Euler-Bernoulli beam model for the modeling of discontinuous slab track subjected to a harmonic load. The analytical equations derived using the receptance method is used to determine the vibration properties of the system.

Fiala et al. (2010) compared the different methods to mitigate ground-borne noise vibrations from underground trains. The countermeasures considered are a floating slab track, base isolation of the structure, and the application of a box-within-box arrangement. The performance of the countermeasures is evaluated using local and

integrated insertion loss indicators, and the results are compared with those obtained by simplified design models.

Forrest and Hunt (2006) modeled the tunnel surrounded by the soil as the infinitely long, thin cylindrical shell and the soil as an infinite homogeneous isotropic continuum to study the track and tunnel interaction.

Degrande and Schillemans (2001) provided the data of the homologation tests of the high-speed train track between Brussels and Paris. They described the characteristics of the Thalys high-speed train and the tracks and the dynamic properties of the soil. The experiment was conducted to measure the vibration levels of the ground both near field and far field.

Jones and Block (1996b) focused on the area of a freight train and vibration generated by its movement. They developed a theoretical model to study both the generation and propagation of vibration to design a low-vibration railway. The vibration generated is a combination of the dynamic forces which include unevenness of the track and the static load which includes track deformation under successive axle loads so to include all this effect, prediction scheme has been developed.

Vogiatzis and Kouroussis (2015) studied the use of floating slab track at the cross-over location in the Athens metro. The finite element modeling has been adopted by them. The slab track system ensured a complete ground-vibration attenuation with an insertion loss of −20 dB with respect to the predominate excitation.

Krylov et al. (2000) discussed the impact of high-speed train on the surrounding. In the track ground system, there are mainly two critical wave velocities which are the velocity of the Rayleigh surface waves in the ground and the minimum phase velocity in the track. Both these mentioned speed can easily be surpassed by the high-speed train which can result in high-amplitude vibration.

Breccolotti et al. (2011) presented in this paper a method for the prediction of vibration levels produced by the railway traffic based on experimental measurements and FE modeling capable of taking into account time varied excitation forces and complex soil conditions. The suggested approach has been implemented in the city of Palermo, Italy.

Hussein and Hunt (2009) gave the new method of modeling floating slab track having discontinuous slabs. Their model included two sub-models that comprises of an infinite track with periodic double-beam unit formulated as a periodic finite structure and a new version of the pipe-in-pipe model that represents tunnel wall embedded in a tunnel half space. The coupling of the two models is done by writing the force transmission equation from the track to the tunnel as a continuous function and satisfying the compatibility condition. Their results showed that the far-field vibrations are increased significantly due to resonance frequencies of slabs with discontinuities.

Ma et al. (2016) studied the long-term effect of metro vibrations on the historical buildings in China. They took up the case study of Bell tower to study the effect of micro-vibrations on the timber structure of the tower. To study this effect, a metro train-track-tunnel-soil 3D dynamic finite element model was developed. In order to validate the model in situ, measurements were also recorded which helped to determine the behavior of timber structure. Their finding indicated that installing

floating slab track and decreasing the train speed helps to control the peak particle velocity.

Galvín et al. (2010) compared the vibrations induced by the high-speed train on the ballasted track and the non-ballasted slab tracks. They have used the 3D multi-body-finite element-boundary element model to study the vibrations induced by the passage of HST. The vehicle is modeled as the multi-body system and the soil is represented as the boundary elements. Three types of loads are considered, i.e., the quasi-static excitation, the parametric excitation and the dynamic excitation due to unevenness and roughness.

Pan et al. (2017) have worked on the base isolation of the buildings constructed near the metro line rather than the isolation of the track as studied by other authors. They studied the use of laminated rubber bearings for the seismic isolation of the buildings from the metro vibrations. Different types of laminated rubber bearings are used in their study, i.e., thick and thin natural rubber bearings and the thick and thin high-damping rubber bearings. They conclude that the thick rubbers of both categories were significantly stable compared to the thin rubbers.

Van Lier (2000) has modeled the slab track with embedded rails. They discussed the vibro-acoustic modeling of the rails embedded in a cork-filled elastomeric material using FE software package. Three types of track are compared using the aforesaid model, an existing slab track with embedded UIC54 rail, a newly designed acoustically optimized slab track, and a reference ballasted track.

Zhu et al. (2015) try to minimize the low-frequency vibrations of floating tracks using dynamic vibration absorbers. Their numerical model result indicated that the proposed dynamic vibration absorbers could effectively suppress low-frequency vibrations of the floating slab track when tuned and attached properly.

Yang and Hung (2008) have used the 2.5D finite/infinite element approach to study the characteristic of the vibration generated by the underground moving trains. The finite element is used to model the near field of half space and infinite element is used to model far filed. To analyze the ground-borne vibration, parameters considered are damping ratio and stratum depth of the supporting soil, depth, and thickness of the tunnel and the moving speed and excitation frequency of the train. Their result showed that moving train loads having non-zero excitation frequencies might induce higher vibrations than the static moving loads.

4 Available Vibration Mitigation Techniques

4.1 Rail Fastener and Rail Pad

Rail fastener keeps the rail at its designated location as shown in Fig. 4. The rail deflection produced can be of large magnitude if flexible fastenings are used. The research has shown that the use of highly elastic rail fastening can reduce the vibrations between 30 to 50 Hz and a higher reduction is observed at 50 Hz.

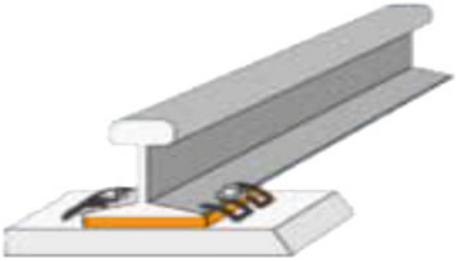

Fig. 4 Rail pad (Rantatalo and Xin 2013)

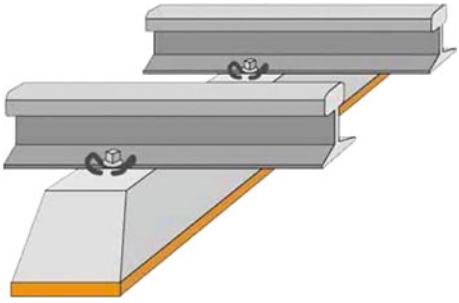

Fig. 5 Under sleeper mats (Rantatalo and Xin 2013)

Rail pads are used between rails and sleepers and are usually made of rubber. They help to reduce fatigue cracking of the sleepers; moreover, it is found that they have a damping effect on the vibrations.

4.2 Under Sleeper Mats

To check the effectiveness of the mats, the padded wooden sleepers of the ballasted track in UK have been replaced by the concrete sleepers with the mats as shown in Fig. 5 (Potocan 2011). Vibration measurement at the lining of the tunnel following track renewal showed that the under sleeper pads were able to prevent any increase of train-born vibration.

4.3 Sub-Ballast Mat

Sub-ballast up to the thickness of 80 can attenuate vibrations in the range of 16–50 Hz (Rantatalo and Xin 2013) where a reduction as high as 20 dB can be reached at 50 Hz. Few types of ballast mat applied on concrete base generated reduction of about 10 dB for frequencies above 40 Hz. Higher attenuation can be observed if mats are placed higher within the ballast. If the thickness of the ballast is increased from 0.3 to 0.6 m in combination with sub-ballast mat, reduction of 4 dB is obtained (Fig. 6).

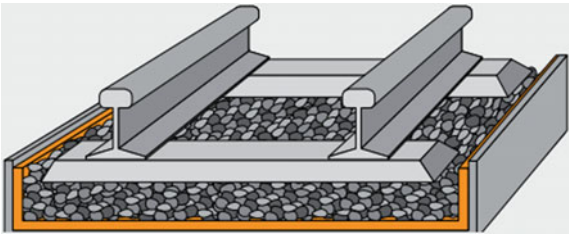

Fig. 6 Sub-ballast mat (Rantatalo and Xin 2013)

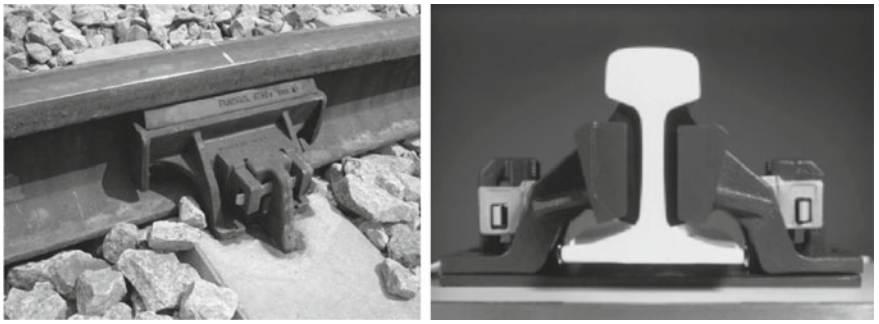

Fig. 7 Pandrol Vanguard system (Rantatalo and Xin 2013)

Sub-ballast mats have proved to be one of the most effective methods of reducing vibration transmission from ballasted track. They isolate the track structure from the supporting foundation and can attenuate the transmission by 20 dB in most of the cases.

4.4 Pandrol Vanguard Systems

The Pandrol Vanguard fastening system (Fig. 7) reduces significantly noise and vibration from underground railways within the constraints of an intensively used small tunnel (Sunley). Recently vanguard system was installed in the Sau Paulo Metro in Brazil and the results were compared with the conventional track system. After the installation of this system, the global vibration level was reduced to 66.2 dBV ("Track report" 2011) at the same frequency and location (Fig. 8). This system has also shown the reduction in the secondary noise measured inside the buildings and was well below the standards set by the Brazilian authority. The natural frequency was 25 Hz prior to replacement.

Afterwards, the natural frequency came down to 16 Hz due to lower-track stiffness causing a vibration diminution in frequency bands between 16 and 25 Hz that was not previously present.

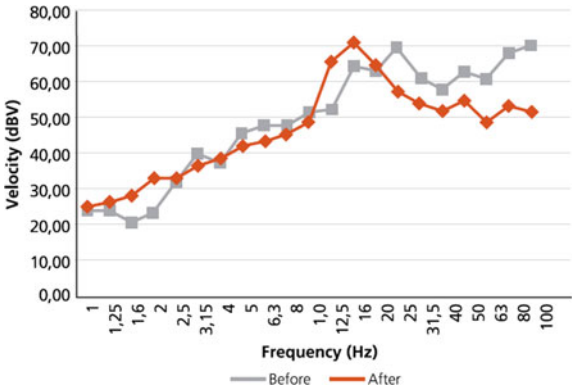

Fig. 8 Vibration measurements ("Track report" 2011)

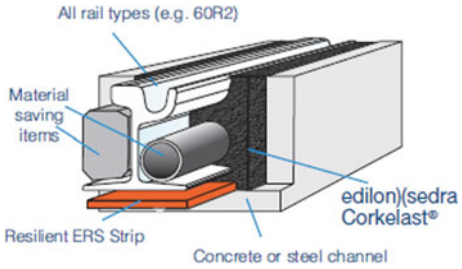

Fig. 9 REMS system (sedra 2015)

4.5 Jet Grouting Technique

Jet grouting is generally done by the cement grout which helps to partially replace the volume of soil loss caused by the tunneling. By doing this between the tunnel and the foundations of a building, the movements affecting the building are significantly reduced. The prominent application of this method can be seen in the tunneling done near the Big Ben clock tower in London (Ng et al. 2008) during the extension of the Jubilee line.

4.6 Removable Embedded Metro System: REMS

The Politecnico di Milano University, (Braghin et al. 2008) studied the dynamic performance of REMS (Fig. 9) through numerical solution of train–track interaction in order to assess its isolation characteristics as well as alignment and gauge variations due to train transit. Their model includes the finite element modeling of track and multi-body model of the metro train. The differential equations of the two subsystems are coupled by the wheel-rail contact forces which are a function of both vehicle and track coordinates.

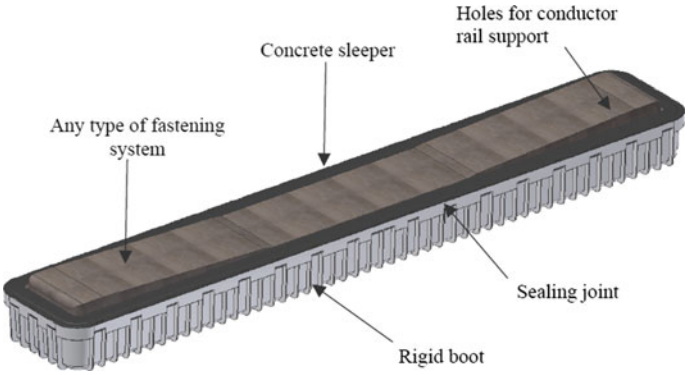

Fig. 10 HAS sleeper (Corre et al., n.d.)

Newmark method of integration is used to integrate the train and track equations. An output of the train–track interaction model includes the displacement of the track and the vibration transmitted to the ground. This system damps out vibrations propagated to the ground but leads to gauge variations which are ten times bigger than those measured on traditional direct fixed tracks.

4.7 High Attenuation Sleeper

HAS is an integrated system dedicated to mitigating ground vibrations (Corre et al. n.d.) generated from rolling stock. Not only does HAS have mitigation properties similar to floating slab tracks (FSTs), it enables tracks to be laid ten times faster. The filling concrete around the sleeper doesn't need to be reinforced. No disruption in the construction method. HAS can be laid in 18 m-long panels using standard installation equipment (Figs. 10 and 11).

Due to the cushion mats under HAS, construction trains can run on the track before concreting. Maintaining HAS is a quick and simple process. If need be, the sleeper can easily be removed from its rigid plastic hull and replaced by a new one. All the system's resilient components—lateral pads, resilient pads, etc.—can be accessed without difficulty (Fig. 12).

The abovementioned vibration mitigation techniques are the most widely used methods both in India and abroad to reduce vibration from the underground movement of the metro trains.

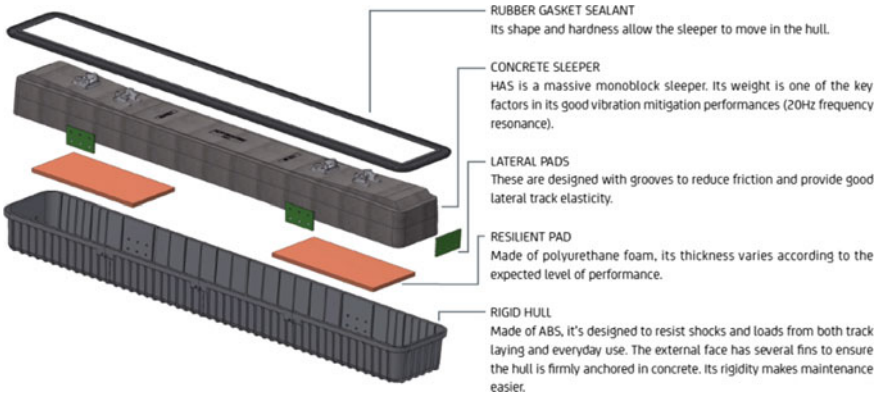

Fig. 11 HAS system (Rail)

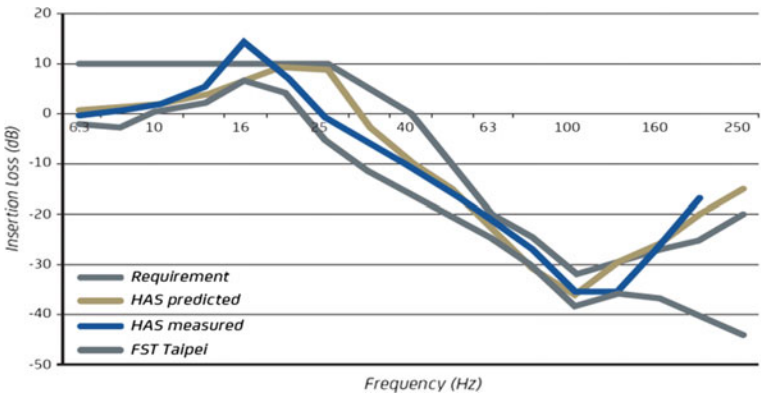

Fig. 12 Effect of high attenuation sleeper (Rail)

5 Conclusions

The ground vibration generated by the subway trains is indeed a practical engineering problem (Yang and Hsu 2006). The review of our study has highlighted the various methods and techniques adopted or implemented worldwide by different researchers to mitigate the underground vibration. The study has revealed that the metro vibration poses no instant danger to the residents; however, it certainly influences the daily life of the residents and those who eventually cannot tolerate.

The study also revealed that vibration generated is in the range of 30–100 Hz, thus, future research should be focused keeping in mind the above frequency range. The finite element modeling technique adopted by some of the authors for the tunnel—soil interaction is bit approximate thus more work is required to be done to incorporate the real situation. The complete wheel-track-soil-tunnel interaction study is done by

few authors (Hussein 2009) and still requires a thorough research to understand the vibration behavior generated by the underground metro.

Moreover, the techniques adopted for the vibration mitigation are not perfect as viewed from the aspect of efficiency and cost especially for the developing economy like India (Goel and Sharma 2016) where infrastructure projects are funded by the outside agency, thus research should also be focused toward more effective and less-costive method.

References

Braghin F, Bruni S, Collina A, Corradi R (2008) Numerical simulation of train-track interaction for the dynamic performance estimation of an innovative metro embedded-rail track system. In: 7th European conference on structural dynamics, EURODYN 2008, Southhampton, E151

Breccolotti M, Materazzi AL, Salciarini D, Tamagnini C, Ubertini F (2011) Vibrations induced by the new underground railway line in Palermo, Italy Experimental measurements and FE modeling. In: Proceedings of the 8th international conference on structural dynamics, EURODYN 2011

Connolly DP, Marecki GP, Kouroussis G, Thalassinakis I, Woodward PK (2016) The growth of railway ground vibration problems—A review. Sci Total Environ Elsevier B.V., 568: 1276–1282

Consolis Rail, Technical report. The HAS system-the solution for urban transport

Corre F Le, Robertson I, Petit C (n.d.) High attenuation sleeper.

COWI (2009) Tunnel engineering. Tunnel Engineering

Dai F, Thompson DJ, Zhu Y, Liu X (2014) Vibration properties of slab track installed on a viaduct. Proceedings of the Institution of Mechanical Engineers, Part F: Journal of Rail and Rapid Transit, 230(1), 235–252

Degrande G, Schillemans L (2001) Free Field Vibrations During the Passage of a Thalys High-Speed Train At Variable Speed. J Sound Vib 247(1):131–144

Degrande G, Schevenels M, Chatterjee P, Van de Velde W, Hölscher P, Hopman V, Wang A, Dadkah N (2006) Vibrations due to a test train at variable speeds in a deep bored tunnel embedded in London clay. J Sound Vib 293(3–5):626–644

Fiala P, Gupta S, Augusztinoviczb F, Degrandea G (2010) A comparative study of different measures to mitigate ground borne noise and vibration from underground trains. Vibac.Hit.Bme.Hu, (July)

Forrest JA, Hunt HEM (2006) A three-dimensional tunnel model for calculation of train-induced ground vibration. J Sound Vib 294(4):678–705

Frederich F (1984) Die Gleislage—aus fahrzeugtechnischer Sicht [Effect of track geometry on vehicle performance]. Zeitschrift fur Eisenbahnwesen und Vekehrstechnik—Glaser Annalen, 108(12): 355–362

Fryba L (1996) Dynamics of railway bridges. Thomas Telford Ltd., London

Galvín P, Romero A, Domínguez J (2010) Vibrations induced by HST passage on ballast and non-ballast tracks. Soil Dyn Earthquake Eng 30(9):862–873

Goel M, Sharma, DRK (2016) An ivestiigation of financial analysis od delhi metro & factors influencing ridership. Int J Res Develop Technol Manage Sci Kailash, 22(4): 17–38

Heckl M, Hauck G, Wettschureck R (1996) Structure-borne sound and vibration from rail traffic. J Sound Vib 193(1):175–184

Hunt HEM, Hussein MFM (2007) Ground-borne vibration transmission from road and rail systems: prediction and control. In: Crocker M (ed) Handbook of noise and vibration control, John Wiley & Sons, Inc, p 1458–1469

Hussein M (2009) A comparison between the performance of floating-slab tracks with continuous and discontinuous slabs in reducing vibration from underground railway tunnels. In: 16th International congress on sound and vibration 2009, ICSV 2009, 1(February)

Hussein MFM, Hunt HEM (2009) A numerical model for calculating vibration due to a harmonic moving load on a floating-slab track with discontinuous slabs in an underground railway tunnel. J Sound Vib 321(1–2):363–374

Jones CJC, Block JR (1996a) Prediction of ground vibration from railways. J. Sound Vibr

Jones CJC, Block JR (1996b) Prediction of ground vibration from freight trains. J Sound Vib 193(1):205–213

Kishore K, Sharma S, Singh K, Kishore N (2017) Effect of underground metro on historical monuments in Delhi. Int J Eng Trends Technol 49(3):158–160

Kouroussis G, Connolly DP, Verlinden O (2014) Railway-induced ground vibrations—a review of vehicle effects. Int J Rail Trans. Taylor & Francis, 2(2): 69–110

Krylov VV, Dawson AR, Heelis ME, Collop AC (2000) Rail movement and ground waves caused by high-speed trains approaching track-soil critical velocities. Proceed Inst Mech Eng Part F J Rail Rapid Transit 214(2):107–116

Ma M, Liu W, Qian C, Deng G, Li Y (2016) Study of the train-induced vibration impact on a historic Bell Tower above two spatially overlapping metro lines. Soil Dyn Earthquake Eng Elsevier 81:58–74

Ming KC, Chiang Lin, C., Rong Lin, Y., and Hao Huang, C. (2016). "Experiments on Vibration Mitigation with a Mass-Spring-Series Model. J Civil Environ Eng 06(05)

Ng C, Simons N, Menzies B (2008) Case study : effect of the Jubilee Line extension on the Big Ben Clock Tower. A short course in soil–structure engineering of deep foundations, excavations and tunnels, Thoams Telford Ltd., London, 357–365

Nielsen JCO (2003) Numerical prediction of rail roughness growth on tangent railway tracks. J Sound Vib 267(3):537–548

Pan P, Shen S, Shen Z, Gong R (2017) Experimental investigation on the effectiveness of laminated rubber bearings to isolate metro generated vibration. Measur J Int Measur Conf. Elsevier Ltd

Potocan S (2011) Vibration protection for Birmingham's Arena Tunnel. 1–4

Rantatalo M, Xin T (2013) Review of countermeasures and regulations for railway induced ground vibrations in tunnels. pp 1–23

sedra, edilon (2015) edilon)(sedra ERS embedded rail system. Haarlem, Netherlands

Singh M, Viladkar MN, Samadhiya NK (2017) Seismic analysis of Delhi Metro Underground Tunnels. Indian Geotech J. Springer India, 47(1): 67–83

Sunley K (n.d.) Track support systems: Pandrol Vanguard on London underground

Track report (2011). J Pandrol Rail Fastening

van Lier S (2000) The vibro-acoustic modelling of slab track with embedded rails. J Sound Vib 231(3):805–817

Vogiatzis KE, Kouroussis G (2015) Prediction and efficient control of vibration mitigation using floating slabs: practical application at Athens metro lines 2 and 3. Int J Rail Trans 3(4):215–232

Yang YB, Hsu LC (2006) A review of researches on ground-borne vibrations due to moving trains via underground tunnels. Adv Struct Eng 9(3): 377–392

Yang YB, Hung HH (2008) Soil vibrations caused by underground moving trains. J Geotech Geoenviron Eng 134(11):1633–1644

Yuan J, Zhu Y, Wu M (2009) Vibration characteristics and effectiveness of floating slab track system. J Comput 4(12):1249–1254

Zhu S, Yang J, Yan H, Zhang L, Cai C (2015) Low-frequency vibration control of floating slab tracks using dynamic vibration absorbers. Veh Syst Dyn 53(9):1296–1314

Construction of Cross-passages Completely Submerged Under Groundwater

Ayush Raj, Ashwani Kumar and Rajesh Kumar Mittal

Abstract This paper is a case study of the construction of cross-passages between South Extension and Lajpat Nagar metro stations of line-7 of phase-III of Delhi Metro. The geological strata at the cross-passages, i.e. CP-18 and CP-19 mainly comprised of silty sand and were completely submerged under groundwater. CP-19 was located below a vacant field and CP-18 was located just below a road junction surrounded by residential houses. Initially, forepoling and TAM grouting were carried at both the cross-passages. At the time of excavation, flowing ground condition encountered at CP-19 and some settlement was also observed at the surface due to ground loss. For stabilizing the ground above CP-19 and to fill any cavity formed because of ground loss, compensation grouting was carried from the top surface. Also during the excavation, TAM grouting was carried on the excavated face of cross-passages to ensure stability of ground inside the cross-passage. At CP-18, due to space constraint and the presence of various utilities, compensation grouting was not possible from the top. Therefore, to encounter the problem faced at CP-19 and to mitigate any risk to the buildings above CP-18, in addition to forepoling and TAM grouting, chemical grouting was carried on the crown of cross-passage to avoid any ground loss. For restraining ingress of water and to provide compressive strength to the ground, polyurethane injection grouting with a very low viscosity was carried. By adopting this methodology, CP-18 was successfully constructed with minimal ground loss and with a maximum settlement of −11 mm observed at the ground surface.

Keywords Cross-passage construction · Submerged underwater · Flowing ground condition · Compensation grouting · TAM grouting · Polyurethane injection grouting

A. Raj (✉) · A. Kumar · R. K. Mittal
Delhi Metro Rail Corporation Limited, New Delhi, India
e-mail: ayush_raj25@yahoo.com

A. Kumar
e-mail: cpm3.track@gmail.com

R. K. Mittal
e-mail: rkmittaldmrc@gmail.com

R. Sundaram et al. (eds.), *Geotechnics for Transportation Infrastructure*, Lecture Notes in Civil Engineering 28, https://doi.org/10.1007/978-981-13-6701-4_19

1 Introduction

The total length covered by metro after the completion of phase-III of project assigned to Delhi Metro Rail Corporation is 329 km. A total of 140 km of the total length is added to the existing network of 189 km in phase-III. In this 140 km, underground twin tunnels of length 53 km (106 km tubes) are constructed in phase-III of the deposit work. The current work discusses about the challenges faced and process used in constructing these underground tunnels.

The network from Mukundpur-shiv vihar also known as line-7 constituted of 58.596 km. Line-7 has 39.479 km of elevated network and 19.117 is km underground network. There are total 38 stations out of which 26 are elevated and 12 are underground. In line-7, four numbers of cross-passage have been constructed between South Extension and Lajpat Nagar stations by NATM methodology. Two cross-passages, namely CP-18 and CP-19 (Fig. 1), amongst the four constructed passages are under groundwater posing the maximum challenge.

The area around the construction site is densely populated and logistically it is difficult to carry out the construction work in these areas. Therefore, the whole construction process requires optimization. Furthermore, any major settlement would have lead into damaging the structures and subsequently, endangering the safety of residents in the vicinity of the construction site. Figure 2 shows the actual location of CP-18 and CP-19, superimposed on Google map.

The geological strata mainly comprised of silty sand with flowing ground condition at CP-18 and CP-19. The permeability of soil encountered at these locations is in the range of 1–9 leugon.

The levels of the top of the crown portion of the two submersed cross-passages, CP-18 and CP-19, from ground level are 21.2 m and 18.6 m, respectively, and levels of groundwater table (GWT) at CP-18 and CP-19 are 18.9 and 16.7 m below the ground level. The GWT, therefore, of 2.3 and 2.2 m above the crown of CP-18 and CP-19, respectively, are shown in Fig. 3.

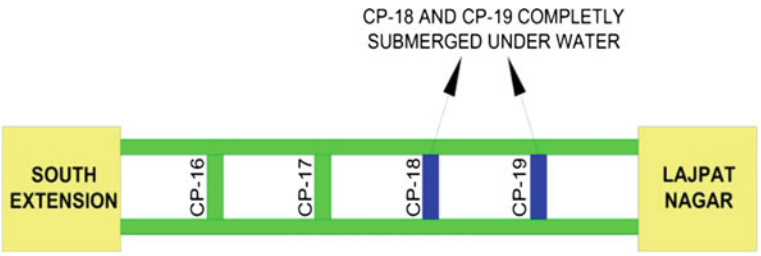

Fig. 1 Schematic diagram of cross-passages between south extension and Lajpat Nagar

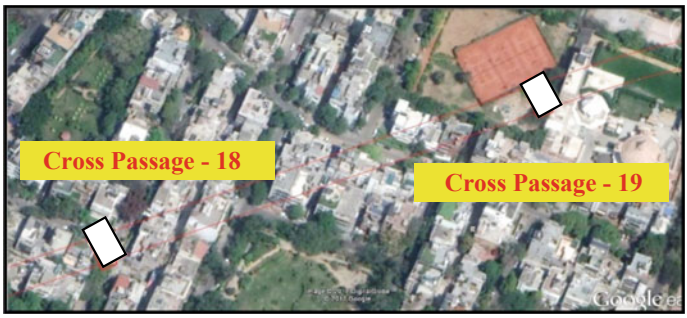

Fig. 2 CP-18 and CP-19 located in densely populated residential area

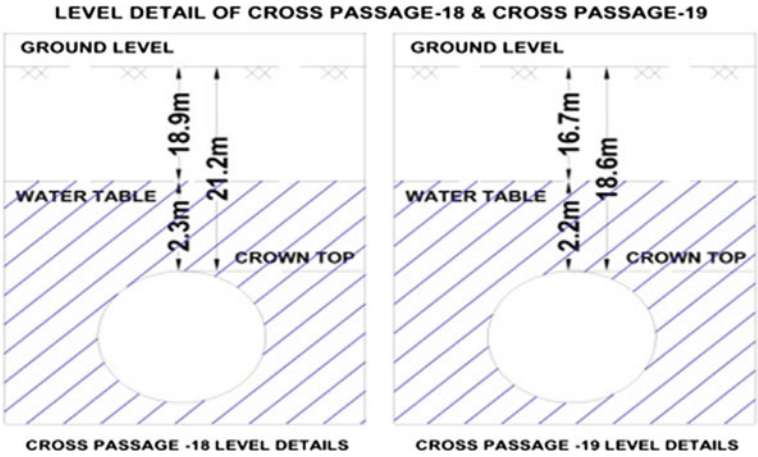

Fig. 3 CP-18 and CP-19 completely submerged under groundwater

2 Initial Construction Methodology for CP-18 and CP-19

The formulization of the construction methodology of cross-passage CP-18 and CP-19 between South Extension and Lajpat Nagar metro stations is carried in such a way that any kind of damages to the nearby buildings is avoided which can ensure the safety of the people residing near the locations of CP-18 and CP-19. It is achieved by minimizing the settlement of ground above cross-passages locations. Ensuring the safety of workers is also of utmost importance in case of any collapse inside cross-passages during the construction phase.

Initially, it is decided that forepoling (Boehm 2014) and Tunbe-A-Manchette (TAM) grouting at CP-18 and CP-19 (as shown in Fig. 4) are performed before commencing the excavation of these cross-passages. Hausmann (1984) mentions the main principles used in ground modification. DMRC (2017) has compiled the method sequence of cross-passage construction under water level which is widely

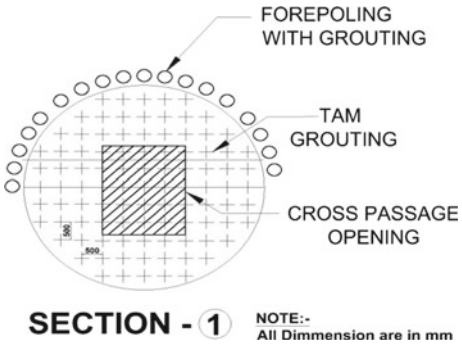

Fig. 4 Forepoling and TAM grouting scheme for CP-18 and CP-19

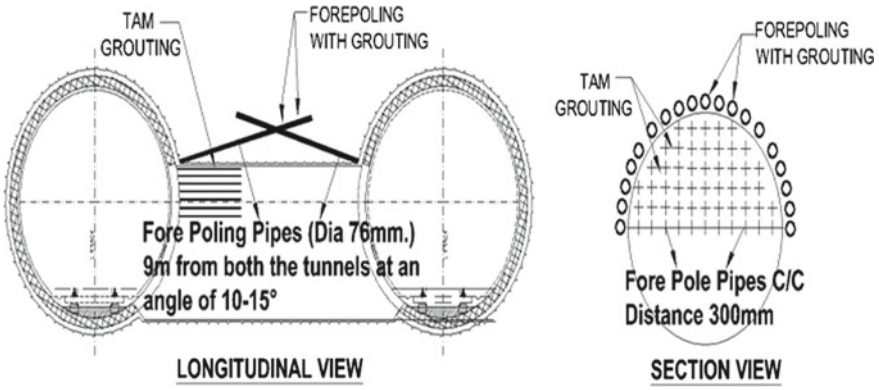

Fig. 5 Forepoling at CP-18 and CP-19

referenced in the current work, apart from that general processes are dealt in brief by Babu in the NPTEL course.

2.1 Forepoling

Ground losses are avoided using insertions of single-layered 76 mm Ø forepoles of 9 m in lengths, at an angle of 10–15° with 300 mm C/C spacing, during the excavation of cross-passages, as shown in Fig. 5. These pipes are inserted in both the tunnels and afterwards, cement is grouted in the inserted pipes. As a result, an umbrella is formed above the crown excavation line of the cross-passages (Boehm 2014). The main purpose of this umbrella of pipes and grout on the top of the crown portion is to avoid sudden ground loss from the top which can result in the ground settlement.

2.2 TAM Grouting

It is necessary to ensure the safety of workers inside the cross-passage by restricting collapses during the excavation. This is achieved by stabilizing the ground through TAM grouting at the excavation face. Grouting is carried by inserting TAM pipes of 50 mm Ø from both the tunnels before commencing the excavation. C/C spacing between TAM pipes is kept less than 500 mm. To ensure the overlapping between the grouting, length of TAM pipes is kept at 6 m. Figure 6 shows the TAM grouting scheme carried during the construction of CP-18 and CP-19.

TAM pipes have 50–75-mm rubber sleeves fixed on them at every 400 mm. These sleeves act as non-return member to the grout holes beneath them. Three grout holes are provided at 120° underneath the sleeves.

After insertion of TAM pipes, consolidation grouting is carried. Grout mix of cement, bentonite and water with varying water–cement ratio is pumped in different stages (as shown in Table 1) using piston type grout pump (Hany pump). The water–cement ratio is in accordance with the strata and site requirement. Deformation in tunnel lining is avoided by gradually increasing the grout pressure from 0.0 to 3.0 bars.

Figure 7 shows the actual site photograph of forepoling and TAM grouting carried at various locations of cross-passage. Pneumatic drilling machine is used in the drilling work for insertion of foreploes and TAM pipes.

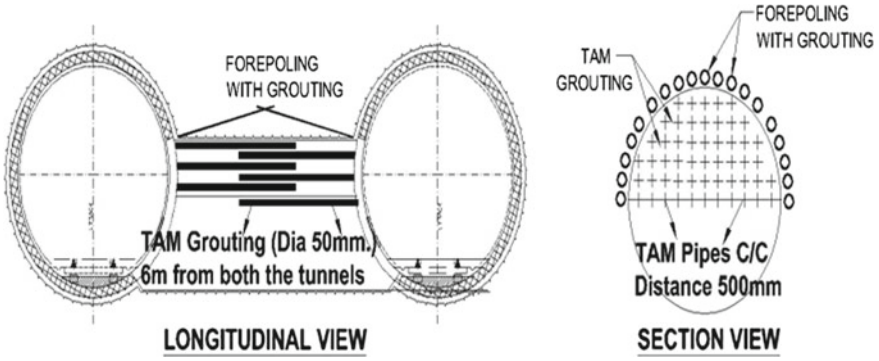

Fig. 6 TAM grouting at CP-18 and CP-19

Table 1 Grout mix in different stages

Grouting stage	Cement (kg)	Water (litre)	Bentonite (kg)
Stage I	50	200	4
Stage II	50	150	4
Stage III	50	100	4
Stage IV	50	50	4

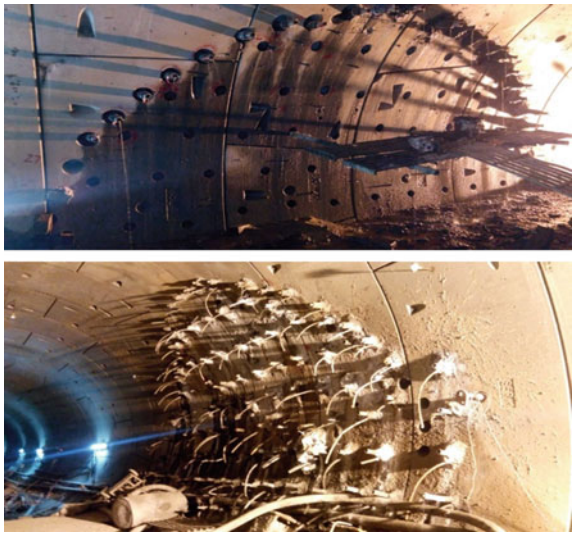

Fig. 7 Forepoling and TAM grouting at site

3 Problem Faced During Construction of CP-19

The construction of these cross-passages is very challenging. The excavation process of CP-19 stared first because it is located just below an open ground as compared to CP-18 which is surrounded by residential houses.

Two lattices at 500 mm c/c are successfully installed after the forepoling and ground stabilization by TAM grouting (as mentioned above). A sudden slush ingress in huge quantity is encountered from the crown of cross-passage and a cavity of around 200 mm is observed on the ground just above CP-19 location. Since CP-19 is located beneath an open ground, no significant damage to any of the property is reported by the sudden ingress of slush, but the excavation activity is stopped and sequence of excavation is again deliberated.

3.1 Remedial Measure for Ground Loss

To avoid further ground settlement and to fill any cavity formed because of slush ingress, cement grouting is carried in the affected area by inserting 12 m long TAM pipes in a grid pattern from the top of CP-19 as shown in Fig. 8. Approximately, 875 cement bags (50 kg/bag) are grouted above CP-19. Table 2 indicates the number of bags grouted in each pipe.

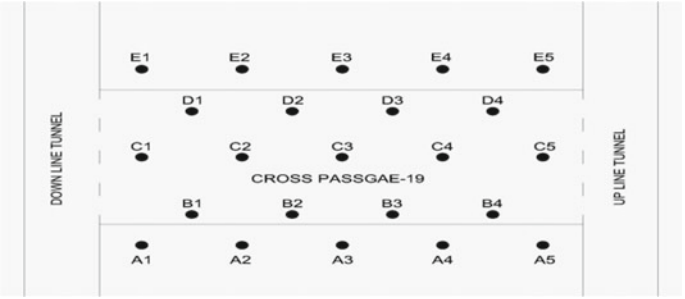

Fig. 8 Plan showing TAM grouting carried from the ground above CP-19

Table 2 Number of bags grouted in different pipes

GRID	1	2	4	5
A	30	29	30	13
B	50	49	71	
C	64	18	19	79
D	54	11	16	
E	24	39	20	21

3.2 Change in the Construction Methodology of CP-19

The detailed deliberation between DDC, site team and DMRC design department lead to a revised construction scheme proposal for both the cross-passages after which the excavation recommenced. To reduce the flow of slush and to ensure the safety of workers, excavation is carried in parts and lattice is erected and shotcreted in pieces. Central hump is always maintained in front of the excavation face to avoid face collapse and additional TAM grouting is carried from front face after every 3 m and also from the locations where slush ingress is encountered. During the entire excavation, a total of 7761 cement bags (50 kg/bag) are grouted to support and stabilize the ground. Figure 9 shows the sequence of excavation followed at CP-19 by applying the precautionary measure mentioned above.

Also, prior to commencement of excavation for benching, 32 mm Ø forepoles of 3 m are inserted at an angle of 45° to support ground during excavation of benching. As shown in Fig. 10, 32 mm Ø forepoles are inserted at the junction of overt shotcrete and temporary benching.

Further, minimal exposure of soil is ensured during the excavation apart from adopting above methodology for the construction of CP-19. The entire process starting from excavation to lattice erection to final shotcrete is completed without any stoppage once the remedies are included in the construction plan.

Figure 11 is the site photograph taken after successful excavation of CP-19.

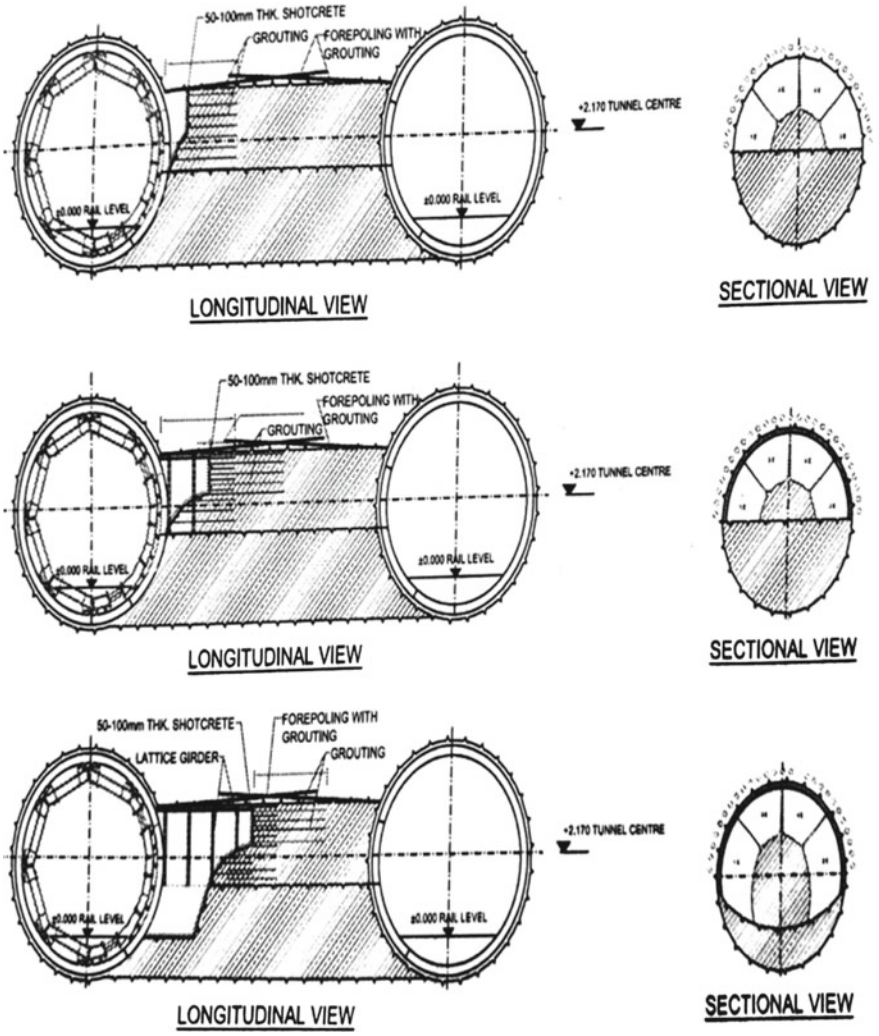

Fig. 9 Revised construction sequence at CP-19

3.3 Contingency Measures

Before the start of any excavation, 1–2 m^3 of concrete is always kept at cross-passage location to immediately seal and stop any slush ingress. Sufficient numbers of gunny bags filled with dry soil are also kept near cross-passages which can be used in case of a sudden collapse from the face of the crown.

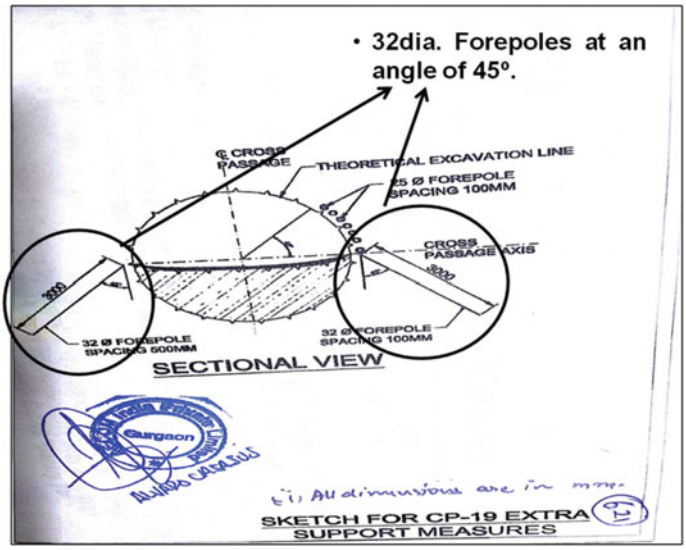

Fig. 10 Forepoling during benching excavation

Fig. 11 Successful excavation of CP-19

4 Modification in Construction Methodology of CP-18

The location of CP-19 is beneath an open ground and its entire construction is carried by supporting ground with forepoling, stabilizing the soil by TAM grouting and complying to additional precautions as mentioned above. CP-18 is located beneath a junction of public road and is surrounded by residential houses in every direction (as shown in Fig. 12). Settlement like CP-19 can lead to major damage to the adjacent properties and can also prove fatal to the lives of residents.

In view of the safety of people and infrastructure in the region adjacent to CP-18, apart for forepoling, TAM grouting and additional precaution adopted for construction of CP-19, chemical grouting is also performed to enhance the stability of the ground in the vicinity of CP-18. During the entire excavation, a total of 3112 cement bags (50 kg/bag) are grouted to support and stabilize the ground using 10930 kg polyurethane grout.

4.1 Chemical Grouting in CP-18

Ground near CP-18 mainly constituted of silty sand having a permeability of 1–9 lugeon. The ground conditions are similar to CP-19 and have a flowing tendency. Considering the location constraint, very low permeability of soil and safety during

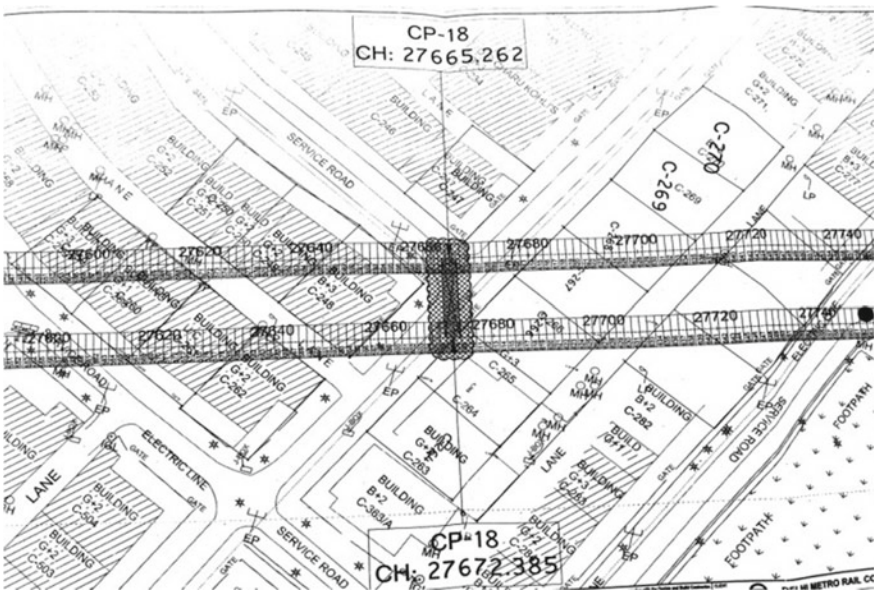

Fig. 12 CP-18 at road junction and surrounded by houses—Topographical map

Table 3 Technical data of product used

S. No.	Properties	Value	
		Polyurethane resins	Catalyst
1	Appearance (colour)	Brown liquid	Clear liquid
2	Viscosity at 25 °C (mPas)	25–50	25–35
3	Density at 25 °C (kg/l)	1.1	0.97

Table 4 Physical properties of end product

S. No.	Properties	Value
1	Compressive strength @ 3 days (Mpa)	3.0
2	Flexural strength (kPa)	1691

excavation, polyurethane injection grouting with a very low viscosity is carried. The resin of the grout used reacts with water to form rigid hydrophobic foam which restrains/diverts water from entering CP-18. Polyurethane resin is used with catalyst. Technical data of the material used and physical properties of the end product are tabulated in Tables 3 and 4.

As tabulated in Table 4, apart from restraining water the resin used also provides 3–4 MPa compressive strength to the soil. The strength provided to the soil helps in ensuring the safety during excavation and also eases the excavation activity by reducing the flowing tendency of soil.

For injecting polyurethane grout, self-drilling anchors (SDAs) 32 mm Ø are inserted to a length of 7.5 m from both the tunnels at an angle of 10–15°, i.e. parallel to inclination of forepoling. The SDAs are provided with perforations of 2–3 mm Ø at an interval of 750 mm along its length, with a non-return valve at it end through which polyurethane grouting is carried. As shown in Fig. 13, spacing of SDAs is kept 300 mm c/c in two rows with zigzag pattern. The first row is inserted 300 mm above the already installed network of forepoling and the second row is inserted 200 mm above the first row.

4.2 Contingency Measures During Construction

In addition to the contingency measures adopted at CP-19, five numbers of weep holes of 76 mm Ø are provided alongside the section of the cross-passage from both the tunnels to divert groundwater outside the curtain formed by polyurethane grouting. Also extra TAM grouting is carried outside the boundary of cross-passage from TAM pipes inserted as shown in Fig. 13.

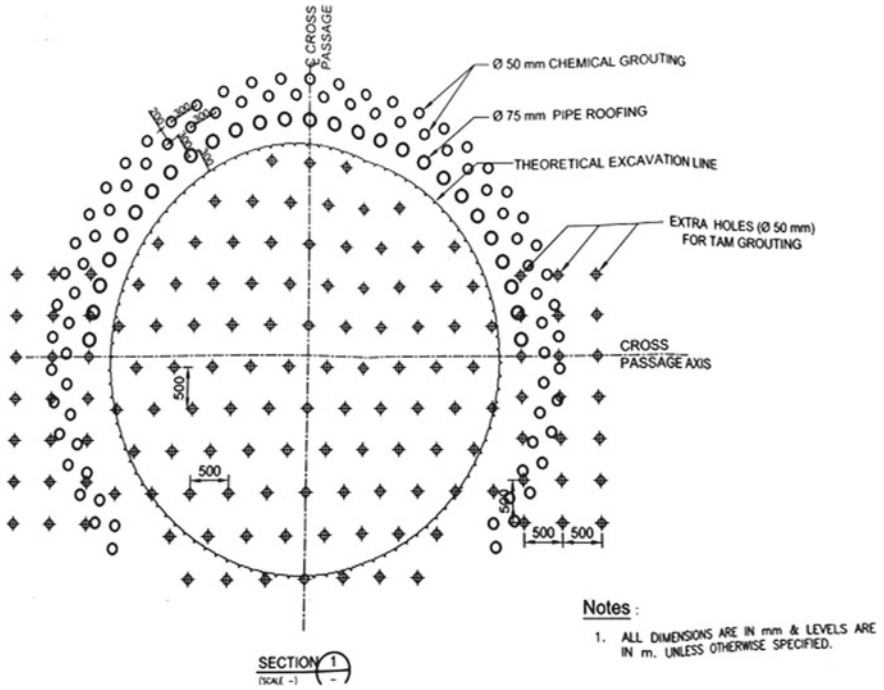

Fig. 13 Revised construction sequence at CP-19

5 Instrumentation Monitoring at CP-18 and CP-19

During the entire construction activity, intensive instrumentation monitoring is carried at the ground surface near the vicinity of CP-18 and CP-19 and also inside the tunnel and cross-passage.

To ensure the safety of houses coming in the influence zone of cross-passages CP-18 and CP-19, on the wall of the houses bi-reflex targets, tiltmeter, crack meter and building settlement markers are installed as shown in Fig. 14. To monitor the settlement of the ground, ground settlement markers are installed. To monitor the movement of excavated surface of cross-passages and tunnel lining segments, bi-reflex targets are installed on the lining segments and shotcrete surface of cross-passages as shown in Fig. 15. The readings are taken after every 12 h by dedicated team of surveyors and depending on the situation encountered during construction, the frequency of monitoring is sometimes reduced to even 3 h.

Fig. 14 Instruments (BTs, CM, TM) on houses

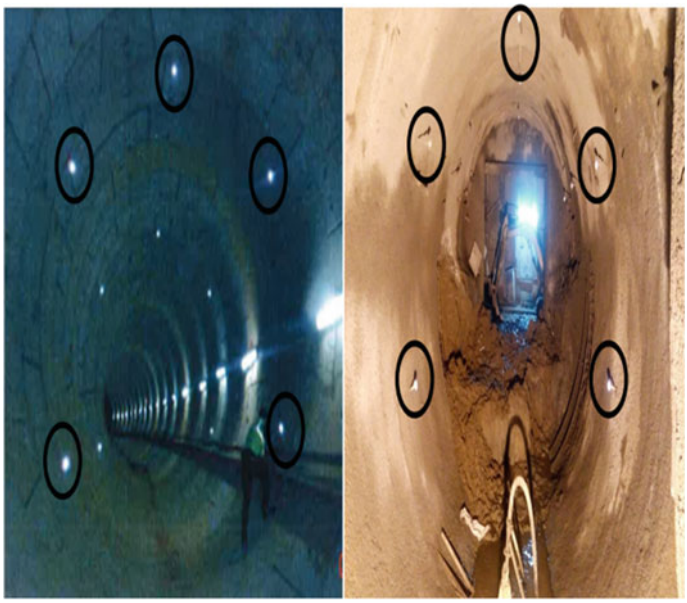

Fig. 15 BTs inside tunnels and CPs

6 Conclusion

CP-18 and CP-19 are successfully constructed by adopting the above methodology and is functional. The settlement observed above CP-19 is restored to its original condition. By using polyurethane grouting, the maximum settlement observed in ground settlement marker above CP-18 is only −11 mm and no damage is noticed to the adjacent houses.

References

Boehm K (2014) Advance forepoling system. NATM Seminar, Sau Paulo, Brazil
Delhi Metro Rail Corporation Limited DMRC (2017) Method statement for cross passage construction under water level, Technical Report
Hausmann MR (1984) Engineering principles of ground modification
Toth A (2015) Tunneling and underground construction technology—ground improvement

Critical Appraisal of Foundation and Substructure Code for Highway Bridges (IRC:78-2014)

Alok Bhowmick

Abstract Harmonization of structural design codes in Europe has been successfully done, where the process culminated in 2010 after 25 years of long and dedicated effort by a group of experts from EU commission. Similar philosophical changes in American codes occurred in the late 1990s and early 2000s through a completely different process. Indian Roads Congress (IRC) is working for more than 15 years now to harmonize the IRC codes pertaining to highway bridge design to limit state philosophy. Significant progress has already been made in this regard. The code on Foundation and Substructure (IRC:78-2014) is, however, still maintaining the working stress philosophy of design and yet to fall in line with the rest of the suite of codes. The philosophical difference between limit state version and working stress version presents a great challenge as well as some confusion in this transition phase. In this paper, a critical appraisal of the current provisions of IRC:78-2014 is highlighted. Inconsistencies between this code and other published codes of IRC are brought out. Some of the contentious provisions in the code which quite often creates confusion to structural and geotechnical engineers in the design of bridge foundations are also highlighted.

Keywords Foundation · Allowable settlement · Liquefaction · Geotechnical investigation

1 Background

The Indian Roads Congress (IRC) Standard Specifications and Code of Practice for Road Bridges in India was first published in the year 1937. Successive revisions over the years reflected incremental improvements, but unfortunately, the Indian codes have not kept up pace with the worldwide explosion of knowledge and advances in new technology. The gaps between national and international codes are getting wider and wider as technology advances even more rapidly. IRC codes therefore need to

A. Bhowmick (✉)
B&S Engineering Consultants Pvt. Ltd, Noida, Uttar Pradesh, India
e-mail: bsec.ab@gmail.com

R. Sundaram et al. (eds.), *Geotechnics for Transportation Infrastructure*, Lecture Notes in Civil Engineering 28, https://doi.org/10.1007/978-981-13-6701-4_20

be updated on a regular basis, on a fast track, for durable, safe and sustainable design of structures.

IRC:78 was first published in July 1980 as Part 1—General Features of Design (covering up to clause 706 of the current code). It was decided to bring out the Part-II of the code subsequently covering the design and construction of foundation (covering clause 707 onwards of the current code). The first revision to the code was published subsequently in December 1983, as a unified code incorporating Part-II. The second revision of the code was published in November 2000. Major amendments were brought into this code in 2003 with regard to seismic provisions. Third revision of this code was published in 2014.

IRC is working for more than 15 years till now to harmonize the suite of codes pertaining to bridges and converting them from working stress (WS) to limit state (LS) philosophy. Significant progress has already been made in this regard. Most of the IRC codes pertaining to structural design have already been upgraded to LS philosophy. The code on Foundation and Substructure (IRC:78-2014) is, however, still maintaining the WS philosophy. The upgradation is presently on the anvil, and it is expected that this code will also be in sync with the rest of the codes soon. Till such time, the bridge engineers have to deal with the contradictions and conflicts that exist between IRC 78 and rest of the bridge design codes.

Carrying out the changes in the code from WS philosophy to LS philosophy, particularly for foundation design, is not an easy task. This change in design philosophy would be a significant departure from the prevailing practice, and it would require a herculean effort from code makers to cross over the usual resistance for change from practicing engineers, for fear of unknown.

In this paper, a critical appraisal of the provisions of IRC:78-2014 is made in its present form. Inconsistencies between this code and other published codes of IRC are highlighted. Some contentious provisions in the code, which quite often creates confusion to structural and geotechnical engineers in the design of foundation are highlighted. The paper also assesses the implications of introducing limit state philosophy for geotechnical design in IRC codes.

2 Scope and Coverage of the Code

This code deals with the design and construction of foundations and substructure for road bridges. The term "road bridges," is a generic term used in IRC codes for all types of highway structures.

Type of structures covered in IRC code is spelt out in IRC:5-2015. Clause 102.1 of IRC:5 classifies the bridges on the basis of function, as follows:

(a) River Bridge/Bridge over stream
(b) Viaduct
(c) Flyover
(d) Grade Separator

(e) Road Over Bridge (ROB)
(f) Road Under Bridge (RUB)
(g) Foot Over Bridge (FOB)
(h) Underpasses
(i) Subways
(j) Overpasses

Foundation for all these types of structures should ideally form a part of IRC:78. However, the codal clauses at present cover only structures under items (a) to (f) and (j). There is no provision in the code regarding design of Underpasses, Subways, and FOBs. Such types of structures are under construction all over the country. Underground (UG) structures have features that make their behavior distinct from above surface structures. Construction of UG structures may involve deep excavations, with sheet piles/diaphragm walls/soil anchors/braced excavations. It is important to include design provisions for UG structures in IRC:78 or supplementary guidelines be prepared by IRC to cover these structural elements

In order for IRC:78 to be consistent with current structural design practice, the scope and coverage of this code would require complete change by the introduction of LS philosophy with partial load factors and material safety factors. Provisions of Euro Code (EC7) on Geotechnical Design is an excellent reference standard and should be considered by IRC code committee for emulation in this regard. Euro code EC7 is in two parts, namely:

(a) Part 1: General Rules
(b) Part 2: Ground Investigation and Testing

Part 1 of EC7 has 12 sections, which are as under:

- Section 1: General
- Section 2: Basis of Geotechnical Design
- Section 3: Geotechnical Data
- Section 4: Supervision of construction, monitoring, and maintenance
- Section 5: Fill, Dewatering, ground improvement, and reinforcement
- Section 6: Spread Foundations
- Section 7: Pile Foundations
- Section 8: Anchorages
- Section 9: Retaining Structures
- Section 10: Hydraulic Failures
- Section 11: Site Stability
- Section 12: Embankments

Part 2 of the code has six sections, which are as under:

- Section 1: General
- Section 2: Planning and reporting of ground investigations
- Section 3: Drilling, Sampling, and GW measurements
- Section 4: Field tests in soil and rocks
- Section 5: Laboratory tests in soil and rocks

- Section 6: Ground investigation report

In addition, there are a number of informative Annexes in EC-7 to supplement. It is a well-structured and comprehensive code with wide coverage of all aspects of foundation design, including the soil–structure interaction. Admittedly, the conversion of present code to limit state mode is a huge challenge. However, this is a bitter pill to be swallowed by the B-3 committee of IRC for harmonization of this code with other codes.

3 Contentious Provisions in the Code

3.1 Geotechnical Issues

3.1.1 Clause 701.4.4: Definition of "Safe Bearing Capacity"

"Safe bearing capacity" is defined in this clause as "net safe bearing capacity" plus "original overburden pressure." The term "original overburden pressure" is not clearly defined in the code, which often leads to confusion and misinterpretation by practicing geotechnical/structural engineers. For scouring river bridges, the bed level is not permanent and during floods, there will be scour around foundation. The confusion is therefore whether the "original overburden pressure" should be calculated with respect to:

(a) Original bed level at the time of boring for investigation or
(b) Maximum scour level (i.e., $2d_{sm}$ below HFL) or
(c) Average scour level (i.e., d_{sm} below HFL)

Figure 1 attached shows the various interpretation of the term "original overburden pressure."

"Overburden pressure" is an important and sensitive design parameter for SBC. It has direct impact on gross SBC calculations and indirect impact on the net safe bearing capacity, since this term is used for the estimation of allowable settlement also. There can be a significant difference in the results depending upon which of the above three assumptions is made by the geotechnical engineer. Therefore, greater clarity in the definition of SBC should be there in the code.

3.1.2 Allowable Settlement for SBC Calculations

- What should be the allowable settlement for bridge foundation?
- Which loads are to be considered for calculation of allowable settlement of foundations?

The above questions do not have suitable answers in IRC:78. Clause 706.3.2.1 of the code mentions about the allowable differential settlement between the two

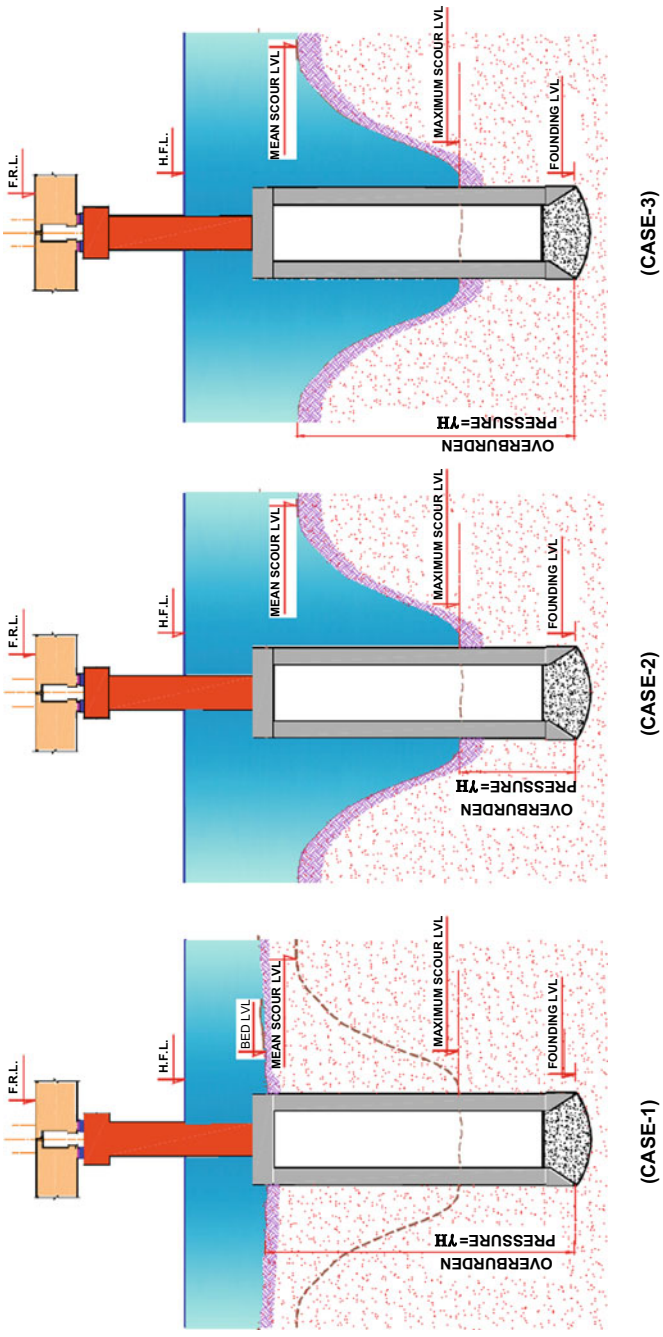

Fig. 1 Various interpretations of "Original overburden pressure" for SBC calculations

adjacent foundations (i.e., 1 in 400), from consideration of serviceability of the bridge structure. Clause 706.3.2.2 states that for structures sensitive to differential settlement, the tolerable limit has to be fixed for each case separately.

It is well recognized that the stability and safety of a bridge depend more upon the distortion of the structure as a result of differential movements of the foundations, rather than upon the absolute magnitude of the overall settlement of the foundation. Experience has shown that bridges can accommodate more settlement and/or rotation than traditionally allowed or anticipated in design of Buildings. Geotechnical engineers responsible for the prediction of SBC for bridges rarely take cognizance of this important clause. Mostly, SBC is derived assuming a fixed allowable settlement for the foundation (which ranges from 25 to 100 mm), without giving importance to the span length, statical system of the bridge, type of structure, and its sensitivity to settlement. This leads to a very conservative and uneconomical design.

In case of bridges, a large fraction of the total load in foundation is dead load and imposed dead load (i.e., to the tune of 80–90%). Most of the dead loads are going to act during the construction stage itself, when the superstructure is yet to be cast/erected. Instantaneous settlements caused by such loads have no consequence in the serviceability of the bridge structure. Therefore depending upon the span length, the statical system of superstructure, the allowable settlement should be decided at the end of the construction period. Only post-construction settlement needs to be considered for geotechnical purpose. Larger total settlement may be allowed.

3.1.3 Clause 704: Sub-Surface Exploration

Quality geotechnical investigation is a pre-requisite for safe and economical design of foundations. Globally, over the years, substantial progress has been made in particular, in the developed world with regard to quality, adequacy, and appropriateness of the geotechnical investigations. On the other hand, most of the investigations in India are lagging behind for a variety of reasons. The practice in India varies very widely. In terms of field investigations, the most primitive equipment to fairly sophisticated equipment are in use at present. Unfortunately in majority of the cases, the practice is nearer to the primitive one. Similarly in the laboratory testing also the practices widely vary. There is very little standardization and there are no requirements of accreditation of investigation agencies. The author is of the view that the code needs to address the following issues:

(a) Code should mention about the need for accreditation of GI firms, which should be made compulsory for bridges. Grading of GI firms depending on the capacity, size/turnover/resources may be done, so as to relate the quality needs as per size and importance of the project.
(b) Detailed procedure for ground investigation and testing should be included in the code, in line with Part 2 of EC-7.

3.1.4 Clause 708.4.2: Procedure for Calculation of Side Earth Resistance of Well Foundation

Clause 708.4.2.1 of the code deals with the side earth resistance for well foundation passing through and resting on sandy or clayey soils. The clause states that "*The side earth resistance may be calculated as per guidelines given in Appendix-3. The use of provisions IRC:45 may be used for pier well foundation in cohesion less soil*".

The above clause is quite confusing and its interpretation quite often leads to the difference of opinion between the designer and proof checker causing inordinate delays in design finalization. One interpretation of this clause is that the side earth resistance can be calculated as per formulas given in Appendix-3. For pier well foundations passing through and resting on cohesionless soil, IRC:45 may also be used. This means that for pier wells on cohesionless soil, the designer has choice to adopt either Appendix-3 or IRC:45-1972. Alternative interpretation is that for pier wells in cohesionless soil, only IRC:45-1972 is permitted in the code. Third interpretation is that for pier wells in cohesionless soils; both the methods are to be followed and design shall satisfy worst of these requirements. The confusion is further compounded in Appendix-3 of the code, wherein the factor of safety over ultimate pressure is given for Pier Wells in "cohesive soils" only, giving the impression that for cohesionless soil, provisions of IRC:78 are not applicable.

Author is of the view that code should avoid prescribing two methods for side resistance calculations. IRC:45-1972 is an outdated code which has not been revised since its first publication. It would be prudent to withdraw this code and delete reference to this code in IRC:78.

3.1.5 Clause 709.3.1: Design Approach for Piles Socketed in Intermediate GeoMaterial and Rock

This clause specifies two methods for socketed piles and stated in Appendix-5 of the code. Method-I is applied when cores of rock sample can be taken and core recovery, as well as RQD data can be established and also UCS, can be established by laboratory tests. Method-II is applicable where strata are highly fragmented with cores and/or core testing results are not available. In this method, shear strength values used for the calculation are related to extrapolated SPT values.

There appears some fallacy in the formulation of the pile capacity. For Method-I, the ultimate shear strength of rock along socket length, 'C_{us}' is given as '$0.225\sqrt{}$qc' subject to a limit of 3 Mpa. For Method-II, the shear strength is related to average 'N' value of socket portion. In many practical situations, author faced a situation where method-II gives a higher capacity as compared to Method-I, since the value of 'C_{us}' in case of method-II is not restricted to '$0.225\sqrt{}$qc'.

3.1.6 Liquefaction of Soil

Liquefaction susceptibility of soil is not addressed in IRC:78. There is a need to address this important consideration holistically. Following aspects in this regard needs to be included in the code:

a. Setting up of a simplified design procedure for the evaluation of liquefaction potential of the soil at bridge locations.
b. Preparation of a detailed guideline on design of bridge foundations in liquefiable soils. This may include recommendations on ground improvement techniques, considerations for liquefaction induced lateral spreading and its impact, neglecting skin friction in liquefiable portion of soil in case of pile foundation, considering negative skin friction in the zone of liquefiable soil, design for lateral loading in the liquefiable zone.

3.2 Issues on Loads, Load Combination, and Structural Design/Detailing Provisions

3.2.1 Loads and Load Combinations

Clause 706.1.1 of the code gives the loads, forces, and their combinations. The clause is ambiguous and in conflict with the corresponding provisions of IRC:6. As per this clause, the load combination given in IRC: 78 is to be followed for structural design of foundation as well as for the stability checks on foundation. Clause 706.1.2 gives increase in permissible stresses in various members under seismic/wind combinations.

Footnote number (9) below Table B.4 of IRC:6 on the contrary states that the structural design of foundation shall be based on limit state philosophy with load combination as given in Table B.4. Load combination is given in IRC:78 shall be followed only for checking base pressure under foundation till such time when IRC:78 changes its philosophy from working stress design approach to limit state approach.

Clause 202.3 and Table 1 of IRC:6 add further confusion to the whole issue. As per this clause, Table 1 load combination shall be adopted for working out stresses in the members. Since there is no provision/scope for working stress design in any of the material codes (IRC 112, IRC 24, IRC 22), this table has become redundant.

Principle difference between the two set of load combination is as shown in Table 1.

The author is of the view that Table 1 load combination of IRC:6 should be shifted to IRC:78, which can be followed for base pressure checks in the interim period till IRC:78 is upgraded to limit state status. Present load combination available in IRC:78 is outdated and should be deleted.

Table 1 Contradiction in load combinations between IRC:78 and IRC:6

Load combination as per IRC:78	Load combination as per Table 1 of IRC:6
1. 100% live load considered under seismic load combination	1. 20% live load in load combination with seismic considered. 50% live load considered under load combination with temperature gradient
2. Snow load and live load not combined in any load combination	2. Snow load and live load combined
3. SV loading and congestion factor loadings not included in load combination	3. SV loading and congestion factor loadings not included in load combination
4. Vehicle collision load, temperature, deformation effects and grade effects not considered	4. Vehicle collision load, temperature, deformation effects and grade effects considered
5. Hydraulic loads and buoyancy considered with accidental load combination	5. Hydraulic loads and buoyancy not considered in load combination with accidental loads

3.2.2 Stability Checks

Clause 706.3.4 of the code provides factor of safety against sliding and overturning for open foundations. Factor of safety against uplift is not specified in this clause. There are situations when foundations may be subjected to uplift. For underpass structures, check against floatation is necessary. Hence, uplift shall also be covered.

3.2.3 Structural Design and Detailing Provisions

IRC 78 has many provisions pertaining to structural design and detailing, which is in conflict with the current provisions of relevant IRC codes. Structural design of substructure and foundation elements is strictly not within the purview of this code and ideally these provisions are supposed to be transferred to respective loading code or material-based codes (such as IRC:112 (concrete), IRC:24 (steel), IRC:40 (Masonry) and IRC:6 (Loads and Load Combination)). Details of these clauses are given in Paragraph 4 below. IRC has already taken steps in this direction, and it is hoped that these amendments will be reflected in the code soon.

3.3 Issues on Hydrology, Hydraulics Including Scour

Determination of general scour during a flood (in the absence of any bridge) is a difficult task due to the fact that a large numbers of geometric, flow, and sediment parameters, e.g., flood peak, duration of flood, bed and plane forms of river, sediment transport, human activities, etc. govern general scour.

Estimation of local scour in the vicinity of piers and abutments poses another added challenging problem to hydraulic engineers. Whereas, any underestimation of scour will result in bridge collapse, overestimation of scour leads to escalation of cost. The best way of assessing the depth of scour in a river is to observe the same during the passage of highest flood.

Real-time scour has been measured at bridge sites by USGS by deploying instruments like fathometer/ADCP and other electronic devices. The observed scour has been verified with predicted scour for proving mathematical model, e.g., HEC-18. Unfortunately, with very little field data regarding bridge scour together with the corresponding flow and geometric parameters governing scour available in India, it has not been possible to prove the various mathematical models used for estimation of scour. Design engineer, therefore, generally relies on the use of empirical formulae for the calculation of scour depth.

Provisions for estimation of general and local scour in IRC:78 is oversimplification of the complexity involved. IRC method of estimation of scour is based on Lacey's regime theory, which was developed by Lacey (1930) and Inglis (1944), based on observations made on canals in India and Pakistan with regime flow condition. There are several limitations in Lacey's method for application in bridge scour calculation. It ignores many parameters which govern the scour around bridge piers. Lacey did not consider the sediment transport and threshold condition of bed motion (Kothiyari 2007; Mazumder 2006; Garde and Kothiyari 1998).

Using Lacey's formula for all types of strata, including clayey and bouldary strata is an abuse of the Lacey's regime theory. Clause 703.2.2.2 refers to Appendix-1 for calculation of mean scour depth, in the absence of any data on scour for such materials, but Appendix-1 covers only formulas for clayey material and not for bouldary strata.

Author is of the firm view that a single comprehensive state of the art document dealing with hydrology and hydraulics of river bridges, covering all possible aspects, should be published by IRC, for the benefit of bridge engineers.

3.4 Depth of Foundation for Bridges in Near-Vicinity of Existing Bridges

Clause 705.1 of the code states that "In case of bridges where the mean scour depth 'd_{sm}' is calculated with Clause 703.2, the depth of foundation shall not be less than those of existing structures in the vicinity." This clause has been misused and abused by many bridge engineers in recent past. The question that remains unanswered in this clause is "what should be considered as 'in the vicinity'?"

In one of the recent major river bridge projects over river Ganga, the Authority's Engineer has demanded that founding level of the bridge foundation shall have to be kept same as that of the next bridge on the stream, located 25 km downstream. The matter could be amicably resolved through persuasion and the Authority's Engineer

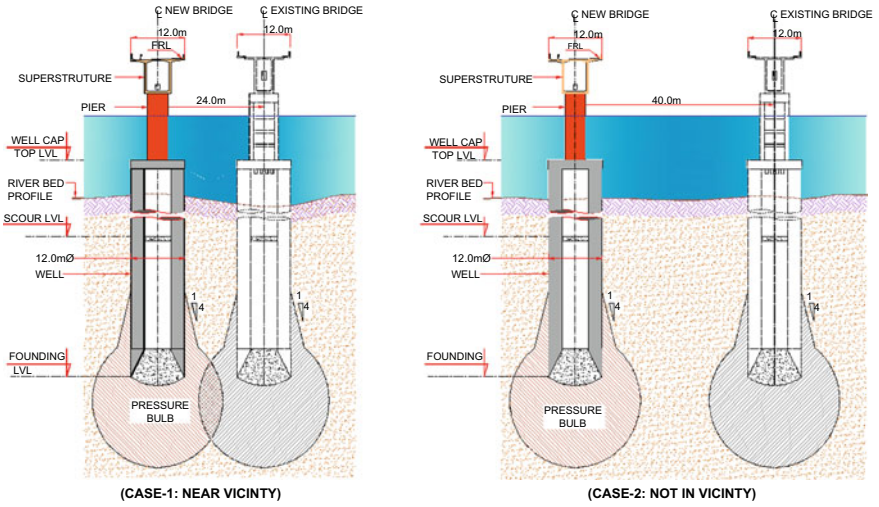

Fig. 2 Foundations of bridges in near-vicinity of an existing bridge

had to withdraw this unjust demand. But the clause is confusing and generates controversies in many projects. It is important for the code makers to clarify the basic intent of this clause and modify this clause to avoid blatant misuse.

Author is of the opinion that this clause is applicable for those foundations which are so close to each other that there "pressure bulbs" interfere with each other within the influence zone (say within 1.5 times the width of foundation below the founding level). In case these foundations are wide apart and the pressure bulbs do not interfere, there is no impact of one foundation over the other and in such cases, the founding level of new bridge need not be kept the same as the old bridge. Figure 2 shows the two possible scenarios for better clarity. In case-1, there is influence of existing foundation to the new foundation, while in case-2, there is no influence of existing foundation to the new foundation.

3.5 Check for Ovalisation of Well Foundation (Clause 708.3.4)

It is stated in this clause that "*The horizontal annular section of well steining shall also be checked for ovalisation moments by any rational method taking account of side earth pressures evaluated as per Clause 708.4.*" The procedure for ovalisation check of well foundation is neither given in any text book nor in the code. Absence of any guideline/literature on this subject makes it difficult for most of the structural designers to carry out this check. Very rarely, this check is performed by Consultants.

It is strongly recommended that an Appendix is added in the code for ovalisation check of well foundation.

3.6 Load Testing and Acceptance Criteria for Pile Foundation (Clause 709)

For pile load testing and acceptance criteria, reference is made to IS:2911 (Part 4), with minor modification in one of the criteria. As per IRC:78, the acceptance criteria for pile foundation are as under:

(1) Two-thirds of the final load at which the total displacement attains a value of 18 mm or maximum of 2% pile diameter whichever is less unless otherwise required in a given case on the basis of nature and type of structure in which case, the safe load should be corresponding to the stated total displacement permissible; and
(2) 40% of the final load at which the total displacement equal to 10% of the pile diameter in case of uniform diameter piles and 7.5% of bulb diameter in case of under-reamed piles.

The first criteria relate to serviceability requirement while the second criteria relate to strength requirement (ultimate limit state).

The serviceability criteria given in the code were fixed in IS:2911 (Part-4)—1985, based on the experience of 400–600 mm diameter piles in the country. With time, the pile diameter has increased and there is also an increase in load-carrying capacity of pile. In light of these changes, this criteria should have been revisited by the code makers. For large diameter piles with high load-carrying capacity, elastic shortening of the pile itself will be quite significant. The upper limit of 18 mm in settlement criteria means that for pile diameter greater than 900 mm, the allowable settlement is independent of the diameter of pile. This leads to very conservative estimate of pile load-carrying capacity. It is very common in bridges to have diameter ranging from 1000 to 2500 mm. The 18 mm limit therefore should be waived. Allowable settlement shall be kept as 2% of pile diameter.

4 Inconsistencies Between IRC:78 and Other Published Codes

There are several provisions in IRC:78 which is at present in conflict with the provisions of other IRC codes. Some of these clauses (as identified by the B-3 committee of IRC) are highlighted below:

a. Structural design and reinforcement detailing provisions for open foundation, pier walls, well foundations …etc. are in conflict with the provisions of IRC:112.

Relevant clauses which need to be shifted to IRC 112 are: Clause 707.2, 708.3.3, 708.3.4, 708.3.6, 709.4, 709.5, 710.1, 710.2.9, 710.3, 710.7, 710.8.7, 710.9, 710.10.3, and 710.10.4

b. Some of the clauses pertain to loading, which should be in the domain of "Loads and Load Combination" and should be shifted to IRC:6 to avoid conflict. Relevant clauses are: Clause 710.2.9, 710.4.2 to 710.4.5, and 710.4.7.
c. Some of the clauses pertain to brick masonry, which should be in the domain of IRC:40. Relevant clauses are: Clause 708.3.2, 708.3.5, Fig. 3 of Appendix-3.

5 Conclusion

It is imperative that national Standards are continually improved and updated to reflect the changes happening in international scenario based on global research and best practices.

There is no need to re-invent the wheels always. IRC is following this philosophy and made a good (though somewhat delayed) progress in this direction. New generation codes with rational limit state design philosophy, which is based on concepts of reliability, safety, serviceability, durability, and economy, are being developed in line with the Eurocodes.

It is only the foundation code which needs to be transformed to limit state version. This is, however, not an easy task. Challenges are much more daunting for the transformation of foundation code, which involves interaction between the structure and soil, combining elementary as well as very advanced construction methods in varying degrees.

It should be considered that knowledge of the ground conditions depends on the extent and quality of the geotechnical investigations. Such knowledge and the control of workmanship are usually more significant to fulfilling the fundamental requirements that is precision in the calculation models and partial factors. Therefore, codification on geotechnical investigation needs urgent attention.

References

Garde RJ, Kothiyari UC (1998) Scour around Bridge Piers, PINSA 64, A, 4:569–580

IRC:5-2015 Standard Specifications & Code of Practice for Road Bridges—Section I—General Features of Design—(Eighth Revision)Design)

IRC:78-2014 Standard Specifications & Code of Practice for Road Bridges—Section VII—Foundation & Substructure (Revised Edition)

Kothiyari UC (2007) Indian practice on estimation of scour around bridge piers—a comment, published in Sadhana, 32(3):187–197

Mazumder SK (2006) Estimation of scour in bridge piers on alluvial non-cohesive soil by different methods, published in Indian Highways

Reddy SA (2011) Fast track design and construction of bridges in India, published in NBM&CW, October 2011

Dynamic Analysis on Multilayer of Cohesionless Soil Subgrade of Railway Track with PLAXIS and MATLAB

R. K. Bharti and Mahabir Dixit

Abstract Dynamic displacement—time response of ballast-subgrade system is very useful result for assessing the soil behavior under dynamic loading for railway track foundation as it can help to gauge the soil suitability for the subgrade which can withstand the dynamic load without much deflection. This paper pertains to study of response of the ballast and subgrade under the dynamic load moving train using analytical and computational methods. The selected ballast and subgrade consist coarser granular material and fine-grained cohessionless material with a dense matrix, respectively. The response of the foundation of the railway track (ballast and subgrade) is presented in terms of "displacement—time" plot. These response curves have been plotted for 1 min duration. Out of this 1 min duration, dynamic load of frequency 26 Hz was applied for the first 6 s only. The analytical and computational (METLAB) results are compared with the results obtained using the FE package PLAXIS. The maximum displacement of the system comprising ballast and subgrade using METLAB and PLAXIS is found to be 2.0 and 2.4 mm, respectively. The maximum deflection observed using the analytical approach and the commercial FE are comparable and acceptable for the railway track embankment.

Keywords Railway track · 2-DOF MSD dynamic model · Finite Element (FE) · Subgrade layer deflection · Ballast

1 Introduction

The most highly built-up railway track consists of rails and sleepers, supported on compacted layers of ballast and subballast. Ballast is generally made from high-quality igneous or metamorphic rocks and locally available material. This accompanies the wheel loading which is imposed on the rails and transfers this to the

R. K. Bharti (✉) · M. Dixit
Central Soil and Materials Research Station, Olof Palme Marg, New Delhi, India110016
e-mail: rk.bharti@nic.in

M. Dixit
e-mail: mdixit@nic.in

R. Sundaram et al. (eds.), *Geotechnics for Transportation Infrastructure*, Lecture Notes in Civil Engineering 28, https://doi.org/10.1007/978-981-13-6701-4_21

subgrade at an acceptable level, while preventing excessive settlement, which may otherwise occur due to the inherent pliant nature of the rail-track system. Among its diverse functions, the rail-track system serves to distribute the large, concentrated time-varying wheel loads longitudinally, laterally, and vertically away from the wheel contact area on the rail surface. The settlement is caused by the repeated traffic loading and the severity of the settlement depends on the quality and the behavior of the ballast, and the subgrade. A well-designed, constructed, and maintained track will distribute the loads in a relatively uniform fashion, with each component supporting its share of the load without failure.

Railway track modeling comprising these two basic components, using various approaches has been one of the important topics of research to the civil engineering fraternity in general and to the geotechnical engineer in particular. Most of the failures of railway tracks occur in the subgrade due to dynamic load as depicted by (Indraratna et al. 1997, 2005; Indraratna and Salim 2002) therefore the topic of this research paper has accordingly been selected. These failures have basically prompted geotechnical engineers to either alter the existing design methodologies by considering a wider spectrum of parameters affecting the performance of the railway track foundation under the influence of the dynamic load of moving train. For example, many researchers have used the classic theory of elasticity for the designing the embankment and for calculating its static deflection (Burmister 1956). These theories are, however, capable of determining the deflection in the homogenous soil strata rather than the multilayer soil strata. A sufficient thick granular layer prevents higher stress, excessive deformation, and subgrade failures due to distribution of wheel load over wider area on the subgrade. These findings also find mention in RDSO (2003) report "guidelines for earthwork in railway projects." These guidelines stipulate the blanket layer of the different thickness on formation based on experience and behavior of the different type of subgrade under repetitive loading. Shahu et al. (2000) studied on a new method to design the formation thickness of a railroad track. This method has been developed based on evaluation of induced subgrade on the subgrade surface. The design method focuses on keeping induced stresses on the subgrade surface below the threshold stress of the subgrade soil by providing a suitable formation thickness. Frost et al. (2004) described the requirements for a better performance of the rail-track system under dynamic load and laid down specifications for pavement foundations and the basic principles of pavement loading, material states, and material behavior for analytical pavement foundation design. A simple relationship to predict material behavior (known as the K-θ model) was proposed. This formula, although describing the general behavior of granular materials, cannot be used to predict precise behavior during loading and other more complex models have been proposed. Indraratna et al. (2006) studied on the stabilizations of rail tracks and underlying soft soil formations. The deformation and degradation behavior of ballast under static and dynamic loading conditions were studied and investigation had been made on the prospective use of different types of geosynthetics to improve the performance of fresh and recycled ballast. Increasing the confining pressure on rail tracks are highlighted in relation to particle breakage and demonstrating the role of the vertical drain for improving the soft subgrade formation drainage condition and

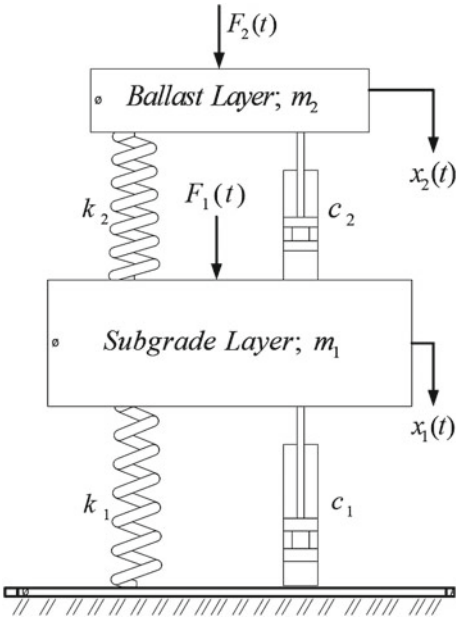

Fig. 1 Mathematical modeling of railway track by mass–spring–dashpot system

use of vegetation to stabilizing the track soft formation. So, treatises are unable to describe the deflection due to dynamic loading easily. And many of them are limited with the many limitations and boundary conditions.

Most of the past work is related to the experiment work that is the time-consuming as well as just covers only the limited aspect. Few of treatises are able to find out the deflection in the layered soil strata but their method to find out the deflection in the layered soil system is very complicated and time-consuming. In this paper, a similar 2-DOF, MSD dynamic model is considered to study the behavior of the ballast and subgrade system beneath the track, which is scarce in literature till date.

Present approach, mass–spring–dashpot system is very useful to determine the deflection in the each layer of soil strata of railway track due to dynamic loading. The main inclination is to find out vertical dynamic deflection in the railway track foundation by the spring—dashpot system which is comparably jibed to find out the deflection due to cyclic loading. An effort is made to model the rail-track system by adopting analytical method by mathematical modeling and computational approach by PLAXIS (a finite element approach). Simple mass–spring–dashpot model has been adopted to develop the analytical model of the rail-track system as per Fig. 1; while PLAXIS has been used to validate these analytical results using the finite element (FE) technique.

2 Methodology

2.1 MATLAB Mass—Spring—Dashpot System

In the mass–spring–dashpot system, analysis for the Indian railway system is adopted as mentioned in Choudhury et al. (2008). The typical mathematical modeling of the railway track has been shown in the Fig. 1 in which ballast layer and subgrade layer of the railway track have been considered. The soil interface has been considered as frictional interface as no horizontal movement allowed at the soil interface. The introducing parameters m_1 and m_2 are the masses of the ballast and subgrade layer on the other hand k_1 and k_2 are the stiffness of the respective soil layer. Consequently, the damping constant of the individual soil layers has been designated by the c_1 *and* c_2. The dynamic coupled equation of this mathematical modeling as given in the Bharti et al. (2006) and choudhury et al. (2008) can be represented by

$$\begin{bmatrix} m_1 & 0 \\ 0 & m_2 \end{bmatrix} \begin{Bmatrix} \ddot{x}_1 \\ \ddot{x}_2 \end{Bmatrix} + \begin{bmatrix} c_1 + c_2 & -c_2 \\ -c_2 & c_2 \end{bmatrix} \begin{Bmatrix} \dot{x}_1 \\ \dot{x}_2 \end{Bmatrix} + \begin{bmatrix} k_1 + k_2 & -k_2 \\ -k_2 & k_2 \end{bmatrix} \begin{Bmatrix} x_1 \\ x_2 \end{Bmatrix} = \begin{Bmatrix} f_1(t) \\ f_2(t) \end{Bmatrix} \tag{1}$$

Since Eq. (1) is a coupled system under dynamic loading—analytical solution of this equation is quiet difficult to obtain. Therefore, above coupled system of equation has been puzzled out by Newmark's method (Bardella and Genna 2005) for obtaining the vertical deflection "x_1 and x_2" in the ballast and subgrade soil layer. For the dynamic analysis, Nermark's method is coded in the MATLAB to find out the value of the dynamic deflection with time. A parametric study for the variation in the displacement with time for ballast and subgrade material under cyclic load has been computed. For cohesionless soil, the adopted Possion's ratio is 0.4 while for granular material (ballast), it is 0.3 (Bowles 1996). Similarly, the values of Young's modulus for cohesionless soil and granular soil are 51.50 and 276 MPa, respectively (Bowles 1996). The geotechnical properties of the ballast and subgrade as used in the model are listed in Table 1.

Table 1 Geotechnical properties considered for the subgrade and ballast materials (Bowles 1996)

Soil type	E (M Pa)	k (10^6) (N/m)	c(10^5)(N-s/m)	ν	ρ(10^3)(kg/m^3)	m(10^3)(kg)
Granular layer	276	396	7.31	0.3	1.76	0.975
Dense uniform sand	51.50	9.81	3.36	0.4	1.84	1.19

Table 2 Rail and sleeper dimensions (SI Units)

Rail and sleeper dimensions			SI unit
Rail parameter	Wheel load of, ***P***	147,150.00	N
	Train wheel diameter, ***D***	0.97	m
	Velocity of the train, ***V***	72	km/h
	Track modulus, ***k***	18,020,970.00	N/m^2
	Young modulus, ***E***	2.1E + 11	N/m^2
	moment of inertia, ***I***	3.59E-05	m^4
Sleeper parameter	spacing between two sleeper, ***S***	0.60	m
	width of the sleeper, ***b***	0.30	m
	Length of the sleeper, ***L***	2.74	m
	Effective length, ***L/3***	0.91	m

For the stiffness ("k" = stiffness per unit area) and the damping constant of granular and subgrade layer ("c" = the stiffness per unit area of the respective soil layer) is calculated as adopted by the Bharti et al. (2006) and Choudhury et al. (2008).

The track properties are mentioned in Table 2. The track system is a Broad Gauge (BG) Indian railway track. The external force "$f_1(t)$" on the sleeper due to wheel load through sleeper has been calculated as per Bathrust and Kerr (1999), which is based on the classical Timoshenko's theory of beams. All the relevant parameters which are adopted from RDSO (2003) report and used in this approach are listed in Table 2.

By using these relevant parameters, vertical deflection has been calculated for finding out the force exerted by the tie on the ballast below the wheel load, i.e., when the horizontal distance of the point of action of the wheel load from the measuring point of the vertical deflection is zero. And the dynamic load has been calculated as per the American Railway Engineering Association (AREA 1996) approach and is given by

$$P_{dl} = \left[1 + \frac{0.0052\ V}{D}\right] P_{sl} \tag{2}$$

where V and D are train speed (in km/h) and wheel diameter (in m), respectively.

The force "$f_2(t)$" is to be zero because entire amount of load is distributed by the ballast layer and transfer it completely to the subgrade layer. It is assumed by the subgrade layer during the cyclic free vibration. The track system properties and dimensions are based on the Ministry of Railways, India.

2.2 PLAXIS Finite Element Analyses

A plane strain as well as axisymmetric model of the railway track has been described as elastic model that was selected from the PLAXIS to describe the dynamic deflection of cohesionless subgrade in this present study. This dynamic deflection has been calculated for the 60 s time when the dynamic train load is acting for 6 s and this time is calculated by the velocity and length of the train as generally mentioned in the RDSO (MC/CB/AC/BG 2002) report. This problem in PLAXIS is simulated using a plane strain model with 15-noded elements and 12-point Gauss integration (Table 4). The geometry model is shown in Fig. 2 which introduces the node point in the embankment discreetly and dimensions are named individually in Table 3.

In analysis, two elastic layers have been taken which is the ballast and subgrade layer, the interface between them is frictional and no horizontal movement occurs between them. Here, the main constrains for the analysis is on the respective vertical deflection in the both the layers. Purpose of PLAXIS analysis is the validation of the mass–spring–dashpot (M–K–C) approach. PLAXIS model involves five parameters, namely Young's modulus "E", Possion's ratio "ν", saturated and unsaturated density of the soils (γ_{sat}, γ_{unsat}), K_0 (earth pressure coefficient at rest) (Table 5). And 26 Hz, exciting frequency of the dynamic loading is taken for the analysis. It has been calculated by adopting the effective length of the track foundation (ballast and subgrade). The effective length of the foundation is based on the sleeper to sleeper spacing "S". Effective length is one-third of the sleeper length (Table 2). Similarly,

Table 3 Model dimensions

Axis	Minimum	Maximum
X	0.00	12.05
Y	0.00	4.86

Table 4 Numbers, type of elements, and integrations

Type	Type of element	Type of integration	Total no.
Soil	15-noded	12-point Gauss	64

Fig. 2 Geometry model

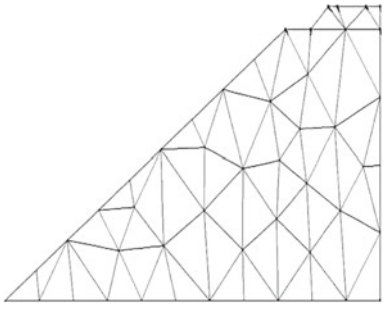

Table 5 Soil data set parameters

Linear elastic		Subgrade layer (Dense sand)	Ballast layer (Granular Layer)
Type		Drained	Drained
γ_{unsat}	[N/m^3]	18,000.00	17,266.00
γ_{sat}	[N/m^3]	28,000.00	19,270.00
E	[N/m^2]	51,500,000.00	276,000,000.00
ν	[−]	0.40	0.30
G_{ref}	[N/m2]	18,392,857.14	106,153,846.15

effective length has been taken in the M–K–C approach. Dynamic force taken in the analysis of the PLAXIS is also similar to spring–mass–dashpot system.

3 Result and Discussions

The total displacements are the absolute accumulated displacements, combined from the horizontal and vertical displacement components at all nodes at the end of the current calculation step, displayed on a plot of the geometry. The soil particles' movement in the discreet direction due to dynamic loading of the train is represented by Fig. 2 which is obtained by the PLAXIS. Directions of movement of the soil particles appear more realistic because the ballast particles motility below the dynamic loading is downward, in the other hand direction of the side particles of the ballast is outward. Arrows signs in Fig. 3 shows the movement of the soil particles which is in outward direction from the slant face of the embankment. Due to dynamic loading, the part just above the toe of the subgrade layer and the ballast layer is affected most as compared to the other parts of the soil embankment. The contour line plot and the shading plot in Figs. 4 and 5 are clearly showing the same. The total displacement is 1.50 mm, which is also clear from the shadings plot shown in Fig. 5 by red color. Combined vertical displacement of the subgrade and ballast is 1.60 mm; Fig. 6 is showing vertical displacement due to movement of the soil particle in downward direction. The dense arrows are signifying more vertical displacement at that explicit area. Again, the vertical displacements are shown by contour lines and shadings by Figs. 7 and 8, respectively. It can be seen from the contour line graph that the vertical displacement (U_y) of the embankment is maximum at the midpoint (1.60 mm) of the slant face of the embankment. The same is clear from the shading plot, which is indicated by the red color in Fig. 8. Therefore, this area is very sensitive and critical for the safety point of view. In PLAXIS analysis, the dense uniform sand is almost stable and not showing any failure. Therefore, 1.60 mm deflection is found to be acceptable for the rail embankments. The results shown in Table 6 are the total displacement obtained by using geotechnical software PLAXIS and using spring-dashpot system. As it can be seen, from Table 6, the displacement is obtained by PLAXIS and the

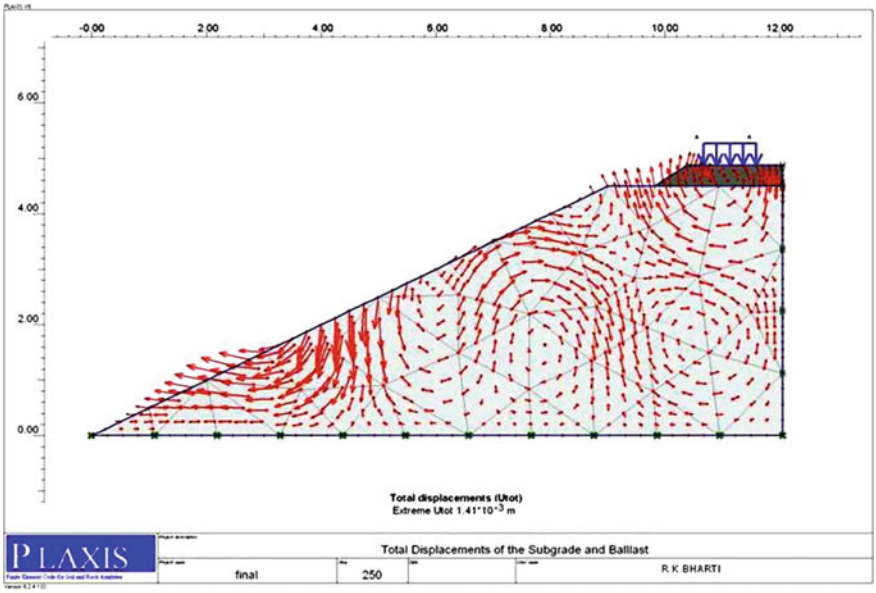

Fig. 3 Plot total displacements (arrows)

Table 6 Comparative results of the PLAXIS and mass–spring–dashpot

Soil type	Maximum displacement (mm)	
	Total displacement PLAXIS	Vertical displacement MSD
Dense Uniform Sand	2.4	2.0

spring-dashpot system. According to PLAXIS, the combined displacement of the ballast and the subgrade layer comes out to be 2.4 mm which is very close to the result obtained by spring–mass–dashpot system analysis. In the present case, the maximum displacement is found to occur at the toe of the subgrade. However, the displacement obtained by spring–dashpot system is the displacement occurring at the centroid of the embankment (Figs. 9 and 10).

4 Conclusions

Equation analyses by mass–spring–dashpot and PLAXIS for finding out the deflection in the foundation of the railway track are comparable and give the acceptable result for the new-made embankment. Under newly compacted sleeper, the deflection on the sleeper takes place like end-bound sleeper. In the end-bound sleeper, maximum deflection has occurred at the center of the sleeper, effective dynamic loading act at this point of the sleeper. Therefore, these analyses are very useful to find out

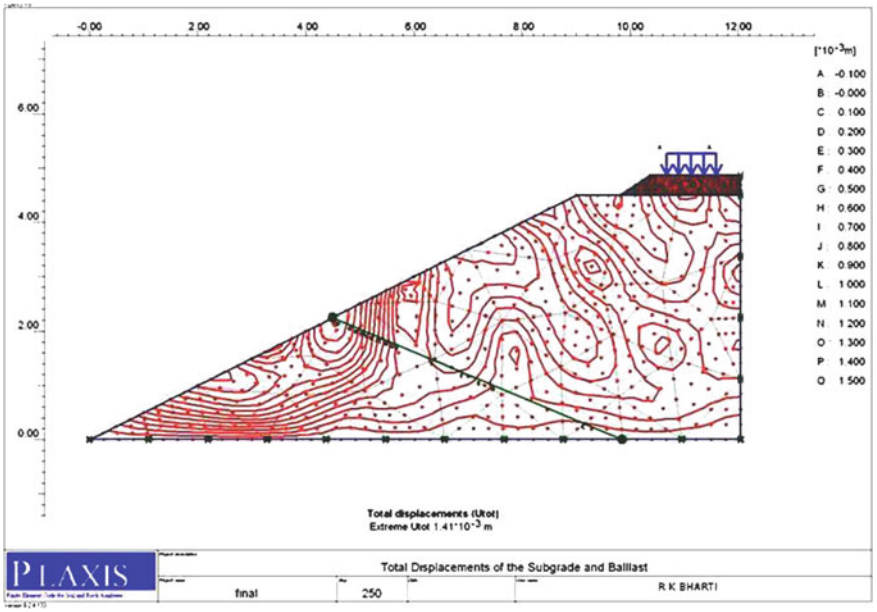

Fig. 4 Plot total displacements (contour lines)

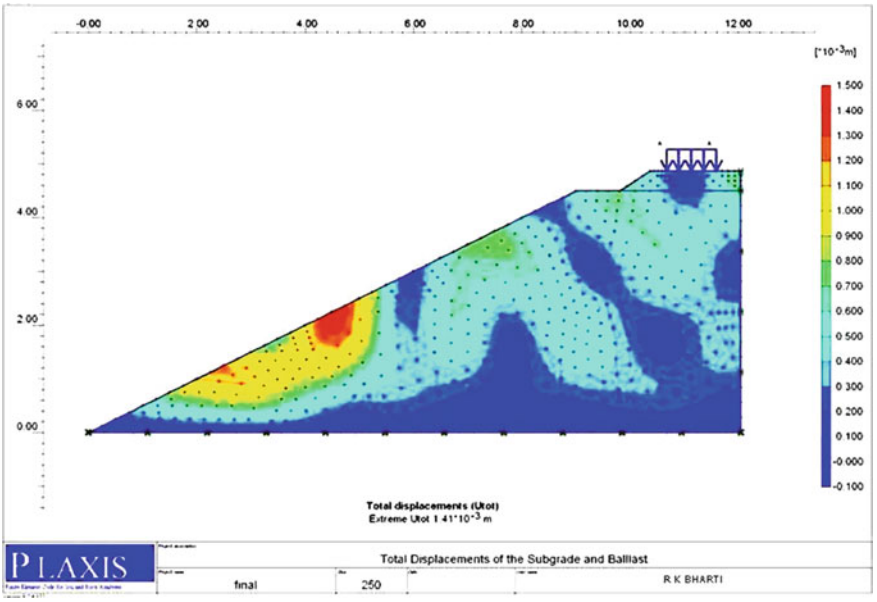

Fig. 5 Plot total displacements (shadings)

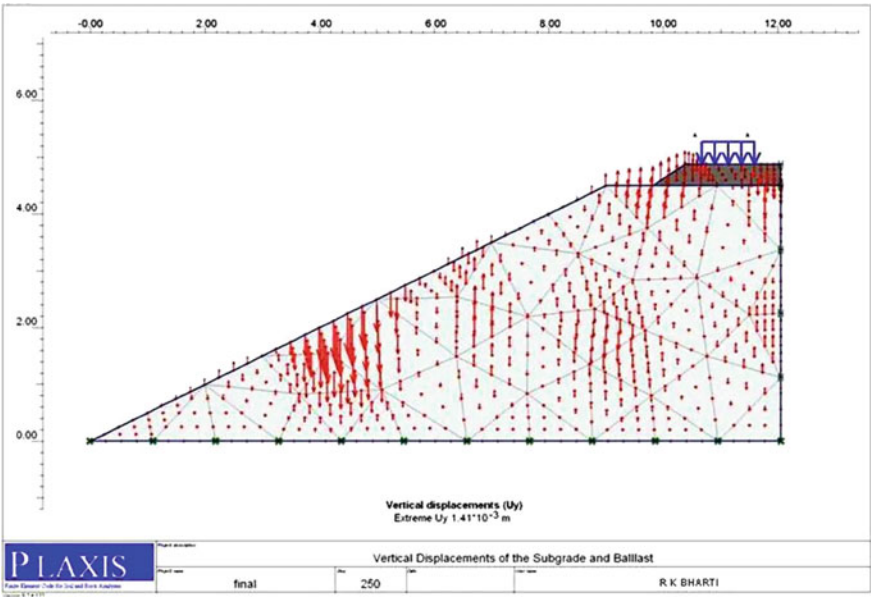

Fig. 6 Plot vertical displacements (arrows)

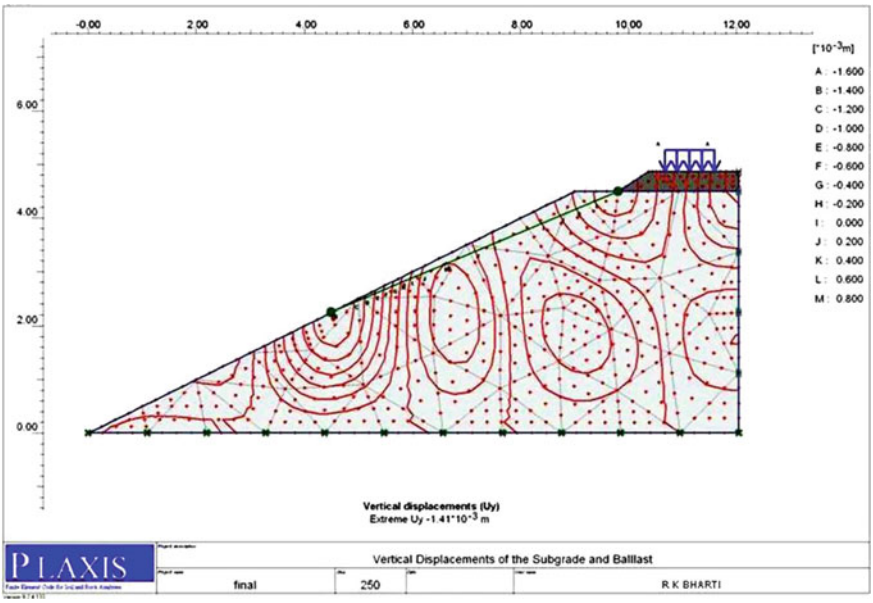

Fig. 7 Plot vertical displacements (contour lines)

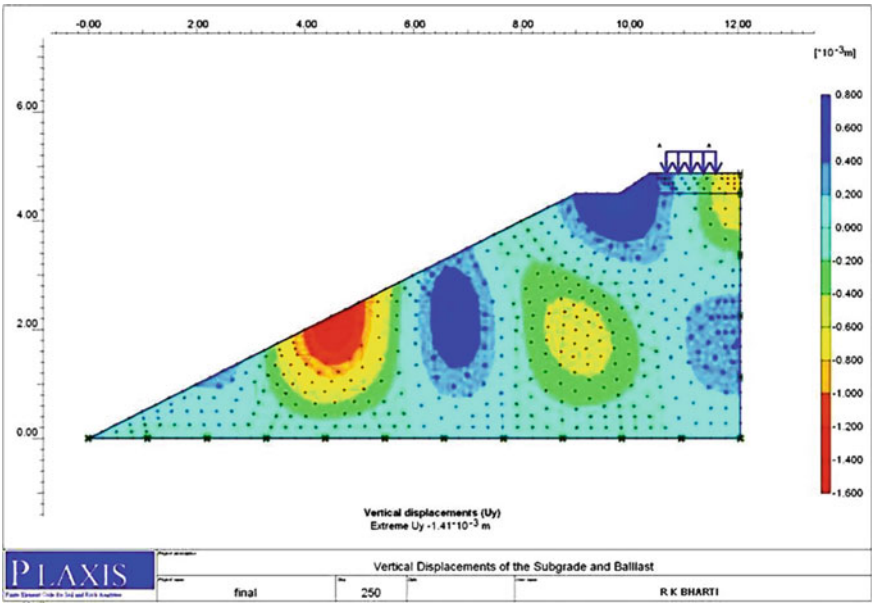

Fig. 8 Plot vertical displacements (shadings)

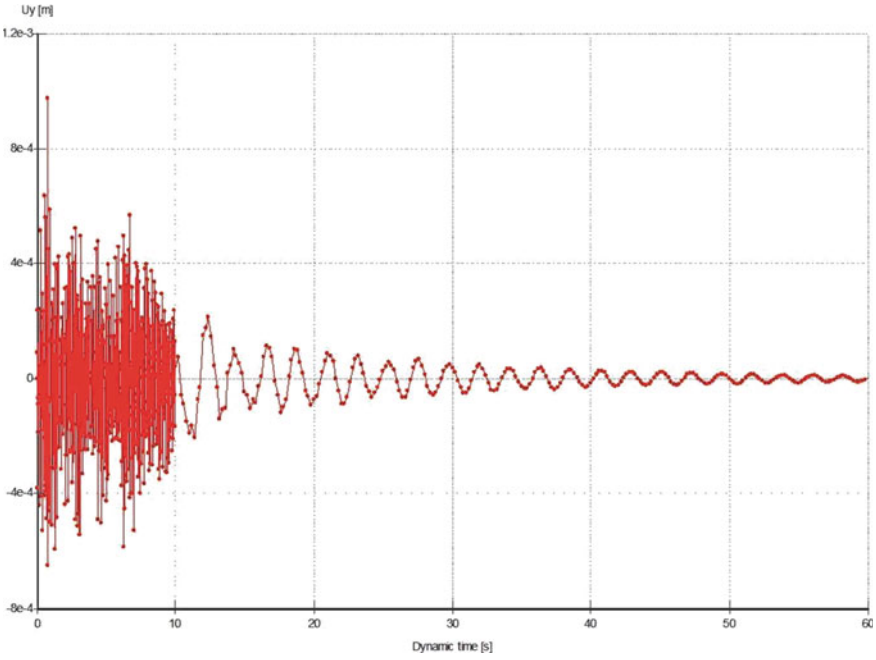

Fig. 9 Time-displacement response curve

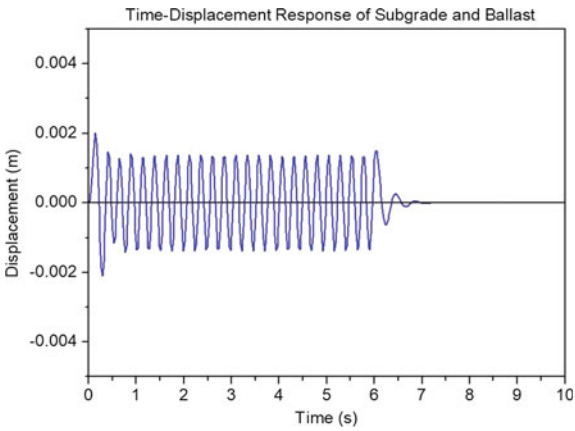

Fig. 10 Time-displacement response curve

Table 7 Physical properties of sands

Soil	D_{60} (mm)	D_{30} (mm)	D_{10} (mm)	C_u	C_c	$\varphi°$
Sand1	0.25	0.20	0.16	1.56	1.00	33
Sand2	0.22	0.19	0.13	1.47	1.09	35

the appropriate soil for the foundation of the railway track. Here, results from both the analyses are showing that results of the finite element (FE) and results of the mass–spring–dashpot are comparatively close (Table 6). So, MSD model is nothing but a FE method that gives better result. It is very fast, simple, and economical method (Table 7).

References

American Railway Engineering Association (AREA) (1996) Manual for railway engineering. AREA, Washington, D.C

Bathrust LA, Kerr AD (1999) An improved analysis for the determination of required ballast depth. In: Proceedings of AREMA on track and structure, Chicago IL, 12–15 Sept 1999

Bardella L, Genna F (2005) Newmark's time integration method from the discretization of extended functional. J App. Mech ASME, 72(4):527–537

Bowles JE (1996) Foundation analysis and design, 5th edn. McGraw-Hill Book Company, New York

Bharti RK, Choudhury D, Chauhan S (2006) Behaviour of subgrade under cyclic load below railway track. In: Proceedings of indian geotechnical conference, IGC-2006, pp 741–742. IIT Madras, Chennai, India, 2 14–16, Dec 2006

Burmister DM (1956) Stress and displacement characteristics of a two-layer rigid base soil system: influence diagram and practical applications. Proc Highw Res 35:773

Choudhury D, Bharti RK, Chauhan S, Indraratna B (2008) Response of multilayer foundation system beneath railway track under cyclic loading, J Geotech Geoenviron Eng 134(10)

Frost MW, Fleming PR, Rogers CDF (2004) Cyclic triaxial tests on clay subgrades for analytical pavement design, J Transp Eng 130(3):378–386
Indraratna B, Balasubramaniam AS, Sivaneswaran N (1997) Analysis of settlement and lateral deformation of soft clay foundation beneath two full-scale embankments, Int J Numer Anal Method Geomech 21:599–618
Indraratna B, Lackenby J, Christie HD (2005) Effect of confining pressure on the degradation of blast under cyclic loading. Geotechnique 55(4):325–328
Indraratna B, Salim W (2002) Modelling of particle breakage of coarse aggregates in incorporating strength and dilatancy. Geotech Eng London, 155(4):243–252
Indraratna B, Shain MA, Rujikiatkamjorn C (2006) Stabilising granular media and formation soil using geosynthetics with special reference to railway engineering. In: Indian geotechnical conference, India, pp 41–50
RSDO (2002) Final maximum permissible speed certificate for operation of Rajdhani FAC coach with modified suspension springs, Luknow
RSDO (2003) Guidelines for earthwork in railway projects, Luknow
Shahu JT, Yudhbir, Kameshwar Rao, NSV (2000) A rational method for design of railroad track foundation, Soils Found 40(6):1–10

Effect of Piled Structures on the Tunnel Stability for Different Pile-Tunnel Configurations

M. Wasif Naqvi and Mohd. Ahmadullah Farooqi

Abstract In view of the rapid pace of urbanization, the demand to enhance the capacity of existing transportation infrastructure and construction of alternative modes of transport is escalating. In the recent pursuit of metro trains in India, the focus toward the construction of underground tunnels has substantially increased. The construction of infrastructure on the ground surface is still growing and may potentially influence the stability of tunnel passing underneath it. The situation may become worse when the structure is to be constructed on deep foundation like piles or wells. In terms of sustainable development, it is of paramount importance to understand the influence of piled structures on the tunnel lining in terms of location and load of pile and pile-tunnel configuration in different subsoil profiles. The present study aims to investigate the effect of the piled structure on stability of the tunnel and the surrounding soil. The 2D multiplier elastoplastic analysis has been carried out using the popular Mohr-Coulomb material model on the commercial finite element-based software OptumG2. The stresses on tunnel lining and the surrounding soil mass have been analyzed under different pile-tunnel configurations under varying load and pile eccentricity with respect to the axis of tunnel. Also, a parametric study has been done to evaluate the displacement and stress distribution of surrounding soils and tunnel lining under increasing pile load, length, and different pile-tunnel placements.

Keywords Pile-Tunnel interaction · Numerical modeling · Limit analysis · OptumG2

M. W. Naqvi (✉) · Mohd. A. Farooqi
Department of Civil Engineering, Z. H. College of Engineering and Technology, AMU, Aligarh 202002, India
e-mail: mwnaqvi@zhcet.ac.in

Mohd. A. Farooqi
e-mail: mafarooqi1@gmail.com

R. Sundaram et al. (eds.), *Geotechnics for Transportation Infrastructure*, Lecture Notes in Civil Engineering 28, https://doi.org/10.1007/978-981-13-6701-4_22

1 Introduction

In the recent economic development in India, urban zones are expanding swiftly over the adjacent rural areas and it is expected that this expansion would reach 60–70% by 2050 (World Urbanization Prospects 2014). On the other hand, in search of jobs, rural population is fast inverting to the nearby metropolitan cities; hence, increasing demand on the already saturated infrastructural capacity. Road traffic congestions and elevated environmental pollution levels are among the worst affected sectors. In Delhi, to slow down this economic exodus, National Capital Region Planning Board has identified national capital regions (NCR), with a view to develop them into regional economic hubs and connect them with the national capital territory (NCT) through peripheral expressways and orbital rail corridors ("National Capital Region Planning Board," n.d.). The metro rail facility through a network of tunnels is an extensively adopted and sustainable solution to regulate elevated traffic volume and to reduce pollution challenges. In urban development scenario, it is relatively more important to investigate the effect of tunneling on existing structures. Significant research has already been done ranging from field studies (Vorster et al. 2005; Li et al. 2014; Selemetas et al. 2006; Kaalberg et al. 2005), experimental work (Loganathan et al. 2000; Chen et al. 1999; Bezuijen and Van der Schrier 1994; Chapman et al. 2001; Pang et al. 2006; Yao et al. 2008; Meguid and Mattar 2009), analytical modeling (Kitiyodom et al. 2005; Lee and Ng 2005; Cheng et al. 2007; Marshall 2012; Marshall and Haji 2015), 2D numerical modeling (Huang et al. 2009; Zhang et al. 2012; Giardina et al. 2015), and 3D numerical modeling (Arunkumar and Ayothiraman 2010; Kitiyodom et al. 2005; Mroueh and Shahrour 2002; Mroueh and Shahrour 2003; Franza et al. 2017; Yao et al. 2012; Zidan and Ramadan 2015) to study the effect of tunneling. However, in an effort to connect remote regional economic areas with sparse developments through metro tunnels, it is of paramount importance to consider the alignment and depth of tunnels and strength and stability of tunnel lining to account for potential future surface infrastructural development.

On account of the prospective future construction of new structures or reconstruction of the old ones, this study aims to explore the effect of construction of piled structures on the lining of existing tunnel. A numerical model has been developed to investigate the effect of piles on tunnel lining by increasing pile load, on four different pile locations, with three different pile-tunnel configurations.

2 Numerical Model

The whole 2D model is modeled using newly developed finite element software OptumG2 ("OptumG2" 2013). Figure 1 shows the typical meshed models of soil with and without pile. The outer dimensions of tunnel of 6 m is taken from the study conducted by Basile (Basile 2014). The thickness of concrete lining used for the modeling is kept 28 cm (Singh et al. 2017). The tunnel concrete lining is made using

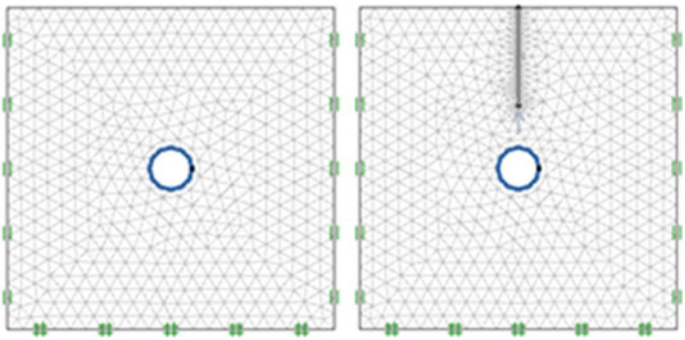

Fig. 1 Discretized domain of problem with and without pile

Table 1 Physical properties of materials

Delhi silty sand	
Unit weight	15 kN/m^3
Young modulus	25,000 kPa
Poisson ratio	0.3
Friction angle	37.5
Cohesion	0.5 kPa
Concrete liner	
Density	25 kN/m^3
Young modulus	23.48 GPa
Poisson ratio	0.2

P800 plate structural element having the properties as shown in Table 1 (Mahajan et al. 2016). The elastoplastic model of the soil is provided using the famous Mohr-Coulomb theory. The dimensions of the soil model are kept 46 m × 46 m with tunnel at its center having diameter of 6 m. All the dimensions are kept such that all the faces are at a distance of 3d, where d is the diameter of tunnels, from the center of the tunnel. This is done because the stress contour is significant up to this distance and the effect is trivial beyond this distance (Jose and Shounak 2015). The soil is considered as Delhi silty sand with properties given in Table 1 (Mahajan et al. 2016). The bottom is provided with a fixed support while the two sides of the soil model are provided with roller support with movement allowed in the vertical direction (Fig. 2).

Piles of varying length are provided at different locations in the soil model. The massive circular concrete piles are modeled using standard beam elements in OptumG2. The diameter of the pile is kept 0.5 m having length varying as 10, 14, and 18 m. the properties of the pile are given in Table 1. The element type used for modelling is 6-node Gaussian elements.

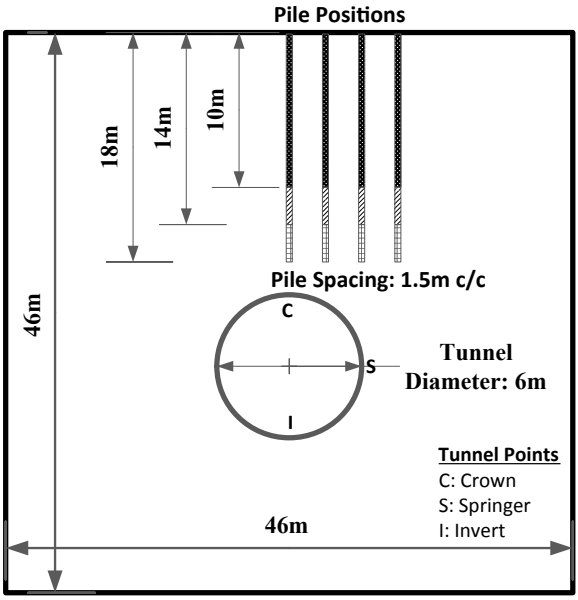

Fig. 2 Geometry of the modeled problem. Pile positions start with eccentricity value of 0 m, at the centerline of tunnel to 4.5 m at a spacing of 1.5 m. Three different depth values are taken: 10, 14, and 18 m. The tunnel crown is located at 20 m from surface

2.1 Stages of Analysis

The analysis is carried out in four sequential stages to simulate the real ground scenario. Initially, the green field analysis is done in which only soil is modeled and the stresses induced due to self-weight are calculated using initial stress analysis of OptumG2. In the second stage, the tunnel is excavated and the tunnel perimeter is provided with full support and elastoplastic analysis is carried out. In this step, a relaxation factor, λ, of 0.5 is specified to consider convergence–confinement method. In the next stage, the perimeter support of tunnel is replaced with a plate element to model the lining and the elastoplastic analysis is carried out to determine the deformation and stress in the model. In the final stage, the pile is inserted at zero eccentricity to simulate the complete problem. The final stage is varied to consider different locations and depths of piles. The analysis carried out in this stage is termed as multiplier elastoplastic analysis which is a combination of limit analysis and elastoplastic analysis. In this type of analysis, the pile is incrementally loaded to a certain value of limiting load and resulting deformations are simultaneously recorded, as shown in Fig. 3. An axial load is applied at pile top to determine the ultimate load-bearing capacity of pile and subsequently, the stresses induced and displacement caused due to varying load is analyzed. The initial displacement is set to zero before this analysis to only observe the effect of gradual loading on piles.

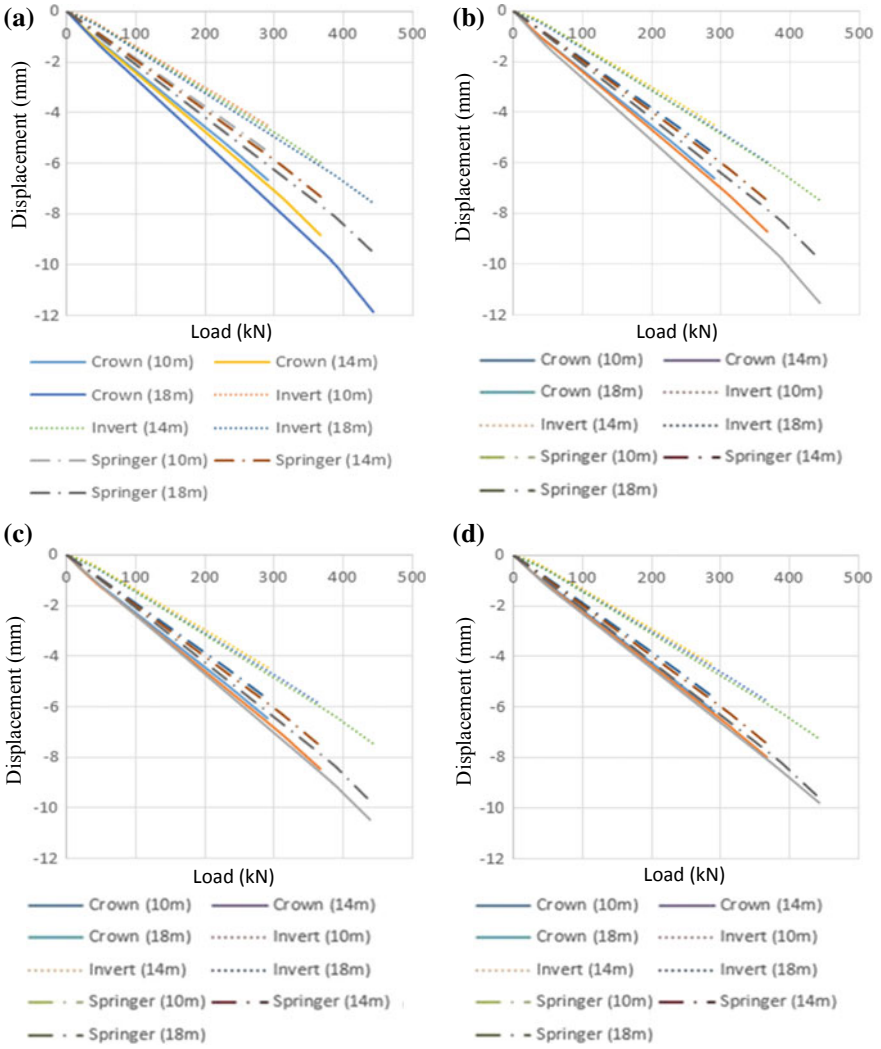

Fig. 3 Critical displacement values against incremental load at the crown, springer, and invert points on tunnel lining. The values in bracket represent eccentricity of pile away from the center line of tunnel

3 Results and Discussions

The vertical displacement induced at crucial tunnel points, namely crown, invert, and springer, subjected to varying loads, are calculated for different depths and eccentricities of pile. The contours of normal force, shear force, and bending moment at maximum loads are simultaneously studied. Finally, the stresses and vertical displacements induced in the surrounding soil are also observed.

3.1 Vertical Displacement of Crucial Tunnel Points

Vertical displacement of crown is found to be the maximum in all cases with a maximum vertical displacement of 11.85 mm in the loading case when the pile is above the crown. The displacement of all crucial tunnel points tends to decrease with the increase in eccentricity with minimum vertical displacement of 4.36 mm is found at invert point in the case of maximum eccentricity of 4.5 m from tunnel axis. The values of maximum displacement at crown, invert, and springer points are found to be 11.85, 4.51 and 9.60 mm at no-eccentricity, no eccentricity and 4.5 m eccentricity cases, respectively. The tunnel point that is most affected by the increase in the depth of pile is the crown with a maximum variation of 5.19 mm in no-eccentric loading case while the least affected point is invert. Crown remained the most affected point under eccentric loading, with variation of up to 2 mm from no-eccentricity to maximum eccentricity case.

3.2 Forces and Moments in Tunnel Lining

The contours of normal forces are as shown in Fig. 4. The normal forces at crown and invert show the usual positive trend while the negative normal forces can be seen at the springer point in all the cases. The maximum magnitude of normal force is at crown and invert points in all cases. The normal forces tend to increase with increase in depth of pile while the change in eccentricity of load has no significant variation in the magnitude of normal force. The minimum and maximum normal forces are −522 and −562 kN in the case of no-eccentricity and at 3 m eccentricity case, respectively.

The contours of shear forces in tunnel lining are also shown in Fig. 4. The shear force is not much influenced with the eccentric loading and is only slightly affected with the increase in depth of the pile. The maximum shear force on tunnel lining is found at 1.5 m eccentric loading case, with magnitude of 156 kN. The contours of bending moment in tunnel lining are shown in Fig. 4; the bending moment is not influenced by the eccentricity significantly but the effect of depth of pile has a significant effect in the bending moment on tunnel lining. The maximum bending

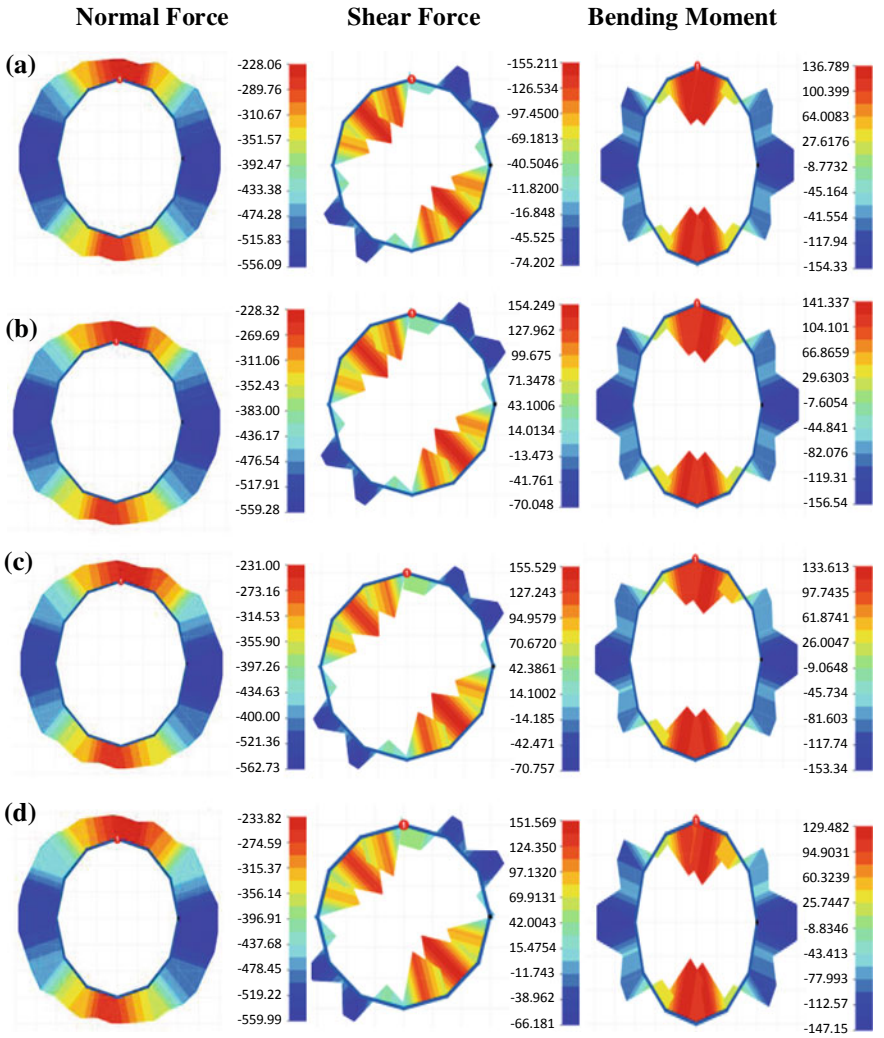

Fig. 4 Contours showing distribution of normal force, shear force, and bending moment along the tunnel lining for **a** eccentricity: 0.0, **b** eccentricity: 1.5, **c** eccentricity: 3.0, and **d** eccentricity: 4.5 meters away from the centerline of the tunnel

moment is found to be 156.5 kNm in the 1.5 m eccentric loading when the pile is at a depth of 18 m while the minimum bending moment of 136 kNm in the tunnel lining is in the 4.5 m eccentric loading case having depth of pile as 10 m.

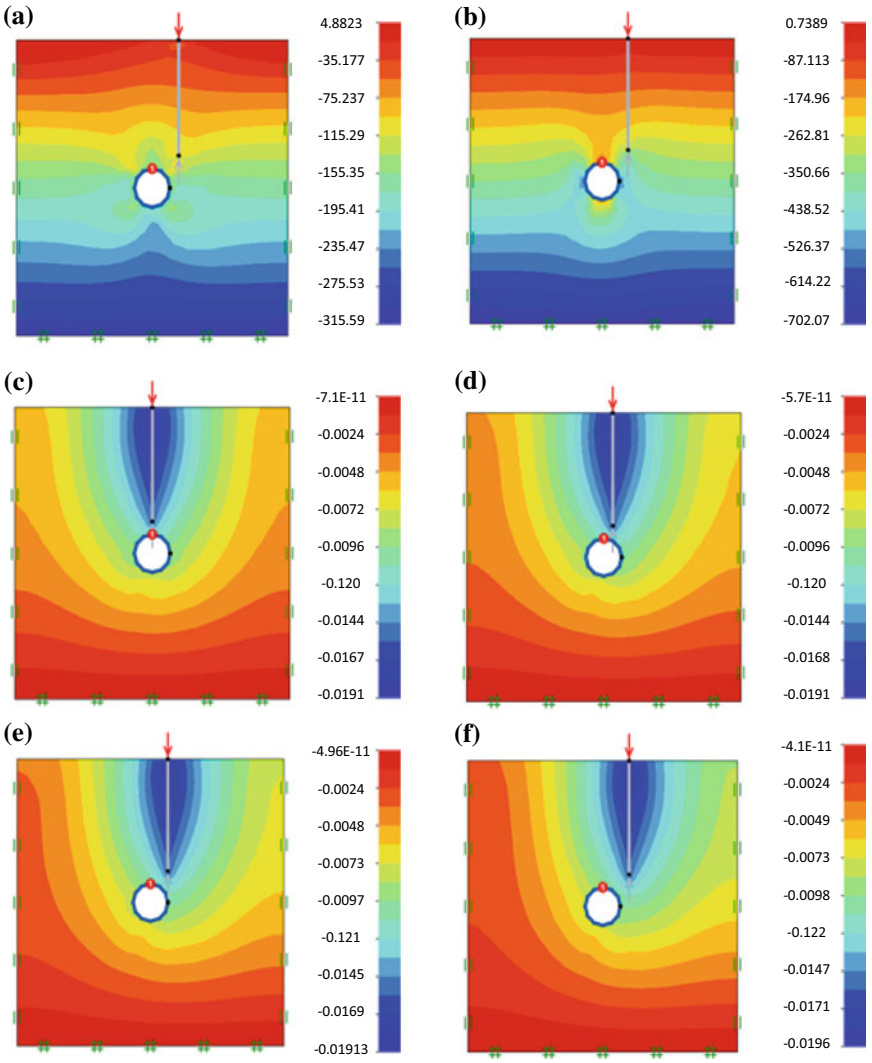

Fig. 5 Stress and displacement distribution in soil mass: principal stresses in soil in **a** vertical direction and in **b** horizontal direction. Vertical displacement in soil mass for **c** eccentricity: 0.0 m, **d** eccentricity: 1.5 m, **e** eccentricity: 3.0 m, and **f** eccentricity: 4.5 m

3.3 Stresses and Displacement in Soil

The maximum principal stresses of soil in *x*- and *y*-directions are shown in Fig. 5. There is no significant variation of stresses in the soil with change in configuration of pile with respect to tunnel. The maximum principal stresses in *x*- and *y*-directions are found to be 316 and 702 kN/m, respectively. The displacements in soil mass in the case

of 18 m depth pile at various eccentricity values are shown in Fig. 5. The maximum displacement in soil occurs at pile top with a maximum downward displacement of 19.6 mm in the case of 4.5 m eccentric loading having pile at 18 m depth. The displacement as expected is influenced with the pile depth and not significantly affected with eccentricity.

4 Conclusions

The present study aims to investigate the effects of construction of piled structure on the stability of existing tunnel. A 2D plain strain model has been developed in OptumG2, and multiplier elastoplastic analysis has been carried out using popular Mohr-Coulomb material model. The displacement and stresses on the tunnel lining and the surrounding soil mass have been studied by increasing pile load and decreasing pile-tip-tunnel distance and increasing pile eccentricity with respect to the axis of tunnel. A parametric study has been done to evaluate the displacement and stress distributions. It has been found that the critical condition for tunnel lining occurs when pile-tip-tunnel distance is reduced and pile is located between crown and springer points. The 18 m long pile challenged the stability of tunnel significantly more than their 10 or 14 m counterparts. In case of surrounding soil, eccentricity played the most challenging role and the worst case scenario existed at 4.5 m eccentricity in terms of both stresses and displacements.

It can be conveniently concluded that heavily loaded long piles located between crown and springer points of tunnel are critical for tunnel lining while those with eccentricity beyond the springer point are critical for surrounding soils.

References

Arunkumar S, Ayothiraman, R (2010) Effect of vertically loaded pile on existing urban tunnel in clay. GEOtrendz pp 751–54

Basile F (2014) Effects of tunnelling on pile foundations. Soils Found 54(3):280–95 Elsevier. https://doi.org/10.1016/j.sandf.2014.04.004

Bezuijen A, Van der Schrier J (1994) The influence of a bored tunnel on pile foundations. In: Proceedings of the international conference. Balkema, Singapore, pp 681–86

Chapman T, Nicholson D, Luby D (2001) Use of the observational method for the construction of piles next to tunnels. In: Jardine FM (ed) Proceedings of international on conference response of buildings to excavation induced ground movements, London:CIRIA

Chen LT, Poulos HG, Loganathan N (1999) Pile responses caused by tunneling. Geotech Geoenviron Eng 125(3):207–215

Cheng CY, Dasari GR, Chow YK, Leung CF (2007) Finite element analysis of tunnel–soil–pile interaction using displacement controlled model. Undergr Space Technol 22(4):450–466

Franza A, Marshall AM, Haji T, Abdelatif AO, Carbonari S, Morici M (2017) A simplified elastic analysis of tunnel-piled structure interaction. Tunn Under Space Technol https://doi.org/10.1016/j.tust.2016.09.008

Giardina G, DeJong MJ, Mair RJ (2015) Interaction between surface structures and tunnelling in sand: centrifuge and computational modelling. Tunn Under Space Technol 50:465–78 Elsevier Ltd https://doi.org/10.1016/j.tust.2015.07.016

Huang M, Zhang C, Li Z (2009) A simplified analysis method for the influence of tunneling on grouped piles. Tunn Undergr Space Technol 24(4):410–422. https://doi.org/10.1016/j.tust.2008.11.005

Jose S, Arjun Shounak GH (2015) Finite element analysis of underground metro tunnels. Int J Civil Eng Technol (IJCIET) 6(2):6–15

Kaalberg FJ, Teunissen EAH, van Tol AF, Bosch JW (2005) Dutch research on the impact of shield tunnelling on pile foundations. In: 5th international symposium on geotechnical aspects of underground construction in soft ground, Amsterdam, The Netherlands, pp 123–131

Kitiyodom P, Tatsunori M, Kawaguchi K (2005) A simplified analysis method for piled raft foundations subjected to ground movements induced by tunnelling. Int J Numer Anal Methods Geomech 29(15). John Wiley & Sons, Ltd, pp 1485–1507. https://doi.org/10.1002/nag.469

Lee GTK, Ng CWW (2005) Effects of advancing open face tunneling on an existing loaded pile. Geotech Geoenviron Eng 131(2):193–201

Li P, Fang Q, Zhang D (2014) Analytical solutions of stresses and displacements for deep circular tunnels with liners in saturated ground. J Zhejiang Univ Sci A 15(6):395–404. https://doi.org/10.1631/jzus.A1400023

Loganathan N, Poulos HG, Stewart DP (2000) Centrifuge model testing of tunnelling-induced ground and pile deformations. Geotechnique 50(3):283–294

Mahajan S, Asaf S, Ayothiraman R, Sharma KG, Ramana GV (2016) Numerical analysis on effect of basement raft l (December) pp 15–18

Marshall AM (2012) Tunnel-pile interaction analysis using cavity expansion methods. J Geotech Geoenviron Eng 138(10):1237–1246. https://doi.org/10.1061/(ASCE)GT.1943-5606.0000709

Marshall AM, Haji T (2015) An analytical study of tunnel-pile interaction. Tunn Undergr Space Technol 45:43–51. https://doi.org/10.1016/j.tust.2014.09.001

Meguid MA, Mattar J (2009) Investigation of tunnel-soil-pile interaction in cohesive soils. J Geotech Geoenviron Eng 135(7):973–979. https://doi.org/10.1061/(ASCE)GT.1943-5606.0000004

Mroueh H, Shahrour I (2003) A full 3-d finite element analysis of tunneling-adjacent structures interaction. Comput Geotech 30(3):245–253. https://doi.org/10.1016/S0266-352X(02)00047-2

Mroueh H, Shahrour I (2002) Three-dimensional finite element analysis of the interaction between tunneling and pile foundations. Int J Numer Anal Methods Geomech 26(3):217–230. https://doi.org/10.1002/nag.194

National Capital Region Planning Board (n.d) http://ncrpb.nic.in/policies_strategies.php

"OptumG2" (2013) http://optumce.com/products/optumg2/
Pang CH, Yong KY, Chow YK, Wang J (2006) The response of pile foundations subjected to shield tunnelling. In: 5th international conference of TC28 of the international society for soil mechanics and geotechnical engineering, ISSMGE; Amsterdam; Netherlands, pp 737–43
Selemetas D, Standing JR, Mair RJ (2006) The response of full-scale piles to tunnelling. Geotechnical aspects of underground construction in soft ground. In: Proceedings of the 5th international conference of TC28 of the ISSMGE pp 763–69
Singh M, Viladkar MN, Samadhiya NK (2017) Seismic analysis of delhi metro underground tunnels. Indian Geotech J 47(1):67–83 Springer India https://doi.org/10.1007/s40098-016-0203-9
Vorster TE, Klar A, Soga K, Mair RJ (2005) Estimating the effects of tunneling on existing Pipelines. J Geotech Geoenviron Eng 131(11):1399–1410 American Society of Civil Engineers https://doi.org/10.1061/(asce)1090-0241(2005)131:11(1399)
Yao A, Yang X, Dong L (2012) Numerical analysis of the influence of isolation piles in metro tunnel construction of adjacent buildings. Procedia Earth Planet Sci 5:150–154 https://doi.org/10.1016/j.proeps.2012.01.026
Yao J, Taylor RN, Mcnamara M (2008) The effects of loaded bored piles on existing tunnels. In: Geotechnical aspects of underground construction in soft ground—6th international symposium (IS-Shanghai), no. 1988:735–741 https://doi.org/10.1201/9780203879986.ch102
Zhang C, Jian Y, Huang M (2012) Effects of tunnelling on existing pipelines in layered soils. Comput Geotech 43:12–25. https://doi.org/10.1016/j.compgeo.2012.01.011
Zidan AF, Ramadan OMO (2015) Three dimensional numerical analysis of the effects of tunnelling near piled structures. KSCE J Civil Eng 19(4):917–928. https://doi.org/10.1007/s12205-014-0741-6

Effect of Underground Blast on Underlying Ground Media Below Substructure

Ranjan Kumar, Kapilesh Bhargava and Deepankar Choudhury

Abstract Geotechnics plays important role in building sustainable civil, pavement, and railroad infrastructure. In recent past, there is an increase in projects related to civil and industrial infrastructure which involves planning, design, and construction of buildings, pavement, railroad track, bridges, metro, and other allied fields. Since last few years, various man-made blast activities have increased which cause increase in threat. This has generated interest in foundation designers to consider effects of blast loads on design of foundations. In case of blast load, protection of human beings, structures, and housed equipment is a major concern in case of blast. Blast load sources are the explosions of penetrated missile into the ground by attack of terrorist. The other sources are the explosions carried out for construction activity, quarrying, mining activities, and soil/rock breaking. Foundation systems resting on ground media may undergo excessive settlement or distortion due to blast phenomenon which in turn may collapse the building. There are challenges in design and construction of substructure considering underground blast. Hence, proper care needs to be taken in the design for the prevention of foundation failure. Solution of geo-mechanical problem involves analysis of soil–foundation interaction which is carried out by various numerical methods. In the present paper, finite difference program Fast Lagrangian Analysis of Continua in 3 Dimensions ($FLAC^{3D}$) is used

R. Kumar (✉)
Civil Engineering Division, Bhabha Atomic Research Centre, Trombay 400085, Mumbai, India
e-mail: ranjancv42@gmail.com

K. Bhargava
Civil Engineering Directorate, NRPSED, Nuclear Recycle Board, Bhabha Atomic Research Centre, Anushaktinagar 400094, Mumbai, India
e-mail: kapilesh_66@yahoo.co.uk

Discipline of Engineering Sciences, Homi Bhabha National Institute, Anushaktinagar 400094, Mumbai, India

D. Choudhury
Department of Civil Engineering, Indian Institute of Technology Bombay, Powai 400076, Mumbai, India
e-mail: dc@civil.iitb.ac.in

Academy of Scientific and Innovative Research (AcSIR), CSIR—Central Building Research Institute (CBRI), Roorkee, India

R. Sundaram et al. (eds.), *Geotechnics for Transportation Infrastructure*, Lecture Notes in Civil Engineering 28, https://doi.org/10.1007/978-981-13-6701-4_23

for soil–foundation interaction. In the present paper, effects of blast on underground soil media have been studied. Effects of blast-scaled distances and type of soil on bearing capacity have been presented.

Keywords Shallow foundation · Blast loading · FLAC^{3D}

1 Introduction

As various man-made activities have increased threat in the recent past, there is a considerable attention of foundation designers to take care of effects of blast loads on foundations. Major concern is to protect the foundation, human beings, and housed equipment when subjected to blast load. Blast can cause severe damage to shallow foundations. Estimation of responses of foundations subjected to blast loading is an important topic of research for geotechnical engineers. A greater understanding regarding the response of foundation subjected to blast loading is required as it is more complex.

When foundation is subjected to underground blast loading, the loading is characterized by short duration and high intensity. The duration of motion in earthquake is in the range from seconds to minutes. However, the duration of motion in blast is in the range of 0.1–0.001 s. Explosions generate ground vibrations. The ground vibration can be resolved in three mutually perpendicular directions, namely longitudinal, transverse horizontal, and transverse vertical. In most of the cases, the transverse horizontal component is much smaller than the other two. There are ground vibration parameters, namely acceleration, velocity and displacement, and their respective frequencies.

Blast involves shock wave propagation in the ground media. In the past, empirical, numerical, and analytical methods have been used to address the problem of foundation when it is subjected to blast. State-of-the-art review for response of foundations subjected to blast has been carried out in the literature (Kumar et al. 2012). It is observed that soil–structure interaction (SSI) in case of foundation subjected to blast has not been paid attention adequately. Response of shallow foundation in rock subjected to underground blast in soil using Fast Lagrangian Analysis of continua (FLAC^{3D} 2009) has been evaluated by Kumar et al. (2014a). Soil material model was validated and experimental vibration parameters were used for the establishment of representative soil parameters before the estimation of response of foundation subjected to blast loading. By using FLAC^{3D}, rock simulation has been carried out in case of underground blasting by Kumar et al. (2015). Reduction of bearing resistance of rock below foundation subjected to underground blast has been presented by Kumar et al. (2016b). In practice, shallow foundations are constructed in soil strata for several residential and industrial buildings.

Soil–structure interaction problem in the soil can be analyzed using Fast Lagrangian Analysis of continua (FLAC^{3D}) software which is based on finite differ-

ence method. Experimental vibration parameters in soil were used for establishing soil model parameters and consequently for validation of material model.

In case of blast loading, shallow foundations may be severely damaged. There is a need for study on the behavior of shallow foundation under underground blast, and there is scarcity of such study.

In the present study, finite-difference-method-based software FLAC^{3D} is used to analyze the SSI problem. The soil medium is calibrated with respect to available experimental data. Consequently, shallow square foundations resting on various types of soils and subjected to underground blast have been analyzed using FLAC^{3D}. Analysis results were compared, and conclusions are provided to understand the complete behavior of such shallow foundations in soils subjected to underground blast.

2 Simulation of Ground Media Under Substructure Under Blast

Peak particle velocity (PPV) is an important blast-induced vibration parameter used for numerical modeling of blast wave propagation on soil/rock to solve soil–foundation interaction problem under blast loading. It is clear from literature that PPV is good general index of damage to structure. PPV should be within permissible limit to avoid damage to foundations. In the absence of field blast data, empirical models are used to estimate PPV. PPV equation for soil site has been developed by present authors as given in Eq. (1). Free field pressure at explosion crater boundary will be estimated by using Eq. (2). The developed PPV model for soil sites has been used for the estimation of free field peak pressure.

$$v = \left(\frac{E}{\gamma}\right)^{0.229} D^{-(1.6985-0.175\times S)} \tag{1}$$

where,

v PPV, m/s;
E Young's modulus of soil, MPa;
γ unit weight of soil, kN/m^3;
S degree of saturation (in fraction, maximum = 1.0);
D scaled distance, m/kg$^{1/3}$.

Calibration of soil model required site field data. Literature survey was carried out, and field data of Leong et al. (2007) and Charlie et al. (1992) were considered belonging to saturated clay and saturated alluvium sand site, respectively. The details of the field data are shown in Table 1.

Soil ground media subjected to blast is modeled in FLAC^{3D}, and PPV is measured at various points and compared with the field data. After blast, PPV is calculated from presently developed model.

Table 1 Summary of field blast parameters for selected saturated clay and saturated alluvium sand sites (modified after Leong et al. 2007 and Charlie et al. 1992)

Author	Type of soil	Blast depth (m)	Charge weight (kg)	Measurement	
				Depth (m)	Distance from blast (m)
Leong et al. (2007)	Saturated clay	1	4.352	1	1.5
Leong et al. (2007)	Partially saturated sand	2, 2.5	4.352	2, 2.5	1.6, 2, 3, 4.3 and 4.8
Charlie et al. (1992)	Saturated alluvium sand	3	0.0045	0.1	6.1, 12.2

Crater is created after the blast. Crater boundary is identified based on literature available. The value of spherical crater diameter is taken as 1 m. Through center of the crater, crater geometry and dynamic load application are symmetrical around a horizontal axis. Blast-free field pressure is estimated and applied at the crater boundary. The load application is normal to the crater boundary. Also, the load is distributed uniformly along the crater boundary.

Soil ground media for both the sites are modeled in FLAC^{3D}. Depths of the blast for these sites are 1 and 3 m, respectively, and spherical crater center is considered accordingly. Free field peak pressure is estimated by using Eq. (2), and the same is applied at the spherical crater boundary.

$$P_o = \rho c v \tag{2}$$

where,

P_o peak pressure (psi);
v peak particle velocity (fps);
ρ_c acoustic impedance (psi/fps).

Figure 1 shows basic soil ground media model in FLAC^{3D}. For these two sites, different brick-zone sizes are considered which are taken as 25 m × 20 m × 11 m and 25 m × 20 m × 13 m, respectively. Soil element size for both sites in all the three directions is taken as 0.5 m. From the constitutive model library of FLAC^{3D}, Mohr-Coulomb model is selected for modeling of soil. Input parameters of soil to FLAC^{3D}, namely Young's modulus, Poisson's ratio, shear modulus, bulk modulus, cohesion, and angle of friction are estimated by correlations. The estimated undrained soil parameters are given in Table 2.

Artificial boundaries are used to limit the model size. At bottom and three side faces, quiet or viscous boundary is considered. At front and top faces, surfaces are kept free. Rayleigh stiffness damping is applied which is independent of dynamic

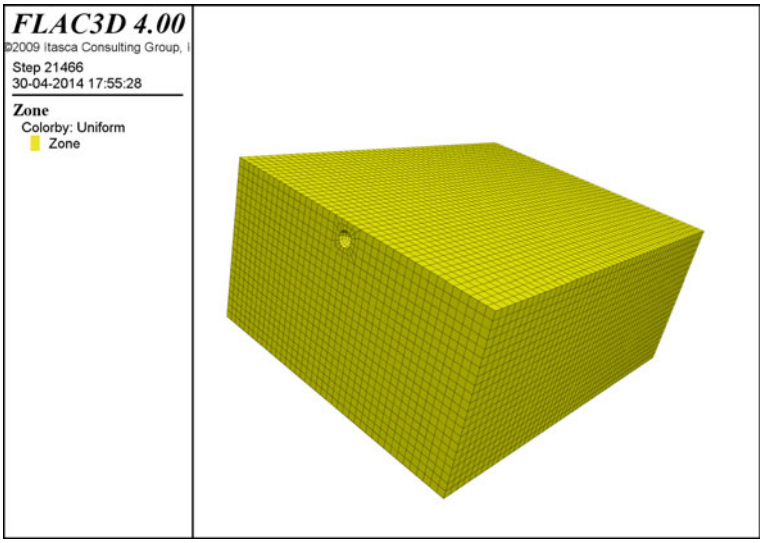

Fig. 1 FLAC model for saturated clay

Table 2 Soil input parameters for FLAC

Parameters	Leong et al. (2007), sat. clay	Leong et al. (2007), part. sat. sand	Charlie et al. (1992), sat. sand
Unit weight (γ, kN/m^3)	19	16.5	18.4
E (MPa)	2724.7	22.02	6854.3
Poisson's ratio (ν)	0.4949	0.2087	0.35
K (MPa)	3569.65	42.53	7615.9
G (MPa)	36.53	30.75	2538.63
c, seismic velocity (m/s)	1380	225	1396
Cohesion (C, kPa)	192.3	10.76	3
Angle of friction (φ, degree)	35.69	14	28
Tensile strength (kPa)	0	0	0
P_o from Eq. (2) (N/m^2)	23.74×10^6	1.6×10^6	5.95×10^6

frequency. The value of damping ratio is taken as 0.01 at 50 Hz frequency. Peak pressure is applied on the crater boundary which is time-independent.

Ground motion is described in terms of time history of acceleration, velocity, and displacement. These time histories are not readily calculated. UFC 3-340-02 (2008) recommends design parameter as peak values of ground motion instead of time histories in case of underground protective structures resisting shock loads. Hence, the time histories may not be required to be obtained.

Table 3 Calculated bearing capacity of soil for square footing

Type of soil	Calculated allowable bearing capacity (kN/m^2)
Saturated clay	184
Partially saturated sand	102.36

Values of soil input parameters were put into the equations given in TM 5-855-1 (1986), and output results were obtained. The results were compared with FLAC^{3D} results for both the soil sites.

Output of the analysis by FLAC^{3D} is generated in terms of history of particle velocity with respect to time for saturated clay, partially saturated sand, and coarse sand sites. The outputs are presented at various distances away from the blast. The point of generation of particle velocity time history for all the sites is different, and it is as per the measurement points given by respective researchers. For saturated clay, the particle velocity time history plot is generated at distances 1, 1.5, and 3.3 m away from the blast point. For partially saturated sand, the particle velocity time history plot is obtained at distances 1.6, 2, 3, 4.3, 4.8, and 6.5 m away from the blast point. The FLAC^{3D} generated PPV values were compared with that obtained from the field value.

3 Simulation of Ground Media with Foundation

In the present study, square shallow footing is modeled in two types of soils, namely saturated clay and partially saturated sand. FLAC^{3D} is utilized to simulate foundation in soil subjected to blast.

The model contains two parts—one is soil and another is footing. Instead of modeling actual footing, footing load is applied at embedment depth. Size of square footing is 2 m $\times$ 2 m at a depth of 1.5 m from ground level. Size of the entire soil model is taken as 25 m $\times$ 20 m $\times$ 11 m based on number of trials to make sure of the stresses in boundaries.

Blast load is considered to act in a sphere of radius 0.5 m at 15 m distance from center of the footing. Spherical cavity of radius 0.5 m is modeled for this blast load simulation. Mohr-Coulomb model of soil is considered for the present analysis. Blast loading of charge weight 100 kg is applied using the soil model developed by present authors (Kumar et al. 2016a). Various soil properties, namely unit weight, degree of saturation, and Young's modulus have been used to develop generalized empirical models for blast-induced parameters (Kumar et al. 2014b). Allowable bearing capacity of the soils for square footing is calculated and applying factor of safety is 2, which is given in Table 3. Pressure at different times is calculated. Compressive stresses are negative in FLAC^{3D}.

Table 4 Reduction in bearing resistance with scaled distance for foundation in various soils

SD (m/kg$^{1/3}$)	Normal stress (kPa), *szz* below center of footing after blasting			
	Partially saturated sand	% reduction	Saturated clay	% reduction
1.7	0	100	0	100
2.6	61	90	0	100
3.4	213.5	65	0	100
4.3	335.5	45	0	100
7	390.4	36	6.2	95
10	427	30	12.4	90
15	457.5	25	24.8	80

4 General Response Below Substructure

Table 4 shows reduction in bearing resistance with scaled distance for foundation in various soils.

The static bearing pressure applied to foundations acts as resistance to external loads. This resistance is affected due to blast wave as evident from Table 4. It is observed that *szz* stress (stress along *z* direction on plane having normal in *z* direction) which initially is the static bearing pressure changes as the blast wave advances toward the footing. As scaled distance decreases, there is a decrease in *szz* below the center of footing. As scaled distance increases, after sometime, it becomes equal to static pressure. This resistance can become zero if high blast pressure is applied. For same scaled distance, reduction in *szz* in partially saturated sand and saturated clay is different. The possible reason can be due to different soil properties.

As evident from Table 4, in case of partially saturated sand and saturated clay, reduction in bearing resistance is 100% at a scaled distance up to 1.7 and 4.3 m/kg$^{1/3}$, respectively.

5 Reduction of Bearing Resistance

Contour of *z*-displacement below footing in both the soils under static condition is generated. Contour of *szz* stress below footing in both the soils under static condition is also generated. Compressive stresses are negative in FLAC^{3D}. Settlements are negative (i.e., vertically downward) in FLAC^{3D}.

6 Conclusions

Soil–foundation interaction has been modeled in FLAC^{3D} and response of foundation was obtained. In case of shallow foundation response analysis, FLAC^{3D} output parameters are displacement, stress, pore pressure versus time history. Contour of *z*-displacement below footing is generated. The displacement is more below the footing, and it gets reduced at a distance away from bottom of the footing. Table 4 shows reduction in bearing resistance with scaled distance for foundation in various soils. In case of saturated clay and partially saturated sand, reduction in bearing resistance is 100% at a scaled distance up to 4.3 and 1.7 m/kg$^{1/3}$, respectively. Increase in displacement is observed under dynamic load.

Effect on bearing capacity will be useful in determining the factor of safety to be applied to allowable bearing capacity. These results can be used by practicing engineers for the design of shallow foundations in soil and soil subjected to blast loadings.

References

Charlie WA, Jacobs FJ, Doehring DO (1992) Blast induced liquefaction of an alluvial sand deposit Geotech. Testing J ASTM 15(1):14–23

FLAC^{3D} (2009) Fast Lagrangian analysis of continua in 3 dimensions, version 4.00. User's Manual Itasca Consulting Group, Minneapolis, Minnesota, USA

Kumar R, Choudhury D, Bhargava K (2012) Response of foundations subjected to blast loadings: state of the art review. Dis Adv 5(1):54–63

Kumar R, Choudhury D, Bhargava K (2014a) Response of shallow foundation in rocks subjected to underground blast loading using FLAC^{3D}. Dis Adv 7(2):64–71

Kumar R, Choudhury D, Bhargava K (2014b) Modeling of soil subjected to underground blast using FLAC^{3D}. In: CD-ROM proceedings of 5th international congress on computational mechanics and simulation (extended abstract), Chennai, India, 10–13 Dec 2014, pp 852–855

Kumar R, Choudhury D, Bhargava K (2015) Simulation of rock subjected to underground blast using FLAC^{3D}, Japanese Geotechnical Society Special Publication, Section 1. Characterization-Rock and expansive soil. In: The 15th Asian regional conference on soil mechanics and geotechnical engineering, Japan 2(12):508–511. http://doi.org/10.3208/jgssp.IND-27

Kumar R, Choudhury D, Bhargava K (2016a) Simulation of soil subjected to underground blast using FLAC^{3D}. In: Proceedings of 6th international congress on computational mechanics and simulation, ICCMS 2016, Mumbai, India, 27 June–01 July 2016, pp 708–711

Kumar R, Choudhury D, Bhargava K (2016b) Reduction of bearing resistance of rock below foundation subjected to underground blast. In: Extended abstract volume of international geotechnical conference on sustainability in geotechnical engineering practices and related urban issues, Mumbai, India, 23–24 Sept 2016

Leong EC, Anand SH, Cheong K, Lim CH (2007) Re-examination of peak stress and scaled distance due to ground shock. Int J Impact Eng 34:1487–1499

TM 5-855-1 (1986) Fundamentals of protective design for conventional weapons united states. Department of the Army Technical Manual, U.S. Department of the Army, Vicksburg, MS

Unified Facilities Criteria (UFC) 3-340-02 (2008) Structures to resist the effects of accidental explosions. Department of Defense, United States of America

Excess Pore-Water Pressure Generation and Mud Pumping in Railways Under Cyclic Loading

Aruni Abeywickrama, Buddhima Indraratna and Cholachat Rujikiatkamjorn

Abstract High-speed heavy haul trains have become one of the most popular and economical modes of transportation in the modern world to cater for increased demand in freight for agricultural and mining activities. However, when these trains travel through vulnerable areas occupying soft subgrade formations, frequent maintenance is required to prevent differential settlement and localized failures of track. The poor performance of track caused by ballast fouling is also often observed where fines are fluidized and pumped into the ballast voids (mud pumping), which in turn create ballast pockets, mud holes and track instability. When saturated subgrade is subjected to short-term undrained cyclic loading, the pore-water pressure can accumulate inducing fine particles to migrate upwards into the ballast layer. Mud pumping causes millions of dollars of damage to heavy haul rail networks every year in Australia. This paper presents a critical review primarily focused on the role of excess pore-water pressure generation on mud pumping under cyclic loading. Mitigation of these issues can result in considerable savings to rail authorities on recurrent track maintenance activities.

Keywords Cyclic loading · Mud pumping · Railway subgrade

1 Introduction

The demand for railway transportation for passengers and freight has been increasing with the expectation of faster trains. As the world searches for greater mobility and environmental issues become more critical, high-speed heavy haul is set to become an

A. Abeywickrama (✉) · B. Indraratna · C. Rujikiatkamjorn
Centre for Geomechanics and Railway Engineering, University of Wollongong, Wollongong, NSW 2522, Australia
e-mail: abkal203@uowmail.edu.au

B. Indraratna
e-mail: indra@uow.edu.au

C. Rujikiatkamjorn
e-mail: cholacha@uow.edu.au

R. Sundaram et al. (eds.), *Geotechnics for Transportation Infrastructure*, Lecture Notes in Civil Engineering 28, https://doi.org/10.1007/978-981-13-6701-4_24

attractive option for freight transport. However, the increasing axle loads and speeds of trains can lead to various track issues including ballast fouling, track failure, ballast degradation and mud pumping. Of all these track problems, mud pumping is considered to be crucial and is generally specific to saturated soft clay subgrades in which the natural water content is close to the liquid limit.

Mud pumping occurs when the cyclic load of passing trains generates excess pore-water pressure that causes upward movement of fluidized subgrade to the upper ballast layer causing differential settlement. Therefore, track maintenance or upgrading is required frequently to establish a liable and safe operation. In many countries including Australia, India and China, as much as hundreds of millions of dollars have been spent each year for track maintenance (Indraratna et al. 2011b). In practice, the fouled ballast is replaced by fresh ballast once significant differential deformation of the track is observed. The cause and mechanisms of mitigating this phenomenon are still poorly understood, and this has resulted in higher track maintenance costs (Li and Selig 1995, Indraratna et al. 2011b). Therefore, it is of paramount importance to investigate the causes of mud pumping and to identify the characteristics of subgrades, which are susceptible to mud pumping.

2 Cyclic Loading of Soft Clay Subgrades

Railway subgrade containing fine-grained soil and excessive moisture content can be susceptible to failure under cyclic loading (Li and Selig 1995).

It is shown that cyclic stress ratio (CSR) is considered to be one of the crucial factors affecting the occurrence of mud pumping.

The cyclic stress ratio is defined by Kalafat et al. (2003) and Saglam and Bakir (2014):

$$\mathrm{CSR} = \frac{q_{\mathrm{cyc}}}{2\sigma_3'} \tag{1}$$

where, q_{cyc} is the cyclic deviator stress which is determined based on train loading and σ_3' is the effective confining pressure.

In Australia, high-speed heavy haul trains (more than 25-tonne axle load with speed greater than 150 km/h) induce high cyclic stresses and high frequency loading onto the rail track substructure. Cyclic stress can affect the behaviour of soft soil, and it is a function of the track gauge, axle load, and train speed. The loading frequency on the subgrade due to a moving train is determined based on the train speed, carriage length, type of bogies and the axle distance (Liu and Xiao 2009).

The drainage condition of cyclic loading can be influenced by the loading period. Undrained conditions which do not allow any dissipation of excess pore-water pressure can be observed in clays for short-term cyclic loading (Saveur 2003) while this condition can change to a partially drained condition for longer term cyclic loading,

where the generation and dissipation of excess pore-water pressure during each cycle is repeated (Hyodo et al. 1992).

The stress–strain behaviour of soft clay subjected to repeated loads is usually nonlinear. It is found that soft clays subjected to cyclic loads tend to fail at very low applied stress compared to ones subjected to static load (Attya et al. 2007a, b). Under cyclic loading, excess pore-water pressure and axial strain are often higher than one under static loading (Loh and Nikraz 2012).

The loading rate is significant on the undrained strength of saturated clay, and as the strain rate increases, the undrained shear strength also increases (Ni et al. 2012; Richardson and Whitman 1963). The shear strength under a low frequency is observed to be lower than when it is loaded at high frequencies (Nieto Leal and Kaliakin 2016).

Due to successive shear deformation over time, the particles are rearranged, and this results in soil destructuration, with a build-up of excess pore-water pressure and a critical loss of shear strength (Kalafat et al. 2003).

3 Cyclic Pore-Water Pressure

The application of cyclic loading on soft, low-permeability soils can affect the corresponding stress–strain behaviour and induces cumulative excess pore-water pressure (PWP) under undrained condition. This results in significant loss of strength and stiffness (Indraratna et al. 2011a; Matasović and Vucetic 1995).

When soft clays are subjected to short-term cyclic loading, cohesive soil can be considered to be under undrained conditions that result in a very high level of pore-water pressure accumulation (Nhan et al. 2015). The loading period and the loading rates affect the generation and accumulation of excess pore-water pressure when higher pore-water pressures are accumulated due to slower loading rates (Krechowiecki-Shaw et al. 2016).

Railway tracks experience cyclic loading at intervals with a rest period between two train passages. For new tracks, this operating interval should be at least 2 h to allow the dissipation of cyclic-induced excess pore-water pressure (Indraratna et al. 2011a). If not, the excess pore-water pressure accumulation due to the subsequent train passage would be much higher, such that it would result in complete loss of soil strength.

In the literature, the normalized excess pore-water pressure is often used instead of the excess pore-water pressure. Attya et al. (2007a) defined the normalized excess pore-water pressure (U^*) as the ratio between excess pore-water pressure (ΔU) and the effective initial confining pressure (P'_{c0}) given by:

$$U^* = \frac{\Delta U}{P'_{c0}} \tag{2}$$

When the normalized pore-water pressure reaches unity, soils have zero effective stress, which initiates liquefaction (Ni 2012). The excess pore-water pressure at which failure starts is termed as the critical pore-water pressure.

Wilson and Greenwood (1974) studied the relationship between pore-water pressures and axial strains. They found that there are two components of pore-water pressures: the non-recoverable component and recoverable component. In addition, they found a linear relationship between pore-water pressures and strains. The recoverable component of excess pore-water pressure is proportional to the recoverable strain, and the non-recoverable component of excess pore-water pressure is proportional to the non-recoverable strain but with a different constant of proportionality (Wilson and Greenwood 1974).

High excess pore-water pressure generation in the subgrade affects the stability of the subgrade, requiring a lengthy period of dissipation. Therefore, soft clay subgrades should be improved in order to control the generation of excess pore-water pressure, as well as curtailing the vertical and lateral displacements (Indraratna et al. 2011a).

3.1 Factors Affecting Cyclic Pore-Water Pressure Generation

Generation of cyclic pore-water pressure in subgrade is affected by repeated load and frequency of train and track substructure characteristics. Cyclic loading factors include cyclic stress, frequency, number of cycles and the drainage condition. Characteristics of the subgrade soil under cyclic load can be influenced by the percentage of fines, confining pressure, plasticity, over-consolidation ratio and in situ moisture content.

3.1.1 Frequency

Mortezaie and Vucetic (2013) conducted a set of cyclic strain-controlled tests on normally consolidated kaolinite clay and showed that for a given number of cycles under low frequency cyclic loading, there is a higher pore-water pressure built up in the soil than that generated by a higher frequency loading. Procter and Khaffaf (1984) came to the same conclusion. However, Yasuhara et al. (1982) carried out a series of stress-controlled cyclic triaxial tests on a remoulded soft marine clay, and they found that the generation of excess pore-water pressure was more predominant when the frequency of the cyclic loading became larger. Zhou and Gong (2001) also state that high excess pore-water pressures are usually generated under high frequencies.

3.1.2 Over-Consolidation Ratio (OCR)

Soralump and Prasomsri (2015) studied the effect of over-consolidation ratio on the cyclic pore-water pressure response. They conducted cyclic hollow cylinder tor-

sional tests in undrained conditions on compacted clay specimens with different OCRs and observed that the normalized residual cyclic excess pore-water pressure is consistently lower at a higher over-consolidation ratio.

Although the excess pore-water pressure in normally consolidated (NC) clay is always positive, negative pore-water pressures can be generated in over-consolidated (OC) clay (Vucetic and Dobry 1988). Therefore, it is comparatively easy to model the relationship between the cyclic pore-water pressure and the degradation in normally consolidated clays.

3.1.3 Drainage Condition

Excess pore-water pressures (PWPs) are generated in the subgrade under undrained and partially drained conditions. Figure 1 illustrates how excess PWP is generated under two different drainage conditions based on the existing literature. Zhou and Gong (2001) conducted several stress-controlled cyclic undrained triaxial tests for different cyclic stress ratios (CSR) without prefabricated vertical drains (PVDs), and they observed a higher excess PWP generation compared to the partially drained conditions as observed by Attya et al. (2007a, b). In the undrained condition also, Zhou and Gong (2001) observed that generated excess PWP was higher with increased CSR.

It is obvious that the partially drained condition with prefabricated vertical drains controls the rapid build-up of pore-water pressure and provides improvement of the soft soil even during cyclic loading (Attya et al. 2007a, b).

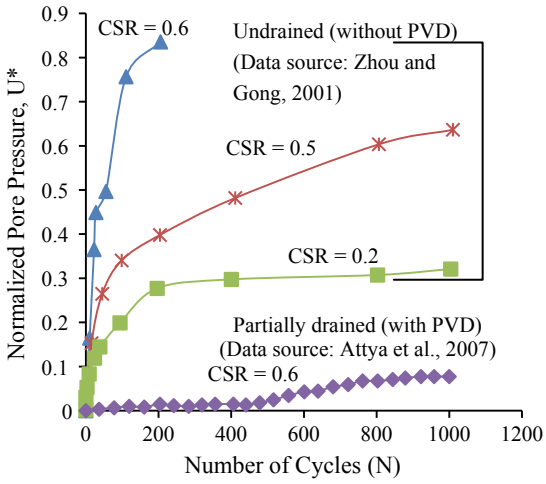

Fig. 1 Excess pore-water pressure generation under undrained and partially drained conditions

4 Mud Pumping in Railways

Mud pumping is a phenomenon in which fine particles from the subgrade migrate upward into the sub-ballast layer voids due to the generation of cyclic excess pore-water pressure; this results in differential track settlement (Alobaidi and Hoare 1996). The mud collected on the ballast appears as solidified mud in relatively dry periods and as slurry during the rainy seasons. When fine particles are pumped up and accumulate in the ballast layer, the ballast becomes clogged and can no longer perform its duty (Aw 2007).

According toARC.gov.au (2017), mud-pumping costs millions of dollars to Australia's rail network every year. Mud pumping occurs mostly in the waterlogged areas of the railway tracks that increase the risk of derailment at certain speeds. This has become a major issue for railways in NSW and in other areas of Australia, especially for trains which are now forced to reduce to speeds as slow as 60 km/h when they cross vulnerable areas. Obviously, finding a solution to this problem can be a huge benefit for railway operations.

4.1 Characteristics of Mud-Pumping Soil

Plastic clay soils are generally considered non-liquefiable. However, some of mud-pumping incidents indicate that cohesive soils are also liquefiable.

The plasticity chart of the subgrade at reported mud pumping sites as shown in Fig. 2 illustrates that medium-to-low plastic clay is also susceptible to mud pumping.

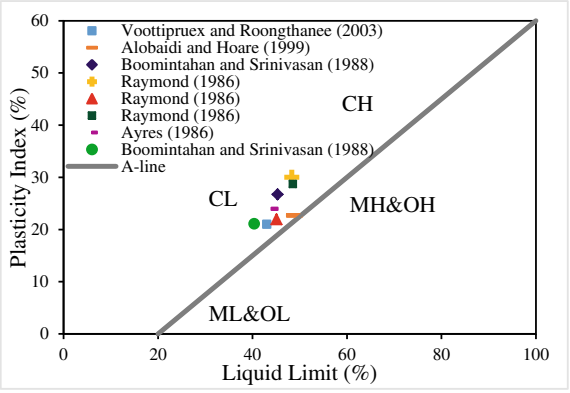

Fig. 2 Plasticity chart of the subgrade at reported mud pumping sites in the literature *Data source* Aw (2007)

4.2 Factors Affecting Mud Pumping

From the existing literature, it is clear that mud pumping is caused mainly by the development of pore-water pressure at the subgrade–sub-base interface, and that the cyclic deformation of subgrade caused by passing traffic is directly related to mud pumping. It is also important to discuss the factors affecting mud pumping.

4.2.1 Initial Dry Unit Mass

Mud pumping usually occurs in sub-soil with a relatively low dry unit mass, whereas with a higher dry unit mass there is a smaller change in volume change and thus a lower pore-water pressure (Duong et al. 2014).

When the initial dry unit mass is higher, the compressibility is lower. Therefore, corresponding to a limited volume change, lower excess pore-water pressures are generated in a subgrade at a higher initial dry unit mass. On the contrary, a subgrade soil with a low initial dry unit mass is highly compressive and enables higher excess PWP to be developed. Thus, the mud-pumping potential is relatively high in subgrade soils with lower dry unit weight.

Duong et al. (2014) defined two types of phenomena that they have observed. The phenomena in which significant migration of fine particles has occurred were defined as mud pumping, while the phenomena in which only a few fine particles have migrated were defined as the interlayer creation.

4.2.2 Permeability

In a marine environment, soft clay normally has a very low permeability, so the dynamic deformation of marine clay is influenced by a significant increase in pore-water pressure, and since most railway lines travel along the coastal belt, the significance of excess pore-water pressure and subsequent mud pumping becomes a serious issue affecting track performance.

According to Alobaidi and Hoare (1996), the main driving force in migrating fine particles in the subgrade into the ballast is the high hydraulic exit gradient created as a result of the dissipation of excess pore-water pressure; however, the high pore pressure is not the sole contributor towards mud pumping.

It has been found that a layer of sand between the subgrade and sub-base/ballast layers could control the pumping of fines (Ayres 1986). As an alternative, if geotextiles are used to control pumping, the excess pore-water pressure at the surface of the subgrade layer can dissipate very quickly, thus setting up a high exit hydraulic gradient which pushes the soil particles upward. The type of geosynthetics used between the subgrade and ballast layers can control mud pumping to some extent.

4.2.3 Plasticity and Fine Content in the Soil

It is generally believed that increase in plasticity increases the resistance against liquefaction in silty or clayey soil. The nature of pore pressure generation in non-plastic silts is the same as that for sands. Guo and Prakash (2000) state that the above-mentioned phenomena may take place if a small percentage of high plastic material is added to non-plastic silt. Those two types of phenomena can be described as follows:

(1) High pore-water pressures are caused due to the reduction in the hydraulic conductivity of the soil resulting from the increase in clay content; and
(2) The liquefaction resistance of the mixture is increased due to the impartation of the cohesive character to this mixture by soil plasticity.

Therefore, it is not fully understood whether the liquefaction resistance increases or decreases with the plasticity in silty or clayey soils. There appears to be a critical PI at which the liquefaction resistance is minimal. The liquefaction resistance of silt–clay mixtures increases with the increase of plasticity index beyond this critical point (Guo and Prakash 2000). Tsai et al. (2010) also investigated the effect of fine content and plasticity on the liquefaction resistance using a series of cyclic triaxial tests with remoulded samples. Samples were prepared by adding silty fines and clay fines separately with different percentages to study both the effect of fine percentage and plasticity on liquefaction resistance. They observed that the generation of excess pore-water pressure increases with the increase in silt percentage. On the contrary, the generation of excess pore-water pressure decreases with the increase in clay percentage. This behaviour is depicted in Fig. 3.

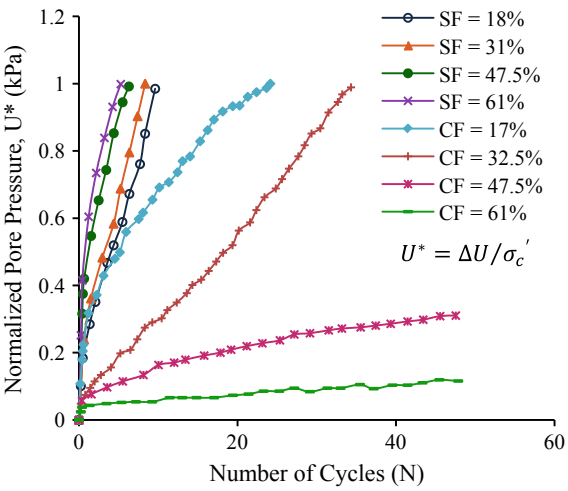

Fig. 3 Effect of fine percentage and plasticity on liquefaction resistance. *Data source* Tsai et al. (2010)

For increased excess pore-water pressure, the liquefaction resistance decreases with the increase in silt percentage and for reduced excess pore-water pressure, the liquefaction resistance increases with the increase in clay percentage.

4.2.4 In Situ Moisture Content

In situ water content and the liquid limit of soil influence mud pumping. According to Seed et al. (1983), fine-grained soils that may be susceptible to liquefaction appear to have a Liquid Limit <35% and an in situ water content >90% of LL. Aw (2007) also has analysed plasticity index (PI) data and liquid limits (LLs) of subgrade soil at reported mud pumping sites, as shown in Fig. 2. Therefore, an approximate range of 35–50% can be taken as the LL of soil that may be susceptible to mud pumping based on past studies.

4.3 Mechanism of Mud Pumping

Various researchers have proposed several contradictory mechanisms for mud pumping; for instance, Alobaidi and Hoare (1996, 1999) state that mud pumping is mainly caused by the development of pore-water pressure at the interface between the subgrade and sub-base or sub-ballast layer. Duong et al. (2014) described mud pumping to occur when high pore-water pressures are generated, and then fine particles lose their apparent cohesion (i.e. segregation). Subsequently, when this pressure dissipates, the particles are brought up to the sub-ballast layer.

However, Tadatoshi (1977) states that mud pumping is caused due to the suction resulting from unloading in a railway track. In this explanation, the sleepers (ties) are suspended from the rail due to the eroded subgrade when there is no trainload, but when a train passes the ties are pushed down into the ground thus generating a high pore-water pressure. According to Tadatoshi (1977), during unloading, the space created by the ties induces a suction pressure that facilitates fine particles in the subgrade to be drawn up to the ballast layer. This mechanism of mud pumping is shown in Fig. 4.

4.4 Remediation of Mud Pumping

In Australia, various field trials have been carried out to remediate mud-pumping problem in vulnerable subgrades, but many of them have not seem systematically studied and reported. Therefore, it is imperative to establish the mechanisms and possible remedial methods related to mud pumping. In practice, track realignment and ballast addition are two of the cheapest and temporary solutions adopted. The rails are lifted to replenish new ballast, so that the contaminated ballast can be discarded.

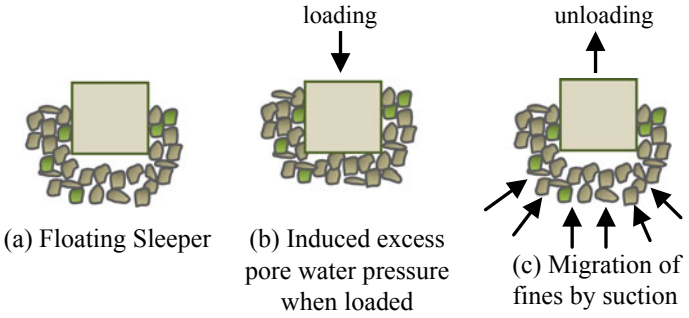

Fig. 4 Mechanism of mud pumping (Tadatoshi 1977)

Sometimes, the fouled ballast layer is completely replaced with fresh ballast and sub-ballast as mud pumping fouls the granular media and impedes drainage. Li and Selig (1998) found that increasing the thickness of the granular layer can improve the lifespan of tracks with problematic soft subgrade, and reduces the adverse effects of mud pumping.

There are a few reported incidents that a sand layer in between the sub-ballast and the subgrade can prevent mud pumping effectively. Permanent filtering of cohesive soil under dynamic conditions for keeping the subgrade from migrating into the ballast is then activated while providing adequate drainage (Ayres 1986).

Some studies have been carried out to investigate the use of geotextiles as separators to prevent migration of fine particles between cohesive subgrade soil and coarse aggregate layers. Although geotextiles are effective in preventing the penetration of the coarse aggregates of the sub-base layer into the subgrade, their action in the reverse direction is not efficient (Raymond 1999).

In addition, a few subgrade improvement methods have been used for the remediation of mud-pumping sites. Soft ground improvement methods such as lime stabilization and hot mixed asphalt can be used to strengthen the subgrade and mitigate mud pumping susceptibility (Aw 2007).

Although there are some techniques adopted to remediate mud pumping, proper solutions cannot be obtained unless the causes and mechanisms of mud pumping are well understood and studied in depth. At University of Wollongong, Ni (2012) conducted a series of cyclic triaxial tests on remoulded soft clay samples with and without prefabricated vertical drains (PVDs) using a large-scale cyclic triaxial apparatus. The excess pore-water pressure generated under cyclic loading with and without PVD was investigated in this study. It was found that the PVD under cyclic loading allows the generated cyclic excess pore-water pressures to dissipate quickly during and after the cyclic load application. These studies imply that PVD would offer a suitable solution for soil fluidization for heavy haul trains that impart instability on soft subgrade at elevated speeds and increased axle loads.

5 Conclusions

It was clear that heavy haul rail industry has to deal with challenges in subgrade fluidization or mud pumping when tracks are built on soft and saturated subgrade. The following conclusions can be made based on past studies:

(a) Railway subgrades subjected to undrained cyclic train loading will cause excess pore-water pressures to be generated and accumulated unless sufficient drainage such as PVDs is provided.
(b) Cyclic loading factors and soil characteristics can influence the rate of generation of excess pore-water pressures in the soft subgrade. These factors include the loading frequency, number of cycles and drainage conditions. The relevant subgrade characteristics include the percentage of fines, confining pressure in track, subgrade soil plasticity, over-consolidation ratio and the natural in situ moisture content in relation to the liquid limit.
(c) Several remediation methods have been proposed to mitigate the occurrence of mud pumping. These include ballast replenishment and the use of either a sand layer or geotextile at the interface between the subgrade and ballast. Some ground improvement methods such as the use of PVD, lime stabilization and hot mixed asphalt used in field trials offer solutions that require further in-depth study.

Acknowledgements The authors would like to acknowledge the financial support from the Australian Research Council (ARC) Linkage Project.

References

Alobaidi I, Hoare DJ (1996) The development of pore water pressure at the subgrade-subbase interface of a highway pavement and its effect on pumping of fines. Geotext Geomembr 14(2):111–135

Alobaidi I, Hoare D (1999) Mechanisms of pumping at the subgrade-subbase interface of highway pavements. Geosynth Int 6(4):241–259

Attya A, Indraratna B, Rujikiatkamjorn C (2007a) Cyclic behaviour of PVD-soft soil subgrade for improvement of railway tracks. In: 10th Australia New Zealand conference on geomechanics. Brisbane, Australia, pp 36–41

Attya A, Indraratna B, Rujikiatkamjorn C (2007b) Effectiveness of vertical drains in dissipating excess pore pressures induced by cyclic loads in clays. In 16th Southeast Asian geotechnical conference. Selangor, Malaysia, pp 447–451

Australian Government, Australian Research Council (2017) Improving our rail network by understanding the process of "mud pumping". Retrieved from http://www.arc.gov.au/Improving-our-rail-network

Aw ES (2007) Low cost monitoring system to diagnose problematic rail bed: case study of mud pumping site. Doctoral dissertation, Massachusetts Institute of Technology

Ayres D (1986) Geotextiles or geomembranes in track? British railways' experience. Geotext Geomembr 3(2–3):129–142

Boomintahan S, Srinivasan G (1988) Laboratory studies on mud pumping into ballast under repetitive rail loading. Indian Geotechn J 18(1):31–47

Duong TV, Cui Y-J, Tang AM, Dupla J-C, Canou J, Calon N, Robinet A (2014) Investigating the mud pumping and interlayer creation phenomena in railway sub-structure. Eng Geol 171:45–58
Guo T, Prakash S (2000) Liquefaction of silt-clay mixtures. In: Proceedings of the 12th world conference on earthquake engineering, Paper no. 0561
Hyodo M, Yasuhara K, Hirao K (1992) Prediction of clay behaviour in undrained and partially drained cyclic triaxial tests. Soils Found 32(4):117–127
Indraratna B, Rujikiatkamjorn C, Ni J (2011a) Cyclic behaviour of soft soil subgrade improved by prefabricated vertical drains. In: International symposium on deformation characteristics of geomaterials. Korea, pp 559–564
Indraratna B, Salim W, Rujikiatkamjorn C (2011b) Advanced rail geotechnology–ballasted track. CRC Press
Kalafat M, Emrem C, Durgunoğlu HT (2003) Behavior of soft Riva clay under high cyclic stresses. In: International conference on new developments in soil mechanics and geotechnical engineering. Lefkosa, pp 177–183
Krechowiecki-shaw C, Jefferson I, Royal A, Ghataora G, Alobaidi I (2016) Degradation of soft subgrade soil from slow, large, cyclic heavy-haul road loads: a review. Can Geotech J 53(9):1435–1449
Li D, Selig E (1995) Evaluation of railway subgrade problems. Transp Res Rec 1489:17–25
Li D, Selig ET (1998) Method for railroad track foundation design. I: development. J Geotechn Geoenviron Eng 124(4):316–322
Liu J, Xiao J (2009) Experimental study on the stability of railroad silt subgrade with increasing train speed. J Geotechn Geoenviron Eng 136(6):833–841
Loh R, Nikraz H (2012) Effective stress method on threshold stress of clay under high rate cyclic loading. In: Proceedings of the 5th Asia-Pacific conference on unsaturated soils (AP-UNSAT 2011). Kasetsart University, Thailand, pp 605–609
Matasović N, Vucetic M (1995) Generalized cyclic-degradation-pore-pressure generation model for clays. J Geotech Eng 121(1):33–42
Mortezaie AR, Vucetic M (2013) Effect of frequency and vertical stress on cyclic degradation and pore water pressure in clay in the NGI simple shear device. J Geotech Geoenviron Eng 139(10):1727–1737
Nhan TT, Matsuda H, Hara H, Sato H (2015) Normalized pore water pressure ratio and post-cyclic settlement of saturated clay subjected to undrained uni-directional and multi-directional cyclic shears. In: 10th Asian regional conference of IAEG, Kyoto, Paper no 1081418
Ni J (2012) Application of geosynthetic vertical drains under cyclic loads in stabilizing tracks. Doctoral dissertation, University of Wollongong
Ni J, Indraratna B, Geng X, Rujikiatkamjorn C (2012) The effect of the strain rate on soft soil behaviour under cyclic loading. 11th Australia—New Zealand conference on geomechanics: ground engineering in a changing world, Australia, pp 1340–1345
Nieto Leal A, Kaliakin VN (2016) General response observed in cyclically loaded cohesive soils. Cienc Ing Neogr 26(1):21–39
Procter DC, Khaffaf JH (1984) Cyclic triaxial tests on remoulded clays. J Geotechn Eng 110(10):1431–1445
Raymond GP (1986) Geotextile application for a branch line upgrading. Geotext Geomembr 3(2):91–104
Raymond G (1999) Railway rehabilitation geotextiles. Geotext Geomembr 17(4):213–230
Richardson AM, Whitman RV (1963) Effect of strain-rate upon undrained shear resistance of a saturated remoulded fat clay. Geotechnique 13(4):310–324
Saglam S, Bakır BS (2014) Cyclic response of saturated silts. Soil Dyn Earthq Eng 61:164–175
Saveur J (2003) (Re)claiming the underground space. In: Proceedings of the ITA world tunnelling congress 2003, vol 1, 12–17 Apr 2003. CRC Press, Amsterdam, The Netherlands
Seed HB, Idriss I, Arango I (1983) Evaluation of liquefaction potential using field performance data. J Geotechn Eng 109(3):458–482

Soralump S, Prasomsri J (2015) Cyclic pore water pressure generation and stiffness degradation in compacted clays. J Geotechn Geoenviron Eng 142(1):04015060(1–13)
Tadatoshi I (1977) Measures for stabilization of Railway Earth structures. Japan Railway Technical Service, p 290
Tsai P-H, Lee D-H, Kung G-C, Hsu C-H (2010) Effect of content and plasticity of fines on liquefaction behaviour of soils. Q J Eng Geol Hydrogeol 43(1):95–106
Voottipruex P, Roongthanee J (2003) Prevention of mud pumping in railway embankment a case study from Baeng pra-pitsanuloke, Thailand. J KMITB 13(1):20–25
Vucetic M, Dobry R (1988) Degradation of marine clays under cyclic loading. J Geotechn Eng 114(2):133–149
Wilson NE, Greenwood JR (1974) Pore pressures and strains after repeated loading of saturated clay. Can Geotech J 11(2):269–277
Yasuhara K, Yamanouchi T, Hirao K (1982) Cyclic strength and deformation of normally consolidated clay. Soils Found 22(3):77–91
Zhou J, Gong X (2001) Strain degradation of saturated clay under cyclic loading. Can Geotech J 38(1):208–212

Flexural Response of Rails on Visco-Elastic Foundations Under Moving Loads

Priti Maheshwari and Shashank Bhatra

Abstract A simple mathematical model has been proposed for the flexural analysis of rails resting on visco-elastic foundations under moving loads. The rail has been modeled as an infinite beam, and the foundation soil has been represented by a series of Burger model interconnected by a tension membrane depicting the time-dependent behavior of clayey soils. The load has been assumed to move with constant velocity from left to right, and only gravitational effect of the load has been considered. The formulation involves the attainment of a quasi-stationary state in which rail is at rest relative to the moving coordinate system. Governing differential equations have been derived and solved with the help of appropriate boundary conditions. Influence of magnitude and velocity of the applied load, parameters of Burger model, tension in the membrane, and viscous damping on the response of rail has been studied. Nondimensional charts have been developed for normalized deflection of the rail. These charts will be useful while analyzing and designing the rails under moving loads.

Keywords Rails · Visco-elastic behavior · Burger model

1 Introduction

The basis of many soil–structure interaction problems is related to the classical problem of beams on elastic foundations. An infinite beam on elastic foundations subjected to moving loads has been treated as a proper representation of rails for quite some time. There are many analytical and numerical solutions available for analysis of infinite beams. Some of the classical works include Kenney (1954), Kerr

P. Maheshwari (✉) · S. Bhatra
Department of Civil Engineering, Indian Institute of Technology Roorkee, Roorkee 247667, India
e-mail: priti_mahesh2001@yahoo.com

S. Bhatra
e-mail: shashankbhatra991@gmail.com

S. Bhatra
Department of Civil Engineering, NIT Uttarakhand, Srinagar, India

R. Sundaram et al. (eds.), *Geotechnics for Transportation Infrastructure*, Lecture Notes in Civil Engineering 28, https://doi.org/10.1007/978-981-13-6701-4_25

(1964), Steele (1967), and Fryba (1972). Few more studies pertaining to the analysis of infinite beams on elastic foundations are Rao (1974), Torby (1975), Saito and Terasawa (1980), Jaiswal and Iyengar (1997), etc. Mallik et al. (2006) studied the response of an infinite beam resting on one parameter as well as two-parameter lumped models, and subjected to a moving load considering both the damped and the undamped cases. Basu and Rao (2013) developed analytical solutions for the steady-state response of an infinite beam resting on a visco-elastic foundation and subjected to a concentrated load moving with a constant velocity. Omolofe (2013) developed a procedure involving spectral Galerkin and integral transformation methods and applied the same to treat the problem of dynamic deflections of beam structure resting on two-parameter elastic subgrade subjected to traveling loads. Ang and Dai (2013) proposed a computational scheme for the dynamic response of a high-speed rail system with consideration to change in foundation stiffness.

In all these studies, the elastic response of rail was obtained. The response having time dependency has not been studied. In view of this, in the present study, an attempt has been made to study the visco-elastic response of rails subjected to concentrated load moving with constant velocity.

2 Analysis

Figure 1 shows the longitudinal section of rail (idealized as an infinite beam) resting on earth bed represented by a series of Burger model interconnected by a tension membrane depicting the time-dependent behavior of clayey soils. This can be observed as a modified version of Filonenko–Borodich model where original linear springs have been replaced by four-element Burger model consisting of springs (k_1, k_2) and dashpots (η_1, η_2). Tension in the membrane is denoted by T.

The response of beam at any time, t, with constant flexural rigidity, EI, on visco-elastic foundation represented by series of Burger model interconnected by a tension

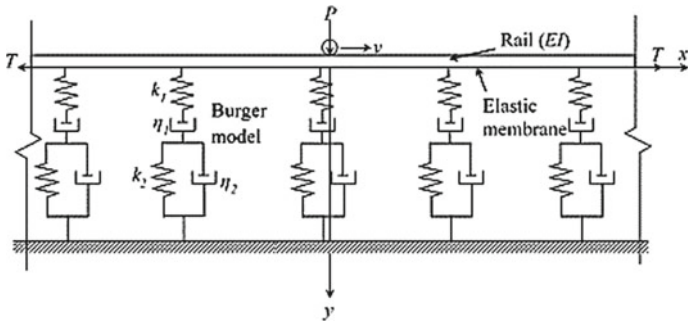

Fig. 1 Rail on visco-elastic foundation

membrane under a load, P, moving with constant velocity (left to right), v, is given by

$$EI\frac{\partial^4 y}{\partial x^4}+\rho\frac{\partial^2 y}{\partial t^2}+c\frac{\partial y}{\partial t}-T\frac{\partial^2 y}{\partial x^2}+k_s y(x,t)=P(x,t) \tag{1}$$

where ρ is mass per unit length of beam (kg), c, the coefficient of viscous damping per unit length of beam (N s/m^2), P, the applied load (N), y, the deflection of the beam (m), x, the space coordinate along length of beam, and

$$k_s=\frac{k_1}{1+\frac{k_1}{\eta_1}t+\frac{k_1}{k_2}\left[1-\exp\left(-\frac{k_2}{\eta_2}t\right)\right]}$$

It has been assumed that a quasi-stationary state is achieved; i.e., the moving load is no longer dependent on time after sufficiently long travel time and is only dependent on space coordinate from the origin which also moves uniformly. For convenience, defining an independent variable, $\xi = x - vt$. Employing this, Eq. (1) transforms to the governing differential equation as

$$EI\frac{\mathrm{d}^4 y}{\mathrm{d}\xi^4}+\rho\, v^2\frac{\mathrm{d}^2 y}{\mathrm{d}\xi^2}-c\, v\frac{\mathrm{d}y}{\mathrm{d}\xi}-T\frac{\mathrm{d}^2 y}{\mathrm{d}\xi^2}+k_s y(\xi)=P(\xi) \tag{2}$$

As ξ tends to infinity, i.e., at both ends of beam, deflection and its slope have been considered to zero as required boundary conditions. Using the following nondimensional parameters, $\xi^* = \xi/L$, $Y = y/L$, $\rho^* = \rho\, v^2/k_1\, L^2$, $I^* = EI/k_1\, L^4$, $c^* = c\, v/k_1\, L$, $k_1^* = k_1\, L^4/EI$, $k_2^* = k_2\, L^4/EI$, $\eta_1^* = \eta_1\, L^4/EI\, t$, $\eta_2^* = \eta_2\, L^4/EI\, t$, $T^* = T/k_1\, L^2$, and $P^* = P/k_1\, L^2$, Eq. (2) has been written in nondimensional form as:

$$\frac{\mathrm{d}^4 Y}{\mathrm{d}\xi^{*4}}+\left(\frac{\rho^*-T^*}{I^*}\right)\frac{\mathrm{d}^2 Y}{\mathrm{d}\xi^{*2}}-\left(\frac{c^*}{I^*}\right)\frac{\mathrm{d}Y}{\mathrm{d}\xi^*}+\frac{Y}{k^*\, I^*}=\frac{P^*}{(\mathrm{d}\xi^*)I^*} \tag{3}$$

This nondimensional form has been written in its finite difference form for any node 'i' as follows:

$$\begin{aligned}&Y_{i+2}+Y_{i+1}\left[-4+A\left(\Delta\xi^*\right)^2-0.5B\left(\Delta\xi^*\right)^3\right]\\&+\ Y_i\left[6-2A\left(\Delta\xi^*\right)^2+\frac{1}{k^*I^*}\left(\Delta\xi^*\right)^4\right]\\&+\ Y_{i-1}\left[-4+A\left(\Delta\xi^*\right)^2+0.5B\left(\Delta\xi^*\right)^3\right]\\&+\ Y_{i-2}=\left[\frac{P^*}{I^*}\right]\left(\Delta\xi^*\right)^3\end{aligned} \tag{4}$$

where $A=\frac{\rho^*-T^*}{I^*}$, $B=\frac{c^*}{I^*}$, and $k^*=1+\frac{k_1^*}{\eta_1^*}+\frac{k_1^*}{k_2^*}\left[1-\exp\left(-\frac{k_2^*}{\eta_2^*}\right)\right]$

Boundary conditions in nondimensional form can be written as:

$$\text{At}\,\xi^* = -1 \quad \text{and at} \quad \xi^* = 1, Y \quad \text{and} \quad \mathrm{d}Y/\mathrm{d}\xi^* = 0. \tag{5}$$

The governing differential equation (4) has been solved along with Eq. (5) to obtain the response of beam in terms of its deflection. Once deflection is determined, the bending moment can be obtained by double derivative of deflection profile.

3 Convergence Criterion and Range for Values of Parameters

A computer program based on the above formulation has been developed to obtain deflection of beam representing the rail. The length of beam has been considered to be large enough so that it depicts the infinite beam condition. The total extent, i.e., $-L \leq x \leq L$, has been considered in the analysis. The results for 801 and 1001 number of nodes have been found to vary by 1–2%, and therefore 801 nodes have been considered for spatial variation for all the parametric studies. The convergence criterion has been taken as: $\left|\frac{Y_i^k - Y_i^{k-1}}{Y_i^k}\right| < 10^{-5}$, where i and k represent node and the current iteration, respectively.

Realistic range of all parameters has been considered from the available literature and has been presented in Table 1.

Table 1 Range of values of input parameters

Parameter	Units	Range
Flexural rigidity of beam (EI)	N m^2	4.5×10^6 (Shahu et al. 2000)
Mass per unit length of beam (ρ)	kg/m	60
Magnitude of applied load (P)	kN	100–250
Velocity of load (v)	km/h	40–140
Ratio (k_1/k_2)	–	0.5–100 (Dey and Basudhar 2012)
Ratio (η_1/η_2)	–	100–10^5 (Dey and Basudhar 2012)
Tension in membrane (T)	MN	5–15
Damping ratio, ζ (percentage of critical damping)	–	0–25% (Vucetic and Dobry 1991)

4 Results and Discussion

4.1 Validation

Before carrying out the detailed parametric study, first developed methodology and the solution have been validated by comparing the results from closed form solution as obtained by Mallik et al. (2006). Mallik et al. (2006) defined velocity ratio as the ratio of the velocity of applied load to the critical velocity. While presenting the results for validation purpose, the distance along length of beam ξ has been multiplied by a factor, $(k/EI)^{1/4}$. Deflection of the beam has been normalized by dividing it with its maximum values in static case, i.e., when $v = 0$. Parameters adopted for validation are: $\rho = 25$ kg/m, $k_s = k_1 = 40.78 \times 10^5$ N/m^2, $EI = 1.75 \times 10^6$ N m^2, $P = 93.36 \times 10^3$ N/m, damping $= 30\%$, and velocity ratio $= 0.50$ (Mallik et al. 2006). Figure 2 shows the comparison of results from both the methods, and a perfect match, therefore, establishes the validity of the developed model and the methodology.

4.2 Retardation Time (t_d) and Nondimensional Elapsed Time (t')

After validation, it has been attempted to first understand some of the adopted terminologies, their physical interpretation, and procedure for determination. One of such terms is retardation time (t_d) of visco-elastic model of foundation which represents the degree of rigidity of visco-elastic material. Figure 3 depicts the effect of elapsed time on maximum normalized deflection of beam for input parameters as mentioned

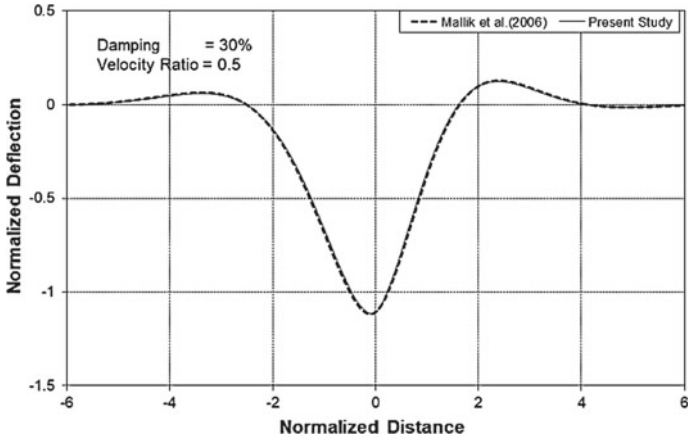

Fig. 2 Validation of the proposed model

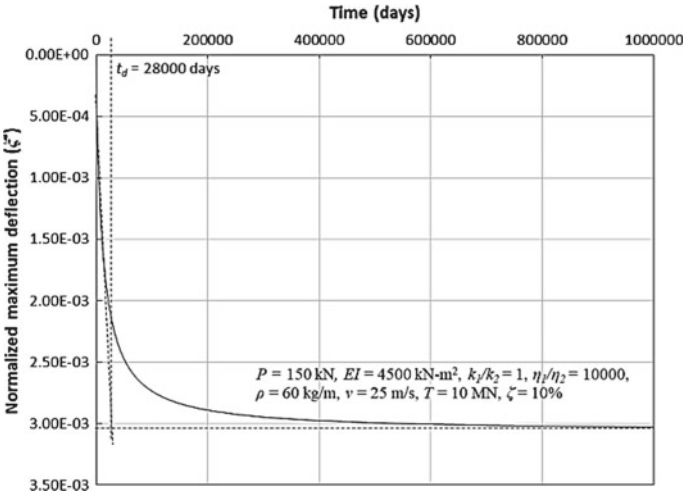

Fig. 3 Variation of maximum normalized deflection of beam with time: determination of t_d

in the figure. Intersection of tangent of the initial portion of the curve with asymptotic part gives the value of retardation time, and in this case, it works out to be about 28,000 days.

This retardation time has been used to normalize the elapsed time. The same results have been presented in order to have standard representation as shown in Fig. 4. A familiar and conventional shape of the curve has been observed (Taylor 1948). Following the standard procedure, time required for 100% primary consolidation can be obtained as depicted in the figure. In the present case, nondimensional elapsed time (t') works out to be about 4, i.e., about 300 years.

4.3 Degree of Consolidation (U)

A four-parameter Burger model is the idealization of coupled primary and secondary consolidation of soft soils. Although decoupling of these two phenomena is not that simple, however, following the conventional procedure, one can obtain the time required for 100% consolidation. Figure 4 can also be replotted with reference to degree of consolidation instead of deflection following the set procedure for its determination as given in Eq. (5). This has been shown in Fig. 5 along with procedure for determination of time corresponding to 50% primary consolidation (t'_{50}). This information is useful in determining the consolidation characteristics of the soil.

$$U = \left[\frac{Y|_{t'} - Y|_{t'=0}}{Y|_{t'=t'_{100}} - Y|_{t'=0}} \right] \times 100 \tag{5}$$

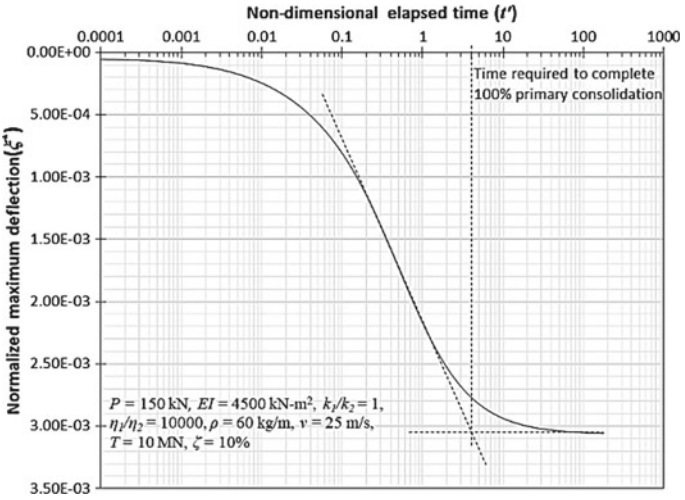

Fig. 4 Variation of maximum normalized deflection of beam with nondimensional elapsed time: determination of time required for 100% consolidation

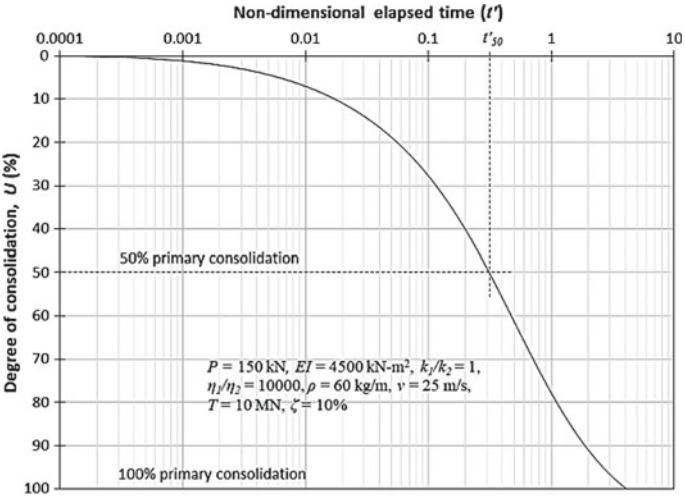

Fig. 5 Variation of degree of consolidation with nondimensional elapsed time

where t'_{100} corresponds to nondimensional elapsed time at completion of 100% primary consolidation.

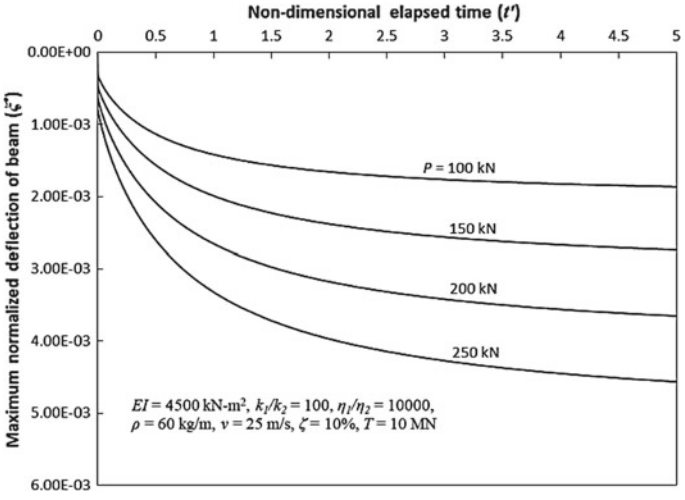

Fig. 6 Maximum normalized deflection: influence of applied load

4.4 Influence of Magnitude of Applied Load (P)

The influence of magnitude of applied load on maximum normalized deflection of beam has been shown in Fig. 6 for input parameters as mentioned in the figure. As expected, the maximum normalized deflection has been found to reduce with reduction in load. The reduction of about 50% has been observed at nondimensional elapsed time of 5 as the load reduces from 250 to 100 kN. Figure 7 depicts the variation of maximum bending moment in beam with applied load at nondimensional elapsed time, t', equal to 1. As the foundation system has been considered to be linear, the maximum bending moment has found to reduce by 60% with reduction in load by the same amount.

4.5 Influence of the Velocity of Applied Load (V)

Figure 8 depicts the variation of maximum normalized load with the velocity of applied load at time, $t = 20{,}000$ days. Other input parameters have been taken as $EI = 4500$ kN m^2, $k_1/k_2 = 100$, $\eta_1/\eta_2 = 10{,}000$, $\rho = 60$ kg/m, $\zeta = 10\%$, and $T = 10$ MN. The normalized deflection has been found to be independent of low values of the velocity of load. However, as the velocity approaches to a critical value, the deflection shoots up. In this case, the value of critical velocity has been obtained as 415 m/s. This helps in designing the track characteristics. For all practically possible situations, the velocity of load never reaches to critical velocity.

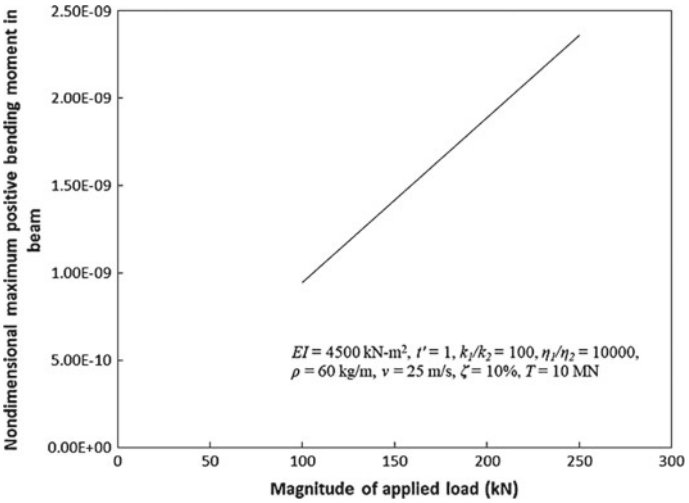

Fig. 7 Maximum normalized bending moment at $t' = 1$: influence of applied load

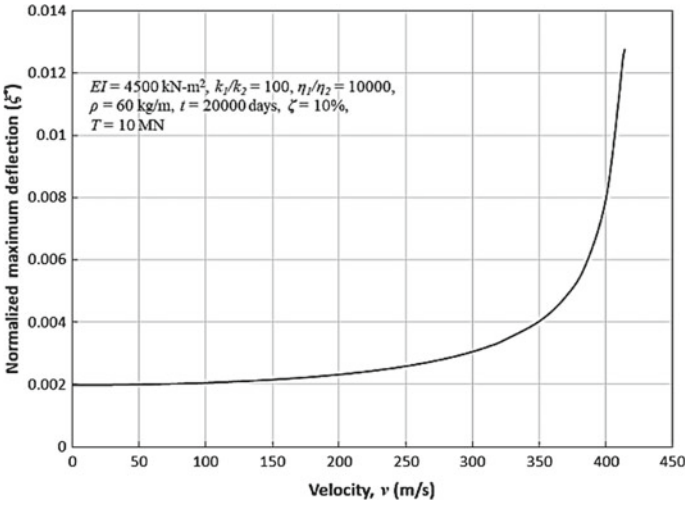

Fig. 8 Influence of velocity on maximum normalized deflection at time, $t = 20{,}000$ days

4.6 Influence of Relative Magnitude of Elastic Coefficients of Burger Model (k_1/k_2)

Influence of relative magnitude of elastic coefficients of Burger model, i.e., ratio, k_1/k_2 on maximum normalized deflection of beam has been depicted in Fig. 9 for other input parameters as mentioned in the figure. The deflection has been found to reduce with reduction in the ratio, k_1/k_2. This reduction at very low value of t' has

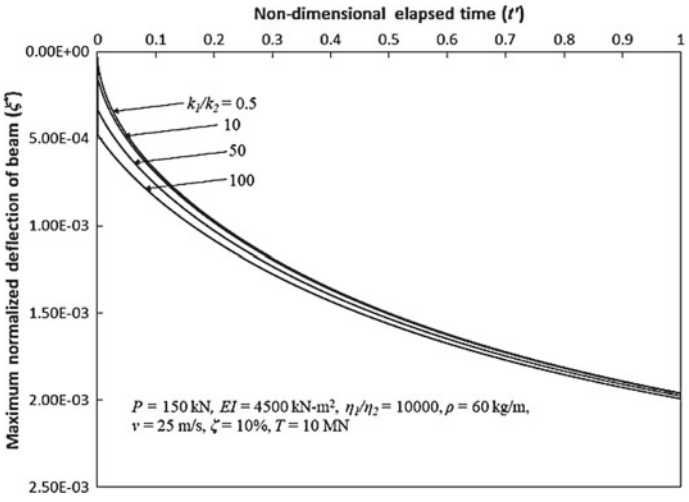

Fig. 9 Influence of relative magnitude of elastic coefficients of Burger model (k_1/k_2) on normalized maximum deflection of beam

been observed to be about 91% which reduces to almost zero for larger values of nondimensional elapsed time. It is to be noted that for very low values of ratio k_1/k_2, the four-parameter Burger model behaves as that of Maxwell model and for very high values, it behaves as three-parameter fluid element.

4.7 Influence of Relative Magnitude of Viscous Coefficients of Burger Model (η_1/η_2)

Figure 10 shows the effect of relative magnitude of viscous coefficients of Burger model for $P = 150$ kN, $EI = 4500$ kN m^2, $k_1/k_2 = 100$, $\rho = 60$ kg/m, $v = 25$ m/s, $\zeta = 10\%$, $T = 10$ MN. The ratio η_1/η_2 has been varied from 10^5 to 100, and the corresponding reduction in the maximum deflection has been found to be about 44% at nondimensional elapsed time t' equal to 5. A relatively higher value of ratio η_1/η_2 signifies higher viscous coefficient of Maxwell part of Burger model. This offers larger resistance to time-dependent deflection which results in smaller deflection for larger value of ratio, η_1/η_2.

4.8 Influence of Tension in Elastic Membrane (T)

The tension in elastic membrane has been found to be very useful in reducing the maximum normalized deflection of the beam (Fig. 11). The tension in membrane has

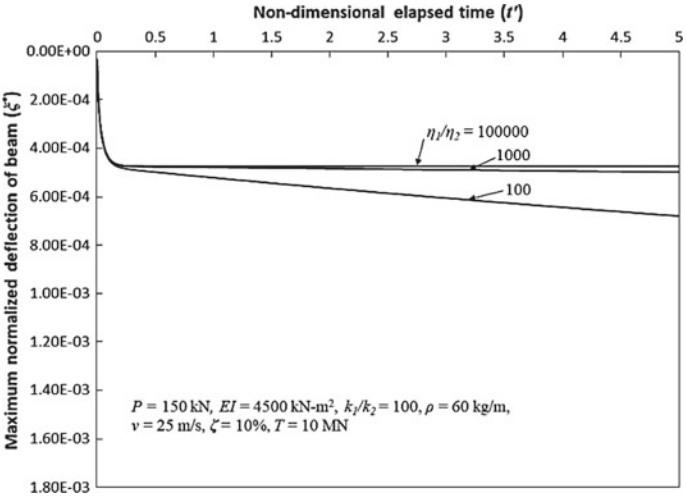

Fig. 10 Influence of relative magnitude of viscous coefficients of Burger model (η_1/η_2) on normalized maximum deflection of beam

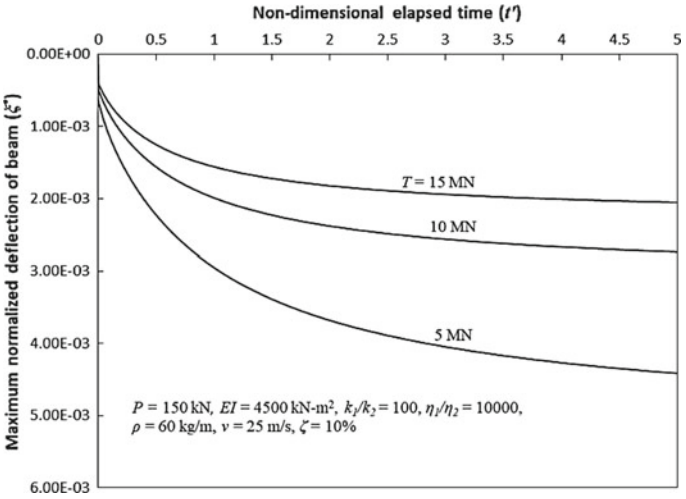

Fig. 11 Influence of tension in elastic membrane on normalized maximum deflection of beam

been varied from 5 to 15 MN, and the corresponding reduction in maximum normalized deflection at t' equal to 5 has been obtained as about 54%. This membrane can very well represent a pretensioned geosynthetic layer lying just above the subgrade below the rail and help in reducing the deflection of the rail.

5 Concluding Remarks

A simple mathematical model has been proposed for the analysis of rails subjected to a moving load with constant velocity and resting on visco-elastic foundation. The subgrade has been represented by a series of Burger model interconnected by an elastic membrane.

All the earlier studies pertaining to such analysis did not incorporate direct time dependency. However, these correlated degree of consolidation indirectly with time. In the present work, direct variation of degree of consolidation with time has been established. It was possible to obtain the consolidation characteristics from the results of such an analysis of rails under moving loads.

The influence of various parameters like magnitude and velocity of applied load, relative magnitude of elastic and viscous coefficients of Burger model, tension in the elastic membrane has been studied on the response of an infinite beam on visco-elastic medium. It has been observed that magnitude of load significantly influences the normalized deflection of the beam. A reduction of about 50% was observed at nondimensional elapsed time of 5 as the load reduces from 250 to 100 kN. For all practically possible values of the velocity of the load, the response of beam was found to be independent of the velocity. However, near the critical velocity, the deflection was found to suddenly shoot up. This information was found to be helpful in designing the railway track with respect to this aspect of critical velocity.

Lower values of relative magnitude of elastic and viscous coefficients of Burger model represent the similar behavior as that of Maxwell model. Deflection of rail was found to reduce with reduction in the ratio, k_1/k_2, and this reduction at very low value of t' can be as high as about 90% which reduces to almost zero for larger values of nondimensional elapsed time, t'. The ratio η_1/η_2 was varied from 10^5 to 100 resulting in a reduction of about 44% in the maximum deflection at nondimensional elapsed time t' equal to 5.

Parameter, c, representing viscous damping has been found to have negligible influence on the response of beam for range of values of parameters considered for the analysis.

The increase in tension in elastic membrane was found to be quite effective in reducing the deflection of the beam. This elastic membrane can be thought of a pretensioned geosynthetic layer. In case of poor subsoil condition, laying of such a layer can be very effective in restricting the deflection of rail. At t' equal to 5, reduction in maximum normalized deflection of about 54% was observed as tension in membrane increased from 5 to 15 MN.

References

Ang KK, Dai J (2013) Response analysis of high-speed rail system accounting for abrupt change of foundation stiffness. J Sound Vib 332:2954–2970

Basu D, Rao NSVK (2013) Analytical solutions for Euler-Bernoulli beam on visco-elastic foundation subjected to moving load. Int J Numer Anal Methods Geomech 37(8):945–960
Dey A, Basudhar PK (2012) Estimation of Burger model parameters using inverse formulation. Int J Geotech Eng 6(3):261–274
Fryba L (1972) Vibration of solids and structures under moving loads. Noordhoff International Publishing, Groningen, The Netherlands
Jaiswal OR, Iyenger RN (1997) Dynamic response of railway tracks to oscillatory moving masses. J Eng Mech Div ASCE 123(7):753–757
Kenney JT Jr (1954) Steady-state vibrations of beam on elastic foundation for moving load. J Appl Mech Div ASME 21(4):359–364
Kerr AD (1964) Elastic and viscoelastic foundation models. J Appl Mech Div ASME 31(3):491–498
Mallik AK, Chandra S, Singh AB (2006) Steady-state response of an elastically supported infinite beam to a moving load. J Sound Vib 291:1148–1169
Omolofe B (2013) Deflection profile analysis of beams on two-parameter elastic subgrade. Latin Am J Solid Struct 10(2):263–282
Rao NSVK (1974) Onset of separation between a beam and tensionless foundation due to moving loads. J Appl Mech Div ASME 41(1):303–305
Saito H, Teresawa T (1980) Steady-state vibrations of a beam on a Pasternak foundation for moving loads. J Appl Mech Div ASME 47(4):879–883
Shahu JT, Yudhbir, Rao NSVK (2000) A rational method for design of railroad track foundation. Soils and Foundations 40(6):1–10
Steele CR (1967) The finite beam with a moving load. J Appl Mech Div ASME 34(1):111–118
Taylow DW (1948) Fundamentals of soil mechanics. Wiley, New York
Torby BJ (1975) Deflection results from moving loads on a beam that reacts upon an elastic foundation reacting in compression only. J Appl Mech Div ASME 42(3):738–739
Vucetic M, Dobry R (1991) Effect of soil plasticity on soil response. J Geotechn Eng ASCE 117(1):89–107

Railway Structure Pile Design Comparison Considered with the Difference of Japan and India

Torajiro Fujiwara, Lalit Kumar, Junya Sawame and Suguru Ikejima

Abstract Design and construction of pile foundation for an important infrastructure project in every country are the acute issues. In most countries, design codes for pile foundation are introduced to enhance the strength and making the construction more economic and viable. Japan also introduced pile foundation design codes and revised it again and again based on lessons learned from field surveys on damaged infrastructure projects. In consequence, the Japanese current design code realizes fairly good performance which was evidenced by different infrastructure projects currently running at good pace. Among various structure design codes, every country design code for foundations is decided and judged based on local soil/rock characteristics, environmental conditions, experimental results and actual structures which have been constructed. The present study shows the comparison of design results of bored cast in situ pile by adopting the Japanese and Indian Railway foundation codes. The study shall also reveal about the validity of the Japanese Railway Structure Foundation Design Code that can be adopted for future India projects, considering a comparison with geotechnical investigation condition, geological condition, materials' difference and the accuracy of execution between Japan and India.

Keywords Bored cast in situ pile · Japanese Railway Standard · Indian Railway Foundation Code · Indian code for pile foundation

T. Fujiwara · J. Sawame
Structural Engineering Center, East Japan Railway Company, 2-2-6 Shibuya, Tokyo, Japan
e-mail: t-fujiwara@jreast.co.jp

J. Sawame
e-mail: sawame@jreast.co.jp

L. Kumar (✉)
Feedback Infra Private Limited, 15th Floor Tower 9B, DLF Cyber City Phase-III, Gurgaon 122002, Haryana, India
e-mail: luckysoni.edu@gmail.com

S. Ikejima
Facilities Department, Kyushu Railway Company, Hakata Fukuoka 3-25-21, Japan
e-mail: s.ikejima@jrkyushu.co.jp

R. Sundaram et al. (eds.), *Geotechnics for Transportation Infrastructure*, Lecture Notes in Civil Engineering 28, https://doi.org/10.1007/978-981-13-6701-4_26

1 Introduction

Recent years have witnessed Japan, both at the government and at the business and academic levels, displaying an increasing interest in India. A number of initiatives have been taken by the two governments to improve bilateral relations in almost every field. To provide more focus and purpose in science and technology between the two countries. The ongoing effort in planning for establishment of advanced skill development, sharing of technology, industrial cluster for investment and mega-infrastructure initiatives India and Japan affirmed the importance of skill development as an important tool for promotion of skills and capacity enhancement of the local youth.

Therefore, there might be some probability to transfer the Japanese technology to India in some projects for the future and also to adopt the Japanese Structure Design Code for upcoming new infrastructure projects. So, this study comprises of comparison of Indian codes for pile foundation design and Japanese codes for pile foundation design.

2 The Purpose of This Study

This study involves the analysis and synthesis of the similarities, differences and patterns across different codes and standards of pile foundation design, which share a common focus or goal. To be able to do this well, the specific factors of each standard have described in depth. The rationale for selecting the specific standards is directly linked to the key evaluation of standards and selection of the same for future Indian infrastructure projects (funded by the Japanese government).

Though, pile foundations are widely discussed by many researchers in order to do research of safer and more economic designs for different types of the infrastructure projects during static and dynamic conditions. The factors used to calculate the pile foundation by the Japanese standards and Indian standards vary significantly, and hence to study the impact of those factors on the calculation of pile foundation is very much necessary for this comparative study. The comparison is part of a major research study on the design of pile foundations done by a Japanese company with interests in performance-based design and the loading response of piles in reclaimed land. There is a different type of pile foundation used internationally. Pile foundation can be categorized based on installation method, forming material, strata in which the pile is supposed to be installed and cross section of pile. The present study reveals the comparison of axial pile capacities and different factors, equations used for the design of concrete circular bored cast in situ pile foundation in cohesive and granular soil types.

Standard penetration test (SPT) is appropriate to estimate the resistance and density of granular soils, also sometimes widely used to find out the cohesion properties of soils and largely practiced in the Japan region while designing the foundation of

mostly railway projects. In most of the railway projects in Japan, the pile capacity has been derived by using standard penetration test (SPT) values; hence for this comparative study, the use of SPT values is taken into preference and capacity has been calculated by the codes and standards of both the countries.

3 Comparison of Different Equations Used for Design of Pile Foundation

Every country has different design factors and often equation for the calculation of pile foundation; in the present study, the factors and equations used for the calculation of pile foundation in India and in Japan are summarized below.

3.1 From Indian Standards and Codes

As per Indian code of practice (IS 2911 Part-1 Section-2), the bearing capacity equations are as follows.

Bearing capacity equation for granular soil is

$$Q_{\mathrm{u}} = A_{\mathrm{p}}\left(0.5D\gamma N_{\gamma} + P_{\mathrm{D}}N_{\mathrm{q}}\right) + \sum_{i=1}^{n} K_i P_{\mathrm{D}i} \tan\delta_i A_{si} \tag{1}$$

where

Q_{u} Ultimate load capacity, in kN
A_{p} Cross-sectional area of pile tip, in m^2
D Diameter of pile shaft, in m
γ Effective unit weight of the soil at pile tip, in $\mathrm{kN/m}^3$
N_{γ} Bearing capacity factors depending on N_{q} and can be calculated as $N_{\gamma} = 2\left(N_{\mathrm{q}} + 1\right)\tan\phi$
P_{D} Effective overburden pressure at pile tip, in $\mathrm{kN/m}^2$
N_{q} Bearing capacity factor depends on the angle of internal friction at pile tip
$\sum_{i=1}^{n}$ Summation for layers 1 to n in which pile is installed and which contributes to positive skin friction
K_i Coefficient of earth pressure applicable to the ith layer (range from 1.0 to 1.5)
$P_{\mathrm{D}i}$ Effective overburden pressure for the ith layer, in $\mathrm{kN/m}^2$
δ_i Angle of wall friction between pile and soil for the ith layer (may be taken equal to the friction angle of the soil around the pile stem)
A_{si} Surface area of pile shaft in the ith layer, in m^2.

To calculate the bearing capacity by static formula, the maximum effective overburden at the pile tip should correspond to the critical depth, which may be taken as 15 times the diameter of the pile shaft for $\phi \leq 30°$ and increasing to 20 times for $\phi \geq 40°$.

Bearing capacity equation for cohesive soil is

$$Q_u = A_p N_c C_p + \sum_{i=1}^{n} \alpha_i c_i A_{si} \tag{2}$$

where

Q_u Ultimate load capacity, in kN
A_p Cross-sectional area of pile tip, in m^2
N_C Bearing capacity factor may be taken as 9
C_p Average cohesion at pile tip, in kN/m^2
$\sum_{i=1}^{n}$ Summation for layers 1 to n in which pile is installed and which contributes to positive skin friction
α_i Adhesion factor for the ith layer depending on the consistency of soil
c_i Average cohesion for the ith layer, in kN/m^2
A_{si} Surface area of pile shaft in the ith layer, in m^2.

Bearing capacity equation based on SPT values for granular soil is:

$$Q_u = 13N\frac{L}{B}A_p + \frac{\overline{N}A_s}{0.50} \tag{3}$$

Q_u Ultimate load capacity, in kN
N Average N value at pile tip
L Length of penetration of pile in bearing strata, in
mB Diameter or minimum width of pile in m
A_p Cross-sectional area of pile tip, in m^2
$\bar{N}$ Average N along the pile shaft
A_s Surface area of pile shaft, in m^2.

In no case, the end bearing resistance should be more than $130NA_p$.

For non-plastic silt or very fine sand, the above formula should be replaced by the following formula.

$$Q_u = 10N\frac{L}{B}A_p + \frac{\overline{N}A_s}{0.60} \tag{4}$$

3.2 From the Japanese Standards and Codes

As per the Japanese code of practice (Design Standards for Railway Structures and Commentary [Foundation]), the bearing capacity equations are:

$$R_{vd} = f_{\mathrm{r}}\left(R_{\mathrm{t}k} + R_{fk}\right) \tag{5}$$

$$f_{\mathrm{r}} = p_{\mathrm{t}} = \left(\frac{R_{\mathrm{t}k}}{R_k}\right) \tag{6}$$

$$R_{\mathrm{t}k} = q_{\mathrm{t}k} A_{\mathrm{t}} \tag{7}$$

$$R_{fk} = r_{fk} U \Delta l \tag{8}$$

$$q_{\mathrm{t}k} = 60N \leq 7500\,\mathrm{kN/m^2} \quad \text{(for Granular soil)} \tag{9}$$

$$q_{\mathrm{t}k} = 51N \leq 9000\,\mathrm{kN/m^2} \quad \text{(for cohesive soil)} \tag{10}$$

$$r_{\mathrm{t}k} = 1.5N \leq 75\,\mathrm{kN/m^2} \quad \text{(forgranular soil)} \tag{11}$$

$$r_{\mathrm{t}k} = 6N \leq 75\,\mathrm{kN/m^2} \quad \text{(for cohesive soil)} \tag{12}$$

where

R_{vd} Design bearing load capacity, in kN
f_{r} Ground resistance coefficient depends on p_{t}
$R_{\mathrm{t}k}$ Basic tip end bearing resistance
R_{fk} Basic shaft friction resistance
R_k Total basic bearing resistance $\left(R_k = R_{\mathrm{t}k} + R_{fk}\right)$
p_{t} The ratio of basic tip bearing resistance by total bearing resistance
$q_{\mathrm{t}k}$ Basic tip end bearing resistance stress, in kN/m^2
A_{t} Cross-sectional area of pile tip, in m^2
N SPT N value
r_{fk} Basic skin friction resistance stress, in kN/m^2
U Circumference of pile, in m
Δl Thickness of strata, in m
f_{r} Depends on p_{t}. As per Japanese Railway Design Standard, the higher p_{t} (the ratio of tip end bearing resistance by total bearing resistance) is, the less the total bearing resistance is evaluated.

The reason is that the reliability of the tip end bearing resistance depends on the quality of tip end, and in Japan, the tip end quality seems to be not good because of the execution uncertainty by almost engineers.

And the design bearing load capacity of long term is evaluated less than that of the short term because of the action load characteristics.

4 Empirical Formulas in Relation to SPT

Pile capacity calculation by standard penetration test (SPT) is one of the earliest applications of this test that includes two main approaches, direct and indirect methods. Direct methods apply N values with some modification factors. Indirect SPT methods employ a friction angle and cohesion values estimated from empirical formulas based on different theories.

4.1 Empirical Formulas in Relation to SPT from Indian Standards and Codes

SPT has been used in correlations for the angle of internal friction, unit weight, shear strength, etc. The real value of these properties requires a special care and laboratory technique. So, prediction of soil properties with the help of field tests such as SPT provides a good opportunity to obtain these parameters without using more laboratory tests. Standard penetration tests (SPTs) roughly measure the strength of soil. Following are the empirical formulas in relation to SPT.

4.1.1 Relation of SPT values with the angle of internal friction is (Varghese 2005)

$$\phi = 0.3N + 27 \tag{13}$$

where

ϕ Angle of internal friction, degrees
N SPT value.

4.1.2 Relation of SPT with cohesion intercept

Even though SPT values are not considered as a good measure of the strength of clays, it is used extensively as a measure of the consistency of clays. The consistency is then related to its approximate strength and then to cohesion intercept

$$q_u = \frac{N}{8} \tag{14}$$

$$c = \frac{q_u}{2} \tag{15}$$

where

q_u Undrained strength of soils, in kg/cm^2
c Cohesion intercept, in kg/cm^2.

4.2 Empirical Formulas in Relation to SPT from the Japanese Standards and Codes

In Japanese Railway Standards, the use of SPT data is taken into priority than the cohesion intercept and angle of internal friction. For granular soil, the angle of internal friction has been calculated by using the empirical formulas as suggested by Gibbs and Holtz (1957), De Beer (1975), Bishop and Eldin (1953), Nash (1953), Kirkpatrick (1965) Aoki and de Alencar (1975). The angle of internal friction calculated by this formula is small (conservative) because of the two-step reduction by the revised data.

4.2.1 Relation of SPT with the angle of internal friction is

$$\phi = 1.85\left(\frac{N}{\frac{\sigma_v'}{100} + 0.7}\right)^{0.6} + 26 \tag{16}$$

$$\sigma_v' = \gamma_t h_w + \gamma'(z - h_w) \tag{17}$$

where

ϕ Angle of internal friction, degrees
N SPT value
σ_v' Effective earth pressure $\leq$50 kN/m^2
γ_t Soil density over the groundwater, in kN/m^3
h_w The depth of water table, in m
γ' Soil density under the groundwater, in kN/m^3
z The depth under the ground surface, in m.

4.2.2 Relation of SPT with cohesion intercept

The formula for the calculation of cohesion intercept by using SPT value is not depicted in the Japanese code of practice (Design Standards for Railway Structures and Commentary [Foundation]). But use of equation below for the calculation of cohesion intercept is widely accepted by most of the engineers in Japan. The equation is based on the statistical analysis result followed by experimental investigated data in Japan.

$$c = \frac{1}{16}N \tag{18}$$

where

c Cohesion intercept, in kg/cm^2
N SPT value.

5 Assumed Ground Condition

Below are the assumed ground conditions to check the differences in the pile capacities calculated from the Japanese standards and Indian standards (Table 1).

Groundwater table is at surface, and pile is circular in diameter with diameter of 1200 mm. Calculate the pile capacity at 20-m depth.

6 Calculations

6.1 Axial Load-Carrying Capacity of Pile as Per Indian Standards and Codes

Axial pile load has been calculated by using two methods: the first method is based on empirical formula interpretation of the angle of internal friction and cohesion intercept, and the second method calculates the pile capacity by using direct formula of SPT value as given in IS 2911-Part-1-Section-2.

Method-1

The results of interpretation of cohesion and angle of internal friction have been summarized in Table 2.

By using the formulas for cohesive soils and granular soils, the axial capacity of pile turnout is 3968.0 kN.

Method-2

To calculate the axial capacity using SPT *N* value, the selection of SPT value is very important factor. Selected SPT value has been taken as per below statistical analysis (Tables 3 and 4).

SPT value of 14 has been considered as average value along the pile shaft and 35 as average SPT value at pile tip. The capacity as calculated by Eqs. 3 and 4 turnout is 2058.4 kN.

Table 1 Physical properties of soil

Depth (m)	SPT (N[a])	Soil type	γ (kN/m^3)
0–5	10	Silty clay	16.0
5–15	25	Silty clay	17.0
15–20	38	Silty sand	17.5
20–25	40	Silty sand	18.0

[a]SPT values are average values of that stratum

Table 2 Calculated strength parameters of soil

Depth (m)	SPT (N^a)	Soil	c^b (kN/m^2)	ϕ^{0b}	γ (kN/m^3)
0–5	10	Silty clay	60	–	16.0
5–15	25	Silty clay	160	–	17.0
15–20	38	Silty sand	–	34	17.5
20–25	40	Silty sand	–	34	18.0

[a]SPT values are average values of that stratum
[b]Values are derived from empirical correlations, and value of the angle of internal friction is taken by limiting to 34°

Table 3 Statistical analysis for selection of SPT

Average	Count	Min	Max	Geomean
28.25	4	10	40	24.83

Table 4 Statistical analysis for selection of SPT

Standard deviation	95% confidence	Selected value
13.87	14.66	14

6.2 Axial Load-Carrying Capacity of Pile as Per the Japanese Standards and Codes

By using formulas for cohesive soils based on SPT values, the cohesion intercept as calculated is found out to be almost same to that calculated by empirical formulas as used by Indian standards and codes. But by using empirical formulas for the calculation of the angle of internal friction based on SPT values in granular soils, it is observed that the results are on higher side than that calculated by Indian standards and codes (Table 5).

As per general practice in Japan, higher SPT values, results higher angle of internal friction and the same has been adopted without any limitations reason being SPT value results have more accuracy based on Japanese Standard and technique in Japan. The method of conducting SPT in boreholes is almost same in Japan and in India, but the difference is in SPT sampler shoe inner diameter. The inner diameter of SPT sampler shoe in Japan is smaller (35 mm) than that of India (38 mm).

The f_r is 0.42 because p_t is small ($p_t = 0.35$), and the long-term design bearing load capacity as calculated by the Japanese codes and standards is 3088.5 kN

$$3088.5\,\text{kN} = 0.42(4775.0 + 2578.6) \tag{19}$$

Table 5 Calculated strength parameters of soil (Japan)

Depth (m)	SPT (N^a)	Soil	c^b (kN/m^2)	ϕ^{0b}	γ (kN/m^3)
0–5	10	Silty clay	63	–	16.0
5–15	25	Silty clay	156	–	17.0
15–20	38	Silty sand	–	40	17.5
20–25	40	Silty sand	–	41	18.0

[a]SPT values are average values of that stratum
[b]Values are derived from imperical coorelations

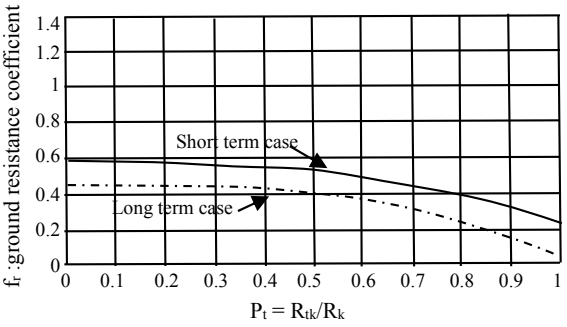

Fig. 1 Relationship between f_r and p_t in case bored cast in situ pile (Japanese standards and codes)

The f_r is determined by Fig. 1 as per the Japanese Railway Standards (JRS) (Design Standards for Railway Structures and Commentary [Foundation]).

7 Comparison of the Bored Cast in Situ Pile Design Results

The calculated bearing capacity result comparison is shown below.

Japanese code estimates the tip resistance of bored cast in situ pile less than that estimated by Indian codes. This is assumed to be the difference of philosophy of bored cast in situ pile performance.

In Japan, the tip resistance of bored cast in situ pile is thought not to be large because of the debris and slimes when bored cast in situ pile is constructed.

Generally the bearing stratum in urban area where infrastructure is constructed is not rocky rather dilluvial soils are prominent resulting in reducing the tip resistance (Table 6).

The friction resistance and tip resistance for given soils types, i.e., silty clay and silty sand, are calculated by static method for axial load. The soil parameters required are calculated by the correlations given in the previous section. The vari-

Table 6 Calculated bearing capacity comparison between Japan and India

Code/standard/method	Friction resistance (kN)	Tip resistance (kN)	Safe bearing capacity (kN)
Japan (Method-1)	4775.0	2578.6	3088.5
India (Method-1)	3883.0	6039.0	3968.0
India (Method-2)	–	–	2058.4

ation of friction resistance and tip resistance for given soil types varies largely in Indian Method-1 and Japanese Method-1. The comparison demonstrated that friction capacity as calculated by using the Japanese method is about 23% higher than as calculated by Indian Method-1; on the contrary, the tip resistance as calculated using Indian Method-1 is about 134% higher than as calculated by the Japanese Method-1. However, the safe bearing capacity as calculated by Indian Method-1 is about 28.5% higher than the Japanese Method-1.

8 Conclusion

Two analyses have been conducted, based on the tip resistance and friction resistance for given case study of silty clay and silty sand. The silty clay encountered in boreholes from ground level to about 15 m followed by the thick layer of silty sand extended down till the end of borehole. Indian codes and Japanese code are used for evaluating the safe axial pile capacity, the capacities were compared for axial load calculations results. In general, the loads calculated using the Indian pile capacity calculation code Method-1 are greater than the safe load-bearing capacity calculated by using Indian pile capacity calculation code Method-2. The Japanese method yields conservative pile capacity compared to the Method-1 of Indian codes. The capacity calculated by Method-2 of Indian codes is much more conservative compared to the Japanese codes and also Method-1 of Indian codes.

The calculated bearing capacity by the Japanese standards and codes is similar to an average of those calculated by Indian standards and codes (Method-1 and Method-2).

This calculation sample shows that there is not much difference between Japan and India codes from the viewpoint of bearing capacity as a result, although the formulas vary largely.

References

Aoki N, de Alencar D (1975) An approximate method to estimate the bearing capacity of piles. In: Proceedings, the 5th Pan-American conference of soil mechanics and foundation engineering, vol 1. Buenos Aires, pp 367–376

Bishop AW, Eldin AK (1953) The effect of stress history on the relation between ϕ and porosity in sand. In: Proceedings of the 3rd ICSMFE, vol 1, pp 100–105

Codes, Indian Standard (1980) Code of practice for design and construction of pile foundations, (IS: 2911), Part I/Sec2. Bureau of Indian Standards, New Delhi

De Beer E (1975) Influence of the mean normal stress on the shearing strength of sand. In: Proceedings of the 6th ICSMFE, vol 1, pp 165–169

Design Standards for Japanese Railway Structures and Commentary (Foundation), Maruzen (2012)

Gibbs HJ, Holtz WG (1957) Research on determining the density of sands by spoon penetration testing. In: Proceedings of the 4th ICSMFE, vol 1, pp 35–39

Kirkpatrick (1965) Effect of grain size and grading on shearing behavior of granular materials. Proceedings of the 6th ICSMFE, vol 1, pp 273–277

Nash (1953) The shearing resistance of a fine closely sand. In: Proceedings of the 3rd ICSMFE, vol 1, pp 160–164

Varghese P (2005) Foundation engineering. PHI Learning Pvt. Ltd., New Delhi

Part III
Advances in Waterways and Pipeline Geotechnics

Controlling Soil and Water Acidity in Acid Sulfate Soil Terrains Using Permeable Reactive Barriers

Subhani Medawela, Buddhima Indraratna, Udeshini Pathirage and Ana Heitor

Abstract There are about 12–14 million ha of acid sulfate soils (ASSs) found throughout the length and breadth of the earth. Bridge and building foundations, pipelines, culverts, and other buried infrastructure in such acidic environments are deteriorated when they are exposed to higher acidity, which is generated due to leaching of sulfuric acid from ASS. Thus, acidic groundwater should be properly treated to avoid detrimental effects on natural environment and strenuous efforts on repairing damaged manmade structures. Since the early 90s, permeable reactive barriers (PRBs) were implemented in several places worldwide and it was proven that PRBs are capable of competently treating poor-quality groundwater with various contaminants. While the acidic groundwater flows through a PRB, contaminants (toxic cations) are removed by mineral precipitation and due to the chemical reactions occur, a near-neutral pH is maintained in the effluent. Nevertheless, longevity of the PRB is alleviated due to coupled clogging in porous media. Physical, chemical, and biological clogging mechanisms and the existing PRB design criteria have been critically reviewed in this paper, including precursory numerical models. It is imperative to extend existing equations and models combining all possible clogging mechanisms, to assure the maximum acid removal capacity of a PRB. Hence, water and soil quality would be enhanced to make the land safe for transport and other infrastructure developments.

Keywords Acid sulfate soils · PRBs · Coupled clogging · Modeling

S. Medawela (✉) · B. Indraratna · A. Heitor
Faculty of Engineering and Information Sciences, Centre for Geomechanics and Railway Engineering, University of Wollongong, Wollongong, Australia
e-mail: skmsj997@uowmail.edu.au

B. Indraratna
e-mail: indra@uow.edu.au

A. Heitor
e-mail: aheitor@uow.edu.au

U. Pathirage
Geo-environmental Engineer, Golder Associates Pty Ltd., Adelaide, Australia
e-mail: UPathirage@golder.com.au

R. Sundaram et al. (eds.), *Geotechnics for Transportation Infrastructure*, Lecture Notes in Civil Engineering 28, https://doi.org/10.1007/978-981-13-6701-4_27

1 Introduction

Acid sulfate soil presents sporadically in the coastal floodplains throughout the globe. They contain a shallow layer of pyrite (FeS_2) that oxidizes in the presence of oxygen. During pyrite oxidation, sulfuric acid is generated. Hence, soil pH is lowered and toxic heavy metals such as aluminum (Al) and iron (total Fe) cations are leached into the groundwater (Regmi et al. 2009). This acidic groundwater flow expands the acidified land area, deteriorating the quality of soil terrains and waterways. Acidic effluents have been shown to be detrimental not only to flora and fauna (White et al. 1997; Sammut et al. 2010), but also to buried infrastructure, as sulfuric acid is highly corrosive and can cause severe damage to pipelines, culverts, and foundations (Van Holst and Westerveld 1973). Thus, remedial measures are required to neutralize the acidic groundwater, in order to reduce the risk and maintenance cost involved with infrastructure in acidic coastal regions.

Naturally occurring acid sulfate soil sediments are very common along estuarine floodplains and coastal lowlands of Australia (White et al. 1997). Several engineering solutions have been implemented over a period of two decades in Shoalhaven floodplain, NSW, Australia, for managing and remediating acidic groundwater. These included v-notch and self-regulating tilting weirs, two-way floodgates (Blunden 2000, Indraratna et al. 2005), and semi-impermeable horizontal lime-fly ash barriers (Banasiak 2004). After numerous trials, permeable reactive barriers have proven to be the most cost-effective and efficient method (Fig. 1) in treating acidic water (Indraratna et al. 2017).

Nevertheless, the main factor potentially compromising the performance of PRBs is physical, chemical, and biological clogging of their pores and associated reduction in permeability due to particle accumulation, mineral precipitation, and bacterial activity, respectively (Banasiak et al. 2015). While physical and chemical clogging has been extensively investigated in past UOW research (Regmi et al. 2009;

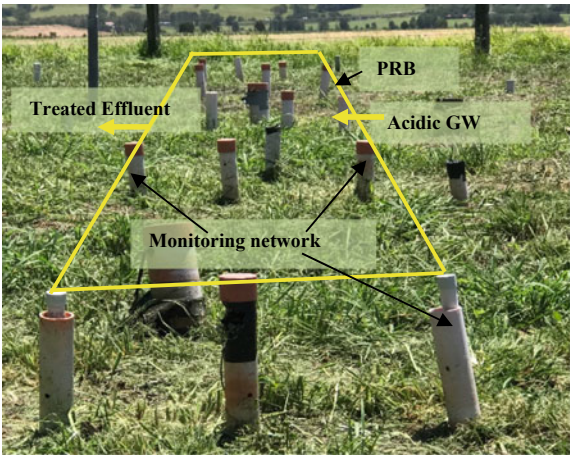

Fig. 1 PRB in Shoalhaven, NSW, Australia

Indraratna et al. 2014), the role of bioclogging has not been critically analyzed in the literature. The bioclogging is associated with acidophilic bacteria which promotes the biofilm growth while catalyzing the chemical reactions and mineral precipitation (Regmi 2012; Pathirage 2014). Therefore, all three types of clogging mechanisms affect the hydraulic characteristics and longevity of PRBs, which arises the need for integrated models to predict the PRB performance.

2 PRBs and Reactive Materials

A PRB is an engineered geostructure which aims to intercept a contaminant plume in situ and is typically a trench constructed as a subsurface treatment zone filled with a permanent, semi-permanent, or replaceable reactive material (Gavaskar 1999). The selection of the filling material of the PRB is vital, since the entire performance of the system to remove contaminants depends on the reactivity of the filling media. Gavaskar (1999) discussed the principal characteristics of the reactive material which should be checked prior to the installation of the PRB. The residence time should be sufficient to maintain an adequate reactivity to remove all the contaminants in an environmentally acceptable manner, without acting themselves as a contaminant. Ability to maintain an economical barrier thickness using a low-cost material is also important. Compatibility with subsurface environment, while maintaining reactivity over a long period without excess clogging and deteriorating, is another key feature that an appropriate filling material should maintain. Availability, correct particle size to maintain the desired porosity, and ability of suppressing precipitation to allow continued flow of water with time are some other factors.

A number of past reviews can be found on various PRB reactive materials (Blowes et al. 2000; Scherer et al. 2008, Obiri-Nyarko et al. 2014). Reactive materials usually act as chemical and/or biological reagents or catalysts to support the chemical reactions associated with the removal of the target contaminants. Prior to the usage of any reactive material in a field PRBs, their effectiveness together with their required properties should be tested in the laboratory. Batch tests are the most commonly used preliminary method for selecting possible materials (Bernier 2005; Golab et al. 2006). Secondly, detailed column tests should be conducted to confirm the treatability of that potential material, while simulating continuous flow of groundwater in the laboratory.

In majority of the PRBs up to date, granular iron media [i.e., zero-valent iron (ZVI or Fe^0)] has been used (Gu et al. 1999; Liang et al. 2000; Scherer et al. 2008; Statham et al. 2016), to treat chlorinated organic contaminants and inorganic contaminants (radionuclides, Ni, Cr, As, U, Cu, Zn, Pb, Cd, Fe, SO_4^{2}). In the case of treating acidic groundwater, reactive materials used in most of the past studies were limestone, mixtures of limestone and organic carbon-rich materials such as wood chips, municipal compost, paper mill pulp (Obiri-Nyarko et al. 2014). In 2006, UOW researchers utilized an economical reactive material, i.e., recycled concrete aggregates (Indraratna et al. 2009; Regmi et al. 2009; Banasiak et al. 2013) for neu-

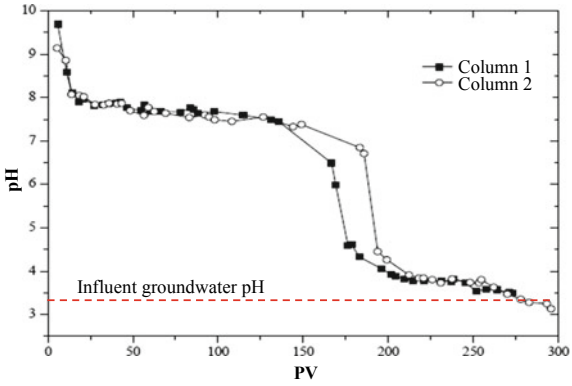

Fig. 2 pH profile of recycle concrete column effluents (modified after Indraratna et al. 2014)

tralizing acidic groundwater in an ASS terrain. Figure 2 depicts the results obtained from laboratory column experiments conducted by Indraratna et al. 2014 in which recycled concrete aggregates were confirmed as a suitable filling material. Although the influent was highly acidic (pH < 3.5), the alkalinity of recycled concrete maintained a near-neutral, contaminant-free effluent (pH > 6.5) throughout 65% of the total time (up to 190 PV) for column tests. Numerical model predicted life span for this field PRB was 17 years (Pathirage and Indraratna 2014).

3 Longevity Reduction of PRBs

The period throughout which the PRB can function in its full capacity within expected design levels is finite and is defined as the longevity or the life span of the PRB (Obiri-Nyarko et al. 2014). In general, when the contaminated groundwater with dissolved constituents encounters the reactive material, the reactivity is exhausted and PRB performance is hindered basically due to aforementioned clogging types. Migration of fine soil particles and suspended matter in groundwater is the primary cause of physical clogging, which is the simplest and mostly studied mechanism of disturbing the pores (Indraratna and Vafai 1997; Reddi et al. 2005). Accumulation of chemically precipitated compounds (most commonly carbonate and sulfate precipitates) was studied in detail (Liang et al. 2000; Li et al. 2005). Biofouling of PRBs occurs due to accumulation of bacteria and by products in pores (Vandevivere and Baveye 1992). Coupled clogging PRB reactive surface can result in reactivity and porosity reductions, reorientations in flow path, changes to flow rates, residence times, and seepage velocities (Li et al. 2005).

3.1 Chemical Clogging and Armoring of PRBs

Indraratna et al. (2014) described armoring as complete encrustation by precipitating material on the reactive surface. The accumulation of the precipitates in void spaces of the reactive material is referred to as clogging of a PRB by Gavaskar (1999). The combination of above two phenomena, chemical clogging and armoring, results in a reduction in the porosity and available pores for water to permeate. For instance, the pilot-scale PRB is designed by UOW using alkaline recycled concrete to treat highly acidic water enriched with Al and Fe; they are precipitated in forms of Al and Fe oxides and hydroxides (i.e., $Fe(OH)_3$, $Fe(OOH)$, Fe_2O_3, $Fe(OH)_2$, $FeCO_3$, $Al(OH)_3$). This chemical reaction process resulted in pore space clogging, reducing the porosity and hydraulic conductivity of the granular assembly. This behavior was examined not only in preliminary column experiments but also it was predicted using a coupled geochemical model (Fig. 3a) (Indraratna et al. 2014). A fully armored and clogged column is shown in Fig. 3b. The hydraulic conductivity reduction was maximum at entrance (Zone 1) and decreased with distance along the column (i.e., clogging in Zone 1 > Zone2 > Zone 3 etc.). This was because of the reduction in dissolved ions in the solution available to precipitate as water moves through the column. In this column, the pores were large enough and the complete blockage of the pores did not occur and hence the flow could be maintained, albeit with an increase in pressure, throughout the experiment.

3.2 Biological Clogging in PRBs

The build-up of microbial biomass [cells and extracellular polymeric substances (EPS)] can lead, when stimulated by sufficiently high nutrient loading, in considerable reductions of hydraulic conductivities. This is due to pores being plugged by the biomass itself from the effect called "bioclogging" (Vandevivere and Baveye 1992). Significant porosity reductions and hence hydraulic conductivity reductions due to bioclogging have been reported in past studies (Taylor et al. 1990; Cunningham et al. 1991; Seki and Miyazaki 2001; Soleimani 2007). For example, the relationship between relative hydraulic conductivity (K/K_0) and relative biomass volume (α) was studied by Vandevivere and Baveye (1992) in relation to clogging intensity and grain-size distribution of the porous medium as shown in Fig. 4.

3.2.1 Bioclogging of PRBs in Acidic Environments

Microbial clogging of other water-logged soils and aquifer materials has been intensely studied in past decades (Baveye et al. 1998) mainly focusing on wastewater treatment units (Dupin and McCarty 2000). In the case of PRBs, biological clogging has not been examined in detail (Liang et al. 2000; Pathirage 2014). Only little

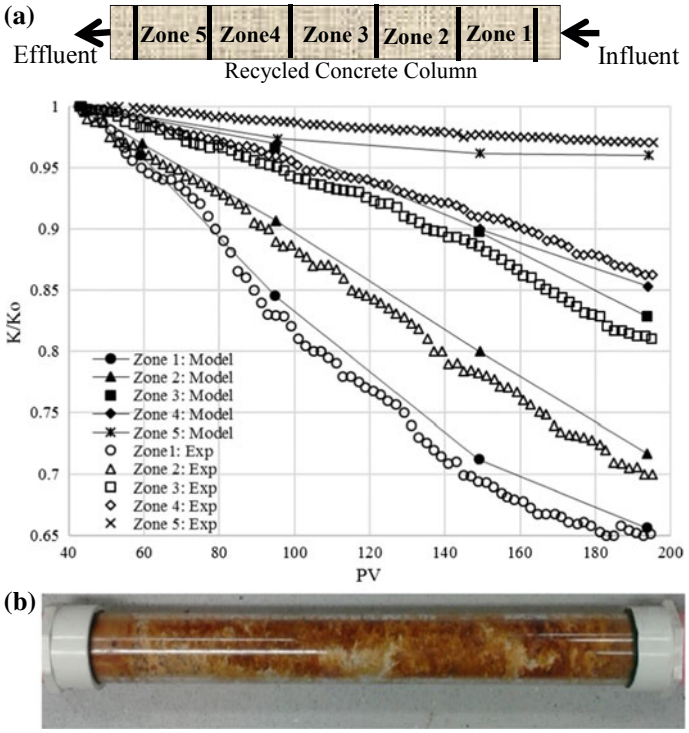

Fig. 3 **a** Permeability reductions along the column due to chemical clogging (modified after Indraratna et al. 2014). **b** A totally clogged column (Dark yellow Fe precipitates and White Al precipitates)

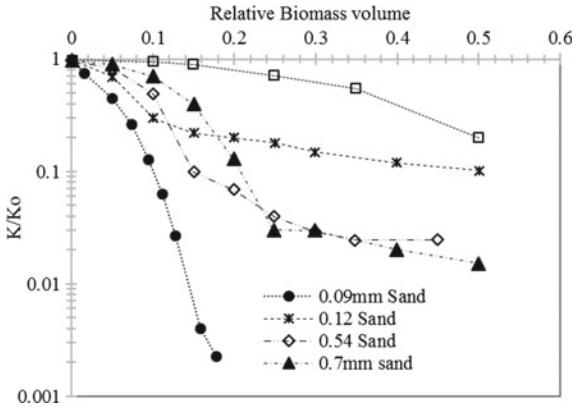

Fig. 4 Relationship between K/K_0 and α. *Data source* Vandevivere and Baveye (1992)

evidence is found regarding microbial clogging in zero-valent iron (ZVI) PRBs. Biofouling was observed in a zero-valent iron/sand reactive barrier in Newbury Park, CA (Gu et al. 1999), and rapid clogging occurred in a filter column at the Portsmouth, OH (Liang et al. 2000). Sulfate-reducing bacteria (SRB) were detected in those water samples in zero-valent iron fillings. SO_4^{2-} ions were acting as electronic acceptors for SRB, and hence, sulfides were produced which caused in biologically mediated mineral precipitation and bioclogging and hence permeability reductions in Fe^0 barriers (Gu et al. 1999). Nevertheless, no past studies reported the role of microbiological activity within in PRBs located in ASS terrains. Acidophiles (particularly termed as *Acidithiobacillus ferrooxidans*) present in ASS environments play a major role in pyrite oxidation and acid generation in ASS terrains. These microorganisms can accelerate porous media clogging. This biotic role is twofold, (a) catalyzing the chemical reactions producing precipitates while neutralizing the acidic groundwater and (b) promoting the biological growth inside the voids leading to armoring of particle surfaces. However, further research is required to evaluate these biofouling effects in PRBs.

4 Modeling of PRB Clogging

In most of the past numerical modeling approaches, Kozeny–Carmen equation has been used for evaluating permeability reductions of the porous media due to physical, chemical, and biological clogging. The hydraulic conductivity (K) after a porosity reduction, Δn_t, can be expressed using the normalized Kozeny–Carmen equation as (Taylor et al. 1990; Clement et al. 1996; Li et al. 2005; Indraratna et al. 2014),

$$K = K_0 \left[\frac{n_0 - \Delta n_t}{n_0} \right]^3 / \left[\frac{1 - n_0 + \Delta n_t}{1 - n_0} \right]^2 \tag{1}$$

When developing a combined clogging model, Δn_t term, the porosity reduction at time t, should capture the effects of physical, chemical, and biological clogging.

4.1 Porosity Change Due to Chemical Clogging

Temporal porosity change only due to chemical precipitates can be obtained by Eq. 2 (Steefel and Lasaga 1994; Li et al. 2005; Indraratna et al. 2014).

$$n_{t_c} = n_0 - \sum_{k=1}^{N_m} M_k R_k t \tag{2}$$

where M_k is the mineral molar volume ($m^3\ mol^{-1}$), R_k is the overall reaction rate of the mineral ($mol\ m_{bulk}^{-3}\ s^{-1}$), N_m is the number of minerals, n_o porosity at the start, and n_{t_c} is the secondary mineral precipitation-affected porosity at time t.

4.2 Modeling of Biological Clogging

Although all past researchers agreed that significant permeability reductions could occur due to biotic growth, they have different views of how the bacteria cause in this dramatic reduction (Vandevivere and Baveye 1992). These biological interactions and clogging mechanisms have been categorized into three main conceptual models, namely (i) strictly macroscopic model, (ii) discrete micro-colony model, and (iii) continuous biofilm model (Baveye and Valocchi 1989). The difference between these bioclogging morphologies is crucial in modeling the associated permeability reduction. In the strictly macroscopic model, bacteria are considered to be attached to the solid particles and growing on them in isolated groups (Clement et al. 1996). The discrete micro-colony model was first developed by Molz et al. (1986) and assumes that microorganisms are growing in micro-colonies (patchy biofilms) attached to the porous medium solid particles. Each of these micro-colonies has a cylindrical plate form with a predefined radius and thickness. Growth of biomass is represented by increase in the number of micro-colonies. Thirdly, the biofilm model postulates that the surface of porous media is covered by a continuous film of biomass (Baveye and Valocchi 1989).

Even though some numerical approaches such as homogenization or network models can be used to scale up the microscopic model parameters into macroscopic level, those methods are complicated. Clearly, due to the complex nature of porous media, it is not possible to simulate the flow through each pore. But macroscopically, pore morphology can be considered without individual visualization of pores. In this way, the microbial activity in the porous media can be considered using the macroscopic properties such as porosity and permeability (Chen-Charpentier 1999). Table 1 summarizes some equations used by several past authors for each conceptual model, which can be used to evaluate the biomass-affected porosity (Δn_{t_b}).

4.3 Flow Models and Transport Models

Using above mathematical expressions, total porosity reduction due to chemical and biological clogging can be written as,

$$\Delta n_t = \Delta n_{t_c} + \Delta n_{t_b} \tag{3}$$

Table 1 Equations for porosity reduction due to bioclogging[a]

Biomass-affected porosity	Approach
Volume fraction occupied by solid-phase biomass, $n_{\mathrm{tb}} = X^{\mathrm{f}}\rho_k/\rho_{\mathrm{f}}$	Macroscopic model (Clement et al. 1996)
Assuming porous medium is comprised equal diameter spheres (homogeneous grain size), $1-\frac{\pi}{\alpha_{\mathrm{m}}}\left[\frac{(2-m)}{12}\left(\frac{2L_{\mathrm{f}}}{d}\right)^3+\frac{(4-m)}{8}\left(\frac{2L_{\mathrm{f}}}{d}\right)^2+\frac{1}{2}\left(\left(\frac{2L_{\mathrm{f}}}{d}\right)+\frac{1}{6}\right)\right]$	Biofilm coating (Taylor et al. 1990; Cunningham et al. 1991)
For heterogeneous grain size, $1-\pi\left[\hat{a}\left(\frac{2L_{\mathrm{f}}}{d}\right)^3+\hat{b}\left(\frac{2L_{\mathrm{f}}}{d}\right)^2+\hat{c}\left(\frac{2L_{\mathrm{f}}}{d}\right)+\hat{d}\right]$	Biofilm coating (Taylor et al. 1990)
Volume of the pores clogged by the biomass $V_{\mathrm{bio}}=\frac{1}{2}\left(1+E\left\{\frac{Z_{\mathrm{n}}}{\sqrt{2\sigma}}-2\sigma\right\}\right)$	Micro-colonies (Thullner et al. 2002)

[a]All terms are defined in Table 2

which can then be used to obtain the hydraulic conductivity reduction in the PRB using Eq. 1. Therefore, a complete mathematical model combining physical, chemical, and biological clogging in porous media can be developed to predict the temporal and spatial variation of saturated hydraulic conductivity based on input data relative to the physical and chemical characteristics of the porous medium and of the liquid phase, the flow characteristics such as pressure gradient or flow rate, and specific features of the microbial population present with in porous matrix. Conceptually, it is convenient to separate such a model into two main components, flow model and transport model (Li et al. 2005; Indraratna et al. 2014). The first component, the flow model, may include a set of equations which describe the mineral precipitation due to chemical reactions and accumulation of microbial cells and their end products that interfere with the flow through the void space. Moreover, it would predict the reductions of saturated hydraulic conductivity and porosity of the porous media as a function of clogging and armoring. The three-dimensional movement of groundwater of constant density through porous earth material may be described by the partial-differential Eq. (4) (Harbaugh 2005), where all terms are defined in Table 1.

$$\frac{\partial}{\partial x}\left(K_{xx}\frac{\partial h}{\partial x}\right)+\frac{\partial}{\partial y}\left(K_{yy}\frac{\partial h}{\partial x}\right)+\frac{\partial}{\partial z}\left(K_{zz}\frac{\partial h}{\partial z}\right)+W=S_{\mathrm{s}}\frac{\partial h}{\partial t} \tag{4}$$

Table 2 Definition of terms

Term	Definition
K	Hydraulic conductivity (L/T)
h	Hydraulic head (L)
W	Volumetric flux per unit volume representing sources and/or sinks of water (T^-)
S_s	Specific storage of the porous material (L^{-1})
t	Time (T)
k	Total number of species
m	Total number of aqueous-phase species
C_k	Aqueous-phase kth species concentration (ML^{-3})
D_{ij}	Hydrodynamic dispersion coefficient (L_2T^{-1}),
v	Pore velocity (LT^{-1})
$\varnothing$	Soil porosity
q_s	Volumetric flux of water per unit volume of aquifer representing sources and sinks (T^{-1})
C_s	Concentration of source/sink (ML^{-3})
r_c	Reaction rates occur in aqueous phase (ML^3T^{-1})
X^f	Microbial cell mass per unit mass of aquifer solids
ρ_k	Bulk density of aquifer solids (ML^{-3})
ρ_f	Solid-phase biomass density (ML^{-3})
α_m	Packing arrangement factor
d	Sphere diameter (L)
L_f	Biofilm thickness (L)
E	Error function
Z_n	$Z_n = f(r)$ is the pore radius
σ	Standard deviation
C_i	Influent contaminant concentration
C_e	Effluent contaminant concentration
C_{lim}	Limit of contaminant concentration
I	Hydraulic gradient

The second part is the development of transport equations which describe the fate and transport of aqueous and solid-phase species in the porous media. Time-dependent variations in concentrations of minerals precipitated and biomass should be captured in this step. The general macroscopic equations describing the fate and transport of aqueous- and solid-phase species, respectively, in multi-dimensional saturated porous media are written as (Clement et al. 1996),

$$\frac{\partial C_k}{\partial t} = \frac{\partial}{\partial x_i}\left(D_{ij}\frac{\partial C_k}{\partial x_j}\right) - \frac{\partial}{\partial x_i}(v_i C_k) + \frac{q}{\varnothing}C_{s_k} + r_c \tag{5}$$

Indraratna et al. (2014) developed one-dimensional contaminant transport modeling based on laboratory column experiments data to explain the geochemical changes in groundwater along the column experiment flow path. Moreover, the model was applied to the field PRB in acidic terrain, along a transect passing through the centerline of the PRB concluding that the model was well matched with laboratory and field data. A geochemical algorithm was formulated and applied, adopting 3D finite difference method (FDM) via commercially available FDM software MODFLOW to simulate the groundwater flow and RT3D to analyze reaction kinetics and contaminant transport. MODFLOW and RT3D were used in tandem, enabling the inclusion of principles of advection, diffusion, and reaction kinetics in numerical analysis. Very similar modeling approach was reported by Li et al. (2005) for a zero-valent iron PRB. Nevertheless, the role of bioclogging component was not considered in these modeling studies (Indraratna et al. 2014).

5 Design Criteria of a Field PRB

Several studies have been carried out to develop methods for determining the design geometry of PRBs. Elder et al. (2002) proposed a simple one-dimensional (1-D) plug-flow model which provides the PRB thickness as:

$$b_{\text{des}} = \frac{-Ki}{k_r n} \text{In}\left(\frac{C_e}{C_{\text{in}}}\right) \quad \text{and} \quad \text{SF} = b_{\text{des}}/b_{\text{opt}} \tag{6}$$

where b_{des} is the design thickness of the PRB, resulting from the optimum thickness b_{opt} by introducing an appropriate safety factor (SF). Based on the numerical simulations explained in Sect. 4.3, an elaborate design criterion for a filed PRB was proposed by Pathirage and Indraratna (2014), as shown in Fig. 5. Only the physical and chemical clogging components were included in the design method, without considering the biofouling. After a detailed experimental and numerical modeling strategy, bioclogging could also be introduced into the geochemical algorithm and into these design criteria.

6 Conclusion

PRB is a one of the foremost technologies in remediating acidic groundwater. Its reactivity and longevity should be critically analyzed, and research into coupled clogging is advantageous in developing advanced biogeochemical computational models and a proper design criteria, which is vital in controlling soil and water acidity, to mitigate negative environmental impacts and to make an appropriate underground for infrastructure development, while diminishing the extra maintenance cost associated mainly with foundations, pipelines, culverts, and many other underground transport

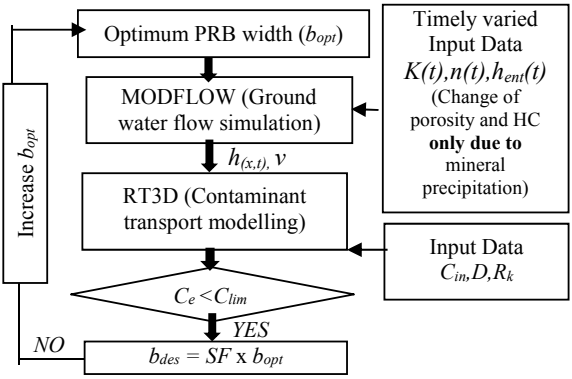

Fig. 5 Flowchart of the PRB design process (modified after Pathirage and Indraratna 2014)

facilities in low-lying acidic belts. In-depth analysis of clogging mechanisms in porous media is not only important for PRB technology, but that knowledge is also essential in controlling clogging in other soil filters, piezometer clogging in dam constructions, and drainage system blockages.

Acknowledgements The authors are grateful for funding received from the Australian Research Council (ARC) and the industry partner Manildra Group, with special thanks to Glenys Lugg. Former research students in UOW ASS research team, Laura Banasiak, and Gyanendra Regmi are gratefully appreciated. The authors acknowledge technical staff at the University of Wollongong for their assistance in field monitoring.

References

Banasiak LJ (2004) The role of a subsurface lime-fly ash barrier in the mitigation of acid sulphate soils. Masters, University of Wollongong

Banasiak L, Indraratna B, Regmi G, Golab A, Lugg G (2013) Characterisation and assessment of recycled concrete aggregates used in a permeable reactive barrier for the treatment of acidic groundwater. Geomech Geo-eng 8:155–166

Banasiak L, Indraratna B, Lugg G, PathiragE U, Mcintosh G, Rendell N (2015) Permeable reactive barrier rejuvenation by alkaline wastewater. Environ Geotech 2(1):45–55

Baveye P, Valocchi A (1989) An evaluation of mathematical models of the transport of biologically reacting solutes in saturated soils and aquifers. Water Resour Res 25:1413–1421

Baveye P, Vandevivere P, Hoyle BL, Deleo PC, de Lozada DS (1998) Environmental impact and mechanisms of the biological clogging of saturated soils and aquifer materials. Crit Rev Environ Sci Technol 28:123–191

Bernier LR (2005) The potential use of serpentinite in the passive treatment of acid mine drainage: batch experiments. Environ Geol 47:670–684

Blowes DW, Ptacek CJ, Benner SG, Mcrae CW, BennetT TA, PulS RW (2000) Treatment of inorganic contaminants using permeable reactive barriers. J Contam Hydrol 45:123–137

Blunden BG (2000) Management of acid sulfate soils by groundwater manipulation. Ph.D., University of Wollongong

Chen-Charpentier B (1999) Numerical simulation of biofilm growth in porous media. J Comput Appl Math 103:55–66

Clement T, Hooker B, Skeen R (1996) Macroscopic models for predicting changes in saturated porous media properties caused by microbial growth. Ground Water 34:934–942
Cunningham AB, Characklis WG, AbedeeN F, Crawford D (1991) Influence of biofilm accumulation on porous media hydrodynamics. Environ Sci Technol 25:1305–1311
Dupin HJ, MCcarty PL (2000) Impact of colony morphologies and disinfection on biological clogging in porous media. Environ Sci Technol 34:1513–1520
Elder CR, Benson CH, Eykholt GR (2002) Effects of heterogeneity on influent and effluent concentrations from horizontal permeable reactive barriers. Water Resour Res 38:27-1–28-2
Gavaskar AR (1999) Design and construction techniques for permeable reactive barriers. J Hazard Mater 68:41–71
Golab AN, Peterson M, Indraratna B (2006) Selection of potential reactive materials for a permeable reactive barrier for remediating acidic groundwater in acid sulphate soil terrains. Q J Eng GeolHydrogeol 39:209–223
Gu B, Phelps T, Liang L, Dickey M, Roh Y, Kinsall B, Palumbo A, Jacobs G (1999) Biogeochemical dynamics in zero-valent iron columns: implications for permeable reactive barriers. Environ Sci Technol 33:2170–2177
Harbaugh AW (2005) MODFLOW-2005, the US geological survey modular ground-water model: the ground-water flow process. US Department of the Interior, US Geological Survey Reston, VA, USA
Indraratna B, Vafai F (1997) Analytical model for particle migration within base soil-filter system. J Geotechn Geoenviron Eng 123:100–109
Indraratna B, Golab A, Glamore W, Blunden B (2005) Acid sulphate soil remediation techniques on the Shoalhaven river floodplain, Australia. Quart J Eng Geol Hydrogeol 38:129–142
Indraratna B, Regmi G, Nghiem LD, Golab A (2009) Performance of a PRB for the remediation of acidic groundwater in acid sulfate soil terrain. J Geotechn Geoenviron Eng 136:897–906
Indraratna B, Pathirage PU, Rowe RK, Banasiak L (2014) Coupled hydro-geochemical modelling of a permeable reactive barrier for treating acidic groundwater. Comput Geotech 55:429–439
Indraratna B, Heitor A, Pathirage P (2017) Acidic groundwater remediation in the Shoalhaven floodplain. In: Geotechnical frontiers 2017
Li L, Benson CH, LawsoN EM (2005) Impact of mineral fouling on hydraulic behavior of permeable reactive barriers. Ground Water 43:582–596
Liang L, Korte N, Gu B, Puls R, Reeter C (2000) Geochemical and microbial reactions affecting the long-term performance of in situ 'iron barriers'. Adv Environ Res 4:273–286
Molz FJ, Widdowson M, Benefield L (1986) Simulation of microbial growth dynamics coupled to nutrient and oxygen transport in porous media. Water Resour Res 22:1207–1216
Obiri-Nyarko F, GrajaleS-Mesa SJ, Malina G (2014) An overview of permeable reactive barriers for in situ sustainable groundwater remediation. Chemosphere 111:243–259
Pathirage PU (2014) Modelling of clogging in a permeable reactive barrier in acid sulfate soil terrain. Doctor of Philosophy, University of Wollongong
Pathirage U, Indraratna B (2014) Assessment of optimum width and longevity of a permeable reactive barrier installed in an acid sulfate soil terrain. Can Geotech J 52:999–1004
Reddi LN, Xiao M, Hajra MG, Lee IM (2005) Physical clogging of soil filters under constant flow rate versus constant head. Can Geotech J 42:804–811
Regmi G (2012) Performance validation of a permeable reactive barrier (PRB) for treating acidic groundwater. Doctor of Philosophy, University of Wollongong
Regmi G, Indraratna B, Nghiem LD (2009) Long-term performance of a permeable reactive barrier in acid sulphate soil terrain. Water Air Soil Pollut Focus 9:409–419
Sammut J, White I, Melville M (2010) Stratification in acidified coastal floodplain drains. Wetlands Aust J 13:49–64
Scherer MM, Richter S, ValentinE RL, Alvarez PJ (2008) Chemistry and microbiology of permeable reactive barriers for in situ groundwater clean up. Crit Rev Microbiol 26:221–264
Seki K, Miyazaki T (2001) A mathematical model for biological clogging of uniform porous media. Water Resour Res 37:2995–2999

Soleimani S (2007) Numerical simulation of biological clogging in biofilters. University of Ottawa
Statham TM, Stark SC, Snape I, Stevens GW, Mumford KA (2016) A permeable reactive barrier (PRB) media sequence for the remediation of heavy metal and hydrocarbon contaminated water: a field assessment at Casey station, antarctica. Chemosphere 147:368–375
Steefel CI, Lasaga AC (1994) A coupled model for transport of multiple chemical species and kinetic precipitation/dissolution reactions with application to reactive flow in single phase hydrothermal systems. Am J Sci 294:529–592
Taylor SW, Jaffé PR, Milly PCD (1990) Biofilm growth and the related changes in the physical properties of a porous medium 2. Permeability. Water Resour Res 26:2161–2169
Thullner M, Zeyer J, Kinzelbach W (2002) Influence of microbial growth on hydraulic properties of pore networks. Transp Porous Media 49:99–122
Vandevivere P, Baveye P (1992) Effect of bacterial extracellular polymers on the saturated hydraulic conductivity of sand columns. Appl Environ Microbiol 58:1690–1698
Van Holst A , Westerveld C (1973) Corrosion of concrete foundations in potential acid sulphate soils and subsoils in The Netherlands. In: Dost H (ed) Proceedings of the international symposium on acid sulphate soils, 373–382
White I, Melville M, Wilson B, Sammut J (1997) Reducing acidic discharges from coastal wetlands in eastern Australia. Wetlands Ecol Manage 5:55–72

Design and Construction Approach of Marine Rock-Socketed Piles for an Oil Jetty Project

Seema Gurnani, K. R. Vinjamuri, A. Usmani and C. Singh

Abstract Jetty structures are supported on marine piles, which are essentially larger diameter piles with long unsupported length exposed to recurrent lateral loadings due to wave attacks, experiencing larger deflections and requiring deeper piles penetration for stability and pile capacity requirement. This particular attribute of long unsupported pile length and high lateral loading on marine piles makes job of an engineer crucial, particularly when the rock is available at a shallow depth thereby imposing restriction on deeper pile penetrations. In such situations, long driven steel piles are not feasible and rock-socketed bored cast-in-situ piles prove to be the most optimum solution. This paper outlines a case history which discusses the methodology of rock socket pile design along with problems encountered during field execution of marine rock-socketed bored cast-in-situ piles for an oil jetty project. Quality and levels of the rock are varying vastly; hence, pile termination criterion based on pile penetration ratio (PPR) is firmed up for execution.

Keywords Large diameter marine piles · Bored cast-in-situ piles · Rock socket · Pile capacity · Pile penetration ratio

S. Gurnani (✉) · K. R. Vinjamuri · A. Usmani · C. Singh
Engineers India Limited, EI Bhawan 1, Bhikaiji Cama Place, New Delhi 110066, India
e-mail: seema.gurnani@eil.co.in

K. R. Vinjamuri
e-mail: kalyan.vinjamuri@eil.co.in

A. Usmani
e-mail: altaf.usmani@eil.co.in

C. Singh
e-mail: c.singh@eil.co.in

R. Sundaram et al. (eds.), *Geotechnics for Transportation Infrastructure*, Lecture Notes in Civil Engineering 28, https://doi.org/10.1007/978-981-13-6701-4_28

1 Introduction

The increasing demand in oil and gas sector and availability of over 7000 km of coastline provides various opportunities for construction of a large number of oil and gas berths in India. Jetty structures and associated facilities are constructed to facilitate large crude and LNG (Liquefied Natural Gas) carriers to transport, berth, and offload crude oil or LNG.

A typical jetty structure comprises of an approach trestle (the approach roadway and piping/cable tray) and a jetty head consisting of an unloading platform, berthing dolphins, and mooring dolphins. The unloading platform and dolphins are interconnected by catwalks and crossovers as shown in Fig. 1.

The jetty structures are RCC structures supported on piles. Generally, marine piles are large diameter vertical/raker steel tubular piles or RCC bored in cast situ piles. The selection of type of pile depends upon subsoil characteristics.

All these structures are designed to resist environmental loads (wave, current, wind), seismic loads, gravity loads, piping, equipment loads, erection loads, mooring loads, berthing loads, and other applied loads.

Approximately, 10–20 m draft is required in front of jetty head for berthing of LNG or crude carriers. To achieve the required draft, dredging is done at jetty head. Elevation of jetty structures is planned in such a manner to keep a minimum required air gap during extreme storm events. Hence, these marine piles have long unsupported pile lengths above seabed level which is exposed to recurrent environmental loads, thereby, causes larger deflections. This particular attribute of marine piles requires deeper pile penetrations to provide stability and achieve higher pile capacity's to resist high lateral and axial loadings.

In case, rock is available at shallow depth, driven steel tubular piles are not feasible. Rock-socketed bored cast-in-situ piles are generally adopted in such a situation. Further, the rock quality and rock levels encountered at the site vary considerably;

Fig. 1 Typical jetty structure

hence, the design of rock socket length and determining pile termination level in field is a challenging task.

This paper presents a case study on detailed design and execution methodology of marine rock-socketed bored cast-in-situ piles for an oil jetty project.

2 Literature Review

Maertens (2003) published a case history about India's first LNG Terminal. Due to the presence of basalt rock, installation of driven piles was not feasible to a depth ensuring sufficient friction to resist design forces. This project involved installation of 610-mm diameter bored sockets through open-end steel pile of larger diameter piles (i.e., 762 mm) in weathered and sound basalt. Comparison of computed design skin friction resistance based on various methods proposed by Tomlinson (1995), Horvath et al. (1983), and Seidel and Collingwood (2002) was presented.

Rosenberg and Journeaux (1976) gave relationship between skin friction of rock socket and unconfined compressive strength of rock based on full-scale tests.

Kulhawy et al. (2005) discussed various methods for computation of skin friction of rock sockets and found that the procedure to quantify skin friction of rock sockets vary considerably.

Davisson and Robinson (1965) have given approximate equations for establishing depth of fixity based on the embedded length of the pile and a relative stiffness factor that depends on the flexural rigidity of the pile and the subgrade modulus of the soil or rock.

Analytical solutions for the rock sockets subjected to lateral loading generated using FEM technique are given by Carter and Kulhawy (1992). Closed-form equations are derived for rigid and flexible shafts. Rock mass is treated as homogeneous and elasto-plastic continuum, without considering secondary structures of rock mass.

Reese (1997) has published procedure for estimation of p–y data for weathered rock. The method is termed as 'interim' due to meager amount of data on which the method was established. This method considers secondary structure of rock by using rock strength reduction factor determined based on RQD.

Singh et al. (2017) carried out numerical analyses of rock sockets subjected to vertical or lateral loading independently and combined vertical and lateral loading. Vertical load—settlement behavior under combined loading is affected by soil cover only whereas lateral load-deflection behavior of pile is governed by both the soil cover and rock socket length. It is further concluded that the vertical load-carrying capacity is not affected by applied lateral load up to a safe load limit for piles with substantial soil cover. Also, total pile length is an important parameter in axial capacity computation as it under the application high loads; elastic compression of pile becomes significant in controlling the limiting settlement of pile.

Datey (1990) has published a detailed paper describing rocks in Bombay region and exploratory methods used. Detailed methodology is discussed to develop design

parameters based on the rate of penetration of chisel with specified energy input in boring.

3 Subsoil Conditions

The subsoil condition at site indicates the following layers:

A. Very soft marine clay layer of 1–8.5 m thick (CH) with very low SPT '*N*' value ($N \leq 1$) below seabed level.
B. Residual soil 0–1.5 m thick (in few boreholes).
C. Completely weathered to unweathered basalt rock (up to borehole termination) with rock quality designation, RQD varying from 0 to 60%, rarely increasing up to 95% and total core recovery (TCR) varying from 10 to 100%.

Huge variation in rock levels and rock quality is encountered in all the boreholes. Alternate bands of slightly weathered rock and highly weathered rock are also found in few boreholes. RQD, TCR, and UCS (unconfined compressive strength) values of one such borehole are given below in Table 1. In most of the boreholes, quality of encountered rock is very poor as tabulated in Table 2.

In weathered zone, the rock is brittle, with loss of color and fabric. TCR indicates 100% core recovery with 'Nil' RQD. The slightly weathered and unweathered rock is fine-grained, hard and tough. The unconfined compression strength of rock ranges from 10.7 to 40 MPa for the entire site.

Table 1 Rock properties in borehole BH 14

Depth in m.	TCR (%)	RQD (%)	UCS (MPa)	Grade based on RQD	
1.13–1.88	10.00	0.00	–	V. Poor	V
1.88–2.88	95.00	41.00	10.72	Poor	IV
2.88–3.58	100.00	0.00	–	V. Poor	V
3.58–5.08	94.00	35.00	19.34	Poor	IV
5.08–6.08	100.00	20.00	21.03	V. Poor	V
6.08–6.58	58.00	20.00	–	V. Poor	V
6.58–8.08	37.00	26.00	27.63	Poor	IV
8.08–9.13	100.00	0.00	–	V. Poor	V
9.13–10.13	80.00	10.00	20.64	V. Poor	V
10.13–11.13	90.00	35.00	19.82	Poor	IV

Table 2 Rock properties in borehole BH 11A

Depth in m.	TCR (%)	RQD (%)	UCS (MPa)	Grade based on RQD	
11.01–11.67	59	0	–	V. Poor	V
11.67–13.31	27	0	–	V. Poor	V
13.31–14.11	70	0	–	V. Poor	V
14.11–14.61	64	0	–	V. Poor	V
14.61–15.07	53	0	–	V. Poor	V
15.07–16.91	100	25	13.57	V. Poor	V
16.91–18.41	100	18	18.72	V. Poor	V
18.41–19.47	73	23	21.03	V. Poor	V
19.47–20.47	85	27	27.83	Poor	IV

4 Pile Design

Pile diameters designed for the jetty project are 1.0, 1.2, 1.4 and 1.5 m. Total pile length ranges from 14 to 39 m and design pile penetration ranges from 11 to 18.5 m. The unsupported pile length ranges from 2 to 26 m. Three-dimensional space frame analysis of the idealized structure is performed for marine structures for all specified load combinations to arrive at the critical design forces/moments and deflections for pile design. Piles were modeled up to virtual depth of fixity of piles.

4.1 Pile Socket Length

Socket length L_s in rock for a pile having diameter D, maximum horizontal force H and maximum moment M at top of rock socket is computed based on IRC-78-2014 given by Eq. 1. Permissible compressive strength, σ (or permissible rock pressure) is considered as minimum of 3000 kN/m^2 and $0.33q_c$ where q_c is unconfined compressive strength (UCS) of rock.

$$L_s = \frac{2H}{\sigma D} + \sqrt{\frac{4H^2}{\sigma^2 D^2} + \frac{6M}{\sigma D}} \tag{1}$$

Minimum required socket length is approximately 1.75–2.25 times pile diameter in moderately weathered rock where RQD is around 25% or more with UCS value of 13 MPa. Sometimes, RQD 25% or more is not encountered continuously in the entire socket length; hence, the design pile socket length is adopted to be three times pile diameter after the start of moderately weathered rock. The design rock socket length shall take care of some variations on rock quality (i.e., the presence of small intermittent very poor quality of rock layers) which may be encountered. However, actual rock socket length is finalized in the field as discussed in subsequent sections.

4.2 Lateral Pile Head Deflection

The presence of huge horizontal force and large moment and long unsupported length of pile causes very large pile head deflections. Allowable deflection of piles is considered as following:

Structure type	Loading condition		
	Extreme storm	Operating (vessel moored)	Operating (without vessel) or seismic
Unloading platform	*H*/350	*H*/500[a]	*H*/350
Approach trestle	*H*/350	*H*/350[a]	*H*/350
Mooring/berthing dolphins	300	300	300

H is unsupported pile length
[a]Deflection limits from piping stress analysis shall also be considered

The large deflections of piles are taken care by providing adequate pile reinforcement.

4.3 Pile Virtual Depth of Fixity

IS 2911 Part 1 Section 2 provides guidelines for determining virtual depth of fixity of piles. However, for bored cast-in-situ piles in rocks, clear guidelines for virtual fixity of piles are not present in the IS code. Thus, pile depth of fixity is computed as described below.

For pile fixity level computation, the stiffness of completely weathered rock is also considered. Say, L_H and L_S are the length of pile in completely weathered rock and design socket length, respectively, then the pile's virtual fixity level is considered at the middle of this extended rock socket below completely weathered rock and pile termination level, i.e., at a level $(L_H + L_S)/2$ below the level where completely weathered rock layer starts. This definition is depicted in Fig. 2.

To validate the above concept, pile fixity depth is empirically determined for the design pile and soil parameters in AllPile software (Version 7.3 h CivilTech 2006).

The pile cutoff level is considered as reference level and pile length below this reference level is measured in positive in increasing order. The dredged level is at 27 m, gravels/completely weathered rock layer starts at 29 m and socketing is considered to be start at 33.3 m length pile terminates at 37.8 m. Three soil layers are modeled in the software residual soft clay layers of 2.4 m thick, completely weathered rock/gravels 3.7 m thick (subgrade modulus ks = 53.5 MN), and weak to moderately weathered rock (ks = 82 MN). The software library is utilized for subgrade modulus which is linked with the shear strength parameters of soil/rock.

Now, virtual depth of fixity is defined by following two ways:

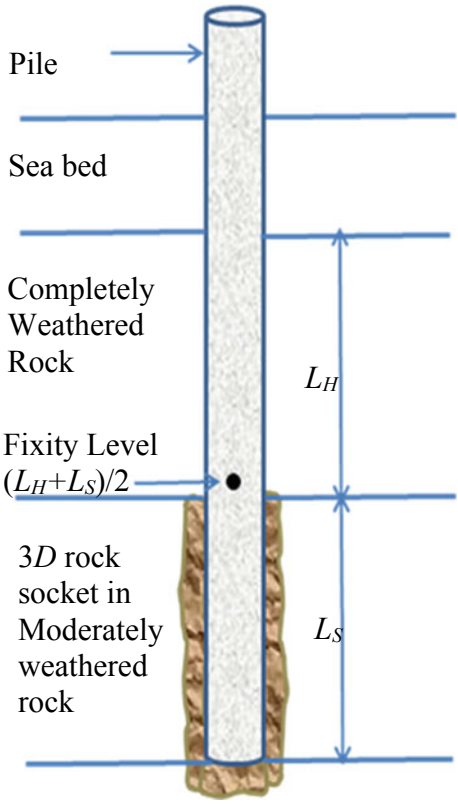

Fig. 2 Rock socket depiction

1. At a level where pile deflection is zero
2. At a level where pile moment is maximum.

Lateral pile analysis is carried out in and depth of fixity for the pile according to the above two definitions is found to be 34 and 31 m, respectively. The pile deflection versus depth and pile moment versus depth diagrams for a typical 1500 mm pile are given below in Figs. 3 and 4, respectively. Software data output for these two graphs is given in tabular format in Fig. 5. The midpoint of the extended rock socket is at 33.4 m which matches with software outcome. Hence, the assumption of considering pile's virtual fixity level at middle of the extended rock socket is a reasonable consideration.

The lateral load on the above pile was around 300 kN. It is also evident from Fig. 5 that corresponding to a lateral load of 300 kN, the lateral deflection is 191 mm. This lateral deflection is within the allowable deflection limit of 300 mm for berthing pile.

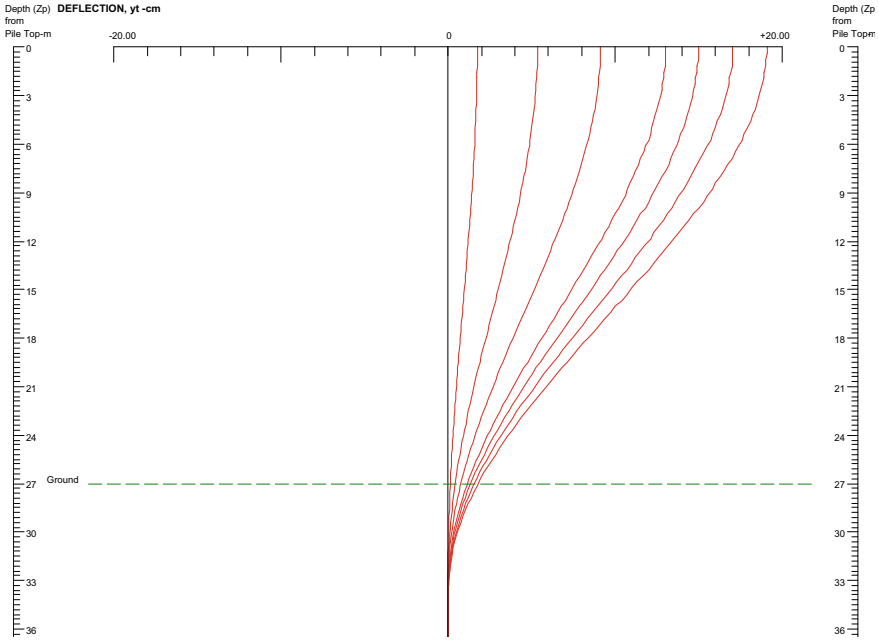

Fig. 3 Depth versus pile deflection for set of lateral loading

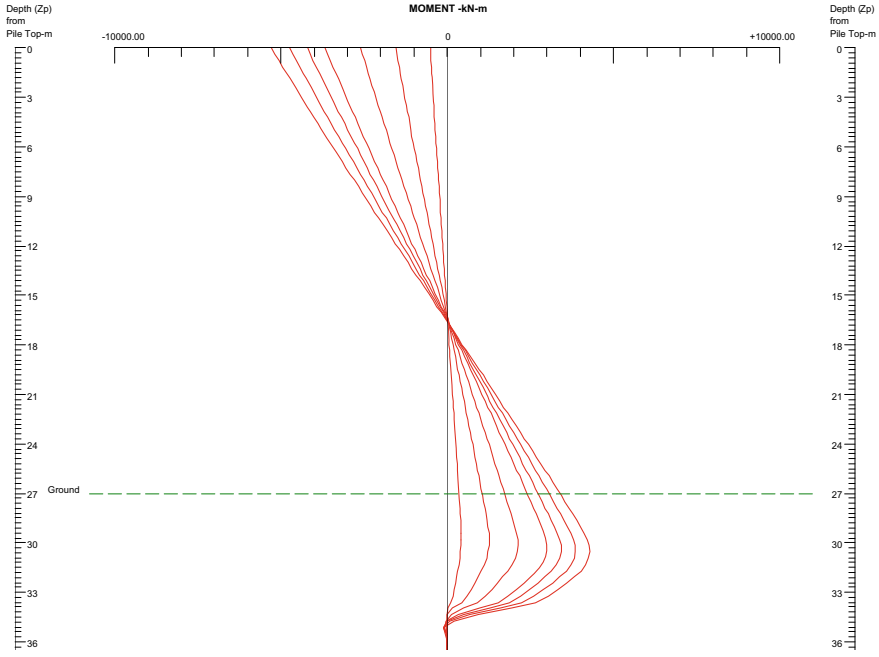

Fig. 4 Depth versus pile moment

Fig. 5 Software data output

No.	Lateral Load (kN)	Slope Restraint (cm/cm)	Vertical Load (kN)	yt at Top (cm)	Slope at Top (cm/cm)	Max. Moment (kN-m)
1	30.0	0.0	3380.0	1.7	0.00	-513.0
2	90.0	0.0	3380.0	5.3	0.00	-1550.0
3	150.0	0.0	3380.0	9.1	0.00	-2610.0
4	210.0	0.0	3380.0	13.0	0.00	-3670.0
5	240.0	0.0	3380.0	15.0	0.00	-4210.0
6	270.0	0.0	3380.0	17.0	0.00	-4750.0
7	300.0	0.0	3380.0	19.1	0.00	-5300.0

4.4 Pile Capacity

Safe axial capacity of pile is computed in accordance with Cl. 6.5.1.1 (method 1) and Cl. 6.5.1.3 (method 2) of IS 14593 (1998). The method 1 (as per Cl. 6.5.1.1) does not require any factor of safety to be applied where as a FOS of 6 is applied for method 2 (as per Cl. 6.5.1.3). The method 1 (as per Cl. 6.5.1.1) yields lesser values for safe pile capacity and the same is considered in design. Further, skin friction developed along the embedded portion in highly weathered rock and in upper very soft clay layer is ignored, conservatively. For tensile pile capacity computation, the socket length of 500 mm is further ignored.

Safe pile capacity Q_s for a pile of diameter D, cross-sectional area $A_{p,}$ and socket length l_s as per method-1:

$$Q_s = q_c N_j N_d A_p + q_c \pi D l_s \alpha \beta \tag{2}$$

where

q_c In unconfined compressive strength = 13 MPa
N_d Depth factor
N_j Empirical coefficient depending on spacing of discontinuities = 0.1 based on IS: 12070 (1995) for spacing of discontinuities 30–100 cm
α Side resistance reduction factor = 0.04
β Rock socket correction factor = 0.4.

Ultimate pile capacity for a pile of diameter D, cross-sectional area $A_{p,}$ and socket length l_s as per method 2:

$$Q_u = C_u.N_c.A_p + C_s.\alpha.\pi.D.l_s \tag{3}$$

where

C_u is shear strength of rock below pile tip
C_s is average shear strength of rock adjacent to shaft in the socket. A.
N_c is bearing capacity factor (equal to 9) and recommended value of α is 0.9 as per IS 14593 (1998).

Table 3 Safe pile capacity for piles

Pile diameter (mm)	Safe pile capacity (method 1) (MT)		Safe pile capacity (method 2) (MT)	
	Compr	Tens	Compr	Tens
1000	330	160	490	280
1200	480	240	635	335
1400	660	335	790	390
1500	760	390	870	420

The factor of safety of 6 is applied to obtain safe pile capacity. The safe pile capacity computed based on method 1 and method 2 in compression and pullout is tabulated in Table 3. It is evident from the following table that the method 1 yields lesser values of safe pile capacity as compared with the method 2.

5 Pile Execution

The project is currently under execution. A fully equipped marine spread is mobilized. A mild steel liner is driven up to the top of soft rock/completely weathered strata for stability. Boring is then done till pile termination level through reverse circulation drilling rig as a pile top rig. After cleaning of borehole, reinforcement cage is lowered and pouring of concrete starts immediately. In order to ensure dense and sound concrete up to pile cutoff level, contaminated concrete is allowed to overflow till good quality of concrete is obtained.

Pile termination level is finalized during design stage; however, taking into consideration the variability in rocky strata, pile penetration ratio (PPR) criterion for hydraulic rigs is utilized to ascertain the pile termination level in field.

As per IRC 78 (2014), the pile penetration ratio (PPR) is defined as the energy in ton-meter required to advance the pile bore of one sq. meter cross-sectional area by 1 cm. PPR for a rotary pile of cross-sectional area 'A' being drilled by a drilling rig at 'n' revolutions per min, running at 'T' torque and taking time 't' in minutes for 'P' penetration is given below:

$$\text{PPR} = \frac{2\pi nTt}{\text{AP}} \tag{4}$$

In case of SPT hammer; energy E spent on 'N' blows is given by $\text{PPR} = 0.747N$.

The actual pile termination level may vary and is decided during execution based on observed energy requirement of rotary piling rig for specified pile penetration ratio (PPR). Moderately (mod.) weathered rock with RQD approximately 25% has been considered for the socketing. This corresponds to 'N' value 200–400 as per Cole and Stroud chart referred from IS 2911-Part 1 sec-2 (2010). Corresponding PPR values are 150 and 300 T-m/m^2/cm.

Initially, it is proposed that the socketing zone shall start when borehole advancing distance does not exceed 100 mm for a rotary energy level (PPR) of 250 T-m/m^2 of cross section of pile for minimum three consecutive trials. However, it was difficult to get 250 T-m/m^2/cm PPR value for consecutive three trials near the design penetration level and in entire socket length. PPR generally varies significantly in the socket length. Hence, the following generic guidelines were drawn:

A. Sequence for PPR Readings:

1. Start taking PPR readings 1–1.5 times pile diameter above hard rock levels indicated in AFC (Approved for Construction) drawings. These tentatively indicated hard rock levels correspond to moderately weathered rock with RQD > 25%.
2. At depth where PPR value of 150 T-m/m^2/cm or more shall be considered as start of mod. weathered rock and thus start of rock socketting zone.
3. Drilling and regular PPR values shall be noted up to 3D (i.e., 3 times pile diameter) below start of rock socketing zone.

B. Pile termination level:

1. In case, PPR values from start of mod. weathered rock are above 150 T-m/m^2/cm and in general increasing to 250 T-m/m^2/cm or more at design pile penetration depth (3D below moderately weathered rock level), terminate the pile at depth 3D below the start of mod. weathered rock level.
2. In case, PPR values from start of mod. weathered rock to designed pile penetration depth (3D socket length) are still around 150 T-m/m^2/cm or more but did not increase up to 250 T-m/m^2/cm at design pile penetration depth (3D socket length); drill further for one-time pile diameter and terminate the pile at depth 4D below mod. weathered rock provided that PPR achieved at termination depth is above 175 T-m/m^2/cm.
3. In case, PPR values after the start of mod. weathered rock falls below 150 T-m/m^2/cm and in general varying or decreasing to 100 T-m/m^2/cm at design pile penetration depth (3D socket length), drilling may be taken further till PPR of 150 T-m/m^2/cm is achieved to ensure that the pile termination is in the rock layer considered in design to get the required end bearing resistance. i.e. Drill further for 2 times pile diameter and terminate the pile at depth 5D below mod. weathered rock level where PPR achieved is 150 T-m/m^2/cm or above.

Above are the general guidelines given to the contractor for execution which covered up almost all possible scenarios.

6 Summary and Conclusions

Although the most popular choice for foundation in marine environment is driven steel piles, installation becomes unattainable when rock is encountered at shallow depth. Marine rock-socketed pile is the feasible solution and methodology for the same is discussed.

Methodology followed for pile fixity and pile capacity calculation is discussed. Rock socket length is computed for allowable socket pressure which depends on UCS of rock layer. Rock socket length is designed as three times pile diameter below the start of mod. weathered rock level (i.e., RQD > 25%). The rock socket length is sometimes increased up to five times pile diameter in case very poor quality of rock is encountered in the entire socket length during field execution.

Based on this study, the following broad conclusions are drawn:

1. Large unsupported length of marine piles causes huge lateral loads, huge moments, and large pile head deflections.
2. Rock socket length is designed based on the required axial capacity and allowable socket pressure.
3. Virtual fixity depth of pile can be considered at middle of rock socket below highly weathered rock and pile termination level.
4. To ensure that desired rock layer is met during execution, the concept of pile penetration ratio (PPR) is very handy for field execution of piles wherein huge variation in rock levels and rock quality is encountered. The actual pile termination level may increase/decrease and is finalized during execution based on observed energy requirement of rotary piling rig for specified PPR.

References

Carter JP, Kulhawy FH (1992) Analysis of laterally loaded shafts in rock. J Geotech Eng Div ASCE 118(6):839–855

Datey KR (1990) Bored piling in Bombay region. In: Proceedings of the I.G.S. conference, Part VI, Session IX, Dec 1990, pp 571–587

Davisson MT, Robinson KE (1965) Bending and buckling of partially embedded piles. In: 6th International conference on soil mechanics and foundation engineering, vol 2, p 243

Horvath RG, Kenney TC, Kozicki P (1983) Methods for improving the performance of drilled piers in weak rock. Can Geotech J 20(1983):758–772

IS: 12070 (1995) Indian standard design and construction of shallow foundations on rocks—guidelines

IS: 14593 (1998) Indian standard design and construction of bored cast in situ piles founded in rocks—guidelines

IS: 2911 (part 1-Section 2) (2010) Code of practice for design and construction of pile foundations

Kulhawy FH, Prakoso WA, Akbas SO (2005) Evaluation of capacity of rock foundation sockets Alaska rocks. In: The 40th U.S. symposium on rock mechanics (USRMS)

Maertens L (2003) Bored sockets in weathered basalt. In: 4th international geotechnical seminar on deep foundations on bored and auger piles, Ghent

Reese LC (1997) Analysis of laterally loaded piles in weak rock. J Geotech Geoenv Eng ASCE 123(11):1010–1017
Rosenberg P, Journeaux NL (1976) Friction and end bearing tests on bedrock for high capacity socket design. Can Geotech J 13(3):324–333
Seidel J, Collingwood B (2002) The SRC method for estimating side resistance of drilled shaft. The Magazine of the Deep Foundations Institute
Singh AP, Bhandari T, Ayothiraman R, Rao SK (2017) Numerical analysis of rock-socketed piles under combined vertical-lateral loading. Proc Eng 191:776–784
Tomlinson MJ (1995) Pile design and construction practice. E & FN Spon, London

Effect of Field Bends on the Response of Buried Pipelines Crossing Strike-Slip Fault

Gautam S. Nair, Suresh R. Dash and Goutam Mondal

Abstract Buried continuous pipelines traversing through large geographical area are subjected to various seismic hazards, among which faulting is one of the most damaging. However, such hazards are usually limited to a small region near the fault crossing. Though the codes of practice, in general, suggest not to have pipe bends near fault zones, however, in reality, these are inevitable. The study on the response of buried pipelines with field bends subjected to faulting is very limited. The present study, hence, is carried out to investigate the effect of pipeline bend and its proximity to the fault line on the response parameter of the pipelines. The pipeline strain is evaluated considering field bends crossing strike-slip fault using beam on nonlinear Winkler foundation (BNWF) model. Parametric study has been conducted by varying bend angles and distance of the fault crossing from the bend. The findings indicate that there is a significant increase in compressive strain when the fault trace is crossing at/near the bends.

Keywords Buried pipelines · Field bends · Faulting

1 Introduction

Pipelines are used in different areas like natural gas transportation, sewage systems, water supply, petroleum transport and industrial sectors. With the improvement of economy and urbanization, damage to pipeline systems severely affects life and economy; hence, more extensive attention is required with regard to performance of pipeline systems during any adverse situations, like in an earthquake. During an earthquake, there are two major hazards which influence the performance of

G. S. Nair (✉) · S. R. Dash · G. Mondal
School of Infrastructure, Indian Institute of Technology Bhubaneswar, Odisha 752050, India
e-mail: gsn10@iitbbs.ac.in

S. R. Dash
e-mail: srdash@iitbbs.ac.in

G. Mondal
e-mail: gmondal@iitbbs.ac.in

R. Sundaram et al. (eds.), *Geotechnics for Transportation Infrastructure*, Lecture Notes in Civil Engineering 28, https://doi.org/10.1007/978-981-13-6701-4_29

buried segmented (brittle) as well as continuous (ductile) pipelines, such as: (a) wave propagation and (b) permanent ground deformation (PGD). In general, the wave propagation hazards associate with transient ground deformation which in turn affects the pipeline network, but with lower damage rates. However, the most damaging seismic hazard for pipelines is PGD which includes surface faulting, lateral spreading due to liquefaction and landslides. Although PGD hazards are usually limited to small regions within the pipeline network, their potential to damage is very high since they impose large deformation on pipelines. Among these different PGD hazards, fault crossing is considered to be one of the most important hazards for buried pipelines. Because the axial strains can reach up to very high levels as a result of excessive bending and axial elongation/shortening caused by fault offset. Presence of bends in the pipelines in fault zones may further increase the strain. Therefore, bends are normally avoided in fault zones. Moreover, as stated in FEMA (1992), bends are the locations that are most vulnerable to earthquake damage especially when compressive strain develops as a result of permanent ground displacement. However, it is not always possible to have only a straight segment of the pipeline crossing the fault zone, mainly owing to the unknown location of fault line (for blind faults).

The active faults in seismic areas have been proven to be one of the most dangerous geological hazards faced by the long-distance pipelines (O'Rourke and Liu 2012). Over the years, several methodologies (analytical, numerical and experimental) have been proposed to calculate the stress and strain responses of pipelines at strike-slip fault crossings (Newmark and Hall 1975; Kennedy et al. 1977; Wang and Yeh 1985; Karamitros et al. 2007; Ha et al. 2008; Abdoun et al. 2009; Trifonov and Cherniy 2010; Vazouras et al. 2010; Uckan et al. 2015; Liu et al. 2016). However, studies on buried pipeline with field bends crossing active strike-slip faults are very limited. A common assumption in majority of the previous studies on buried pipelines subjected to fault crossing is that the pipeline axis remains straight for a large distance away from the considered PGD zone. The only known exception is the analytical solution by O'Rourke and Liu (1999), which refers to the special case of pipelines with 90° elbows, under the simplifying assumptions that the arc-shaped geometry of the bend may be overlooked and that both the pipeline steel and the transverse soil resistance remain within the elastic range. Later, Yoshizaki and Oguchi (2000) described in-plane bending experiments that were conducted to evaluate the response of various kinds of low-angle pipeline elbows to earthquake-induced permanent ground displacement. A very few experimental works have been done to investigate the response of pipe with bends. One of the most notable works was done by Yoshizaki et al. (2001), where they conducted full-scale tests by applying PGD to simulate the effect of landslides on the response of pipeline with elbows (Fig. 1). The experimental results were validated with the numerical results. Available design guidelines for pipelines of fault crossing (Eurocode 8 2006; IITK-GSDMA 2007) recommend that the pipelines should be constructed without field bends, elbows and flanges that tend to anchor the pipeline to the ground.

From the aforementioned literature review, it has been observed that the response of pipelines with field bends subjected to faulting has got limited attention from the

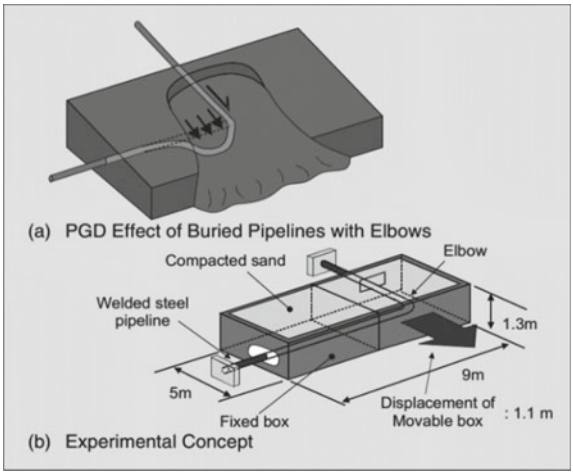

Fig. 1 Experimental concept for PGD effects on buried pipelines with elbows (adapted from Yoshizaki et al. 2001)

researchers. However, the situation may become critical and pipeline may fail at the location of bends due to stress concentration. Hence, the present study focuses on evaluating the response of buried pipelines with field bends crossing active faults. The pipeline strain is evaluated using BNWF model considering different cases of the pipeline with different bend angles and variation of distance of fault line from the bend part of the pipeline.

2 Modelling Pipeline—Soil Interaction

A schematic representation of the numerical model developed in this study is shown in Fig. 2. A continuous pipeline is modelled as beam elements supported on soil springs using SAP2000 v16 (2014) finite element software. Both ends of the pipeline are assigned with fixed supports as shown in Fig. 2. The length of the pipeline is considered to be long enough such that the boundary effect is not prominent. Therefore, based on mesh convergence study, the length of the pipeline is considered as 400 m in the zone of application of displacement loads, a minimal curved length as per the bend angle considered and a straight segment of pipeline of 100 m beyond the bend part. The pipe is considered as steel pipe with external diameter of 0.610 m and a wall thickness of 25.4 mm. The grade of steel for the pipe is considered as API X70 having a modulus of elasticity of 200 GPa.

The soil around the pipeline is considered as loose sandy backfill with an angle of internal friction (ϕ) of 30° and effective unit weight (γ) of 17 kN/m^3. The soil is modelled as nonlinear spring elements. The spring properties used in the model is

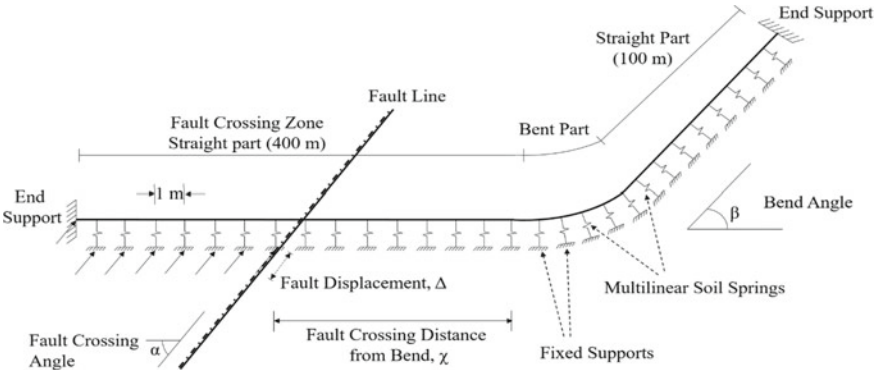

Fig. 2 Schematic representation of the numerical model

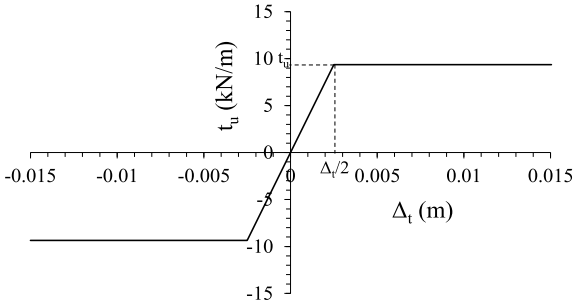

Fig. 3 Bilinear axial soil spring representing 1 m of soil as per ALA (2001)

Table 1 Axial and lateral soil spring properties

Soil spring parameters	Value
Axial spring:	
Maximum axial soil resistance per unit length of the pipe, t_u (kN/m)	9.4
Mobilizing displacement in axial direction, Δ_t (m)	0.005
Lateral spring:	
Maximum transverse soil resistance per unit length of the pipe, P_u (kN/m)	66.0
Mobilizing displacement in lateral direction, Δ_u (m)	0.052

calculated based on ALA guidelines (ALA 2001). Both axial and lateral soil springs are modelled. Based on mesh convergence study, the spacing between the soil springs is kept as 1 m. This is to make the model more efficient in terms of computational requirement. Typical axial and lateral soil springs representing 1 m soil are shown in Figs. 3 and 4, respectively. Table 1 gives the axial and lateral soil spring properties used in the model. The burial depth considered for the present study is 1 m (~1.6 times the pipe diameter).

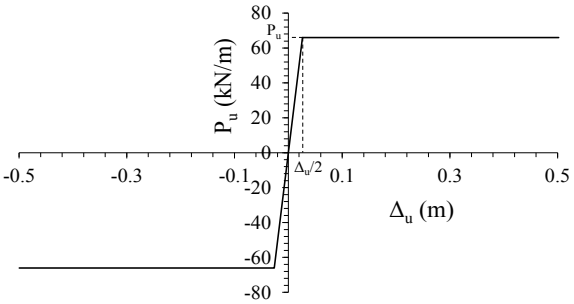

Fig. 4 Bilinear lateral soil spring representing 1 m of soil as per ALA (2001)

Table 2 Pipeline and faulting parameters used in the model

Parameter	Value
Pipe diameter, D (m)	0.610
Pipe thickness, t (mm)	25.4
Burial depth, H (m)	1
Effective unit weight of soil, γ (kN/m^3)	17
Angle of internal friction, ϕ (°)	30
Fault displacement, Δ (m)	2
Fault crossing angle, α (°)	90
Pipe bend angle, β (°)	0, 30, 45, 60, 90, 120, 135
Fault crossing distance, χ (m)	0, 5, 10,15, 20, 25, 50, 75, 100, 125, 150, 200

This study is limited to strike-slip fault where the fault crossing angle (α) is 90°. The parameters used in this study to investigate the response of buried pipeline with field bends subjected to strike-slip fault are the bend angle (β) and the fault crossing distance (χ) as summarized in Table 2. The magnitude of fault displacement is increased gradually to reach 2 m and the response of the pipeline is monitored. The displacement is applied to the fixed nodes of the soil spring elements. A nonlinear static analysis with P-Δ effect has been carried out in this model by incorporating material nonlinearity associated with soil as represented through nonlinear backbone curves.

3 Results and Discussion

The response of buried pipelines with field bends subjected to strike-slip faulting has been presented here. The variation of maximum bending moment, maximum shear force and maximum axial force with respect to distance of the fault line from the bend for different bend angles has been shown in Figs. 5, 6, and 7, respectively. When the

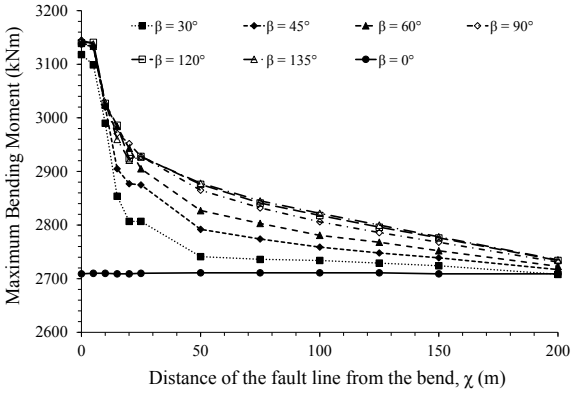

Fig. 5 Variation of maximum bending moment with fault crossing distance with respect to different bend angles

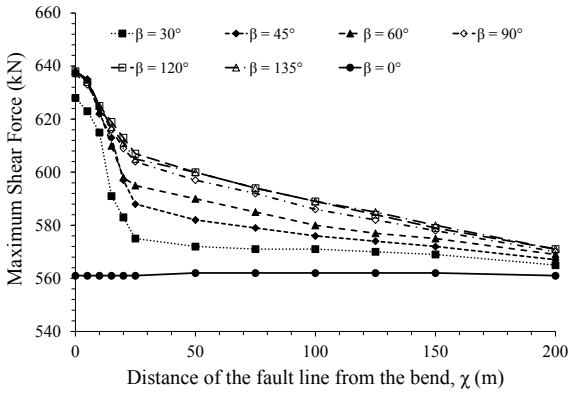

Fig. 6 Variation of maximum shear force with fault crossing distance with respect to different bend angles

fault trace is crossing at the bend, it was observed that maximum bending moment and maximum shear force in the pipeline increase by about 16% and 14%, respectively, irrespective of bend angle, when compared with that for a straight pipeline ($\beta = 0°$). It was also observed that there is a decrease of 91% in the maximum axial force in the pipeline with bends when compared with that for a straight pipeline. In other words, use of bends near the fault crossing play a vital role in the response of pipeline. Moreover, it can also be inferred from the figures that with the increase in distance between the fault trace and the bend, the response of pipeline with bends comes in close agreement with that of a straight pipeline.

Figures 8 and 9 show the variation of tensile and compressive strains with respect to distance of the fault line from the bend for different bend angles, respectively. When the fault trace is crossing close to the bend, compressive strain is higher than

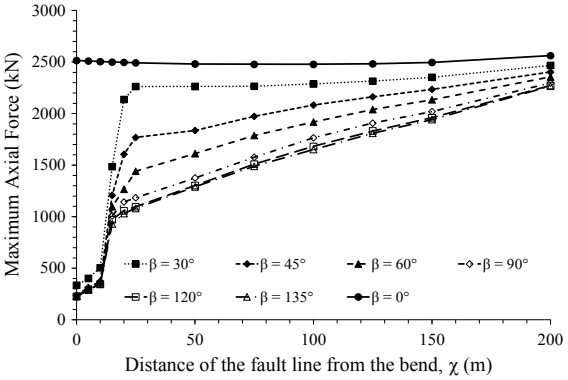

Fig. 7 Variation of maximum axial force with fault crossing distance with respect to different bend angles

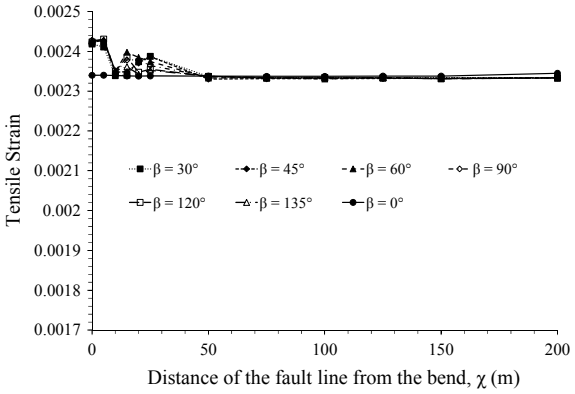

Fig. 8 Variation of tensile strain with fault crossing distance with respect to different bend angles

tensile strain in the pipeline for different bend angles. Moreover, when the pipe bend is at a considerable distance away from the fault trace (~120*D*), there is no much influence of bend angle on the response of pipeline significantly.

4 Conclusion

The present study focused on understanding the response of buried pipelines with field bends subjected to fault crossing. Influence of parameters such as bend angle and fault crossing distance on the response of the pipeline has been examined. It was observed that maximum bending moment and maximum shear force increase with increase in bend angle whereas maximum axial force decreases with increase in bend

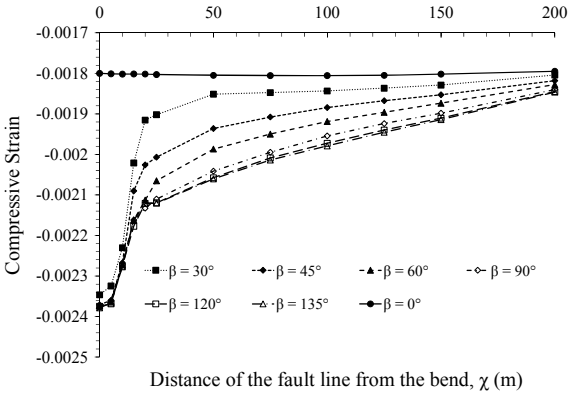

Fig. 9 Variation of compressive strain with fault crossing distance with respect to different bend angles

angle when the fault trace is crossing at/near the bend. Also, it was found that bends near to the fault trace is highly undesirable since it induces high compressive strain in the pipeline. Therefore, presence of bends near to the fault trace can severely affect the structural integrity of pipeline leading to rupture/failure. It was also observed that there is no significant influence of bend angle on the response of pipeline when the distance between the fault trace and bend is greater than or equal to 120*D* for the case considered. The present study is limited only to strike-slip faulting with 90° fault crossing angle. Hence, in view of the importance of various parameters on pipeline response, more studies are required to understand the influence of different soil and pipe parameters on the response of pipeline subjected to different types of faulting.

Acknowledgements The first author would like to thank Ministry of Human Resources Department (MHRD), Government of India for providing financial assistance during the research work. The authors would like to thank Mr. Deepak Kumar of School of Infrastructure, Indian Institute of Technology Bhubaneswar for his help and support during the parametric study.

References

Abdoun TH, Ha D, O'Rourke MJ, Symans MD, O'Rourke TD, Palmer MC, Stewart HE (2009) Factors influencing the behavior of buried pipelines subjected to earthquake faulting. Soil Dyn Earthq Eng 29(3):415–427

ALA (2001) Guidelines for design of buried steel pipes, A report by public-private partnership between American Society of Civil Engineers (ASCE) and Federal Emergency Management Agency (FEMA), American Lifelines Alliance (ALA), USA, p 83

Eurocode 8 EN 1998-4 (2006) Design of Structures for earthquake resistance—part 4: silos, tanks and pipelines. European Committee for Standardization, Belgium, p 83

FEMA (1992) Earthquake resistant construction of gas and liquid fuel pipeline systems serving or Regulated by the Federal Government, earthquake hazard reduction series 67, Federal Emergency Management Agency, USA, p 77

Ha D, Abdoun TH, O'Rourke MJ, Symans MD, O'Rourke TD, Palmer MC, Stewart HE (2008) Centrifuge modelling of earthquake effects on buried high density polyethylene (HDPE) pipelines crossing fault zones. J. Geotech Geoenv Eng. ASCE 134(10):1501–1515

IITK-GSDMA (2007)Guidelines for seismic design of buried pipelines. In: Dash SR, Jain SK (eds) Prepared by Indian Institute of Technology Kanpur (IITK) and Gujarat State Disaster Management Authority (GSDMA). National Information Center of Earthquake Engineering (NICEE), India, p 105

Karamitros DK, Bouckovalas GD, Kouretzis GP (2007) Stress analysis of buried steel pipelines at strike-slip fault crossings. Soil Dyn Earthq Eng 27(3):200–211

Kennedy RP, Chow AW, William RA (1977) Fault movement effects on buried oil pipeline. J Transp Eng ASCE 103(1):617–633

Liu X, Zhang H, Li M, Xia M, Zheng W, Wu K, Han Y (2016) Effects of steel properties on the local buckling response of high strength pipelines subjected to reverse faulting. J Nat Gas Sci Eng. 33(1):378–387

Newmark NM, Hall WJ (1975) Pipeline design to resist large fault displacement. In: Proceedings of U.S. national conference on earthquake engineering, USA, pp 416–425

O'Rourke MJ, Liu X (1999) Response of buried pipelines subject to earthquake effects, Monograph No. 3. In: Multidisciplinary center for earthquake engineering research (MCEER), University at Buffalo, New York, USA, p 276

O'Rourke MJ, Liu X (2012) Seismic design of buried and offshore pipelines, monograph series, MCEER-12-MN-04, Multidisciplinary Center for Earthquake Engineering Research (MCEER), University at Buffalo, New York, USA, pp 297–309

SAP2000 v16 (2014) Finite element analysis and design of structures, computers and structures, Inc. USA

Trifonov OV, Cherniy VP (2010) A semi-analytical approach to a nonlinear stress-strain analysis of buried steel pipelines crossing active faults. Soil Dyn Earthq Eng 30(11):1298–1308

Uckan E, Akbas B, Shen J, Rou W, Paolacci F, O'Rourke M (2015) A simplified analysis model for determining the seismic response of buried steel pipes at strike-slip fault crossings. Soil Dyn Earthq Eng 75(1):55–65

Vazouras P, Karamanos SA, Dakoulas P (2010) Finite element analysis of buried steel pipelines under strike-slip fault displacements. Soil Dyn Earthq Eng 30(11):1361–1376

Wang LRL, Yeh YH (1985) A refined seismic analysis and design of buried pipeline for fault movement. Earthq Eng Struct Dyn 13(1):75–96

Yoshizaki K, O'Rourke TD, Bond T, Mason J, Hamada M (2001) Large scale experiments of permanent ground deformation effects on steel pipelines. Research Progress and Accomplishments, MCEER, USA, pp 21–28

Yoshizaki K, Oguchi N (2000) Large deformation behavior of low-angle pipeline elbows subjected to in-plane bending. In: Proceedings of the 12th world conference on earthquake engineering (12WCEE), New Zealand, pp 1–8

Response of Pile Foundation in Alternate Liquefying and Non-liquefying Layers in Spreading Ground

Praveen M. Huded and Suresh R. Dash

Abstract Pile foundations are often preferred in high seismic zones; however, even having high factor of safety against bending strength many historic evidences showed that pile foundations are vulnerable during earthquakes, especially when liquefaction occurs. Major code specification treats pile as beam element subjected to lateral loading, and no definitive provisions are available on analysis method for pile foundation embedded in alternate liquefiable and non-liquefiable soil. The present study is conducted to model layered liquefiable soils for pile foundation response considering state-of-the-art understating along with available code recommendations. Both force-based and displacement-based approaches for typical layered soil profile were chosen in this study. The soil liquefaction depth of the middle layer was varied to understand the behavior during successive stages of liquefaction. The pile-soil interaction was modeled through *p-y* lateral springs, and suitable reduction was made for the *p-y* springs which represent liquefaction by various methods available in literature. The static nonlinear analysis was carried out for various models, and the response such as bending moment, shear force, and displacement have been studied. A great variability was seen among the results of pile response for any typical layered soil profile, when different analysis approaches have been adopted.

Keywords Pile foundation · Liquefaction · Lateral spreading · *p-y* curve

1 Introduction

Many pile founded structures subjected to earthquake loads and have shown damages in past earthquake (San Francisco 1906: Kanto 1923; Fukui 1948; Alaska 1964; Niigata 1964; Nihonkai-Chubu 1983; Bhuj 2001). Investigations have reported one of

P. M. Huded (✉) · S. R. Dash
School of Infrastructure, Indian Institute of Technology Bhubaneswar, Bhubaneswar, Odisha 752050, India
e-mail: ph01@iitbbs.ac.in

S. R. Dash
e-mail: srdash@iitbbs.ac.in

R. Sundaram et al. (eds.), *Geotechnics for Transportation Infrastructure*, Lecture Notes in Civil Engineering 28, https://doi.org/10.1007/978-981-13-6701-4_30

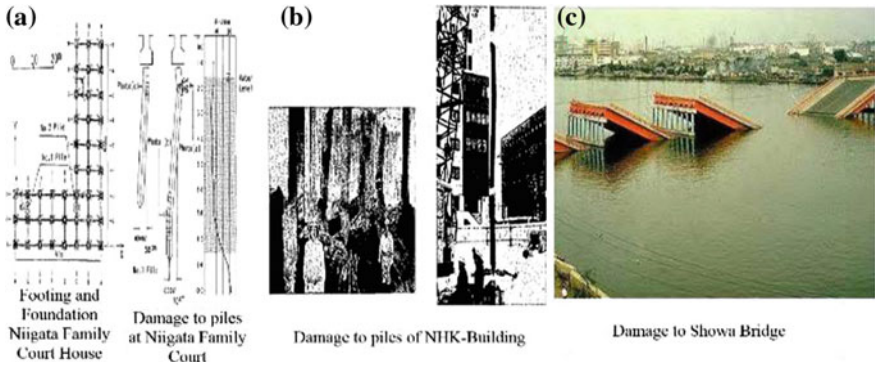

Fig. 1 Damage to Building and Showa Bridge during Niigata earthquake (Hamada and O'Rourke 1992)

the causes of major damages as liquefaction (Kramer 1996), including liquefaction on level ground and/or lateral spreading (Boulanger et al. 2003; Hamada and O'Rourke 1992). In liquefiable deposits, the soil behavior often decides the response of pile foundation. Increase in excessive pore pressure in liquefiable soil reduces strength and stiffness of the soil. If reduced soil strength is less than the static shear stress then the soil may move laterally in a sloping ground and result in high lateral pressure on pile or on foundation which may lead to failure (Finn and Fujita 2002).

With large unsupported length and lateral pressure from flowing soil, pile foundation is subjected to higher bending moment and significant *p*-delta effect leading to its failure by forming plastic hinges.

Figure 1 shows some of the damaged structures due to liquefaction caused by the 1964 Niigata earthquake. Niigata Family court house (Fig. 1a) suffered differential settlement and was inclined about one degree, but with minor repairs the building was used 25 years after earthquake. During reconstruction work after 25 years, excavation revealed that piles were failed with plastic hinges during the 1964 Niigata earthquake. Further analyses have shown that the lateral movement of the liquefied soil was the cause for the failure (Hamada and O'Rourke 1992). It infers that bending moment and shear force exceeded those predicted by design methods. O'Rourke et al. (1994) proposed three failure mechanisms of pile foundations in liquefiable soils as bending, buckling, and lateral soil flow. However, recently Bhattacharya et al. (2005)and Dash et al. (2009) have analyzed some of these cases where the pile foundations have failed despite having high factor of safety against bending and suggested that another probable cause of failure of pile foundations in liquefiable soils can be bending-buckling interaction.

The phenomenon of lateral spreading of soil and its effects on pile foundation is still under development through laboratory test, field tests, and numerical analysis. Analysis of pile foundations for earthquake loads requires the consideration of inertial loads due to soil-pile-super structure interaction and also needs the evaluation of kinematic interactions due to the movement of the surrounding soil and the pile.

National Research Council (1985) reported that lateral spreading is responsible for most of the damages during earthquake than any other form of liquefaction-induced ground failure, the mechanism was adopted later by Japanese Code of Practice (1996, revised 2002). First empirical model to estimate lateral earth pressure due to spreading was presented (Hamada et al. 1986) using field data of Niigata earthquake (1964). Tokimatsu and Asaka (1998) explained that inertia force from super structure may dominate before the development of pore pressure, and at the end of earthquake vibrations, kinematic force from liquefaction dominates the pile behavior. A series of centrifuge experiments conducted by Abdoun (1997) on two-layer soil system concluded that non-liquefied soil layer exerts passive pressure on pile foundation. Dobry and Abdoun (1998) proposed the application of inverted triangular pressure distribution to calculate the maximum bending due to lateral spreading.

Berrill et al. (2001) have shown that the flow of non-liquefied crust layer causes more damage than that of the flow of liquefied soil alone. To quantify the lateral spreading, Zhang et al. (2004) proposed the use of standard penetration test (SPT) and cone penetration test in addition to experimental data to assess the soil displacement in free field. A simplified method using reduction factor for initial modulus of subgrade reaction was given by Cubrinovski and Ishihara (2004) for liquefied soil. However, the literature is still scarce in terms of experimental and numerical study on the seismic response of pile foundation if founded on layered liquefiable soils.

The present study is thus aimed to understand the current practices of estimating the response of pile foundation for soil profiles with alternating liquefiable and non-liquefiable soils. Analysis includes *force-based* and *displacement-based* approaches. Response of pile foundation such as bending moment, shear force, and displacement is studied critically in this paper.

2 Current Understanding of Pile Failure in Layered Liquefiable Soils

Some of the code provisions for designing pile foundations in layered liquefiable soils are presented below.

The Japanese highway code of practice (JRA 2002) gave a model as shown in Fig. 2, based on damaged analysis of bridge in Hyogo-ken Nanbu earthquake. The liquefaction-induced ground flow force acting upon the foundations located inside the liquefying layer is taken as 30% of the total overburden pressure.

Eurocode (EN 1998-1:2004) suggests that structure shall be designed for no local and global collapse, for an earthquake event of 10% in 50 years with return period of 475 years. According to Sect. 5.4.2, side resistance of soil layers should be ignored, if the soil is susceptible to liquefaction or strength reduction. Additional load due to lateral spreading should be considered. Piles should remain elastic but plastic hinges may be allowed to develop at pile heads under certain situations.

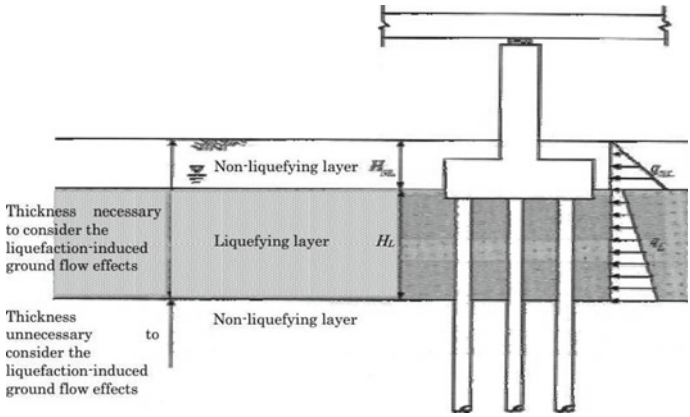

Fig. 2 Model for calculating lateral movement force (JRA 2002)

ASCE 7-10 does not provide any specific guidance for the design of pile foundation in layered liquefiable soils. As per clause 12.13.6.3 "*Piling shall be designed and constructed to withstand deformations from earthquake ground motions and structure response. Deformations shall include both free-field soil strains (without the structure) and deformations induced by lateral pile resistance to structure seismic forces, all as modified by soil–pile interaction*" implies that both inertia and kinematic loads should be considered for designing the pile foundation.

Similarly, NEHRP code (2000) and IS-1893 (2000) also emphasize on strengthening pile against bending. In summary, pile is treated as beam element subjected to lateral load causing bending failure.

Although most of the codes of practice only recognize bending failure as mechanism which will govern the pile design and suggest designers to design for higher bending strength, many recent studies have shown that the buckling (Bhattacharya and Bolton 2004) or bending-buckling interaction (Dash et al. 2009) could also be a possible failure mechanisms, which shall be considered during design. To consider buckling in the design, the *p*-delta effect due to axial load on pile in the lateral spreading analysis must not be neglected.

Hence, a parametric study has been carried out in this paper to estimate the response of pile foundation founded in alternating liquefiable soil layers according to various available models as per code provisions or literature, including *p*-delta effect.

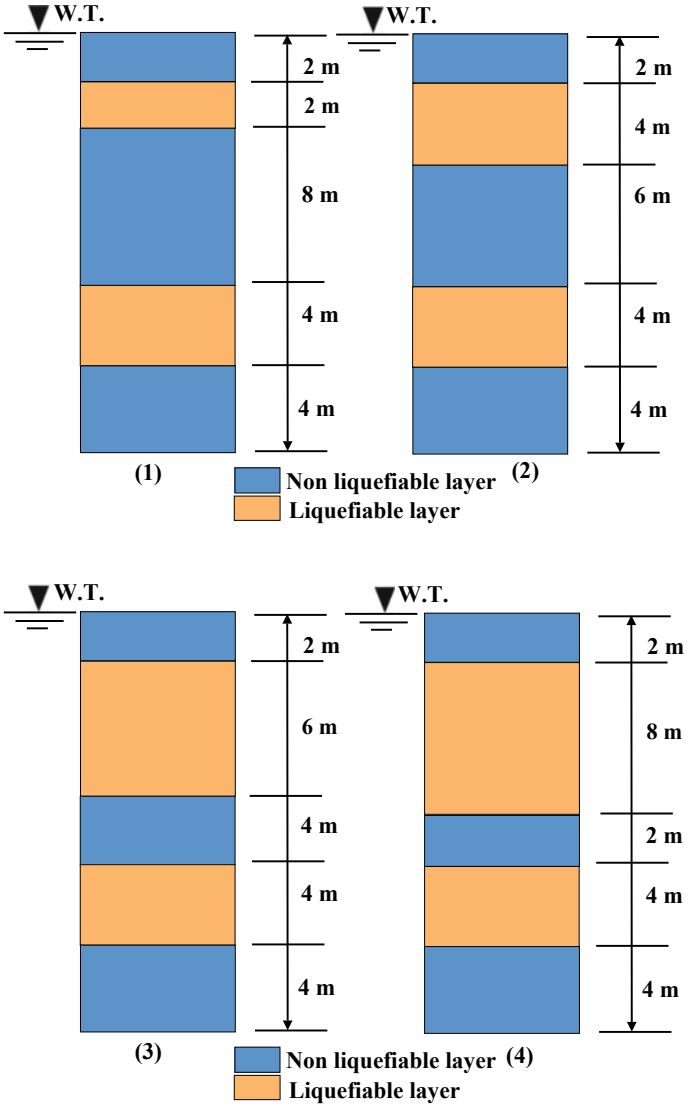

Fig. 3 Soil profile with alternate liquefiable and non-liquefiable soil

3 Numerical Study of a Typical Pile Foundation in Layered Liquefiable Deposit

A typical soil profile with alternate liquefiable and non-liquefiable soil is considered in this study as shown in Fig. 3. Table 1 shows the details of pile and soil properties used.

Table 1 Details of pile and soil properties

Soil	C_u	$(N_1)_{60}$	γ	$\varphi°$
Non-liquefied layer at top	12	6	16	–
Non-liquefied layer at middle	48	8	16	–
Non-liquefied layer at bottom	100	10	17	–
Liquefied soil	–	15	16	33

Pile dia (mm): 1000
Pile material: Concrete

The concrete pile of 18 m long is modeled as a Beam on a Nonlinear Winkler Foundation (BNWF) using the finite element program SAP2000 (2014). Nonlinear behaviour of concrete pile was assigned to the model in the form of lumped plastic hinges (P-M-M and Moment Rotation types). The pile passes through alternate layers of liquefiable and non-liquefiable soils of different combinations as given in Fig. 3. The pile was fixed at the bottom and was subjected to the combination of axial and lateral loads. The lateral loads are basically the representation of the soil pressure from lateral spreading modeled as a force-based approach. The lateral soil pile interaction was modeled as closely spaced soil springs, normally called *p-y* springs. The depth of soil liquefaction of second layer from top was increased by 2 m till full liquefaction of 8 m, so there were four soil profiles for which analyses were performed. The length of pile in the liquefiable soil zone increased from 2 m to 8 m, and the underlying dense clay layer (4 m thick) provided end fixity to the pile foundation. The pile was assumed to be a bearing pile resting on a hard rock layer. API guidelines (2000) were used to calculate the nonlinear soil spring properties for non-liquefied sandy soil and clayey soil. A typical nonlinear lateral soil spring for non-liquefying soil is plotted in Fig. 4. For liquefied soil, the soil springs are estimated by two methods (a) *p*-multiplier and (b) hyper-elastic model. In *p*-multiplier method, the *p-y* spring properties of the liquefied soil are modeled as the *p-y* spring of its non-liquefied state as per API (2000) with 90% reduction. In case of hyper-elastic model, the *p-y* spring properties were calculated according to the procedure suggested by Dash et al. (2017) for upper bound and lower bound values of lateral pressure.

A nonlinear static analysis with *P*-delta effect was carried out in SAP (CSI 2004). The lateral spreading was modeled in two major ways, (a) force-based approach and (b) displacement-based approach, which are detailed below.

3.1 Force-Based Approach

In this approach, the loading from soil flow on pile foundation was estimated from maximum soil strength and applied to the pile as lateral force. Two models (Fig. 5) were analyzed in the present study, namely JRA model and Madabhushi model for the pile foundation in soil profile 4. The JRA model was prepared based on guidelines given in JRA (2002), which suggest that liquefied soil layer applies 30%

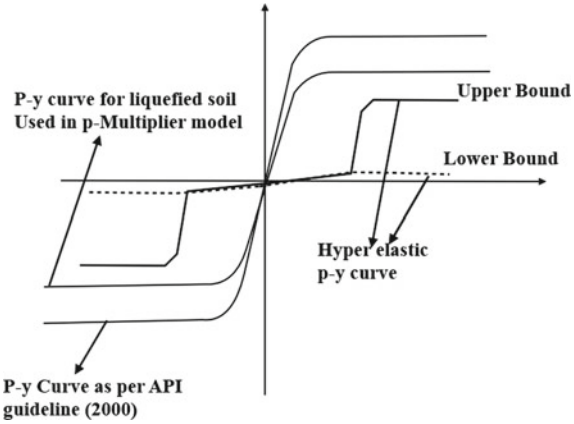

Fig. 4 Nonlinear lateral soil spring (*p-y* spring) used in the BNWF model

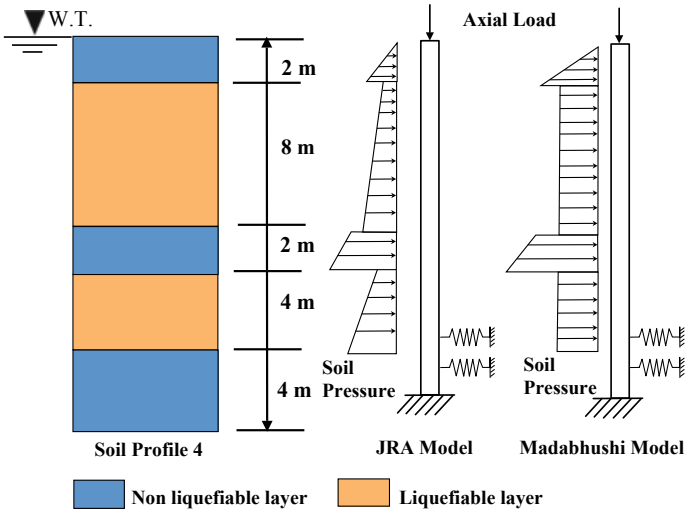

Fig. 5 Pile subjected to lateral force from soil flow (JRA 2002)

of overburden pressure on pile. Whereas Madabhushi et al. (2010) recommended the value of constant pressure of 30 kPa that the liquefied soil can apply during its flow. For these two models, the pile responses including its yielding pattern and allowable deflection were monitored.

3.2 Displacement-Based Approach

In this approach, the lateral flow of liquefied soil is modeled as finite displacements applied at the free ends of the *p*-*y* springs as inverted triangular patter with displacement of 0.5 m at top and 0 m at the bottom of liquefied soil. Three models were prepared for displacement-based approach for the same scenario as used in force-based approach, namely (a) Eurocode model (Fig. 6a), (b) *p*-multiplier model (Fig. 6a), and (c) hyper-elastic model (Fig. 6b). In Eurocode model, the soil springs were removed for the liquefied layer, but the non-liquefied layers were having *p*-*y* curves as per API (2000). For *p*-multiplier and hyper-elastic models, the non-liquefied layer springs remained same, but the springs in liquefied layers have been modified as described earlier.

Force-based approach is simple but displacement-based approach is more representative of the actual behavior of laterally spreading soil. From different force-based approach and displacement-based approach models, pile response for a typical field condition had been analyzed and comparison of the results has been made as follows.

4 Evaluation of Pile Response for a Typical Soil Profile

The considered pile foundation in force-based approach was yielding at small percentage of lateral pressure in both JRA and Madabhushi models. Table 2 represent the percentage of lateral loads at which pile has developed full plastic hinge and in the verge of getting into instability zone. The effect of passive pressure from non-liquefiable soil layer was significant in JRA and Madabhushi models. The plot of bending moment for soil profile 4 is shown in Fig. 7. The present pile foundation is observed to undergo yielding before even subjected to full load as estimated. Although the pattern of bending moment is similar for both the models, the pile was found to collapse completely by forming plastic hinges at bottom for different percentage of loading as given in Table 2 for various soil profiles. There also lies significant variation in the prediction of pile response from these two methods.

Table 2 Percentage load at which pile entered nonlinear zone

Model type	Soil profile 1 (%)	Soil profile 2 (%)	Soil profile 3 (%)	Soil profile 4 (%)
JRA model	30	32	42	66
Madabhushi model	26	29	35	49

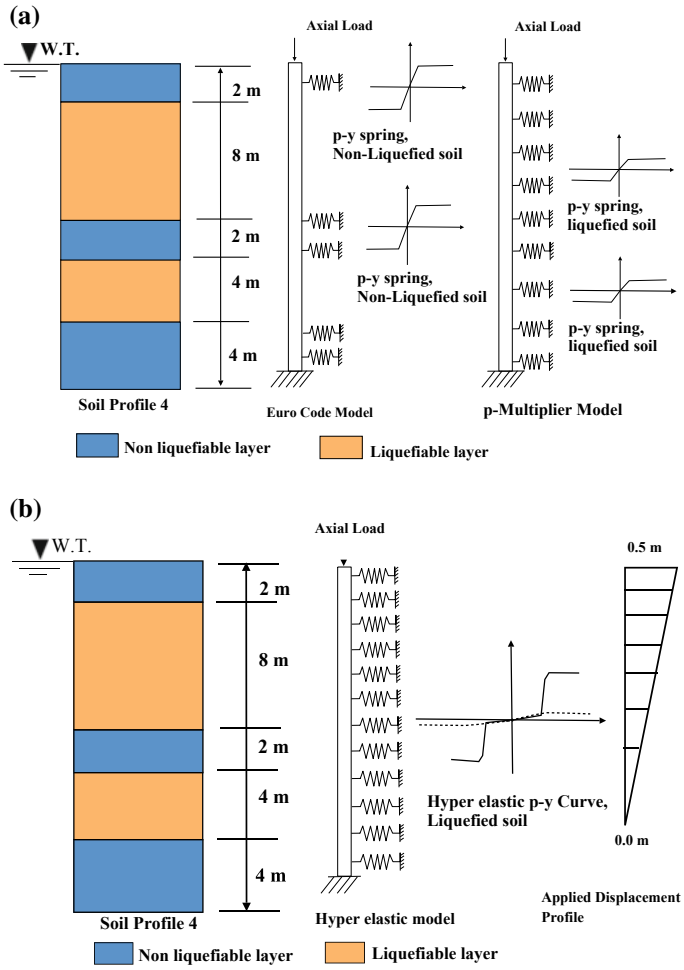

Fig. 6 **a** and **b** Pile subjected to lateral displacement from soil flow

In case of displacement-based model, bending moment variation was approximately same for soil profile 1 and 2. However, in case of soil profile 3, upper bound hyper-elastic model gives lesser value of bending moment than all other models, and it is interesting to note that all the other models are giving values in between hyper-elastic upper bound model and lower bound model (Fig. 8). In case of soil profile 3, hyper-elastic model with higher limit was giving 60% less displacement than hyper-elastic lower limit model (Fig. 9). In soil profile 4, Eurocode model was giving 72% lesser bending moment than hyper-elastic model with higher limit at a depth of 10.5 m (Fig. 10). Displacement predicted by Eurocode method was 67% less than that predicted by upper bound hyper-elastic model (Fig. 11). The maximum bending moment variation with respect to different soil profile is shown in

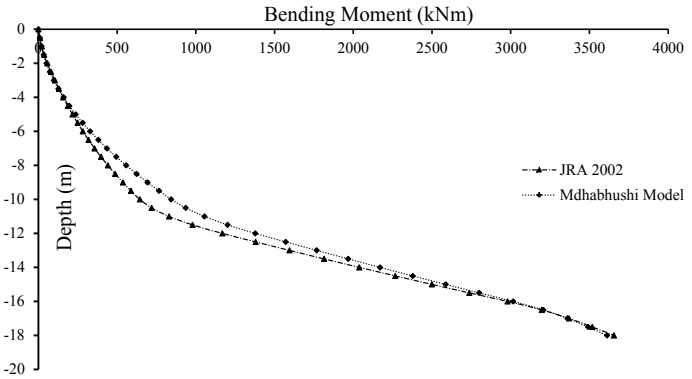

Fig. 7 Variation of bending moment with depth for soil profile 4 (JRA loading 66%, Madabhushi model loading 49%)

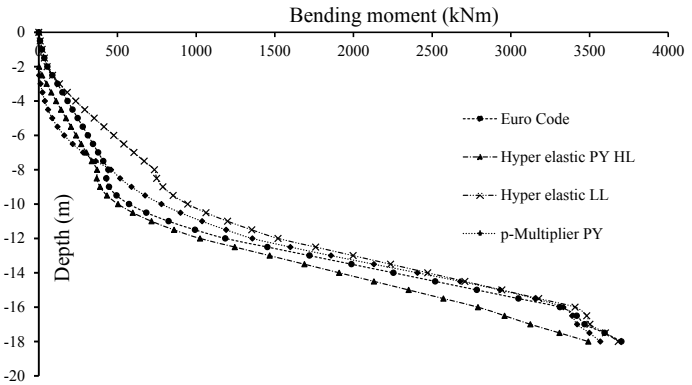

Fig. 8 Variation of bending moment with depth for soil profile 3

Fig. 12. It has been observed that when the depth of non-liquefying layer is higher and sandwiched by liquefying layers at top and bottom, the bending moment tends to be higher as compared to the case where the depth of non-liquefying layer is less. It can be clearly seen that a great variability lies in the evaluation of pile response for a same liquefiable soil profile if different analysis approaches are being adopted. For instance, in soil profile 1, the variation of bending moment is about 28%, whereas for soil profile 4, the variation is about 0.3%.

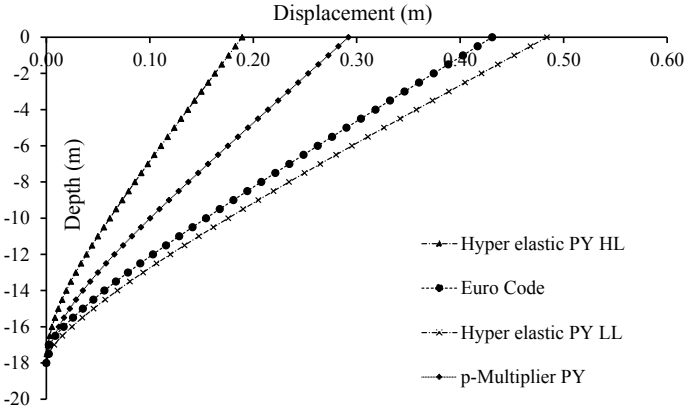

Fig. 9 Variation of displacement with depth for soil profile 3

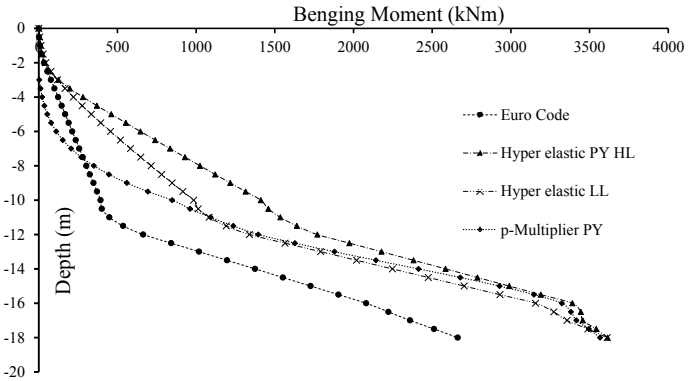

Fig. 10 Variation of bending moment with depth for soil profile 4

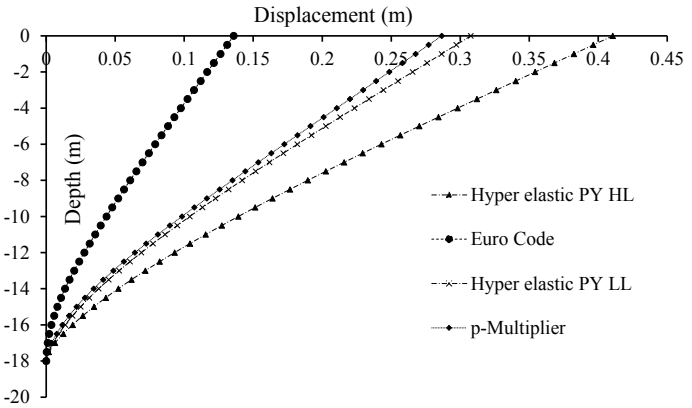

Fig. 11 Variation of displacement with depth for soil profile 4

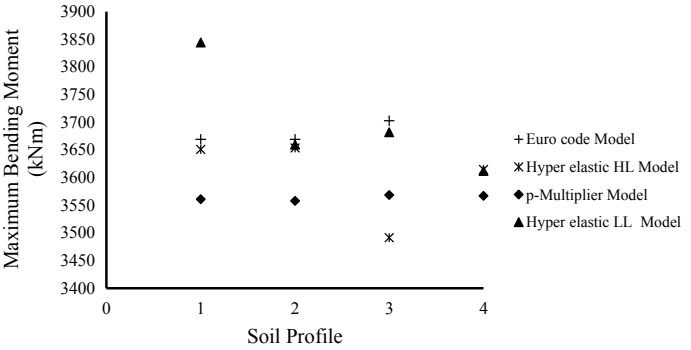

Fig. 12 Variation of maximum bending moment for different soil profile for 0.5 m lateral spreading value at top

5 Conclusion

The present study is focused on the evaluation of pile response in layered liquefiable soils, using force-based approach and displacement-based approach. In the force-based approach, the pile foundation considered in this study has developed plastic hinges even before the application of full load. It was found that the force-based approach was too conservative in comparison with displacement-based approach. For any typical soil profile, much variation in bending moment and displacement was observed between different approaches of analyses. Also, this variability increases with increase in depth of non-liquefying layer sandwiched between liquefying layers at top and bottom, because of the increased lateral earth pressure due to the flow of the non-liquefied soil layer.

Acknowledgements The first author would like to thank Ministry of Human Resources Department (MHRD), Government of India for providing financial assistance during the research work.

References

Abdoun TH (1997) Modelling of seismically induced lateral spreading of multilayered soil and its effect on pile foundations. Ph.D. Thesis, Rensselaer Polytechnic

API (2000) 2A (WSD), Recommended practice for planning, designing, and constructing fixed offshore platforms-working stress design. Version 21st

Berrill JB, Christensen SA, Keenan RP, Okada W, Pettinga JR (2001) Case studies of lateral spreading forces on a piled foundation. Geotechnique 51(6):501–517

Bhattacharya S, Bolton M (2004) Buckling of pile during earthquake liquefaction. In: 13th World Conference on Earthquake Engineering, Vancouver, B.C., Canada, 1–6 Aug

Bhattacharya S, Bolton MD, Madabhushi SPG (2005) A reconsideration of the safety of the piled bridge foundations in liquefiable soils. Soils Found 45(4):13–26

Boulanger RW, Kutter BL, Brandenberg SJ, Singh P, Chang D (2003) Pile foundations in liquefied and laterally spreading ground during earthquakes: centrifuge experiments and analyses. Center for Geotechnical Modeling, University of California, Davis, USA. Report No. UCD/CGM-03/01

CSI (2004) Sap 2000: V11.0—integrated software for structural analysis and design. Computer and Structures Inc (CSI), Berkeley, California, USA

Cubrinovski M, Ishihara K (2004) Simplified method for analysis of piles undergoing lateral spreading in liquefied soils. Soil Found 44(5):119–133

Dobry R, Abdoun T (1998) Post-triggering response of liquefied sand in the free field and near foundations. In: Proceedings of 3rd ASCE speciality conference on geotechnical engineering and soil dynamics, Seattle, WA, pp 270–300

Eurocode (1998) Design provisions for earthquake resistance of structures- foundations, retaining structures and geotechnical aspects. European Committee for Standardization, Brussels

Finn WDL, Fujita N (2002) Piles in liquefiable soils: seismic analysis and design issues. Soil Dyn Earthq Eng 22(9–12):731–742

Madabhushi G, Jonathan K, Stuart H (2010) Design of pile foundation in liquefiable soils. Imperial College Press

Hamada M, O'Rourke (1992) Case studies of liquefaction and lifeline performance during past earthquakes, vol 1, Japanese case studies, Technical report NCEER-92–0001

Hamada M, Yasuda S, Isoyama R, Emoto K (1986) Study on liquefaction induced permanent ground displacement. Report for the association for the development of earthquake prediction

IS-1893 (2000) Part-1: criteria for earthquake resistant design of structures. Bureau of Indian Standard (New Delhi)

JRA (2002) Specification for highway bridges, part v-seismic design

Kramer SL (1996) Geotechnical earthquake engineering. Prentice- Hall Inc, Upper Saddle River, USA

National Research Council (1985) Liquefaction of Soils during earthquakes. Report No. CETS-EE-001, Committee on Earthquake Engineering, NationalAcademy Press, Washington, D.C

NEHRP (2000) NEHRP recommended provisions for seismic regulations for new buildings and other structures. In: Rep. Nos. FEMA 368 (Provisions) and 369 FEMA (Commentary). Council, B.S.S

O'Rourke TD, Meyersohn WD, Shiba Y, Chaudhuri D (1994) Evaluation of pile response to liquefaction-induced lateral spread. In: O'Rourke TD, Hamada M (eds) Proceedings from the 5th US-Japan Workshop on earthquake resistant design of lifeline facilities and countermeasures against soil liquefaction, Technical report NCEER 94–0026. National Centre for Earthquake Engineering Research, State University of New York at Buffalo, pp 457–479

Dash S, Mehdi R, Domenico L, Subhamoy B (2009) Bending–buckling interaction as a failure mechanism of piles in liquefiable soils. Soil Dyn Earthq Eng 30:32–39

Dash S, Mehdi R, Domenico L, Subhamoy B (2017) A practical method for construction of p-y curves for liquefiable soils. Soil Dyn Earthq Eng 97:478–481

Tokimatsu K, Asaka Y (1998) Effects of liquefaction-induced ground displacements on pile performance in the 1995 Hyogeken-Nambu earthquake. Soil Found 163–177

Zhang G, Robertson PK, Brachman RWI (2004) Estimating liquefaction-induced lateral displacements using the standard penetration test or cone penetration test. J Geotech Geoenviron Eng ASCE 130(8):861–871

Part IV
Slope Stability, Landslides, Debris Flows, and Avalanches on Hilly Roads and Remedial Measures

Applicability Evaluation of Slope Disaster Risk Assessment Method in Snowy Cold Regions

Tatsuya Ishikawa, Srikrishnan Siva Subramanian and Tetsuya Tokoro

Abstract Climate change-induced large-scale natural hazards are problematic for confrontation. Many of the snowy cold regions of Japan, i.e. Hokkaido, experience multifaceted types of natural disasters, i.e. slope failures and debris flows due to abnormal weather and rainfall patterns which were never encountered in the past. In consideration of the change of extreme weather patterns in future, this study has attempted to develop a wide-area disaster risk assessment at first with introducing an early warning criterion for snowy cold regions and then by proposing and analysing the applicability of a wide-area slope failure analysis method. To this end, we have performed early warning and wide-area numerical modelling studies for various cases of soil slope failures in Hokkaido which shows new paths for the disaster mitigation.

Keywords Slope failures · Snowy cold regions · Wide-area disaster risk assessment · Climate change

1 Introduction

In snowy cold regions such as Hokkaido, Japan, many sediment-related disasters, which are thought to cause freezing of soil ground, frost heave phenomenon or infiltration of snowmelt water into soil ground, occur at soil slopes during thawing period (Ishikawa et al. 2015). For example, the main cause of the serious slope failure at the Nakayama Pass along the National Highway No. 230 (Fig. 1) occurred in April 2013 was that snowmelt has progressed rapidly due to heavy rain in the snowmelting

T. Ishikawa (✉) · S. Siva Subramanian
Faculty of Engineering, Hokkaido University, Sapporo, Japan
e-mail: t-ishika@eng.hokudai.ac.jp

S. Siva Subramanian
e-mail: srikrishnan@frontier.hokudai.ac.jp

T. Tokoro
Department of Engineering for Innovation, National Institute of Technology, Tomakomai College, Tomakomai, Japan
e-mail: t-tokoro@tomakomai-ct.ac.jp

R. Sundaram et al. (eds.), *Geotechnics for Transportation Infrastructure*, Lecture Notes in Civil Engineering 28, https://doi.org/10.1007/978-981-13-6701-4_31

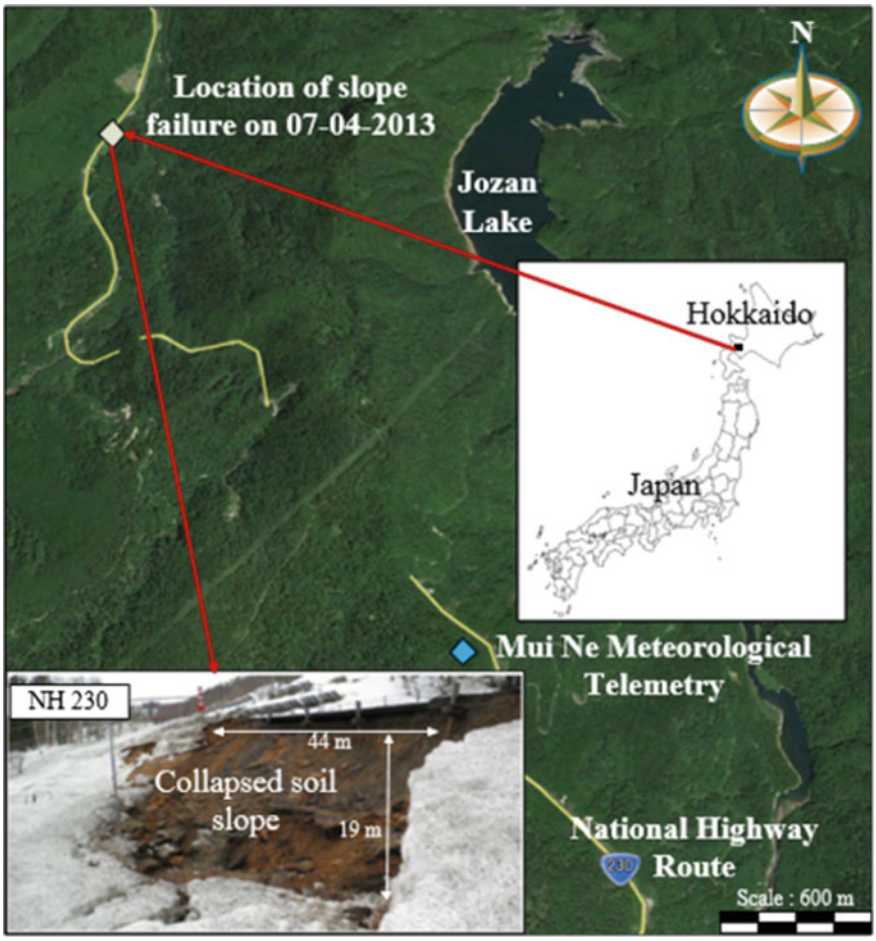

Fig. 1 Slope failure at the Nakayama Pass along the National Highway No. 230

season and a large amount of snowmelt water infiltrated into the embankment along with rainwater. According to the result of the data analysis recorded in a nearby meteorological telemetry (Fig. 1), the amount of day-equivalent rainfall obtained by adding snowmelt water to rainfall for a day was ranked higher in the past 10 years. Therefore, it is important to evaluate the slope stability by taking the change of the water content in the slope accompanying the freezing/frost heave-thawing of the ground and the infiltration of snowmelt water into consideration, when discussing the geotechnical disaster prevention in snowy cold regions.

On the other hand, slope disasters caused by weather conditions that have not so far been experienced are increasing due to climate change in Hokkaido recently. For example, a heavy rainfall due to the proximity of the front and the typhoon No. 10, in which the cumulative rainfall amount was ranked first in the observation history,

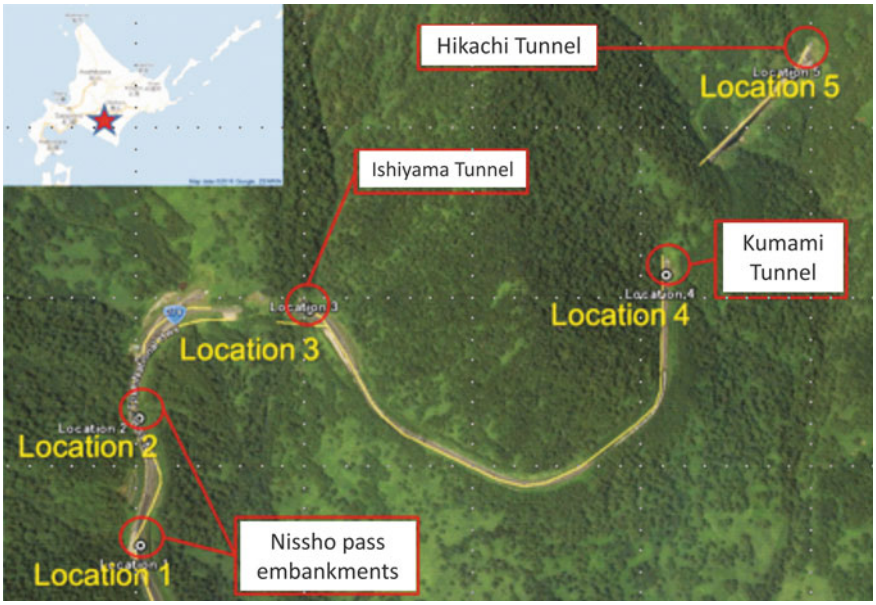

Fig. 2 2016 typhoon-induced slope failures in Hokkaido

caused many large slope failures at the Nissho Pass (Tokachi side) along the National Highway No. 274 (Fig. 2) on 29 to 31 August 2016 (Japanese Geotechnical Society 2017). One of the main causes for these serious slope failures is a large amount of surface runoff water that was not able to permeate into the ground because of a very high water content induced by the preceding three typhoons No. 7, 9 and 11, which were attacked before the typhoon No. 10. At present, in order to predict the occurrence of such slope failures, macro-indexes such as Soil Water Index are currently widely used in Japan as a criterion which simply assesses a wide-area disaster risk. However, in case of the external forces such as heavy rainfall in a summer and sudden rise in the ground temperature in a spring beyond past observation data due to extreme weather and climate change, it is impossible to predict and evaluate various complex geotechnical disaster risks, which are caused by multiple factors such as wetting and drying process and freeze-thawing by using a risk assessment approach based on past geotechnical disaster records.

The objective of this research is developing a risk assessment method of slope failure disasters in snowy cold regions, which are likely to happen in future due to the progression of climate change, in terms of soil mechanics for freeze-thawed soil ground in unsaturated conditions. In case there are no observation data, the areas of future potential disasters are identified based on the rainfall history of sediment-related disasters that occurred in the past (Gariano et al. 2017). However, in Chap. 2, through assuming cases where it is difficult to set the threshold value for early warnings of rainfall-/snowmelt-induced soil slope failures, we developed a disaster risk

assessment method for snowy cold regions using a numerical analysis approach. The numerical analysis approach considers non-isothermal coupled seepage analysis and pseudo-coupled mechanical analysis. Using the numerical analysis, parametric studies are performed under various magnitudes of rainfall and snowmelt water assuming actual ground conditions. Based on the results of the numerical analysis, the practicality of the early warning criterion is verified. In Chap. 3, to develop a wide-area risk assessment method for heavy rainfall-induced slope failures, a prediction method to integrate wide-area runoff analysis into local-area slope stability analysis is proposed. Through the detailed factor analysis for cases of typhoon-induced slope disasters in Hokkaido, the applicability of the approach handled in this study to couple the wide-area hydrological analysis with the explicit geotechnical analysis is examined. Overall, this study has shown ways to construct a disaster risk assessment method for future climate change-induced soil slope failures and brought a very good understanding of the failure characteristics of heavy rainfall-induced soil slope failures in snowy cold regions.

2 Prediction of Slope Failure Using Macro-index in Cold Regions

2.1 Macro-index Used in Japan

An early warning criterion (macro-index) to predict soil slope failures in cold regions should consider the influencing factors like freeze-thaw action and snowmelt water infiltration because of the complex nature of frozen–unfrozen soils (Okimura and Ichikawa 1985). In Japan, the Japanese Meteorological Agency (JMA) (Japan Meteorological Agency 2012) uses the Soil Water Index for the prediction of rainfall-induced slope failures. Distinctly, slope failures in seasonally cold regions like Hokkaido are influenced by many other factors than the rainfall alone. Owing to these reasons, a method to predict the soil slope failures in cold regions is developed in this study.

The prediction of rainfall-induced slope failures in Japan is performed using the relationship between 60-min cumulative rainfall and Soil Water Index (SWI) (Osanai et al. 2010) by JMA. Okada (2001) proposed the method of SWI as shown in Fig. 3. The Soil Water Index is a conceptual model of the availability of moisture of the surface soil calculated using a value of the total water depth of a three-layer tank model. The storage of the tanks is estimated using the coefficients of the model as shown in Fig. 3, and it is referred from Okada (2001). The runoff, outflow water and storage amount calculations are also shown in Fig. 3.

The concept of the current early warning system presently practised in Japan is shown in Fig. 4.

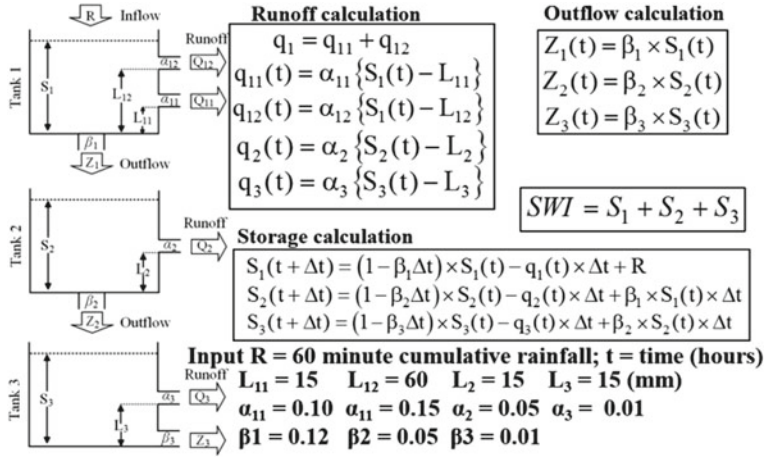

Fig. 3 Method to calculate the Soil Water Index. Adapted from Osanai et al. (2010)

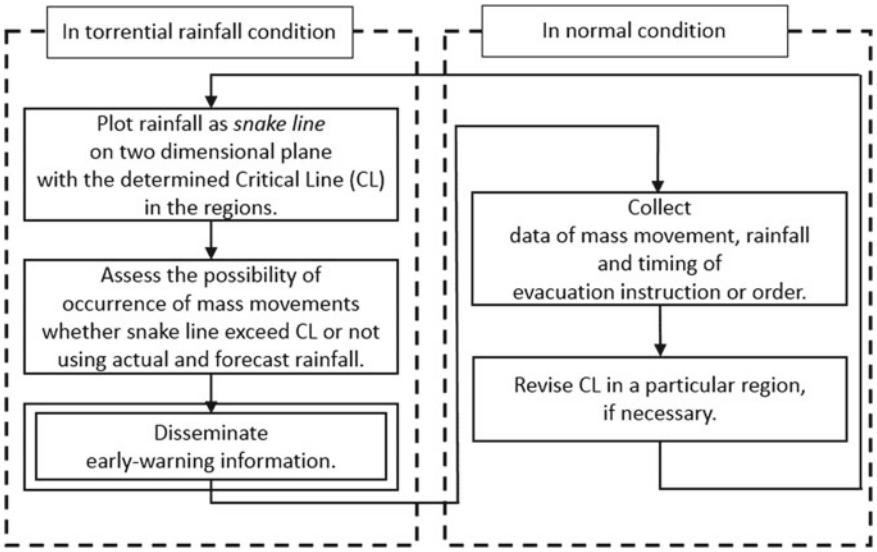

Fig. 4 Basic concept of the currently operating Japanese early warning. Adapted from Osanai et al. (2010)

Okada (2001) performed a statistical analysis to determine the fixed parameters of the SWI. The inflow for the model includes the hourly rainfall amount of the target period.

$$S_1(t + \Delta t) = (1 - \beta_1 \Delta t) \times S_1(t) - q_1(t) \times \Delta t + R \tag{1}$$

$$\mathrm{SWI} = S_1 + S_2 + S_3 \tag{2}$$

Figure 3 shows the calculations of S_2, S_3 and other parameters. The outflow coefficients of the tank are noted using the symbols $\alpha_1, \alpha_2, \alpha_3$ and α_4; L_1, L_2, L_3 and L_4 are noted as the heights of the outflow holes of the tanks; the penetration volumes of the tanks are β_1, β_2 and β_3; the cumulative hourly rainfall is R, t is present time, and Δt is increased time step, and in this case, it is a 60-min rainfall. A threshold line is used for the SWI by JMA for every 5 km by 5-km grid all over Japan for the early warning of debris flows and slope failures. Each 5 km by 5-km area is given a CL based on the occurrences and non-occurrences of sediment disasters corresponding to a value of 60-min rainfall and Soil Water Index (Osanai et al. 2010).

For the soil slope failure occurred on April 2013 along National Highway Route 230, the SWI is calculated and shown in Fig. 5. Critical line (CL) designated for the slope failure region Minami Ward of Sapporo district is obtained from Hokkaido Regional Development Bureau. As the CL is determined only based on the occurrence of disasters induced by rainfall, it could not consider the long-term snowmelt water infiltration and cannot be used to predict the snowmelt-induced slope failures as shown in Fig. 5.

In Fig. 5, the CL is never reached because the ultimate value of hourly rainfall alone is not enough and the moisture contributed by the snowmelt should also be considered. This is because in cases of slope failures induced by rainfall (i.e. heavy rain and typhoon) a maximum amount of hourly rainfall would be about 50–60 mm/h, whereas observation of the climate data of Hokkaido for the last decade emphasizes that such high hourly rainfall never happened during snowmelt season. In consideration of these facts, it is very clear that incorporation of snowmelt water and a new CL for SWI are necessary. Figure 6 shows the 60-min cumulative rainfall and Soil Water Index (SWI) relationships for the climate data collected from Nissho Pass Telemetry. The total duration of the calculation is set as 01-04-2016 to 31 August 31 2016, to visualize the occasions when the CL is exceeded and to validate it against the actual slope failure data.

For the case of sediment disasters induced by the typhoon during August 2016 in Hokkaido, the occurrences are predicted and the snake lines exceed the CL for location Nissho Pass. The threshold level is deemed applicable to predict such a large amount of rainfall disasters in Hokkaido. Through this observation, it is very clear that the 60-min cumulative rainfall and Soil Water Index relationships are precisely applicable to the prediction of large-scale sediment disasters induced by heavy rainfall. At the same time, the SWI may not predict the slope failures induced

by the snowmelt water and the existing CL designated for Sapporo Minami-Ku region is not applicable and needs to be revised.

2.2 Method to Estimate Hourly Snowmelt Water

Importance of the estimation of the hourly rate of snowmelt water for early warnings is well known, and many energy balance methods are introduced in practice for this purpose (Berris and Harr 1987; Kondo and Yamazaki 1990 and Motoyama 1990). In this study, an empirical estimation method of the snowmelt water is introduced considering most of the physical processes governing the melting process of snow (Riley et al. 1969). Air temperature, snow surface temperature, melt factor and other key influencing climatic factors are considered. Climate data obtained from the Automatic Meteorological Data Acquisition System (AMeDAS) and from some meteorological telemetries is used for the estimations. The equation of the method is given below

$$\mathrm{SM} = 0.4 \times \mathrm{SD} \times \mathrm{RI} \times (T_a - T_{st}) \times (1 - \mathrm{Al}) + \left[(T_a - T_{st}) \times \frac{P}{144} \right] \quad (3)$$

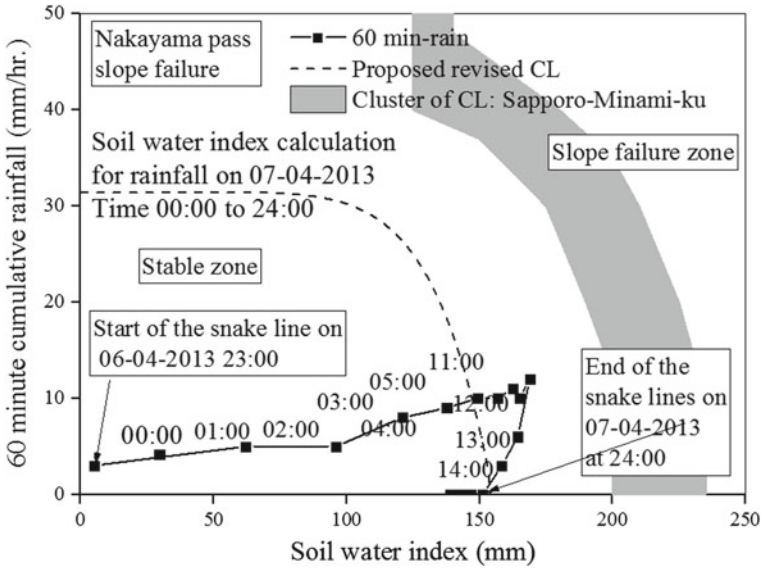

Fig. 5 Early warning of slope failure on April 2013 along Nakayama Pass, National Highway Route 230

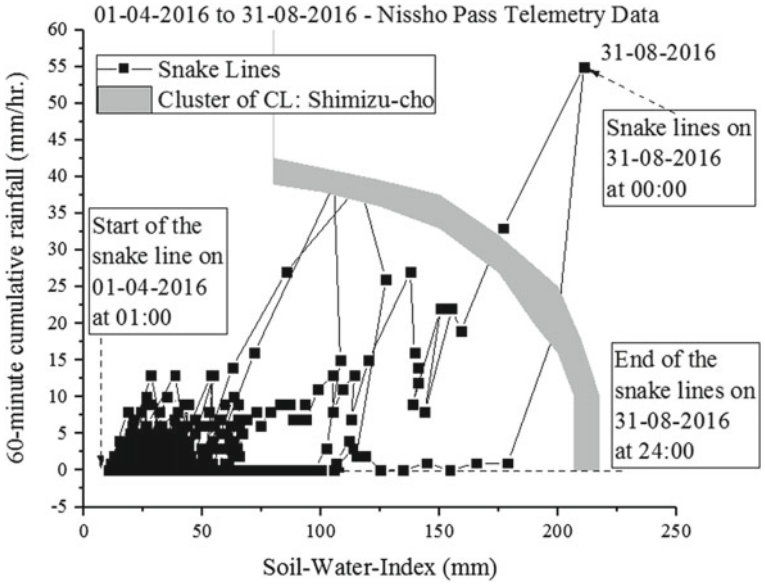

Fig. 6 Early warning of slope failure on April 2013 along Nakayama Pass, National Highway Route 230

where SM is hourly snowmelt water per increment in air temperature (mm/h °C), T_a is air temperature (°C), T_{st} is snow freezing temperature (°C), SD is hourly amount of decrease in depth of snow cover (mm/h), RI is radiation index (%), Al is albedo (%) and P is precipitation (mm/h).

2.3 Parametric Studies to Produce Conceptual Slope Failures Using Numerical Modelling

To propose a new CL for snowmelt-induced soil slope failures in Hokkaido, in this study, a series of parametric studies are performed. Through the parametric studies, many numbers of soil slope failures are produced under a set of assumed predefined analytical conditions using numerical modelling. Numerical simulations were performed based on a recommended slope stability assessment approach validated explicitly by Siva Subramanian et al. (2017). The analytical slope model used for the parametric studies is a two-dimensional plane strain model assuming a full-scale embankment slope shown in Fig. 7. As the boundary conditions, the horizontal and vertical sides of the analytical model were fixed, the climate boundary was applied on the slope surface, the adiabatic boundary and a non-drainage boundary were applied on the sides, and then an isothermal boundary and a nondrainage boundary were applied at the base, respectively.

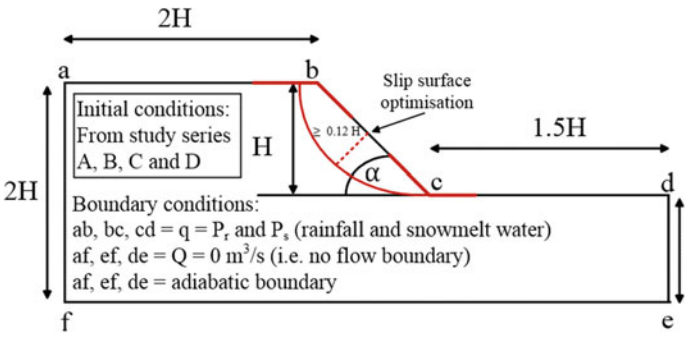

Fig. 7 Two-dimensional FEM analysis model and boundary conditions

Table 1 Analytical conditions used in parametric studies

Slope heights *H* (m)	Slope angle *α* (°)	Initial water content distribution	Rainfall *P* (mm/h), Time *T*	Snowmelt rates *P* (mm/h)
5	30	2013.02.16 A. Freezing	(a) 10 *T*: 24 h	(i) 0
10	35	2013.04.07 B. Thawing	(b) 30 *T*: 6 h	(ii) 0–4
15	40	2013.05.27 C. Post thaw	(c) 30 *T*: 6 h	(iii) 0–15
20	45	2013.10.16 D. Prefreeze	(d) 30 *T*: 6 h	
			(e) 30 *T*: 6 h	

In this case, the shape and dimensions of the analytical model were varied between the slope height H and the slope inclination angle α in four ways (Table 1).

Nine hundred and sixty numbers of numerical simulations were performed, and out of those 512 numbers of slope failures and 448 numbers of stable scenarios were obtained. For the revision and proposal of early warning criterion, these slope failures and stable scenarios are used as discussed in the following section.

2.4 Revisions for the CL of Macro-index SWI Using Results of Numerical Parametric Studies

The revisions for the CL of the macro-index SWI are studied by introducing the amount of hourly snowmelt water in addition to the hourly rainfall in the calculation of storage of tank 1 (S1) and then determining/revising the threshold—critical line

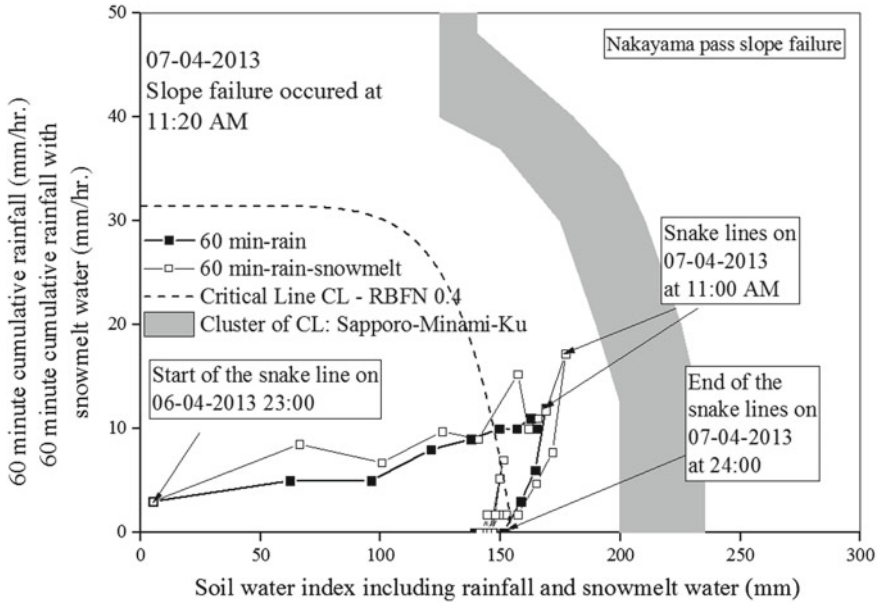

Fig. 8 Early warning of slope failure occurred on April 2013 along Nakayama Pass, National Highway Route 230, with consideration of snowmelt water in SWI

(CL). In the calculation of SWI, the snowmelt water is considered as an input as shown in Eq. 4.

$$S_1(t + \Delta t) = (1 - \beta_1 \Delta t) \times S_1(t) - q_1(t) \times \Delta t + P \tag{4}$$

P is the cumulative hourly precipitation including rainfall and snowmelt water (mm/h). The revised SWI and the storage of the tank 1, S_1, include the contribution of moisture supplied by snowmelt water. The SWI is then applied to the slope failure occurred on April 2013 along National Highway Route 230 as shown in Fig. 8.

It is clearly seen that even after incorporation of the snowmelt water in the storage calculation, the SWI does not predict the slope failure. Since the SWI fails to predict the slope failures due to a higher threshold value (CL), a revision for the CL is necessary. Figure 8 also shows a dotted line conceptually considered as the revised CL for this particular slope failure. Anyhow, the revisions of the CL should be done by utilizing the slope failure scenarios observed from the conceptual numerical slope failure cases. From those simulations performed as explained in Sect. 2.4, the failure, as well as stable scenarios, is classified based on the factor of safety (FOS) value. The FOS values lower than 1 are considered as slope failures.

For the case of initial water content during thawing season with 45° slope angle, 5-m slope height, 10-mm/hr. rainfall for 24 h and 0, 0–4, 0–15-mm/h snowmelt water, the stability of the slope is shown in Fig. 9.

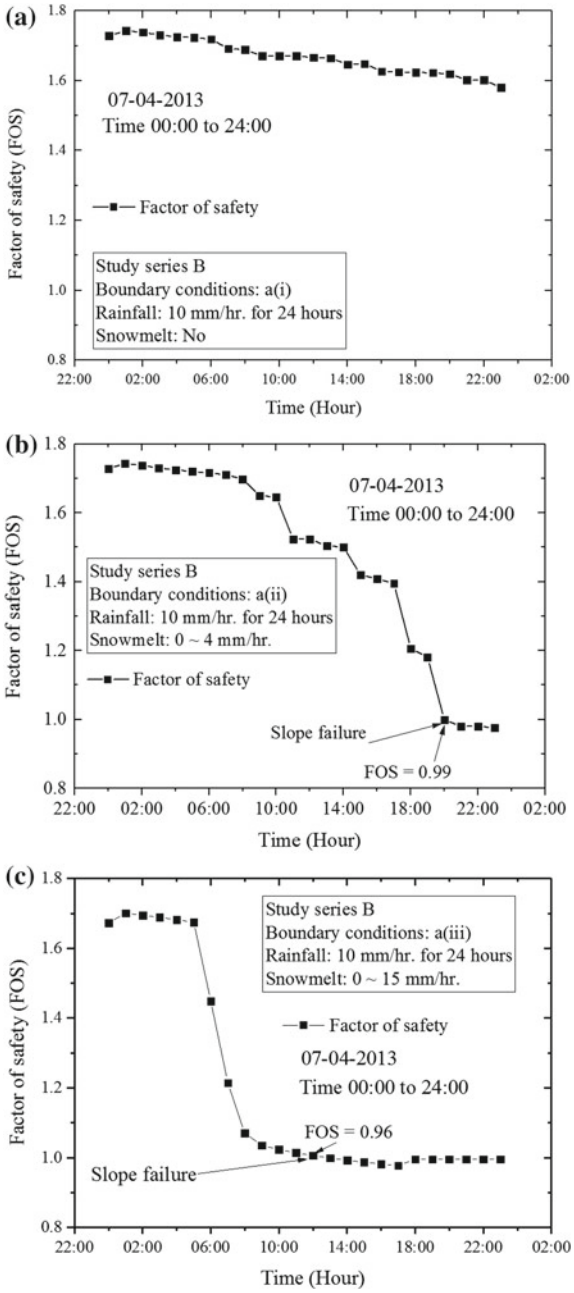

Fig. 9 Stability of slope for series B with 45° slope angle, 5-m slope height, 10-mm/h rainfall and snowmelt

For the same study series B with initial water content during thawing season with 45° slope angle, 5-m slope height, 10-mm/h rainfall for 24 h and 0, 0–4, 0–15-mm/h snowmelt, the calculated SWI is shown in Fig. 10.

Figure 9 shows two slope failure cases with snowmelt rates 0–4 and 0–15 mm/h, whereas in Fig. 10 the SWI CL is never reached. Though there are slope failures indicated by the FOS values in Fig. 9, there is no early warning made in Fig. 10. It could be said that the CL designated for the location Sapporo Minami-Ku is not applicable to predict the slope failures occurred during snowmelt season. Similar plots have been made with higher rainfall intensities with the same amount of snowmelt water. For the case of initial water content during thawing season with 45° slope angle, 5-m slope height, 30-mm/h rainfall for 24 h and 0, 0–4, 0–15-mm/h snowmelt water, the stability of the slope is shown in Fig. 11.

In the case of 30-mm/h rainfall, a slope failure could be seen even without the influence of snowmelt water. All three cases in Fig. 11 show FOS value less than 1 and slope failure occurred due to very high amount of rainfall. For the same study series B with initial water content during thawing season with 45° slope angle, 5-m slope height, 30-mm/h rainfall for 24 h and 0, 0–4, 0–15-mm/h snowmelt, the calculated SWI is shown in Fig. 12. In Fig. 12, the slope failure is predicted for the case of 30-mm/h rainfall for 24 h with 0–15-mm/h snowmelt water, whereas for the other two cases with 0-mm/h snowmelt water and 0–4-mm/h snowmelt water, the CL still stays above the snake lines and there is no early warning made.

The CL for a particular region can be revised with reference to the guidelines given in the basic concept of the currently operating Japanese early warning system (Osanai et al. 2010). As many researchers have found that the CL designated for many regions of Hokkaido is not an appropriate snowmelt season, in this study the revisions are studied. The critical line designated for location Sapporo Minami-Ku is revised based on the slope failure data using the conceptually derived Radial Basis Finite Network (RBFN) lines as shown in Fig. 13. The RBFN is a cluster of slope failure as well as stable data through which JMA and local governments delineate the CL. At JMA, the RBFN lines are derived from years and years of occurrences and non-occurrences of slope failures within the preferred area. Of those RBFN lines, the one which can precisely delineate the margin between the failure and the stable scenarios is selected as a CL. A similar rule is followed in this study as well.

For all the 448 numbers of slope failures from series B and C and 64 numbers of slope failures from series D, the corresponding SWI is plotted in a two-dimensional plane along with many CLs as shown in Fig. 14a, b respectively. The failures are identified by checking the FOS is lesser than 1 or not.

The designated CL does not predict the failures and stable scenarios clearly in Fig. 14a. A CL line can be delineated between the occurrence and the non-occurrences of failures with a minimum of 30-mm 60-min cumulative rainfall and 150-mm SWI. This CL is found to be appropriate for the prediction of snowmelt-induced soil slope failures.

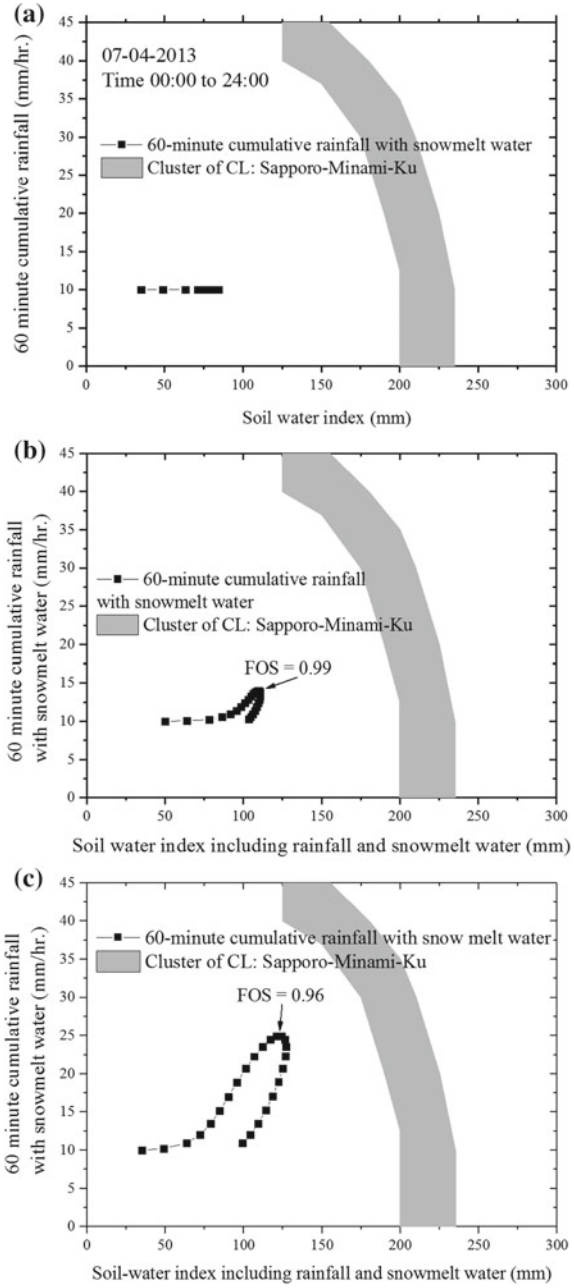

Fig. 10 Calculated SWI for series B with 45° slope angle, 5-m slope height, 10-mm/hr. rainfall and snowmelt water. **a** 0 mm/h, **b** 0–4 mm/h and **c** 0–15 mm/h

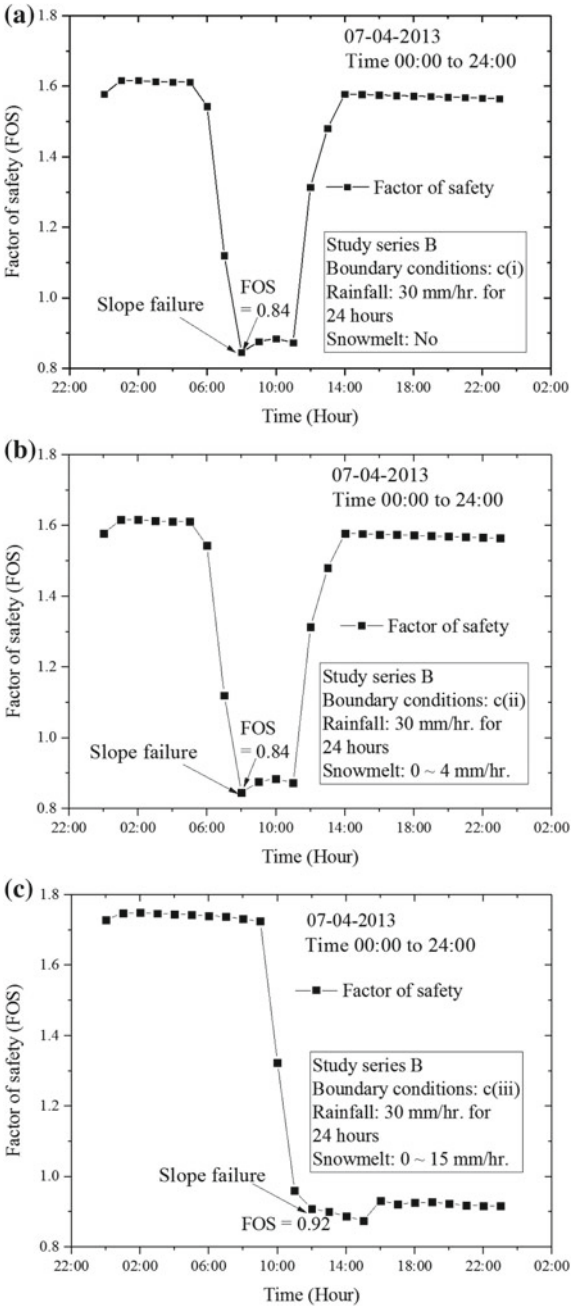

Fig. 11 Stability of slope for series B with 45° slope angle, 5-m slope height, 30-mm/h rainfall and snowmelt

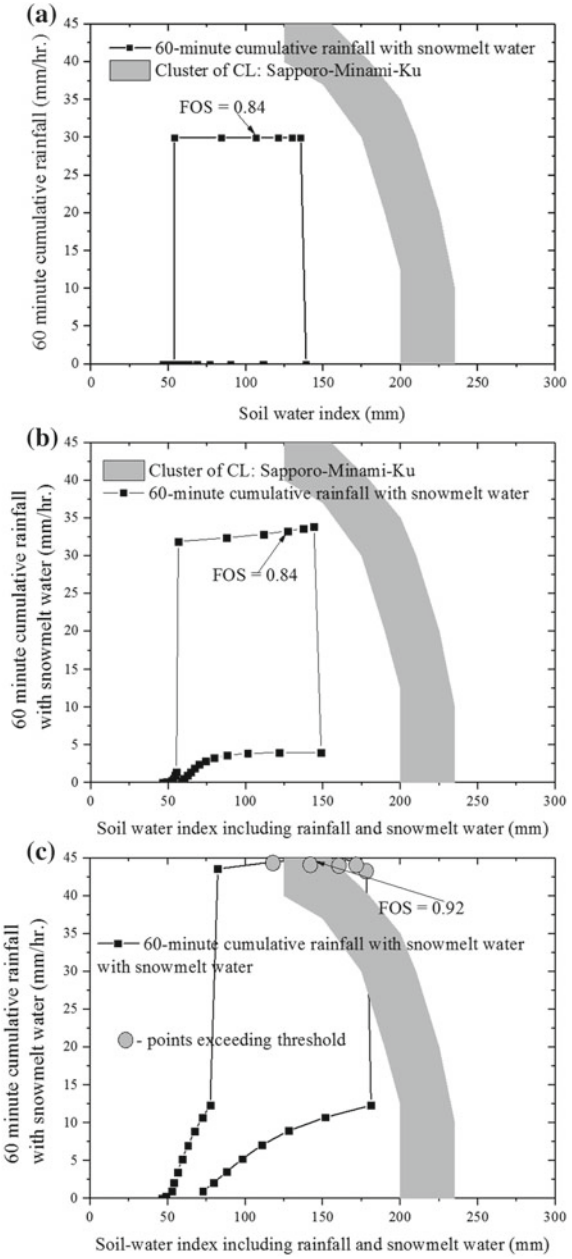

Fig. 12 Calculated SWI for series B with 45° slope angle, 5-m slope height, 30-mm/h rainfall and snowmelt water. **a** 0 mm/h, **b** 0–4 mm/h and **c** 0–15 mm/h

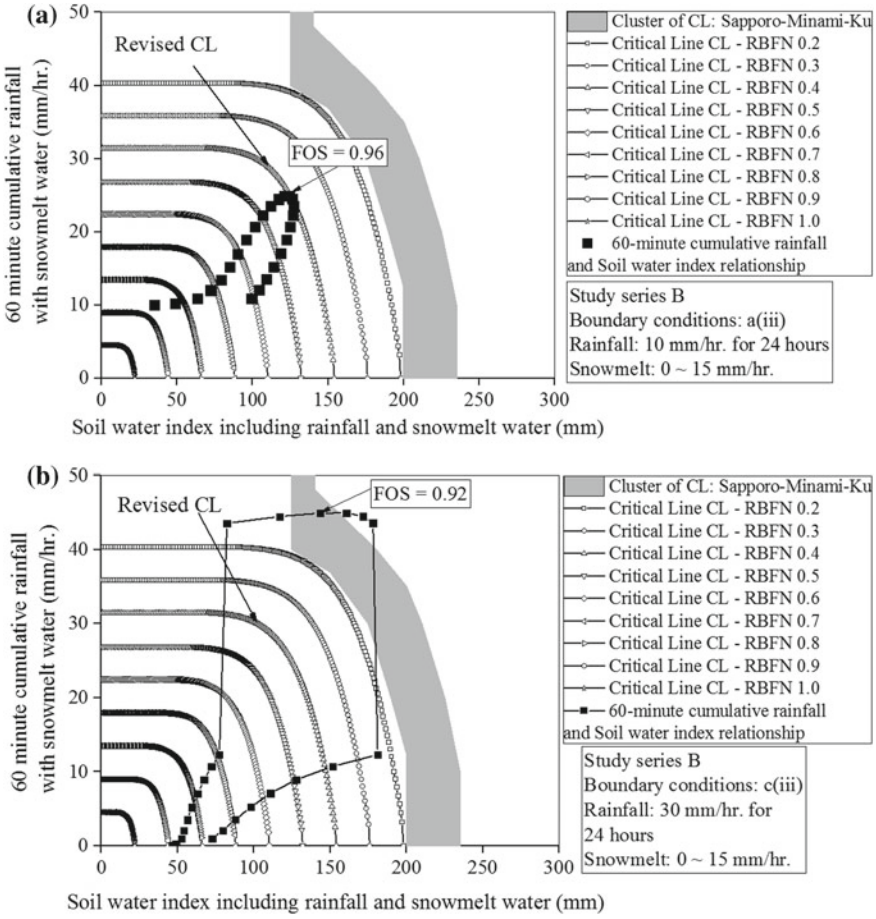

Fig. 13 Revision of CL for SWI based on occurrence and non-occurrence of slope failures using data from study series B with 45° slope angle, 5-m slope height, 10- and 30-mm/h rainfall with two different snowmelt rates

3 Wide-Area Slope Stability Analysis Under Climate Change

Warming of the climate system is unequivocal; this is according to the Intergovernmental Panel on Climate Change (IPCC 2014) report, which further contended that the evidence of observed climate change impacts is strongest and most comprehensive for natural systems (Montgomery 1994; Martinovic et al. 2016). In a more related scenario, the series of roadside slope failure along the Nissho Pass National Highway 274 in Hokkaido, which happened during the occurrence of Typhoon 10 on August 2016 is shown in Fig. 15. This has caused closure of the road, which

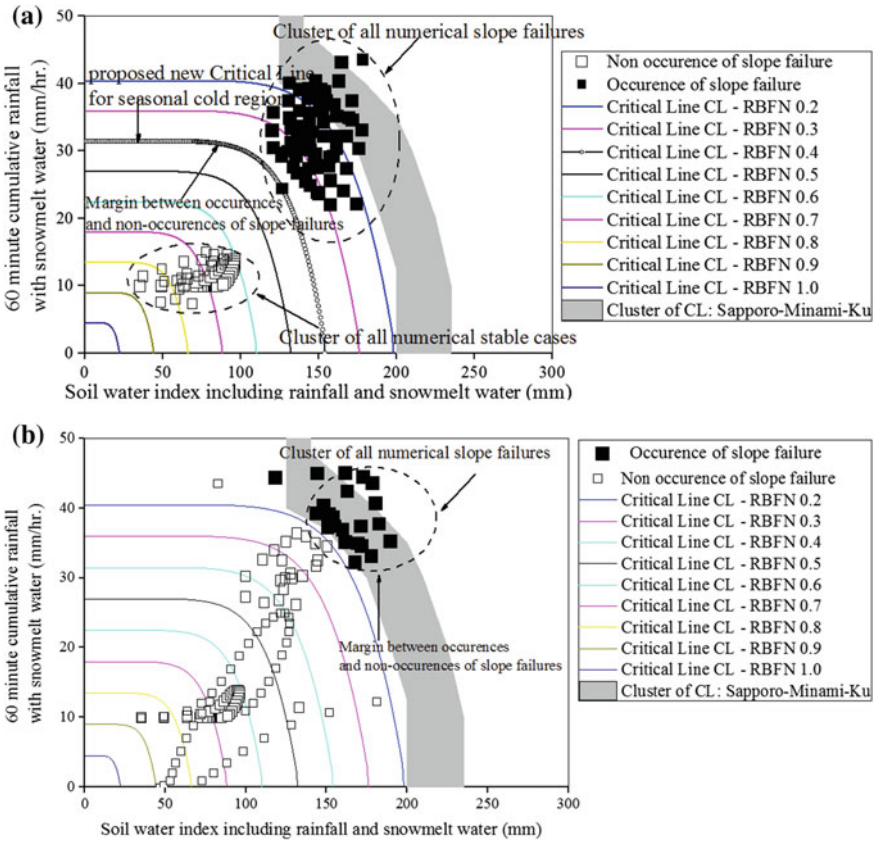

Fig. 14 Revision of CL for SWI using numerical results

connects the towns of Shimizu and Sapporo, which is also a major trunk line in Hokkaido, including a series of rehabilitation and repair activities. Extreme rainfall observed during the typhoon peaked at 55 mm with a cumulated 488 mm overtopping the monthly average for Hokkaido according to the Japanese Meteorological Agency (JMA).

Climate and landslides act at only partially overlapping spatial and temporal scales, complicating the evaluation of the climate impacts on landslides (Gariano and Guzetti 2016). During heavy rain or storm, runoff generated on the surface of the slope would erode the slope and induce large-scale landslides or slope failures. For example, referring to Fig. 16, it is recognizable that during the typhoon 10 hit Hokkaido, in four days from 01:00 on 28 August to 23:00 on the 31 August, the maximum observed cumulative rainfall exceeded 500 mm, far exceeding the average rainfall in the area. Hence, the occurrence of slope runoff has replaced the direct infiltration of rainfall as the cause of the disaster.

Fig. 15 Damages caused by the typhoon 10

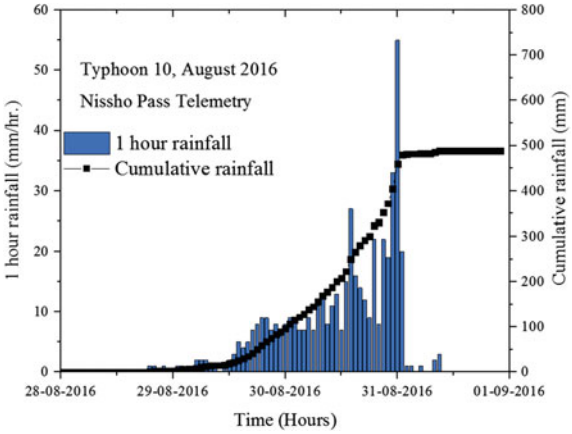

Fig. 16 Rainfall recorded at typhoon 10 at Nissho Pass Telemetry

In this study, to analyse the impacts of climate change-induced abnormal typhoon rainfall on slope stability, we gave an attempt to consider the effects of runoff and high-velocity flow of water during a typhoon in slope stability analysis. However, using conventional geotechnical methods, i.e. unsaturated/saturated seepage and slope stability analyses, which is often adopted to analyse rainfall-induced slope failures, the continuous flow of water above the slope and runoff cannot be considered. Therefore, we calculated the amount of runoff water flow from the received rainfall from typhoon 10 by employing large-scale hydrological analysis using geographical information system (GIS) tools and two-dimensional (2D) surface water

flow module using Nays2D Flood solver of the International River Interface Cooperative (iRIC) programme (Shimizu et al. 2014). After that, the calculated amount of water depth was used as a boundary condition in the continuum mechanics programme Fast Lagrangian Analysis of Continua (FLAC) to estimate the surface runoff and consider the influence of water depth on infiltration, to calculate the infiltration volume and the variation of pore water pressure within the slope.

3.1 Spatial Analysis of the Disaster Terrain

To visualize the topography of the disaster site, which would also be helpful to understand the nature of the slope failures, at first, spatial analyses were performed using ArcGIS. Using digital elevation model (DEM) with 0.000111 arc degree resolution, the terrain profile and distribution of the drainage network along sub-catchment areas across Nissho Pass were plotted as shown in Fig. 17.

The roadway along the Nissho Pass has an elevation of 950 m to 1050 m above mean sea level (MSL). Each of the disaster sites is located inside an individual sub-catchment. The drainage network inside each sub-catchment confirms that the flow of water from the mountain part over an elevation of 1300 m should always cross the highway to reach the lower elevations as shown in Fig. 17b. The distribution of slope of the mountainous terrain along the Nissho Pass is shown in Fig. 18.

3.2 Simulation Method

Rainfall-induced slope failures are induced by increasing pore pressures and seepage forces during periods of intense rainfall. This study was performed to determine the rainfall runoff of the slope surface by using iRIC programme, and then the iRIC calculations were used as boundary conditions for the FLAC programme, as shown in Fig. 19. During a typhoon disaster, the surface soil would be affected by rainfall intensity and topography conditions, at the valleys or trenches of the mountains. Water was collected above the surface soil making the depth of water constantly changing. Hence, setting the constant infiltration boundary or constant pore pressure boundary in the FLAC would not reflect the real situation. We attempted to use iRIC to get the changing water depth as the FLAC boundary condition to simulate the impact of slope infiltration on slope failure in the case of runoff.

In this study, the runoff analyses were done in Nays2D Flood solver of the iRIC software, which is a flood flow analysis solver that relies on unsteady two-dimensional plane flow simulation using boundary-fitted coordinates as the general curvilinear coordinates (Shimizu et al. 2014). Through entering the rainfall data (Fig. 16) and the elevation of the terrain based on the digital elevation model (DEM) which was sourced from Geospatial Information Authority of Japan using ArcGIS software (Fig. 18), iRIC could get the time-based water depth of the target point by

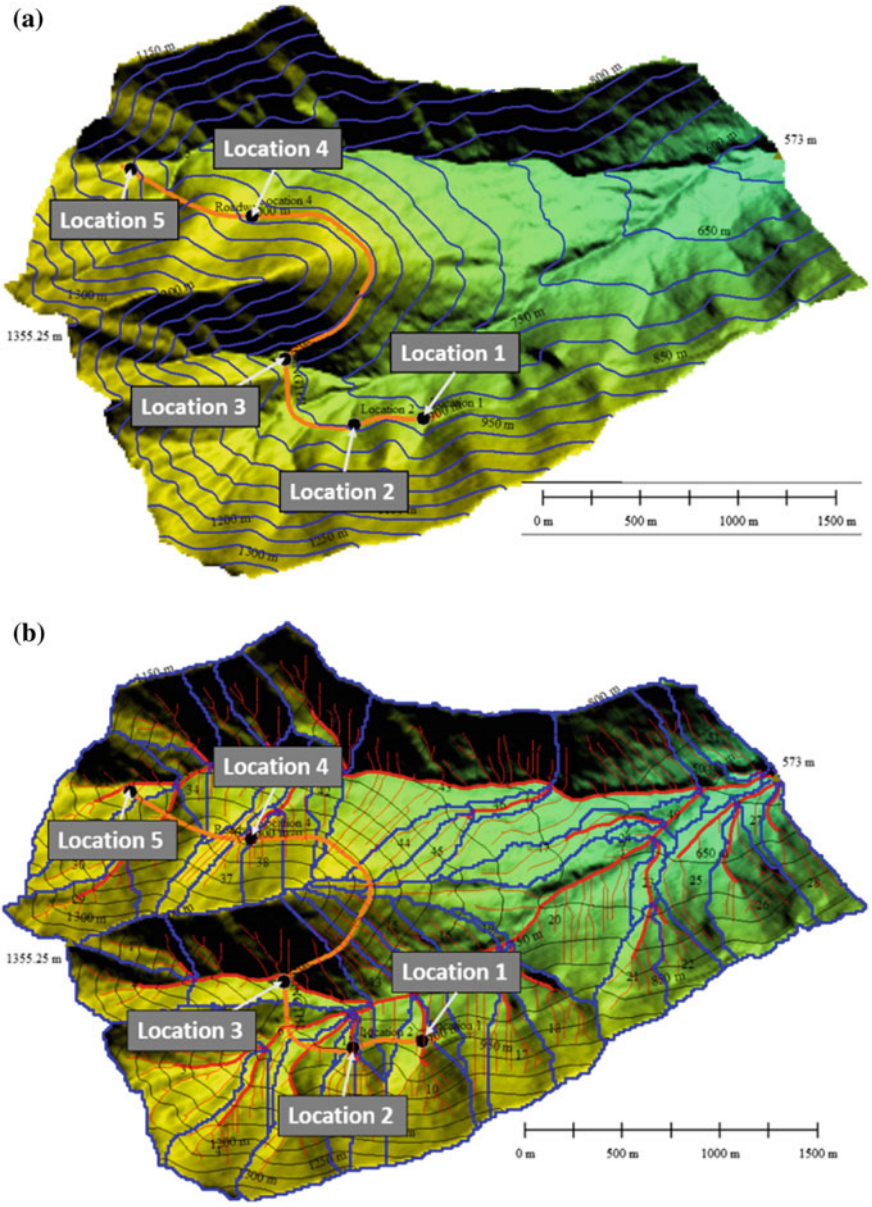

Fig. 17 **a** Terrain profile and **b** drainage network along Nissho Pass in National Highway 274

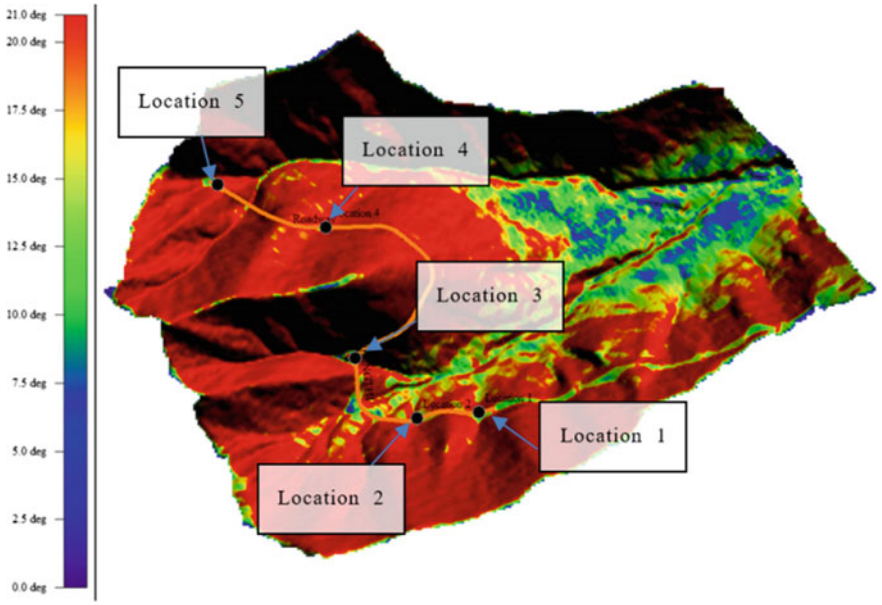

Fig. 18 Slope distribution of the typhoon disaster area

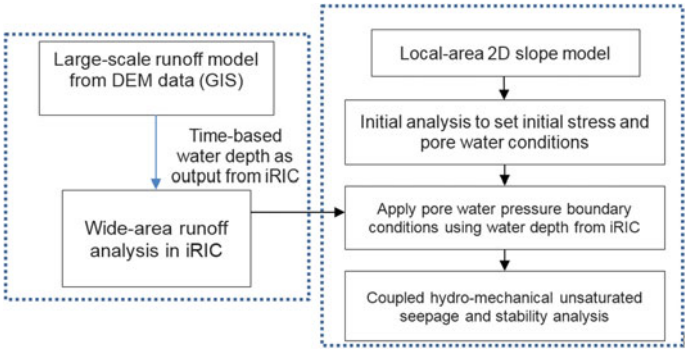

Fig. 19 Flow chart of coupling wide-area runoff analysis and slope stability analysis

runoff analysis; after that, time-based pore pressure was used instead of the depth of water as the boundary condition in the FLAC model and then coupled hydro-mechanical unsaturated seepage, stability analysis using two-phase flow module (Fluid-Mechanical Interaction 2011) was done in FLAC to simulate the process of soil saturation under boundary infiltration in the above time-based pore pressure and factor of safety of the slope was analysed subsequently. The concept showing the coupling between wide-area runoff analysis and coupled slope stability analysis is shown in Fig. 20.

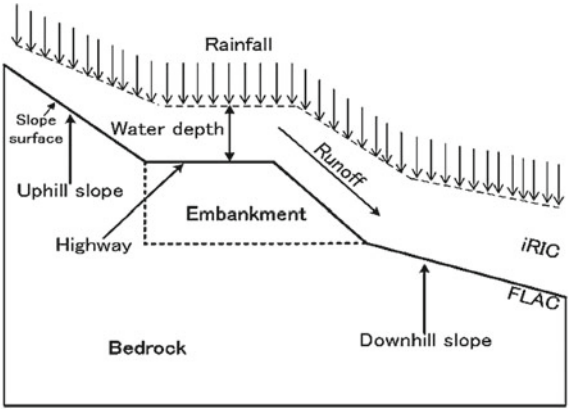

Fig. 20 A schematic of the numerical modelling adapted in this study using iRIC and FLAC

3.3 Wide-Area Runoff Analysis Using IRIC

The basic equations of a synthetic storage routing model and flow in a rectangular coordinate system (x, y) used in the Nays2D Flood solver can be referred from Shimizu et al. (2014) and SRM Solver Manual (2014). The overlay grid of the iRIC model is shown in Fig. 21.

The grid was created in the area near the target point to make the calculation more rapid and efficient; in the meantime, the boundary at the higher elevation was set as the inflow boundary and the boundary at the lower elevation was set as the outflow boundary to consider the impact of runoff in the large area. The inflow value at the inflow boundary was calculated from the catchments in the adjacent area. On the contrary, the outflow boundary was defined as free flow. Within the analysis domain, the effects of rainfall are also considered by entering the amount of rainfall observed per hour. Taking location 2 as an example, the grid produced runoff within 345,600 s (4 days). The water accumulated at lower altitudes was increased in runoff velocity and has the same tendency as rainfall. As shown in Fig. 21, the location 2 is situated at the valley. The velocities at a different time calculated by iRIC are shown in Fig. 22 at different times during the typhoon. It shows that at location 2, which is surrounded by the yellow dotted box (140 m $\times$ 160 m), the velocities of water increased at first and then decreased with the change in rainfall intensity. The yellow dotted box shows the area which is comparatively lower in elevation than the surrounding area shown in Fig. 22. The velocity vectors can be seen accumulating towards the shallow areas. The shallow areas within the yellow dotted box collected more amount of water from the deep mountain. It is understandable that the water flowed through the low-lying areas, especially surrounding the location 2 and across the roadway which induced the slope failure. The increase in water velocity was found to be spontaneous with the increase in rainfall intensity. The maximum water

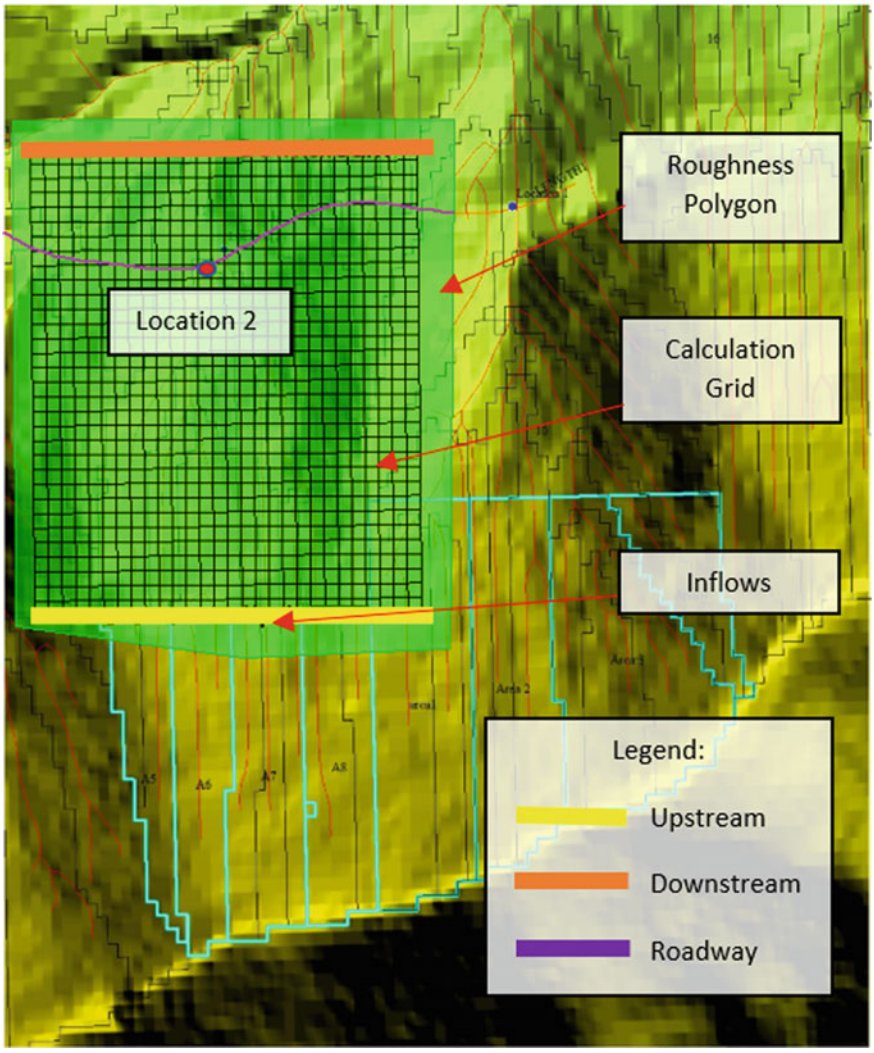

Fig. 21 Overlay grid layer for iRIC—Nays2D Flood analysis

velocity estimated is 1.26 m/s. Apart from the velocity of water, the depth of water at locations also played a significant role in the disasters which is discussed further.

At location points 1, 2, 4 and 5, the typhoon-induced increase in water depth and water velocity was calculated. Figure 23 shows that the depths of water and magnitude of velocities at location points 1, 2, 4 and 5 (each location was a point approximately at the centre point of the road and calculated in iRIC, as shown in Figs. 17 and 18) were slowly increased with the increase of rainfall intensity and steeply decreased after a sudden drop in rainfall. At location points 1 and 2, the maximum depth of

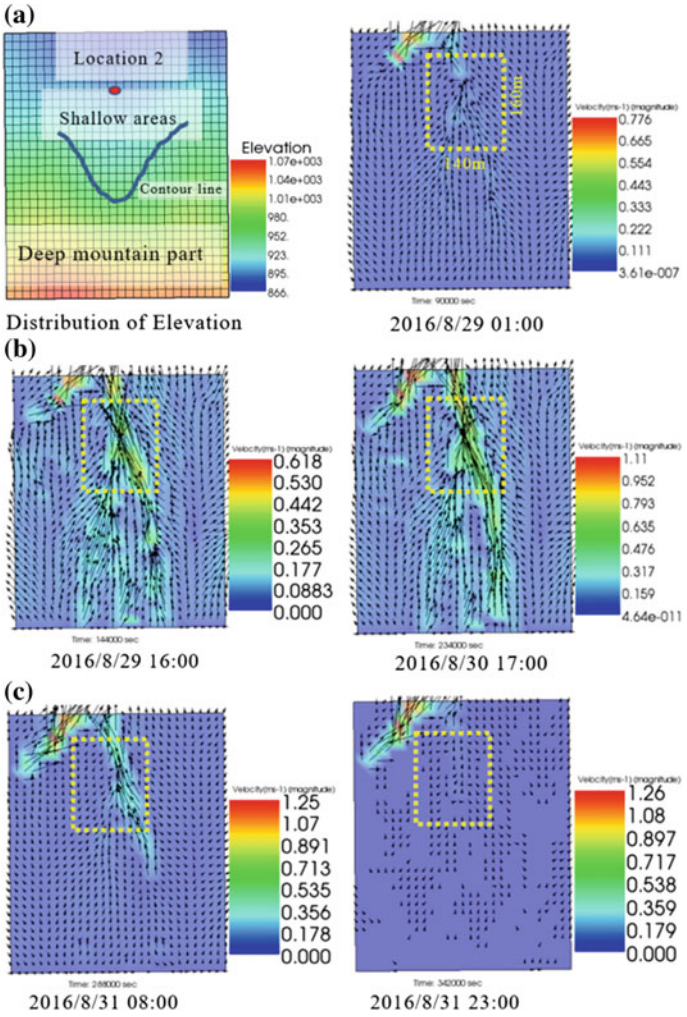

Fig. 22 **a** Distribution of elevation and velocity at 2016/8/29 01:00, **b** increase in water velocity at 2016/8/29 01:00, 2016/8/30 17:00, 2016/8/31 08:00 and **c** 2016/8/31 23:00

water was more than 0.1 m. The highest magnitude of the velocity during the typhoon 10 event approximately ranges up to 1.6 m/s at location 1, where both embankment collapse and debris flow were occurred. In these failure sites, it is recognizable that rainfall event is not the only major contributor to the increased runoff concentration at the exploratory points, and it is a combination of the following conditions: (1) initial state set by the previous intense rainfall that the catchment received from the previous typhoons which made the soil almost in saturated condition that ultimately affected the infiltration, thus increasing the runoff volume; (2) the drainage network

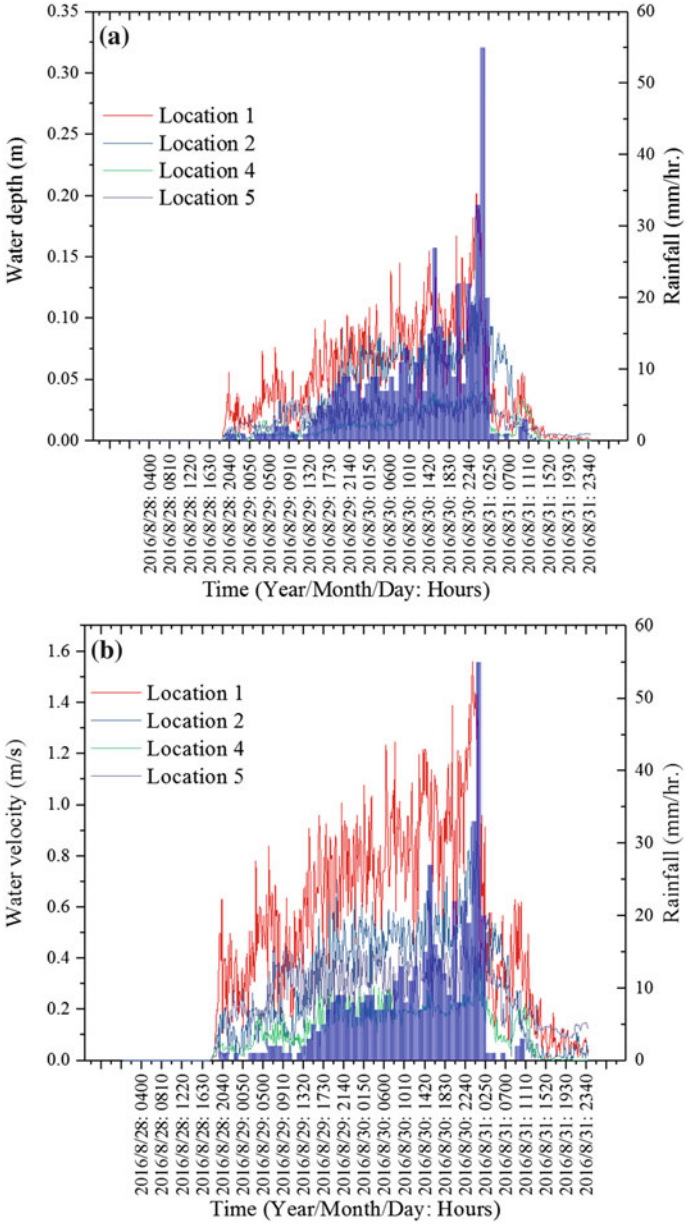

Fig. 23 iRIC calculations of **a** water depth and **b** magnitude of water velocity at each location

suggests that the site where the failure occurred is a collection point of runoff water; (3) the topography of the site, where the average slope of the uphill portion of the road is 20° which increased the flow.

3.4 *Coupled Hydro-mechanical Unsaturated Seepage and Slope Stability Analysis Using FLAC*

Stability analysis of the slope was computed by using the two-phase flow model in FLAC. The governing equations for the unsaturated coupled hydro-mechanical analysis can be referred from Itasca (2011). The stress–strain relationship of the soil is based on extended Mohr–Coulomb failure envelope. The slope stability analysis has been performed using the strength reduction method for determining factor of safety, and it is based on Mohr–Coulomb elasto-plastic material model using the bracketing approach. Unlike conventional limit-equilibrium stability analyses based on the method of slices, the shear strength reduction technique has a number of advantages. In the above technique, it is not necessary to specify the shape of the failure surface in advance, as the critical failure surface (or multiple failure surfaces) evolves automatically through the weakest zone during the solution. The anticipated failure surface has been determined for the limiting case of overall slope stability by reducing the strength parameters of the soil until hypothetically bringing the slope to an unstable state. The factor of safety value was then back calculated.

Referring to the disaster report of JGS, at location 3, the debris flow occurred at the embankment by concentrated heavy water flow on the centre point of the road which collapsed the embankment. Debris flow was also occurred at location 1, 3 and 5, which was the factor that could not be considered in FLAC. At locations 2 and 4, the main factor of roadside slope failure was runoff-induced collapse of earthfill road embankment. However, as shown in Fig. 23, the water depth and magnitude of the velocity of location 2 were much higher than location 4. Thus, the stability analysis of the slope mainly focused on location 2. As shown in Fig. 24, points 25, 26, 27 and 28 were calculated as exploratory points in iRIC. The FLAC model and boundary conditions are shown in Fig. 25. The model is configured with a mesh made up of quadrilateral elements and specified with zero displacement boundaries applied at the lateral and bottom sides. At the top portion of the slope, the time-based water depth computed by iRIC (Fig. 26) was converted into average pore water pressure (average value in 6 h) which was applied as the FLAC model's boundary conditions as a pore water pressure to reflect the impact of rainfall-induced runoff. In this study, slope stability analysis without considering the runoff (only rainfall) was also performed.

The soil and fluid properties used in FLAC are shown in Table 2.

The numerical analysis results are shown as follows. Figure 27a, b is distribution of degree of saturation, and Fig. 28a, b is distribution of shear stain increment before runoff generation and after slope failure, respectively. Figure 27b implied that the water content of soil was increased at the embankment. As can be seen in Fig. 27b, under the influence of runoff, pore water pressure increased means that the suction was reduced, which made the occurrence of roadside slope failures and embankment collapse. Figure 28b suggested that the deformation area of the slope became more concentrated and the failure shape became steeper as the shear strain increased where it was consistent with the actual location and size of the roadside slope failure (Fig. 24).

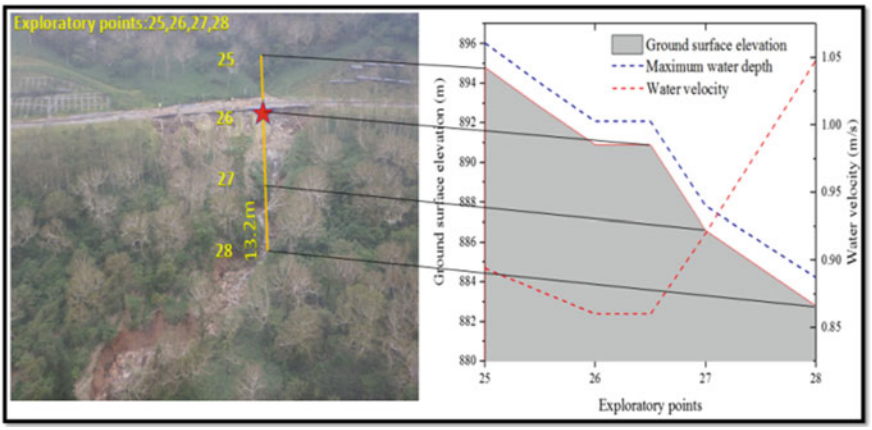

Fig. 24 Elevation and maximum of water depth and velocity at location 2

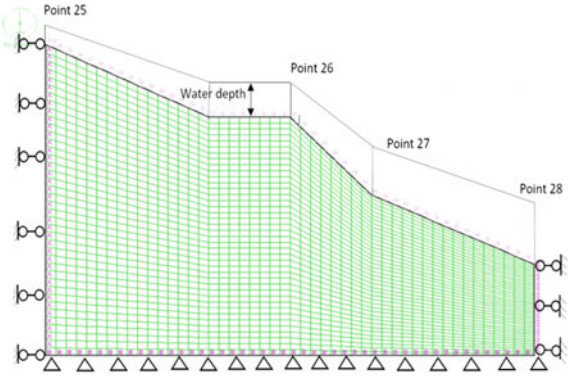

Fig. 25 FLAC model and boundary conditions

The change in factor of safety (FOS) of slope with runoff analysis and without runoff analysis is shown in Fig. 29. With runoff analysis, the factor of safety of slope was 1.42 at 5:30 on 29 August that suggested the slope was stable. In the early rainfall, after the runoff generation, the infiltration has greatly reduced the stability of the slope with factor of safety reducing to 1.2 at 09:00 on 29 August. Along with the increase of water depth, factor of safety continued to reduce and approached to 1.0 at 18:00 on 30 August, which suggested that the stability of the slope reached the limit state at the time.

Finally, the roadside slope failure occurred between 18:00 and 23:00 on 30 August with the advent of greater rainfall. However, if without considering the impact of runoff and using precipitation as boundary conditions, the factor of safety was not less than 1 that implied the importance of runoff in slope stability analysis. In heavy rains or storms, especially in the valleys or trenches of the mountain, the runoff

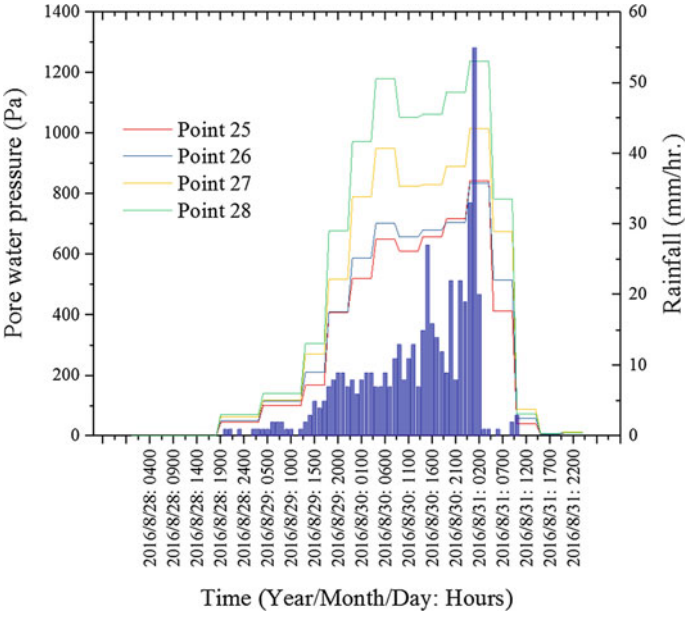

Fig. 26 Pore water pressure at exploratory points

Table 2 Soil and fluid properties used in FLAC

Parameters	Value	Parameters	Value
Dry density ρ_s (kg/m^3)	1695	Density of water ρ_w (kg/m^3)	1000
Drained bulk modulus K (MPa)	200.0	Density of air ρ_g (kg/m^3)	0.0
Shear modulus G (MPa)	100.0	Van Genuchten parameter, m	0.468
Drained cohesion c' (kPa)	0	Van Genuchten parameter, b	0.5
Drained friction angle φ' (degrees)	37	Van Genuchten parameter, c	0.5
Dilation angle Ψ (degrees)	0	Van Genuchten parameter, α (kPa)	0.81
Permeability coefficient k^w (m^2/(Pa*s))	8.3E^{-8}	Bulk modulus of water K_w (MPa)	1.0
Porosity n	0.36	Bulk modulus of air K_a (Pa)	1.0
Residual degree of saturation of water S_r	0.1	Undrained coefficient	0
		Viscosity ratio	1.0

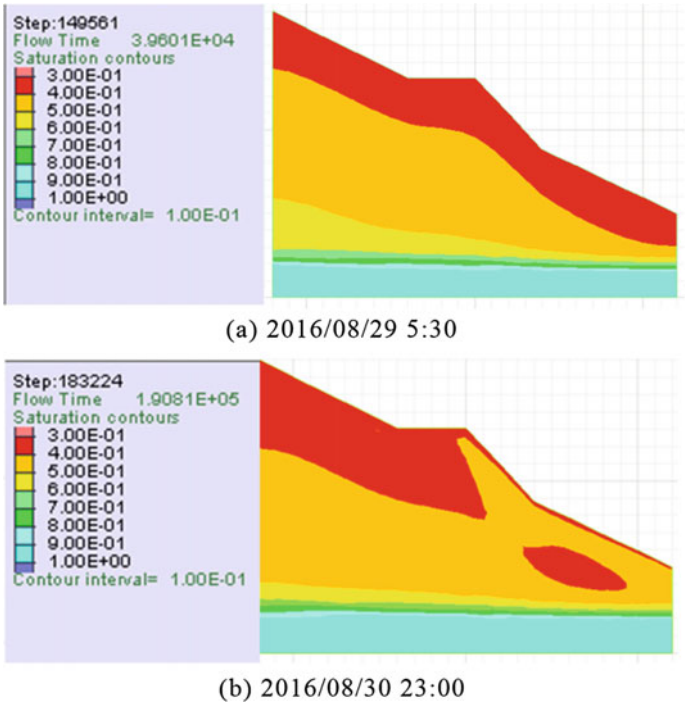

Fig. 27 Increase in degree of saturation

generation will be the real situation. Therefore, it is unsuitable to assume the boundary conditions of the slope as a constant rainfall velocity infiltration in slope stability analysis by using FLAC.

4 Conclusions

The first part of this paper evaluated the applicability of Japanese early warning criteria Soil Water Index (SWI) for the prediction of snowmelt-induced soil slope failures in Hokkaido, Japan. Considering the change of climate in future, construction of a risk assessment method is shown through adopting a numerical analysis approach for slope disasters in snowy cold areas through which various limit state scenarios of conceptual soil slope failures are studied under different magnitudes of snowmelt water and rainfall. A revision for the SWI is introduced by incorporation of snowmelt water in the calculation. Following findings can be outlined from the early warning portion of this study.

– The SWI is improved and predicts the snowmelt-induced slope failures only when snowmelt water is considered provided with a revision in the CL.

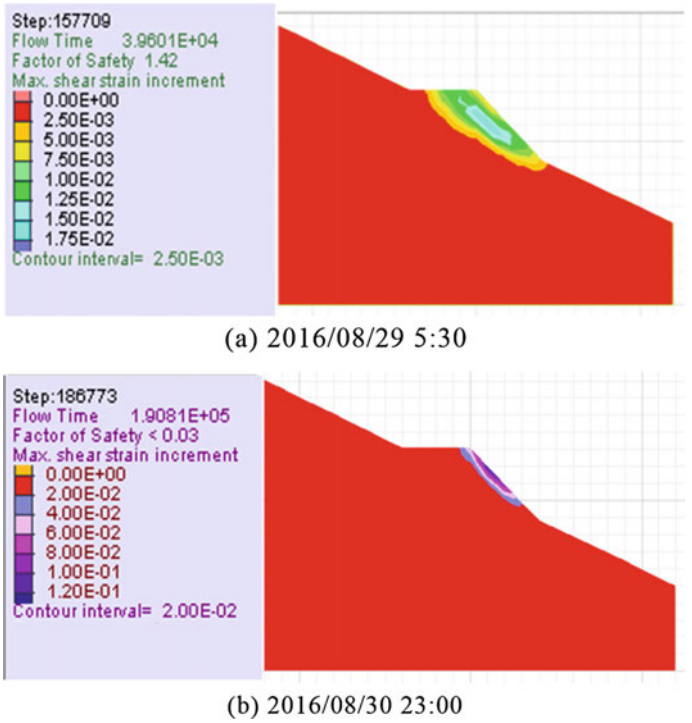

Fig. 28 Decrease in factor of safety and slope stability

- The revisions to the SWI criteria suggest an hourly threshold rainfall + snowmelt value is 30 mm/h instead of the present value of about 45 mm/h. For SWI, a value of 150 mm is recommended.
- The different critical lines presented for snowmelt as well as rainfall-induced slope failures predict the failures and stable scenarios more accurately than the existing CLs.
- The results of the parametric numerical simulations performed in this study, both stable cases and slope failures, agree well with the newly proposed CL of SWI.
- The numerical simulation approach proposed in this study can be practically used to set the CL for both snowmelt and rainfall-induced soil slope failures.

In order to model and analyse the 2016 typhoon-induced large-scale slope failures in Hokkaido, in the second part of this paper, wide-area runoff analysis was used to simulate the rainfall-induced runoff in the mountain region, and the slope stability analysis based on coupled hydro-mechanical unsaturated seepage and stability analysis was performed using the results of hydrological analysis as boundary conditions. The results show that

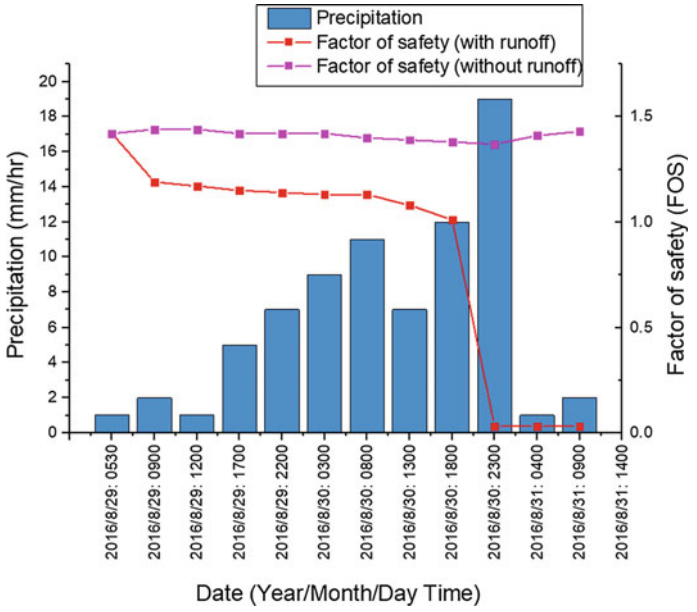

Fig. 29 Change in factor of safety with time

- The runoff simulation for each site suggested that the concentration of runoff at each location is a common scenario, where high water surface runoff depth alongside the high velocity is observed.
- The likely combination of topography, slope, drainage network and the initial wet state of soil at the site has exacerbated the amount of runoff.
- The drainage concentration magnified the effect of rainfall, which could lead to surface erosion and channel enlargement.
- The runoff generation and concentration at the failure locations therefore have contributed to the debris flows and ultimately embankment collapse.
- During the early rainfall, after the runoff generation there was heavy flow of water along the mountains and the highways.
- The infiltration has greatly reduced the stability of the slope, along with the increase in water depth, and the scale of the failure was widened, which is suggested by the slope stability analysis.
- The coupled numerical modelling approach used in this study by integrating wide-area runoff analysis with local-area slope stability analysis is found to reproduce the real phenomenon of runoff generation and slope failure with rational precision.

The proposed early warning criterion for snowmelt-induced soil slope failures in snowy cold regions is expected to be adapted in practice and predict the slope failures in advance. The numerical modelling method using wide-area runoff analysis and coupled hydro-mechanical slope stability analysis are expected to be useful for the

prediction of large-scale slope failures which are predicted in future. Nevertheless, much more developments in many aspects are indeed necessary.

Acknowledgements We gratefully acknowledge the Hokkaido Regional Development Bureau and the Hokkaido Government for the provision of their surveyed data. The authors thank Mr. Yulong Zhu of Hokkaido University for performing some parts of the analysis. This research was supported in part by Grants-in-Aid for Scientific Research (A) (16H02360) from Japan Society for the Promotion of Science (JSPS) KAKENHI.

References

Berris SN, Harr RD (1987) Comparative snow accumulation and melt during rainfall in forested and clear-cut plots in the western Cascades of Oregon. Water Resour Res 23(1):135–142

Fluid-Mechanical Interaction, (2011) FLAC Version 7.0, ITASCA

Gariano SL, Guzzetti F (2016) Landslides in changing climate. Earth-Sci Rev. 162:227–252

Gariano SL, Rianna G, Petrucci O, Guzzetti F (2017) Assessing future changes in the occurrence of rainfall-induced landslides at a regional scale. Sci Total Environ 596–597:417–426

Intergovernmental Panel on Climate Change—IPCC (2014) Climate change synthesis report summary for policymakers. Available at: http://www.ipcc.ch/pdf/assessment-report/ar5/wg2/ar5_wgII_spm_en.pdf

Ishikawa T, Tokoro T, Seiichi M (2015) Geohazard at volcanic soil slope in cold regions and its influencing factors. Jpn Geotech Soc Spec Publ 1(1):1–20

Japanese Geotechnical Society (2017) The final report of ground disaster investigation report due to heavy rain in Hokkaido during August 2016. https://www.jiban.or.jp/wp-content/uploads/2017/08/final_report_ver0.12s.pdf (in Japanese)

Japan Meteorological Agency (JMA) (2012) Soil water index calculation 3 layer tank model. http://www.jma.go.jp/jma/kishou/know/bosai/dojoshisu.html (in Japanese)

Kondo J, Yamazaki T (1990) A prediction model for snowmelt, snow surface temperature and freezing depth using a heat balance method. J Appl Meteor 29:375–384

Martinovic K, Gaven K, Reale C (2016) Development of landslide susceptibility assessment for a rail network. Engg Geol 215:1–9

Montgomery DR (1994) Road surface drainage, channel initiation, and slope instability. Water Resour Res 30(6):1925–1932

Motoyama H (1990) Simulation of seasonal snow cover based on air temperature and precipitation. J Appl Meteorol 29:1104–1110

Okada K (2001) Soil water index, Sokkoujihou No. 69, **5**(5):67–100 (in Japanese)

Okimura T, Ichikawa R (1985) A prediction method for surface failures by movements of infiltrated water in a surface soil layer. Nat Disaster Sci 7:41–51

Osanai N, Shimizu T, Kuramoto K, Kojima S, Noro T (2010) Japanese early-warning for debris flows and slope failures using rainfall indices with Radial Basis Function Network. Lands **7**:325–338. https://doi.org/10.1007/s10346-010-0229-5

Riley JP, Chadwick DG, Eggleston KO (1969) Snowmelt simulation, Reports, Paper 122. http://digitalcommons.usu.edu/water_rep/122

Siva Subramanian S, Ishikawa T, Tokoro T (2017) Stability assessment approach for soil slopes in seasonal cold regions. Eng Geol 221:154–169. https://doi.org/10.1016/j.enggeo.2017.03.008

Shimizu Y, Inoue T, Suzuki E, Kawamura S, Iwasaki T, Hamaki M, Omura K, Kakegawa E, Yoshida T (2014) Nays2D flood solver manual

Storage Routing Model (SRM) Solver Manual (2014) International River Interface Cooperative (iRIC)

Unified Prediction Method for the Rainfall-Induced Landslides and Debris Flows

Sangseom Jeong, Jeongsik Park, Moonhyun Hong, Junghwan Kim and Kwangwoo Lee

Abstract In this study, a unified method was proposed for the analysis of rainfall-induced landslides by using GIS based landslides prediction model (YS-Slope model) and a prediction method by using a large deformation analysis method. A susceptibility assessments of landslides and debris flows in Umyeonsan (Mt.), South Korea were conducted as a case study by using the landslides prediction model and ABAQUS/CEL large deformation method. It is shown that the result of the analysis has a good agreement with historical landslides and debris flows. Based on the case study for Umyeonsan (Mt.) landslides, failure behaviors of landslides and debris flows are well predicted by the method described in this study. These procedure can be apply to the prediction of landslides and debris flows of another study area.

Keywords Landslide · Debris flow · Prediction method · YS-Slope · GIS · CEL

1 Introduction

Landslides cause many loss of lives and properties as well as failures in slopes, and debris flows triggered by landslides induce serious damage to several infrastructures. Therefore, landslides susceptibility assessment and the simulation of debris flows are

S. Jeong · J. Park · M. Hong (✉) · J. Kim · K. Lee
School of Civil and Environmental Engineering, Yonsei University, Seoul 03722, South Korea
e-mail: homh12@yonsei.ac.kr

S. Jeong
e-mail: soj9081@yonsei.ac.kr

J. Park
e-mail: hlpcs@hanmail.net

J. Kim
e-mail: hwanee2@gmail.com

K. Lee
e-mail: geokwoo@hotmail.com

R. Sundaram et al. (eds.), *Geotechnics for Transportation Infrastructure*, Lecture Notes in Civil Engineering 28, https://doi.org/10.1007/978-981-13-6701-4_32

important issues for the safety of urban and human lives (Liao et al. 2011; Kim et al. 2012; Hong et al. 2017). Landslides can be occurred by severe rainfalls and earthquake in the world, especially rainfall induced landslides are expected to accelerate more and more because of the climate change causing increase of rainfall and severe fluctuation in rainfall patterns.

There are several methods for landslide susceptibility assessment, these methods can be classified into four groups in general: heuristic, statistic, and deterministic approaches called physically-based model (Mantovani et al. 1996; Dai et al. 2002; van Westen 1997). Physically-based models were proven its applicability globally, and these models are usually used to assess susceptibility of landslides. Recently, regional scale landslides prediction methods have been used depending on topographic, geologic, hydrologic variables and changes in land use (Cotecchia et al. 2010; Pardeshi et al. 2013). Landslide susceptibility assessment on regional scale, the problem is recognized before the landslide event, is useful for avoiding landslide losses (Brabb 1993). Implementing data for landslide factor, such as weather conditions, topography and vegetation, in Geographic Information System (GIS) might be start for a regional landslide susceptibility assessment (van Western 1997). Due to the ability to spatial data process, Geographic information systems (GISs) are broadly used for landslide analyses (Burrough 1986; van Westen 1993; Tarboton 1997; Simoni et al. 2008; Lepore et al. 2013). In particular, physically based models combine a geotechnical model and a hydrological model for analysis of rainfall-induced landslides. They can be used for determining of locations and the timing of the occurrence of a rainfall-induced landslide on a regional scale using GIS.

Consequently, susceptibility assessments of landslides on regional scale are needed for avoiding landslide losses, and combining between hydrologic models with geotechnical models. Slope stability analysis and debris flow simulations are very important to predict landslide that is recognized before the landslide event. In this study, a unified prediction method for landslides and debris flows based on geological and hydrological models are described. An assessment of landslides susceptibility in Umyeonsan (Mt.) and the simulation of debris flows were conducted as a case study of the unified method.

2 Research Methodology

The initial volume of debris flows is a very important factor in the simulation of debris flows. In order to determine the initial volume of debris flows, some empirical equations can be applied, but in recently, the estimation based on the analysis results of landslides is applied for more accurate simulation results. In this study, the initial volume of debris flows are calculated by the prediction results from the GIS based landslides analysis model called YS-Slope. Rainfall input such as recorded rainfall and probability rainfall, geotechnical properties, hydrological properties and topography are needed for the landslides analysis. Based on the hazard map and the results of landslides analysis such as the depth of wetting front and failure area, the initial

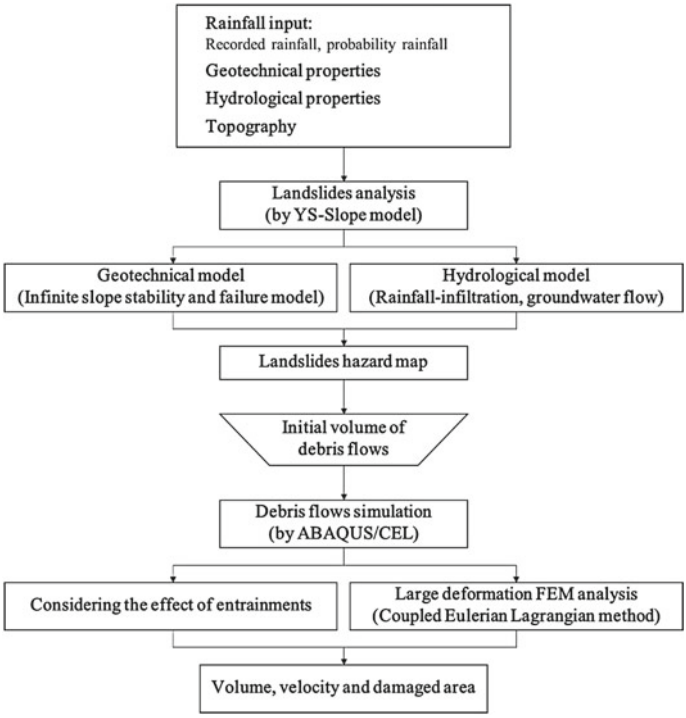

Fig. 1 The conceptual flow chart of unified prediction method for landslides and debris flows

volume of debris flows are calculated. Finally the calculated initial volume and the location of debris flows are applied to the simulation of debris flows as an input data. These unified analysis procedure is shown in Fig. 1.

2.1 YS-Slope Model

YS-Slope model had been developed using a methodology as shown in Fig. 2. This model uses unsaturated soil properties including the field matric suction and soil water characteristic curve (SWCC) represented by the relationship between the volumetric water content and the soil matric suction, as well as the soil strength coefficients such as internal friction angle and cohesion. In addition, the model reflects the influence of the increase in soil strength and load, and interception loss due to vegetation. DEM and soil depth of the regional area are entered as raster data of the matrix structure. The infinite slope failure model is used for slope stability analysis, and hydrological analysis is performed to simulate rainfall-infiltration and the groundwater recharge and flows. Various types of rainfall events such as real-time precipitation and probability rainfalls can be used in the analysis (Kim et al. 2014).

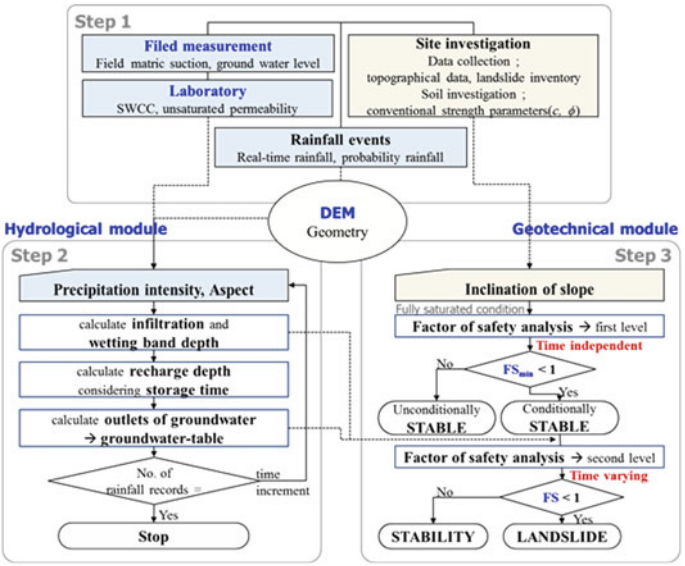

Fig. 2 The process of landslides susceptibility assessment in YS-Slope model

2.1.1 Geotechnical Infinite Slope Model

The general mechanism of rainfall-induced landslides can be classified into three cases: (1) failure along the wetting front, (2) failure at the bottom of the groundwater, and (3) failure affected by both of wetting front and the groundwater recharge. The infinite slope failure method, a physically-based limit equilibrium method, was applied to calculate safety factors of rainfall-induced landslides based on the aforementioned mechanisms.

The factor of safety of infinite slope failure for failure under the wetting front (case 1) can be calculated by below equation:

$$FS = \frac{\left(c_s^{'} + c_r^{'}\right) + \left(q_0 + \left(\gamma_{sat} - \gamma_w\right) \cdot D_w\right) \cdot \cos^2 \beta \cdot \tan \phi^{'}}{\left(\gamma_{sat} \cdot D_w + q_0\right) \cdot \sin \beta \cdot \cos \beta} \tag{1}$$

where $c_s^{'}$ is the soil cohesion, $c_r^{'}$ is the shear strength by tree roots, q_0 is the tree loads on slope surface, D_w is the wetting front depth, γ_t is the total unit weight of the soil, γ_{sat} is the saturated unit weight of the soil, γ_w is the unit weight of water, and β is the slope angle.

Failure on the bedrock (case 2 and 3) can be calculated as follows:

$$\mathrm{FS} = \frac{\left(c_{\mathrm{s}}^{'} + c_{\mathrm{r}}^{'}\right) + \left(\gamma_{\mathrm{t}} \cdot D_{\mathrm{s}} + q_0 + \left(\gamma_{\mathrm{sat}} - \gamma_{\mathrm{w}}\right) \cdot D_{\mathrm{w}}\right) \cdot \cos^2 \beta \cdot \tan \phi^{'}}{\left(\gamma_{\mathrm{t}} \cdot D_{\mathrm{s}} + \gamma_{\mathrm{sat}} \cdot D_{\mathrm{w}} + q_0\right) \cdot \sin \beta \cdot \cos \beta} \tag{2}$$

where D_{s} is the depth of the unsaturated soil.

2.1.2 Hydrological Model

A Green and Ampt model (Green and Ampt 1911) was modified by Mein and Larson (1973), and we used the modified Green-Ampt model to estimate rainfall-infiltration and groundwater recharge while considering the behavior of the unsaturated soil as shown in Fig. 3.

Groundwater flow was calculated by linking GIS based raster model with Darcy's law (Soller et al. 1999; Smit et al. 2013), and recharge by rainfall-infiltration was used as input variable. Groundwater flow analysis was performed on small unit volumes assumed to be homogeneous in soil characteristics. The fluxes were calculated to balance the masses of water entering to the unit volume and the water flowing out, satisfying Darcy's law (Fig. 4).

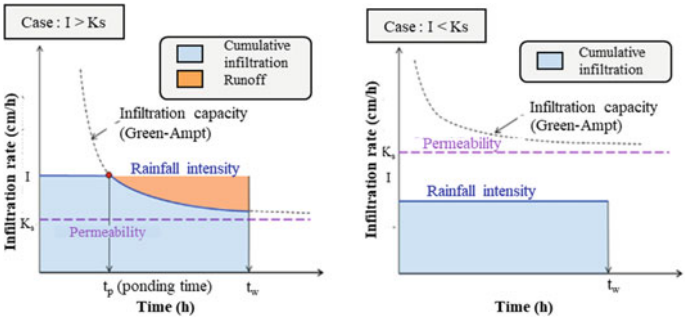

Fig. 3 Infiltration rates (Mein and Larson (1973)

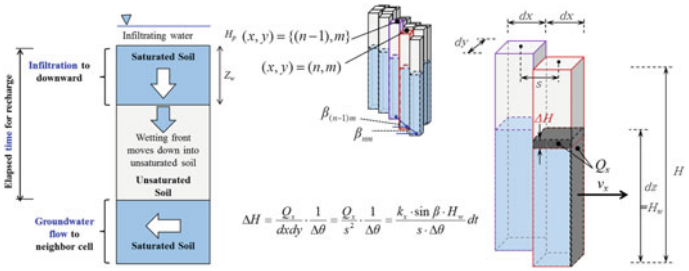

Fig. 4 Unit volume fluid flows in YS-Slope

2.2 Debris Flows Model

ABAQUS/CEL large deformation method was used to simulate debris flows considering the erosion and entrainment of soils. CEL analysis was developed to simulate fluid-structure interaction accommodate fluid-structure interaction problems and combines Lagrangian and Eulerian methods. Lagrangian method is usually applied to solid analysis, and Eulerian method is generally employed in fluid analysis. In Lagrangian analysis, each node moves with properties of the element. The node should be shared, and properties of the interface should be accurately defined between two objects.

3 A Case Study on Landslides and Debris Flows

3.1 Study Area

Mountain Umyeonsan is located in south-east of Seoul, Korea (Fig. 5). This area is located in temperate monsoon zone and is generally hot and wet in summer while cold and dry in winter. Most precipitation falls in the summer. The altitude ranges from 50 to 312 m, and various terrains are distributed. Approximately 1100–1500 mm of precipitation measured in annual and 70% of the precipitation falls from June to September. Landslides are common in the area in the summer, and landslides that occurred on the 27th July 2011 at umyeongsan (Mt.) were the most disastrous catastrophic landslide and debris flow recorded.

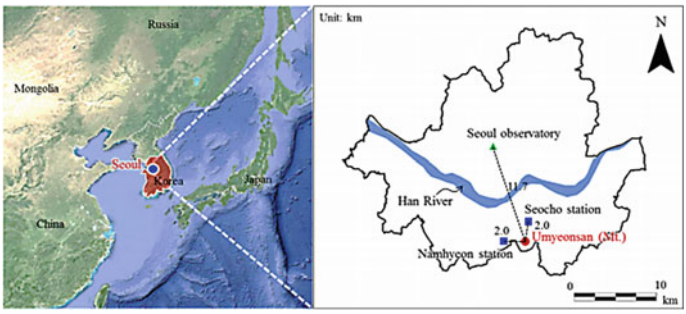

Fig. 5 Location of the Umyeonsan debris flows in Seoul, Korea

3.2 Rainfall Characteristics

Rainfall records which are the cumulative and hourly rainfall from July 26 to 27, 2011 by the rain gauges at the Namhyun and Seocho stations are shown in Figs. 6a, b. The cumulative rainfall during 24 h ending at 4 p.m. on July 27 were 425.5 (Namhyun) and 364.5 (Seocho) mm. The maximum rainfall intensities (hourly rainfall) at the two stations were 112.5 (Namhyun) and 85.5 (Seocho) mm, occurred between 7:30 and 8:30 a.m. The maximum hourly rainfall recorded from Namhyun station was more severe, reaching at the 120 years of return period rainfall. Interestingly, the occurrence of the debris flow in the Raemian watershed starting at 9:00 p.m. coincided well with the peak hourly rainfall. In 2011, the heaviest cumulative rainfall recorded since the emplacement of the rain gauge (Fig. 6c). Rainfall in 2011 was characterized by the analysis as a long duration and high intensity, which can be a major cause of occurrence of the debris flows.

An empirical ID curve that can be used to the landslide prediction have a general form like the following power law equation (Guzzetti et al. 2008; Hong et al. 2017):

$$I = \alpha \cdot D^{\beta} \tag{3}$$

where I is the rainfall intensity and D is the rainfall duration, and α and β are empirical constants. ID curves proposed by previous researchers are highlighted in Fig. 7 (Caine 1980; Innes 1983; Guzzetti et al. 2008; Hong et al. 2017), and rainfall records at July 27, 2011 are compared with these thresholds. Recorded rainfalls were highly intensive and long, and they over various ID curves.

3.3 Geotechnical Characteristics

Ground investigations were performed to determine hydrogeological and geotechnical properties for the analysis of the landslide initiation and the debris flow simulation. Five boreholes (B-1, B-2, B-3, B-4 and B-5) and six trial pits (TP-1, TP-2, TP-3, TP-4, TP-5and TP-6) were drilled and investigated to conduct various soil samplings for laboratory tests and site investigations such as SPT, in situ permeability tests, and borehole shear tests. Figure 8 shows the location of the borehole and the seismic survey conducted in the watershed, and the properties by the survey were summarized in Tables 1 and 2.

3.4 Vegetation Characteristics

The effects of vegetation on slope stability can be represented by mechanical stabilization of the soil by roots, additional loading by the weight of trees, and soil water

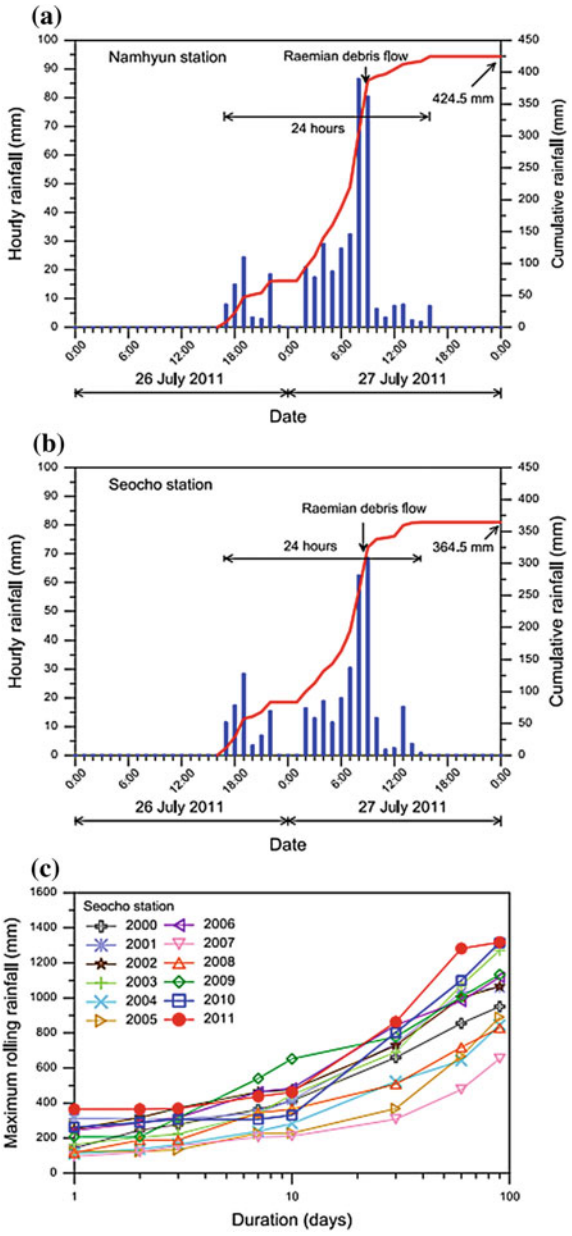

Fig. 6 Rainfall records for 26–27 July 2011 (Namhyun and Seocho station) and maximum rolling rainfall at Seocho station

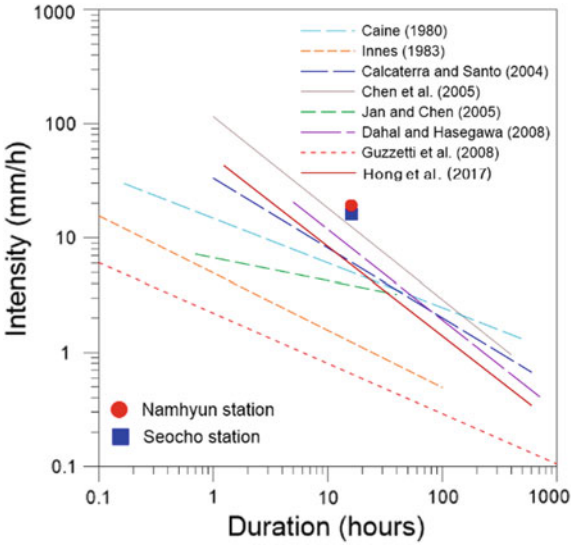

Fig. 7 Comparison of the recorded rainfall intensity-duration data with previous ID curves

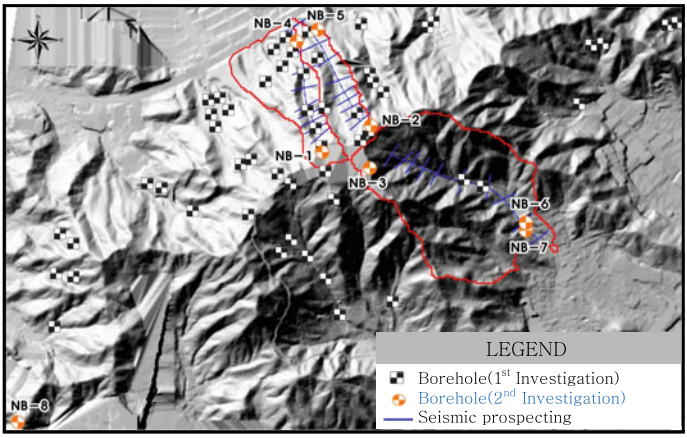

Fig. 8 The location of boreholes and seismic prospecting

degradation through evapotranspiration or interception loss (Nilaweera and Nutalaya 1999). Tree roots penetrating the entire soil at shallow slopes serve as tensile elements within the soil matrix and connect soft soil to adjacent stable soil. The type, soil depth and roots characteristics determined by hydrologic conditions, species and cultivars change roots fiber reinforcement (Wu and Sidle 1995).

To explore the nature of the vegetation community, extensive field surveys have been conducted in the Ramian Basin. A sampling plot of 400 m^2 parallel to the debris flow canyon has been established. As a result of measuring the characteristics

Table 1 In situ properties by constant head permeability and borehole shear tests

Borehole	Depth (m)	Soil type	k (m/s)	c (kPa)	ϕ (°)
B-1	1~2	Colluvium	4.67×10^{-6}	7.5	22.3
B-2	3~4	Colluvium	8.08×10^{-6}	6.9	25.1
	5~6	Weathered rock	1.99×10^{-6}	18.1	27.3
B-3	1~2	Colluvium	3.54×10^{-6}	9.7	25.8
	4~5	Weathered rock	2.24×10^{-7}	15.4	27.6
B-4	1~2	Colluvium	4.45×10^{-6}	7.5	24.7
	3~4	Weathered rock	8.23×10^{-7}	33.8	32.6
B-5	1~2	Colluvium	2.08×10^{-6}	11.2	27.1

Table 2 Properties from laboratory tests

Test pot	Depth (m)	w (%)	PL (%)	LL (%)
TP-1	0.5	18.2	21.2	36.6
TP-1	0.5	14.1	22.3	31.6
TP-3	0.5	32.1	23.7	40.6
TP-4	0.5	15.8	20.9	35.9
TP-5	0.15	28.1	23.8	30.2
TP-6	0.15	30.6	23.0	42.1
Test pot	% Fines	USCS	c (kPa)	ϕ (°)
TP-1	51.9	CL	9.2	21.7
TP-1	28.9	SC	10.9	23.7
TP-3	55.7	CL	11.3	23.1
TP-4	44.4	SC	11.8	22.7
TP-5	28.8	SM	6.6	32.1
TP-6	54.2	CL	5.1	25.4

of vegetation including the diameter at the depth and height of rape seeds, species, roots, the total number of rainforest species was 149, and the survival water having a height of 0.06 m or more was investigated. The plant species in the Umyunsan area are abundant and dominated by Mongolian (Quercus mongolica), which has a ratio of 43%. A dense lower layer of vegetation within a height of 2 m, such as shrubs and herbs with well-branched stems, was rarely distributed in this area. The depth of the root is limited to the surface below 1 m, and the depth of the space is in the range of 1–2 m (Fig. 9).

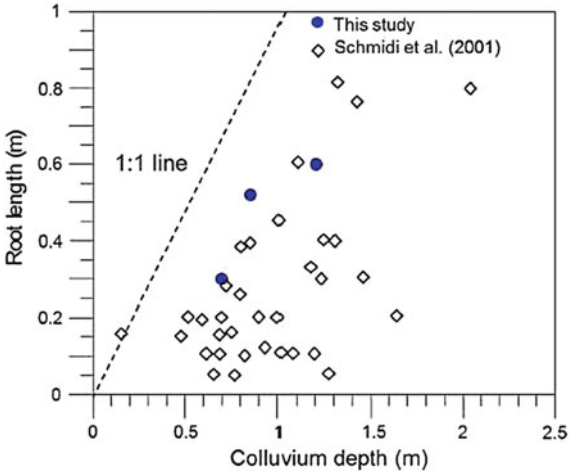

Fig. 9 Relationship between root length and colluvium depth

3.5 Spatial Data Sets

The DEM data shown in Fig. 10a was established from light detection and measurement (LiDAR). It has a spatial resolution of 1 m and grid cells for landslide analysis in the study area and was provided by LiDAR data in 2009. Elevations, the spatial location, and slope angles are included in the spatial data sets. The LiDAR data in 2011 was also used for validation of the incidences of landslides in 2011. The slope aspects data was also established as shown in Fig. 10b. In the study area, the face of the northwest slope was the most dominant (47.1%).

3.6 Analysis Results

3.6.1 Landslides Analysis

A series of landslide analyses were conducted to compare with other physically-based models, such as SINMAP and TRIGRS. The analysis result from YS-Slope model was compared with the landslide inventories in 2011. Soil data from 5 × 5 m grid DEM, detailed survey and field measurements converted from 2009 LiDAR data, and precipitation measured by the KMA Automated Weather Station (AWS) (Korean Society of Metrology 2011). Rainfall infiltration-groundwater flow was calculated by SINMAP model (A) and YS-Slope (B)–(D) in the Raemian watershed (Fig. 11). The wetness index is defined as a ratio of the saturated depth by the soil depth, and the saturated depth is determined based on the results of the rainfall infiltration and the groundwater flow analyses. As shown in Fig. 11a, the analytical results from the

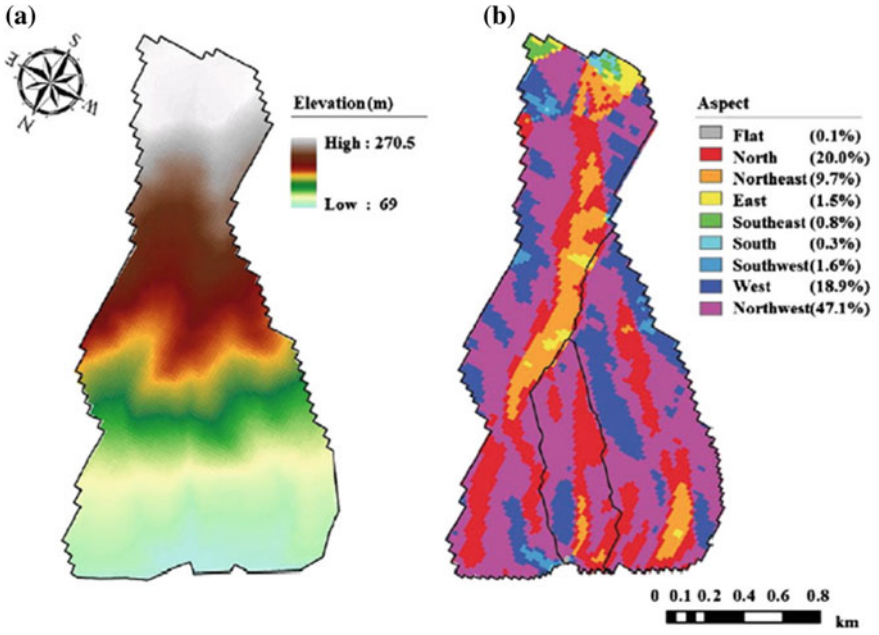

Fig. 10 Digital elevation model and slope direction of the study area

SINMAP shows the surface outflow. However, recharge rates, precipitation periods, and groundwater flow times regarded with the rainfall-infiltration and storage were not considered. The wetness index at the 34th day when the first rainfall was dropped (Fig. 11b) was ranged from 0.0 to 0.5. The wetness index value was maximized over the watershed on the 40th day (Fig. 11c). On July 27, the day landslides occurred, the groundwater rose on the surface, and the wetness index values were ranged from 0.2 to 0.4 in the watershed. The amount of recharged water in each matrix node was analyzed during a 57 day rainfall period (Fig. 12a). Groundwater flow was analyzed for 13 days (57–70 days) after the final rainfall (Fig. 12b). Figure 13a shows the results of the analysis using the YS-Slope model. Landslide locations on the site are indicated by black dots. All safety factors without landslides were less than 0.8. Figure 13b shows the results of slope stability analysis by the TRIGRS model considering the downward motion of the wetting front. The depth of the wet front is estimated to be about 2.0 m. The safety factor for four dots was less than 1.0, and a larger difference between prediction and observation of landslides was obtained.

Based on the field surveys using a GPS and clinometers historical landslide areas were estimated, 0.53% (685 m^2) of the watershed area. The results of numerical analysis using YS-Slope and TRIGRS were compared with the estimated results from the GPS and clinometers (Table 3).

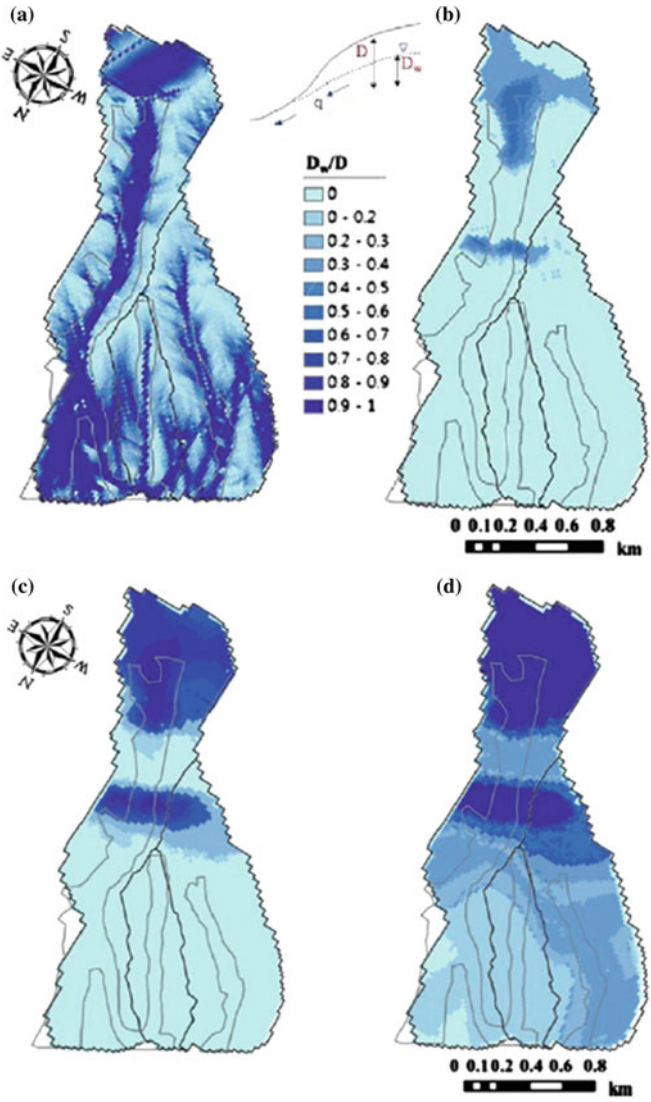

Fig. 11 Analysis results of wetness index (D_w/D)

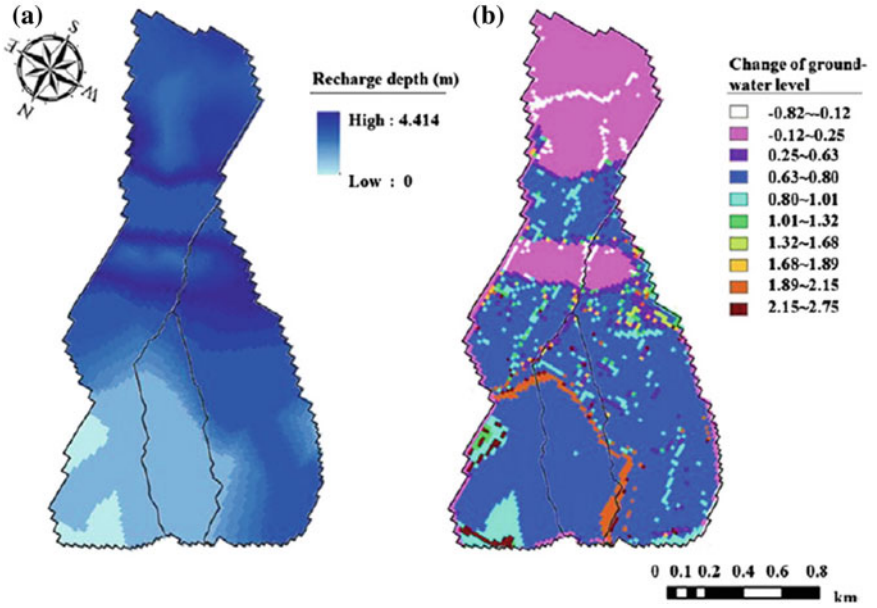

Fig. 12 Recharge and groundwater flows during 57 day

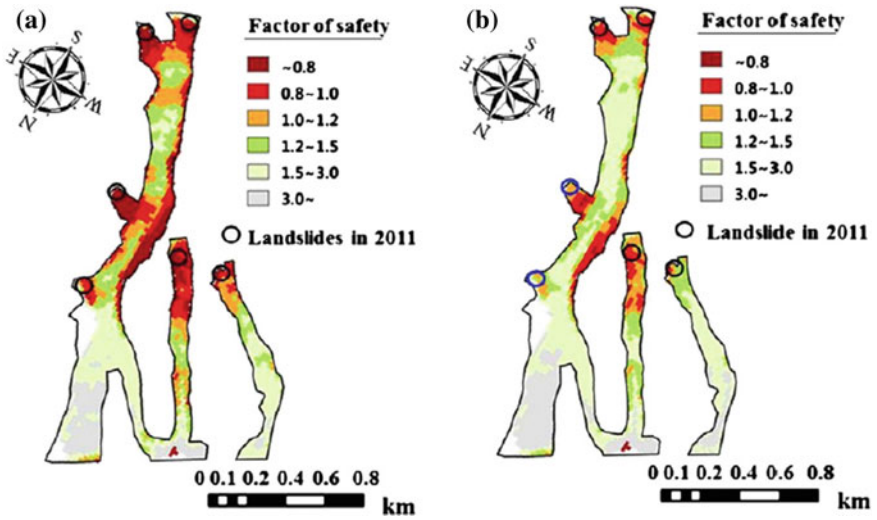

Fig. 13 Analysis results by YS-Slope and TRIGRS

Table 3 Landslides occurrence areas in the study area

	Survey	YS-slope	TRIGRS
Area (m^2)	685	4672	1647
% of area	0.53	3.63	1.28
Landslides	6	6	3
% landslides	–	100	50

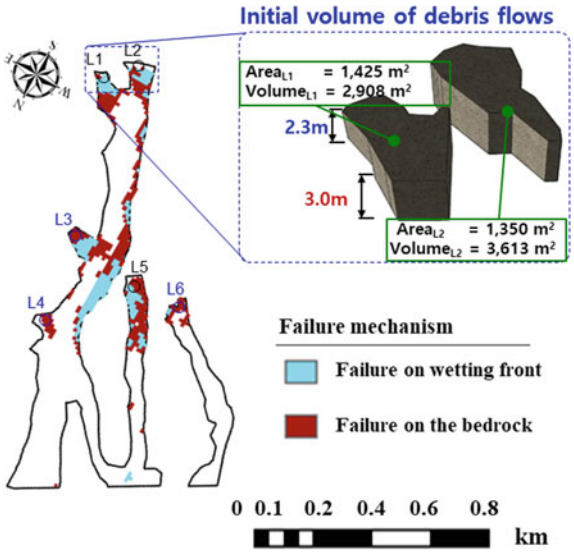

Fig. 14 The estimation of initial volume of debris flows from the result of the landslides analysis

3.6.2 Debris Flows Analysis

Analysis results from the debris flows simulation were compared with the recorded values from the actual events in the study area, volume, inundation area of debris flow and velocity. The initial volume of the debris flows due to landslides near the top of the Raemian basin was estimated as 6500 m^3 (Fig. 14), and debris deposition at the downstream was estimated to be 42,500 m^3. In case of the simulation without the entrainment of soil layers, the initial volume of debris flow reached the bottom of the basin without changing volume. Based on the estimated initial volume of debris flows the result of simulation shows the volume of the debris flows increased by considering the entrainment of soils, and the sediment volume was 40,500 m^3. The actual damage area from the analysis results is shown in Fig. 15. It is shown that the damaged area increase with the entrainment of soils. While debris flows reached the bottom of the watershed, the velocity of the flow front was increased to 25.2 m/s.

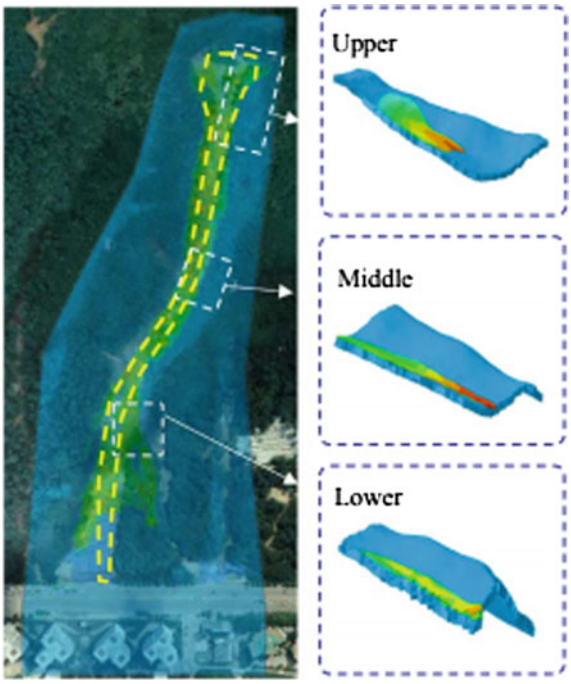

Fig. 15 Inundation area and shape of debris flows

4 Conclusions

In this study, a unified prediction method for landslides and debris flows based on geological and hydrological models are described. An assessment of landslides susceptibility in Umyeonsan (Mt.) and the simulation of debris flows were conducted as an application example of the method. From the analytical results of this study, the significant findings are summarized as follows:

(1) GIS based landslides prediction model (YS-Slope) and ABAQUS/CEL large deformation method were used to predict landslides and debris flows on a test site. Based on the results of landslides analysis, a landslides hazard map was established and initial volume of debris flows were estimated.
(2) The simulation of debris flows were conducted by using the initial volume of debris flows from the landslides analysis. As a result, the unified method to predict landslides and debris flows were used on a case study, and the prediction results have good agreements with historical landslides and debris flows.
(3) The catastrophic debris flow in the study area was used to analyze the topographical characteristics of debris effluent valleys and to investigate various factors controlling landslide and debris flow.

(4) Based on the case study for Umyeonsan (Mt.) landslides, failure behaviors of landslides and debris flows are well predicted by the method described in this study. These procedure can be apply to the prediction of landslides and debris flows of another study area.

Acknowledgements This work was supported by the National Research Foundation of Korea (NRF) grant funded by the Korean government (MSIP) (No. 2011-0030842).

References

Brabb EE (1993) Proposal for worldwide landslide hazard maps. In: Novosad S, Wagner P (eds) Proceedings 7th international conference and field workshop on landslides, Balkema, Rotterdam, pp 15–27

Burrough PA (1986) Principles of geographical information systems for land resources assessment. Claredon Press, Oxford, p 194

Caine N (1980) The rainfall intensity: duration control of shallow landslides and debris flows. Geogr Ann A 62:23–27

Calcaterra D, Santo A (2004) The January 10, 1997 Pozzano landside, Sorrento Peninsula, Italy. Eng Geol 75:181–200

Cotecchia F, Santaloia F, Lollino P, Vitone C, Mitaritonna G (2010) Deterministic landslide hazard assessment at regional scale. In: GeoFlorida 2010: Advances in analysis, modeling & design, pp 3130–3139

Dai FC, Lee CF, Ngai YY (2002) Landslide risk assessment and management: an overview. Eng Geol 64(1):65–87

Green WH, Ampt G (1911) Studies on soil physics, 1. The flow of air and water through soils. J Agric Sci 4:1–24

Guzzetti F, Peruccacci S, Rossi M, Stark CP (2008) The rainfall intensity–duration control of shallow landslides and debris flows: an update. Landslides 5(1):3–17

Hong M, Kim J, Jeong S (2017) Rainfall intensity-duration thresholds for landslide prediction in South Korea by considering the effects of antecedent rainfall. Landslides 1–12

Innes JL (1983) Debris flow. Prog Phys Geogr 7:469–501

Jeong S, Kim Y, Lee JK, Kim J (2015) The 27 July 2011 debris flows at Umyeonsan, Seoul, Korea. Landslides 12(4):799–813

Kim J, Jeong S, Regueiro RA (2012) Instability of partially saturated soil slopes due to alteration of rainfall pattern. Eng Geol 147:28–36

Kim J, Lee K, Jeong S, Kim G (2014) GIS-based prediction method of landslide susceptibility using a rainfall infiltration-groundwater flow model. Eng Geol 182:63–78

Le T, Bae DH (2013) Evaluating the utility of IPSS AR4 GCMs for hydrological application in South Korea. Water Resour Manag 27:3227–3246

Lepore C, Arnone E, Noto LV, Sivandran G, Bras RL (2013) Physically based modeling of rainfall-triggered landslides: a case study in the Luquillo forest, Puerto Rico

Liao Z, Hong Y, Kirschbaum D, Adler RF, Gourley JJ, Wooten R (2011) Evaluation of TRIGRS (transient rainfall infiltration and grid-based regional slope-stability analysis)'s predictive skill for hurricane-triggered landslides: a case study in Macon County, North Carolina. Nat Hazards 58(1):325–339

Mantovani F, Soeters R, Van Westen CJ (1996) Remote sensing techniques for landslide studies and hazard zonation in Europe. Geomorphology 15(3–4):213–225

Mein RG, Larson CL (1973) Modeling infiltration during a steady rain. Water Resour Res 9:384–394

Nilaweera NS, Nutalaya P (1999) Role of tree roots in slope stabilisation. Bull Eng Geol Environ 57(4):337–342

Pardeshi SD, Autade SE, Pardeshi SS (2013) Landslide hazard assessment: recent trends and techniques. SpringerPlus 2(1):523

Simoni S, Zanotti F, Bertoldi G, Rigon R (2008) Modelling the probability of occurrence of shallow landslides and channelized debris flows using GEOtop-FS. Hydrol Process 22(4):532–545

Smit AL, Bengough AG, Engels C, van Noordwijk M, Pellerin S, van de Geijn SC (eds) (2013) Root methods: a handbook. Springer Science & Business Media

Soller D, Duncan I, Ellis G, Giglierano J, Hess R (1999) Proposed guidelines for inclusion of digital map products in the National Geologic Map Database. In: Digital mapping techniques' 99—workshop proceedings. US Geological Survey Open-File Report, pp 99–386

Tarboton DG (1997) A new method for the determination of flow directions and upslope areas in grid digital elevation models. Water Resour Res 33(2):309–319

Van Westen CJ (1993) Application of geographic information systems to landslide hazard zonation

Van Westen CJ (1997) Statistical landslide hazard analysis. ILWIS 2:73–84

Wu W, Sidle RC (1995) A distributed slope stability model for steep forested basins. Water Resour Res 31(8):2097–2110

Design Approach to Rockfall-Related Problems

Marco L. Deana, Giorgio Giacchetti and Minimol Korulla

Abstract Nowadays the correct dimensioning of rockfall mitigation systems is possible with the aid of numerical simulation programs, which study the behavior of a falling rock (actually a series of them) and allows to define the most relevant parameters of the mitigation system. Unfortunately, the input parameters for the numerical simulations are not always easy to define, moreover, the uncertainty linked to some aspects of the problem is very high. For these reasons, experience plays a major role in rockfall design, especially without a worldwide defined approach. Starting from some case histories the authors have defined how to develop a design approach, based on a national standard, which allows the correct dimensioning of a solution, considering the various aspect of the problem and the sources of uncertainty. The goal is to allow the designers' community to approach this kind of project with some formal tools even in the absence of specific experience and to arrive at safe results.

Keywords Rockfall · Rockfall barriers · Rockfall mitigation systems

1 Introduction

The use of rockfall barriers to protect infrastructures like rails, power lines and roads are becoming more and more common as there is an increase in number rockfall problems.

Rockfall barrier offers many positive aspects such as the speed of installation and the possibility to be installed next to the road in comparison with the other rockfall

M. L. Deana (✉)
Officine Maccaferri Spa, 40069 Bologna, Zola Predosa (BO), Italy
e-mail: m.deana@maccaferri.com

G. Giacchetti
Alpigeo Consultant Company, 32100 Belluno, Italy
e-mail: giorgio.giacchetti@alpigeo.it

M. Korulla
Maccaferri Environmental Solutions Pvt. Ltd., Gurugram 122005, India
e-mail: m.korulla@maccaferri.com

R. Sundaram et al. (eds.), *Geotechnics for Transportation Infrastructure*, Lecture Notes in Civil Engineering 28, https://doi.org/10.1007/978-981-13-6701-4_33

mitigation solutions. However, it needs a sound input data and a clear and sound design approach.

While the first of the above issues is linked to the definition of a suitable geological and geotechnical survey, with particular attention to the study of the possible detaching volume of rock and the possible trajectories, the second is a more sensitive subject, which depends on the culture and sensitivity of the designer.

At the moment, there is no international standard dealing with the design of this kind of solution. The most relevant references available are "Guideline for European Technical Approval of Falling Rock Protection Kit" (ETAG 027 2013) which deals with the testing of the barriers and "Italian Standard "Opere di difesa dalla caduta massi—Rockfall Mitigation Measures" (UNI 11211 2012) which deals with the design of this kind of measures.

The knowledge of both these two standards allows the designer to consider all the major parameters relevant for a safe design.

It has to be underlined that rockfall events are highly unpredictable. For this reason, a standard approach, with defined parameters, which takes into account the main causes of unpredictability, can help to have a safer and sounder design.

The last issue to be evaluated is the Risk Analysis. When facing a rockfall mitigation project, a Risk Analysis has to be performed, also a simple one. This is needed to properly evaluate the effectiveness of the design and to identify the most relevant aspects of the specific situation.

The paper describes three case histories showing the design forecast and the feedback about the effectiveness of the design itself.

2 Case History 1—Effect of Large Impacts

In May 2010, rock with an approximate volume of 8 m^3 reached the HWY National Highway A3—Ch 425. The event had no consequence on human life and very low consequence on the infrastructure. The detachment niche was approx. 250 m above the road level. In this area, a vertical cliff crowns the inclined slope at 35° (Giacchetti 2014) (Fig. 1).

The total volume of rock fallen was 1200 m^3. Out of which about 85–90% of the scree arrested the movement within the first 50 m from the toe of the cliff and almost 10–15% of the scree ran further 60 m.

The road administration has required fast and cheap intervention since the alternative route would be ready in a short time. Moreover, in order to avoid interferences with the estates near to the highway, the administration has imposed to design the intervention in the area close the detachment area (Fig. 2).

The geomechanical investigation pointed out that on the detachment niche still there were more than other 1000 m^3 of unstable rock mass. The situation was very dangerous for the workers on the rockfall area as well as for the traffic along the highway.

The remedial measures constituted the followings (Fig. 3):

Fig. 1 Debris close to the detachment area. Down the slope the HYW is shown

Fig. 2 Boulder on the HWY 3

- Draping the unstable cliff by using steel rope panels in order to protect the workers on the lower area and to reduce the energy of further collapses expected from the cliff by wrapping the blocks up.
- Primary rockfall barrier line which is aimed to withstand large multiple impacts.
- Secondary rockfall barrier to be placed just below the main one (Fig. 3) as a backup.

The suitable position of the primary rockfall barrier has been optimized with a rockfall simulation (refer Fig. 4). The rockfall trajectories analysis was adjusted with

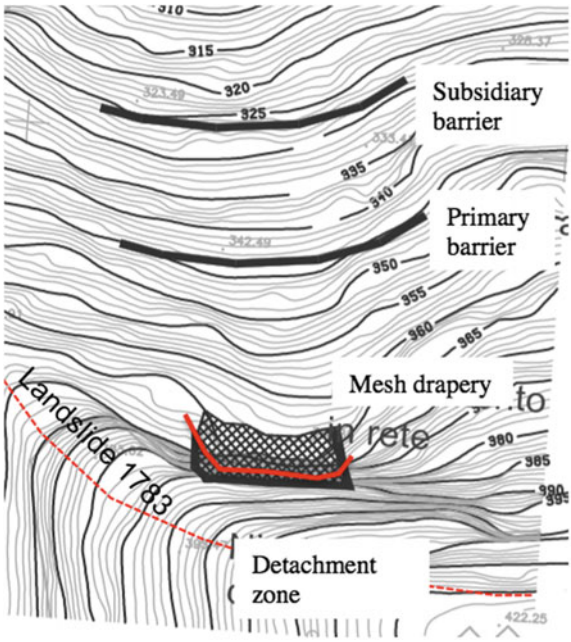

Fig. 3 Plan view of the interventions

a back analysis, considering the distribution of the arrest-points on the slope in the case of blocks with 70 m^3 volume. UNI 11211 design standard, the Maximum Energy Level design criteria and the previous experiences on large impacts were utilized to define the energy capacity, the height and the position of the barrier.

For this project, a 5000 kJ deformable rockfall barrier (highest energy capacity barrier available in the market during that time) with 6 m in height and 70 m length was built. In order to reduce the installation time, and consequently to increase the safety condition for the workers (prone to rockfall risk), the base plates of posts were directly founded on the soil of the slope by means of fully grouted 5 m long 830 MPa vertical steel bars with 26.5 mm diameter and without any concrete plinth (Giacchetti et al. 2015).

After seven months, the unstable rock mass newly collapsed. A fast swarm of large blocks impacted the primary barrier, which was severely damaged but preserved a residual height of 35% (refer Figs. 5 and 6) catching almost all of the blocks.

The only one block which passed over the first barrier was withstood by the second barrier, placed 15 m downslope the first. The total arrested volume estimated was more than 50 m^3 and the largest block had a volume of approx. 7 m^3 (refer Fig. 6).

Further a back analysis of the event was performed. There was an assumption that the largest blocks mainly rolled on the slope and stretched the lower bearing rope of the barrier while other boulders (1–2 m^3 in volume) jumped along the slope and impacted somewhere on the barrier with an energy up to 5000 kJ. It must be

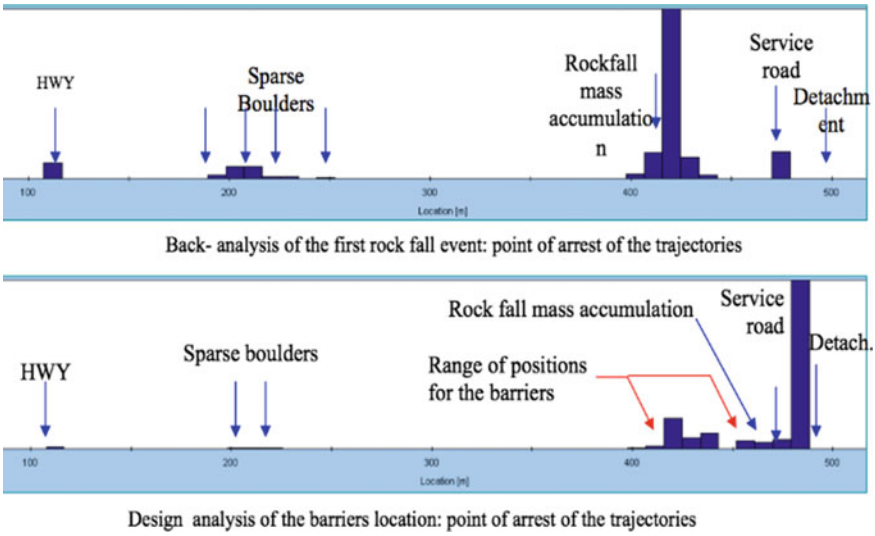

Fig. 4 Diagrams of the arrest point of the trajectories in back analysis (upper diagram) and of design (lower diagram)

highlighted that only one of them was able to pass over the first alignment and reach the second fence. Therefore, the barrier performed systematically as the high residual height allowed it to be effective for a swarm of blocks that generated multiple impacts with total energy far higher that it is tested Maximum Energy Level (Giacchetti et al. 2015).

Besides, a relevant aspect was the performance of the base footplates of the post that allowed a little bit of energy dissipation. Several footplates sunk down and stripped the vertical anchor bars for a length of approx. 0.2 m (Fig. 7). Several bent rods showed the action of a lateral stress, in good accordance with the crash test measurements and the theoretical calculations (Fig. 7). The barrier was designed for an extreme condition that is comparable to a dry flow of debris. The impact energy exceeded the capacity of the barrier that was largely damaged but resisted to the impact. The falling velocity estimated by mean of back analysis was between 9 and 15 m/s, that is 2–3 times larger than the design one (4.5 m/s). The consequences of the impact were the extraordinary deformation in terms of deflections and reduction of the residual height and the sinking of the footplates foundations.

When the impacts are out of the standard conditions (meaning crash test conditions), it is difficult to foresee the behavior of the barriers, but as shown by Case History 1; if the design has been made following an existing standard, the outcome can be safe.

Concerning the foundation, ETAG 027 standard does not consider the connections to the ground as a part of the tested kit, since they must be sized in accordance with the soil characteristic by the designer who has to consider the forces supplied by the

Fig. 5 Massive impact of the "dry flow" of blocks

Fig. 6 Only one block over passed the primary barrier and impacted on the secondary one

Fig. 7 Settlement of the footplates after the impact

manufacturer. Many designers consider such forces, but verify the post foundations in accordance with the standard building codes (e.g., bridges foundations). Hence, the final result is a stiff and massive foundation with concrete plinth or very deep micro-piles that does not admit settlements. The design of the connection to the ground of the base plates of the posts of a rockfall barrier should be approached in a different way than the foundation of a bridge pillar. The performance should be defined, and then, the design shall be made accordingly. Moreover, the settlements of the base plates dissipate energy which helps the main performance of the barrier that is to stop the boulder.

3 Case History 2—Impact with MEL Energy

A small village close to Colle Santa Lucia municipality (Dolomite Alps, Italy) is placed at the foot of a very steep woody slope. At the top, there is an almost vertical rocky cliff of 50–90 m height. The rock mass is constituted by a volcanic complex (sequence of pillow lava and volcanic tuff) which is moderately jointed. The presence of some trees and the ice results in opening of cracks in the rock mass and further release of blocks. However, the weathering process is quite slow and the wood/thick vegetative cover act as a good natural protection, hence, the falling blocks rarely reach the village. The local experience confirms that the real rockfall hazard is related to large blocks that can smash the wood and run down the slope, whereas the trajectories of the small ones are quickly arrested. In 2010, the administration has decided to reduce the risk after an accurate inspection of the slope. The interventions like scaling and draperies were not feasible on the vertical cliff hence a rockfall barrier was scheduled.

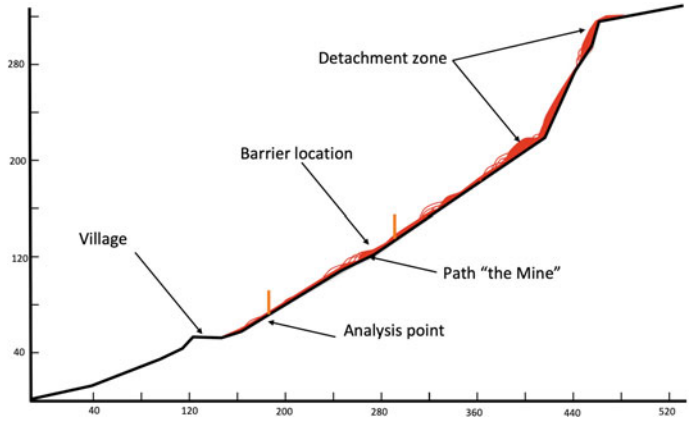

Fig. 8 Trajectories obtained from the analysis

The design of the barrier was carried out by considering a suitable safety margin, reducing the nominal barrier capacity and increasing the impact energy, following the design procedure of the standard UNI 11211. Based on the geomechanical survey on the cliff and the observations on the slope, the size of the design block volume considered was near 3.0 m^3 which included the 97% of the blocks seen on the slope. The rockfall simulation was calibrated considering available information like the traces of impact on the slope and the height of the impacts on the trees close to the cliff toe.

The design velocity at the 95% was 19.8 m/s. The design features required for the barrier was energy capacity of 1775 kJ and nominal height of 2.3 m (refer Fig. 8). Hence, a barrier with a nominal capacity of 2000 kJ, 4.0 m height was chosen (an ETAG027 certified 2000 kJ barrier with 2.5 m height does not exist on the market). Since in the present case there was the probability that the large block was followed by a swarm of smaller blocks, a barrier with a very high residual height to increase the safety margin was required.

Later the 2000 kJ barrier was impacted by 3 main blocks. One of them, of approx. 4 m^3 (approx. 11,000 kg) crashed directly against one of the intermediate posts (refer Fig. 9).

The estimated velocity of impact was (by simulation based on a back analysis) 22 m/s with an energy level next to 2600 kJ. Considering the other 2 blocks, the smallest one (~0.6 m^3) impacted against the interception structure with an energy of ≈400 kJ, while the largest one (~0.8 m^3) impacted on the upper part of the fence, next to the upper longitudinal cable with an estimated energy of 530 kJ. These three boulders developed a total cumulative energy close to 3600 kJ. Considering the swarm of other secondary blocks, the total amount of energy was probably higher than 5000 kJ. Despite the event's high energy level, compared to the maximum energy absorption capacity of the barrier, it was able to withstand all the boulders. Actually, only one block had the same energy level than the barrier's maximum, whereas

Fig. 9 Effect of the impact against the post of a 2000 kJ barrier

the other ones had energy level a little bit smaller than the Service Energy Level and moreover impacted on the screen on positions distant one from the other. The structure was able to maintain a considerable residual height of 30-35% even though one post was directly impacted by the largest block (Fig. 10). The deformation of the mesh, after the 3 impacts, was close to 6 m (Sassa et al. 2014).

The foundations of the post were composed of 4 rods. The footplates of the barrier were installed directly on the slope surface, without any concrete base-plinths, but just a very thin level of concrete aimed at getting a regular base. The impact was very strong as it exceeded the nominal barrier capacity, with a sequence of multiple impacts and moreover with a hit on an intermediate post.

After the impact, the rod bars and the footplate of the impacted post got lifted from the ground by approx. 0.3–0.4 m. The bending of the steel bars was due to the action of lateral shear stresses (Fig. 9). In any case, these foundations allowed dissipation of the energy on the stiffest portion of the barrier, helping the overall performance (Sassa et al. 2014).

Despite of that, the good design approach allowed to withstand impacts higher than the MEL of the barrier, even if the barriers were severely damaged. The good performance in terms of residual height was really appreciated since it prevented the swarm of blocks to overpass the screen.

Fig. 10 The barrier was able to preserve 30–35% of residual height despite the large impact

4 Case History 3—Impact with SEL Energy

The village of Pietracamela (central Apennins, Italy) lies below a wide moderately steep woody slope. Its top is crowned by an irregular vertical rock face (Fig. 11) constituted by a massive conglomeratic formation. The morphology is quite irregular with several unstable pillars. In order to protect the village with a cost-effective solution, the administration has asked a consultant to define a solution. The consultant decided for a rockfall barrier to be placed 30–50 m below the toe of the vertical face and some minor intervention of consolidation on the vertical slope. Looking at the size of the potentially unstable blocks and at the past experiences, the final design foresaw a barrier 7 m high with nominal capacity 5000 kJ (Fig. 11).

In November 2009, only 2 months after the installation of the barriers, while the work on the slope was still going on, a large block fallen down from the rock slope.

The size of the fallen block was 2.5–3.0 m^3 and the impact energy was estimated 1500 kJ. The detachment niche was 35 m above the barrier itself and the potential energy was estimated 2800 kJ. The motion of the boulder was of free fall for a short section of the vertical slope and of rolling with small jumps with negligible

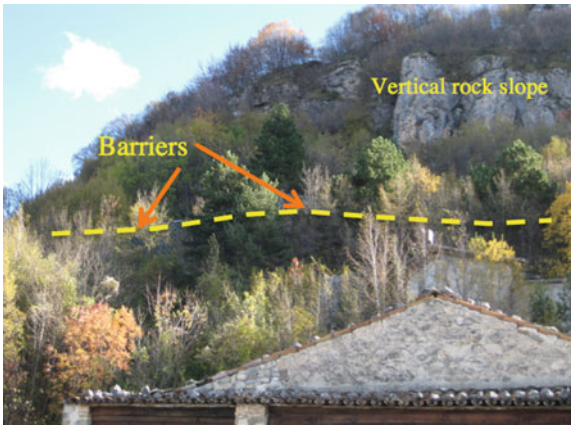

Fig. 11 Vertical rock face with above the village. The barriers are located in the middle of the wood (yellow line)

energy reduction on the inclined slope. The impact happened on lower part of the screen barrier (Fig. 12). The barrier did not suffer large damages, only there was stretching of some ring of the screen in the impact area which was close to 3.5 m after the deflection. The brake systems were engaged just for some centimeters and their substitution was not required. Post foundations and anchors of bracing cables did not show any stretching or settlements. The rehabilitation of the barrier was comprised only in the demolition of the boulder and the arrangement on site of the fragments in a stable way.

The case shows that the maintenance cost becomes negligible if the barriers work with its Service Energy Level. Obviously, this means that the chosen barrier must have capacity equals or greater than three times the design energy.

5 Lessons Learned

Rockfall events are highly unpredictable, for the variability of the involved parameters as well as for the knowledge of the single event. The review of the three projects highlights some important aspects of the design of rockfall barriers.

1. The presence of uncertainties needs to be assessed, and the designer has to deal with them.
2. A good survey activity (topographic, geomechanical, geotechnical) can help to minimize and manage the uncertainties.
3. The use of amplifying and reduction coefficients can help to manage the uncertainty and to help to deal with the risk.

Fig. 12 The fallen block was 2.5–3.0 m^3, and impact energy 1500 kJ, close to the Service Energy Level (SEL) of the barrier

4. The definition of energy levels can help to minimize the cost of the mitigation measures in the lifetime of the material.
5. The investigation of the performance of the barrier and of the related works (post foundations) leads to a better design.

It has to be underlined that the performance of the barriers is known only by the tests, their behavior in natural environment will be different.

Case History 1 and 2 show that the use of an approach which considers amplifying and reduction factors brings to safe and reliable solutions, while Case History 3 shows that the reference to Energy Levels lower than the maximum of the barrier can minimize the maintenance cost and can optimize the barrier performance. In particular, Case History 1 helps to understand how a precise definition of the parameters, using back analysis, is a key factor to properly understand the on-site situation.

6 Risk and RockFall

To properly design a Rockfall Mitigation Solution, it should be mandatory to perform a Risk Analysis. A proper assessment of the risk level is unavoidable if a proper design is the final goal of the process, where "proper design" means not only technically valid but also cost-effective.

Rockfall events are highly unpredictable, and the magnitude of the design event often can be only estimated. For this reason, this kind of projects is often referred to as "Hazard Mitigation Solution," to underline this fact that there is a high grade of uncertainty in some parts of the design process. For this reason, when facing a Rockfall Mitigation Measure, it becomes mandatory to perform a Risk Analysis, even a very simple one, to estimate the uncertainty and the risk to be mitigated.

From the beginning of the 1980s', a number of Rock Hazard Rating Systems (RHRS) were developed, the first being the one developed by the Oregon Department of Transportation (1984), afterward which was modified many times to match various needs. This method does not provide a sound method of assessment of risk as it is intended today. Especially, it does not provide a method to evaluate the risk reduction due to mitigation measures.

Risk has become a most investigated topic, even though nowadays different analytical approaches are available, the one to be used has to be chosen depending on the situation and the data available.

6.1 Definitions and Terminology

The following terminology is accepted worldwide:

- Risk (R): quantitative value of the consequences of the occurrence of the event.
- Hazard (H): the likelihood that a particular (dangerous) event may occur.
- Vulnerability (V): the degree of loss within the area affected by a hazard.
- Element at Risk (value of) (E): the total value of all threatened items, including human lives, infrastructures, buildings, economic activities, etc.

Hazard can be expressed as

$$R = H \times V \times E \tag{1}$$

All the terms of Eq. (1) can be expressed both in a quantitative way and in a qualitative way. In Eq. (1), H is the probability of occurrence of the event which poses the Risk, V is the vulnerability, and E is the value. Equation (1) is also helpful when written in this way because it can be used to underline the terms affected by the mitigation measure hence to evaluate the effectiveness of the proposed measures.

6.2 Risk Analysis and Assessment

To properly use Eq. (1), it is important to have a sound assessment of the values of the variables, which means that the data collection about the element at risk and their value, about the Vulnerability of the elements at risk and about the assessment of the spatial and temporal probabilities for the elements at risk, must be reliable and extensive.

It has to be understood that when possible numeric approaches have to be performed, but it is not always possible to have sound numerical data or to ascribe correct values to the required variables. In these cases, a qualitative approach is possible, leading to results depicted in Fig. 13.

If a quantitative approach has been followed the same table (Fig. 13), it should show numbers (Currency) instead of qualitative descriptions.

Once the risk level is defined, it is possible to define if it is acceptable or not and to define whether a mitigation measure is required or not. Once the Risk Analysis and assessment is performed, decisions have to be taken (Mikos et Al. 2017; Hungr et Al. 2005).

Typically the following choices are available:

i. Accept the risk
ii. Avoid the risk
iii. Reduce the likelihood of Rockfall
iv. Reduces the consequences of Rockfall
v. Transfer the risk

The first two options are the extreme: either do nothing (Risk acceptance) or choose another solutions. Option (iii) is related to Active Measures (like scaling, rock bolting, the use of steel meshes) while option (iv) is related to Passive Measures (rockfall barriers, embankments). The last option is related to the use of insurance or development of regulatory controls like hazard mapping.

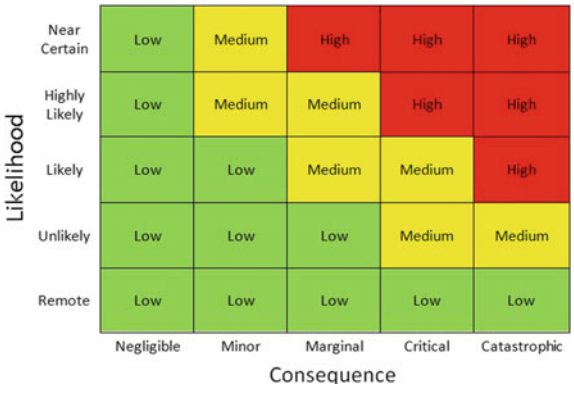

Fig. 13 Qualitative risk rating matrix

It is now clear that in Eq. (1), the different terms are influenced by different mitigation measures:

– H (related to probability of occurrence) is affected by Active Measures, which prevent the detachment of rock volumes from the slope;
– V (related to the rock reaching the target) is affected by Passive Measures, which prevent the rock volume to reach the target;
– E is related to the residual risk, which can be estimated only by running again the Risk Analysis with the presence of the mitigation measures.

7 International Standards

Once the Risk Analysis and Assessment is performed, and the need of a Remedial Measure is clear, a good design is required. Most of the times good judgment of experienced designers is the most used approach, but it cannot be enough, even if in this field the experience plays a role. Standards do exist to help in the choice of the correct solution and to help the designer to properly input correct values of the most important parameters, taking into account the randomness which is a characteristic of this phenomena.

There are two relevant international standards which are at the moment used as worldwide reference viz., "Guideline for European Technical Approval of Falling Rock Protection Kit" (ETAG 027 2013) and "Rockfall Mitigation Measures" (UNI 11211-1/2/3/4 2012). The first one is a European Standard and it is mandatory for the producer to get the CE Marking. It deals with the definition of the procedure for the testing of rockfall barriers. It is important because in the definition of the testing methodology it introduces some concepts which can influence the design. The second one (which is an Italian Standard) deals with the design of all kind of mitigation measures, from bolting to barriers, to sheds and it is intended as a guideline for designers who approach this specific field.

7.1 Guideline for European Technical Approval of Falling Rock Protection Kit (ETAG027)

As specified it is a product standard which means that it regards mainly the product and how it is made, characterized and tested, in order to get the CE marking (mandatory in Europe for a product to be used in public works). The standard defines the parts of the barriers, how they have to be tested and the performances which need to be recorded. The standard also defines the minimum values of some specific performance that the barrier has to reach in order to get the certification. In the description of the testing methodology, it defines two different energy levels for the test:

- MEL (Maximum Energy Level)

- SEL (Service Energy Level).

The two levels are defined in a way that:

$$\text{MEL} = 3 \cdot \text{SEL} \tag{2}$$

The performances required at the two energy levels are different. At the Service Energy Level, two impacts are foreseen, the barrier has to stop the impacting block and after the impact the barrier must have a residual height not lower than 70% of the initial height. Also between the two impacts, the barrier cannot be maintained. At MEL impact, the barrier has to stop the block. After the MEL impact, the residual height will be measured and a class will be assigned to the barrier depending on the residual height viz., (a) Class A: for residual height more than 50% than the initial height (b) Class B: for residual height between 30 and 50% of the initial height and (c) Class C: for residual height less than 30% of the initial height.

The performance about the residual height after SEL test is required because the Service Energy Level is thought to be associated to an event which can happen in the life of the barrier and which should not require the maintenance of the barrier. The Maximum Energy Level is an impact which the barrier can withstand but after which it has to be maintained. Following this approach, the residual height after the MEL test is a sort of index about how far from the collapse the barrier is; somehow it can be read (not literally and for sure without a concrete data) as the capacity of overperforming the certified energy level.

ETAG027 is a valid reference to understand how a barrier works under impact and which can be the relevant parameters and performance characterizing a barrier.

7.2 Rockfall Mitigation Measures (UNI 11211)

UNI 11211 is a design standard which means that it is intended to help designer to properly approach the design of Rockfall Mitigation Measures, starting from the beginning.

In the first parts (1–3), it deals with definitions and recommendations about the preliminary studies, in order to get all the needed data, while part 4 deals with the actual design of the protection measures.

The main contribution of this norm to the field of designing rockfall measures is the introduction on partial safety factors (that is coefficients for increasing the actions and coefficients for reducing the resistances) to be applied to the main parameters characterizing the event.

Regarding the barriers, the norm assumes (as it is done worldwide) as the main parameter the Energy of the impacting rock (Wyllie 2015; Turner and Schuster 2012).

In general terms, the Energy of a falling rock volume is:

$$E = \frac{1}{2} \cdot m_{\text{d}} \cdot v_{\text{d}}^2 + \frac{1}{2} \cdot I_{\text{d}} \cdot \omega_{\text{d}}^2 \tag{3}$$

where

– m_d is the design impacting mass
– v_d is the design impact velocity
– I_d is the design Moment of Inertia
– ω_d is the design rotational velocity.

Usually, the rotational contribution to the total energy is neglected because it is not that big and it is difficult to evaluate.

Hence, Eq. (3) becomes

$$E = \frac{1}{2} \cdot m_d \cdot v_d^2 \tag{4}$$

To properly design a Mitigation Measure—such as a rockfall barrier—the parameters have to be defined, moreover in their definition should be taken into account the soundness of their definition.

8 Proposed Approach

The approach proposed is the one illustrated in UNI 11211-4. The main feature of the standard is to introduce partial safety coefficient to multiply the characteristic values of the parameters in order to get the design values; moreover, the values of the partial coefficient are related to the accuracy of the geological or geotechnical survey done to define the parameters; the same is done for the definition of the minimum height of the barrier. Afterward it uses the SEL and MEL as defined in ETAG027 to outline two different approaches for the definition of the Energy Level of the barrier.

8.1 Actions on the Barrier

The general approach is

$$x_d = \prod_i \gamma_i \cdot x_k \tag{5}$$

Using this formulation and defining the parameter x_k, which is the characteristic value of the parameter, and the safety coefficients γ_i (there can be many different coefficients for a single parameter) allows to arrive at the design value of every single input parameter.

The parameters to be defined are the one present in the equation of the kinetic energy (4), m and v, but since m is the product of Volume and Volume Weight the parameters are:

- V_k: Characteristic volume of the impacting Rock
- γ_k: Characteristic volume weight
- v_k: Characteristic value of the impact velocity.

The way these characteristic values are defined has an influence on the values of the safety coefficients.

Moreover also the height of the barrier has to be defined and also for the height a safety is introduced, in the following way:

$$h_{\mathrm{d}} = h_{\mathrm{tr}} + f_{\mathrm{min}} \tag{6}$$

where

In the following paragraphs the way to impute the values of the safety coefficients will be explained.

8.1.1 Velocity

Design Velocity is defined as

$$v_{\mathrm{d}} = \gamma_{\mathrm{F}} \cdot v_k \tag{7}$$

where v_k is the velocity coming from numerical trajectory analysis, while γ_{f} is defined as

$$\gamma_{\mathrm{F}} = \gamma_{\mathrm{Tr}} \cdot \gamma_{\mathrm{Dp}} \tag{8}$$

where γ_{Tr} is the coefficient which takes into consideration the reliability of the numerical analysis, in particular, the bouncing coefficients attributed to the surface of the slope. The values vary between 1.02 for coefficients defined from back analysis to 1.10 for coefficients defined from tables or bibliography. The values may seem to be small, but they have to be squared, and it is important to note that a good back analysis gives a lot of useful information.

8.1.2 Mass

The design mass of the impacting block is defined as

$$m_{\mathrm{d}} = (\mathrm{Vol}_{\mathrm{b}} \cdot \gamma_k) \cdot \gamma_m \tag{9}$$

where

- $\mathrm{Vol}_{\mathrm{b}}$: is the characteristic volume of the impacting rock
- γ_k: is the characteristic value for the volume weight of the rock

- γ_m: is the safety coefficient, expressed as

$$\gamma_m = \gamma_{\text{VolF1}} \cdot \gamma_\gamma \tag{10}$$

where:

- γ_{VolF1}: is a coefficient related to the precision of the topographic survey, and varies between 1.02 (for accurate surveys) and 1.10 for situation where the topographic survey is not specific for the project;
- γ_γ is a coefficient related to the definition of the volume weight, which is usually accurate, so the coefficient is usually set to 1.00; it can have higher values if there are uncertainties about the type of rock or its weight.

8.1.3 Energy

With the definition of the partial safety coefficients, it is now possible to calculate the kinetic energy of the impacting rock.

Usually, it is calculated by performing a numerical simulation with a dedicated software (many commercial software are available). In which topography (3D and 2D software are available), the bouncing coefficients of the slope and the design volume are the inputs parameters and as result it gives a series of trajectories (stochastically generated) obtained with small variations of the main parameters (Fig. 14). Once the energy and height have been defined, the design of the barrier is done. The final step is the choice of the barrier.

The next step is to define if the Design Energy E_d is to be compared with the MEL or with the SEL

For each simulation usually several hundreds of events are created, and for each point of the slope the velocity and the Maximum Bouncing height is plotted, in this way it is possible to study the value of the most important parameter in each point of the slope.

Cumulative curves, for the section of interest, can be plotted, showing the distribution of the inspected parameter (Fig. 15).

The standard suggests using the 95% percentile of the cumulated curve as characteristic value v_k, since the use of maximum value could be too much overdesigning.

Once the velocity v_k and the mass m_k have been defined, it is possible to calculate the energy as:

$$E_\text{c} = \frac{1}{2} \cdot \gamma_{\text{VolF1}} \cdot \gamma_\gamma m_k \cdot \left(\gamma_{\text{Tr}} \cdot \gamma_{\text{Dp}} \cdot v_k\right)^2 \tag{11}$$

The value calculated as shown above can be amplified depending on the importance of the target:

$$E_\text{d} = I \cdot E_\text{c} \tag{12}$$

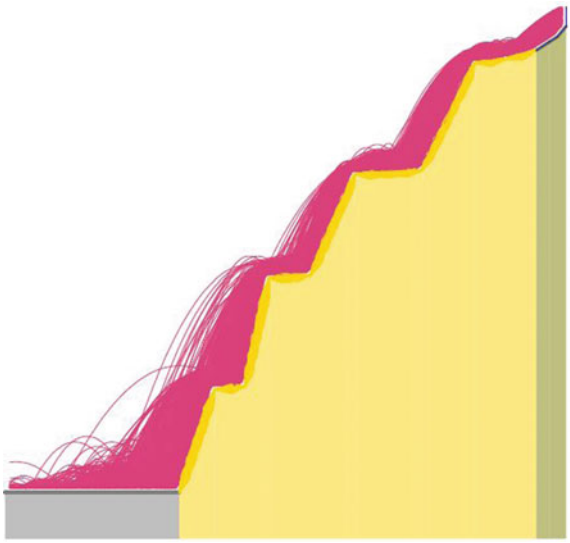

Fig. 14 Example of numerical simulation, trajectories

I is the factor of importance, and its possible values are:

- $I = 1.00$ for target whose damage causes small economic consequences, with damages easy to repair;
- $I = 1.05$ for target whose damage causes significant economic consequences, with damages easy to repair;
- $I = 1.10$ for target whose damage causes significant economic losses and damages difficult to repair (popular places, places of small artistic value);
- $I = 1.20$ for target whose damage causes very significant economic losses and extensive damages, threat for human lives (strategic structures, very popular places, places of high artistic value).

Equation (12) gives the design actions to be considered.

8.1.4 Barrier Height

To complete the design the height of the barrier has to be defined. Starting from the calculation of bouncing height h_{tr}, the design height h_d is defined as for Eq. (6):

$$h_d = h_{tr} + f_{min} \tag{6}$$

where:

- h_{tr} is the height resulting from the numerical simulation;
- f_{min} is the safety, which is the greater between;

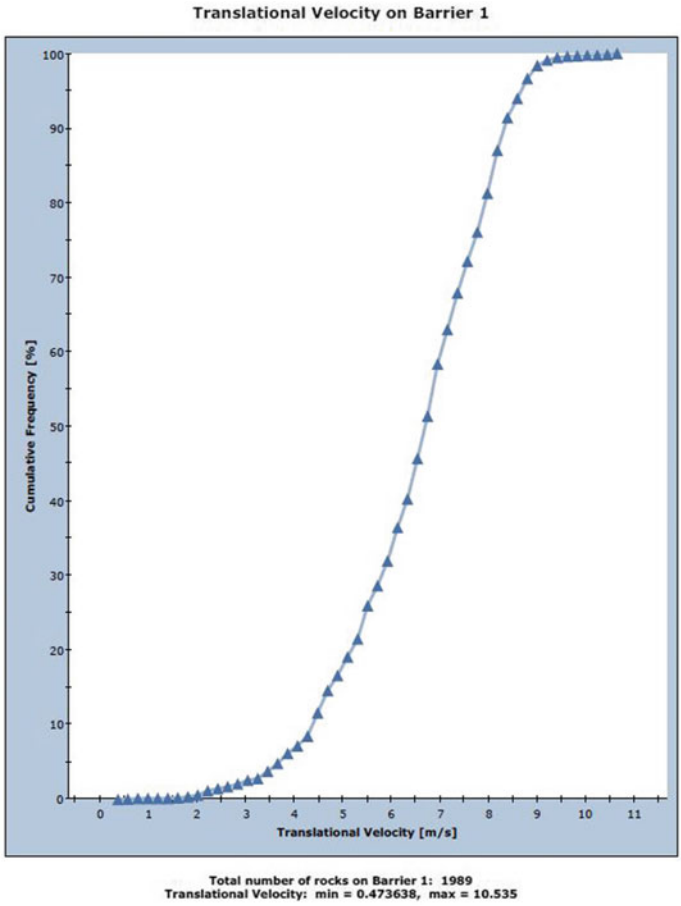

Fig. 15 Example of cumulated curve—velocities

- 0.5 m;
- Radius of the impacting rock.

8.2 Design Check

Once that the Design Energy (E_d) and Height (h_d) have been designed, the correct barrier must be chosen. At this stage, the decision has to be done about the reference Energy Level (as per ETAG 027).

If the scenario is to choose the MEL as reference Energy Level which means that the barrier has to withstand the impact but most probably it will have to be

maintained afterward. Choosing MEL as reference energy level means also that our Design Energy Level will be next to the maximum event that the barrier can withstand.

The other scenario is to have SEL as reference Energy Level the, which means that the design impact must be under the 33% of the Maximum Energy Level of the barrier. In this case, after the design impact the barrier is not supposed to need any maintenance.

For the above reasons, the standard foresees an amplifying factor, γ_E, to be used when comparing the Design Energy (E_d) and the Energy Level of the barrier (E_b) to be selected:

$$E_d \leq \frac{E_b}{\gamma_E} \tag{13}$$

where γ_E can have the following values:

- $\gamma_E = 1.20$ for project developed having the MEL as reference Energy Level of the barrier;
- $\gamma_E = 1.00$ for project developed having the SEL as reference Energy Level of the barrier.

The standard foresees also special cases: when for any reason if there is a need to use a barrier shorter than the standard field tested barrier, then, there are 2 options:

1. Use $\gamma_E = 1.20$ and design for two parallel alignment;
2. Use one alignment and use $\gamma_E = 2.00$.

8.3 Definition of the Alignment

As prescribed in ETAG027, during the test should be conducted in the center field (out of three the impact) and the lateral fields should be out of the possible impact zone, when possible.

Two consecutive alignments should have an overlap of at least one field, to avoid any unpredictable trajectory to pass through.

The last issue is to deal with the proximity of the barrier to infrastructures or buildings. ETAG027 prescribes the recording of the maximum elongation during the impact, d_b at the time of testing. The minimum distance between the alignment of the barrier and another object should be

$$d_A = d_b \cdot \gamma_d \tag{11}$$

where γ_d can have the following values:

- $\gamma_d = 1.30$ if the project was developed having the MEL as reference energy level;
- $\gamma_d = 1.00$ if the project was developed having the SEL as reference energy level.

In this way, it is possible to have also a planimetric setting of the barrier.

8.4 Overall Considerations

The use of both the cited standards, with a full comprehension of the consequences of all the aspects, can be the key factor for an effective design of a rockfall barrier.

It is possible to relate Eq. 1

$$R = H \times V \times E \tag{1}$$

to the type of solution chosen. Since a rockfall barrier is a passive solution, which intercepts the rock after it has started the motion along the slope, it will influence the term V, it is possible to compare the overall risk with or without the mitigation measure.

It is also possible to evaluate the opportunity to spend money in survey activity running the dimensioning with different values of the safety coefficients and arriving to different solution for the barrier resulting different costs.

A correct design activity starts with a Risk Analysis, together with the survey activity, to arrive at the choice of the solution and its design. The various phases are the following.

1. On-site visit to assess the situation and to interview the Owner and collection of the relevant information
2. Preliminary Risk Analysis
3. Design and execution of the survey activities
4. Imputation of the values of the relevant parameters
5. Execution of the Complete Risk Analysis, together with the draft design
6. Choice of the solution
7. Running of the numerical simulations
8. Final Design.

9 Conclusions

Rockfall is an almost unpredictable event, in which a lot of parameters, play a major role which even more difficult to define. For this reason, it is not a most studied and standardized subject. The correct dimensioning of mitigation measures such as rockfall barriers implies the reduction of the risk for infrastructure and people.

At the moment, there are few relevant standards, the most known are

- ETAG 027 as a testing standard
- UNI 11211-4 as a design standard.

A correct use of these standards allows the designer to properly approach the dimensioning of a rockfall barrier, considering both the uncertainty in the definition of the parameters and the risk involved in the event of a rock overrunning the barrier.

The correct imputation of the numerical value of the safety coefficients is dependent from the accuracy of the survey conducted to define the main parameters which mean that the result will consider the accuracy (that means lowering the uncertainties) put in the design.

The variation of the combination of the entire safety coefficient considered with their minimum or maximum value is in the range of 1.34–2.55.

References

EOTA, ETAG 027 (2013) Guideline for European technical approval of rockfall protection kits. EOTA

Giacchetti G, Grimod A, Peila D (2015) Strategy for the foundation design of rock-fall barriers. In: Lollino G, Dr. Giordan D, Crosta GB, Corominas J, Azzam R, Wasowski J, Sciarra N (eds) Engineering geology for society and territory, vol 2. Springer International Publishing

Hungr O, Fell R, Couture R, Eberthardt E (2005) Landslide risk management. In: Proceedings of the international conference on landslide risk management, Vancouver, Canada, Taylor & Francis, London

Mikos M, Tiwari B, Yin Y, Sassa K (2017) Advancing culture of living with landslides, vol 2–4. Springer International Publishing

Sassa K, Canuti P, Yin Y (2014) Landslide science for a safer geo-environment, vol 1. Springer International Publication

Turner AK, Schuster RL (2012) Rockfall, characterization and control. TRB

UNI 11211-4 (2012) Rockfall protective measures. UNI

Wyllie DC (2015) Rock fall engineering. CRC Press, Taylor & Francis Group

A Comparison of 1D and 2D Spatial Variability in Probabilistic Slope Stability Analysis

Rubi Chakraborty and Arindam Dey

Abstract Slope stability analysis is a highly challenging task in geotechnical engineering as the influence of uncertainty involved in geotechnical properties on failure behavior of slopes is inevitable. Traditional deterministic slope stability approach, based on a single factor of safety (FoS) parameter, cannot explicitly encounter the uncertainties involved in geotechnical properties and failure mechanism, leading to erroneous results of slope stability. Hence, slope stability practice is highly persuadable to probabilistic treatment, which allows quantification of the uncertainty and rationally integrating the same into the analysis. The present study investigates the influence of inherent spatial variation of soil domain in probabilistic slope stability analysis. To accomplish this, a hypothetical slope is analyzed, considering 1D spatial variation, with the aid of GeoStudio 2007, using Morgenstern-Price limit equilibrium method (LEM) coupled with Monte Carlo simulation (MCS). The results are compared with those of Griffiths et al. (2007), wherein 2D random field for soil shear strength was considered and the analysis was carried out with the help of random finite element method (RFEM). The influence of correlation lengths on the probabilities of failure is compared. The results reveal that the probability of failure highly depends on spatial variation of soil property in both the methods. When correlation length is small, the failure probability is essentially zero; failure probability increases rapidly for intermediate correlation lengths, and for large correlation lengths, the failure probability becomes constant. It is also found that combining LEM with one-dimensional random field gives lower probabilities of failure than RFEM, as RFEM is more efficient in simulating the field uncertainty. Moreover, RFEM can search and identify the weakest path through the soil domain for the failure to occur, whereas LEM presumes a predefined failure plane.

R. Chakraborty (✉)
Department of Civil Engineering, National Institute of Technology, Meghalaya 793003, India
e-mail: rubi.rc.nit@gmail.com

A. Dey
Department of Civil Engineering, Indian Institute of Technology Guwahati, Guwahati 781039, India
e-mail: arindamdeyiitg16@gmail.com

R. Sundaram et al. (eds.), *Geotechnics for Transportation Infrastructure*, Lecture Notes in Civil Engineering 28, https://doi.org/10.1007/978-981-13-6701-4_34

Keywords Factor of safety · Probability of failure · Correlation length · Monte Carlo simulation · Random finite element method

1 Introduction

Several issues of uncertainty in slope stability analysis originate mainly due to geological anomalies, inherent spatial variability of soil properties, lack of data availability, uncertainty in potential failure surface, simplifying approximations adopted in geotechnical modeling as well as human errors in design and construction. Soil structure is the result of a complex combination of various geological, environmental, and physical–chemical processes. Soil heterogeneity is classified into two main classes: lithological heterogeneity (described as the presence of a different lithology within a uniform soil domain or one soil layer overlying another layer of soil) and inherent spatial soil variability (variation of soil properties from one point to another in space within one layer). The latter uncertainty originates due to different depositional conditions and loading histories (Elkateb et al. 2003, Lloret-Cabot et al. 2014). A one-dimensional random field showing the cone tip resistance measured during a cone penetration test (CPT) is shown in Fig. 1 as an example of spatial variation of soil. Among all the uncertainties, soil heterogeneity plays a crucial role in assessment of failure mechanism of slope and this paper mainly focuses on the influence of inherent spatial variability of failure probability of a soil slope. The conventional way to tackle with spatial variability in geotechnical engineering was to depend upon high safety factor, experience, and engineering judgement. However, Morgenstern (2000) reported several case histories where relying entirely on high safety factor lead to poor predictions in 70% of the cases. Therefore, it has been realized that more reliable tools to incorporate geotechnical uncertainty are necessary. In order to incorporate uncertainty in geotechnical practice, limit equilibrium analysis in combination with Monte Carlo simulation (MCS) technique was introduced. Later on, the stochastic finite element method was introduced in combination with MCS to incorporate soil spatial variability into a numerical analysis.

The contemporary studies on spatial variability in geotechnical engineering mainly focuses on the inherent soil variability within a homogeneous soil layer (Griffiths and Fenton 2000; Griffiths et al. 2004; Ji et al. 2011; Hicks et al. 2014; Li et al. 2014; Jiang et al. 2014; Li et al. 2015; Jamshidi and Alaie 2015). Ji et al. (2011) observed that failure probability can be overestimated when spatial variation of soil is not considered; i.e., a slope will be predicted comparatively safer when spatial variability is ignored. Allahverdizadeh et al. (2015) stated that there exists a critical correlation length value which results in an unconservative design due to underestimation of failure probability. This critical spatial correlation length resulting in maximum failure probability was shown to $0.5H$ to H, where H is the height of the slope. Other researchers (e.g., Griffiths and Fenton 2000) have also reported this critical spatial correlation length. Chakraborty and Dey (2017) showed that there exists a threshold correlation length beyond which the probability of failure

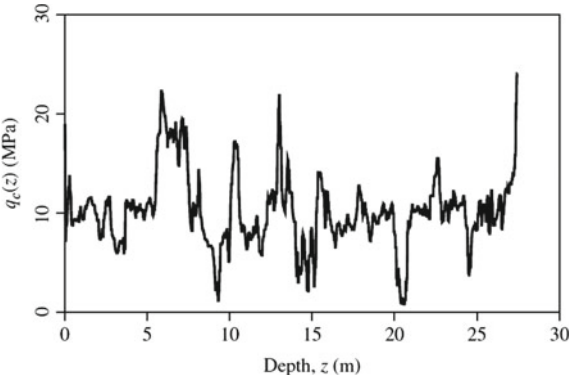

Fig. 1 Variation of cone tip resistance (q_c) with depth using a cone penetrometer (Griffiths and Fenton 2007)

is underestimated by conventional probabilistic analysis without considering spatial variation. In this paper, a hypothetical slope is analyzed, considering 1D spatial variation of soil properties, with the aid of GeoStudio 2007. The Morgenstern-Price limit equilibrium method (LEM) is coupled with MCS technique to assess the probability of slope failure for different spatial variabilities of soil domain. The results are compared with those of Griffiths et al. (2007), where 2D random field for soil shear strength was considered and analyzed with the help of random finite element method (RFEM). The probabilities of failure for different correlation lengths are compared. It is found that combining LEM with one-dimensional random field underestimates the probability of failure in comparison with that obtained from RFEM.

2 LEM-Based Probabilistic Approach Considering 1D Spatial Variation

A 2(H):1(V) slope having 60 m length and 15 m height (Fig. 2) is analyzed considering 1D spatial variation with the aid of GeoStudio 2007, using Morgenstern-Price limit equilibrium method (LEM) coupled with Monte Carlo simulation (MCS). The mean cohesion (c) of 5 kPa and angle of internal friction (ϕ) of 20° are considered with a standard deviation of 1.5 kPa and 6.22°, respectively. A correlation coefficient of 0.5 is considered between c and ϕ. The soil properties are taken as per Griffiths et al. (2007) for further comparison. In a probabilistic approach, soil properties are considered to be random variables and the failure probability of (P_f) is computed. To execute this, the Monte Carlo simulation (MCS) method is generally preferred for its simplicity and ease of computation. MCS simply generates a series of trial values of the random variables and evaluates the *limit state function* for each trial value. A *limit state function,* generally denoted by $g(x)$, is a mathematical function that determines whether the system is in failure or not. The limit state function is universally (though arbitrarily) defined such that $g(x) < 0$ indicates a failed state and $g(x) > 0$ indicates

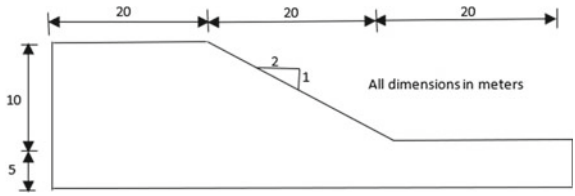

Fig. 2 Slope geometry considered in the present study

a safe state. The number of failures that occur among all the realizations of random variables is counted, and the probability of failure is approximated as

$$P_{\mathrm{f}} = \frac{n_{\mathrm{f}}}{N} \tag{1}$$

where n_{f} is the number of failures and N is the total number of realizations.

2.1 Basic Probability Principles

This section briefs the basic probability concepts required for the present study. A continuous random variable, for example, undrained shear strength, S, can be expressed by probability density function (PDF), usually denoted as $f_s(s)$. Normal or Gaussian distribution function is generally used in geotechnical problem. Figure 3a illustrates a PDF for normally distributed random variable undrained shear strength S. The equation for the normal probability density function is

$$f_s(s) = \frac{1}{\sqrt{2\pi}\sigma_s} \mathrm{e}^{-(s-\mu_s)/2\sigma_s^2} \tag{2}$$

where μ_s is the mean value of S, and σ_s is the standard deviation of s.

Normal distribution is most commonly used to characterize geotechnical properties, because the sum of random variables tends to be in normal distribution as per the central limit theorem. For example, it is a common practice to characterize the distribution of cohesion using the normal distribution, as the cohesive strength of soil is defined as the sum of electro-chemical interactions at its molecular level. However, the disadvantage of using normal distribution is that it allows negative values. A simple technique to avoid this limitation is to characterize geotechnical properties by a nonnegative distribution, such as lognormal distributions.

The cumulative distribution function is related to the probability density function (Fig. 3b), usually denoted as $F_s(s)$. The cumulative distribution function (CDF) gives the probability that the random variable S having a value less than s, i.e.,

$$P(S < s) = F_s(s) \tag{3}$$

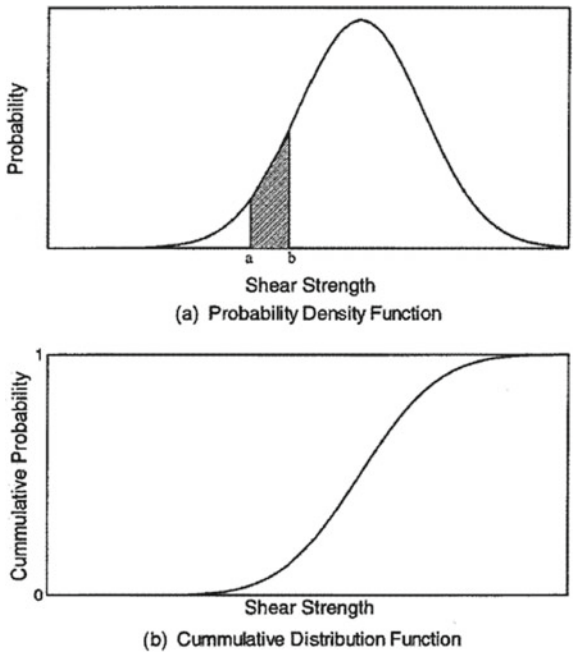

Fig. 3 **a**. Probability density function; **b**. cumulative density function (Kitch 1994)

While the PDF or CDF leads to a complete characterization of a random variable, it is convenient to have some simpler descriptors for random variables. The most obvious characteristic of a random variable is the mean, denoted by

$$\mu_s = \int_{-\infty}^{\infty} s f_s(\mathrm{s}) \mathrm{d}s \tag{4}$$

The mean, also known as the expected value of a random variable, is denoted by $E[S]$. Further, the next most important characteristic is the variability of a random variable; i.e., how much does the value of the random variable differ from its mean. The measure of the average deviation is called the variance, σ_s^2, and is defined as

$$\sigma_s^2 = E[(s - \mu_s)^2] = \int_{-\infty}^{\infty} (s - \mu_s)^2 f_s(s) \mathrm{d}s \tag{5}$$

The square root of the variance is known as the standard deviation, denoted as σ_s, and is thus defined as $\sigma_s = \sqrt{\sigma_s^2}$.

While comparing two different random variables with different mean values, it is often required to normalize the standard deviation of a random variable by its mean value. This quantity is called the coefficient of variation, (COV) defined as

$$\text{COV} = \frac{\sigma_s}{\mu_s} \tag{6}$$

Most geotechnical engineering problems are functions of more than one variable. For example, the drained shear strength of a soil is a function of both cohesion, c', and the friction angle, ϕ'. If the cohesion (c') and friction angle (ϕ') are both random variables, then the joint probability distribution should be considered for a particular range of soil cohesion and friction angle values. When two random variables are considered together, there is often a statistical relationship between them. The correlation between two random variables is measured by the covariance of the two variables. Given two random variables, X and Y, the covariance of X and Y, denoted as Cov [X, Y], is defined as

$$\text{Cov}[X, Y] = E[(X - \mu_X)(Y - \mu_Y)] \tag{7}$$

As with the variance, there is a normalized version of the covariance, which is called the correlation coefficient, ρ, and is defined as

$$\rho_{X,Y} = \frac{\text{Cov}[X, Y]}{\sigma_X \sigma_Y} \tag{8}$$

where σ_X and σ_Y are standard deviations of random variable X and Y, respectively.

Therefore, based on the above discussion, in this study, a lognormal PDF is assigned for soil shear strength parameters (cohesion, c, and angle of internal friction,ϕ) with a correlation coefficient of 0.5 having a one-dimensional spatial variation. In this study, it is assumed that the soil property varies only in horizontal direction within the slope soil domain and the vertical spatial variation is ignored. To simulate 1D random field in SLOPE/W 2007, the soil shear strength properties (cohesion, c, and angle of internal friction,ϕ) are sampled at specified distances to evaluate the probabilities of failure for different correlation lengths. The pattern of spatial variability in soil property is aptly represented by the correlation distance or scale of fluctuation (Vanmarcke 1977), which is further described in detail in Sect. 2.2.

2.2 Scale of Fluctuation or Correlation Length

The scale of fluctuation (SOF) represents the spatial range over which the soil property shows a relatively strong correlation in space. An approximate method of estimating the SOF is presented by Vanmarcke (1977) as

$$\delta_v = 0.8\overline{d} \tag{9}$$

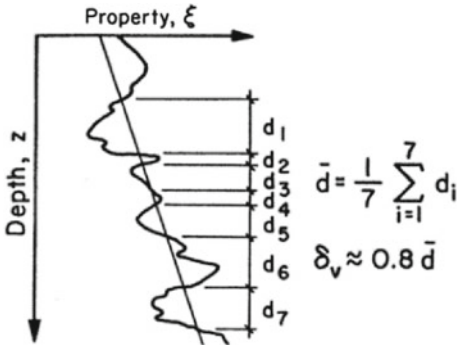

Fig. 4 Estimation of vertical scale of fluctuation (Vanmarcke 1977)

where δ_v is the vertical scale of fluctuation and $\overline{d}$ is the average distance between intersections of the fluctuating component with its trend line, as shown in Fig. 4.

A large correlation length reflects smooth variation of properties, whereas a small length means erratic variability as shown in Fig. 5. Estimation of correlation distance is illustrated in DeGroot (1996) as well as Lacasse and Nadim (1996). In this study to generate 1D random field in horizontal direction, soil properties are sampled for specified distances to estimate failure probability for different correlation lengths. When soil domain of 60 m length is sampled for specified distance, for example 25 m, there will be two complete sampling distances of 25 m and a partial sampling distance of 10 m. A partial sampling distance is considered to be correlated with the immediate preceding sampling section. The correlation coefficient between two soil sections can be estimated as follows (Vanmarcke 1983):

$$\rho(\Delta Z, \Delta Z') = \frac{Z_0^2\Gamma(Z_0) - Z_1^2\Gamma(Z_1) + Z_2^2\Gamma(Z_2) - Z_3^2\Gamma(Z_3)}{2\Delta Z\Delta Z[\Gamma(\Delta Z)\Gamma(\Delta Z')]^{0.5}} \tag{10}$$

where

$\Delta Z, \Delta Z' =$ the length between two sections
$Z_0 =$ the distance between the two sections,
$Z_1 = \Delta Z + Z_0$,
$Z_2 = \Delta Z + Z_0 + \Delta Z'$
$Z_3 = \Delta Z' + Z_0$ and
Γ is a dimensionless variance function and can be approximated as (Vanmarcke 1983):

$$\Gamma(Z) = 1.0 \text{ when } Z \leq \delta, \text{ and}$$
$$\Gamma(Z) = \frac{\delta}{Z} \text{ when } Z > \delta \tag{11}$$

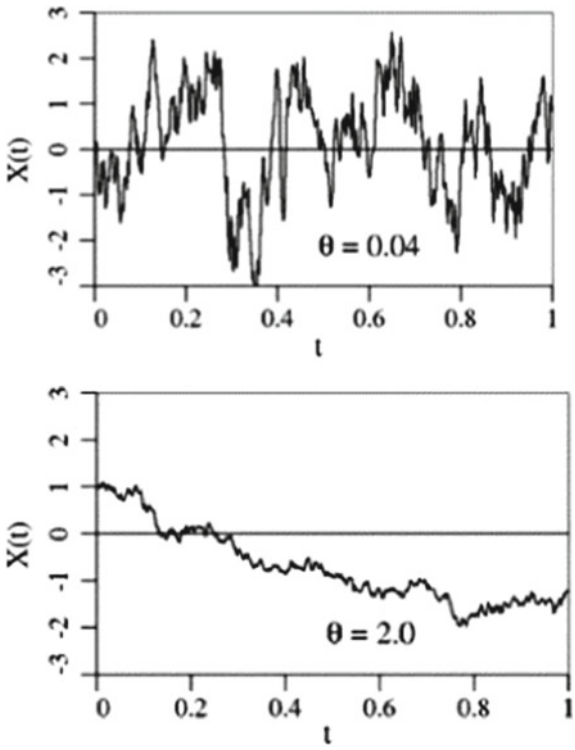

Fig. 5 Simulation of *X(t)* for different scales of fluctuation (Griffiths and Fenton 2007)

Here, δ is the scale of fluctuation. To incorporate spatial variation of soil property in SLOPE/W, the value of scale of fluctuation is decided by the user-defined desired sampling distance along the slip surface.

A legitimate criticism of these LEM-based probabilistic approaches, however, is that they are not capable to encounter spatial variation in the soil domain properly and are inextricably linking with conventional slope stability approaches. To overcome these disadvantages, a more realistic and advanced approach called the random finite element method (RFEM, Fenton and Griffiths 1993) is recommended, wherein the random field theory is combined with the deterministic finite element analysis, as described in Sect. 3.

3 Random Finite Element Method (RFEM)

A more advanced method of probabilistic analysis in geotechnical engineering for the incorporation of spatial variability of soil, called the 'random finite element method' (RFEM), (Fenton and Griffiths, 1993; Paice 1997; Griffiths and Fenton 2000), was developed in 1990s. RFEM is a completely different approach for failure probability

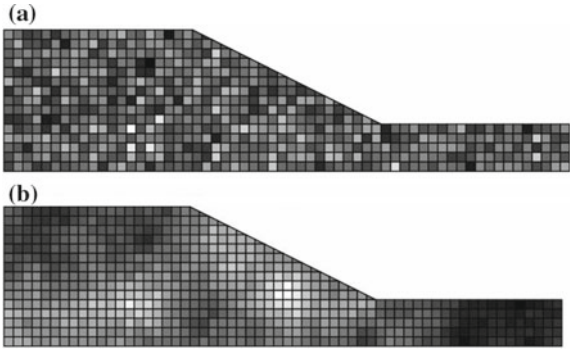

Fig. 6 A typical 2D random filed for slope with **a**. Small correlation length; **b** high correlation length (Griffiths et al. 2007)

prediction. In RFEM, a soil property is considered as a random variable at any location within a soil domain since the soil property is an uncertain quantity at every point of the soil domain. The pattern of variability of soil is characterized by the correlation distance or scale of fluctuation as described in Sect. 2.2. A typical two-dimensional random field with low and high correlation length is shown in Fig. 6.

Generally, all engineering properties are the result of local average of some sort. Uncertainty of the average shear strength along the slip surface is a more accurate measure of uncertainty than the strength at discreet locations. Because failure in slope is more probable when the average shear strength along the failure surface is less than the applied shear stress rather than because of the presence of some local weak zones. Therefore, geotechnical engineers are much more interested in studying the behavior of random field considering the average properties of the field, rather than the properties at discreet locations. Consider the moving local average defined as

$$X_T(t) = \frac{1}{T} \int_{t-T/2}^{t+T/2} X(\xi) \mathrm{d}\xi \tag{12}$$

where $X_T(t)$ is the local average of $X(t)$ over a window of width T centered at t (Fig. 7). The upper plot (in the figure) is averaged over the moving window length T to get the lower plot. Local averaging reduces the contribution of the high-frequency components and thus attenuates the variance. The variance of any property at their discrete points is always less than the variance spatially averaged over a particular domain. As the extent of the length (T, over which the soil property being averaged) increases, the corresponding variance decreases.

In RFEM, each random variable is characterized by a PDF. RFEM also correlates the random variables at adjoining locations. A joint probability distribution function characterizes the set of random variables at all locations within the soil domain, which are considered as a random field. RFEM combines nonlinear finite element methods with random field theory. It essentially overlays a random field upon a

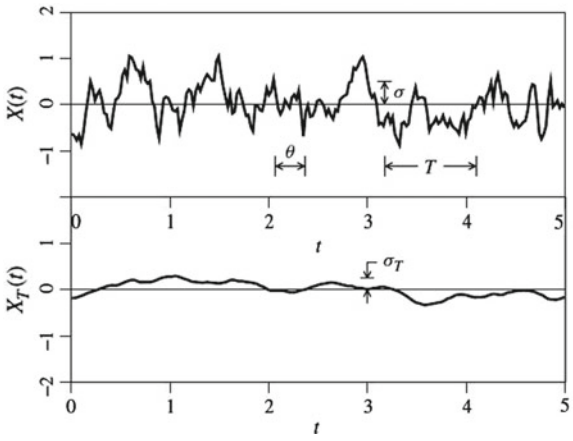

Fig. 7 Effect of local averaging on variance (Fenton and Griffiths 2008)

finite element mesh, resulting in each mesh behaving as a random variable. RFEM completely accounts for spatial correlation and averaging. It does not presume the shape or position of the critical slip surface of failure as it can identify the actual weakest failure path through the soil mass.

If the mean and covariance of a random field vary with position, mathematically it is difficult to estimate the governing joint PDF from the real data. Therefore, further simplifications of stationary or statistically homogeneous random field are required. A stationary random field signifies that the joint PDF governing the random field is invariant in space; i.e., the CDF, mean, and variance are constant at any location within the random field. Rather than their absolute locations within the random field, the covariance of two random variables depends only on their separation distance. Under the simplifying assumptions of stationary random field, a random field can be aptly characterized if the mean, variance, and their rate of variation in space are known. The rate of variation can be characterized by the second moment of the joint PDF governing the random field, equivalently using covariance function, variance function, or spectral density function.

4 Results and Discussions

In this study, the failure probabilities of the hypothetical slope considering 1D random field, based on traditional probabilistic approach, are compared with the probabilities of failure considering 2D random field (Griffiths et al. 2007) for different correlation lengths (Fig. 8). It is observed that combining LEM with one-dimensional random fields underestimates failure probabilities of slope structure as compared to RFEM. Because the 2D random field can simulate field uncertainty better than 1D spatial variation, hence increasing the probability of failure. Moreover, LEM method presumes the failure mechanism using deterministic methods (using Morgenstern-Price

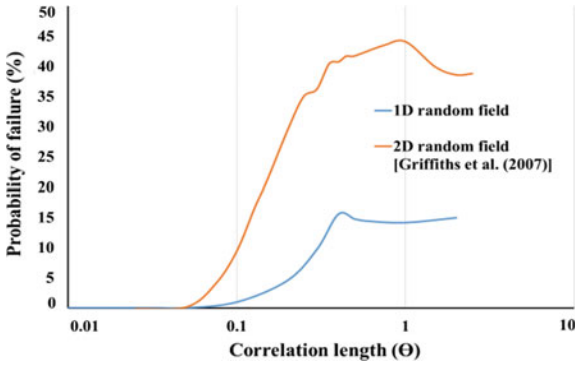

Fig. 8 Comparison of effect of 1D and 2D spatial variation of soil on the probability of failure

method in the present study), whereas the RFEM allows the failure surface to originate through the weakest path in the soil layers in a particular realization. When correlation length is small, the failure probability is essentially zero; failure probability increases rapidly for intermediate correlation lengths, and for large correlation lengths, the failure probability becomes constant. The local averaging gets maximized for a very small value of correlation length. Therefore, for small correlation length, the soil properties tend to take their mean values, and for each realization, the soil domain becomes essentially homogeneous. Considering the mean values of soil properties result in a safe slope (having FoS greater than unity), the failure probability is always zero. When the correlation length is very large, the soil for the entire domain becomes strongly correlated. Hence, within each realization, the slope becomes essentially homogeneous, but different from one realization to the next. Whereas, the slope is not homogeneous for intermediate values of correlation length. RFEM is able to search out the weakest path through the soil mass, and hence, the anomalies, such as locations of weak areas, govern the failure probability.

5 Conclusions

The paper highlights the contrast between the results obtained by traditional LEM-based probabilistic approach and a more advanced random finite element method (RFEM) for stability analysis of slope. Both the methods evaluate the failure probability of slope as opposed to the deterministic FoS measure of slope safety. It is noticed from the results that the probability of failure highly depends on spatial variation of soil property, as failure probability changes with different correlation lengths in both the methods. However, depending on the value of the correlation length, the methods show a significant difference in results. It is observed that the LEM probabilistic approach considering one-dimensional random fields underestimates the probabilities of failure in comparison with RFEM. The reason behind this is 2D random field can simulate field uncertainty better than 1D spatial variation,

hence increasing the probability of failure. Moreover, LEM method presumes the failure mechanism by the means of deterministic methods, while the RFEM allows the failure plane to develop through the weakest path in the soil layers. Therefore, traditional LEM-based probabilistic approach leads to unconservative predictions of slope failure probability and may end up producing erroneous design solutions. Hence, the incorporation of spatial variation properly with the aid of more advanced techniques (RFEM) is recommended.

References

Allahverdizadeh P, Griffiths DV, Fenton GA (2015) The random finite element method (RFEM) in probabilistic slope stability analysis with consideration of spatial variability of soil properties. IFCEE 2015. American Society of Civil Engineers, Reston, VA, pp 1946–1955

Chakraborty R, Dey A (2017) Importance of spatial variability on probabilistic slope stability. In: Indian geotechnical conference IGC 2017, IIT Guwahati, Guwahati, India, 14–16 December 2017

DeGroot DJ (1996) Analyzing spatial variability of in situ soil properties. In: Uncertainty in the geologic environment : from theory to practice: proceedings of Uncertainty '96, pp. 210–238

Elkateb T, Chalaturnyk R, Robertson PK (2003) An overview of soil heterogeneity: quantification and implications on geotechnical field problems. Can Geotech J 40(1):1–15

Fenton GA, Griffiths DV (1993) Statistics of block conductivity through a simple bounded stochastic medium. Water Resour Res 29(6):1825–1830

Fenton GA, Griffiths DV (2008) Risk assessment in geotechnical engineering. John Wiley & Sons, Inc, Hoboken, NJ, USA

Griffiths DV, Fenton GA (2000) Influence of soil strength spatial variability on the stability of an undrained clay slope by finite elements. Slope stability 2000. American Society of Civil Engineers, Reston, VA, pp 184–193

Griffiths DV, Fenton GA (2007) Probabilistic methods in geotechnical engineering. CISM courses and lectures, vol 491

Griffiths DV, Fenton GA, Denavit MD (2007) Traditional and advanced probabilistic slope stability analysis. Probabilistic applications in geotechnical engineering. American Society of Civil Engineers, Reston, VA, pp 1–10

Griffiths DV, Asce F, Fenton GA, Asce M (2004) Probabilistic slope stability analysis by finite elements, 130: 507–518

Hicks MA, Nuttall JD, Chen J (2014) Influence of heterogeneity on 3D slope reliability and failure consequence. Comput Geotech 61:198–208

Jamshidi Chenari R, Alaie R (2015) Effects of anisotropy in correlation structure on the stability of an undrained clay slope. Georisk Assess Manage Risk Engineered Syst Geohazards 9(2):109–123

Jiang SH, Li DQ, Cao ZJ, Zhou CB, Phoon KK (2014) Efficient system reliability analysis of slope stability in spatially variable soils using monte carlo simulation. J Geotech Geoenviron Eng 141(2):1–13

Ji J, Liao HJ, Low BK (2011) Modeling 2-D spatial variation in slope reliability analysis using interpolated autocorrelations. Comput Geotech 40:135–146

Kitch W (1994) Deterministic and probabilistic analyses of reinforced soil slopes. Ph.D. dissertation, University of Texas, Austin, TX

Lacasse S, Nadim F (1996) Uncertainties in characterizing soil properties. In: Uncertainty in the Geologic Environment: from Theory to Practice, pp. 49–75

Li DQ, Qi XH, Phoon KK, Zhang LM, Zhou CB (2014) Effect of spatially variable shear strength parameters with linearly increasing mean trend on reliability of infinite slopes. Struct Saf 49:45–55

Li DQ, Jiang SH, Cao ZJ, Zhou W, Zhou CB, Zhang LM (2015) A multiple response-surface method for slope reliability analysis considering spatial variability of soil properties. Eng Geol 187:60–72
Lloret-Cabot M, Fenton GA, Hicks MA (2014) On the estimation of scale of fluctuation in geostatistics. Georisk Assess Manage Risk Eng Syst Geohazards 8(2):129–140
Morgenstern NR (2000) Performance in geotechnical practice—FCCN. In: The inaugural Lumb lecture. Hong Kong Institution of Engineers
Paice GM (1997) Finite element analysis of stochastic soils
Vanmarcke E (1977) Probabilistic modeling of soil profiles. J Geotech Eng Div
Vanmarcke E (1983) Random fields, analysis and synthesis. MIT Press, Cambridge

Analysis of Effect of Reinforcement on Stability of Very Steep Slopes

Akshay Kumar Jha, Madhav Madhira and G. V. N. Reddy

Abstract The present paper analyses reinforced steep slope to optimize the length of geosynthetic reinforcement from the face or near end of the slope with respect to its location, length and combination of multiple layers of reinforcement to obtain the desired minimum factor of safety. In case of walls, the reinforcement needs to extend up to and be tied to wall face due to functional requirement. But in case of slopes, no such requirement exists and hence curtailment of reinforcement from face end is feasible. The effect of providing geosynthetic layer in shifting the critical slip circle has been studied. The interaction between layers of reinforcement has been identified, modelled and quantified. The study facilitates understanding the mechanics of reinforcing slopes which is very different from that of reinforced soil walls.

Keywords Reinforcement · Optimization of length · Critical slip circle · Reinforced steep slope · Geosynthetics · Interaction

1 Introduction

The analysis of earth slopes is one of the oldest geotechnical engineering problems that engineers have been dealing with using various techniques. The methods of analyses can be classified as limit equilibrium methods, finite element method based on c and ϕ reduction, finite element modelling/finite difference method, combination of FEM and LEM, limit analysis (LA) method, etc. Geosynthetic reinforcement

A. K. Jha (✉)
Indian Railways, Hyderabad, India
e-mail: akshayghungru@gmail.com

M. Madhira
JNTU Hyderabad, Hyderabad, India
e-mail: madhavmr@gmail.com

G. V. N. Reddy
JNTUH, Hyderabad, India
e-mail: gvnreddy@jntuh.ac.in

R. Sundaram et al. (eds.), *Geotechnics for Transportation Infrastructure*, Lecture Notes in Civil Engineering 28, https://doi.org/10.1007/978-981-13-6701-4_35

of earth slope results in reducing the land requirement and preservation of natural resources (land and backfill requirements) apart from time and cost. Designing geosynthetic-reinforced slope with minimum length of geosynthetics leads to further economy.

Jewell et al. (1985), Bonparte et al. (1987), Verduin and Holtz (1989) present design methods for earth slopes reinforced with geotextiles or/and geogrids using LEM assuming different types of failure surfaces such as circular or/and bilinear wedges. Jewell et al. (1985) used limit equilibrium analysis and local stress calculation for design of reinforced slope. Rowe and Soderman (1985) present a method for estimating the short-term stability of reinforced embankment incorporating soil—structure interaction derived from FEM. (Leshchinsky and Reinschmidt 1985; Leshchinsky and Boedeker 1989) present an approach based on limit equilibrium and variational extremization of factor of safety multilayer-reinforced slope. Schneider and Holtz (1986) present a design procedure for slopes reinforced with geotextiles and geogrids for a bilinear surface of sliding and considering pore water pressures and the initial stress conditions in the slope. Jewell (1991) presented revised design charts for steep slopes valid for all polymer reinforcement materials. These revised charts lead to savings of the order of 20–30% in reinforcement quantity. Leshchinsky (1992) and (Leshchinsky et al. 1995) used log spiral failure mechanism to determine the required reinforcement long-term strength. (Baker and Klein 2004a, b) modified the top-down approach of (Leshchinsky 1992) to obtain the reinforcement force needed for a prescribed factor of safety everywhere within the reinforced mass. Han and Leshchinsky (2006) present a general analytical framework for designing flexible-reinforced earth structures, i.e. walls and slopes. Leshchinsky et al. (2010) presented a limit equilibrium methodology to determine the unfactored global geosynthetic strength required to ensure sufficient internal stability in reinforced earth structures. Leshchinsky et al. (2014) introduced a limit state design framework for geosynthetic-reinforced slopes and walls. Leshchinsky and Ambauen (2015) presented use of upper bound limit analysis (LA) in conjunction with discretization procedure known as discontinuity layout optimization (DLO) for comparison with rigorous LE Methods. Gao et al. (2016) in their study considered three-dimensional effects on reinforced earth structure stability and determined the required strength and length of reinforcement using limit analysis approach. The three-dimensional effects are more significant for the minimum required length of reinforcement than for the minimum required tensile strength.

None of the above approaches optimizes the length of geosynthetics by curtailing the same from the slope face. The paper detail analysis carried out to optimize the length of reinforcement from the face end of steep slope and also identifies interaction between layers of reinforcement and its effect on overall stability.

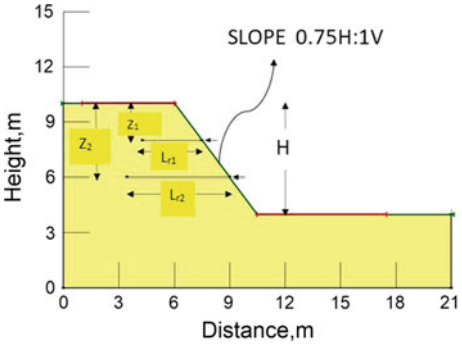

Fig. 1 Problem definition

2 Problem Definition

An embankment of height, H, of 6.0 m with relatively steep side slopes of 0.75 H to 1 V vertical is considered in (Fig. 1). The embankment and foundation soil have cohesion, c, of 5 kPa, unit weight, γ, of 18 kN/m^3 and angle of shearing resistance, ϕ, of 23°. The geotextile reinforcement used has a nominal adhesion, c_a, of 3 kPa, angle of interface friction between soil and reinforcement, δ, of 18° and ultimate tensile strength, T_{ult}, of 250 kN/m. All the stability analyses have been carried out using Morgenstern–Price method.

3 Stability Analysis

3.1 Unreinforced Slope

Unreinforced embankments of heights 2, 3, 4, 5 and 6 m have been analysed using SLOPE/W of Geostudio 2004 version and FS_{min} obtained as 1.48, 1.27, 1.0, 0.902 and 0.831, respectively.

3.2 Reinforced Slope

6 m High unreinforced slope is not stable for heights greater than 2.0 m as FS_{min} is much lower than desirable value of 1.5. To study the interaction of reinforcement and the slope, the slope reinforced with single layer of geosynthetic at $Z_2 = 4.0$ m was analysed. Length of reinforcement has been optimized on lines as detailed in Jha and Madhav (2015). Reinforcement length is optimized by curtailing reinforcement length from the non-face end to get FS_{min} of 1.5. *A new and original contribution of this work is optimization of reinforcement length from the face end by curtailing*

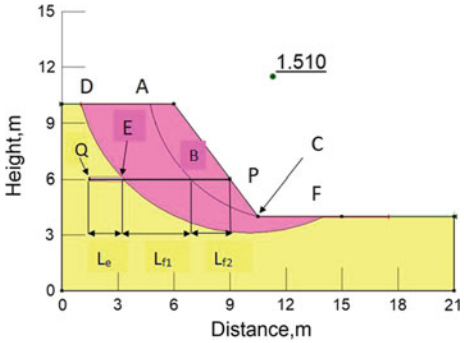

Fig. 2 Slope with one layer of reinforcement at depth 4.0 m—conventional design

Table 1 Factors of safety for slope with reinforcement at 4.0 m

Sn.	Length of reinforcement (L_r), m	Reinforcement load (F_r) (kN/m)	FS_{min}
1	7.10	50.59	1.452
2	7.20	53.61	1.467
3	7.25	55.15	1.474
4	7.50	62.63	1.510
5	7.60	65.21	1.524

its length without sacrificing stability, that is still maintaining the minimum factor of safety of 1.5. Optimization of the total length of reinforcement leads to FS_{min} of 1.51 for $L_{r2} = 7.50$ m (Fig. 2). *The search mechanism for locating critical slip circle includes all possible slip surfaces including those that pass through toe and deep slip circles passing through base*. The critical slip circle with a single layer of reinforcement at 4.0 m depth having minimum safety is depicted in Fig. 2.

It should be noted that one of the effects of inclusion of reinforcement in embankment soil is to shift the critical slip circle from ABC to DEF. This shift of the critical circle increases the factor of safety by involving larger slide mass. The effect of varying $L_r(L_e + L_{f1} + L_{f2})$ with right end fixed at point P and left end (Q) moved towards slope face successively on mobilized force in the reinforcement (F_r) and the factor of safety (FS) is studied and the results are summarized in Table 1.

The length $L_f(L_{f1} + L_{f2}) = (L_r - L_e)$ of reinforcement in the failure zone is much larger than L_e, the effective length of reinforcement contributing to increase in the stabilizing moment/force. The required pullout force in the reinforcement in the stable zone gets mobilized and limited by the corresponding length of the reinforcement in the unstable zone. It would serve no useful purpose if the length of the reinforcement in the unstable zone is more than that required for generating the required stabilizing force. Hence, minimizing $L_f = (L_r - L_e)$ by moving point P inside the soil mass and away from the slope face by curtailing length of reinforcement but still maintaining FS_{min} above 1.50 can lead to economy. Accordingly, for reinforced slope of Fig. 2, L_r has been curtailed from the face end of the slope. As point P is moved inside gradually by reducing L_r, the critical circle continues to be DEF or close to it (Fig. 3), i.e. no

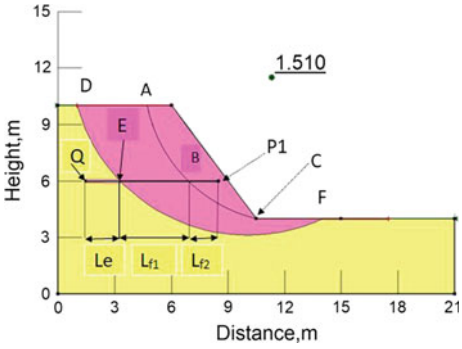

Fig. 3 Slope with one layer of reinforcement at depth 4.0 m but length curtailed near the face

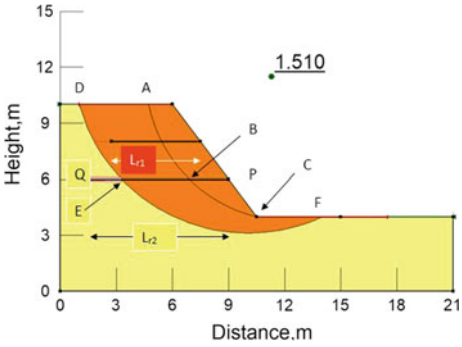

Fig. 4 Slope with two layers of reinforcement at depths 2.0 and 4.0 m

shift of the critical circle. The minimum length, $L_{r,}$ which provides $FS_{min} = 1.51$ is obtained as 7.0 m (Fig. 3). *The search mechanism of locating critical slip circle, while arriving at minimum length of reinforcement after curtailment from face of slope as detailed above, includes the shallow slip surfaces between face of slope AC and end of curtailed end of reinforcement, i.e. Point P_1 in* Fig. 3. *Slip surface with the minimum factor of safety has been depicted in* Fig. 3 *and does not lie between sloping face AC and Point P1.*

However, 4 m high slope itself is unstable as FS_{min} is lower than the desired minimum value. Therefore, from stability consideration of this slope, there is a need to reinforce the slope in the top 4.0 m zone. Accordingly, slope was reinforced with geosynthetic reinforcement of length 4.75 m at $Z_1 = 2.0$ m. This slope with reinforcement at $Z_1 = 2.0$ and $Z_2 = 4.0$ m was optimized from non-face end of the slope leading to FS_{min} of 1.51 with $L_{r2} = 7.50$ m and ensures no shallow failure in (Fig. 4).

It was also observed that even with T_{ult} of 120 kN/m for reinforcement at $Z_1 = 2.0$ m FS_{min} of 1.51 can be maintained.

Slope with two layers of reinforcement at depths of 2.0 and 4.0 m (Fig. 4) was optimized by curtailing reinforcement from the face end of slope and reduction in lengths of reinforcement L_{r1} by 0.65 m and L_{r2} by 1.10 m is achieved (Fig. 5). *In order to arrest shallow sloughing, i.e. erosion of slope face, protective measures like*

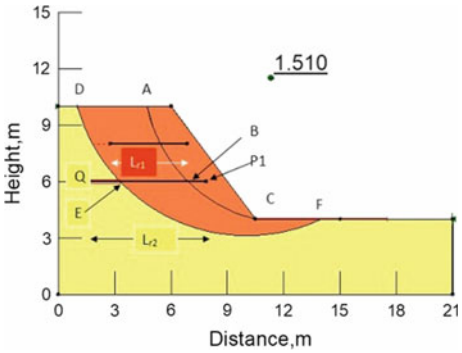

Fig. 5 Slope with two layers of reinforcement at depths 2.0 and 4.0 m—reinforcement curtailed near the face

turfing, pitching, etc. *need to be undertaken. The codal provision of minimum vertical spacing of reinforcement needs to be taken care of at detailed design stage.* Further reduction in length of L_{r1} leads to decrease in FS_{min} to 1.435.

It is observed that reinforcements at Z_1=2.0 m *and* Z_2=4.0 m *affect contributions from each other.*

Analyses of 4 and 6 m high slopes independently with reinforcement at $Z_1 = 2.0$ m and $Z_2 = 4.0$ m, respectively, provide optimum lengths, $Lr_1 = 4.10$ m and $Lr_2 = 7.50$ m. However, combined analysis of the slope, i.e. with both the reinforcements placed simultaneously in 6 m high slope provides optimum lengths Lr_1 and Lr_2 values, respectively, as 4.10 and 6.40 m duly considering the stability of 4 m high slope during construction phase. *Thus, the presence of reinforcement at* $Z_1 = 2.0$ m *reduces the length of* Lr_2 *at* $Z_2 = 4.0$ m *by* 1.10 m. Bottom 4 m of embankment slope during construction phase will have a FS_{min} of 1.30. From consideration of 4.0 m slope which will be the case during construction phase, minimum length of reinforcement required at $Z_2 = 4.0$ m is 4.10 m starting from 1.10 m from face of slope. This is a temporary phase and FS_{min} of 1.3 is **adequate** and *after construction with both reinforcements in place* FS_{min} *of* 1.51 *for slope as whole is ensured due to the presence of reinforcement at* $Z_1 = 2$ m.

Reinforced slope as in Fig. 5 above, with the minimal lengths of the reinforcement arrived at, has been analysed for the slip circle ABC of unreinforced slope to quantify the FS so obtained. FS for this case works out to be very high at 2.12 indicating that the critical circle that gives minimum factor of safety with reinforcement is very different from the one without the reinforcement. Slope as in Fig. 5 has been analysed further for the critical slip circle DEF of reinforced slope but without considering the effect of contribution of the reinforcement to get FS of 1.265 (Fig. 6).

Table 2 presents results in concise from for different cases.

Legend: **I**: FS_{min} for unreinforced slope with critical circle ABC; **II**: FS_{min} for reinforced slope with critical circle DEF; **III**: FS for reinforced slope analysed for fixed circle ABC and **IV**: Reinforced slope analysed for critical slip circle DEF without considering effect of reinforcement.

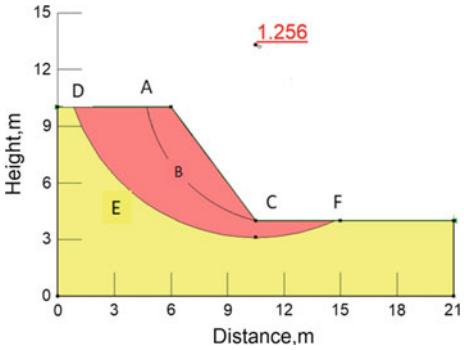

Fig. 6 Unreinforced slope analysed for critical slip circle of reinforced slope (DEF)

Table 2 Factors of safety and lengths of geosynthetics for reinforced slope with Z_1 = 2.0 m, and Z_2 = 4.0 m

FS				L_{r1}, m	L_{r2}, m
I	II	III	IV		
0.831	1.51	2.12	1.265	4.10	6.40

From Table 2, *it can be seen that* FS_{min} *for unreinforced slope is 0.831 and critical slip circle is ABC* (Fig. 5). *For reinforced slope,* FS_{min} *is 1.51 and critical slip circle is DEF* (Fig. 5). *Hence, an increase in* FS_{min} *of 81.70%. The unreinforced slope analysed for critical slip circle DEF of reinforced slope provides FS of 1.265 which is 51.62% higher as compared to* FS_{min} *of unreinforced slope. This increase in FS is due to shifting of critical circle from ABC to DEF which involves larger slide mass. Due to effect of reinforcement by way of increase in stabilizing moment FS min increases from 1.265 to 1.51 an increase of about 30.08%. Analysis of reinforced slope for critical circle ABC of unreinforced slope provides FS of 2.12 indicating that critical slip circle ABC of unreinforced slope is no more critical after reinforcing the slope with geosynthetics.*

4 Results and Discussion

4.1 Reinforcement at Z_1 = 2.0 M and Z_2 = 4.0 M

The contribution of reinforcement in enhancing the stability of a slope is observed to be twofold: (i) shifting of critical slip circle deeper into the slope involving larger slide mass or forward involving smaller slide mass and thus enhancing the factor of safety of the slope and (ii) due to contribution of reinforcement to stabilizing force/moment. The contribution in terms of change in FS is defined as follows:

ΔFS_1—change in factor of safety due to overall effect of reinforcement

Table 3 Changes in factors of safety for cases with reinforcement placed simultaneously at $Z_1 = 2.0$ m and $Z_2 = 4.0$ m

ΔFS_1 %	ΔFS_2 %	$(\Delta FS_1 - \Delta FS_2)$ %
81.70	51.62	30.08

Table 4 Results of analysis of slope reinforced with two layers of reinforcement at 2.0 and 4.0 m

Z (m)	L_r (m)	$L_{opt} = P_1Q$ (m)	$L_{shift} = P_1E$ (m)	L_e (m)	$L_r - L_{opt}$	FS_{minDEF}	FS_{shift}
2	4.75	4.10	–	–	0.65	1.51	1.26
4	7.50	6.40	4.52	1.78	1.10		

$$\Delta FS_1 = \frac{FS_{\text{min DEF}} - FS_{\text{min ABC}}}{FS_{\text{min ABC}}} \tag{1}$$

ΔFS_2—change in factor of safety due to shift of critical circle due to effect of reinforcement

$$\Delta FS_2 = \frac{FS_{\text{DEF without effect of reinforcement}} - FS_{\text{min ABC}}}{FS_{\text{min ABC}}} \tag{2}$$

The difference between the two factors of safety $(\Delta FS_1 - \Delta FS_2)$ is the contribution of the reinforcement (Table 3).

The increase in FS due to reinforcement of slope is 81.70% out of which 51.62% is due to shifting of critical slip circle from ABC to DEF (Fig. 5) *and balance 30.08% is due to increase in stabilizing moment due to effect of geosynthetic reinforcement.*

4.2 Summary of Results

The results of the analysis L_r and FS are summarized in Table 4.

Legend: FS_{shift} = FS for DEF slip circle without considering effect of reinforcement; P1Q & P1E lengths of reinforcement (Fig. 5).

Optimal length of reinforcement from non-slope face end leads to L_{r1} and L_{r2} values of 4.75 m *and 7.50* m*, respectively. The optimization of reinforcement from face end leads to reduction in length of reinforcement of L_{r1} and L_{r2} by 0.65* m *and 1.10* m*. This leads to saving of 1.75* m *in reinforcement length which is about 14.30%.*

5 Conclusions

An analysis of interaction between a very steep embankment slope and reinforcement are carried to identify and quantify the mechanisms contributing to increased slope stability as reflected in higher factor of safety and to optimize the length of reinforcement to be provided. Interaction between reinforcement layers has been identified and quantified. A typical embankment slope 0.75H:1 V of height 6.0 m with two layers of reinforcement at 2.0 and 4.0 m depths is examined for stability using Morgenstern and Price method.

The critical slip circle for the slope with reinforcement shifts inward and is very different from that for unreinforced slope. The increase in factor of safety for the reinforced slope is because of the shift of the critical slip circle deep into the slope and involving larger sliding mass as the slip circle gets shifted deeper into the soil and away from the critical circle corresponding to that for unreinforced embankment soil.

1. *The effect of providing reinforcement in the slope is twofold,* viz. *shifting of critical circle inside of the embankment involving larger slide mass and thereby increasing in stabilizing force/moment.*
2. It is possible to achieve about 14% shorter length of the reinforcement without endangering the stability of the embankment slope by curtailing the length of the reinforcement from the face end.
3. *The upper layer of reinforcement at* $Z_1 = 2.0$ m *can be of relatively lower tensile strength, as low as* T_{ult} *of 120 kN/m in the presence of reinforcement at 4.0* m *depth.*
4. Reinforcement placed at $Z_1 = 2.0$ m affects the length of reinforcement required at $Z_2 = 4.0$ m as its length gets reduced from 7.50 to 6.40 m due to the presence of reinforcement at $Z_1 = 4.0$ m. Thus, interaction of reinforcement layers has been identified leading to reduction in length by 14.7%.

Acknowledgements Comments and suggestions of Prof K. Rajagopal IIT Madras are gratefully acknowledged and appreciated.

References

Baker R, Klein Y (2004a) An integrated limiting equilibrium approach for design of reinforced soil retaining structures. part I—formulation. Geotext Geomembr 22(3):119–150

Baker R, Klein Y (2004b) An integrated limiting equilibrium approach for design of reinforced soil retaining structures: part II—design examples. Geotext Geomembr 22(3):151–177

Bonaparte R, Holtz RD, Giroud JP (1987) Soil reinforcement design using geotextile and geogrids. In: Fluet JE Jr (ed) Geotextile testing and design engineer, ASTM STP 952. American Society for Testing Materials, Philadelphia, pp 69–116

Gao Y, Yang S, Zhang F, Leshchinsky B (2016) Three dimensional reinforced slopes: evaluation of required reinforcement strength and embedment length using limit analysis. Geotext Geomembr 44:133–142

Han J, Leshchinsky D (2006) General analytical framework for design of flexible reinforced earth structures. J Geotech Geoenviron Eng ASCE 132:1427–1435
Jha AK, Madhav MR (2015) Analysis of effect of reinforcement on stability of slopes. In: Proceedings 50th Indian geotechnical conference, Pune, India
Jewell RA, Paine N, Woods RI (1985) Design methods for steep reinforced embankments, Polymer Grid Reinforcement. Thomas Telford Ltd., London, pp 70–81
Jewell RA (1991) Application of the revised design charts for steep slopes. Geotext Geomembr 10(1091):203–233
Leshchinsky D (1992) Issues in geosynthetic reinforced soil. Keynote paper, Proc. Int. Sym. Earth Reinforcement practice, Kyushu, Japan, Balkema, Rotterdam, The Netherlands, 2: 871–897
Leshchinsky B, Ambauen S (2015) Limit equilibrium and limit analysis: comparison of benchmark slope stability problems. J Geotech Geoenvironmental Eng, 04015043-1–04015043-8
Leshchinsky D, Boedeker RH (1989) Geosynthetic reinforced soil structures. J Geotech Eng 115(10):1459–1478
Leshchinsky D, Kang B, Han J (2014) Framework for limit state design of Geosynthetic Reinforced walls and slopes. Transp Infrastruct Geotech 1:129–164
Leshchinsky D, Ling H, Hanks G (1995) Unified design approach to geosynthetic reinforced slope and segmental walls. Geosynthetics Int 2(5):845–881
Leshchinsky D, Reinschmidt AJ (1985) Stability of membrane reinforced slopes. J Geotech Eng 111(11):1285–1300
Leshchinsky D, Zhu F, Meehan CL (2010) Required unfactored strength of geosynthetic in reinforced earth structures. J Geotech Geoenvironmental Eng 136(2):281–289
Rowe K, Soderman KL (1985) An approximate method for estimating the stability of geotextile reinforced embankments. Can Geotech J 22(3):392–398
Schneider HR, Holtz RD (1986) Design of Slopes reinforced with geotextiles and geogrids. Geotext Geomembr 3:29–51
Verduin JR, Holtz RD (1989) Geosynthetically reinforced slopes: a new procedure. Proc Geosynthetics, San Deigo, IFAI, pp. 279–290

Analysis of Slope Failures on Sagam–Inderwan Road and Suggested Remedial Measures

Muzamillah Mohi-ud-din and F. A. Mir

Abstract Slope failure is one of the frequent geological events occurring along the road network in the hilly areas of Kashmir, creating inconvenience to the public and huge expenses for repairs, maintenance, and stabilization measures of such roads. This work presents the results of investigations and analyses for two failed slopes on Sagam-Inderwan road located in Anantnag district of Jammu and Kashmir. The main purpose of this research was to evaluate the safety status of these slopes. The soil data obtained from DST tests was used as input in the SLOPE/W software using limit equilibrium method. The FOS values obtained in the study range from (0.655–0.827) at Rd 500 m and (1.796–2.601) at Rd 1200 m. The FOS was also calculated manually to compare the results with software. Back analysis was also done to find the actual strength mobilized at the time of failure. The conclusions derived from the analysis suggest that the slope at Rd 500 m is unsafe and the slope at Rd 1200 m is marginally safe. The factor of safety obtained after using shear strength parameters from back analysis at Rd 500 m was less than 1.5 indicating slope is at risk of failure and needs stabilization.

Keywords Shear strength parameters · Limit equilibrium method · Factor of safety · Slope/W software · Back analysis

1 Introduction

Shallow slips occur frequently on the Sagam–Inderwan road. Major slips that occurred in 2014/2015 resulted in road blockage, damage to pavement, masonry toe walls, and blockage of road drains. The failure of the slopes also poses threat to inhabitants of Inderwan besides repair and road clearance expenses. The Sagam–In-

M. Mohi-ud-din (✉) · F. A. Mir
Department of Civil Engineering, National Institute of Technology Hazratbal Srinagar (J&K), Srinagar 190006, India
e-mail: rathermuzamillah@gmail.com

F. A. Mir
e-mail: fayazamir@yahoo.co.in

R. Sundaram et al. (eds.), *Geotechnics for Transportation Infrastructure*, Lecture Notes in Civil Engineering 28, https://doi.org/10.1007/978-981-13-6701-4_36

derwan road located in the south Kashmir (Anantnag district) receives annual rainfall of 1103 mm and the temperature varies from minimum of sub-zero in winter to maximum of 33 °C in summer. The geology/lithology of the area reveals that the soils are karewa soils. The problems associated with the karewa soils are soil erosion and depleting soil fertility. Major slope failures occur during rains in these soils causing deprivation of production, additional stripping, cost for recovery, and excessive handling of failed material. Damage of pavements leads to accidents and loss of property. As large number of roads are constructed along these hilly karewa lands to provide connectivity to far flung areas and to provide transport facilities to orchards to boost economy, etc., it is therefore essential that safety status of these slopes is ascertained so as to have the knowledge of risk prior to finalizing the design of the slope and any improvement measure which will be feasible and economical for a reasonable life span. Software called SLOPE/W, developed by GEO-SLOPE International Canada, was used for slope stability analysis. The basic principle used for the analysis is limit equilibrium.

1.1 Causes of Slope Failure

The causes for the landslide at the given site have been identified as under

a. Deforestation on account of excavation for roadwork.
b. Rainfall leading to both surface erosion as well as sub-surface seepage.
c. Snowfall and the associated problem of freeze–thaw.

2 Methodology

The steps followed to achieve the aim were as shown in Fig. 1

2.1 Site Description and Data Collection

The site is located in Anantnag district about 23 Kms from district headquarters. The rock formations underlying the area ranges in age from Cambrian to Quaternary Panjal traps forming hilly and mountainous terrain of the district with hard formations of igneous and metamorphic rocks. The Karewa soils and alluvium soils of Quaternary and Tertiary age (Plio-Pleistocene) underlie the valley area and consist of bands of sand, silt, and clay, interspersed at two to three levels locally by glacial boulder beds. The vegetation/land cover of the area consists of mix of Bren, Deodar, Kail trees, etc.

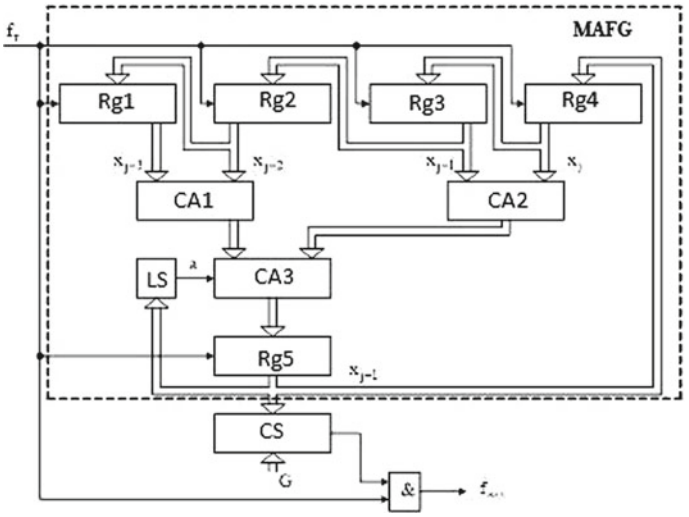

Fig. 1 Flowchart showing steps followed to achieve the aim of the project

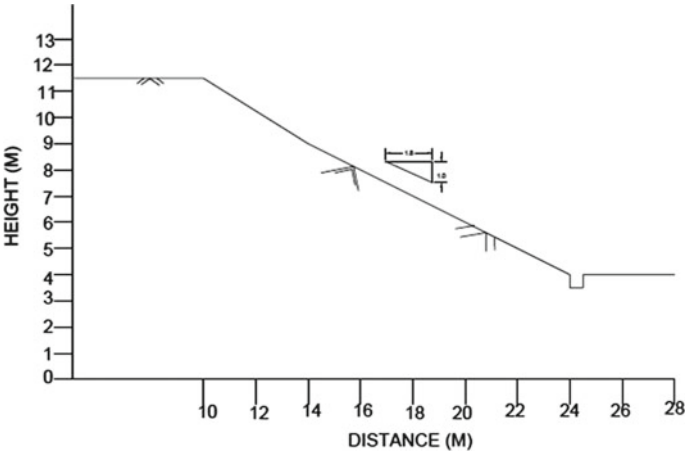

Fig. 2 Cross section at Rd = 1200 m

(a) The cross-sectional details of the slope subjected to failure were taken (At Rd 1200 m and Rd 500 m) shown in Figs. 2 and 3.

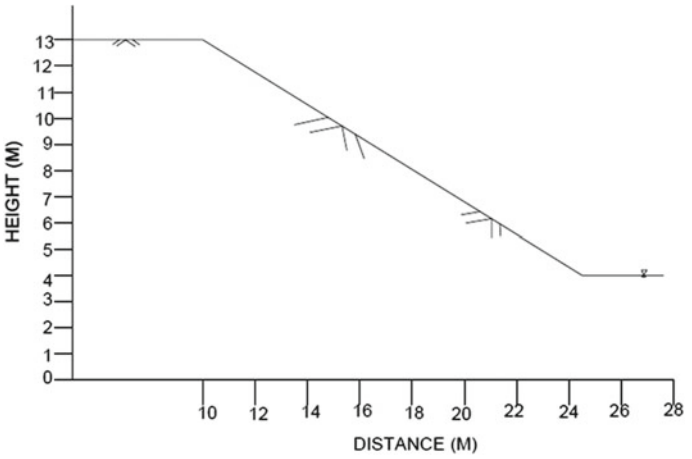

Fig. 3 Cross section at Rd = 500 m

2.2 Sample Preparation and Collection

Sampling was done to get disturbed and undisturbed samples for laboratory tests of all required soil parameters.

- Disturbed samples were used to classify soils by grain size analysis, Atterberg's limits, and specific gravity.
- Undisturbed samples were used for finding soil unit weight and shear strength parameters.

The samples were obtained from six different places of the two slopes on 15–01–2017. Initially, the ground was dug up to half meter to take samples of proper moisture content representing the total slope. The locations from where the samples sourced were selected after careful consideration to represent the whole area. The location was first cleared of vegetation and soft soil cover. The samples were collected using the routine core-cutters. The samples were properly sealed to prevent loss of moisture. Proper care was taken to ensure that the parameters of the sample do not change while bringing these to the laboratory (Fig. 4).

2.3 Factor of Safety Calculation

The factor of safety for slope stability analysis is usually defined as the ratio of the ultimate shear strength divided to the maximum shear stress at incipient failure. There are several ways in formulating the factor of safety. The most common formulation for FOS assumes the FOS to be constant along the slip surface, and it is defined with respect to the force or moment equilibrium (Cheng and Lau 2008).

Fig. 4 Collection of sample

2.4 Limit Equilibrium Methods

Several limit equilibrium (LE) methods have been developed for slope stability analyses. According to Sivakugan and Das (2010), the major components in solving a slope stability problem includes:

- Geometry of the slope is defined as a first step in modeling.
- Soil properties are defined and assigned to the specific regions.
- The third step involves defining the water table.
- Fourth step involves defining slip circles and the method used for analysis purpose.
- Once the method is selected, then the problem is solved.
- The last step involves displaying of the results.

3 Results and Discussions

3.1 Atterbergs Limits

Based on the values of L.L., P.L., P.I. of the two soil samples, soils are classified as inorganic silts of medium plasticity and inorganic clays of medium plasticity, respectively. The results are shown in Table 1.

3.2 Shear Strength Tests

Direct Shear tests were done on both saturated and unsaturated samples. Samples were saturated in order to simulate worst field condition during rainfall. The shear strength values obtained from sample collected at Rd 500 m were much lower than that of sample from Rd 1200 m location as shown in Table 2. Unconfined compression tests showed the results similar to DST as shown in Table 3.

Table 1 Showing results of Atterbergs limits

Location	Rd 1200 (m)	Rd 500 (m)
Liquid limit (%)	37	40
Plastic limit (%)	30	17
Plasticity index (%)	7	23
Soil classification	MI	CI

Table 2 Results of DST tests

Location	Cohesion, c (kpa)	Angle of internal friction, φ
Rd 1200 m	39.84	15.7
Rd 1200 m	30.71	22.9
Rd 500 m	9.68	10.7
Rd 500 m	3.87	10.7

Table 3 Results of UC tests

Location (m)	Unconfined compressive strength, q_u (kpa)	Undrained Cohesion c_u (kpa)
Rd 1200	92.0	46.0
Rd 500	43.0	21.5

Table 4 Results of factor of safety under different conditions and different methods

Location Rd (m)	Ordinary method	Morgenstern–price method	For total stress condition
1200	1.931	1.904	
500	0.700	0.793	
1200	2.483	2.601	For effective stress condition
500	0.766	0.827	
1200	2.420	2.601	
500	0.585	0.585	

3.3 Factor of Safety

The factor of safety was calculated by first defining geometry of the two slopes having slope of 1 in 2 m at Rd 1200 m and 1 in 1.4 m at Rd 500 m. The shear strength parameters obtained from laboratory tests were used as input data in SLOPE/W software. The factor of safety was calculated for both total stress condition and effective stress condition. The results are shown in Table 4. The factors of safety for sample at Rd 1200 m are more than 1.0 even under worst ground conditions indicating the current slope is safe. The factors of safety for the sample from Rd 500 m are less than 1.0 indicating the slope is unsafe and will reactivate and fail if water table rises to current slope surface. The factor of safety was calculated using ordinary method of slices and compared with Janbu's and Morgenstern–Price method. The factor of safety values computed with different methods showed a difference of 6%.

The factor of safety lies outside grid for total stress condition using grid and radius slip circle method for slope at Rd 1200 m as shown in Fig. 5 and for slope at Rd 500 m as shown in Fig. 6. The shear strength values from UC tests were used for total stress condition for obtaining the short-term stability of the two slopes (Geostudio slope tutorials 2012 by Geo-Slope International).

The factor of safety for total stress condition lies inside grid for effective stress condition. The groundwater conditions are drawn with piezometric line assuming the groundwater rises up to toe of slope (worst groundwater condition) as shown in Figs. 7, 8, 9 and 10.

3.4 Back Analysis

Back analysis was done taking the cross section of slope before failure to find the actual shear strength mobilized at the time of failure. The type of analysis done was $\varphi = 0$ analysis. The slip surfaces of the two slopes are shown in Figs. 11 and 12. The cohesion values are shown in Table 5.

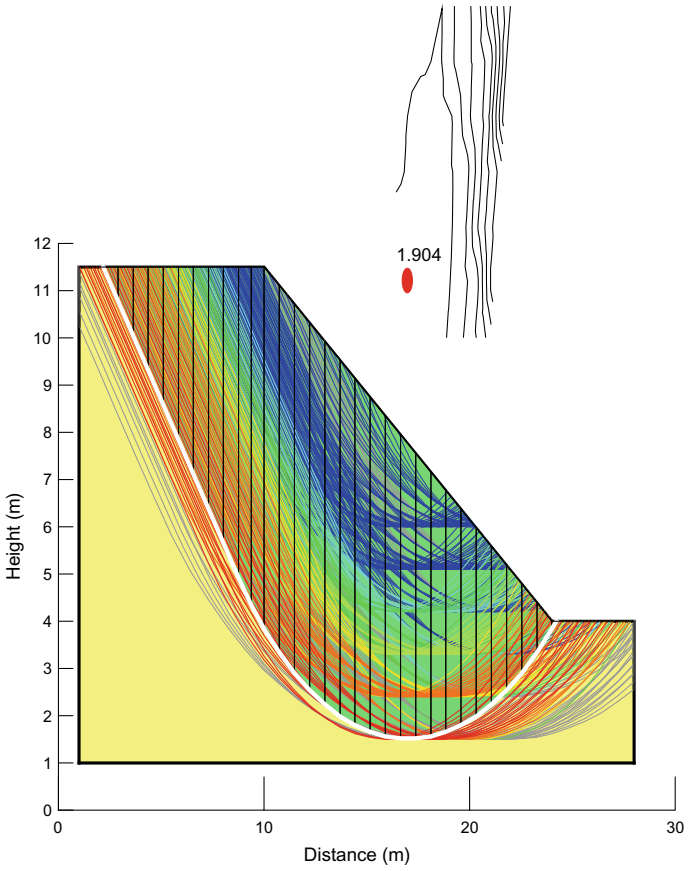

Fig. 5 FOS at Rd 1200 m for total stress condition

Table 5 shows results of shear strength parameters after back analysis

Location (m)	Cohesion c (kpa)
Rd 1200	12.5
Rd 500	11.8

4 Stability Measures

The flattening/benching of slope at Rd 500 m resulted in improvement to the factor of safety. The other stability measures include vegetation cover and construction of retaining walls with proper weep holes for drainage of water behind the wall. The most feasible and economical method at a particular site is to do the benching of the slope and construction of retaining walls at various spots (where there is maximum deformation) along the cross section of the slope. The purpose of benching a slope is to transform the behavior of one high slope into several lower ones. The slope of

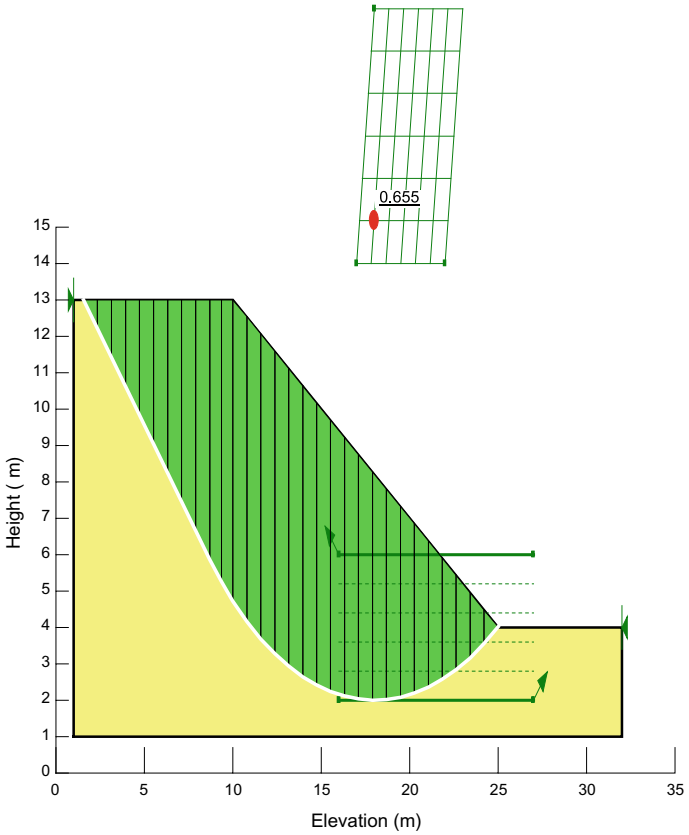

Fig. 6 FOS at Rd 500 m for total stress condition

1 in 1.6 m at bottom, 1 in 3.3 m at middle, and 1 in 1.8 m at top was given for this particular slope at Rd 500 m as shown in Fig. 13, which resulted in improvement to the factor of safety.

Th flattening of slope increases the length of failure surface within the weak stratum to create more sliding resistance. Flattening of slope with overall slope of 1 in 2.75 resulted in improvement to the factor of safety as shown in Fig. 14. Provision of drainage ditches in slope also improved the factor of safety as shown in Fig. 15 (slope modelling 2012 edition an engineering methodology by Geo-Slope International).

5 Conclusions

- The shear strength values obtained from different test methods did not exactly match, but they were comparable and showed reasonable agreement.

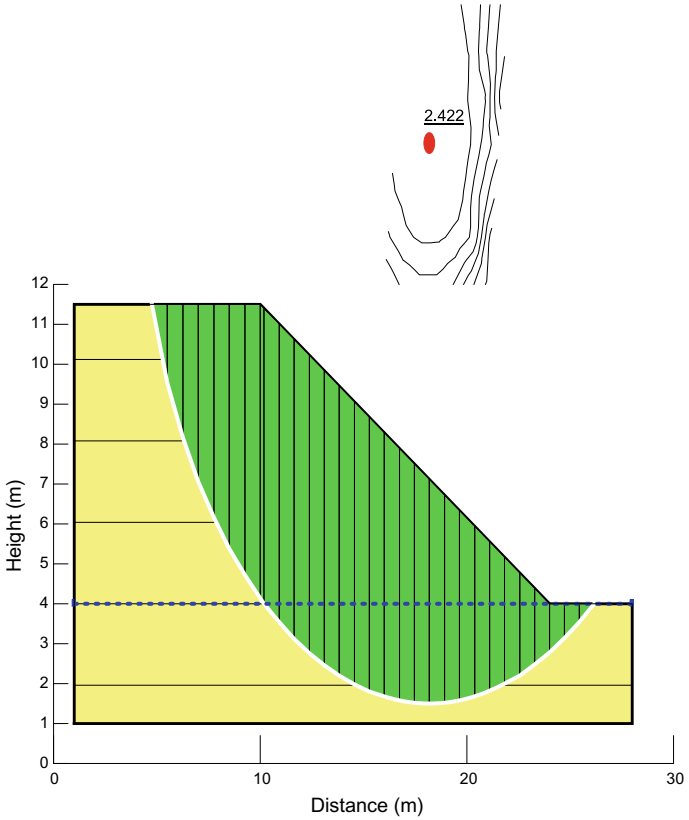

Fig. 7 FOS at Rd 1200 m for effective stress condition (unsaturated)

- The results show that the factors of safety for the slope (Rd 1200 m) are higher than 1.0 (1.796–2.601) even using the worst ground water conditions indicating current slope is safe which is contradictory to actual field situation.
- The factor of safety for slope (Rd 500 m) is much lower than 1.0 (0.585–0.827) indicating the large displacements of the slope after failure which is in good agreement with the field conditions.
- The mobilized shear strength parameters obtained from back analysis were much less than laboratory values.
- The factor of safety obtained after using shear strength values from back analysis at Rd 500 m was less than 1.5 indicating slope is at high risk of failure and needs stabilization.
- The flattening of slope at Rd 500 m resulted in improvement to the factor of safety and can be adopted as a feasible slope stability measure.
- The provision of drainage ditches and benching of slopes also help in improving the factor of safety by about 50%.

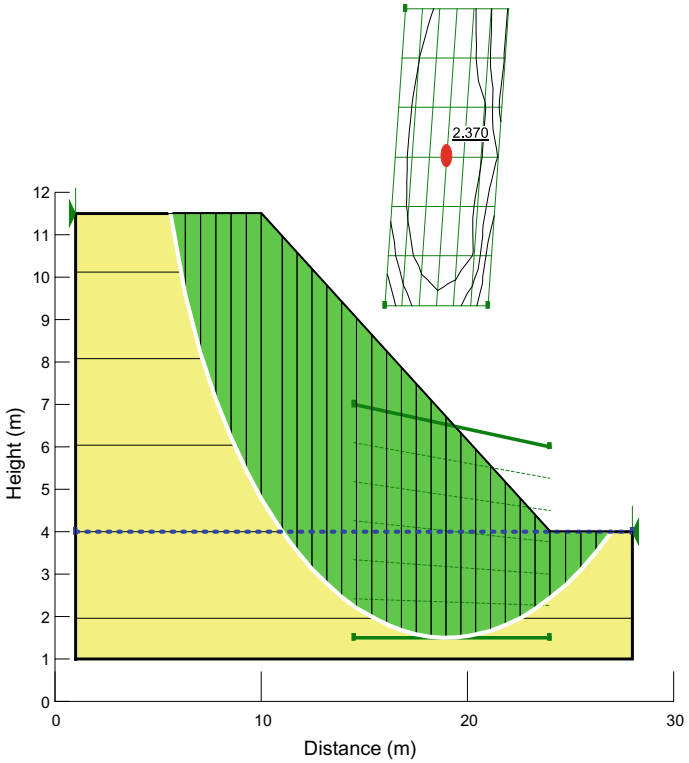

Fig. 8 FOS at Rd 1200 m for effective stress condition (saturated)

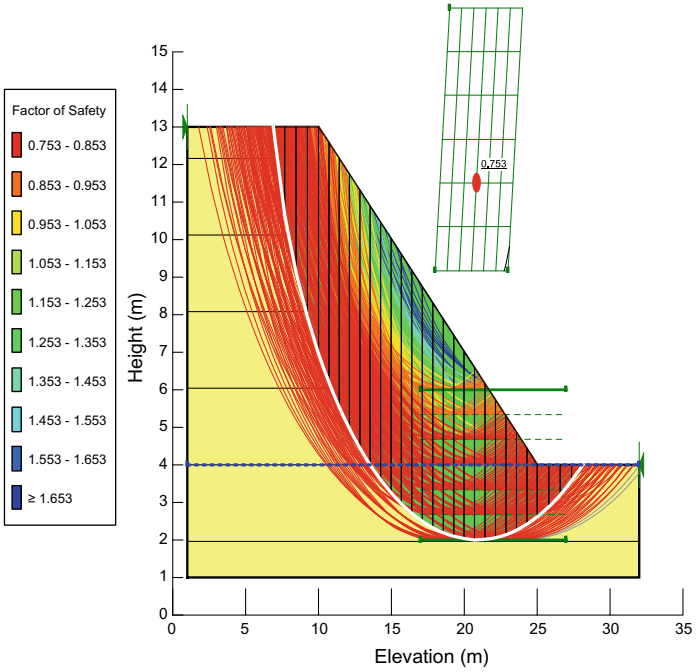

Fig. 9 FOS at Rd 500 m for effective stress condition (unsaturated condition)

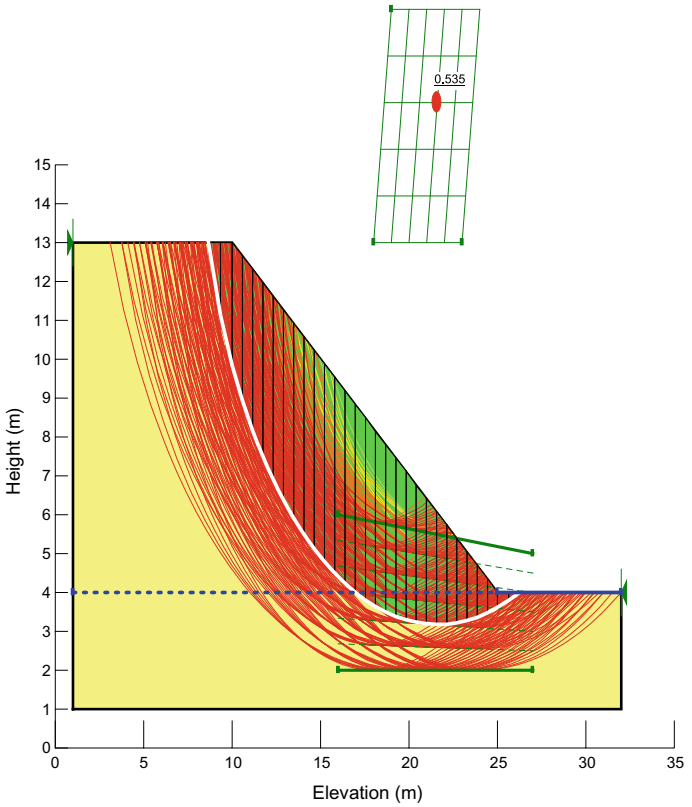

Fig. 10 FOS at Rd 500 m for effective stress condition (saturated condition)

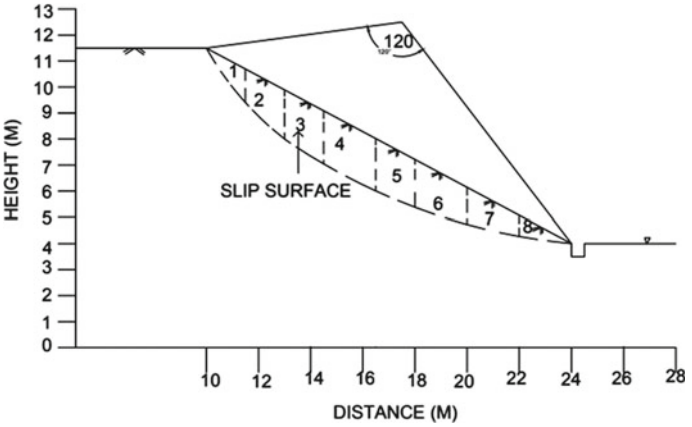

Fig. 11 Slip surface at Rd = 1200 m

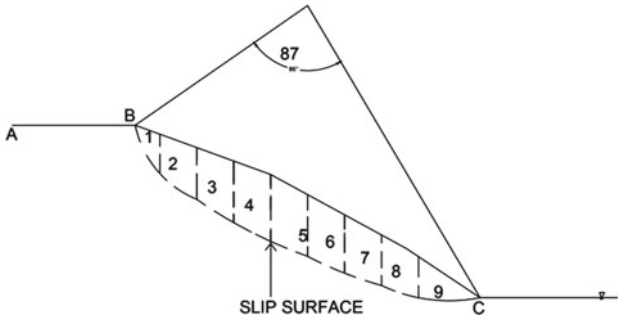

Fig. 12 Slip surface at Rd = 500 m

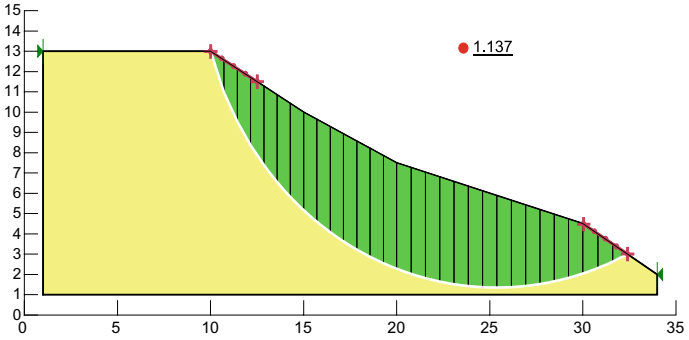

Fig. 13 FOS at Rd 500 m after benching of slope

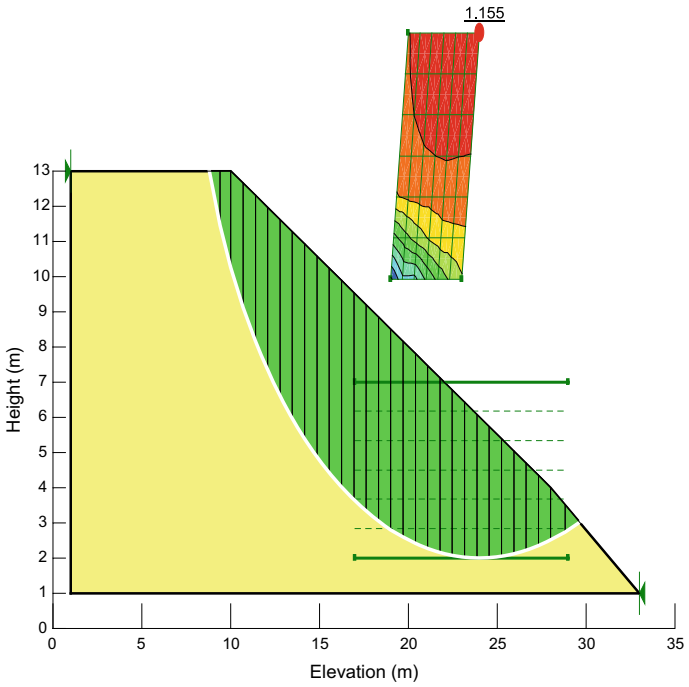

Fig. 14 FOS at Rd 500 m after flattening of slope

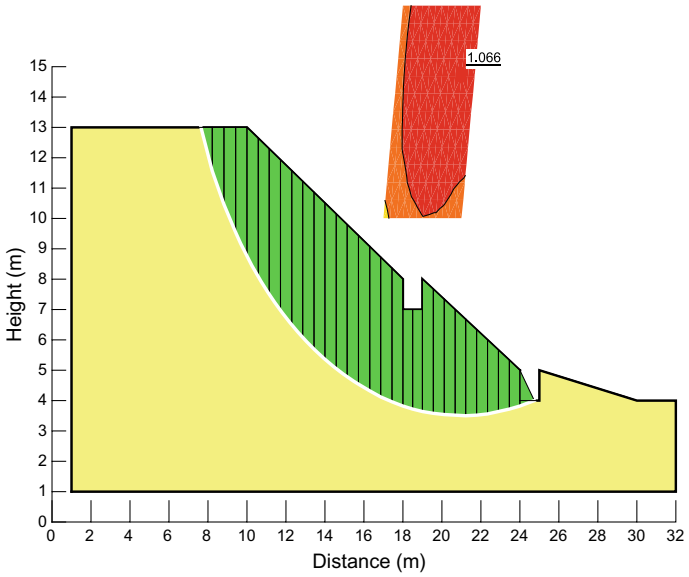

Fig. 15 FOS at Rd 500 m after using drainage ditches in slope

References

Abramson LW, Lee TS, Sharma S, Boyce GM (2017) - http://www.pubs.geoscienceworld.org
ASTM Standard D698 (2007) Standard test methods for laboratory compaction characteristics of soil using standard effort. ASTM International, West Conshohocken, PA
Elia G, Cotecchia F, Pedone G Geo studio slope tutorials 2012 by Geo-slope International - Quarterly Journal
Geotechnical control office (1984) Geotechnical manual for slopes, 2nd edn. Hong Kong: civil engineering services department
Murthy VNS (2001) Principles of soil mechanics and foundation engineering, 5th edn. UBS Publisher's Ltd
Slope modeling (2012) edition an engineering methodology, Geo-slope International limited

Geotechnical Evaluation of a Landslide in the Lesser Himalayas

Ravi Sundaram, Sorabh Gupta, Rudra Budhbhatti and Kinjal Parmar

Abstract A landslide at Birahi in Chamoli District of the Lesser Himalayas had affected traffic along NH-58. The paper presents details of the geotechnical and geophysical investigations done to evaluate the failure and to develop remedial measures. A slide zone of overburden with boulders was clearly identified which matches well with the borehole data. The probable causes of failure and remedial measures such as drainage planning, erosion control, and reinforcement on the valley side are discussed.

Keywords Landslide · Geotechnical investigation · Seismic refraction test · Stabilizing and destabilizing forces · Drainage and erosion control · Reinforced soil structure

1 Introduction

Landslide is a complex geological process, and interplay of a number of factors is known to trigger these. The Himalayas alone count for landslides of every fame, name, and description—big and small, quick and creeping, ancient and new.

Geology and structural setup of the area combined with heavy rains and seepage of water through fragile jointed rock can play havoc on the overall stability of region.

R. Sundaram (✉) · S. Gupta
Cengrs Geotechnica Pvt. Ltd, A-100 Sector 63, Noida 201309, India
e-mail: ravi@cengrs.com

S. Gupta
e-mail: sorabh@cengrs.com

R. Budhbhatti · K. Parmar
Macaferri Environmental Solutions Pvt. Ltd, 403-409 Suncity Success Tower, Sector 65, Gurgaon 122005, India
e-mail: rudra@macaferri-india.com

K. Parmar
e-mail: kinjalwdc@macaferri-india.com

R. Sundaram et al. (eds.), *Geotechnics for Transportation Infrastructure*, Lecture Notes in Civil Engineering 28, https://doi.org/10.1007/978-981-13-6701-4_37

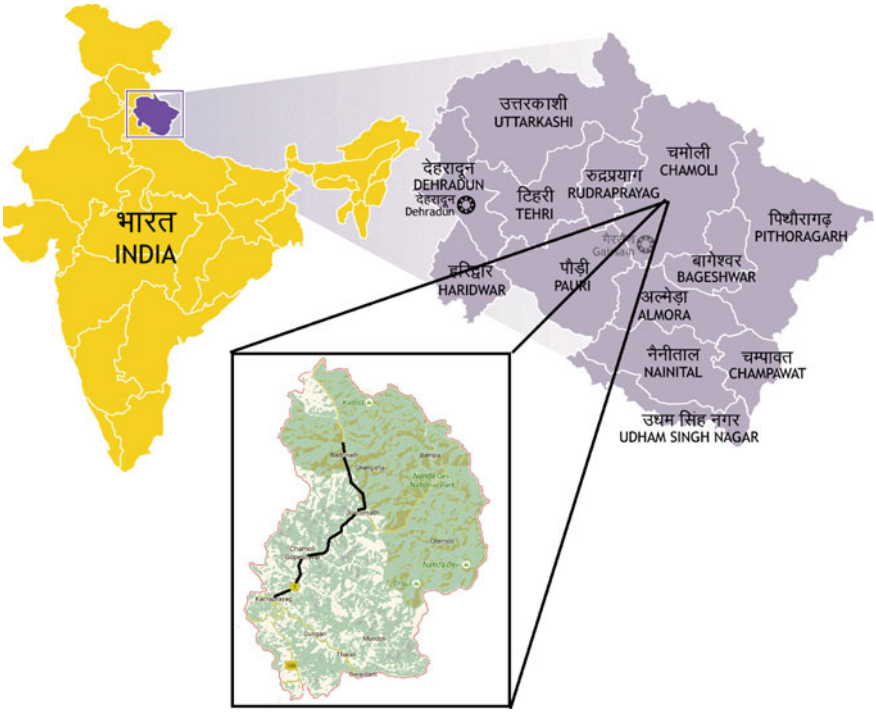

Fig. 1 Vicinity map

The cloudburst in June 2013 triggered several landslides along the Rudraprayag–Badrinath section of NH-58. The paper presents a case study of one such landslide at Birahi along the highway on the bank of River Alakhnanda. A vicinity map of the alignment of the highway is presented in Fig. 1.

The project road has distinct importance because of variety of destinations of pilgrim and tourists interest like Badrinath, Hemkund Sahib, Valley of Flowers, and Auli. Chamoli occupies the northeastern corner of the Garhwal tract and lies in the central or mid-Himalayas in the very heart of the snowy range.

Detailed geotechnical investigation including boreholes and seismic refraction tests were used to characterize the landslide and assess the extent of the failure. The results have been used to develop engineering solution to mitigate the distress and make the highway safe under such extreme climatic events.

2 Generalized Geology and Strata Conditions

2.1 Geological Setting

Geologically, the area belongs to the Lesser Himalayas and lies in a tectonic fore-deep. It is sandwiched between North Almora Thrust and Main Central Thrust (DMMC 2014). The rocks of the Lesser Himalayas belong to the Central Crystalline Group.

The rocks comprise gneisses and quartzites which are extremely deformed during ductile regime to form different types of myolinites, myolinitic gneisses, schists, amphibolites, etc. The gneisses and quartzites are sheared and give rise to sericite schists, sillimanite-bearing mica-schists.

The area has a highly rugged topography characterized by moderate to steep slopes that are intervened by narrow valleys. The exposed rocks at Birahi are highly jointed and fractured quartzitic schist belonging to the Garwal Group.

2.2 Site Conditions

The rocks are highly folded and faulted with the Birahi fault zone passing toward NE of landslide location.

The surficial soils and boulders along the slope are prone to landslide during heavy rains. Since Birahi fault is in the vicinity, it makes the landslide seismically disturbed.

The NH-58 section continues into a hairpin bend at Birahi. A photograph showing the disturbed zone at higher and lower levels of the bend is presented in Fig. 2.

Fig. 2 Slide at the hairpin bend

Fig. 3 Satellite image showing the locations of geotechnical investigation *source* Google Earth

2.3 Geotechnical Investigation

Geotechnical investigation has been carried out to evaluate the stratigraphy of the area. The investigation included four boreholes and seismic refraction tests along two lines.

A satellite image showing the locations of the geotechnical investigation on the upper and lower elevations of the hairpin bend is presented in Fig. 3 along with the Alakhnanda River at the bottom.

A photograph of the borehole drilling in progress is illustrated in Fig. 4.

2.4 Stratigraphy

An overburden of boulders (colluvial deposit) is encountered to about 2–4 m depth on the higher elevation and to 11–12.5 m depth. The overburden is the mostly slide material accumulated along the slope. It is underlain by quartz-mica-schist. Typical data from boreholes drilled on the lower elevation below the hairpin bend is presented in Fig. 5.

Fig. 4 Borehole drilling in progress—Note the slide material on the hillslope

2.5 Geophysical Profile

Seismic refraction test was done along the road alignment to characterize the ground conditions at the higher and lower elevations, evaluate the geophysical lithology and to make an assessment of the extent of the landslide.

The geophysical lithology encountered along the line at lower level is illustrated in Fig. 6. It indicates a two-layered geological model. A slide zone of overburden with boulders was clearly identified which correlates very well with the borehole data.

The seismic profile at lower elevation illustrates a two-layer lithology. Both layers are landslide materials. Hard rock is at deeper depth.

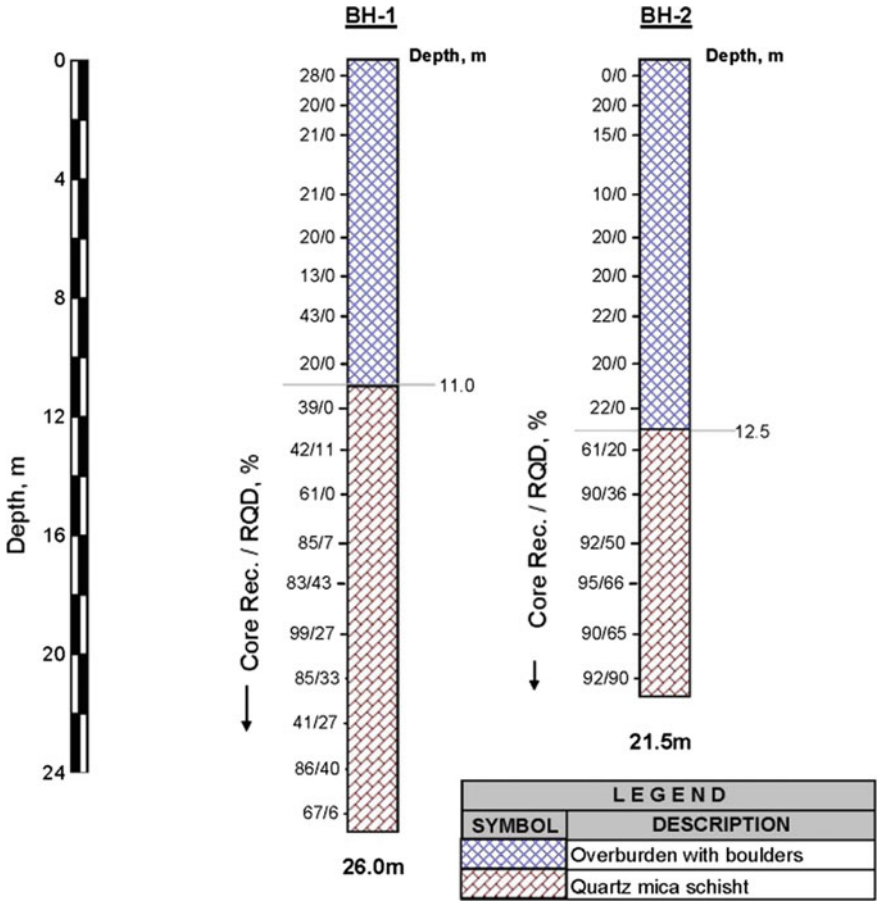

Fig. 5 Borehole profiles at lower elevation

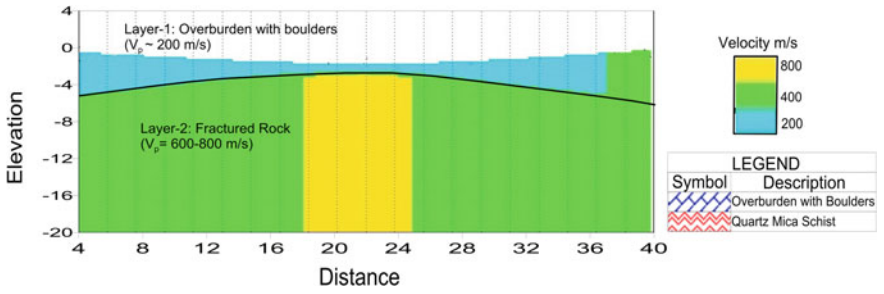

Fig. 6 Typical seismic sectional profile along the landslide at lower elevation

3 History and Background of Slide

Birahi is a village in the Chamoli District of Uttarakhand State, India at an altitude of 1200 m above sea. It is situated on the riverbanks of Alaknanda and Birahi Ganga on NH-58.

The landslide at Birahi was probably activated during Chamoli earthquake in March 1999 (as per locals). At Birahi, there are two landslides—one on the hillside and the other between the roads of hairpin bend. Satellite images taken since 2006 illustrate the progression of the landslide over the years (see Figs. 7, 8, 9, and 10).

Fig. 7 Satellite image taken in 2006. *source* Google Earth

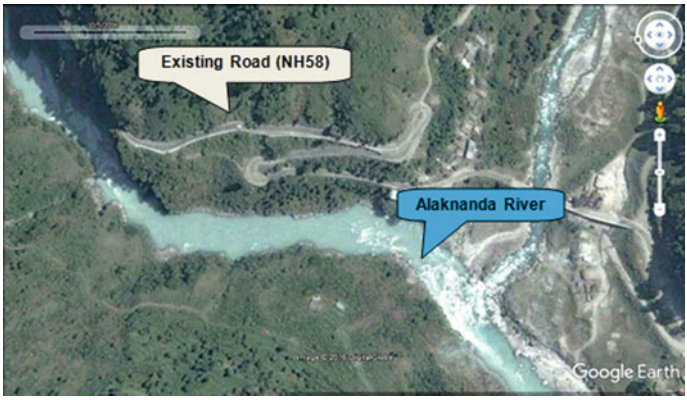

Fig. 8 Landslide at Birahi location in 2011. *source* Google Earth

4 Engineering Assessment

The section along this landslide reveals that the rocks are highly folded and faulted with fault zone passing toward NE of landslide location. The exposed rocks are highly jointed and fractured. It is classified as quartzitic-schist that belongs to Garhwal group. Surficial material on the slope in between the roads consists of loose soil-boulders matrix and is prone to slide. Towards hillside, the rocks are highly weathered and jointed.

Fig. 9 Satellite image taken in 2014 shows the landslide. *source* Google Earth

Fig. 10 Landslide at Birahi—photograph taken in 2016

The rock mass dips unfavorably toward the valley side. Further, proximity to the Birahi fault makes the area seismically prone. A sketch showing the unfavorable dip and the failure zone is illustrated schematically in the geological section in Fig. 11.

The unfavorable dip of the rock combined with the buildup of pore-water pressure behind the gabion wall and erosion of the river bank toe during heavy rains resulted in increased instability of the area. This combined with human activities such as slope cutting for infrastructure development and leaving the steep cut slopes untreated made the rock mass vulnerable to movement.

Excavating into hillside resulted in removal of base support. This caused hillslope failures in slightly concave depressions. These depressions are believed to be former landslide scars which have gradually filled with soil and organic materials through time. As soil depth in these depressions increases with time, the stability of the site decreases.

This coupled with episodic occurrence of precipitation over years has decreased soil strength substantially resulting in slope failure.

On the valley side, overloading or increase in head load accompanied by intense rainfall and addition of runoff from new roads on compacted fill has increased pore-water pressure destabilizing the slope and caused slide.

5 Probable Causes of Failure

A discussion on the various destabilizing forces that had an impact on the overall instability and progression of the landslide are discussed below:

Anthropogenic Activities: Construction activity for widening of road was a major destabilizing force at Birahi. Cutting of hillside vegetative-slope probably resulted in release of in situ stresses in the rock mass and disturbed the equilibrium of forces. This remained untreated without any proper support system which makes the hillslope vulnerable to slide.

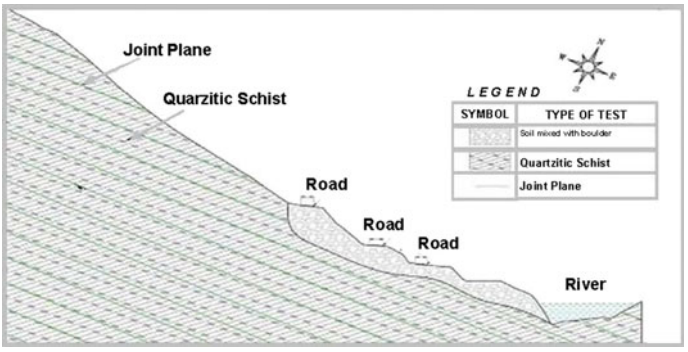

Fig. 11 Geological section illustrating the dip of the rock

Tectonic Settings: Birahi landslide area is in the vicinity of Birahi fault that makes area seismically active. Two major joint sets are present at the landslide location and one of them is dipping toward road-side (see Fig. 12). This unfavorable dip caused the slide due to water seeping through the joints.

Surface Erosion: Accumulation of colluviums on the valley side slope starts erodes when comes in contact with surface runoff water. This surface erosion disturbed the stability of road. Figures 13 and 14 are photographs of the accumulation of debris and erosion on the valley side.

6 Remedial Measures

Several remedial measures were implemented to enhance the stability of the area and ensure that the road and surrounding areas are safe from geotechnical perspective. Some of the major measures implemented in accordance with IRC-SP-048 1998 are highlighted below.

Drainage Planning: Although there is an existing culvert for drainage, there are no proper channels for diverting the water to the culvert and then to the nearest water stream. A proper drainage channel was provided on hill as well as valley side including edge drains and chute drains as per IRC-SP-042 (2014).

Water was channelized from the hill and discharged in the culvert through the road-side edge drain. The culvert water was then directed to river through chute drains in accordance with IRC-SP-013-(2013). This proper drainage network has reduced the danger of further accumulation of water in the in situ soil.

Erosion Control: To stabilize the road portion where erosion has occurred, self-drilling anchors of 25 mm diameter were provided at 3-m spacing in longitudinal

Fig. 12 Photograph showing the unfavorable dip of joints in the rock mass

Fig. 13 Photograph accumulated debris at foot of the slide

Fig. 14 Photograph showing erosion and consequent accumulated debris

and transverse direction. For surface stability and erosion control, bio-engineering measured and secured with provision of geogrid. For the entire stretch, 3-m-high gabion toe wall is provided as illustrated in Fig. 15 [FWHA-NHI-00-043 (2001)].

Reinforcement on Valley Side: On valley side, for retention of proposed 12-m-wide road, reinforced soil system of 25 m maximum height has been provided on valley side of the road. This was done to stabilize the road that had been cut for road construction without appreciation of the stability aspects [IRC-HRB-Special Report-23 (2014)]. At this location, retention was provided by the combination of reinforced soil system and gabion wall as per the guidelines in MORTH (2013) section 3100 and BS-8006 Part 1(2010). (see Fig. 16).

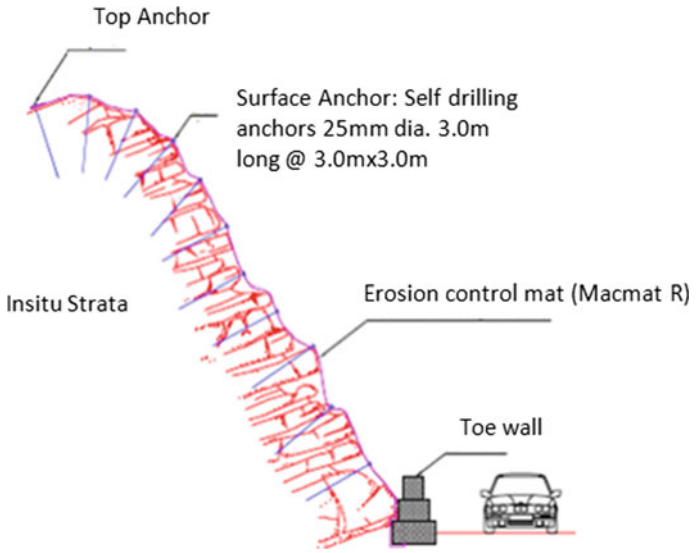

Fig. 15 Typical hillslope protection work

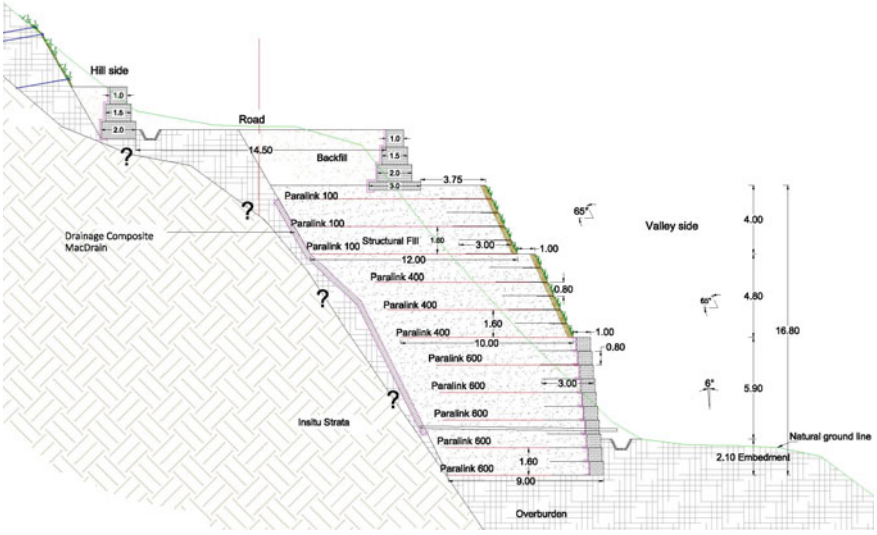

Fig. 16 Typical section of valley retention system

Gabion and wrap-around facing units (made up of double-twisted wire mesh) with geogrids, considering geogrids as "primary reinforcement" and the "integrated tail" of the facing units as "secondary reinforcement" (Grimod and Giacchetti 2014).

Here in this location, bottom portion of the wall is made of gabion facia units with integrated tail. The top portion is made of green facia with integrated tail. High-strength geogrids have been used as primary reinforcement, and integrated tail acts as secondary reinforcement. For reinforced soil section, trapezoidal section with minimum 0.4-m reinforcement as per the guidelines is adopted. On the top of this reinforced soil system gabion retaining wall of maximum 6 m height is provided.

7 Concluding Remarks

The study illustrates the use of seismic refraction test in characterizing the ground conditions in landslide zones. The engineering solutions developed and the remedial measures adopted in the landslide zone have been carefully worked out to ensure the development goes hand-in-hand with environmental sustainability.

Construction of roads in the fragile Himalayan Mountains requires appreciation of the geological interplay of forces for sustainable development. It is essential that human development is in harmony with nature.

References

BS 8006-1 (2010) Code of practice for strengthened/reinforced soils and other fills, British Standards Institute

Disaster Mitigation and Management Centre (2014) Geological investigations in Rudraprayag with special reference to mass instability, A DMMC publication, Dehradun, Uttarakhand

FHWA-NHI-00-043 (2001) Mechanically stabilized earth walls and reinforced soil slopes design and construction guidelines, Publication of U. S. Department of Transportation Federal Highway Administration

Grimod A, Giacchetti G (2014) Design approach for secured drapery systems. In: Proceedings, World Landslide Forum 3, Beijing, 2–6 June 2014

IRC:SP:102 (2014) Guidelines for design and construction of reinforced soil walls, Indian Roads Congress

IRC-HRB-Special Report-23 (2014) State of the art: design and construction of rockfall mitigation systems, Indian Roads Congress New Delhi

IRC-SP-013 (2013), Guidelines for the design of small bridges & culverts, Indian Roads Congress, IRC Special Publication

IRC-SP-042 (2014) Guidelines of road drainage, Indian Roads Congress, IRC Special Publication

IRC-SP-048 (1998) Hill road manual, Indian Roads Congress, IRC Special Publication

MORTH (2013) Section 700 and 3100, 5th Revision

Performance-Based Procedure for Prediction of Lateral Resistance of Slope-Stabilizing Piles

Sajid Iqbal

Abstract Piles (or drilled shafts) have been an effective slope-stabilization scheme since the 1970s. However, limited knowledge regarding load transfer for piles within moving soil may cause design of the piles to be more conservative than is actually needed. The objective of this study is to provide guidance on the effects of pile diameter and spacing, so designers can reasonably account for these effects when predicting response of piles from lateral loading within moving soils. Based on measured soil movements and sliding surface locations from full-scale field monitoring of slopes stabilized with drilled shafts at different pile-spacing-to-diameter ratios (S/D), *p*-*y* analyses are performed to back-calculate "best fit" *p*- and *y*-multipliers that would lead to prediction of the measured bending moments in drilled shafts. The back-calculated *p*-*y* parameters are compared with values from literature and with one another to develop recommendations for predicting lateral resistance in piles for slope-stabilization applications.

Keywords Slope stabilization · Drilled shafts under lateral loading · Soil movement · p-y analysis · LPILE

1 Introduction

There are many ways to deal with unstable slopes. One way is to increase the stability of slope using piles or drilled shafts. The use of piles emerged as a most effective scheme for slope stabilization and has been successfully practiced to enhance the safety of natural slopes against instability. The piles must be embedded deeply enough into a bearing stratum to provide resistance against the lateral forces transmitted from the unstable soil mass. However, limited knowledge regarding load transfer for piles within moving soil may cause design of the piles to be more conservative than is actually needed. This work is intended to better understand the mechanism of transfer of load from moving soils onto the piles. Specifically, a better understanding

S. Iqbal (✉)
National Engineering Services Pakistan (NESPAK), Lahore 54000, Pakistan
e-mail: sajid_gunjial@yahoo.com

R. Sundaram et al. (eds.), *Geotechnics for Transportation Infrastructure*, Lecture Notes in Civil Engineering 28, https://doi.org/10.1007/978-981-13-6701-4_38

of the load transfer process includes knowledge of the member spacing and pile diameter. The main objective of this study is to provide guidance on the effects of pile spacing and diameter when predicting loads in piles for slope stabilization. Six well-documented field-based measurements of in situ performance of piles to stabilize the slope from full-scale field testing involving a single/leading row of vertically drilled shafts were selected for this research that was carried out by author during his graduate research studies (Iqbal 2015).

2 Design Methodology

Reese et al. (1992) described an approach for analyzing the laterally loaded slope-stabilizing piles. The approach considers pile to be vertically installed and subjected to soil movement induced lateral loading above the sliding surface. The approach involves *p-y* method for the prediction of lateral forces acting on pile. *p-y* method is established on the philosophy of soil–pile interaction. Isenhower (1999) presents a method for predicting loads that develop in piles subjected to deep-seated soil movement. Although the method was not specifically developed for slope-stabilization applications, it nevertheless provides a framework for predicting forces that can be applied to limit equilibrium analysis. Like Reese et al. (1992) method, Isenhower (1999) method is based on soil–structure interaction analysis. To solve for the lateral response of the pile, a variation of the *p-y* method is used. It presents version of the beam-column equation that governs the *p-y* method, modified to account for the effect of moving soil, and a finite difference solution for beam-column equation. Ensoft's LPILE v2013 (Isenhower and Wang 2013) that automates the solution is used to perform such analysis. Once *p-y* analyses are completed to predict lateral resistance provided by pile, limit equilibrium slope stability analyses can be performed by incorporating that resisting forces (Boeckmann and Loehr 2013; Loehr and Brown 2008).

3 Analysis Procedure

The measured response of drilled shafts (bored piles) due to soil movement induced lateral loading from six full-scale field monitoring cases was analyzed to develop a better understanding of the load transfer to drilled shafts from moving soils. *p-y* analyses were performed using Ensoft's LPILE v2013. For these analyses, measured soil movements were used as input to predict the lateral response of drilled shafts from moving soil using common *p-y* models.

The API sand model in LPILE v2013 was used for modeling sands and clays under drained conditions in all cases. Weak rock (Reese) and strong rock (Vuggy Limestone) in LPILE v2013 were used to model soft rock and weathered limestone where appropriate. The API sand model is primarily used for modeling lateral pile

response in sand. However, it is also logical to use the API sand model for performing lateral analysis of piles in clays under drained conditions. The available models in LPILE v2013 for clays are based on undrained shear strength properties of clay and may not be appropriate for analyses under drained conditions; because, reliability of predicted results can be questioned. Instead, sand models available in LPILE v2013 predict reasonable lateral response under drained conditions (Personal communication with William Isenhower, Ensoft's LPILE Developer in 2014; Bellew 2015).

Soil movement was assumed to be uniform above sliding surface with a triangular shape of soil movement for drag zone (Poulos 1995). *p*-multipliers serve to increase or decrease the resistance or limit soil pressure without modifying the required relative movement between the pile and soil. Usual practice for slope-stabilizing piles is to enter a value of 1.0 for *y*-multipliers and to enter values equal to or less than 1.0 for *p*-multipliers. Initial analyses were performed with *p*- and *y*-multipliers equal to 1.0 for a given soil movement and depth of sliding surface taken from inclinometer measurements. *p*-multipliers were then varied to modify API sand model for producing a best fit between the predicted bending moment and measured bending moment responses.

4 Analyses and Results

Results of pile response analyses are presented in this section along with brief background information regarding site conditions, slope monitoring, and geotechnical properties of soil and instrumented piles for each case.

4.1 Railway Embankment Slope-Stabilization Project, Kent, UK

A railway track resting on 7.9-m-high soil embankment in Hilderborough located near Kent area in UK experienced serviceability issues due to side-slope movements causing settlement of railway track. Embankment was stabilized by installing 0.6-m-diameter piles. Soil parameters for lateral pile analysis were established using geotechnical site investigations and laboratory testing data. Table 1 summarized the soil parameters for design purpose. The 10-m-long bored piles were installed at spacing ratio (*S/D*) of 4.0 (Smethrust and Powrie 2007).

The results from inclinometer records (Smethrust and Powrie 2007) showed that the depth of sliding surface lied 4 m below the pile head along with a drag zone depth of 1.5 m below the sliding surface. Bending moments and soil movement were measured on day 42 and day 1345 after the piles were constructed. At day 42, soil movement of 6.25 mm was observed over the top 4 m of slope and increased

Table 1 Soil parameters at the pile location

Stratum	Nominal thickness (m)	Unit weight, γ (kN/m^3)	Friction angle, ϕ' (deg.)	Effective cohesion, c′ (kPa)
Rockfill	1.75	18.9	35	0
Weald clay embankment fill	1.75	18.9	25	1.0
Weathered weald clay	1.0	18.9	25	1.0
Intact weald clay	–	20.0	30	5.0

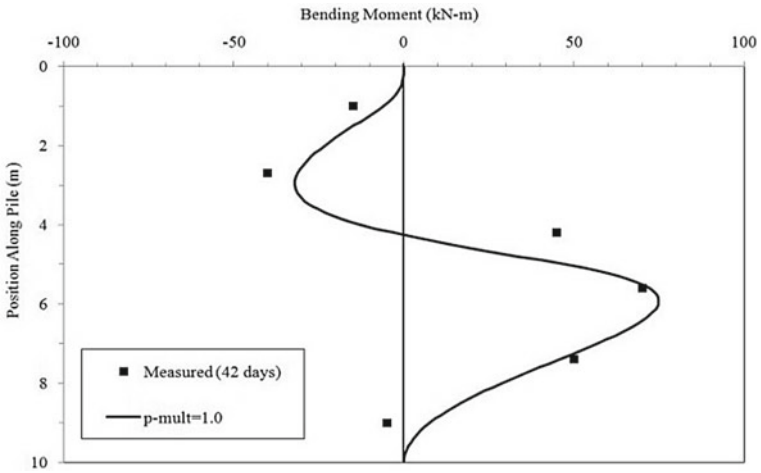

Fig. 1 Comparison of measured and predicted bending moment response at 4-mm soil movement

additional soil movement up to 25 mm by day 1345. The *p*-multiplier of 1.0 produced the best fit with measured results for instrumented pile. The measured and predicted moments for the instrumented pile are shown in Figs. 1 and 2 at given soil movements.

4.2 Masseria Marino Landslide Stabilization Project in Basento Valley, Italy

Five piles were installed and monitored in an active mudslide in the Basento Valley, Southern Italy. The drained shear strength properties at the pile location are summarized in Table 2 for lateral response analysis of pile (Lirer 2012). For the stable clay layer, drained friction angle was estimated from plasticity index (PI) using correlations presented by Terzaghi et al. (1996).

The instrumented middle pile is 10 m long, 0.4-m steel pipe pile with 6 mm thickness constructed at pile-spacing-to-diameter ratio (S/D) of 2.25, which has about

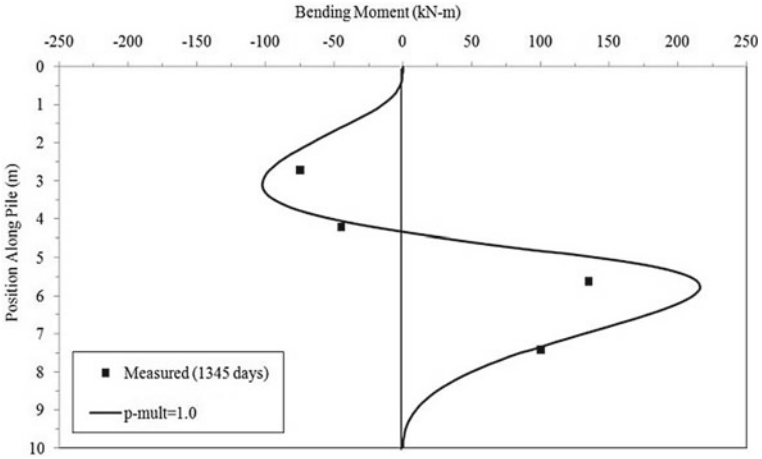

Fig. 2 Comparison of measured and predicted bending moment response at 25-mm soil movement

Table 2 Soil parameters at the pile location

Stratum	Nominal thickness (m)	Unit weight, γ (kN/m^3)	Friction angle, ϕ' (deg.)	Effective cohesion, c′ (kPa)	PI (%)
Sliding layer (c- ϕ soil)	5.0	17.9	23	4.0	22
Stable layer (clay)	–	18.9	30	–	27

the same flexural stiffness value as that of 0.4-m-diameter reinforced concrete bored pile (Lirer 2012). The readings at uphill inclinometer placed 1.5 m away from row of piles revealed the presence of sliding surface at a depth of about 4.75 m. Pile response was analyzed for three different values of soil movement from the uphill inclinometer record to match the predicted response with measured values of bending moment. From construction of piles in July, 1999 till 6 April, 2000, soil movement of 25 mm was observed up to depth of sliding surface. Soil movement of 62.5 mm and 100 mm was observed above the sliding surface on 8 June, 2000 and 13 September, 2000, respectively, as reported by Lirer (2012). Drag zone depth of 0.6 m was observed from inclinometer record. The *p*-multiplier of 0.35 produced the best possible fit with measured values of bending moment for the instrumented pile. The measured and predicted moments for the instrumented pile are shown in Figs. 3, 4, and 5 at given soil movements.

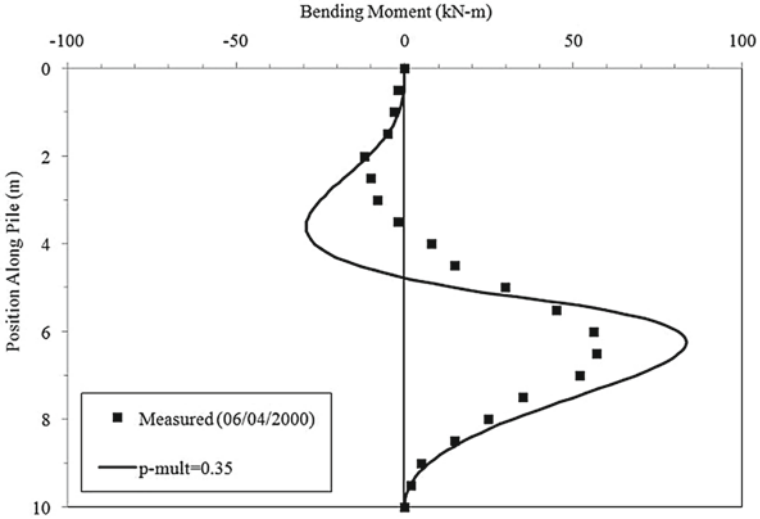

Fig. 3 Comparison of measured and predicted bending moment response at 25-mm soil movement

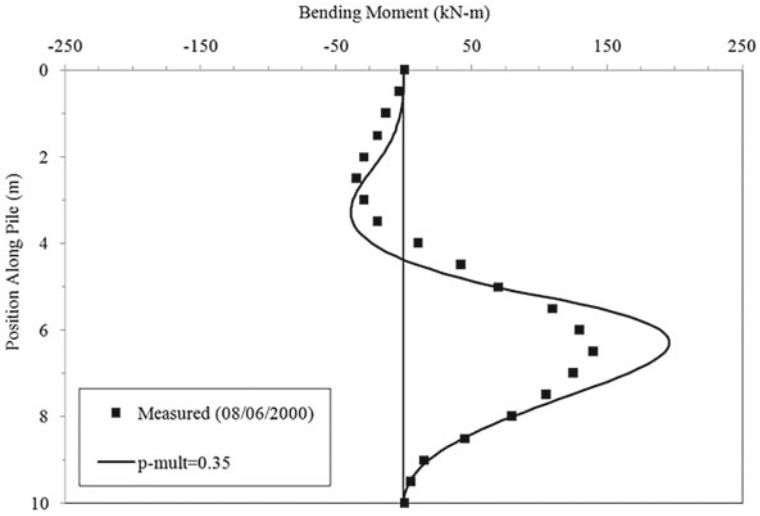

Fig. 4 Comparison of measured and predicted bending moment response at 62.5-mm soil movement

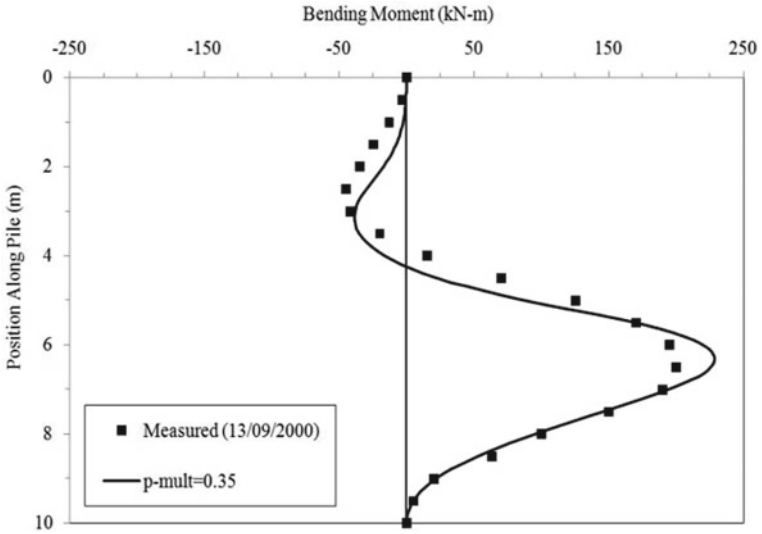

Fig. 5 Comparison of measured and predicted bending moment response at 100-mm soil movement

4.3 National Road Slope-Stabilization Project, Atkea, Greece

Cracks were observed in a road passing over a bridge located near Atkea, Greece after two years following construction. Wing wall of bridge also experienced a tilt. Cracks and tilt were majorly attributed to an active landslide movement near bridge structure. 12-m-long piles of 1.0 m diameter were constructed as spacing ratio (S/D) of 2.5 (Kalteziotis et al 1993). Correlations developed by Terzaghi et al. (1996) were used to estimate the drained frictional angle using plasticity index (PI). The drained shear strength properties reported by Kalteziotis et al (1993) at the pile location are summarized in Table 3 for lateral response analysis of pile.

Two measurements of soil movement and bending moments were presented by Kalteziotis et al (1993), and each was used for two different time periods after the construction of piles. The inclinometer record indicates that the sliding surface was about 3.0 m below the ground surface with drag zone depth of 0.95 m. Soil movements of 6 mm were observed from the end of construction through 14 January, 1992. An additional 1 mm of soil movement occurred on 21 October, 1992. The *p*-

Table 3 Soil parameters at the pile location

Stratum	Nominal thickness (m)	Unit weight, γ (kN/m^3)	Friction angle, ϕ' (deg.)
Sliding layer (c- ϕ soil)	4.0	20.4	25
Stable layer (c- ϕ soil)	–	20.4	30

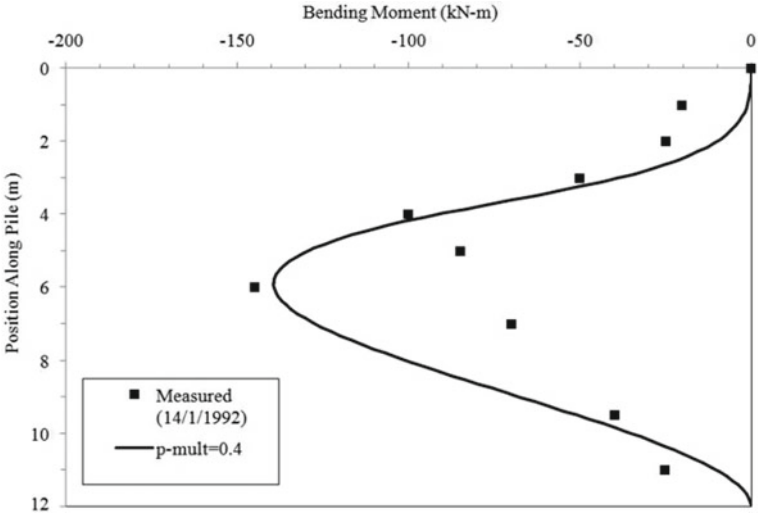

Fig. 6 Comparison of measured and predicted bending moment response at 6-mm soil movement

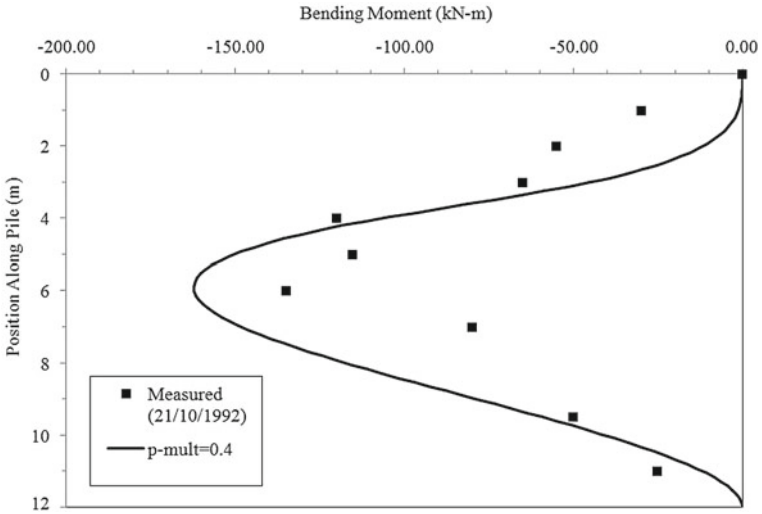

Fig. 7 Comparison of measured and predicted bending moment response at 7-mm soil movement

multiplier of 0.4 produced the best fit with measured values of bending moment for instrumented pile at two soil movements. The measured and predicted moments for the instrumented pile are shown in Figs. 6 and 7 at given soil movements.

4.4 River Bank Slope-Stabilization Project, Alabama, USA

Between 1988 and 2004, movements of a 18-m-diameter coal unloader cell adjacent to the power plant in southern Alabama, USA, accumulated to about 1.2 m of lateral movement and 50 mm of vertical movement. However, during the planning stages for the construction of new facility at project site, soil movements along the riverbank may result into a threat to safety of unloading facility and halt its operation and ultimately cause the instability of project site area during the design life of power plant. For the zero tolerance to long-term instability, proposals were made for slope stabilization to arrest riverbank movements. The selected stabilization scheme included construction of three rows of drilled shafts. One hundred drilled shafts of 1.4 m diameter along the bank of river. Shafts within each row were constructed with spacing-to-diameter ratio (S/D) of 3.3. The shafts averaged 34.5 m in length and have embedded length of 24.4 m into the soil stratum. Drained shear strength properties at the pile location are summarized in Table 4 (Ghahreman et al 2007).

Inclinometer records of Ghahreman et al (2007) revealed the presence of sliding surface at a depth of about 16.2 m near location of drilled shafts. Following construction of drilled shafts, only 5 mm of soil movement was observed and then soil movement arrested. The *p*-multiplier of 0.85 produced the best possible fit with measured values of bending moment for instrumented pile. The measured and predicted moments for the instrumented piles are shown in Fig. 8 at given soil movement.

Table 4 Soil parameters at the pile location

Stratum	Nominal Thickness (m)	Soil density, γ (kN/m^3)	Angle of internal friction, ϕ' (deg.)	Drained cohesion, c' (kPa)	q_u^a (kPa)
Soft-to-stiff clay	4.3	18.1	32.8	20.1	–
Mixed loose to firm sand	3.7	17.3	25.6	15.3	–
Stiff clay	4.3	19.5	27.1	34.7	–
Stiff-to-hard fat clay	6.1	17.3	25.4	16.5	–
Weathered limestone	–	25.1	–	–	120

[a]Uniaxial compressive strength (UCS)

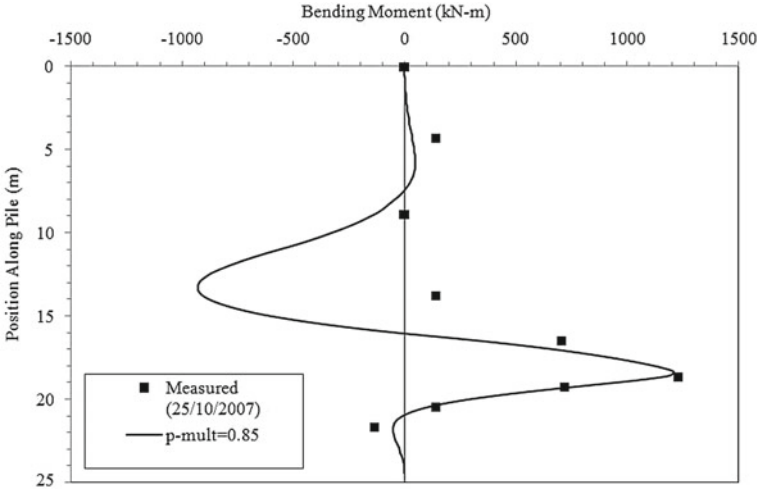

Fig. 8 Comparison of measured and predicted bending moment response at 5-mm soil movement

4.5 State Route RS-152 Slope-Stabilization Project, Ohio, USA

A sliding surface observed parallel to ground surface and was located at the interface zone of overburden and mudstone basal rock. 13.7-m-long drilled shafts of 1.1 m diameter were constructed at the spacing ratio (S/D) of 2. About 6.1 m length of drilled shaft was embedded into the weak rock. Drained shear strength properties for soil layers and compressive strength properties of the weak rock are summarized in Table 5. Pressuremeter test was performed on the rock with 100% RQD to measure the strength properties (Liang 2010).

Inclinometer records of Liang (2010) revealed the presence of sliding surface at a depth of about 6.1 m at an inclination of 30° from horizontal, with additional drag zone depth of 1.5 m. 12.5 mm of lateral soil movement was observed on 1 August, 2006 since the construction of the drilled shafts ended on 25 March, 2006. An additional movement of 12.5 mm was observed on 28 May, 2010. The *p*-multiplier of 0.31

Table 5 Soil parameters at the pile location

Stratum	Nominal thickness (m)	Unit weight, γ (kN/m^3)	ϕ' (deg.)	c′ (kPa)	q_u^a (kPa)	E_{int}^b (kPa)
c- ϕ soil	7.6	19.6	20	4.8	–	–
Weak rock	–	22.0	–	–	4.8	670

[a]Uniaxial compressive strength (UCS)
[b]Initial rock modulus

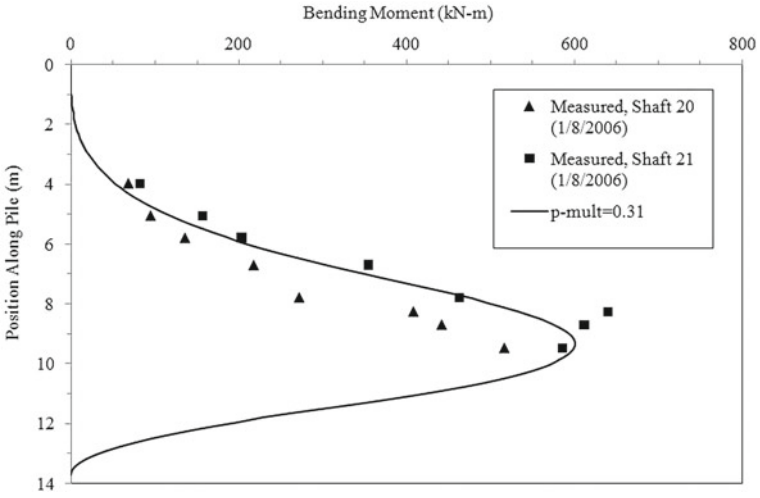

Fig. 9 Comparison of measured and predicted bending moment response at 12.5-mm soil movement

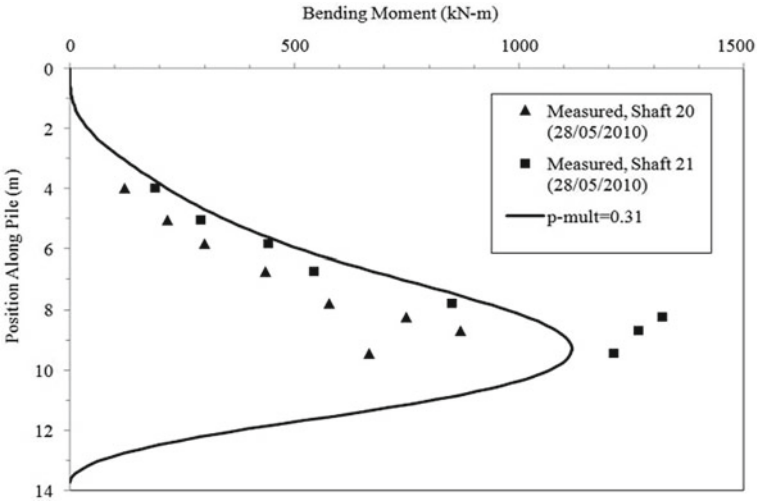

Fig. 10 Comparison of measured and predicted bending moment response at 25-mm soil movement

produced the best fit with measured values of bending moment for instrumented pile at measured soil movements. The measured and predicted moments for the instrumented piles are shown in Figs. 9 and 10 at given soil movements.

Table 6 Soil parameters at the pile location

Stratum	Nominal thickness (m)	Unit weight, γ (kN/m^3)	ϕ' (deg.)	c′ (kPa)	q_u^a (kPa)	E_{int}^b, (kPa)
Colluvium soil	9.15	15.7	22	2.4	–	–
Soft Rock	–	19.6	–	–	27.7	33,865

[a]Uniaxial compressive strength (UCS)
[b]Initial rock modulus

4.6 State Route RS-7 Slope-Stabilization Project, Ohio, USA

The 335-m-long deep-seated slope failure penetrating through interface zone of soil and soft rock occurred in Washington, Ohio. 9.2-m deep sliding surface was observed at the project site. Slope was stabilized by constructing 128 piles in a single row. Piles were constructed 30.5 m off the centerline of highway. Piles of 12.2 m length and 1.2 m diameter were installed at spacing ratio (S/D) of 3. About 3 m length of the total length of shaft was embedded into soft rock. Drained shear strength properties for soil layer and compressive strength properties of soft rock underlain by soil layer at the pile location are summarized in Table 6. Pressuremeter tests were performed on the rock sample with 33% RQD to measure the strength properties (Liang 2010).

The inclinometer record of Liang (2010) indicates that the sliding surface was about 6.1 m below the ground surface at an inclination of 30° from the horizontal, along with drag zone depth of 1.5 m. Inclinometer record revealed that 2.5 mm of lateral soil movement was observed on 1 August, 2008 since the end of construction of drilled shafts. An additional movement of 1.25 mm occurred on 11 August, 2009. A comparison between prediction of analyses and measured response for instrumented piles is shown in Figs. 11 and 12 at given soil movements.

The *p*-multiplier of 0.45 was back-calculated to produce best possible fit with response for the pile at measured soil movements.

5 Interpretation of Results

Lateral pile response analyses were presented, and *p*-multipliers were back-calculated to study the effect of spacing on resistance provided by the continuous row of piles. *p*-multipliers determined from the pile response analyses are plotted versus spacing ratio in Fig. 13. This figure shows the *p*-multiplier needed to match the observed pile response increases with increasing spacing ratio, which suggests that for a given set of pile and soil conditions, resistance increases as the distance between piles increases. The observed trend is in agreement with data presented by

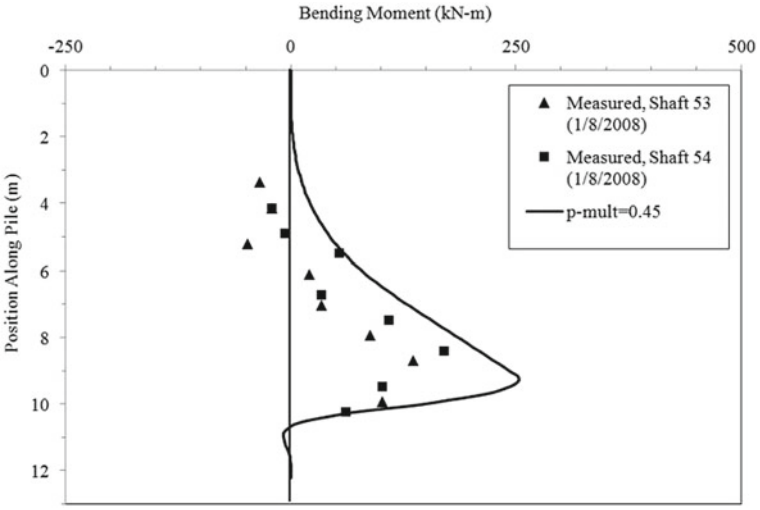

Fig. 11 Comparison of measured and predicted bending moment response at 2.5-mm soil movement

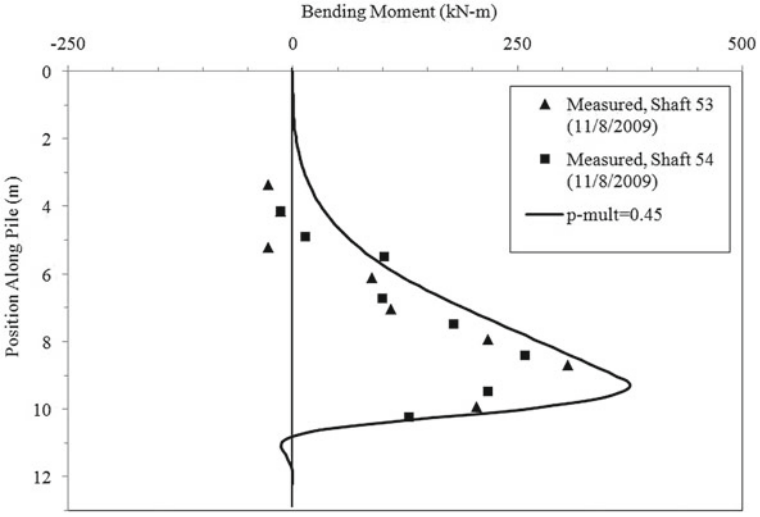

Fig. 12 Comparison of measured and predicted bending moment response at 3.75-mm soil movement

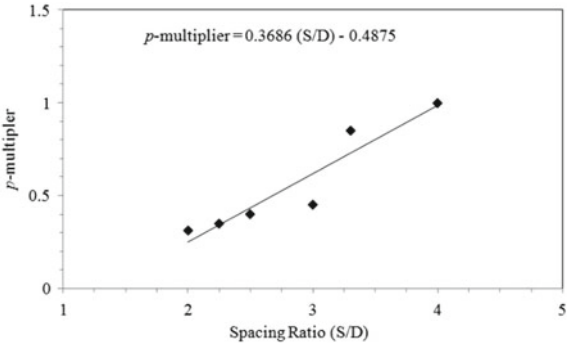

Fig. 13 Back-calculated *p*-multipliers versus spacing to diameter ratio (S/D)

Reese et al (2006) and by Goh et al (2008). Results presented by Kourkoulis et al. (2011) also justify this predicted trend.

It is also important to note that *p*-multipliers were established relative to the API sand *p*-*y* model for drained conditions. Predicted pile responses showed best possible fit with measurements in terms of both general shape and magnitude of moment along the length of pile and no moments were observed at the pile head.

6 Conclusion

Resistance of vertical piles increases as spacing between piles increases if installed in a continuous row without through capping beam. It is recommended that *y*-multiplier of 1.0 should be used and *p*-multiplier should be selected on the basis of pile-spacing-to-diameter ratio (S/D) as shown in Fig. 13, using *p*-*y* analysis for predicting lateral resistance in piles for slope-stabilization applications under drained soil conditions. These multipliers are not recommended for undrained loading conditions. Once lateral resistance provided by piles is predicted, limit equilibrium slope stability analyses can be performed by incorporating that resisting force.

References

Bellew G (2015) Effective stress design for floodwalls on deep foundations—U.S. Army corps of engineers project at Fairfax Jersey Creek levee along Missouri river, Weekly Geotechnical seminar at University of Missouri, Columbia, Missouri, USA

Boeckmann A, Loehr J (2013) A procedure for predicting Micropile resistance for earth slope stabilization. ASCE Geo-Congress, San Diego, California, USA

Ghahreman B, Loehr J, Ang E (2007) Instrumentation and monitoring for a riverbank slope stabilization project, ASCE FMGM 2007. In: Seventh international symposium on field measurement in geomechanics, Boston, Massachusetts, USA

Goh A, Wong K, The C, Miao L (2008) Ultimate soil pressure for pile groups in soft clay subjected to lateral soil movement. J Deep Found Inst 2(1):42–51

Iqbal S (2015) Development of *p*- and *y*- multipliers for design of slope stabilizing piles. In: Thesis presented to the University of Missouri-Columbia in partial fulfillment of the requirements for masters of science degree

Isenhower W (1999) Analysis of pile groups subjected to deap-seated soil displacements. In: Proceedings of the OTRC conference: analysis, design, construction, and testing of deep foundations, Austin, Texas, USA

Isenhower W, Wang ST (2013) Computer program LPILE version 2013: a program to analyze deep foundations under lateral loading, Ensoft Inc., Austin, Texas, USA

Kalteziotis N, Zervogiannis H, Frank R, Seve G, Berche J (1993) Experimental study of landslide stabilization by large diameter piles. In: International symposium on geotechnical engineering of hard soil-soft rocks, Athens, Greese

Kuorkoulis R, Gelagoti F, Anastasopoulos I, Gazetas G (2011) Slope stabilzing piles and pile-groups: parametric study and design insights. ASCE J Geotech Geoenviron Eng 137(7):663–677

Liang R (2010) Field instrumentation, monitoring of drilled shafts for landslide stabilization and development of pertinent design method, Report submitted ohio department of transportation and federal highway administration, Report no. 134328

Lirer S (2012) Landslide stabilzing piles: experimental evidences and numerical interpretation. Eng Geol 149–150:70–77

Loehr J, Brown D (2008) A method for predicting mobilization of resistance for Micropiles used in slope stabilization application, Report submitted to the joint the international association of foundation drilling/deep foundation institute's Micropile committee

Puolos H (1995) Design of reinforcing piles to increase slope stability. Can Geotech J 32:808–818

Reese L, Wang S, Fouse JL (1992) Use of drilled shaft in stabilizing a slope, stability and performance of slopes and embankments. ASCE GSP 31(2):1318–1332

Reese L, Isenhower W, Wang S (2006) Analysis and design of shallow and deep foundations. John Wiley & Sons, New York

Smethurst J, Powrie W (2007) Monitoring and analysis of the bending behavior of discrete piles used to stabilize railway embankment. Geotechniques 57(8):663–677

Terzaghi K, Pack R, Mesri G (1996) Soil mechanics in engineering practice. John Wiley and Sons, New York

Seismic Response of a Steep Nailed Soil Slope: Shaking Table Test and Numerical Studies

S. Sahoo, B. Manna and K. G. Sharma

Abstract The shaking table test was conducted on a steep nailed soil slope having slope angle of 80° to understand its seismic behavior. The earthquake excitation was carried out along the axial direction of the model slope using the input time history, i.e., the 1989 Loma Prieta earthquake. The displacement and acceleration responses of the slopes and the nail forces along the length of nails were recorded. Finite element analysis was also performed on the same model slope to examine its response. A prototype nailed soil slope having slope angle of 80° was also prepared using finite element method which was subjected to the 1991 Uttarkashi earthquake. A comparison has been made between the results obtained from prototype slope and the model slope. This has been done to examine the applicability of shaking table tests on model slope to the real field conditions and to ascertain the same under Indian earthquake condition. A combination of translation and rocking movement is found in the model slope. The maximum nail force has been found toward the farther end of each of the nails from slope facing both in case of prototype and model slopes.

Keywords Shaking table test · Finite element analysis · Seismic behavior · Steep nailed soil slope

S. Sahoo (✉)
Department of Civil Engineering, National Institute of Technology Meghalaya, Bijni Complex, Laitumkhrah, Shillong 793003, India
e-mail: s.sahoo.iitd@gmail.com

B. Manna · K. G. Sharma
Department of Civil Engineering, Indian Institute of Technology, Delhi, New Delhi 110016, India
e-mail: bmanna@civil.iitd.ac.in

K. G. Sharma
e-mail: kgsharma@civil.iitd.ac.in

R. Sundaram et al. (eds.), *Geotechnics for Transportation Infrastructure*, Lecture Notes in Civil Engineering 28, https://doi.org/10.1007/978-981-13-6701-4_39

1 Introduction

Soil nailing is an important and popular technique used to reinforce and strengthen the existing ground for protecting slopes especially steep slopes. The design of nailed soil structures and their reinforcement mechanism under only static load have acquired most of the attention of some of the potential researchers (Murthy et al. 2002; Patra and Basudhar 2005; Fan and Jiun 2008; Li et al. 2008) and very limited studies (Hong et al. 2005; Giri and Sengupta 2009) are available to evaluate their seismic response. Therefore, the seismic behavior of steep nailed soil slopes is worthy of investigation to establish some design guidelines accordingly. The seismic response of steep nailed soil structures is of great importance especially for the earthquake-prone zones (Bathurst and Alfaro 1996). During the Northridge earthquake in California (1994), the performances of a number of reinforced soil structures were documented (Sandri 1994; Stewart et al. 1994; Bathurst and Cai 1995; White and Holtz 1996). During the 1989 Loma Prieta earthquake in the San Francisco Bay, it was observed that many of the nailed soil structures were subjected to considerable levels of shaking which has been reported by Barar et al. (1990). However, no details were available in the literature about the reinforcement failures to identify the reason precisely from the observations made from the failed reinforced soil structures because of earthquakes.

Hence, more research is required to properly understand the behavior of nailed soil structures under earthquake conditions.

An attempt has been made to understand the seismic behavior of model and prototype soil slope having slope angle of 80° with the help of shaking table tests and finite element analyses, respectively.

2 Experimental Investigation on the Model Slope

The shaking table test was conducted on a steep nailed soil slope having slope angle of 80° and slope height of 0.4 m to understand its seismic behavior. The shake table present at the Heavy Structures Laboratory (HSL) at Indian Institute of Technology (IIT) Delhi, India, has been used to provide the uniaxial excitation to the base of the model slope.

The model slope with two rows and three columns of nails having nail length of 0.3 m and nail inclination of 0° was placed in the soil with horizontal and vertical distances between each pair of 225 and 130 mm, respectively. The front view of the complete shaking table test setup with all the instrumental arrangements has been depicted pictorially in Fig. 1.

The earthquake excitation was carried out only along the horizontal/axial direction of the model slope using the input time history, i.e., the 1989 Loma Prieta earthquake having the peak ground acceleration (PGA) of 0.57 g recorded at Los Gatos Presen-

Fig. 1 Front view of complete shaking table test setup

Table 1 Comparison of original and generated earthquake on shake table

Earthquake		Loma Prieta
Year		1989
Peak ground displacement, PGD (mm)	Original	410.02
	Generated	60.43
Peak ground acceleration, PGA (g)	Original	0.57
	Generated	0.58
Predominant frequency (Hz)	Original	1.56
	Generated	1.57

tation Center, California, USA. The range of displacements of the earthquake history is large, falling well outside the range of the strokes of the shake table actuator.

The shake table that was available for the earthquake simulations has only a 150-mm stroke (±75 mm). Figure 2a shows that the earthquake displacements exceed this value, in some instances substantially. To carry out the earthquake tests, the signals were processed using moving average method (Elvin 2009) to fall within the stroke capabilities of the uniaxial shake table without substantially changing the original earthquake history. Figures 2b, c shows the acceleration history and their Fourier transformation, respectively, for both original earthquake acceleration history and the acceleration history recorded at base of the shake table from the accelerometer attached there. The acceleration history recorded at base of the shake table from the accelerometer attached there is considered as the input acceleration history in the experimental investigation. The maximum values of acceleration, displacement, predominant frequencies, and maximum values of acceleration response spectrum have been compared in Table 1.

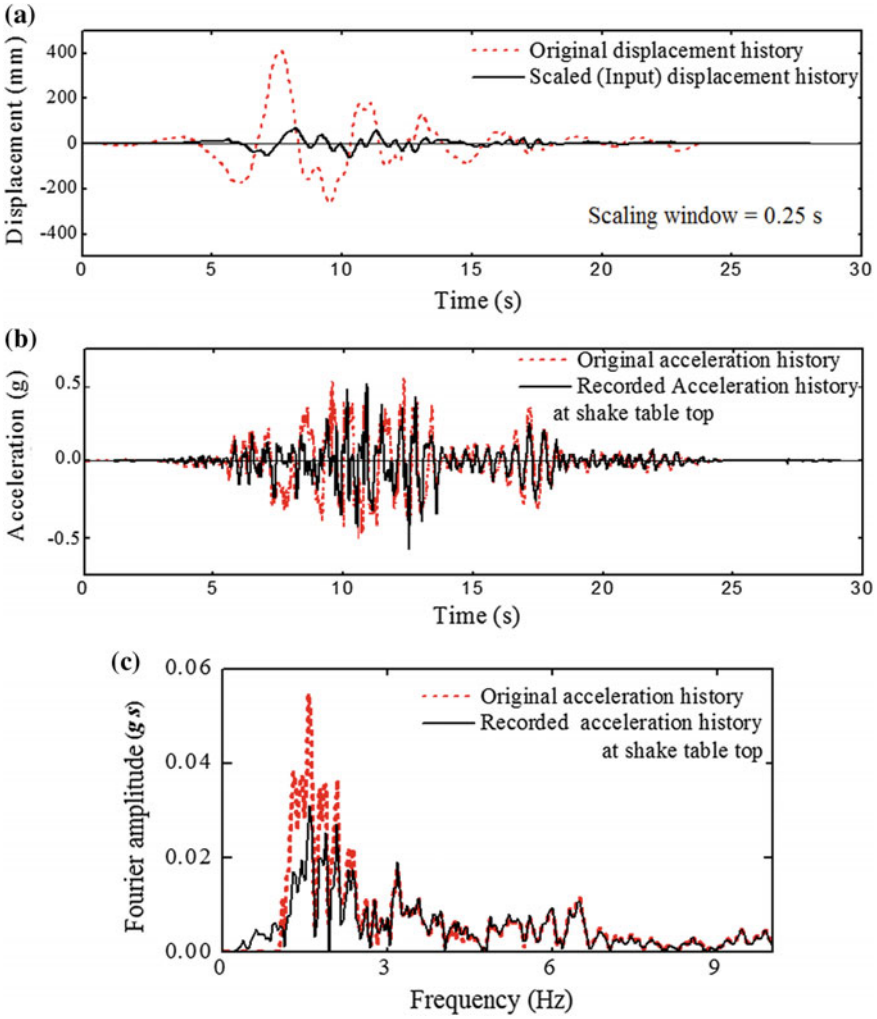

Fig. 2 Scaling of the earthquake time histories of N00E component of the 1989 Loma Prieta earthquake recorded at Los Gatos Presentation Center with peak ground acceleration (PGA) of 0.57 g. **a** Displacement time history; **b** acceleration time history; **c** Fourier transformation of acceleration history

Table 2 Material properties of model slope

Properties	Results
Material and grain size distribution	Yamuna sand and poorly graded (SP)
Maximum and minimum density (γ_{max} and γ_{min})	17.1 kN/m^3 and 13.1 kN/m^3
Angle of shearing resistance (ϕ) and cohesion (c)	33° and 0.5 kPa
Young's modulus of elasticity (E) and Poisson's ratio (υ)	9.5 MPa and 0.3

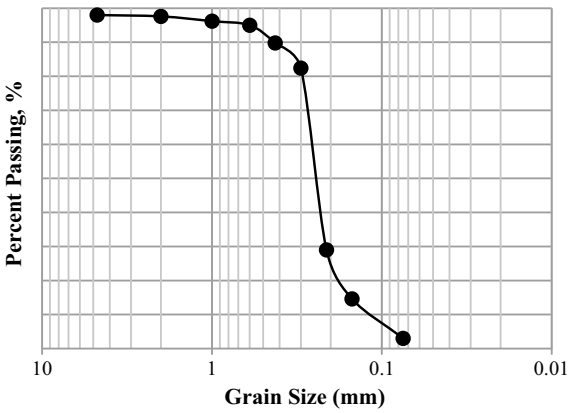

Fig. 3 Grain size distribution of backfill soil (Yamuna sand)

A similitude derived for shaking table tests in a 1-g gravitational field derived by (Iai 1989) has been adopted in determining the characteristics of the material involved in the model tests.

Yamuna sand has been used in making of the model slopes. The sand has been filled into the box through the screen hopper from the fixed falling height of 1 m to maintain the relative density of soil approximately at 65%. The properties of the Yamuna sand used have been given in Table 2. Figure 3 shows the grain size distribution of Yamuna sand.

Hollow aluminum pipe with an outer diameter of 10 mm and thickness of 2 mm has been used as the reinforcing soil nail. The smaller-sized square (0.04 m × 0.04 m × 0.002 m) aluminum plates at the slope face acting as nail heads termed hereafter as facing plates to which the nails were attached. The unit weight (γ), Young's modulus of elasticity (E), and Poisson's ratio (υ) of aluminum tubes (and/or plates) have been found as 21.03 kN/m^3, 10.5 GPa, and 0.24, respectively.

The interface properties between soil and nail have been provided in terms of shear stiffness modulus (K_s), normal stiffness modulus (K_n), and angle of internal friction (ϕ_n) which are found as 90,000 kN/m^2/m, 4,000,000 kN/m^2/m, and 38°, respectively.

The displacement and acceleration responses of the slopes and the nail forces along the length of nails were recorded through the entire instrumental arrangements for further result analysis.

3 Numerical Investigation on the Model Slope

Finite element analysis was also performed using finite element software, (MIDAS/GTS 2013) on the same model slope to examine its response to the same seismic condition, i.e., the 1989 Loma Prieta earthquake having the peak ground acceleration (PGA) of 0.57 g, and the results are compared with the laboratory shaking table test results. The FE results such as maximum lateral displacements at various heights of the facing for both slopes, forces developed along the length of the nails for nailed soil slopes are compared with the test results. The dimensions of aluminum tubes (as nails) and small aluminum plates (as facing plates) used in the present FE analysis are considered as per the shaking table test on model soil slopes. The nails are modeled as one-dimensional beam elements, and the facing plates are modeled as two-dimensional plate elements. The Mohr–Coulomb model has been adopted for soil to simulate the elasto-plastic behavior of soil which combines Hooke's law and the Coulomb's failure criterion. The meshing for soil elements of both the model slopes has been done using 10-noded tetrahedron elements, whereas for the facing plate and nail elements, it has been done with 8-noded quadratic elements and linear elements, respectively. In this analysis, two types of boundary conditions are considered: free-roller and full-fixity. The free-roller and the full-fixity boundary conditions are considered for the side soil boundary nodes and the bottom soil boundary nodes, respectively. The hollow isometric view, the generated mesh diagram, the accumulated displacement diagram, and variation in maximum axial nail force in Newton with its contour diagram at the end of the seismic sequence of model slope are shown in Figs. 4a, b, c and d.

4 Numerical Investigation on the Prototype Slope

A prototype nailed soil slope having slope angle of 80° and slope height of 10 m was also prepared using finite element method which was subjected to the 1991 Uttarkashi earthquake having PGA of 0.0188 g recorded at Almora earthquake station, India.

To evaluate displacements and stresses developed in a nailed soil slope due to seismic loading condition, a three-dimensional finite element model of a prototype nailed soil slope was prepared. The prototype nailed soil slope is representative of typical nailed soil slope on Indo-Gangetic soil located in the vicinity of Delhi, India. The prototype simulates the actual boundary value problem for the present study. The prototype has been created using FE-based Midas/GTS (2013) software, while post-processor facility of the software makes it possible to retrieve the output data in the form of discrete values, contours, or graphics of the required output parameter.

The meshing for soil elements of the prototype slope has been done using 10-noded tetrahedron elements. For the facing plate and nail elements, it has been done using 8-noded quadratic elements and linear elements, respectively.

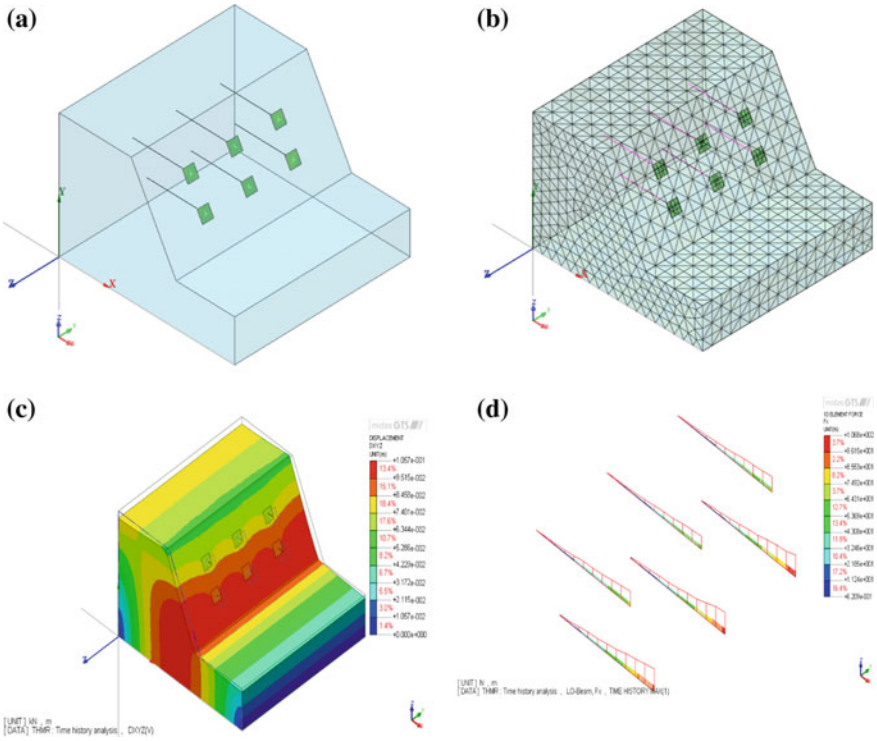

Fig. 4 **a**. Hollow isometric view; **b** the generated mesh diagram; **c** the accumulated displacement diagram; and **d** variation in maximum axial nail force in Newton with its contour diagram at the end of the seismic sequence of model slope

For boundary conditions, roller supports were provided on vertical faces and the bottom face was fixed. In the present investigation, the seismic load was applied uniaxially at the bottom nodes along the axial direction of the prototype slope, i.e., here *X*-direction. Therefore, the bottom nodes are considered fully fixed in all directions but released in *X*-direction under seismic loading at the bottom of the prototype slopes. Elasto-plastic finite element analysis of the prototype slope has been carried out based on simulation of soil by Mohr–Coulomb model.

The initial stress conditions were generated considering self-weight of the prototype slope through linear static analysis whose results do not affect the time-history analysis. The time-history analysis was carried out on the prototype slope using nodal mass concept in which the self-weight of all elements is converted to nodal masses automatically by the in-built features of Midas/GTS (2013).

The acceleration time history of the 1991 Uttarkashi earthquake (PGA = 0.184 m/sec^2) recorded in the longitudinal direction at Almora station and its Fourier transformation are shown in Figs. 5a, b. This acceleration time history of the 1991

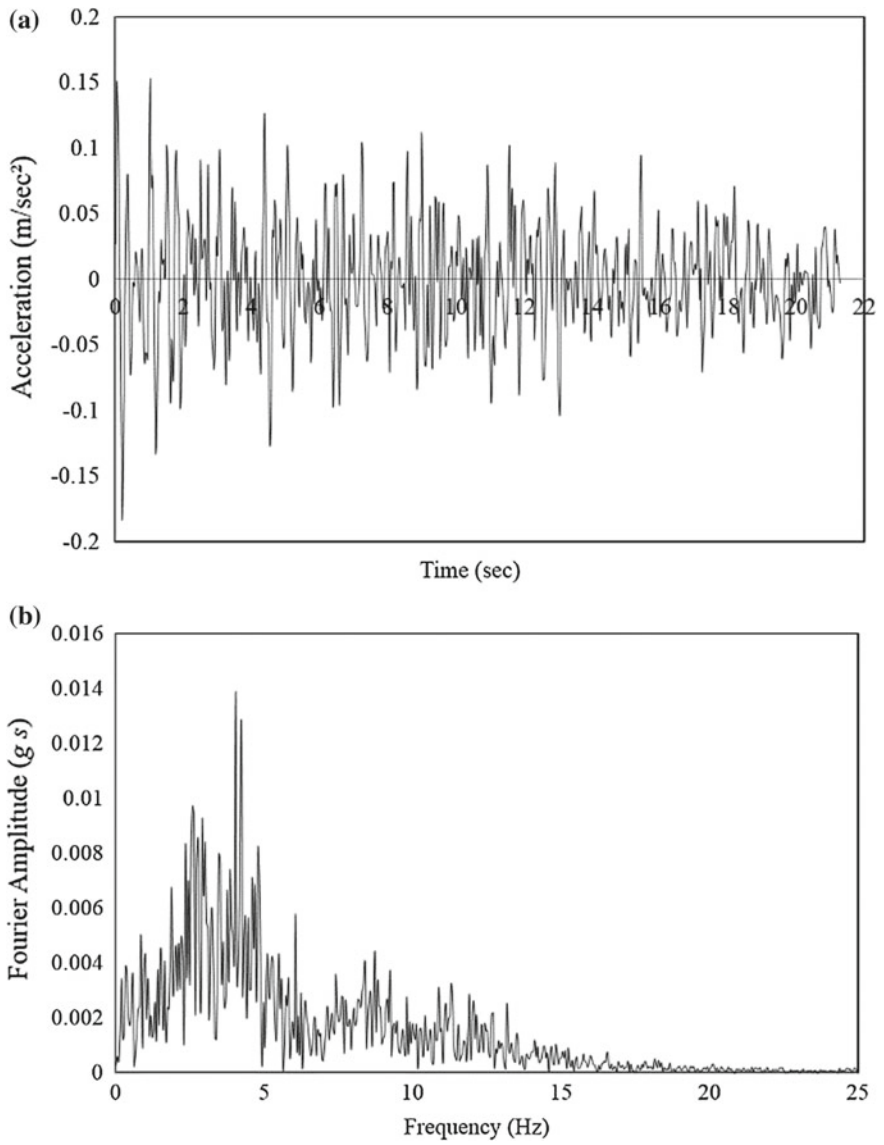

Fig. 5 **a**. Input acceleration history (1991 Uttarkashi earthquake); **b** Fourier transformation of acceleration history (1991 Uttarkashi earthquake)

Uttarkashi earthquake has been considered as the input acceleration history to provide unidirectional (horizontal) seismic excitation at the base of the prototype slope.

The hollow isometric view, the generated mesh diagram, the accumulated displacement diagram, and variation in maximum axial nail force in Newton with its

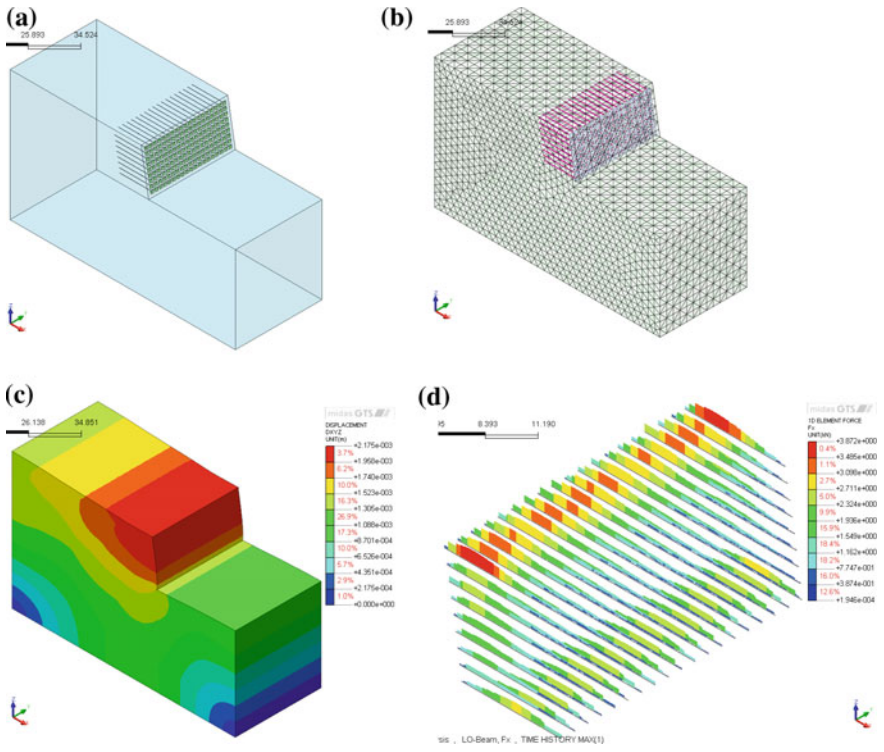

Fig. 6 **a** Hollow isometric view; **b** the generated mesh diagram; **c** the accumulated displacement diagram; and **d** variation in maximum axial nail force in Newton with its contour diagram at the end of the seismic sequence of prototype slope

contour diagram at the end of the seismic sequence of model slope are shown in Figs. 6a, b, c and d.

5 Results and Discussions

A comparison has been made between the results obtained from prototype slope and the model slope in terms of response acceleration at their respective crests, accumulated displacement at various heights of the slope facing, and nail forces developed along the entire length of soil nails. This has been done to examine the applicability of shaking table tests on model slopes to the real field conditions and to ascertain the same under Indian earthquake condition. A combination of translation and rocking movement is found in the model slope. The predominant displacement mechanism found in the prototype slope at every measured level is translation. The

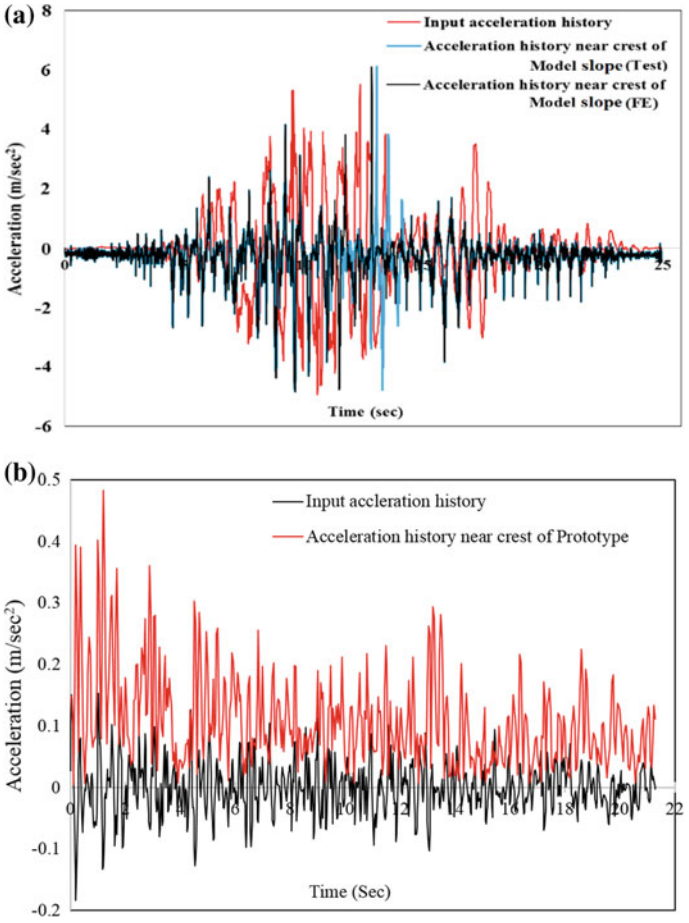

Fig. 7 Response acceleration history in the soil mass near crest versus input acceleration history **a** model slope; **b** prototype slope

maximum nail force has been found toward the farther end of each of the nails from slope facing both in case of prototype and model slopes.

The acceleration response of the model slope and prototype slope has been shown in Fig. 7a, b.

It can be concluded that the accelerations were not uniform in nature throughout the soil mass as there is a significant difference in magnitude of acceleration at the base and at the crest of the prototype slope. It can also be seen that the occurrence of peak acceleration at the crest of the prototype slope is approximately at the same occurrence time of the peak input acceleration.

The normalized accumulated displacements of the slope facing at the end of seismic excitation for model slope and prototype slopes are presented in Fig. 8a, b.

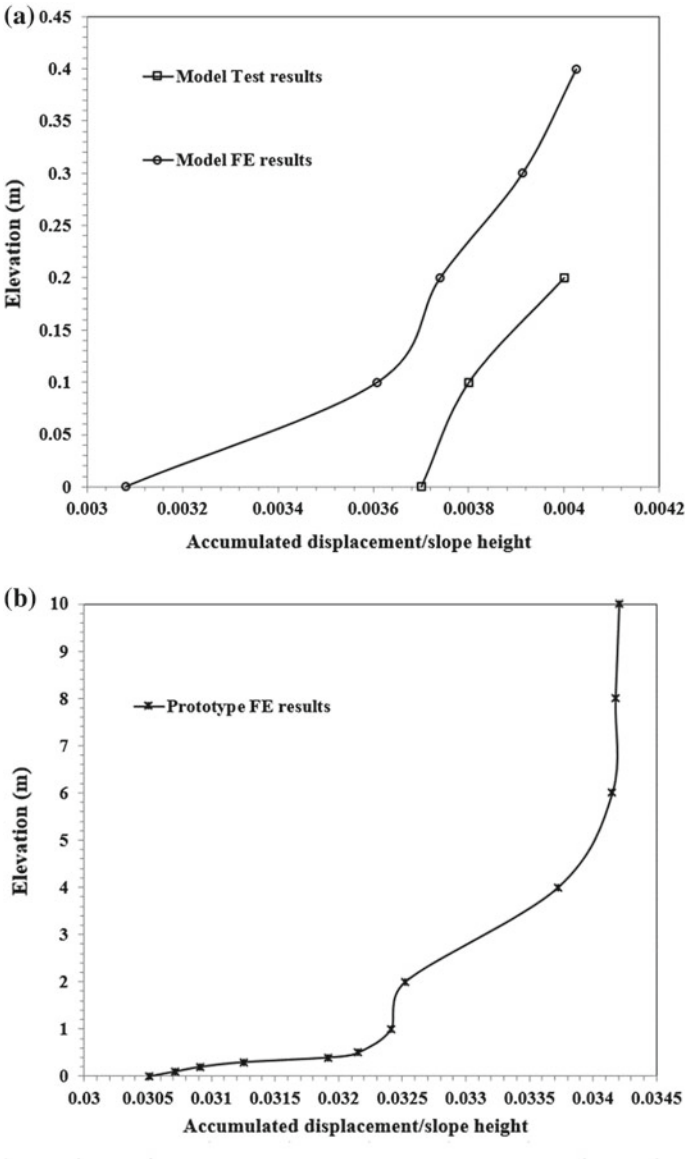

Fig. 8 Normalized accumulated displacements of the slope facing at the end of seismic excitation **a** model slope; **b** prototype slope

The facing displacement of prototype slope from FE results is investigated in terms of ratio of average facing displacement to slope height. The normalized accumulated displacement of the facing which is defined as the ratio of facing displacement to slope height accumulated at the end of the seismic excitation of the prototype slope at every measured level is shown in Fig. 8.

The plot of normalized accumulated displacement of the facing with slope height of the various prototype slopes obtained from FE analysis is shown in this figure.

The predominant displacement mechanism found in the prototype slope at every measured level is translation. The facing displacement in the upper portion of the slope is higher than the lowermost end of the slope facing. It seems from the movement pattern of the prototype slope that a larger mass of soil pulled out along with the nails at the end of the seismic excitation.

6 Conclusions

Thus, from the above discussions, it is apparent that the use of soil nails can improve the stability of a steep slope of slope angle 80° effectively for seismically active regions.

A combination of translation with rocking movement is found in reinforced soil slopes although translational movement is predominant. A greater translational movement than the reinforced model soil slope with rocking movement has been found in case of reinforced prototype slope. The use of soil nails reduces the acceleration amplification at the crest of both the slopes. The maximum nail forces have been found toward the farther end of each of the nails from slope facing in case of reinforced prototype slope, whereas in case of the reinforced model slope, maxima for all the nails are concentrated at the slope facing itself.

The use of finite element simulation of shaking table test on model slopes can also provide a remarkable insight into the seismic behavior of steep nailed soil slopes. Hence, it can be concluded that the testing method and also the numerical method used in the present paper in studying the seismic behavior of steep nailed soil slopes can also be used under Indian earthquake conditions for the same purpose.

References

Barar P, Felio G, Vucetic M, Hudson M, Chapman R (1990) Performance of soil nailed wall during the October 17, 1989 Loma-prieta earthquake. In: Proceedings of the 43rd Canadian Geotechnical Conference, Quebec, 1, pp. 165–173

Bathurst RJ, Alfaro MC (1996) Review of seismic design, analysis, and performance of geosynthetic reinforced walls, slopes and embankments. In: Proceedings of international symposium on earth reinforcement, Fukuoka, Japan, pp. 887–918

Bathurst RJ, Cai Z (1995) Pseudo-static seismic analysis of geosynthetic-reinforced segmental retaining walls. Geosynthetics international 2(5):787–830

Elvin A (2009) Experimentally applied earthquakes and associated loading on a full-scale dry-stacked masonry structure. J S Afr Inst Civil Eng 51(1):15–25 Paper 689

Fan CC, Jiun HL (2008) Numerical study on the optimum layout of soil—nailed slopes. Comput Geotech 35(4):585–599

Giri D, Sengupta A (2009) Dynamic behavior of small scale nailed soil slopes. Geotech Geol Eng 27(6):687–698.

Hong YS, Chen RH, Wu CS, Chen JR (2005) Shaking table test and stability analysis of steep nailed slopes. Can Geotech J 42:1264–1279

Iai S (1989) Similitude for shaking table tests on soil-structure fluid model in 1 g gravitational field. Soils Found 29(1):105–118

Li J, Tham LG, Junaideen SM, Yue ZQ, Lee CF (2008) Loose fill slope stabilization with soil nails: full-scale test. J Geotech Geoenviron Eng 134(3):277–288

MIDAS/GTS (2013) Modeling, integrated design & analysis software—A geotechnical and tunnel analysis system, based on state-of-the-art finite element and graphical technology, manual, GTS 2013 (v1.1)

Murthy S, Babu GLS, Srinivas A (2002) Analysis of prototype soil nailed retaining wall. J Ground Improv 6(3):129–136

Patra CR, Basudhar PK (2005) Optimum design of nailed soil slopes. Geo-Tech Geol Eng 23(3):273–296

Sandri D (1994) Retaining wall stand up to the Northridge earthquake. Geo-Tech Fabrics Rep 12(4):30–31

Stewart JP, Bray JD, Seed RB, Sitar N (1994) Preliminary report on the principal geotechnical aspects of the January 17, 1994 Northridge earthquake. Earthquake Engineering Research Centre, University of California at Berkeley, California, USA, June 1994, Report No. UCB/EERC-94/08

White DM, Holtz RD (1996) (Draft) performance of geosynthetic-reinforced slopes and walls during the Northridge, California earthquake of January 17, 1994. Earth Reinforcement Practice, (Ochiai, Hayashi and Otani, Eds.), Balkema, Proc. Int. Symp. on Earth Reinforcement Practice, IS-Kyushuí96, Fukuoka, Japan, November 1996

Soil Nailing for Failed Slope Stabilization on Hilly Terrain

Shuvranshu Kumar Rout, Manos De, Anup Kumar Mandal and Biswajit Das

Abstract In applications where it is required to enhance stability of vertical cut faces or natural slopes, soil nailing techniques are being increasingly used. The nails improve the ability of soil mass to take care of tensile forces by acting as reinforcement. From the reported literature, it is found that such applications have been made mostly in highway projects with favorable soil conditions. The advantages can be extrapolated for applications in mine infrastructure projects and difficult soil conditions with undulated terrain. This paper aims to highlight a unique case on the rehabilitation of a failed slope in lateritic soil mixed with iron-ore fragments and stabilization of 33 kV transmission tower foundation which is situated just edge of the hill slope. This achieved the desired purpose for stabilization of failed slope and restoration of conveyor operation which is just beneath the hill slope in a shortest possible time. The site-specific design aspects along with modified construction methodologies in difficult geological situations have been reported, and lessons are learned for future implementation.

Keywords Soil nailing · Grouting · Shotcrete · Limit equilibrium method · Factor of safety

S. K. Rout (✉) · M. De · A. K. Mandal · B. Das
Tata Consulting Engineers Ltd, Pipe Line Road, Sakchi, Jamshedpur 831001, Jharkhand, India
e-mail: skrout@tce.co.in

M. De
e-mail: mde@tce.co.in

A. K. Mandal
e-mail: akmandal@tce.co.in

B. Das
e-mail: biswajitd@tce.co.in

R. Sundaram et al. (eds.), *Geotechnics for Transportation Infrastructure*, Lecture Notes in Civil Engineering 28, https://doi.org/10.1007/978-981-13-6701-4_40

1 Introduction

Conventionally, soil nails are used in situations where vertical excavation faces are required to create necessary working space. Soil nailing techniques with appropriate facing element finds wide application in various situations across the world. Not all types of soils are suitable for application of soil nailing techniques. Of particular interest to the present study is the application of this technique in laterite which is a highly weathered soil. Only few references of such studies and applications are available (Atefeh and Erwin 2014).

The current study attempts to evaluate the adaptability of soil nailing techniques for restabilizing failed soil mass caused due to landslides in lateritic soil mixed with iron-ore fragments. The intent of this paper is to present a case study in an application where collapse of existing slope led to disruption of ongoing plant operation and endangered the stability of structures previously built at top of the slope and mitigation of the problem by stabilizing the failed slope through application of soil nailing.

2 Brief History of Problems

The site is located in an iron-ore mine area in eastern region of India. The property owner had installed a new ore processing and handling plant at site comprising of long conveyors and junction houses.

There exists a 33 kV transmission line tower at the top of the slope of this hill. The 33 kV transmission line is also crossing the railway lines further downhill of the slope and is connected to state electric grids. The 33 kV tower is the lifeline of the total operation of plant. The foundation for this tower was constructed by cutting into the slope and subsequently backfilling the foundation pit.

Following completion of the new expansion project, excavation into the hill side was made by the mine developer to create bench for installation of material carrying conveyor. The alignment of the bench was roughly parallel to the slope of the hill. It was noted at the time that the rock formation had discontinuities with inward inclination.

In the next phase of construction on this hill slope, the conveyor foundation was constructed by again cutting into the hill slope along the conveyor route including the portion below the tower foundation. The construction activities which required cutting into this hill side had also endangered the stability of the foundation for this vital installation. In order to prevent failure of the excavated slope for creation of the bench, the conveyor contractor constructed a gabion wall of height 3 m.

After one year of operation, initial signs of shallow failure were noticed just above the gabion wall after significant rainfall at project site. The bulging of gabion boxes was observed in the bottom portion. As a protective measure, a stepped random rubble masonry wall was constructed by local contractor just above the gabion wall

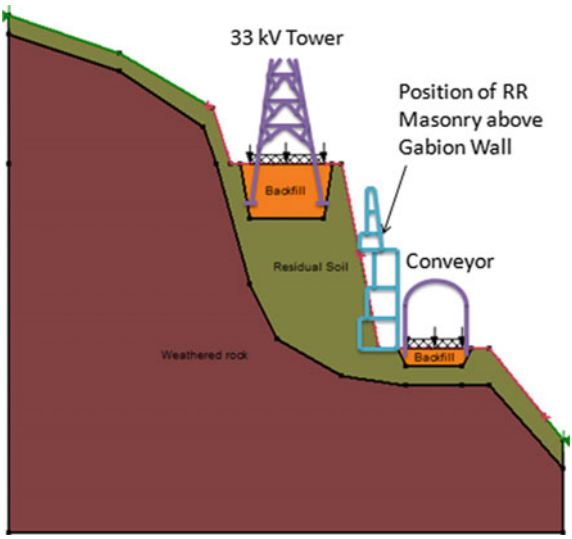

Fig. 1 Project location showing the hill slope with 33 kV tower at top and conveyor at bottom along with position of collapsed RR masonry wall above gabion wall

and backfilled the cut with locally available fines from mine spoils. Heavy rainfall during the retreating period of monsoon had further detrimental effect on the already vulnerable situation. Failure of the soil slope caused extensive damage to the conveyor in operation. The damage was for a length of approximately 30 m. The slope failure additionally threatened the stability of 33 kV tower foundation which is present just at the edge of the slope. The poorly managed drainage water from uphill of this conveyor location, pass through this stretch during rainy season which further destabilized the soil mass. It was concluded that RR masonry wall which was constructed over existing gabion wall could not sustain the earth pressure and pore pressure developed due to the seepage water. The typical location of transmission tower and conveyor has been presented in Fig. 1.

3 Site Constraints, Geology, and Sub-surface Profile

The disruption of the conveyor system led to shut down of the mining plant, and the operation was required to be restarted on urgent basis. There was no scope for new geotechnical investigation at the landslide location. Therefore, considering the urgency previous geotechnical reports of nearby area was considered for design purpose. The geological formation is of hematite rock. The soil layers encountered at site comprise a thin fill layer of hard silty clay underlain by completely weathered to highly weathered reddish brown laterite and rock with steel gray fine-grained iron-ore mixture. The input design parameters for sub-soil profile as obtained from field and laboratory test results are shown under Table 1.

Table 1 Geotechnical parameters for design

Sub-strata	Unit weight (kN/m^3)	Cohesion (kN/m^2)	Internal friction angle (degree)
Filled up soil	18	0.5	28
Residual soil	19	5	30
Weathered rock	22	25	35

The lateritic soil being of residual formation is naturally of high porosity. The presence of water in the soil mass highly aggravates tendency for slope failure and also impedes slope protection schemes. Parametric study on residual soils with various values of internal friction angle and cohesion have already shown that such soil slopes tend to have probability of collapse when cohesion values are less than 10 kN/m^2 with factor of safety less than the acceptable value of 1.5 (Atefeh and Erwin 2014).

4 Design Basis and Formulation of Inputs

There is very little previous available reference of any successful slope protection scheme applied in such type of iron-ore-rich soils. Detailed discussions and literature survey were done to evaluate the merits and demerits of slope protection treatments in similar type of conditions. Based on the available input data, design charts by Federal Highway Administration (FHWA 1994, 1998, 2003) were initially used for the analysis in absence of IS codes.

Subsequently, stability of 33 kV tower under various operational circumstances was established to reach acceptable level of confidence. Therefore, design aspects were investigated for different stages throughout the site progress and inputs are collected from drilling time in different strata, volume of grout consumptions, etc. Accordingly, the stability of the slope was assessed under different operating conditions, e.g., variation in nail length and spacing, diameter, inclination with varying slope profile, varying geotechnical parameters, etc. For optimum design, iterations were continued until the required minimum factor of safety was obtained. Ultimate bond strength of nail and grout was taken from design guidelines initially and verified by pullout test results on sacrificial nails on adjacent locations. Stability of slopes is commonly analyzed by established classical limit equilibrium methods of slope stability analysis using commercial software package (GeoStudio 2007). The following Table 2 presents the basic design inputs for soil nails.

Table 2 Design parameters for soil nails

Item description	Value
Vertical wall height, m	7–13
Nail length, m	4–11
Nail spacing, m	1–1.3
Grade of nail bar	Fe 500
Grade of steel plate	Fe 250
Grade of grout and shotcrete	M 30
Drill hole diameter, mm	150
Ultimate bond strength, kN/m^2	80

5 Challenges in Design Stage

At the start of the design, full-length nails were planned in equal grid spacing. However, when drilling started at top layers, full length could not be achieved due to collapse of holes. This was because of the heterogeneous back-fill material in the tower foundation zone. Manually, 1-m casing were pushed to facilitate further drilling. However, success was not achieved beyond 4 m drilling. Due to the presence of large iron-ore boulders, the equal spacing was not maintained both vertically and horizontally. Also, the top nails had to be drilled with sufficient safe distance from underground tower foundation. After removal of debris at bottom level, civil, mechanical, and electrical erections for conveyor were started along with nailing. The bottom-row nailing was not feasible due to space constraint. To compensate the short-length top

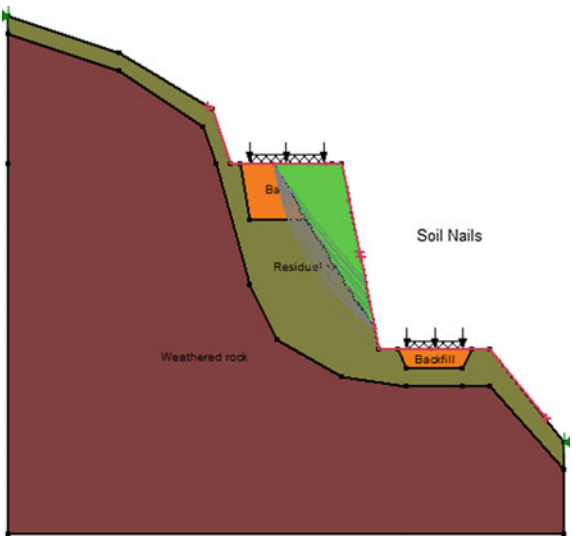

Fig. 2 Prediction of FOS < 0.5 under condition of complete debris removal and without nails (Case-A)

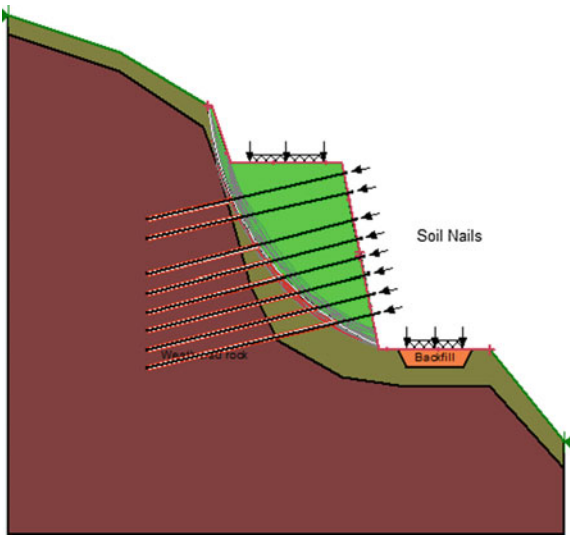

Fig. 3 Prediction of FOS > 1.5 with eight rows of designed length nail (Case-B)

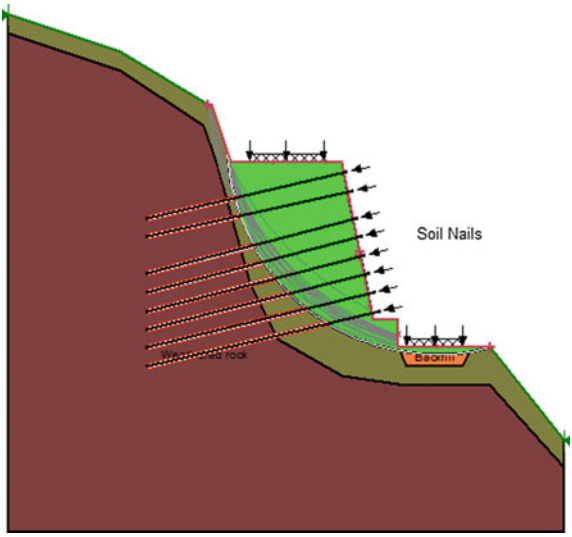

Fig. 4 Prediction of FOS > 1.7 with eight rows of designed length nail and RCC toe wall at bottom (Case-C)

nail, a concrete toe wall with 3-m vertical nails was introduced at bottom portion as additional protection.

Based on continuously changing soil properties, time, space constraint, and all possible construction issues that arose during and after excavation, various situations have been analyzed. Results of the minimum "Factor of Safety (FOS)" are summarized in tabular form below, and outcome figures are shown in thereafter (Figs 2, 3, 4, 5, and 6).

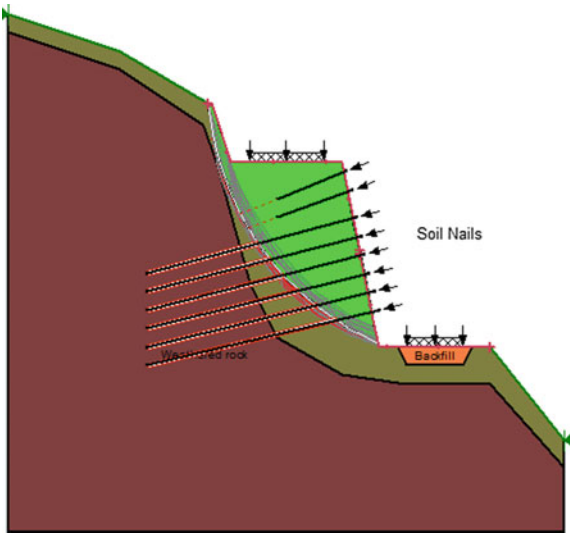

Fig. 5 Decrease of FOS to 1.5 with two top rows of short length and six rows of designed length nail (Case-D)

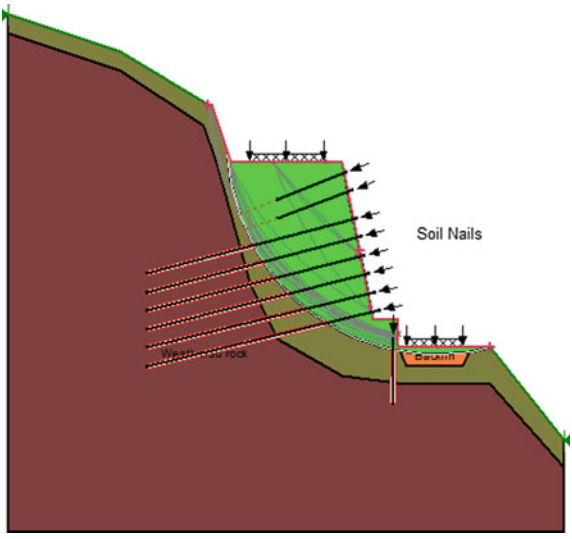

Fig. 6 Increase of FOS to 1.7 with addition of vertical nail and RCC toe wall at bottom (Case-E)

The factor of safety in Case-A is very low to work under these conditions. To maintain minimum factor of safety of 1.0, step-wise debris removal of 1–1.5 m depth from top-down approach was adopted during execution.

6 Challenges in Construction Methodology

Soil nailing is generally carried out in top-down approach with staged excavation. Hence, the general approach is to create benches to accommodate drilling and grouting operation. The bench heights are restricted to desired depths for which the face of excavation can safely remain unsupported till the drilling and grouting of last-row nail. The bench heights are also guided by the requirement of the nozzle operator to hold the nozzle at an angle normal to the face of the slope. Detailed analysis of the convenient bench height for nailing and shotcreting operations is presented by Kutschke, Tarquinio, and Petersen (DFI 2007).

In the present case, the slope reinforcing is carried out on an existing failed slope and hence required a different approach in planning the execution activities. The collapsed soil mass actually provided additional support to the failed slope and was preventing further slide. It was decided to take advantage of this mass of collapsed soil to facilitate the normal top-down approach for carrying out the slope reinforcing work.

6.1 Anchoring Tower

The first requirement at the site was to immediately ensure and enhance the stability of the slope beneath the 33 kV tower foundation. In order to enhance the stability of the tower in this modified profile of the slope, tie-back structure with massive anchor blocks embedded in soil was provided to the tower structure. Additionally, sand bags were placed on the slope for additional support during drilling.

6.2 Staging Platform, Debris Removal, and Bench Excavation

Staging platform was erected from limited space at bottom, taking support from existing trestles of conveyors. Benches were created with scaffolding material resting on the collapsed debris at bottom. Stages were created at different levels at intervals corresponding to convenient operating height of 1.5 m. The working platforms were connected by ramps fabricated from scaffolding material to allow the drilling machine to reach the topmost level of the slope. Similarly, construction schedule was compressed by drilling and grouting at daytime and shotcreting and scaffolding erection during night time.

6.3 Nail and Drainage Pipe Installation

Due to the non-cohesive nature of the residual soil, undulated surface profile resulted during the drilling operation. Modified design approach was adopted by providing one layer of shotcrete on the exposed surface prior to start of drilling to prevent sloughing of loose soil. This technique was also beneficial to enhance the stability of the vulnerable soil mass below the 33 kV tower foundation.

The other aspect of nail installation is the insertion of nails inside the hole. Special care needs to be taken so that the nails do not touch the mouth of the drilled hole at insertion point causing it to collapse. Manual lifting and insertion of nails cause needless striking of the nail against the hole face and can create holes to collapse. Therefore, for long holes and nails at heights, support system with the help of crane at nail end was deployed to minimize the hole collapse. Since there was no space to operate a crane at this location for both vertical (due to active high 33 kV transmission line) and horizontal clearance (due to conveyor and trestles), nail insertion was carried out manually.

Normal steel reinforcement bars were used for nailing. For extra precaution against corrosion, one coat of galvanization was applied at site.

Similarly, inclined drilling was done for installation of drainage pipes of length 2–3 m. The drainage pipes were perforated PVC pipes wrapped with non-woven geo-textiles over the perforation and end of pipes.

6.4 Shotcrete and Grouts

During simultaneous drilling operation for both ends of platform, the disturbance to the loose soil mass from the vibrations caused large soil mass to collapse when the drilling depth had reached about 3 meters. As indicated earlier, the drainage through the soil mass on the slope further aggravated the situation. Therefore, in many cases, large quantity of shotcrete was required to fill the pockets created by collapsed soil. The same thing happened for grouting operation also. In some places, the grout consumption was very high; about 50–200% greater than the usual grout consumption. The presence of fracture planes or pockets inside the strata which can account for higher grout consumption could not be quantified accurately even with proper investigation report. Portland cement with plasticizers was used for grouting with water–cement ratio of 0.45.

7 Instrumentation

Conventional surveying methods were adopted for any movement of ground and displacement of tower pedestals. Due to schedule and time constraints, special geotechnical field instrumentation was not installed. However, dedicated safety inspection teams were engaged for 24/7 monitoring of site activity.

8 Conclusions

The soil nailing method was successfully implemented at site comprising of lateritic soil mixed with iron-ore boulders in a constrained area especially with 33 kV tower at top and conveyor at bottom. This achieved the desired purpose for stabilization of failed slope and restoration of conveyor operation in a shortest possible time. Successful implementation of soil nailing work in situation presented in this study was possible through the following:

i. Detailed analysis and design for the soil nailing system coupled with micro-planning of all site activities considering various constraints at the site.
ii. Rechecking and modification of the design calculations to incorporate site-specific design issues during execution.
iii. Continuous monitoring of site conditions as per the progress and modifying execution methodology accordingly.

The major learning from the present case study is presented herein which will be beneficial for future design as well as implementation practices (Tables 3 and 4).

The solution for slope stabilization should be looked at holistically considering existing facilities and structures in the vicinity of the work site. Special attention has to be paid to ensure safety and stability of nearby structures in brown-field projects.

Most of instability occurs in hill slope due to inefficient drainage networks. To avoid such type of failure, an extensive study of existing drainage networks and periodical maintenance plans has to be addressed.

Table 3 Preliminary cases considered in design stage

Sl. No.	Method of analysis			
	Fellinious	Bishop	Janbu	Spencer
Case-A	0.47	0.48	0.47	0.47
Case-B	1.57	1.65	1.61	1.64
Case-C	1.72	1.84	1.82	1.84

Case-A After complete removal of debris from slope face at one go
Case-B Installation of eight rows of designed length nails
Case-C Installation of eight rows of designed length nails with 1-m height RCC toe wall

Table 4 Additional cases considered at execution stage

Sl. No.	Method of analysis			
	Fellenius	Bishop	Janbu	Spencer
Case-D	1.54	1.62	1.57	1.61
Case-E	1.71	1.84	1.78	1.83

Case-D Installation of two rows of short nail and six rows of designed length nails
Case-E Installation of two rows of short nail, six rows of designed length nails, and one row of vertical nail with 1-m height RCC toe wall

In order to facilitate the evaluation of long-term risk and the probable detrimental effect, continuous monitoring of slope movement and water table is recommended with installation of appropriate field instrumentation.

9 Site Photographs

The site photographs showing site conditions and construction stages are enclosed (Figs 7, 8, 9, 10, 11, 12, 13, and 14).

Fig. 7 Project site of 33 kV tower with damaged conveyor due to collapse of gabion and random rubble masonry wall

Fig. 8 Step-wise debris removal and lowering platform for smooth movements of drilling machine and resources

Fig. 9 Installation of grouted nails by wagon drilling machine after phase-wise debris removal from top

Fig. 10 Drilling and placing of perforated PVC drainage pipes and wire mesh for shotcreting layer

Fig. 11 Application of shotcrete layer with additional cavity filling by concrete, small boulders

Fig. 12 Bottom debris removal and installation of vertical nails for RCC toe wall between slope toe and conveyor

Fig. 13 Final layer of shotcrete along with provision of top surface drainage to channelize surface run-off water

Fig. 14 Final finished slope face showing 33 kV tower at top and restored conveyor along with toe wall at bottom

Acknowledgements The authors gratefully recognize Tata Steel Limited, Jamshedpur, India, for giving opportunity to Tata Consulting Engineers to work as "Consultant" in such a complex brownfield project. Similarly, the authors would like to thank L&T Limited, India, for their continuous support on site-specific inputs throughout the project execution.

References

Atefeh A, Erwin Oh (2014) Strength parameter selection in stability analysis of residual soil nailed walls. Int J Geomate, 7(1, Sl. No. 13)

FHWA (1994) Soil nailing field inspector manual—Soil nail walls. FHWA-SA-93-068, U.S. Department of Transportation, Federal Highway Administration, Washington D.C., USA

FHWA (1998) Manual for design & construction monitoring of soil nail walls. FHWA-SA-96-096R, U.S. Department of Transportation, Federal Highway Administration, Washington D.C., USA

FHWA, (2003) Geotechnical circular no.7—Soil nail walls. FHWA-IF-03-017, U.S. Department of Transportation, Federal Highway Administration, Washington D.C., USA

GeoStudio (2007) Geoslope International Limited, Alberta, Canada

Kutschke WG, Tarquinio FS, Petersen WK (2007) Practical soil nail wall design and constructability issues. In: DFI's 32nd annual conference on deep foundations, Nicholson Construction Company, Colorado Springs, Colorado, USA

Stability Assessment of Reinforced Rock Slope Based on Two-Dimensional Finite Element Approach: A Himalayan Case Study

C. K. Aswathi, Amalesh Jana, Arindam Dey and S. Sreedeep

Abstract Himalayan rock slopes are highly vulnerable to landslides due to geological and tectonic activities. The study area lies along NH 109 road from Rudraprayag, the only pilgrimage route to holy Kedarnath, which experiences high vehicular traffic. There are many cases of landslides reported due to the unpredictable weather and landslide-prone rocks in this seasonal pilgrimage route. Stability analysis is essential, and effort should be given to understand their failure mechanism which resembles the actual field instability. It is important to take mitigation measurements to minimize the losses due to slope failure and to ensure the safe transportation along this route. In this case study, stability analysis of the rock slope, located on national highway (NH 109), is performed using Phase^2 of Rocscience software by considering rock mass as continuum. Reinforcement is provided for the protection of vulnerable rock slope. Two methodologies, equivalent continuum method and combined continuum-interface numerical method, are adopted for the analysis. Equivalent continuum model considers rock slope as continuum mass without any joints, and the effect of discontinuity is introduced by reducing the strength and properties of intact rock to that of the jointed rock mass. In the combined continuum-interface numerical method, the joints are explicitly introduced in the numerical model which accurately represents the behavior of rock slopes in actual field condition. Based on this analysis, end-anchored rock bolts are given as reinforcement to achieve the target factor of safety against failure.

C. K. Aswathi · A. Jana · A. Dey (✉) · S. Sreedeep
Department of Civil Engineering, Indian Institute of Technology Guwahati, Guwahati 781039, India
e-mail: arindamdeyiitg16@iitg.ernet.in

C. K. Aswathi
e-mail: aswathi@iitg.ernet.in

A. Jana
e-mail: janaaamalesh@gmail.com

S. Sreedeep
e-mail: srees@iitg.ernet.in

R. Sundaram et al. (eds.), *Geotechnics for Transportation Infrastructure*, Lecture Notes in Civil Engineering 28, https://doi.org/10.1007/978-981-13-6701-4_41

Keywords Equivalent continuum method · Combined continuum-interface method · Shear strength reduction technique · Finite element method · End-anchored bolts

1 Introduction

Hilly terrains of Himalaya are highly vulnerable due to geological and tectonic activities. The study area which lies along NH 109 road from Rudraprayag is the only pilgrimage route to holy Kedarnath which experiences high vehicular traffic. There are many cases of landslides reported due to the unpredictable weather and landslide-prone rocks in this seasonal pilgrimage route. Stability analysis of rock slopes in this region is essential to minimize losses due to landslides, and appropriate mitigation measures should be taken to achieve the target factor of safety against failure.

Stability of rock slopes is mainly influenced by the anisotropy induced by the structural discontinuities present in the rock such as bedding plane, schistosity, foliation, joint, cleavage, fracture, fissure, crack, or fault plane.

In case of a heavily jointed rock slope, the failure mechanism is guided by a general failure surface which might be developed through intact rock and joints. In order to perform stability analysis of a heavily jointed rock slope, incorporation of all the joints in numerical model requires immense computational efficiency. It is, as well, practically impossible to explore orientation of all joints and to find out all the mechanical and geological characteristics for implementing them in the numerical model. Under such cases, equivalent continuum model (Hoek et al. 2002) considering isotropic, homogeneous system of reduced rock mass strength parameter derived from Geological Strength Index (GSI) is useful to predict the stability of rock slope. Equivalent continuum model considers rock slope as continuum mass without any joints, and the effects of discontinuity are introduced by reducing strength and properties of intact rock to that of the jointed rock mass.

Numerical modeling by considering rock mass as a homogenous medium does not resemble the actual field conditions in all cases. In case of blocky rock slope failures, the main cause of failure is the anisotropy created by the joints. This anisotropy created by the joints changes the stress–strain distribution in rock mass. For such cases, it is important to incorporate to joint properties to study the actual instability. Combined continuum-interface numerical method focuses on the explicit simulation of interfaces through joint elements (Tiwari and Latha 2016). In this method, the joints are considered as interface elements with zero thickness.

In the present study, numerical modeling is performed in both equivalent continuum method and combined continuum-interface numerical model in Phase^2 software. Factor of safety is calculated using shear strength reduction (SSR) technique which is based on finite element method (FEM). SSR technique has ability to predict the stresses and deformation at the support elements at failure and visualize the development of failure mechanism.

Suitable stabilization technique is provided to ensure the stability of rock slopes. End-anchored rock bolts of appropriate mechanical and geometrical properties are used for the mitigation purpose to attain target factor of safety in the present case study.

2 Study Area

The study area lies along NH 109 in Uttarakhand, India, which runs from Rudraprayag to Kedarnath, and is situated at the confluence of the Mandakini and the Alaknanda rivers (Fig. 1). The study area is located between Rudraprayag and Agastmuni [(N30°17′6.30″; E78°58′59″) and (N30°23′34.5″; E79°1′42.4″), respectively]. The highest and lowest elevations in this area are 1650 and 600 m, respectively. The study area lies in the Garhwal Group of the Lesser Himalaya, which comprises diverse rock types of Paleoproterozoic to Mesoproterozoic ages (Umrao et al. 2014).

2.1 Description of Rock Slope

Slope geometry of 25 m height and 80° slope angle is used in this case study as shown in the Fig. 2. Discontinuities are primarily slightly weathered joints of high persistence in the study area. Hariyali quartzite rock slope consists of slightly rough, weathered, and three major joint sets. All three joints have a length of 3 m and spacing 0.6 m. The joint dip angle, dip direction, and spacing are listed in Table 1.

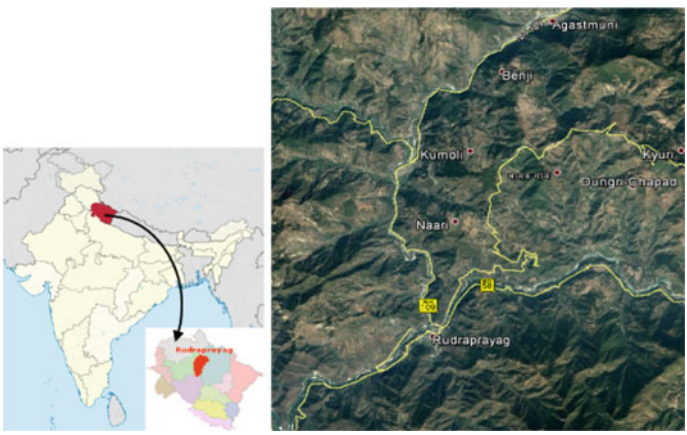

Fig. 1 Location map of study area

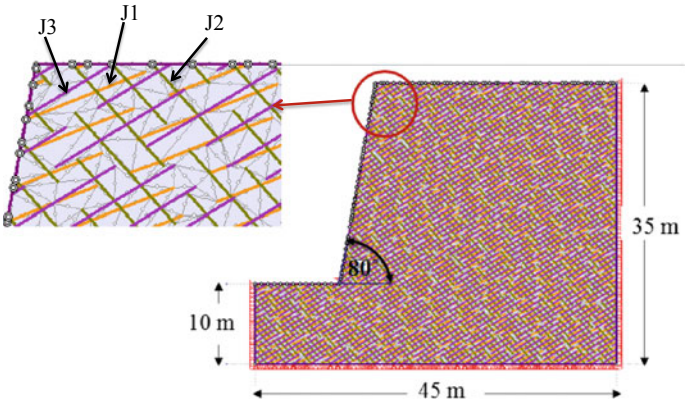

Fig. 2 Description of rock slope

Table 1 Orientation of joints

Joint set	J1	J2	J3	Slope face
Dip/dip direction	30/315	52/155	56/65	80/180

3 Methodology

FEM numerical analysis is carried out in Phase^2 (Rocscience 2016b) by considering the rock mass as continuum. Two methodologies, equivalent continuum method and combined continuum-interface numerical method, are adopted for the analysis.

3.1 Equivalent Continuum Model

Equivalent continuum model assumes that material is continuous throughout the body and discontinuities are introduced into the model by reducing the properties and strength of intact rock to those of rock mass. FEM analysis is carried out in Phase^2 (Rocscience 2016b) for the selected rock slope in two-dimensional plain strain approaches. Phase^2 software uses shear strength reduction (SSR) technique (Matsui and Sam 1992), which is based on FEM, used to find the factor of safety of the rock slope. The geomechanical properties of intact rock obtained from the laboratory test (Umrao et al. 2011) are used to obtain corresponding rock mass properties. RocLab software program is used to obtain the rock mass strength parameters, which is based on generalized Hoek–Brown failure criterion. Since there are some difficulties in applying SSR technique directly to Hoek–Brown criteria in FEM analysis, the equivalent Mohr–Coulomb envelope is used to obtain the rock mass properties. Six nodded triangular finite elements, with an average mesh size of 1.5 m, were used

to discretize the model geometry. Roller-type boundary condition is given at the right boundary, and base of the model is restrained against vertical and horizontal movements.

3.2 Shear Strength Reduction Technique

The shear strength reduction technique is used widely in numerical modeling which gives better results compared to the conventional methods. SSR does not need to assume failure shape and location, failure mechanism. SSR automatically satisfies all the equilibrium conditions, and the factor of safety of a slope can be computed by reducing the rock shear strength based on the Eqs. 1 and 2, until the failure occurs. Actual shear strength properties cohesion (c) and internal friction angle (φ) are reduced for each trial using equations. The trial strength reduction factor is gradually increased until the slope fails, and the shear strength reduction factor at failure is taken as the factor of safety value.

$$C_f = \frac{C}{\text{SRF}} \tag{1}$$

$$\phi_f = \tan^{-1}\left(\frac{\tan\phi}{\text{SRF}}\right) \tag{2}$$

An energy convergence criterion with tolerance 0.1% is used in this study. This convergence criterion is satisfied when the energy imbalance of the iteration falls below a specified value. Phase^2 stops the iteration when the energy imbalance of current iteration becomes small fraction of energy imbalance of initial energy imbalance.

3.3 Evaluation of Rock Mass Properties

RocLab software program is used to obtain the rock mass strength parameters which is based on generalized Hoek–Brown failure criterion. A Hoek–Brown criterion calculates rock mass strength properties based on the following equation (Hoek et al. 2002).

$$\sigma_1 = \sigma_3 + \sigma_{ci}\left(m_b\frac{\sigma_3}{\sigma_{ci}} + s\right)^a \tag{3}$$

where σ_1 and σ_3 are major and minor principal stresses at failure, σ_{ci} is the uniaxial compressive strength of the intact rock, m_b is the reduced value of the material constant m_i and is given as

$$m_b = m_i \exp\left(\frac{\text{GSI} - 100}{28 - 14D}\right) \tag{4}$$

s and a are constants for the rock mass given as

$$s = \exp\left(\frac{\text{GSI} - 100}{28 - 14D}\right) \tag{5}$$

$$a = \frac{1}{2} + \frac{1}{6}\left(e^{-\text{GSI}/15} - e^{-20/3}\right) \tag{6}$$

GSI is the Geological Strength Index, and D is the disturbance factor which depends upon the degree of disturbance to which the rock mass has been subjected by blast damage and stress relaxation. The value of the D varies from 0 for undisturbed rock mass and 1 for the disturbed rock mass.

The equivalent Mohr–Coulomb parameters, cohesion, and friction angle are obtained by fitting a line to the curve generated by Eq. 3 as shown in Fig. 3 (Tables 2 and 3).

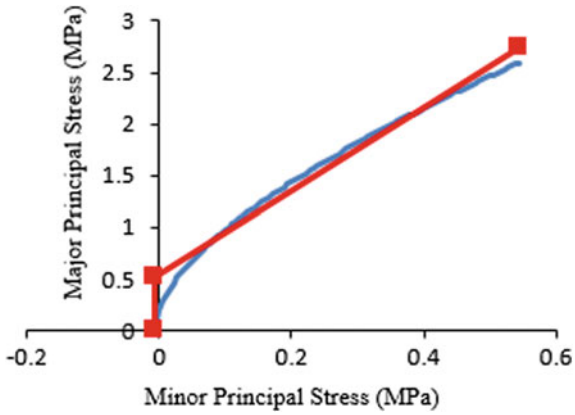

Fig. 3 Mohr–coulomb fitting curve

Table 2 Intact rock properties

Unit weight (kN/m^3)	Cohesion (kPa)	Friction angle (°)	Tensile strength (kPa)
25.91	132	37	6

Table 3 Rock mass properties

UCS (MPa)	GSI	m_i	D	Ei (MPa)
54	35	18	1	22,000

3.4 Kinematic Analysis

The orientation of a joints relative to slope also controls the possibility of failure in the rock slopes. Kinematic analysis is performed in DIPS (Rocscience 2016a) which gives the information about most unstable joint orientation and potential for planar, wedge, and toppling failures. The difference between dip direction of slope face and joint sets is more than 20º; the failure due to planar sliding is not possible for this case.

The plunge (44°) of the line of intersection of two intersecting joints J2 (52/155) and J3 (56/65) is less than the dip of the slope face. This indicates mainly wedge type of failure. The critical zone of failure is shown in stereographic plot (Fig. 4).

3.5 Combined Continuum-Interface Method

Combined continuum-interface numerical method has been attempted in which the discontinuities are represented as interface elements in between the intact rocks. Discontinuities are treated as joint elements which provide a relaxed connectivity between the two adjacent intact rock portions. The joint element is considered as a one-dimensional four-nodded quadrilateral finite element of zero thickness. Normal and shear displacements are simulated in term of relative displacement of nodal pairs at the edge of interface. The constitutive relation between force and displacement is derived in terms of normal (*kn*) and tangential (*ks*) stiffness coefficients. *kn* is estimated using Barton equation (Barton 1972), and *ks* is assumed to be one-tenth of this value. Barton and Bandis (1990) failure criteria are used to determine the shear strength parameters of the joint.

Joint properties used in the analysis are shown in Table 4. All three joints have a length of 3 m, and spacing 0.6 m is used in the analysis as shown in the figure. Shear

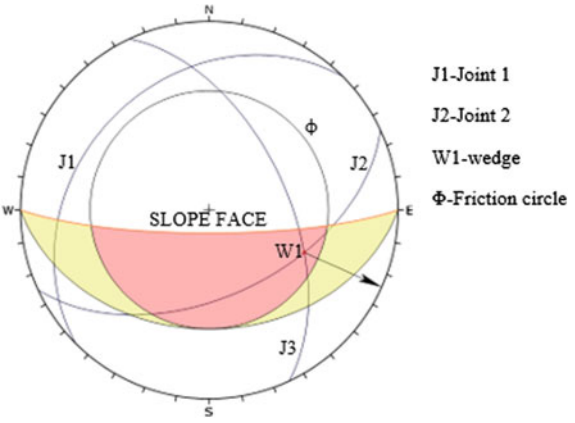

Fig. 4 Stereographic plot for wedge failure

Table 4 Properties of joint sets

Joint set	Normal stiffness (MPa/m)	Joint shear stiffness (MPa/m)	Equivalent joint friction angle (φ)	Equivalent Joint cohesion (kPa)
J1, J2, J3	1244.85	124.485	33°	3

strength reduction (SSR) technique (Matsui and Sam 1992) is used to find the factor of safety value of jointed rock slope.

4 Results and Discussions

Numerical analysis using shear strength reduction (SSR) technique which is based on FEM is conducted for both equivalent continuum and combined continuum-interface models. Failure mechanism (as depicted by contours of total displacement) predicted by FEM-SSR is shown in Figs. 5 and 6. Equivalent continuum model considering isotropic, homogeneous system of reduced rock mass strength predicted a factor of safety value of 1.28, indicating that the slope is marginally stable. The factor of safety obtained is less than the limiting value of 1.5 in static condition. A general failure surface is developed through intact rock and joints which is nearly circular.

The numerical modeling by considering rock mass as a homogenous medium does not resemble the actual field conditions in all cases. Discontinuities are highly persistent in the study area which cannot be captured with equivalent continuum method. Combined continuum-interface method of analysis is done by explicitly introducing the joints. This method predicts a factor of safety value 0.81 that shows the slope to be highly vulnerable to failure. The SRF value for the equivalent continuum model is found to be substantially higher than the combined continuum-interface method because it considers a homogeneous system. The very low factor of safety value predicted by combined continuum-interface method implies that anisotropy

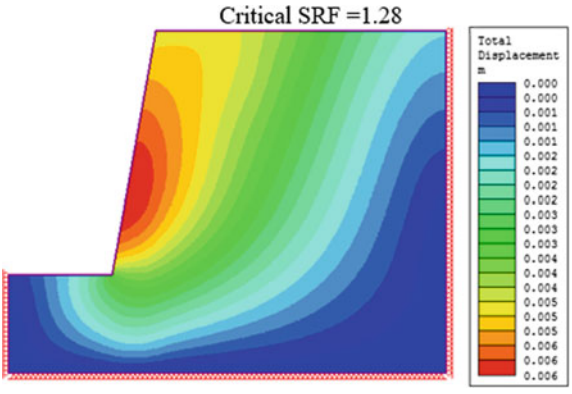

Fig. 5 Failure mechanism (as depicted by contours of total displacement) predicted by FEM-SSR equivalent continuum model

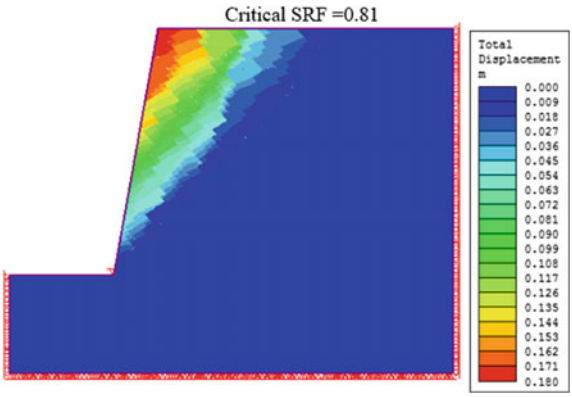

Fig. 6 Failure mechanism predicted by FEM-SSR combined continuum-interface model

created by the joints significantly influence the stability of slope. Since the factor safety is less than limiting value of 1.5 in static condition, appropriate protection should be adopted to prevent failure.

5 Design of Reinforcement

From the results obtained from the two-dimensional finite element analysis, it is well understood that rock slope is highly unstable. It is essential to provide suitable stabilization technique to prevent the rock slope failure. In the present study, end-anchored bolts are used for rock slope stabilization. In Phase^2, end-anchored rock bolts are modeled as one-dimensional deformable element. The bolt transmits the load in terms of relative deformation of two ends. From the kinematic analysis and two-dimensional finite element analysis, potential sliding is found to occur along the joint set J3 with dip angle 56°.

The axial force of bolt (T) is resolved into normal component (T_n) which acts perpendicular to the joint plane and the shear component (T_s) of mobilized tension which acts parallel to the joint plane. When the bolts are installed flatter than normal to the joint plane (Fig. 7), T_n counteracts the dilation and T_S resists the sliding of the joint. FOS has been found to be maximum for this orientation due to the combined effect of these two components. When the bolt is installed at an angle steeper than normal to the joint plane (Fig. 8), T_S results in an increment of the driving force along the potential sliding plane which causes the reduction of factor of safety of the rock slope.

A parametric study is conducted to evaluate the influence of different parameters on rock slope stability by considering cost effectiveness. The orientation of bolts is varied between 0° and 45° with the horizontal for different bolt length, bolt spacing, and bolt tensile capacity to obtain the optimum bolt orientation, and SRF is evaluated

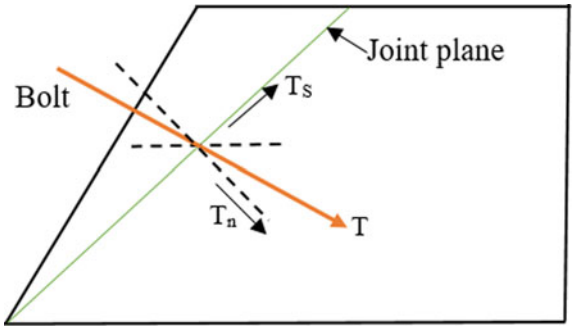

Fig. 7 Bolts installed at an angle flatter than normal

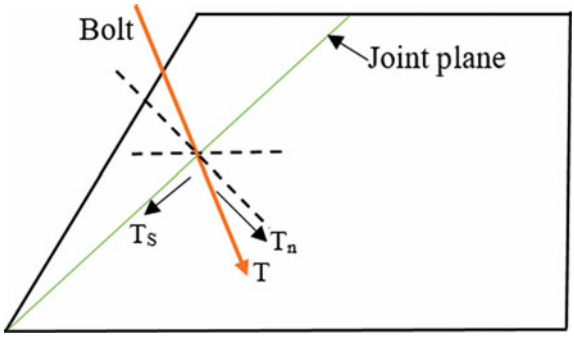

Fig. 8 Bolts installed at an angle steeper than normal

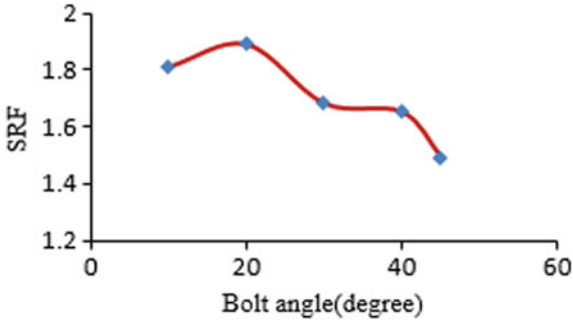

Fig. 9 Variation of SRF with bolt angle

for each case. The maximum SRF value obtained from the two-dimensional finite element analysis is for 20° bolt angle as shown in the Fig. 9.

End-anchored rock bolts of 32 mm diameter at 20° angle with the horizontal are selected from this iterative procedure. The bolt is of 6 m length and 1 m spacing in both in-plane and out-of-plane directions. The tensile capacity of the bolt provided is 0.25 MN. The stability analysis is done for the reinforced slope, and the SRF value obtained for this bolted system is 1.89 (Fig. 10), which is significantly higher than the limiting value in static case, and the deformations are within the limit as well.

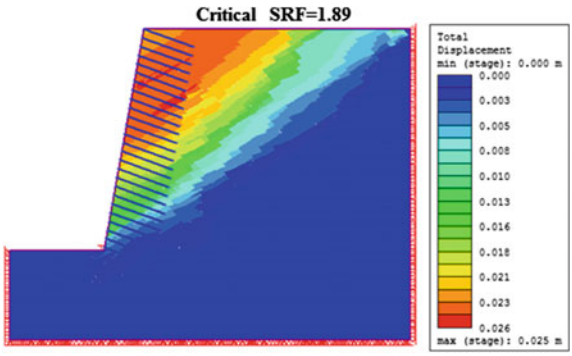

Fig. 10 Failure surface predicted by numerical analysis for reinforced rock slope

The analysis shows that the reinforcement provided in the study area is adequate to sustain the static loading condition.

6 Conclusions

In the present case study, stability assessment of the rock slope, located on national highway (NH 109), is performed in two different approaches: equivalent continuum method and combined continuum-interface method. Equivalent continuum model considering isotropic, homogeneous system of reduced rock mass strength predicted higher factor safety but failed to capture the anisotropy created by the discontinuities. Even though it reduces the complexity in implementing all the joints in a heavily jointed rock slope, it does not resemble the actual field conditions in all cases. A general failure surface is developed through intact rock and joints which is nearly circular. In the second case, for combined continuum-interface method, the joints are introduced in the model explicitly which resembles the actual field condition. The lesser factor of safety predicted from this method implies that the instability of rock slope is highly influenced by anisotropy created by the discontinuities. From the numerical modeling, it is well understood that the combined continuum-interface method, which considers the instability caused by discontinuities present in the rock slope, predicts more accurate and better results. End-anchored rock bolts are provided for the stabilization of vulnerable rock slope. The stability assessment of reinforced rock slopes showed that designed rock bolts are adequate to attain the target factor of safety under static condition.

References

Barton NR (1972) A model study of rock joint deformation. Rock Mech Min Sci Abs 9(5):579–582

Barton NR, Bandis SC (1990) Review of predictive capabilities of JRC-JCS model in engineering practice. In: Rock joints" Proceedings of the international symposium on rock joints, CRC Press, Loen, Norway, 603–610. Boca Raton, FL, pp 4–6

Hoek E, Carranza-Torres C, Corkum B (2002) Hoek-Brown criterion-2002 edition. In: proceedings of the NARMS-TAC conference, 10 July 2002, University of Toronto Press, Toronto, Canada 1, pp 267–273

Matsui T, Sam KC (1992) Finite element slope stability analysis by shear strength reduction technique. Soils Found 32(1):59–70

Rocscience (2016a) Dips version 6.015: Graphical and statistical anallysis of orientation data. Rocsicence Inc., Ontario, USA

Rocscience (2016b) Phase2 version 8.020: Finite element analysis for excavations and slopes. Rocscience Inc., Ontario, USA

Tiwari G, Latha GM (2016) Design of rock slope reinforcement: an himalayan case study. Rock Mech Rock Eng 49:2075–2097

Umrao RK, Singh R, Ahmad M, Singh TN (2011) Stability analysis of cut slopes using continuous slope mass rating and kinematic analysis in Rudraprayag District, Uttarakhand. Geomaterials 1:79–87

Umrao RK, Singh R, Singh TN (2014) Stability evaluation of road-cut slopes in the Lesser Himalaya of Uttarakhand, India: conventional and numerical approaches. Bull Eng Geol Environ 73:845–857

Stability Assessment of Rock Slope and Design of Rock Slope Reinforcement

Kallam Naveen Reddy and Adapa Murali Krishna

Abstract The stability analysis of rock slopes has been a challenging task because of the presence of discontinuities in various forms which result in different types of slope failures. Discontinuities are the weakest zones in the rock mass. Failure mechanism of a rock slope mainly depends on the characteristics of discontinuities. Discontinuities in the form of joints, bedding planes, and faults create anisotropy in the rock mass. Stability assessment of rock slope is very much essential for suitable mitigation measurements. The stability of a rock slope is increased by using various stabilizing techniques. Rock bolting is one of the most common techniques used to stabilize the slope. In this paper, stability analysis of a rock slope located at Sairang station along the alignment of the Bairabi–Sairang railway project is carried out. The study mainly focuses on the kinematic analysis of the rock slope to obtain the possible mode of failure using DIPS, and the stability of the rock slope is analyzed using PHASE^2 which is a finite element method-based shear strength reduction technique .

Keywords Rock slope · Kinematic analysis · Finite element method · Shear strength reduction · Rock bolting

1 Introduction

Failure mechanism of rock slope is very intricate phenomenon and mainly depends on the characteristics of discontinuities. Discontinuities in the form of joints, bedding planes, and faults mainly decide the stability of rock slopes. Discontinuities are the weakest parts in the rock mass and get affected when sheared under the load. Discontinuities create anisotropy in the rock mass and change the stress–strain distribution

K. N. Reddy (✉) · A. M. Krishna
Department of Civil Engineering, Indian Institute of Technology Guwahati, Guwahati 781039, India
e-mail: naveen2016@iitg.ernet.in

A. M. Krishna
e-mail: amurali@iitg.ernet.in

R. Sundaram et al. (eds.), *Geotechnics for Transportation Infrastructure*, Lecture Notes in Civil Engineering 28, https://doi.org/10.1007/978-981-13-6701-4_42

within the rock mass. The mechanical behavior of rock masses is strongly affected by the properties and geometry of the discontinuities (Cai and Horri 1992). Rock slope fails in one or more combination of failure mechanisms, like circular failure, plane failure, wedge failure, toppling failure, and buckling failure.

Kinematic analysis is the most simplified failure analysis in terms of joint sets, bedding plane, cut slope, and angle of internal friction, but it is only suitable for preliminary design (Hoek and Bray 1981; Coggan et al. 1998). Preliminary analysis of slope stability problem using kinematic approach is necessary to identify the orientation of critical discontinuity before proceeding into the strength-based analysis.

Static stability analysis is performed using finite element method based on shear strength reduction (SSR) approach, which calculates the factor of safety based on strength reduction phenomenon. In order to introduce joints in the finite element model, combined continuum interface element method is used in this study. In finite element combined continuum interface method, joint element is assumed as negligible thickness element in between intact rock element and deformation characteristics of interface elements follow Goodman's joint element model (Goodman et al. 1968). Stability assessment of rock slope is very much essential for suitable mitigation measures. The stability of a vulnerable rock slope is increased by using various stabilizing techniques. Rock bolting is one of the most common techniques used to stabilize the slope (Tiwari and Latha 2016).

The primary objective of this study is to investigate the mode of failure and critical discontinuity based on kinematic analysis and to determine the nature of rock slope failure based on the result obtained by performing stability analysis.

2 Background

Kinematic analysis using friction method can be conducted in DIPS (Rocscience 2016a). Several researches have done to determine the mode of failure by kinematic analysis using DIPS (Ghosh et al. 2014; Singh et al. 2015; Sarkar et al. 2016; Umrao et al. 2011; Kumar and Sanoujam 2007). Kinematic analysis is done to obtain a relationship and understanding between existing surface slope steepness and structural discontinuities. Kinematic analysis revealed that the landslides are caused by the wedge failure for the slope instability (Kumar and Sanoujam 2007).

Stability analysis using finite element method can be conducted in PHASE^2 (Rocscience 2016b). Several researchers conducted the stability analysis of a jointed rock slope using different techniques. Gupta et al. (2016) conducted the stability analysis of Surabhi landslide in the Uttaranchal located in Mussoorie using the FEM-SSR technique in PHASE^2. Pal et al. (2012) conducted the dynamic analysis of Surabhi landslide in the Uttaranchal located in Mussoorie using the distinct element method (DEM) in UDEC. Kainthola et al. (2015) conducted the stability analysis of cut slopes along State Highway 72, using the finite element method in PHASE^2. Liu et al. (2014) on the seismic stability analysis of a layered rock slope using pseudo-static analysis in UDEC. Tiwari et al. (2014) performed the stability analysis of Himalayan rock

slope using continuum interface approach by FEM-SSR technique in PHASE^2. Hatzor et al. (2004) carried out dynamic 2D stability analysis of upper terrace of King Herod's palace in Masada, which is a highly discontinuous rock slope. Latha and Garaga (2010) performed the seismic slope stability analysis of a 350-m-high slope using the equivalent continuum approach in FLAC. Kanungo et al. (2013) performed the stability analysis of rock slopes using finite element method in PHASE^2.

In this paper, stability analysis of a rock slope located at Sairang station along the alignment of the Bairabi–Sairang railway project is carried out. The study mainly focuses on the kinematic analysis of the rock slope to obtain the possible mode of failure using DIPS, and the stability of the rock slope is analyzed using PHASE^2 which is a finite element method-based shear strength reduction technique. The observations further utilized to obtain the details of rock bolt installation, i.e., bolt diameter, bolt length, bolt orientation, tensile strength, and spacing of the bolts.

3 Description of the Site

The site is located at Sairang station between chainage of 49.2–51.2 km along the alignment of the Bairabi–Sairang railway project. The rock slope is about 18 m high with an intermediate bench of 3 m width. The area has been subjected to control blasting to pave the way for the railway track alignment. The application of blasting has induced severe instability at the location which is mainly due to the presence of bedding planes dipping out of the face. The mineralogy of the rock slope is mainly composed of thinly bedded fully persistent fine-grained shale (Mithresh 2017).

The rock slope has undergone serious fragmentation due to the blasting process, resulting in formation of rock debris at various sections of the slope. Joint orientation was measured using the Brunton compass to determine the dip and dip direction of the joint planes. For the present slope, in addition to the bedding plane, two other prominent joint sets were observed. The details about the orientation of the slope and the discontinuities are given in Table 1. The joint planes are impersistent with persistence ranging from 2 m to about 8 m (Mithresh 2017).

Table 1 Slope and joint orientation details

Discontinuities	Dip (°)	Dip direction (°)
Bedding plane (*B.P*)	20	280
Joint 1 (J_1)	47	173
Joint 2 (J_2)	55	295
Slope	45	270

4 Evaluation of Rock Strength Parameters

The strength parameters are evaluated by conducting the simple point load test on rock lumps of varying thickness which then utilizes various empirical relations to arrive at a detailed geotechnical data for stability analyses of the rock slope. The strength parameters are adopted from the laboratory test results presented in Mithresh and Krishna (2017). The value of point load index is found with respect to standard size of 50 mm using the equation,

$$I_L(50) = \frac{P}{(A)^{0.75}\sqrt{50}} \tag{1}$$

The conversion factor of point load value to UCS value is taken as 14 which is as preferred for soft rocks (Agustawijaya 2007). The UCS value thus obtained confirms shale to be classified under soft rocks.

Intact rock parameter m_i and modulus ratio "MR" for shale rocks are considered to be 6 and 200 (Hoek 2000), respectively. The value of elastic modulus is found out using the equation,

Table 2 Properties of rock mass and joints

Parameter		Value
Point load strength, $I_{L(50)}$ (MPa)		0.69
Uniaxial compressive strength, σ_{ci} (MPa)		9.71
Elastic modulus, E_i (GPa)		2
Unit weight (KN/m^3)		21.33
Geological strength index (GSI)		27
Rock mass parameter	m_b	0.109
	s	0.00002543
	a	0.527
Joint compressive strength, JCS (MPa)		7
Joint roughness coefficient, JRC		7
Joint cohesion, kPa		20
Joint internal friction angle (°)		30
Normal stiffness (MPa/m)	J_1	665
	J_2	222
	J_3	222
Shear stiffness (MPa/m)	J_1	66.5
	J_2	22.2
	J_3	22.2

$$E_i = \text{MR} * \sigma_{ci} \tag{2}$$

Geological Strength Index (GSI) and Rock Mass Rating (RMR) are other important parameters which require to be evaluated for a complete understanding of the characteristics of the rock mass in the area. The damage factor was taken as $D = 0.7$ due to good blasting carried out at Sairang site location. Properties of rock mass and joints are shown in Table 2.

5 Kinematic Analysis of Rock Slope

The most causative factors of slope failure are multiple joint sets, weathering of the rock mass, and high intensity of rainfall. The analysis has been carried out using friction cone method in DIPS (Rocscience 2016a). A friction circle of 30° equal to joint friction angle was plotted on the stereo-net to obtain the mode of failure for the rock slopes which are depicted in Fig. 1.

From Fig. 1, it is clearly observed that the rock slope section has potential for occurrence of wedge failure. The values of trend and plunge at the point of intersection of two discontinuity planes are 229° and 30°. In kinematic analysis, only the effect of joint orientation is studied. Influence of joint spacing, persistence, strength characteristics of rock, self-weight of slope, and external forces are not considered.

6 Static Stability Analysis of Rock Slope

Numerical model (Fig. 2) of the rock slope has been developed in two-dimensional elasto-plastic finite element analysis program, PHASE^2 (Rocscience 2016b). Joints are introduced in between intact rock as negligible thickness interface elements formulated by Goodman et al. (1968), which connects two intact rock elements. Shear and normal stiffness of the interface element govern the displacement of the jointed system. Joints are introduced as elastic-perfectly plastic elements where Mohr-Coulomb strength criteria have been considered to represent joint strength parameters. Generalized Hoek–Brown failure criteria are used for intact rock. The ratio of the horizontal stress to vertical stress in the rock mass is considered to be 0.5 (Eberhardt et al. 2004). Six nodded triangular meshing element of gradation factor 0.1 and uniform size 1 m is used to generate the finite element mesh. Optimum size of mesh in this study is obtained using mesh convergence study. In the process of mesh convergence analysis, the size of mesh is changed until the mesh size does not change the solution results. Fixed boundary condition is assumed at the base of the model which will restrict displacement in x- and y-direction at the base, and roller boundary condition is assigned to the side of the slope which will allow movement in the vertical y-direction.

Static stability analysis was conducted using the shear strength reduction technique proposed by Matsui and San (1992). An iterative search algorithm was used in shear strength reduction technique to obtain the critical strength reduction factor (SRF). In this method, the parameters of joints and intact rock are reduced by sequential factor, and the stress-deformation behavior of the same is obtained in each step until the slope failed. The reduction factor at the point of failure is the critical strength reduction factor, which is similar to factor of safety of the slope. If the initial material strength parameters are c and ϕ, then the reduced strength parameters, c_f and ϕ_f, can be obtained using the following equations.

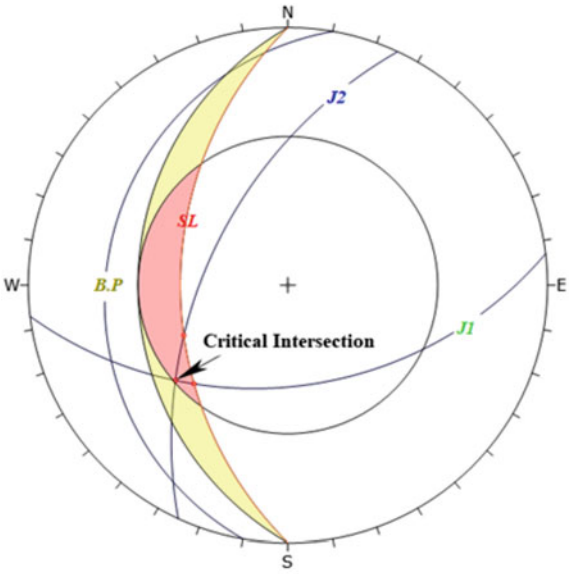

Fig. 1 Kinematic analysis for wedge failure

Symbol	Feature
	Critical Intersection

Kinematic Analysis	Wedge Sliding
Slope Dip	45
Slope Dip Direction	270
Friction Angle	30°

	Critical	Total	%
Wedge Sliding	3	6	50.00%

Plot Mode	Pole Vectors
Vector Count	1 (1 Entries)
Intersection Mode	Grid Data Planes
Intersections Count	6
Hemisphere	Lower
Projection	Equal Angle

$$c_f = \frac{c}{\text{SRF}} \tag{3}$$

$$\phi_f = \tan^{-1}\left(\frac{\tan \phi}{\text{SRF}}\right) \tag{4}$$

where SRF is the strength reduction factor.

Figure 3 represents the critical strength reduction factor (SRF) and displacement response of the rock slope. The critical strength reduction factor (SRF) for the slope is 1.22 (less than recommended value 1.5) and the displacement of the rock slope observed after the analysis was 40.8 mm, and hence, the slope is to be stabilized to reduce the displacement and to increase the stability.

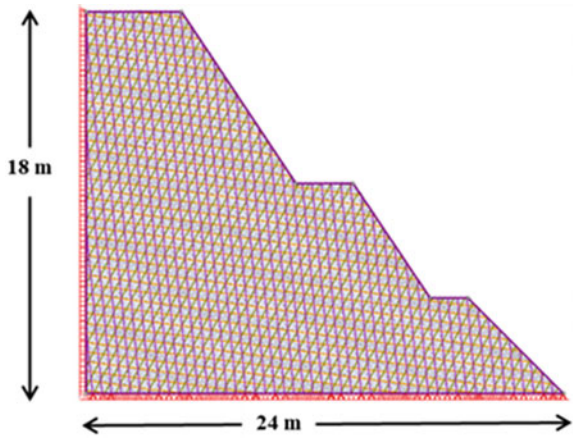

Fig. 2 Numerical model of rock slope

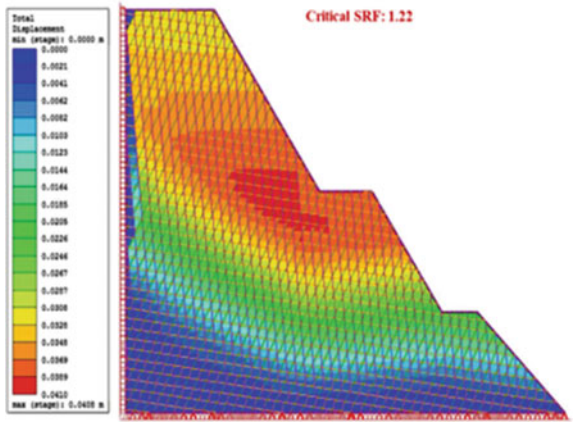

Fig. 3 Critical SRF and displacement response of rock slope

7 Design of Reinforcements

In the present study, end anchorage bolts are used to reinforce the slope. An end-anchored bolt is represented as a 1D deformable element whose interaction with the finite element meshes is through the end points only (Rocscience 2016b).

When the bolts are installed at an angle flatter than the normal to the joint (Fig. 4a), FOS has been found to be maximum for this orientation. The normal component of mobilized tension (*Tn*) neutralizes dilation, and the shear component of mobilized tension (*Ts*) acts in reverse direction of the driving force. Combined effect of these two mechanisms increases the FOS of the rock slope if the bolts are installed at an angle flatter than the normal to the joint.

If the bolts are installed steeper than the normal to the joint (Fig. 4b), the shear component of the bolt tension (*Ts*) acts down the joint plane which increases the total driving force, resulting in the reduction in factor of safety of the rock slope.

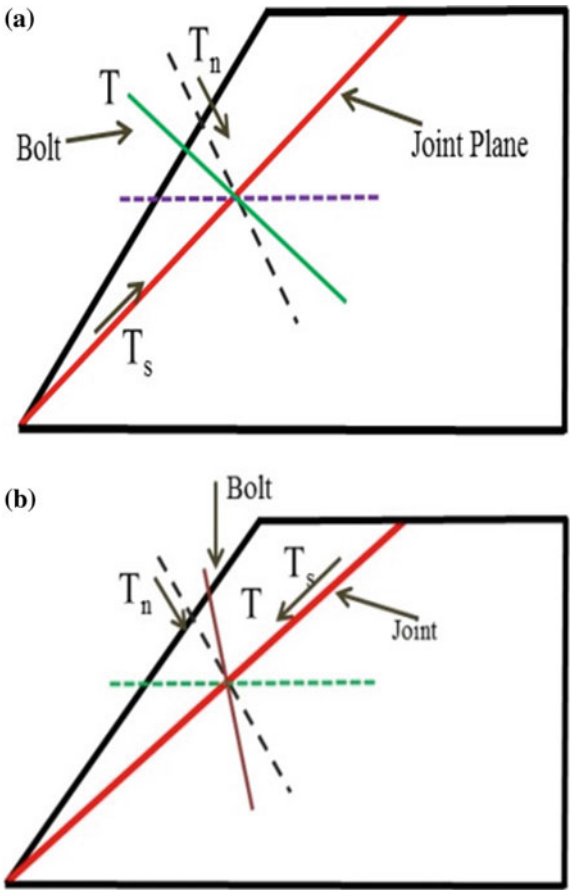

Fig. 4 Bolts installed at an angle **a** flatter than normal to the joint and **b** steeper than normal to the joint

For the current analysis, bolts are installed normal to the slope face (flatter than normal to the joint, J_2). The bolt orientation, bolt length, and bolt spacing are evaluated based on the trial and error method. Different combinations of bolt parameters such as bolt diameter, bolt length, bolt spacing, and bolt tensile capacity are used to obtain the effective parameters of the bolt. Figure 5 represents the numerical model of the reinforced rock slope.

Based on the trial and error results, the optimum bolt parameters for the current study are as follows:

Bolt orientation = Normal to the slope (45°)
Bolt diameter = 20 mm
Bolt length = 4 m
Bolt spacing = 0.75 m
Bolt tensile capacity = 0.25 MN.

The factor of safety obtained after stabilization of rock slope is 1.62 which is more than the required value 1.5 and the displacement of the rock slope observed after the analysis was 29.7 mm, and the displacement response of the rock slope after stabilization is shown in Fig. 6.

From the analysis, the factor of safety for the unreinforced case under static condition was 1.22, which was increased to 1.62 after reinforcing the slope. Provision of reinforcement increased the factor of safety because it modifies the normal and shearing forces acting along a sliding plane. Similarly, the maximum displacement observed for the unreinforced case under static condition was 40.8 mm, which was decreased to 29.7 mm after reinforcing the slope.

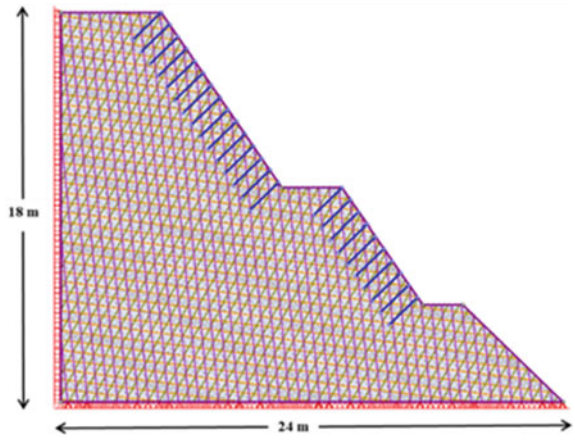

Fig. 5 Numerical model of reinforced rock slope

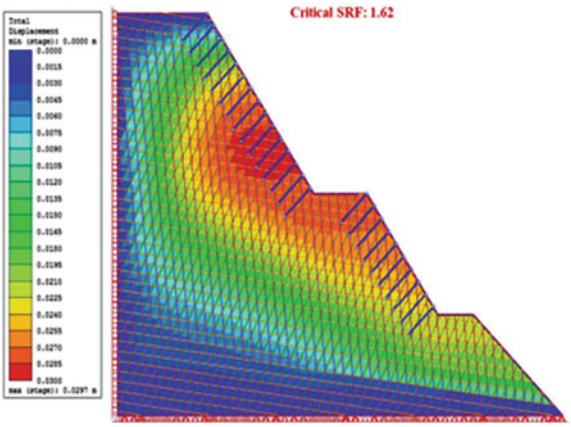

Fig. 6 Critical SRF and displacement response of reinforced rock slope

8 Summary and Conclusions

Stability analysis of a rock slope located at Sairang station along the alignment of the Bairabi–Sairang railway project is presented in this paper. Kinematic analysis of the rock slope is carried out to obtain the possible mode of failure using DIPS, and the stability of the rock slope is analyzed using PHASE^2 which is a finite element method-based shear strength reduction technique.

Kinematic analysis concludes that the rock slope had the potential for occurrence of wedge failure. The slope is found to be unstable as the critical strength reduction factor (SRF) is less than recommended value. Hence, the slope is to be stabilized to reduce the displacement and to increase the stability.

Reinforcement in the form of rock bolts was recommended for stabilizing the slope sections, and the reinforcement layout was arrived at based on trial analyses. Provision of reinforcement increased the factor of safety or strength reduction factor of the slope section.

References

Agustawijaya DS (2007) The uniaxial compressive strength of soft rock. Civil Eng Dimension 9(1):9

Cai M, Horii H (1992) A constitutive model of highly jointed rock masses. Mech Mater 13:217–246

Coggan JS, Stead D, Eyre JM (1998) Evaluation of techniques for quarry slope stability assessment. Transactions of the institution of mining and metallurgy. Section B. Appl Earth Sci, 107

Eberhardt E, Stead D, Coggan JS (2004) Numerical analysis of initiation and progressive failure in natural rock slopes—the 1991 Randa rockslide. Int J Rock Mech Min Sci 41(1):69–87

Ghosh S, Kumar A, Bora A (2014) Analyzing the stability of a failing rock slope for suggesting suitable mitigation measure: a case study from the Theng rockslide, Sikkim Himalayas, India. Bull Eng Geol Env 73(4):931–945

Goodman RE, Taylor RL, Brekke TL (1968) A model for the mechanics of jointed rock. J Soil Mech Found Div

Gupta V, Bhasin RK, Kaynia AM, Kumar V, Saini AS, Tandon RS, Pabst T (2016) Finite element analysis of failed slope by shear strength reduction technique: a case study for Surabhi Resort Landslide, Mussoorie Township, Garhwal Himalaya. Geomatics, Nat Hazards and Risk 7(5):1677–1690

Hatzor YH, Arzi AA, Zaslavsky Y, Shapira A (2004) Dynamic stability analysis of jointed rock slopes using the DDA method: King Herod's Palace, Masada, Israel. Int J Rock Mech Min Sci 41(5):813–832

Hoek E, Bray JD (1981) Rock slope engineering. CRC Press

Kanungo DP, Pain A, Sharma S (2013) Finite element modeling approach to assess the stability of debris and rock slopes: a case study from the Indian Himalayas. J Int Soc Prev Mitigation Nat Hazards 69:1–24

Kumar A, Sanoujam M (2007) Landslide studies along the national highway (NH 39) in Manipur. Nat Hazards 40(3):603–614

Latha GM, Garaga A (2010) Seismic stability analysis of a Himalayan rock slope. Rock Mech Rock Eng 43(6):831–843

Liu Y, Li H, Xiao K, Li J, Xia X, Liu B (2014) Seismic stability analysis of a layered rock slope. Comput Geotech 55:474–481

Matsui T, San KC (1992) Finite element slope stability analysis by shear strength reduction technique. Soils Found 32(1):59–70

Mithresh KP (2017) Characterization and stability analyses of rock slopes, Post Graduation Thesis, Indian Institute of Technology, Guwahati

Mithresh KP, Krishna AM (2017) Stability of rock slopes in soft and stratified rock mass. In: Geotechnics for natural and engineered sustainable technologies: Indian geotechnical conference (GeoNEst: IGC-2017), Guwahati, India, pp 1–4

Pal S, Kaynia AM, Bhasin RK, Paul DK (2012) Earthquake stability analysis of rock slopes: a case study. Rock Mech Rock Eng 45(2):205–215

Rocscience Inc (2016a) DIPS v7.0. Graphical and statistical analysis of orientation data. Toronto, Ontario, Canada. www.rocscience.com

Rocscience Inc. (2016b). PHASE^2 Version 9.0 - Finite Element Analysis for Excavations and Slopes. Toronto, Ontario, Canada. www.rocscience.com

Sarkar K, Singh AK, Niyogi A, Behera PK, Verma AK, Singh TN (2016) The assessment of slope stability along NH-22 in Rampur-Jhakri Area, Himachal Pradesh. J Geol Soc India 88(3):387–393

Singh PK, Kainthola A, Singh TN (2015) Rock mass assessment along the right bank of river Sutlej, Luhri, Himachal Pradesh, India. Geomat Nat Haz Risk 6(3):212–223

Tiwari G, Latha GM (2016) Design of rock slope reinforcement: An himalayan case study. Rock Mech Rock Eng 49(6):2075–2097

Tiwari G, Gali ML, Rao VR (2014) Finite element study of a rock slope using continuum-interface approach

Umrao RK, Singh R, Ahmad M, Singh TN (2011) Stability analysis of cut slopes using continuous slope mass rating and kinematic analysis in Rudraprayag district, Uttarakhand. Geomaterials 1(03):79

Steep Slope Stabilization Under Seeping Water

R. Besra, A. Usmani and V. K. Panwar

Abstract Construction of structures on a land created between the upper and the lower plateau of a hill slope has always been a challenging task for geotechnical engineers. Creating adequate space under such conditions involves huge earthwork in cutting and filling, resulting in unstable steeper slopes in several locations. The problem gets further aggravated with the presence of high water table pressure and seeping water through the slope. This paper refers to a case study of constructing refinery unit road used for the movement of product-laden trucks across a slopy terrain where a maximum rainfall of 4000 mm is recorded annually. Due to the space constraint at the site, construction of stable slope with gentle inclination was not feasible. Hence, the steeper slope of 80–85° inclination was constructed with reinforced earth (RE) wall on filling side (650-m length) and 65–70° slope of 350-m length was constructed using soil nailing with gabion toe wall in the cutting side. This paper discusses in detail construction methodology carried out at the site along with various challenges faced during execution of soil nailing slope including details of nails, load test results, gabion toe wall details, reasons of local slope failure and rectification measures adopted.

Keywords Soil nail · Gabion · Soldier pile · Geo-textile · Grouting

1 Introduction

Construction of access roads across slopy terrain has always been a challenging task for engineers. Long-term stability of such structures always remained questionable in view of the various problems encountered at such sites. Intrinsic stabil-

R. Besra (✉) · A. Usmani · V. K. Panwar
Engineers India Limited, Bhikaiji Cama Place, New Delhi 110066, India
e-mail: rimil.besra@eil.co.in

A. Usmani
e-mail: altaf.usmani@eil.co.in

V. K. Panwar
e-mail: vk.panwar@eil.co.in

R. Sundaram et al. (eds.), *Geotechnics for Transportation Infrastructure*, Lecture Notes in Civil Engineering 28, https://doi.org/10.1007/978-981-13-6701-4_43

ity of slopes having different types of geo-materials like soil, weathered rocks and bedrocks requires specific ways of stabilization under different field conditions. Soil nailing is one of the commonly used techniques of reinforcing and strengthening steep slopes under varying environmental conditions. Tan and Chow (2004) defined nails as closely spaced steel bars installed, as construction proceeds from top-down. Nailing is classified as passive anchors and develops their reinforcing action through nail–ground interactions as the ground deforms during and after construction. BGS report (1991) identified the range of soils amenable for nailing works as cemented granular soils to over-consolidated clays, marls and soft rocks. Properly designed soil nail wall has proven to be an efficient and cost-effective slope stabilization measure. Shaw Song (2005) reported the use of soil nailing technique to many civil engineering projects at Mexico City back in the 1960s and has gained popularity in Europe since 1970. Commonly referred design codes and manuals for soil nailing works are FHWA-SA-96-069R (1998), FHWA-IF-03-017 (2003) and BS-8006 Part-2 (2011). This paper includes a case study of slope stabilization carried out using soil nailing technique along with remedial slope stabilization work post-failure at a particular location.

2 Topography and Subsoil Condition of the Site

Large diameter oil tanks are located on the northern side, and water filtration plant is located on the southern side of the proposed area to be developed for construction of refinery unit at RL 35 m. This case study deals with slope stabilization work between RL 61.50 m at the tankage area and finished ground level of the refinery unit (refer to Fig. 1). Deep excavation on the northern side of the refinery unit is proposed for construction of building structures, slope for which needs to be protected using soil nails and grid beam system. The plan slope length of nearly 400 m on the north side is required to be stabilized.

Top strata soil of thickness 7–18 m mainly consists of medium dense to very dense clayey sand/silt and sandy clay of lateritic nature with significant voids. This is underlain by slightly weathered to highly weathered brownish-colored granite rock. The top layer of thickness 3–3.50 m is hard lateritic soil which can stand unsupported at the steeper slopes. Hard lateritic soil is followed by a layer of yellowish white-colored fine silty sand with high lime content of varying thickness existing in the interface of soil and weathered rock at several locations. Properties of these geo-materials used for analysis are given in Table 1.

Groundwater table (GWT) observed during rainy season varies from RL 52 m on one side to RL 35 m on the other side, and annual rainfall in the region is more than 4000 mm. During rainy season, rainwater percolates in the higher plateau catchment area and gushes out from the exposed voids of the cut slope. Standard penetration test (SPT) of soil (hard laterite region) was reported as 20 and refusal in some soil locations. Bulk density of the soil was 15–16 kN/m^3, and natural moisture content was 23–25%; cohesion (C) of 70–80 kN/m^2 and angle of internal friction ($Ø$) as 30–35°

were estimated for top hard lateritic soils. Rock quality designation (RQD) as nil to 100%, uniaxial compressive strength (UCS) of 4700–103, 500 kN/m^2, porosity of 0.02–8.32%, dry density of 24–29 kN/m^3 were reported for rock. Based on these results of the site investigations, an initial scheme for slope stabilization comprised of three tiers of soil nailing wall up to level 40 m with RCC tieback prestressed anchor toe wall of 5 m retaining height was conceived.

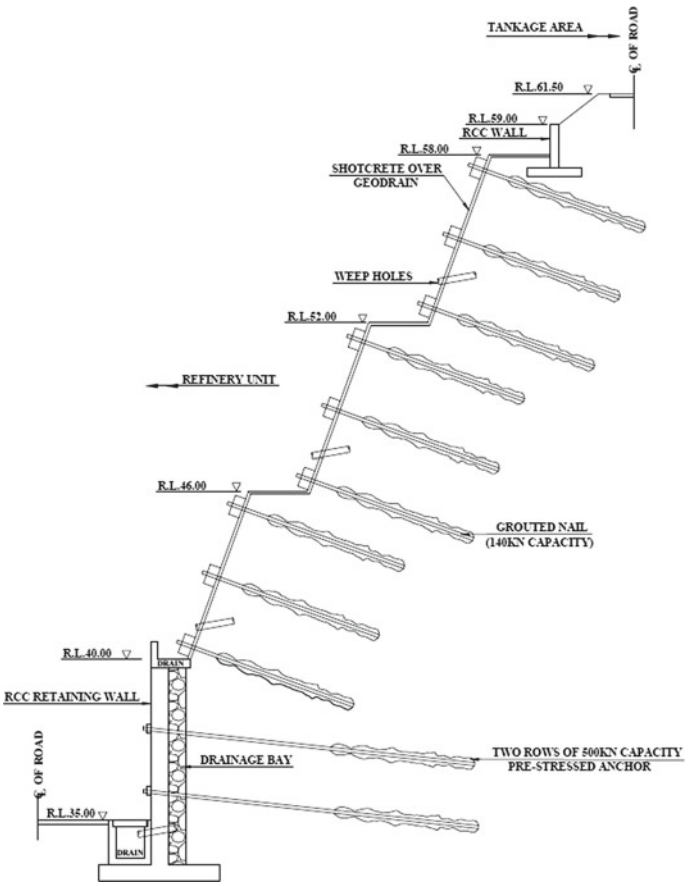

Fig. 1 Slope stabilization using grouted soil nail

Table 1 Properties of slope layers

Layers	E (MPa)	C (KPa)	ϕ^o	γ (kN/m^3)
Hard laterite	50	25	30	20
Soft clay	20	10	20	18
Hard rock	75	400	35	22

3 Slope Stability Scheme

Proposed slope lies in between existing roads at the top and proposed bottom peripheral unit road. Slope was divided into three levels (RL 58-52, RL 52-46 and RL 46-40) each separated by a berm of 1 m (Fig. 1).

Initial slope stability scheme typically consists of 15-m-long grouted soil nails along with weep holes of 2-m length at regular intervals followed by retaining wall at the bottom. Eight rows of soil nails of 15-m length were installed at 2 m c/c with shotcrete facing and grid beams as permanent facing (Fig. 2), when a part of partially treated slope gave away during the deep excavation works carried out beneath the treated slope area in the monsoon period with heavy continuous downpour (Fig. 3).

Slope failure occurred in the second and third tier (from RL 40 to RL 52) for a length of approximately 60 m. Temporary remedial measures with the help of sandbags were placed to restrain damage in surrounding tiers of the nailed slope. An investigation carried out post-failure revealed that uncontrolled seepage of water into the slopes appears to be the prime reason for the distress of the soil slope at the western end of the treated slope. The soil at the site is predominantly lateritic which is very hard and strong in dry conditions and becomes soft when in contact with water. The water was seen gushing through the soil during the site visit. Some wet soil lumps were also seen coming down from behind the gunited face (Fig. 4).

The affected soil slope seems to have slid down due to loss of toe support. It appears that the soil has gradually moved down during the deep excavation work for construction of foundations just in front of the toe of the slope.

Fig. 2 Slope stabilization using grouted soil nail

Fig. 3 Slope failure during monsoon season

Fig. 4 Seepage water from the cut slope

4 Remedial Measure and Post-stabilization Scheme

Immediately after the failure, slope was stabilized temporarily using sandbag support laid up to RL 42 m. Sandbags were also placed at the base of tier-2 to provide additional support. Since the most probable cause of failure was assessed to be excessive seepage forces due to the heavy downpours during the monsoon rains, this aspect was primarily given a major impact in the revised design. The revised proposal includes stabilization of the slope with soldier piles going up to RL 31 m and stone-filled gabion units at the toe of slope. The free drainage of groundwater is facilitated by providing a 500-mm-thick drainage layer made of stones and leading the water to nearby drains. The proposed section between E-4108 and E-4160 is shown in Fig. 5. It is proposed to install fresh soil nails of 20-m length. These soil

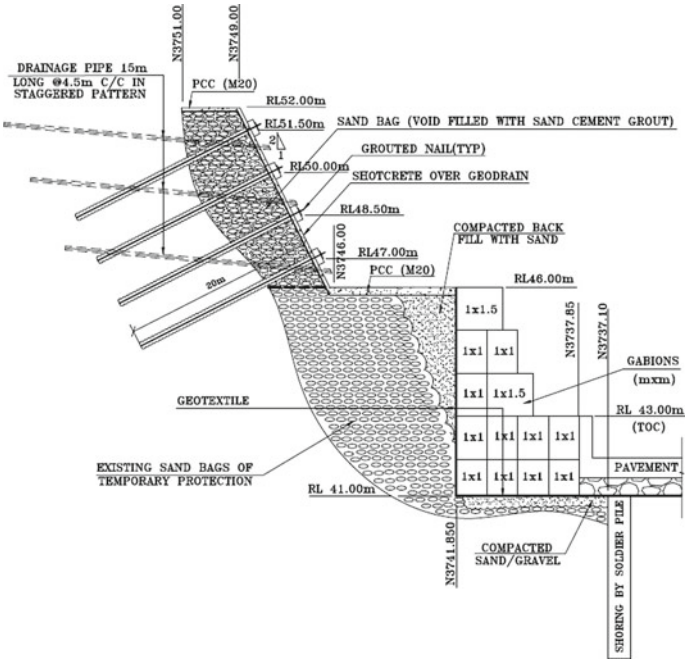

Fig. 5 Revised slope stabilization scheme

nails were in addition to those which are already installed at the site. The drainage of the subsurface water in slope soil was proposed to be improved by installing 15-m-long perforated pipes with a downward inclination to help in water flow. Distressed slope was rebuilt with sandbags, and void between bags was filled with sand–cement grout (1:1 ratio by weight). Refer to Fig. 5 for detailed rectification scheme. Slope stability with a modified scheme was analyzed with PLAXIS 2D, and factor of safety evaluated was 1.60.

5 Challenges During Execution

Following challenges were faced during the execution of slope stabilization work.

(i) Yellowish white-colored silty fine sand with high lime content under water seepage condition is prone to collapse. Ability of this soil to stand unsupported is for a short duration of time, and hence, shotcreting is needed to be carried out immediately for face stability of designed slope. Furthermore, a large quantity of additional shotcrete was required to fill in voids where sloughing has taken place at the wall face.

(ii) Shotcreting in the cut slope with high seepage water causes adhering problem. Flowing-out seepage water carries fine cement particles from newly placed shotcrete and converts it to a weak porous medium.
(iii) Drilled hole was collapsing due to subsoil seepage water and for execution temporary casing was used for bore stability.
(iv) Cleaning of the borehole with compressed air was forming soil lumps with seepage water. In some areas, water jet had to be used for cleaning of drill holes although use of drilling mud, water or other fluids to remove cuttings is not suggested for nail installation.
(v) While cleaning the drill hole with compressed air or water jet, adjacent drill holes were getting interlinked resulting in higher consumption of nail grout.

6 Load Test Results

Verification and proof load tests (pull out) were carried out as per IS: 11309 (1985) on nails of 140 kN capacity in the rectified slope area, and the displacement was within the allowable limit of 40 mm. Load test results are shown in Fig. 6.

7 Summary and Conclusions

The entire project was executed successfully by the year 2013 after overcoming all impediments, and it is performing well with no instances of slope failure till date.

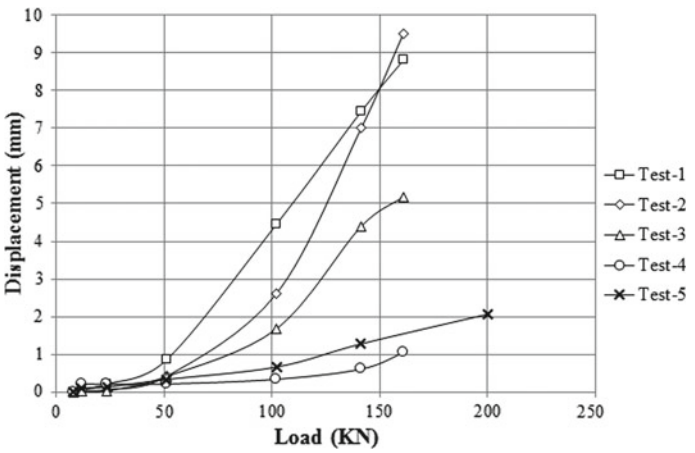

Fig. 6 Load test results

Following lessons were learned during implementation of steep slope stabilization work:

1. Soil nailing is not well suited for the cut slopes with seeping water. It poses difficulty in excavation, drilling, grouting and shotcreting.
2. Lower part of the soil layer consisted of yellowish white-colored fine silty sand with high lime content. Seeping water from slope surface carries the fine particles, resulting in gradual impairment of soil matrix.
3. Seeping water from the soil pores gradually reduces the bond strength between grout and soil. Exposure of nail reinforcement to moist condition also increases the risk of nail corrosion. These phenomena may result in capacity reduction of nail and eventually to slope failure.
4. Soil nail intended to be installed in excessive seepage slope shall accompany with appropriate long-term drainage control measures to effectively control and direct the seepage water. Use of deep horizontal perforated drainage pipes, weep holes, geo-strip drains, scupper drain, garland drain, etc., has been effective for seepage water control.
5. During slope failure studies, inadequate drainage arrangement (to facilitate free flow of seepage water) is required to be taken care. Accumulation of seepage water behind shotcrete facing generates unexpected additional lateral pressure which could damage the overall slope stabilization scheme.

References

BS-8006 Part-2 (2011) Code of practice for strengthened/reinforced soils—Soil nail design, British Standard Institute

BGS (British Geotechnical Society) Report on Soil Nailing: a solution looking for problems (1991) Ground Engineering, Jan/Feb 1991

FHWA (2003) Geotechnical circular no. 7, soil nail walls, Publication FHWA-IF-03-017, U.S. Department of Transportation, Federal Highway Administration, Washington, D.C

FHWA (1998) Manual for design and construction monitoring of soil nail walls, FHWA-SA-96-069R, U.S. Department of Transportation, Federal Highway Administration, Washington, D.C

IS: 11309 (1985) Method for conducting pull-out test on anchor bars and rock bolts

Shaw Song L (2005) Soil nailing for slope strengthening, Geotechnical Engineering, Kuala Lumpur, Malaysia

Tan, Y-C, Chow, C-M (2004) Slope stabilization using soil nails—design assumptions and construction realities

Taming the Hill Roads—A Case Study

Arun Kumar Singh, Atasi Das and Anand Raghuwanshi

Abstract Engineering of hill roads is always a daunting task, especially owing to unstable strata of the young fold Himalayan Mountains as geologically, and rocks in outer and lesser Himalayas are in formative stage and inherently very weak like highly weathered or fractured sedimentary formations such as sandrocks, siltstones, claystones. Some rocks' formation primarily shows good in situ strength, but weathering exposure weakens its strength. Located in Seismic Zone IV, even minor tremors instigate weak rocks to behave as flowing soil mass/tend to swell and fail along bedding/structural weak planes, resulting in disastrous slope failures. To make a safe and reliable access to the remotest hilly region, hill slopes are required to be stabilized artificially by mechanical means besides stabilization by natural phenomenon and vegetative growth. Hill roads are normally constructed by part-cut and part-fill method. To construct the required formation width of highway, provisions of retaining structures in valley side are necessarily desired. Retaining structures contribute 20–30% of the total project cost in hill road construction. Parwanoo to Solan section of NH 22 is also proposed to be widened to four lanes from existing two lanes by cut-and-fill method. This paper presents a case study on design and construction of embankment on valley side using reinforced soil slope at steeper angle due to ROW constraint.

Keywords Reinforced soil slope (RSS) · Geogrid · Hill road · Valley-side widening

A. K. Singh
Kameshwar Buildcon & Infrastructure Pvt. Ltd, New Delhi, India
e-mail: arun.ritjsr@gmail.com

A. Das (✉) · A. Raghuwanshi
GR Infraprojects Ltd., 2nd Floor, Novus Tower, Plot 18,
Sector 18, Gurugram, Haryana 122002, India
e-mail: atasid@gmail.com

A. Raghuwanshi
e-mail: andi.rag22@gmail.com

R. Sundaram et al. (eds.), *Geotechnics for Transportation Infrastructure*, Lecture Notes in Civil Engineering 28, https://doi.org/10.1007/978-981-13-6701-4_44

1 Introduction

Efficient transportation contributes all-round development of a country and advances its progress. Highways have enriched road transportation in India. As India has vast areas of hilly region, massive projects are underway to expand highway network to connect remotest hilly regions for economic development and strategic needs. National Highway No. 22 is also one of the important roads as per commercial and tourism perspective besides connecting two state capitals of Punjab and Haryana from the capital of Himachal Pradesh as well; it needs widening of existing two-lane national highway to four-lane standards to cater the present as well as anticipated future traffic. Existing road is passing through 15–55 m high hill on one side and 10–45 m steep deep valley on the other side. Land available for widening of existing two-lane national highway to four-lane standard is only 30–35 m. Keeping in view steep deep valley and ROW constraint, it was decided to adopt geogrid reinforced soil technique for widening of existing road in valley side to achieve the required formation width of the project highway.

1.1 Hill Road—The Challenge

Hill road is formed predominantly by cutting into the hillside and filling onto the valley side. To achieve the required formation width of highway, the construction of retaining walls onto the valley side is imminent in places along the alignment, where cutting into hill is not economical or has to be restricted due to other reasons. The Hill Road Manual (IRC:SP:48-1998) covers the retention of the cut slope of the hillside adequately; however, experiences in India for the use of retention of earth for valley side widening is meagrely documented. The use of conventional gabion walls, crushed rubble masonry (CRM) walls, and buttress walls is common up to low heights. When a two-lane road is to be widened to a divided four-lane carriageway, reinforced soil slopes (RSSs) and walls (RSWs) offer both technical and economic advantages over conventional mass gravity wall systems and portrays as a blessing for the highway community.

2 Reinforced Soil Slopes (RSSs)

The concept of reinforced earth has been developed and propagated by Henri Vidal in 1960 (FHWA-NHI-10-024: 2009) and has been constructed as reinforced earth (RE) or reinforced soil (RS) walls with vertical faces from as early as 1974 in many countries. RE systems are a form of mechanically stabilized flexible earth structure that incorporate planar inextensible tensile reinforcing elements in the form of strips, sheets, and typically geosynthetics like geogrids and geotextiles to enhance

the strength of the fill. When reinforced earth fill is constructed to have a slope face angle flatter than 70°, it is referred as a reinforced soil slope (RSS) as per the provision of specifications for road and bridge works by the Ministry of Road Transport and Highways (MORTH-2013).

Apart from the economics, the general behaviour of the RE system is found satisfactory, even under conditions where the hill slopes experience movements, when rigid structures would suffer damage and REs exhibit good deformability characteristics.

Reinforced soil slopes (RSSs) are safer than flatter, unreinforced soil slopes if designed at the same factor of safety and compare in terms of its performance, due to inherent conservatism in design. So, the risk of long-term stability is lower with reinforced soil slopes than that of flatter and unreinforced soil slopes. The various components of the RSS include the granular fill, the reinforcing element using geogrid, and the facia choice.

RSSs with the face angle between 70° and 45° are classified as steep slopes and the face angle $\leq 45°$ are classified as shallow slopes.

There is dearth of design and implementation guidelines for the RSS in the Indian highway fraternity. The only plausible reference is the MORTH-2013 specifications covered in Clause 3107 both for design and specification. The specification for the components and factors is briefly described here.

2.1 Granular Fill Material

Selected soil/earth fill having drained or effective angle of friction, $\varphi \geq 28°$ and gradation meeting the following criteria is specified and has been used as reinforced fill in RSS for the case study.

Sieve size	Percentage passing
75 mm	100%
425 micron	0–60%
75 micron	less than 15
PI ≤ 6	

2.2 Facia

The specified variety of facia includes:

(i) Wrap-around facing using geosynthetics;
(ii) Gabion facing;

(iii) Metallic facing, prefabricated in different shapes including welded wire grid and woven steel wire mesh;
(iv) Precast reinforced concrete panels;
(v) Precast concrete blocks and hollow blocks.

For this case study, welded steel mesh of 8 mm diameter and having 150 × 150 mm apertures has been used as the facing of RSS.

2.3 Reinforcing Element

Polyester knitted geogrid with PVC coating, which has already seen use on projects in India, has been used in this project case study.

2.4 Other Components and Factors

A nonwoven coir/jute fibre mat of natural geotextile is provided behind the mesh facing to protect the reinforcing geogrids against UV degradation from direct sunlight as well as to act as a medium to established and promote continued growth of vegetation.

Wherever the height of RSS is more than 10 m, to break the continuity, a berm/bench of width 1.0–1.5 m is provided at every 10 m height from the bottom of the slope.

3 Project Case Study

The Site of the Four-Lane Project Highway comprises the section of National Highway in the state of Himachal Pradesh. The project comprises the existing two-lane road to be developed as four-lane road.

Relevant field investigations were conducted prior to design and execution of the RSS system.

4 Field Investigation

Field investigations broadly included geotechnical investigations and geological mapping of the project corridor.

4.1 Geotechnical Investigation

Extensive field and laboratory investigation were conducted to determine the suitability of soil/rock to support foundation of structures and to generate adequate data for design and stability analysis of reinforced soil slopes. Other information like actual site condition and topographic features, lithology, groundwater condition, geological features, discontinuities, likely construction difficulties was also investigated and recorded.

4.1.1 Borehole Investigation

Field investigation was carried out for physical examination, excavation, drilling of boreholes to collect undisturbed and disturbed soil/rock samples at different depths. SPT was also conducted, and 'N' values were observed at respective depths during bore drilling for detail analysis and laboratory investigations. Samples of filling material from different sources were collected for testing of acceptance criterion as per codal provisions and to be used as reinforced soil fill. The borehole data in the vicinity are included here in Table 1 below.

4.1.2 Laboratory Investigation

Laboratory investigation like grain size analysis, Atterberg limit tests, density, specific gravity, shear strength, RQD, RMR was carried out on the collected cores and soil samples to determine soil parameters and rock characteristics. Relevant laboratory tests on collected samples for reinforced fill were also carried out for acceptance criterion.

Table 1 Typical bore log data

Depth from GL (m)		0.0–1.0	1.0–2.0	2.0–3.0	3.0–4.0
Soil description		Gravelly sand	Gravelly sand	Weathered rock	Weathered rock
Grain size	Sand	–	33.68	–	–
	Gravel	–	29.32	–	–
Atterberg limits%	LL	–	29	–	–
	PI	–	12	–	–
Core recovery		–	–	18.00%	42.00%
R.Q.D.		–	–	Nil	33.00%
Specific gravity		–	–	2.65	2.65

4.1.3 Plate Load Test

Plate load test has been conducted on the excavated bed of RSS for re-conformity of the safe bearing capacity at founding level, which was calculated based on the field and laboratory investigations and considered as 30 t/m^2 in the design.

4.2 Geological Studies

The project area falls at the boundary line of the outer and lesser Himalaya. A geological mapping study was conducted to guesstimate the type of the rock anticipated for the slope stabilization works on the hillside and the uncertainty involved in the excavation of the valley-side slopes for the purpose of insertion of the geogrids into the RSS.

The rocks in the area are highly jointed and at most places shattered and fractured. Even shear zones have also been observed at a number of places. All these are mainly due to the tectonic activities, i.e. the Himalayan orogeny.

The seismic sensitivity in the state of Himachal Pradesh is very high, as over the years a large number of damaging earthquake has struck the state and its adjoining areas. Seismically, Himachal Pradesh lies in Zone IV and Zone V. The project area, however, falls under the Seismic Zone IV; i.e., the area is in high damage risk with expected intensity of MSK VIII or more.

5 Design Framework for the RSS

5.1 Design Standard

As per guidelines given in fifth revision of MORTH-2013 specifications, design principles and provisions prescribed in BS 8006-1 (2010), FHWA-NHI-10-024 (2009), and FHWA-NHI-10-025 (2009) are being followed and Software, ReSSA, version 3.0 of Adama Engineering has been used for the designing of reinforced soil slopes (RSS).

5.2 Stability Analyses

As per Clause A3-1.1 of MORTH-2013 specifications, the design of reinforced soil slopes are mainly based on the rotational stability analysis for different loading conditions. Accordingly, the factors of safety (FOS) for dynamic/seismic loading

and static loading condition being checked as per the design standard indicated above.

5.3 Design Considerations

5.3.1 Factors of Safety

FOS for dynamic/seismic loading = 1.1
FOS for static loading = 1.3

5.3.2 Load Surcharge

Live Load = 24 kN/m^2

5.3.3 Seismic Factors

Maximum ground acceleration = a_{max}: 0.24 g for Zone IV
Horizontal ground acceleration = $k_h = 0.5 \times a_{max} = 0.12$

5.3.4 Subsurface Properties

Based on interpretation of the borehole investigation, weathered rock strata is encountered and found to fall under Class V as per RMR calculation. Hence, the shear strength parameter, i.e. Cohesion = 100 kPa and angle of internal friction = 15°, are arrived from Table 1 of IS 13365-1 (1998).

6 Accessory Considerations

6.1 Drainage

At the outset, it is anticipated that there will be large surface run-off due to heavy rains at the project locations and the hilly terrain. Subsurface seepage from hillside to valley side was also observed from few locations. In order to prevent surface and/or subsurface water entering into backfill soil, efficient drainage is provided over the full height of the soils in the form of chimney drains. The chimney drain consists of uniformly graded coarse aggregate.

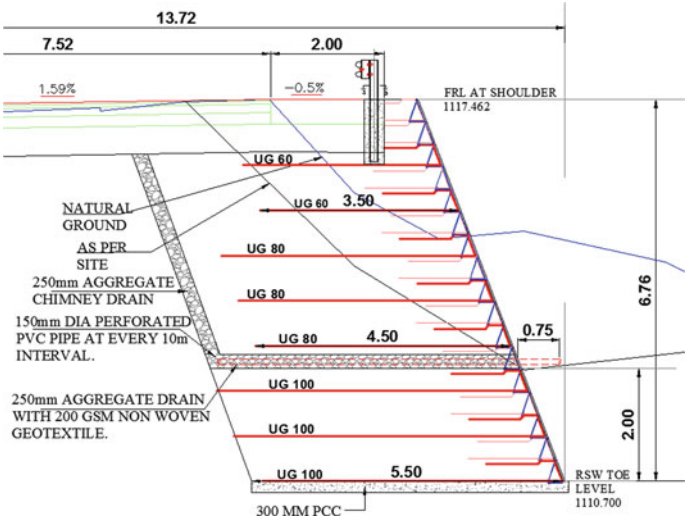

Fig. 1 Collection of groundwater behind RSS using aggregate drainage blanket referred as chimney drain

Fig. 2 PVC pipe details

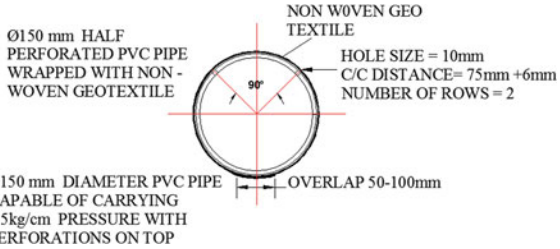

Though granular fill is the preferred material for use in the RSS due to their high strength, ease of compaction, ability to dissipate excess pore water pressure, often, in hill roads, the variability in the availability of suitable fill materials is inherent due to weathered rock conditions; thus, making the use of marginal fill is unavoidable. The designer may not have control on the material QA/QC. Thus, analysing the soil properties to be used as reinforced backfill a suitable means to mitigate the potential development of excess pore water pressures are also taken care of. On the slope behind reinforced soil fill, 250 mm drainage media is provided and continued at base above the ground level along with 200 GSM geotextile as chimney/aggregate drain depicted in Fig. 1. 150-mm-diameter perforated PVC pipe at every 10 m interval is also provided at base and its outlet kept at rear side of the reinforced soil slopes shown in Fig. 2

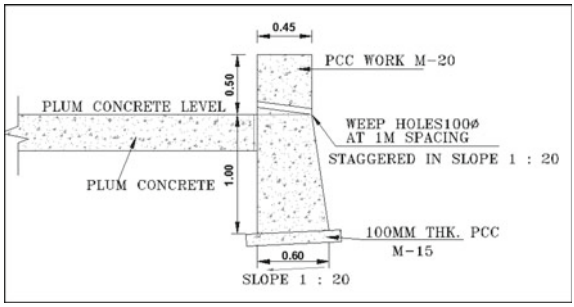

Fig. 3 Toe wall typical section

6.2 Toe Protection

At selected locations (where height is more than 10 m), a toe wall is provided at the junction of reinforced soil slope and the virgin slope so as to protect the toe of RSS from damage and/or soil erosion if any and also to prevent the RSS from any possibility of sliding down. The toe wall is founded on a strip footing of 600 mm wide and 100 mm thick of M15 grade plain cement concrete (PCC) as per RSS drawings. The founding level of toe wall is kept 1.0 m below the founding level of RSS. Weep holes also were provided in toe wall to ensure drainage if required (Fig. 3).

6.3 Foundation

A sound foundation is desirable for resting the RSS. Two types of foundation have been considered based on the ground profile and the weathered rock conditions.

6.3.1 Gabion Foundation

In this case study, a particular location along the project highway is discussed where widening was required to get sufficient carriageway width for smooth traffic flow of four lanes at a sharp curve. Due to dense commercial establishment on the adjacent uphill slope, National Highway could not be widened towards uphill slope. Therefore, required road formation was proposed towards the downhill side, which is at steeper inclination. And more so, a running stream/gorge is also present at the downhill side. Citing the predominant site situation, a combination of reinforced soil slope and gabion retaining wall was proposed as shown in Fig. 4.

This hybrid wall was proposed for the construction in stepped fashion with limitations of partial cutting towards downhill side of existing slope; otherwise, it disturbs the existing carriageway and affects the traffic movement badly, since, as explained above, neither widening nor diversion is possible towards uphill side. Keeping in view all the constraints and limitations, gabion wall was proposed at the bottom of

Table 2 Summary of global slope stability analysis

S. no.	Section	FOS				Status of slope
		Static		Seismic		
		Rotational	Translational	Rotational	Translational	
1	Figure 4	1.37	1.50	1.20	1.39	Safe
2	Figure 5	1.46	1.40	1.30	1.27	Safe

reinforced soil slope to act as a platform for the construction of tiered RSS with each tier of 8 m height. The gabion wall was concreted and encased from three sides with M15 grade of PCC as a solid impermeable foundation platform. The overall stability along with the suggested remedial measures was rechecked using ReSSA software under static and seismic conditions. The FOS of the structure was obtained as shown in Table 2.

The details of geogrid used in section (Figs. 4 and 5) are shown in the Table 3.

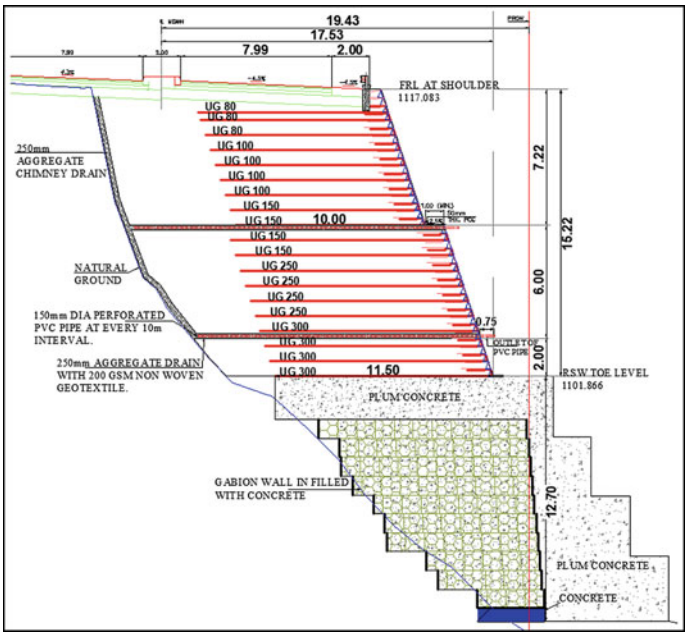

Fig. 4 RSS on gabion foundation

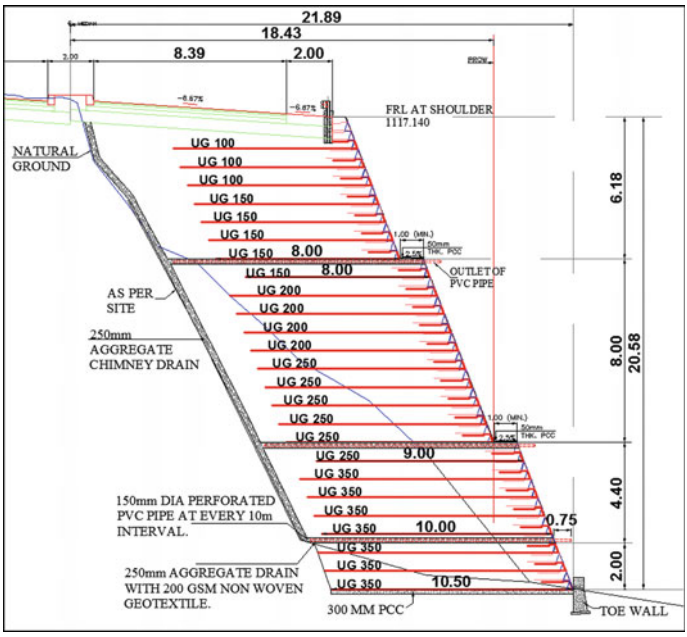

Fig. 5 RSS on PCC foundation

6.3.2 Plum Concrete (PCC) Foundation

To serve as a bedding/foundation, a 200 mm thick layer of Plum Cement Concrete (PCC) is laid as shown in the RSS Drawings (Figs. 1, 4 and 5).

Table 3 Summary of geogrids

Section	Height form base	Geogrid type
Figure 4	Up to 3 m from Toe	UG 300
	3–6 m	UG 250
	6–9 m	UG 150
	9–12 m	UG 100
	12–15 m	UG 80
Figure 5	Up to 5 m from Toe	UG 350
	5–10 m	UG 250
	10–13 m	UG 200
	13–17 m	UG 150
	17–20 m	UG 100

Note UG 300 means uniaxial geogrid having tensile ultimate strength, $T_{ult} = 300$ KN/m

7 Construction Methodology

7.1 Excavation

All the debris and loose materials on cuttings areas were removed and then excavation being done up to desired level indicated in RSS Drawings. While executing excavation, contractor has taken all adequate precautions against the soil erosion. After the excavation/cutting of slopes, foundation for reinforced soil slope has been prepared. Before laying the foundation and toe wall, the excavated trenches inspected properly to ensure that there are no loose pockets and unfilled depressions left in the trench as well as the soil at the founding level is properly compacted too.

7.2 Laying and Compaction in RSS System

8-mm-diameter welded steel mesh having 150 × 150 mm apertures placed over PCC as a facing of RSS. Primary geogrid of desired specification is laid for the designed length. Care has been taken that geogrids are laid free from all kinks, damage and displacement during placement, spreading, levelling, and compaction of the fill. After the placement of geogrids, selected soil is filled in layers up to the level of secondary geogrids. Thereafter, secondary geogrid of 1.50 m length has been laid followed by the selected fill. The sequence has been repeated so on as per design. The thickness of embankment layers is 200 mm, compacted to 95% of maximum laboratory density measures as per IS 2720-8 (1983). Care has also been taken that no construction of machineries/vehicles moves directly on the reinforcing elements/geogrids. The movement of machineries/vehicles only allowed after providing compacted thickness of 150 mm of soil fill over the geogrids.

Manmade geotextiles and natural geotextiles made of coir and jute (JGT) help to reduce the velocity of overland flow and entrapping the dissociated soil particles

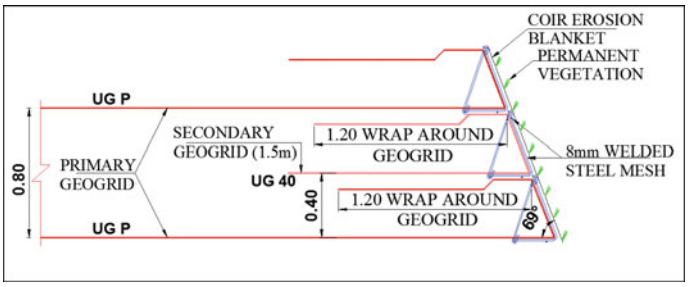

Fig. 6 Typical arrangement for reinforcement and facia

while fostering growth of vegetation concurrently that is very much effective for slope protection. This is provided all along the slope as shown in Fig. 6.

7.3 Permanent Vegetative Cover

Permanent vegetative cover is provided at face of RSS with nonwoven coir/jute fibre mat of natural geotextile to act as erosion blanket as well as medium to established and promote continued growth of vegetation.

8 Pictorial View of Sequence of Construction

The critical location discussed in this case study is shown in contour in Fig. 7. The lowest height for this curve portion is 8.76 m and highest is 27.92 m (Figs 8, 9, 10, 11, 12, 13 and 14).

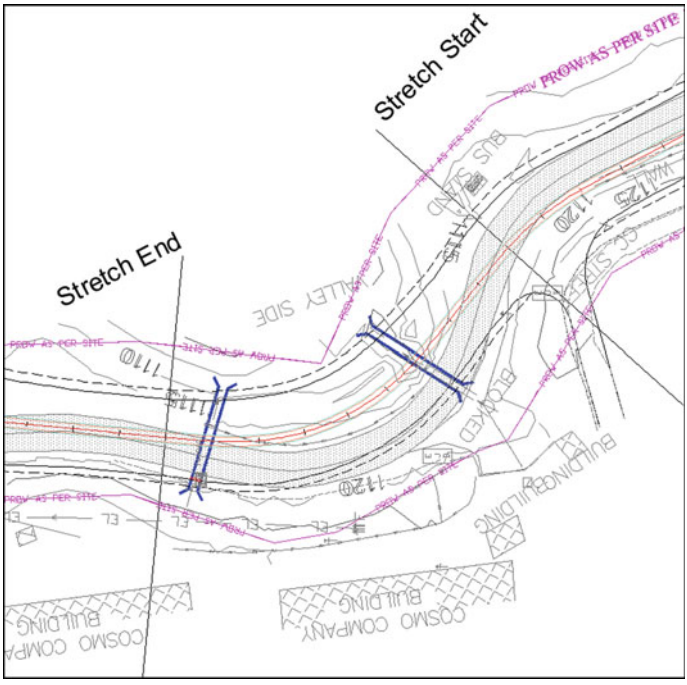

Fig. 7 Contour and plan of steady stretch

Fig. 8 Gabion foundation and dump on slope to receive RSS

Fig. 9 Steady seepage is noticed on the hillside after clearing of slope face

Fig. 10 RSS construction underway after the first berm

Fig. 11 RSS reaching second berm

Fig. 12 Culverts to address the seepage water shown in Fig. 9

9 Conclusions

The project highway passing through the outer and lesser Himalaya region is still in the formative stage consisting of mixer of soil, weathered and fractured sedimentary rock, boulders, etc. It also has steep slopes requiring very deep retaining structures to construct the formation width of the project highway. Based on the results of field and laboratory investigations, stability analysis and design, limitations and constraints in construction, the following are the conclusions:

- Reinforced soil slopes (RSSs) with and without combination of conventional retaining walls have been introduced and satisfied with all design standards and specifications criterion along with better stability where retaining structures with conventional method like RCC retaining wall, gabion wall, coarse rubble masonry wall have certain limitations and are neither technically feasible nor very economical at several stretches of the project highway.

Fig. 13 Surface and/or subsurface water draining through chimney system

Fig. 14 Opened to traffic after RSS completion

- Reinforced soil slopes (RSSs) are ease in construction and embankment filling with the material originated from hill cutting for road widening.
- Provision of chimney drain along the existing slope for the full depth of the filling is effective and efficient in catching and channelizing the subsurface seepage. It may be seen in Fig. 12. It is difficult to identify sources of subsurface seepage in hilly region, and so, improper drainage affects the highway badly, resulting which pre-matured failure occurs.

- Provision of nonwoven coir/jute fibre mat of natural geotextile is effective in protecting the reinforcing geogrids against UV degradation from direct sunlight and acting as erosion blanket as well as a medium to established and promote continued growth of vegetation.
- Provision of vegetation being introduced which may act as a biotechnical stabilization after full and permanent growth of vegetative cover and make the region eco-friendly and identical with the surroundings.

Acknowledgements The authors are thankful to the management team of M/s. G R Infraprojects Ltd, especially Mr. Ajendra Agarwal, Director (Technical), for guidance and providing all facilities in carrying out the reported work.

References

BS 8006-1 (2010) Code of practice for strengthened/reinforced soils and other fills, British Standard

FHWA-NHI-10-024 (2009) Design and construction of mechanically stabilized earth walls and reinforced soil slopes—Volume I, Federal Highway Administration, U. S. Department of Transportation

FHWA-NHI-10-025 (2009) Design and construction of mechanically stabilized earth walls and reinforced soil slopes—Volume II, Federal Highway Administration, U. S. Department of Transportation

IRC: SP: 48 (1998) Hill road manual, Indian Roads Congress, New Delhi

IS 2720-8 (1983) Determination of water content-dry density relation using heavy compaction, Indian Standard, New Delhi.

IS 13365-1 (1998) Quantitative classification system of rock mass—Guidelines, Part 1: RMR for predicting of engineering properties, Indian Standard, New Delhi

MORTH (2013) Specifications for Road and Bridge Works (Fifth Revision), Ministry of Road Transport & Highway, New Delhi

Use of Hybrid Geosynthetics in Mitigating Rainfall-Induced Slope Instability

Dipankana Bhattacherjee and B. V. S. Viswanadham

Abstract The objective of the present study is to investigate the mechanism of rainfall-induced instability in steep mountainous slopes and to mitigate the same by the inclusion of hybrid geosynthetics. For this purpose, a typical hilly terrain subjected to heavy rainfall was chosen for case study, and the local geology, recorded rainfall data and shear strength parameters measured at the site were replicated numerically by incorporating unsaturated soil parameters related to volumetric water content, permeability and soil matric suction. Hydro-mechanical infiltration analysis was performed on the selected slope profile using finite-element software SEEP/W, and corresponding pore water pressure values obtained during rainfall were incorporated in limit equilibrium-based software SLOPE/W for monitoring the factor of safety with time. The results indicated that slope instability occurred due to rapid loss of matric suction from an initial value of −200 kPa at the onset of rainfall to −60 kPa, resulting in a safety factor lying below the critical limit of 1.0. A global failure surface passing through the toe was observed in this case, thereby indicating that rainfall-induced slope instability may not necessarily be attributed solely to increasing ground water levels. As a remedial measure, the inclusion of dual-function hybrid geosynthetics has been suggested, which exhibit both reinforcement and drainage characteristics. The hybrid geosynthetics are proposed to be installed from the bottom to the top, following the sequence of slope construction or during slope reprofiling as a part of road widening projects in hilly areas. Subsequent numerical analysis conducted on the reinforced slope depicted considerable retention of soil suction at the end of rainfall and an enhanced global stability value of 2.29, which may be attributed to the drainage potential of hybrid geosynthetics in dissipating the excess pore water pressure generated within the slope during rainfall, coupled with reinforcement action which prevents loss of soil shear strength and associated softening, thereby averting possible slope instability.

D. Bhattacherjee · B. V. S. Viswanadham (✉)
Department of Civil Engineering, Indian Institute of Technology Bombay, Mumbai 400076, India
e-mail: viswam@civil.iitb.ac.in

D. Bhattacherjee
e-mail: dipankanabhattacherjee@gmail.com; dipankanabhattacherjee@iitb.ac.in

R. Sundaram et al. (eds.), *Geotechnics for Transportation Infrastructure*, Lecture Notes in Civil Engineering 28, https://doi.org/10.1007/978-981-13-6701-4_45

Keywords Slope stability · Rainfall · Hybrid geosynthetics

1 Introduction

Recently, the frequency of rainfall-induced landslides has been increasing globally, coincident with the effects of climate change, causing innumerable deaths and severe damages to infrastructures. Although geotechnical failures may occur due to construction activities, many cases of total/partial collapse have been reported in natural and excavated slopes, soil walls and road sub-grades simply due to rainwater infiltrating in an otherwise stable structure. In the last decade, several cases of disasters triggered by heavy monsoon rain have been reported in India (number exceed 2700 annually, as per the Geological Survey), a few of which include the major landslide blocking tracks along a section of the Konkan Railway in 2010, the cloudburst conditions in Uttarakhand rendering masses homeless in 2013, 2014 and 2016, and landslides along the Mumbai–Pune expressway in 2015 and in Arunachal Pradesh in 2016. The annual statistical review report of the Centre for Research on the Epidemiology of Disasters reveals that, in the year 2016, almost 75% of the natural disasters that occurred globally may be attributed to rainfall, and the estimated average losses due to rainfall-triggered landslides exceed 92 million US$/annum (Dahal and Hasegawa 2008). Hence, there arises the necessity to investigate the behaviour of geotechnical soil structures especially that of hilly soil slopes under various rainfall intensities.

The problem aggravates in hilly terrain on account of the local geology and prevalence of rainfall in mountainous regions. Drawing parallel to the above, an attempt is made in the present paper to investigate the mechanism of rainfall-induced instability in mountainous slopes and to mitigate the same by the inclusion of a composite geosynthetic material, referred herein as geocomposites or hybrid geosynthetics. Till date, the studies on the potential use of hybrid geosynthetics in reducing pore water pressures and retaining stability of soil slopes subjected to rainfall is limited in the literature, rendering the above as a topic of major research interest. In the present study, a typical case of slope instability induced by heavy rainfall in hilly areas is modelled numerically using Geostudio (2012) software package. The local geology, recorded rainfall data and shear strength parameters at the site are replicated numerically by incorporating unsaturated soil parameters related to volumetric water content, permeability function and soil matric suction. Hydro-mechanical-based infiltration analysis is subsequently performed on the selected slope profile using finite-element software SEEP/W, and corresponding pore water pressure values obtained during rainfall are incorporated into limit equilibrium-based software SLOPE/W for monitoring the variation of slope factor of safety with time. The next phase of analysis involves the inclusion of hybrid geosynthetics within the selected slope section, which exhibit both reinforcement and drainage characteristics. The hybrid geosynthetics are proposed to be installed from the bottom to the top, following the sequence of slope construction or during slope reprofiling undertaken as a

part of road widening projects in hilly areas. The analysis results related to seepage and stability aspects of hilly slopes reinforced with and without hybrid geosynthetic layers under rainfall condition are discussed in subsequent sections.

2 Properties of Model Materials and Rainfall Records

The geotechnical properties of the residual soil type existing at the site under consideration were documented by Oh and Lu (2015) during post-investigation analysis of slope instability. Based on the values reported, laboratory investigations were carried out in the present study on various locally available soil types to replicate the soil properties close to that obtained by Oh and Lu (2015). The shear strength, permeability and compaction characteristics of the model soil formulated in this case is presented in Table 1, which were given as input parameters in the seepage and slope stability analyses. Further, the average rainfall data of the hilly terrain was assumed in Fig. 1 based on typical values suggested by Oh and Lu (2015) depending on past rainfall records.

In addition to the above, wide-width tensile tests and radial transmissivity tests were performed on the hybrid geosynthetic material proposed to be incorporated in the reinforced slope model for determining tensile load–strain characteristics and drainage properties, respectively. The soil–geosynthetic interface behaviour was assessed based on modified direct shear tests, as summarized in Table 2.

3 Modelling of Unreinforced Mountainous Slope

A typical mountainous slope having a height of 10 m and inclination of 51° with the horizontal was adopted in the present study for studying the effects of rainfall on slope stability. As per existing geological conditions at the site, an initial ground water table at a depth of 2 m below the slope toe was considered in the numerical analysis prior to rainfall infiltration. The basic mesh configuration and overall geometry adopted

Table 1 Properties of model soil used in the present study

Soil properties	Field data[c]	Present study
Unit weight, γ, (kN/m^3)	13.93	16
Cohesion[a], c' (kPa)	0	0
Friction angle[a], ϕ' (°)	31.6	29
Permeability[b], k_s (m/s)	3.4×10^{-6}	3.0×10^{-6}

[a]CU triaxial tests conducted on moist-compacted soil
[b]Falling head tests at $\gamma = 16$ kN/m^3
[c]Oh and Lu (2015)

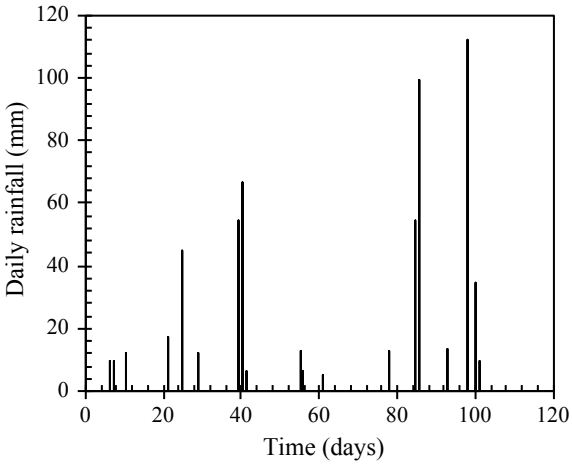

Fig. 1 Input rainfall data (based on Oh and Lu 2015)

Table 2 Properties of hybrid geosynthetic material

Property	Value
In-plane permeability[a] (m/sec)	1.02×10^{-3}
Cross-plane permeability (m/sec)	8.16×10^{-4}
Tensile load[b] (kN/m)	30.42
Soil–geosynthetic interface[c] (°)	30.6

[a]Based on radial transmissivity tests as per ASTM D6574 (2006)
[b]Wide-width tensile tests as per ASTM D4595 (2005)
[c]Modified direct shear tests as per ASTM D5321 (2002)

for the unreinforced slope are shown in Fig. 2. The results of seepage and stability analysis conducted under rainfall condition on the above slope profile are discussed in subsequent sections.

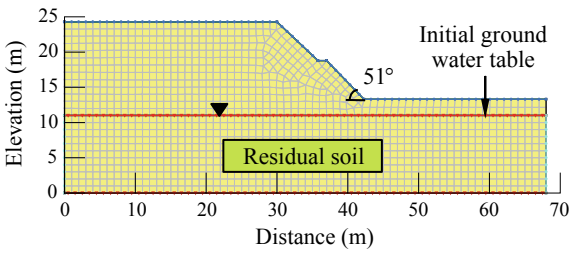

Fig. 2 Basic mesh configuration of existing hilly slope

3.1 Seepage Analysis Using SEEP/W

Seepage analysis was carried out using SEEP/W, a finite-element method-based geotechnical software package of Geostudio (2012). The rainfall event shown in Fig. 1 was applied in the form of a positive seepage boundary flux on the slope surface, and a no-flow boundary condition was established at the slope base to ensure adequate build-up of positive pore water pressures during rainfall. The 'saturated/unsaturated' constitutive material model was selected for predicting the response of slopes during rainfall infiltration, which requires specification of the hydraulic conductivity function and the water content function of the soil involved as input parameters. In the present analyses, the soil–water characteristic curve (SWCC) was estimated using the Van Genuchten method (1980), whereas the hydraulic conductivity function was developed by utilizing the saturated soil properties (Table 1) in conjunction with the SWCC as outlined in the Van Genuchten model. The SWCC and conductivity function thus developed for the model soil are given in Figs. 3 and 4, respectively, along with corresponding field curves suggested by Oh and Lu (2015), which indicate a close correlation between the input parameters and field values.

Figure 5a–c presents the pore water pressure distribution (in kPa) and corresponding phreatic surfaces observed in the unreinforced mountainous slope at different time intervals with rainfall, up to the penultimate stage of slope collapse. A rapid decrease in soil suction can be observed in this case from an initial value of −200 kPa existing within the slope during the hydrostatic pore pressure analysis shown in Fig. 5a to −60 kPa at the end of 96 days of rainfall as depicted in Fig. 5c. This resulted in a steady rise of the phreatic surface towards the slope crest, which is detrimental for the slope stability, as discussed in details during stability analysis presented in Sect. 3.2.

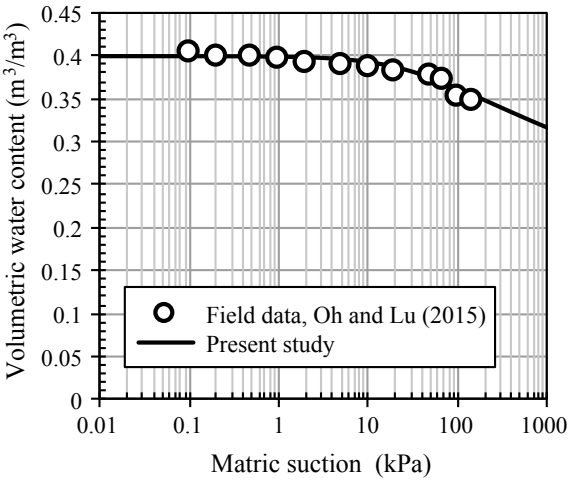

Fig. 3 SWCC curve used in the present study

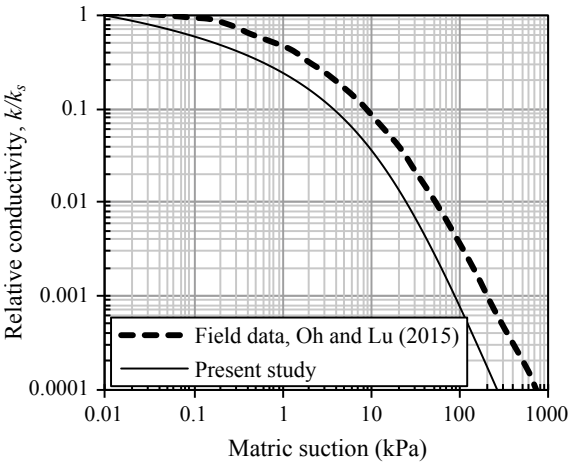

Fig. 4 Hydraulic conductivity function used in the study

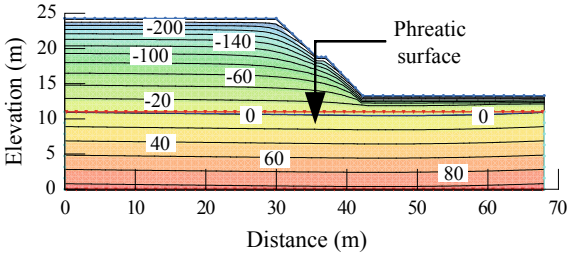

(a) At the onset of rainfall

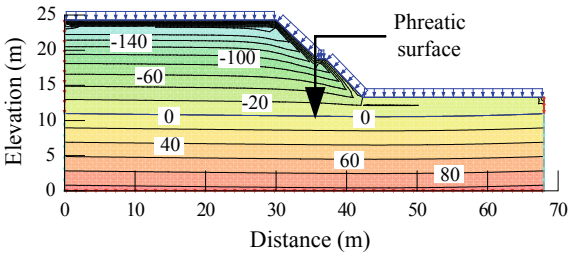

(b) 20 days after rainfall [Intermediate period]

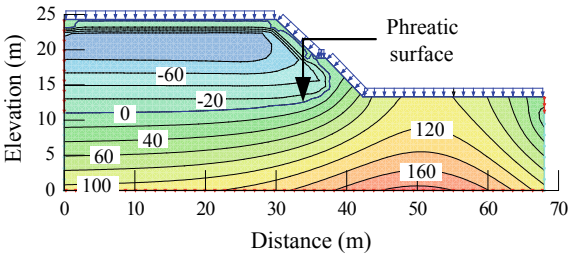

(c) 96 days after rainfall [At failure]

Fig. 5 Pore water pressure distribution (in kPa) within the unreinforced mountainous slope

3.2 *Stability Analysis Using SLOPE/W*

The phreatic surfaces obtained from SEEP/W analyses during various stages of rainfall were incorporated into limit equilibrium-based software SLOPE/W of Geostudio (2012) package for performing the stability analysis of the hilly slope under rainfall condition. Thirty slices were considered in each iteration conducted using modified Bishop's method of slices to achieve convergence for maximum of 2000 iterations with a tolerance of 0.01 in factor of safety (FOS) values. Circular failure surfaces were assumed in this case, and the entry and exit method was adopted for specifying the potential slip surface. The unit weight, cohesion and internal friction of the model soil presented in Table 1 were considered as input values in the analysis. In addition, the variation of negative pore water pressures in the unsaturated zone above the water table was incorporated in the slope stability analysis by

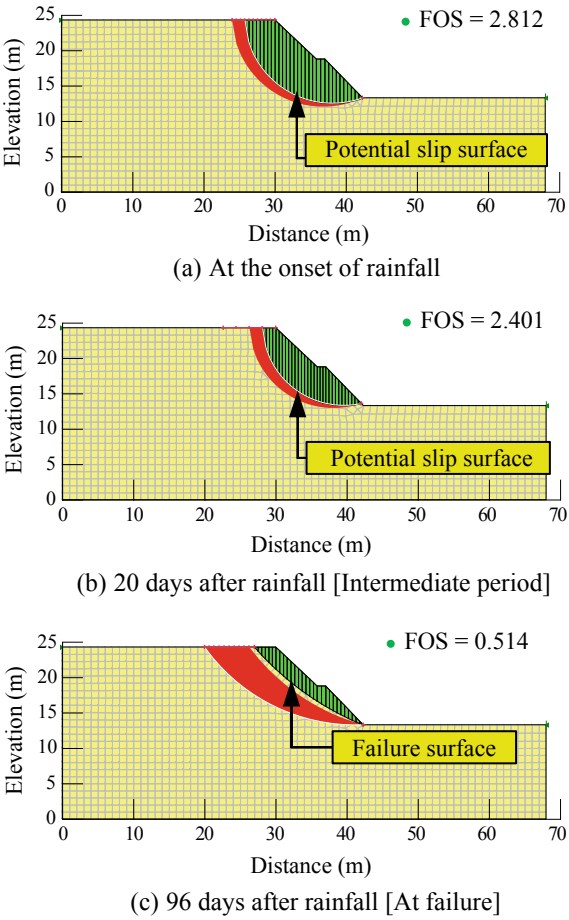

(a) At the onset of rainfall

(b) 20 days after rainfall [Intermediate period]

(c) 96 days after rainfall [At failure]

Fig. 6 Stability analysis results of the unreinforced slope

adopting the modified Mohr–Coulomb failure criterion proposed by Fredlund et al. (1978). Figure 6a–c presents the results of stability analyses for the unreinforced slope in terms of the variation of FOS values with rainfall, which indicate a gradual slope destabilization due to a steady reduction in FOS values from 2.812 at the onset condition to 0.514 at the end of 96 days of rainfall. The above observations are consistent with gradually decreasing matric suction levels with rainfall observed within the unreinforced slope model during seepage analysis as shown previously in Fig. 5a–c.

4 Modelling of Hybrid Geosynthetic-Reinforced Slope

In the next phase of analysis, the possibility of the inclusion of hybrid geosynthetics has been explored as a remedial measure against slope instability, which exhibit both reinforcement and drainage characteristics. The hybrid geosynthetics are proposed to be installed from the bottom to the top, following the sequence of slope construction during slope reprofiling as a part of road widening projects in hilly areas. The modified geometry of the slope having an inclination of 70° with the horizontal post the proposed reprofiling is shown in Fig. 7, which indicate an additional road space of 7.9 m gained at the base of the hilly terrain on account of reduction in the existing slope angle from 51° shown in Fig. 2 to the newly acquired inclination of 70°. The road width of 7.9 m thus gained at the slope base can be subsequently utilized for construction of two-lane highways in the above mountainous settings, provided adequate measures are adopted to ensure stability of the reprofiled slope section under rainfall condition. In order to address these concerns, the seepage and stability aspects of the reprofiled slope reinforced with hybrid geosynthetic layers are discussed in subsequent sections, subjected to the same rainfall event as considered in Fig. 1 during analysis of the unreinforced slope.

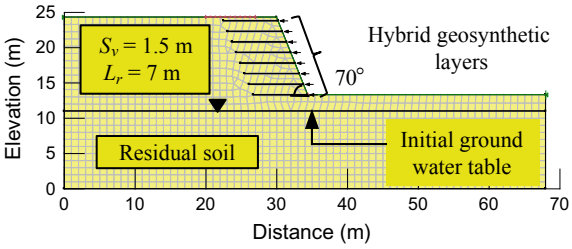

Fig. 7 Basic mesh configuration of reinforced slope

4.1 Seepage Analysis

The hybrid geosynthetics were modelled as interface elements added to the mesh to represent the thickness of the geosynthetics. In this case, in-plane conductivity and normal conductivity values were incorporated separately in the analysis (Table 2), to simulate reduced flow in the cross-plane direction compared to tangential direction. Further details related to modelling aspects are presented in Bhattacherjee and Viswanadham (2015, 2016). The length of the reinforcement layers was selected as 0.7H in the present case (7 m), and the vertical spacing between consecutive layers was considered as 1.5 m, as shown in Fig. 7. The seepage analysis of the reinforced slope at various time intervals during rainfall is presented in Fig. 8a–c. From Fig. 8a–c, it can be observed that the inclusion of hybrid geosynthetic layers within the profiled slope section was effective, as it caused negligible changes in the phreatic surface for the same intensity and duration of rainfall. This may be attributed to the freely draining conditions provided by the hybrid geosynthetics within the slope, which resulted in alternative drainage paths for dissipation of the excess pore water pressure generated during rainfall. As a result, considerable retention of the soil matric suction can be observed within the reinforced slope from Fig. 8a–c until the end of rainfall, which is beneficial for the slope.

4.2 Stability Analysis Using SLOPE/W

While performing the stability analysis, the reinforcement functions of hybrid geosynthetic layers were considered together with their in-plane drainage capability. The ultimate tensile load in machine direction (kN/m) and soil–geosynthetic interface friction angle presented in Table 2 was considered as input values in the analyses. Further, a value of one was specified for the orientation of the tensile load along the hybrid geosynthetic layer to be applied parallel to the slice base. Figure 9a–c presents the results of stability analyses for the reinforced slope in terms of the variation of FOS values with rainfall, obtained by incorporating the pore water pressure conditions observed in corresponding seepage analysis. As can be observed from Fig. 9a–c, the hybrid geosynthetic-reinforced slope exhibited an initial FOS of 3.77 just at the onset of rainfall, which dropped down to 2.29 at the end of 96 days of rainfall, thereby indicating a stable slope. The above observation highlights the importance of reinforcement function provided by hybrid geosynthetics in stabilizing steep hilly slopes subjected to rainfall, as the dual-function layers prevent soil softening taking place under rainwater infiltration, thereby averting possible slope deformations or collapse.

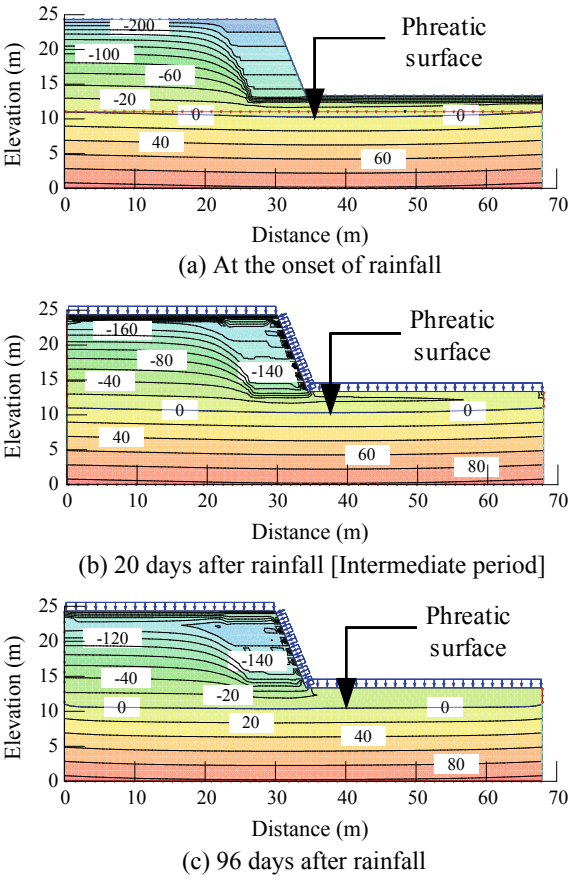

Fig. 8 Pore water pressure distribution (in kPa) within the reinforced mountainous slope

5 Results and Discussion

This effectiveness of hybrid geosynthetics in mitigating rainfall-induced slope instability in hilly areas and preventing associated landslides is further highlighted in this section through the comparison of the response of slopes reinforced with and without geosynthetics under rainfall.

The effectiveness of the hybrid geosynthetic layers from seepage point of view can also be expressed in an alternative way in terms of the variation of normalized pore water pressure ($u/\gamma H$), obtained by dividing the pore pressure value (u) measured along the toe of the slope by the unit weight of the soil (γ) times the height of the slope (H). The variation of $u/\gamma H$ against the duration of rainfall with and without hybrid geosynthetic layers is shown in Fig. 10, which signifies that there occurred a significant reduction in the $u/\gamma H$ values by about 48% within the hybrid geosynthetic-reinforced slope with rainfall, as compared to the unreinforced slope.

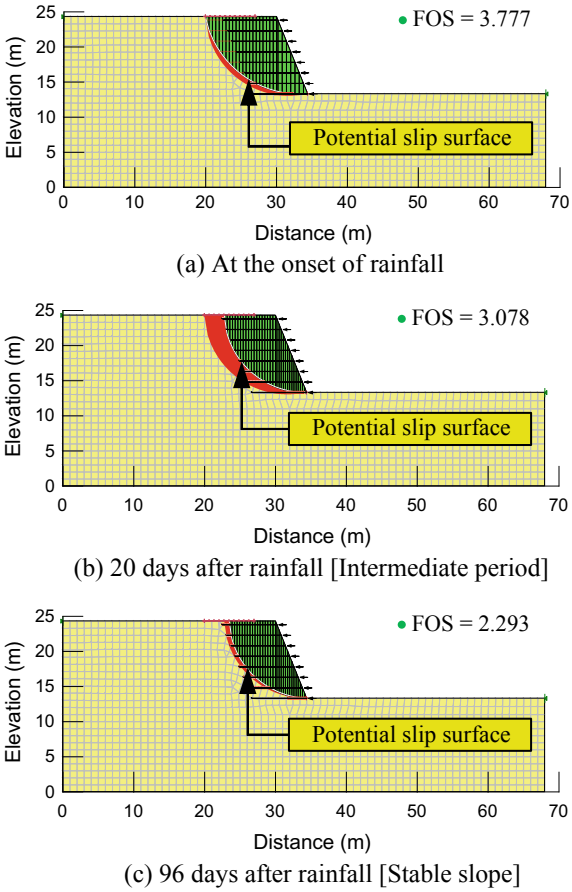

(a) At the onset of rainfall

(b) 20 days after rainfall [Intermediate period]

(c) 96 days after rainfall [Stable slope]

Fig. 9 Stability analysis results of the reinforced slope

This may be attributed to the continuous build-up of positive pore water pressure (u) within the unreinforced slope in the absence of drainage elements, resulting in continuously increasing values of $u/\gamma H$. Contrary to this, the hybrid geosynthetic layers provided the necessary drainage path for dissipation of excess pore water pressure generated due to rainfall, on account of which the $u/\gamma H$ values were considerably low in this case, and became constant within a short period of rainwater infiltration. The corresponding slope stability analysis results plotted for the unreinforced and reinforced slopes for the entire duration of rainfall is presented in Fig. 11a, b, respectively. As can be observed from the stability analyses in Fig. 11a, the unreinforced slope underwent a reduction in FOS values with increasing pore water pressure levels, experiencing failure (FOS = 0.514) at the end of 96 days of rainfall. The above finding corroborates the failure observed in the field for the above slope section at the end of 87 days of rainfall, as reported by Oh and Lu (2015). On the other hand,

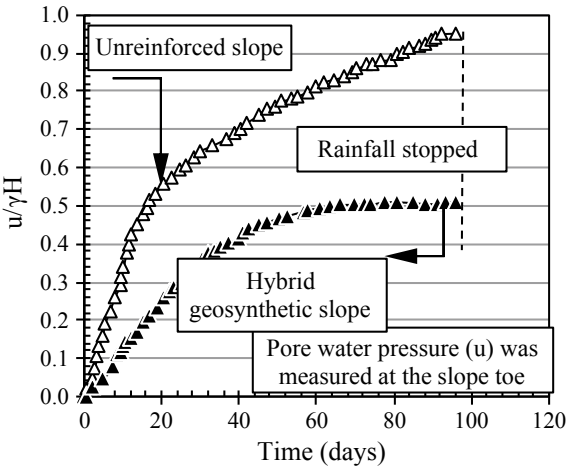

Fig. 10 Normalized pore pressure variation with time

the hybrid geosynthetic-reinforced slope was stable for the entire duration of rainfall as presented in Fig. 11b, and the FOS at the penultimate stage was 2.293.

6 Conclusions

In the present study, the response of a typical mountainous slope subjected to rainfall was analysed numerically, and the effect of inclusion of hybrid geosynthetic layers within the slope section was further investigated. The hybrid geosynthetics are proposed to be installed from the bottom to the top, following the sequence of slope construction during slope reprofiling undertaken as a part of road widening projects in hilly areas. Based on the analysis and interpretation of results, the following conclusions can be drawn:

(1) The seepage analysis results indicated that the unreinforced slope experienced rapid loss of matric suction in the unsaturated zone above the ground water table from an initial value of −200 kPa to about −60 kPa, resulting in a gradual build-up of excess positive pore water pressure within the slope. On the contrary, the hybrid geosynthetic-reinforced slope was capable of dissipating the excess pore water pressure generated during rainfall, resulting in depleted phreatic surface levels and retaining considerable soil matric suction within the slope for the entire duration of rainfall. As a consequence, the positive pore water pressures were reduced by about 48% in the hybrid geosynthetic-reinforced slopes as compared to the unreinforced slope.

(2) The stability analysis results indicated that the FOS of the unreinforced slope started dropping with the progress of rainfall due to the loss of soil matric suction, resulting in a safety factor lying below the critical limit of 1.0. A global

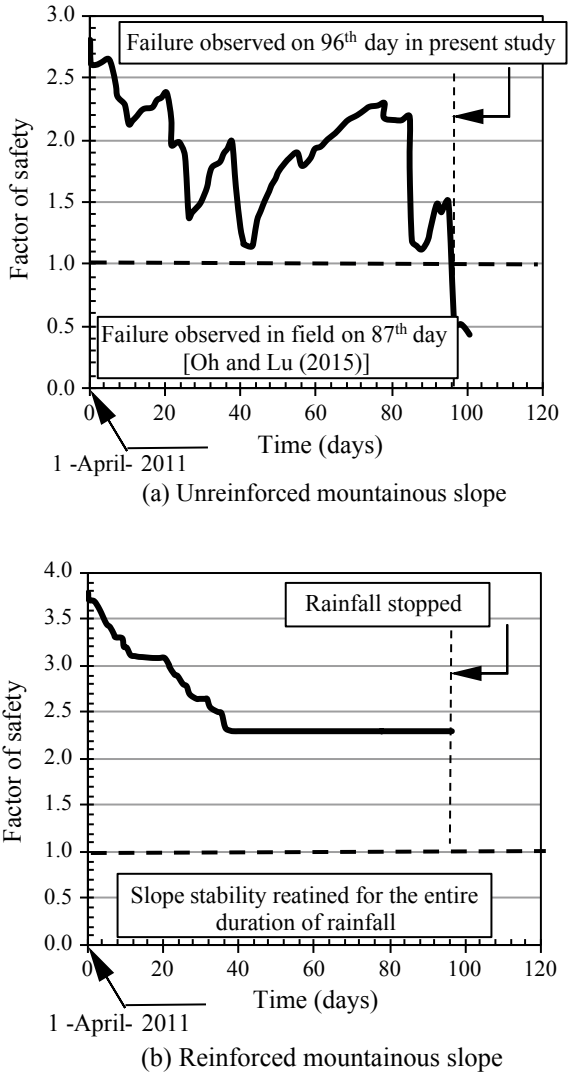

Fig. 11 Variation of slope FOS with rainfall

failure surface passing through the toe was observed in this case, thereby indicating that rainfall-induced slope instability may not be necessarily attributed solely to increasing ground water levels. The time corresponding to failure observed numerically was found to corroborate well with that observed in the field, thereby validating the numerical model and reconstructing the failure event encountered in the field. The next stage of analysis conducted on the hybrid geosynthetic-reinforced slope indicated higher FOS values during rainfall due to the reinforcement action of the geocomposites, which prevented the

loss of soil shear strength and associated softening, thereby averting possible slope instability.

(3) The findings derived from the present study indicate that the inclusion of hybrid geosynthetics ensured the stability of reprofiled slope sections located in mountainous regions under heavy rainfall. As a consequence, road widening projects can be successfully undertaken at the base of existing hilly slopes, and the additional road space gained can be utilized for construction of roadways and two-lane highways. However, further studies are warranted in this regard on various slope profiles subjected to a wide range of rainfall events to ensure economization of project costs.

References

ASTM D 4595 (2005) Standard test method for tensile properties of geotextile by the wide-width strip method, annual book of ASTM standards, Section 4, vol 04.1. Geosynthetics, American Society for Testing and Materials, West Conshohocken, Pennsylvania, U.S.A

ASTM D 5321 (2002) Standard test method for determining the shear strength of soil-geosynthetic and geosynthetic-geosynthetic interfaces by Direct Shear, American Society for Testing and Materials, West Conshohocken, Pennsylvania, USA

ASTM D 6574 (2006) Standard test method for determining the (in-plane) hydraulic transmissivity of a geosynthetic by radial flow, American Society for Testing and Materials, West Conshohocken, Pennsylvania, U.S.A

Bhattacherjee D, Viswanadham BVS (2015) Numerical studies on the performance of hybrid-geosynthetic-reinforced soil slopes subjected to rainfall. Geosynthetics Int 22(6):411–427

Dahal RK, Hasegawa S (2008) Representative rainfall thresholds for landslides the Nepal Himalaya. Geomorphology 100(3–4):429–443

Fredlund DG, Morgenstern NR, Widger A (1978) Shear strength of unsaturated soils. Can Geotech J 15(3):313–321

Geostudio (2012) SLOPE/W and SEEP/W, Ver. 7.15, User's Guide, Geo-Slope International Ltd, Calgary, Canada

Oh S, Lu N (2015) Slope stability analysis under unsaturated conditions: case studies of rainfall-induced failure of cut slopes. Eng Geol 184:96–103

Van Genuchten MTh (1980) A closed-form equation for predicting the hydraulic conductivity of unsaturated soils. Soil Sci Soc Am J 44(5):892–898

Viswanadham BVS, Bhattacherjee D (2016) Studies on the performance of geocomposite reinforced low-permeable slopes subjected to rainfall. Jpn Geotech Soc 2(69):2362–2367